RAL-85-047

Science and Engineering Research Council
Rutherford Appleton Laboratory
CHILTON, DIDCOT, OXON, OX11 0QX

Science and Engineering Research Council Central Laser Facility

Annual Report to the Laser Facility Committee 1985

Laser Division
Rutherford Appleton Laboratory

RAL-85-047

SCIENCE AND ENGINEERING RESEARCH COUNCIL

CENTRAL LASER FACILITY

ANNUAL REPORT TO THE LASER FACILITY COMMITTEE

PREFACE

The report describes research and facility development work carried out at or in association with the Central Laser Facility (CLF) during the year ended 31 March 1985.

The primary purpose of the CLF is to give UK University research workers access to advanced laser facilities for academic research. Funding by the Science Board of SERC, organisation and procedures for approval of scientific work are outlined in the Introduction to Part I of the report.

In Part I Sections A, B and C respectively cover the multi-disciplinary scientific programmes of the high power neodymium glass laser (VULCAN), the smaller frequency tunable lasers of the Ultra-Violet Radiation Facility (UVRF) and the developmental high power krypton fluoride laser (SPRITE). Part I is a compilation of contributions from University staff describing the results of their research, and from CLF staff, describing development of the facilities, and it includes related theoretical work. It is not a catalogue of scheduled work: the criterion for inclusion of material is that it should contain scientifically or technically useful information.

Part II describes a new in-house R&D programme aimed at industrial applications of lasers in microcircuit fabrication. This work is separately funded by the Engineering Board of SERC and the Department of Trade and Industry, and is a spin-off from the work of the UVRF. Some of the more significant achievements of this programme are not reported in detail because they are the subject of patent applications and confidential discussion on industrial exploitation.

All other aspects of the work of the Central Laser Facility are published in the open literature as shown in the Publications Section at the end of the report.

The year's work has been characterised by intensive operation of the facilities leading to some notable scientific successes. Development of new facets in the programme has increased the number of facility users and the scientific scope of their research. International collaboration with our counterpart laboratories overseas, (particularly ILE Osaka in Japan, PN Lebedev Institute Moscow in the USSR, Ecole Polytechnique Palaiseau in France, MPIQ Garching in West Germany, and the Lawrence Livermore Los Alamos and Brookhaven Laboratories in the USA) has been of great value.

In the glass laser scientific programme a notable feature has been the growth of interest in non plasma physics applications of intense single pulse X-ray emission, with the most dramatic example being the first demonstration of in vivo soft X-ray microscopy of biological cells. The commissioning in mid year of a sophisticated new facility for 12-beam irradiation of spherical targets, at λ = 0.53 and 1.05μm led to important new compression and energy transport studies and theoretical work on energy transport has also been strong. Vigorous efforts have gone into the (delayed) construction of new facilities for X-ray laser research and X-ray source production and a novel aberration-free line focus system of great promise for X-ray laser target irradiation has undergone successful one-beam tests and will be included in the final six-beam system.

The UVRF has sustained a broad range of experiments in physics, chemistry and biology. A particularly successful line has been the use of time-resolved UV resonance Raman spectroscopy to study excited states and reaction intermediates, with a notable first in the detection of vibrational frequencies of an enzyme substrate intermediate, acyl papain. There was also important action off stage with a decision to provide more funds to add a laser loan pool service and a picosecond laser system to the existig UVRF, the whole to be renamed the Laser Support Facility (LSF) and to start operations in May 1985.

The high power KrF laser, SPRITE, reached a major milestone becoming the world's first such laser to be used for irradiation of targets.

Strong X-ray production of great promise for a variety of scientific applications was demonstrated for the first time. Important progress was also made towards the next goal of optical and Raman multiplexing to shorten the pulse duration and increase the power of the laser, which has attracted strong international collaboration particularly from Japan.

Technically important developments leading to patent applications were made in the new "lasers for microcircuit fabrication" project as well as very topical scientific progress in the area of phase conjugate imaging.

The overall position is encouraging with many new scientific opportunities to exploit and novel facilities just completed or shortly to be completed. Morale and progress have recovered considerably from the cuts and threats of 1983/84, not least because of approval of accelerated funding for the capital programme in 1985/86.

M H Key

CONTENTS

PART I

INTRODUCTION

P T Rumsby (RAL)

The Central Laser Facility (CLF) is funded by the Science Board of the Science and Engineering Research Council and in the year covered by this report, April 1984 to April 1985, its allocation was £2.475M

The Science Board has provided the facility for research whose major themes are:

A	High Density Plasma Physics
B	High Intensity Laser Plasma Interactions
C	Energy Transport in Laser Produced Plasmas
D	Laser Driven Implosions
E	X-ray Lasers
F	Other Applications of Laser Produced Plasmas (eg as X-ray sources)
G	High Power UV Gas Laser Development
H	Applications of Short Pulse Frequency Tunable Lasers
I	Ultra Violet Lithography

The programme is managed by the Laser Facility Committee (LFC) whose membership is given in Table 1. The LFC delegates responsibility to the Rutherford Appleton Laboratory for the operation of the Facility.

The Laser Division of RAL was allocated 52 man years of effort, 50 of which as deployed in the organisational structure shown in Table 2 and a further 2 man years used as support in other RAL Divisions. Staff costs and overheads used 43% of the allocation while facility operations and minor development costs used 40%. 17% of the total allocation was spent on the Phase 1 programme of capital facility development (discussed in more detail in Sections A6 and C). The major facilities provided by the CLF and a brief indication of their principal scientific applications is given in Table 3.

The Nd glass laser VULCAN is the major facility and about 63% of resources was used to support its programme of research by UK Universities described in Section A.

Multidisciplinary scientific applications of excimer lasers and excimer pumped dye lasers by UK Universities has been catered for by the rapidly developing Ultra Violet Radiation Facility (using 13% of resources) (Section B). It should be noted that the CLF is to operate a new laser loan pool (LLP) scheme from 1 April 1985. This will be operated alongside the UVRF and the joint operation has been named the Laser Support Facility (LSF).

Development of a high power UV gas lasers is an in house project which now provides X-ray source facilities for University users. About 13% of resources are committed to this work (Section C).

A target preparation service (7%) and a small group giving theoretical support by maintaining computer codes (4%) support all CLF activies.

Use of the CLF by UK Universities is free of charge to those successful in a peer review process. Research grants of typically three years duration covering expenditure in University Laboratories and research assistants' salaries may be obtained from the LFC by application to SERC. LFC Grant holders are entitled to bid for time on the CLF's lasers through a procedure described below.

A few per cent of the time may also be allocated to bids for short trial experiments from University researchers working in the Science Board area who do not hold LFC grants.

The SERC encourages use of the CLF by industry or other organisations on the basis of payment for the full cost of laser time. Such use is limited to not more than 10% of available laser time.

International collaboration in the research programme is particularly welcomed, either through collaborative participation in approved experiments of UK University groups or through agreements negotiated with the CLF and SERC.

Selection and scheduling of University experiments using the VULCAN glass laser and SPRITE UV laser is via proposals to one of six informal specialist scientific groups which anyone may join. Each has a

University Chairman and an RAL secretary (Table 4). Each group places its proposals in order of priority prior to the preparation of a draft schedule (by the programme coordinator and group secretaries). The draft schedule, which includes as many of the high priority proposals as possible (typically <50% of proposals), is then discussed and modified at a meeting of the more formal High Power Laser Scientific Programme and Scheduling Committee (HPLSPSC). All University staff members involved in the programme have voting rights, together with the group secretaries and programme coordinator. The Committee is chaired by the Division Head of Laser Division and is formally advisory to him.

During the year the Chemistry, Biology and Physics Committees of the Science Board decided to commit funds to set up a laser loan pool scheme to be operated by the staff of the CLF. This scheme will operate in parallel with the UVRF and the joint operation is to be called the laser support facility (LSF). This unit came into operation on 1.4.85. The LFC has delegated LSF Management duties to a panel whose membership is given in Table 5. Selection of experiments requiring loan pool lasers or use of the lasers based at the CLF is carried out by this panel and scheduling is performed by an ad hoc committee of users chaired by the Laser Division Head.

Scheduled experiments are supported by the operating budget of the CLF which covers travel and subsistence costs for University users and minor engineering work and other costs of experiments.

The experimental programme is linked to theoretical work in Universities which is supported by grants from the LFC and coordinated by the Theory and Computation group (Section A5).

There is a large and diverse community of University researchers participating in the programme. They number about 130 staff and research students. The majority are physicists but there has been a rapid growth of participation from chemists and most recently biologists.

TABLE 1

Membership of the Laser Facility Committee 1984/85

Professor G J Pert (Chairman)
Dept. of Applied Physics
University of Hull.

Dr J E Allen
Department of Engineering Science
University of Oxford

Dr E H Evans
Department of Biology
Preston Polytechnic

Dr T A Hall
Department of Physics
University of Essex

Dr H Hutchinson
Imperial College of
Science and Technology
London

Professor E W Laing
Department of Natural Philosophy
University of Glasgow

Dr C L S Lewis
Department of Pure &
Applied Physics
The Queen's University of
Belfast

Dr A Maitland
Physics Department
St Andrew's University

Prof. D. Phillips
Dept. of Chemistry
Royal Institution

Professor J P Simons
Department of Chemistry
University of Nottingham

Dr I J Spalding
Culham Laboratory
UKAEA

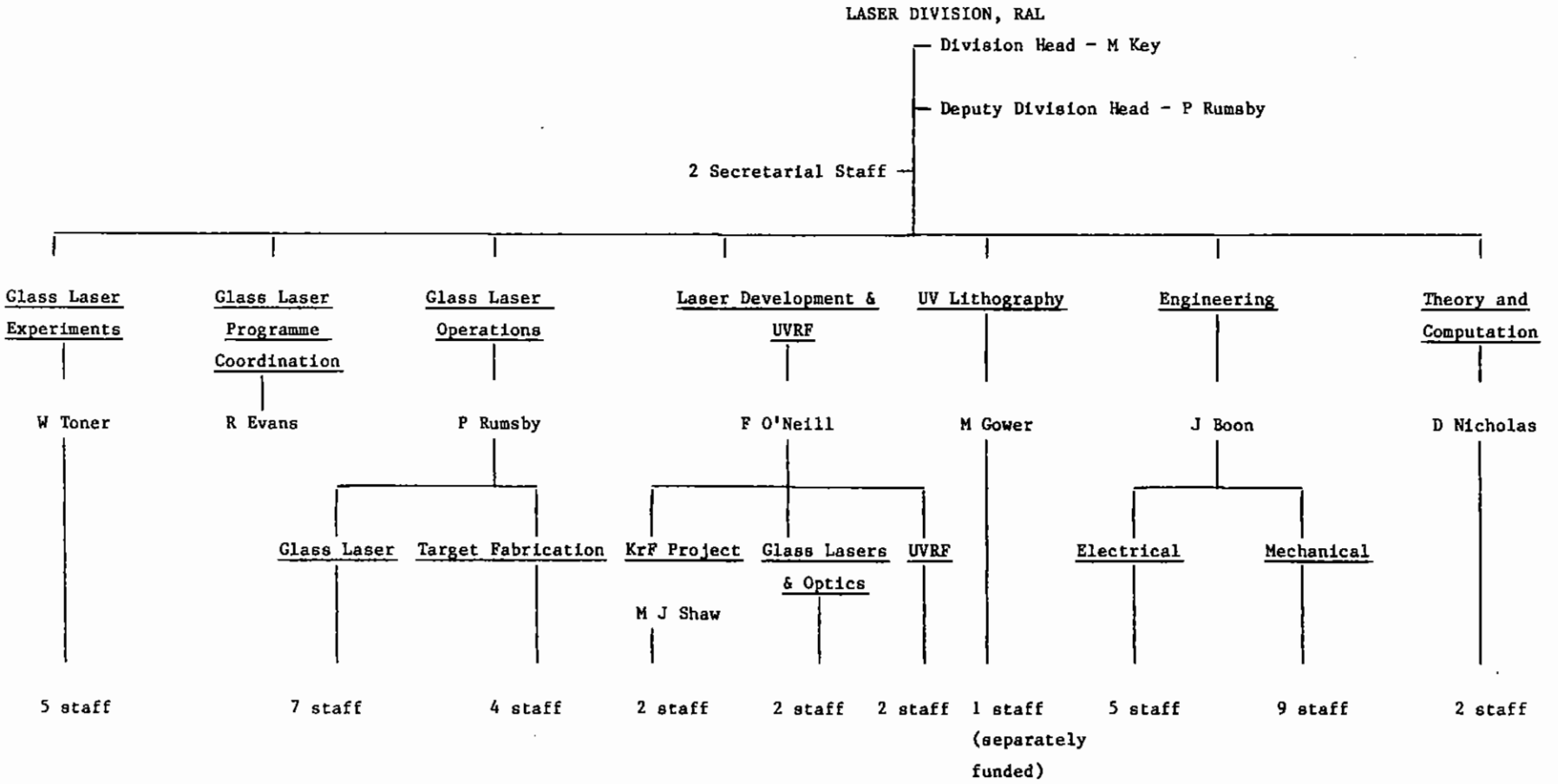
LASER DIVISION, RAL
Division Head - M Key
Deputy Division Head - P Rumsby
2 Secretarial Staff
Glass Laser Experiments
Glass Laser Programme Coordination
Glass Laser Operations
Laser Development & UVRF
UV Lithography
Engineering
Theory and Computation
W Toner
R Evans
P Rumsby
F O'Neill
M Gower
J Boon
D Nicholas
Glass Laser
Target Fabrication
KrF Project
Glass Lasers & Optics
UVRF
Electrical
Mechanical
M J Shaw
5 staff
7 staff
4 staff
2 staff
2 staff
2 staff
1 staff (separately funded)
5 staff
9 staff
2 staff

TABLE 2

TABLE 3 Major Facilities at the CLF

Nd glass Laser facility	Ultra - violet radiation facility	High power KrF laser facility
VULCAN	UVRF	SPRITE
Plasma Physics Applications of intense X-ray and particle sources X-ray laser Research	Photo chemistry Photo biology Materials processing Non linear optics Plasma diagnostics Tunable VUV source	Facility utilizing the high X-ray brightness of UV laser produced plasmas High power UV laser research.
Target Preparation Service		
Theoretical support service		

Table 4

Groups of the HPLSPSC	Chairman	Secretary
Laser plasma Interaction and Energy transport	Dr A E Dangor	Dr D Nicholas
Laser plasma Compression and Dynamics	Dr T A Hall	Dr A J Cole
Dense plasma and radiation physics	Dr C L S Lewis (acting for Prof.D D Burgess)	Dr S J Rose
XUV lasers and applications of laser produced plasmas	Dr C L S Lewis	Dr O Willi
Theory and Computation	Dr R A Cairns	Dr A R Bell
Glass Laser Facility Operations and Development	Dr P T Rumsby	Mr J E Boon
Scientific programme coordinator	R G Evans	

TABLE 5

Laser Support Facility Panel

Professor J P Simons - Chairman of LSFP
Nottingham University

Professor R E Hester for Chemistry Committee
York University

Dr P B Davies for Chemistry Committee
Cambridge University

Dr C W Wharton for Biological Sciences Committee
Birmingham University

Dr C Webb for Physics Committee
Oxford University

Dr H Evans for Laser Facility Committee
Preston Polytechnic

SECTION A GLASS LASER SCIENTIFIC PROGRAMME

A GLASS LASER SCIENTIFIC PROGRAMME

R G Evans (RAL)

INTRODUCTION

This section of the Annual Report describes results obtained in the research programme of the VULCAN Nd glass laser. During the period of this report 24 experiments were scheduled out of 45 bids. The single most notable facility enhancement was the provision of the twelve beam target area for symmetrical illumination of spherical targets. The twelve beam system has provided its first X-radiographic implosion results and has demonstrated its versatility by being used for high density plasma experiments using planar foil targets.

A major part of the research programme has been the use of laser produced plasmas as X-ray sources, providing an instantaneous brightness which is much greater than synchrotron sources and the opportunity to study phenomena on a nanosecond time scale. A particularly notable result has been the production of X-ray microscopic images of biological samples in vivo with exposure times of 1ns and a resolution of 300Å. This is a major development since the biological samples are usually destroyed by the X-ray dose required for microscopy but in 10^{-9}s they do not have time to change their structure. Work has continued on the examination of solid structure using EXAFS and REFLEXAFS, again utilising the short exposure time made possible using laser produced plasmas.

There is considerable topical interest in X-ray laser research with the hope of a coherent soft X-ray source in the near future. A major breakthrough at the CLF has been the invention of diffraction limited line focus optics using an off-axis spherical mirror. This reduces the laser power required per unit length and conversely enables longer targets to be irradiated with a given laser.

A significant new part of the plasma physics programme has been the

production in the laboratory of an unmagnetised collisionless shock by obstructing part of the ablation flow from a laser irradiated target. This is of great astrophysical interest, complementing observations of magnetised collisionless shocks such as the earth's bow shock.

Theory and facility development work have started in preparation for an investigation of the "beat wave" produced by two laser frequencies in an under dense plasma. This is exciting both from the production of relativistic plasma oscillations and the likely application to high energy particle accelerators. For the first time two different laser rods have been operated in the same mode-locked cavity, giving synchronous pulses at 1.053μm and 1.064μm, each of less than 200ps duration.

A1 LASER PLASMA INTERACTION AND ENERGY TRANSPORT

Editor D J Nicholas

A1 LASER PLASMA INTERACTION AND ENERGY TRANSPORT

A1.1 INTRODUCTION

A E Dangor (Imperial College) and D J Nicholas (RAL)

The problem of thermal transport in laser plasms with large temperature gradients continues to be of major importance. Studies have been made of various aspects of the problem by a number of groups with a variety of approaches being adopted from the Z-pinch plasmas to dot spectroscopy. Laser plasma interactions are represented by further analysis of Raman scattering in long scale length plasmas and new data is described on the energy loss of charged particles in high temperature plasmas.

A1.2 MEASUREMENT OF THE HEAT FLUX AND ION ACOUSTIC TURBULENCE IN PRE-FORMED PLASMA

A E Dangor, A K L Dymoke-Bradshaw (Imperial College), D A Pepler and W T Toner (RAL)

The objectives of this experiment were to measure heat flow in a plasma in the presence of a large temperature gradient, to investigate the spectrum of ion acoustic waves and to determine if their level is above thermal.

The principal of the experiment is to produce a high temperature gradient in a uniform plasma by focusing ~ 100 Joules of 1.053 micron light in a 1.5ns pulse at the centre of a z-pinch hydrogen plasma of density ~ 10^{17} cm^{-3}. Temperature rises in the plasma of the order of 20eV (initial 10eV final 30eV) were achieved. This rise, and its spatial distribution and time evolution, was then measured using Thomson scattering with a 0.52 micron probe beam. The scattered light was spectrally resolved and then recorded with a streak camera.

In a previous experiment (A1.1) we obtained a measure of the heat flow, but the results suffered greatly from a lack of knowledge of the background plasma conditions due to irreproducibility in the plasma source and a poorer signal to noise ratio than would have been desired. In the current experiment both these drawbacks have been successfully overcome producing data of exceptionally high quality.

The changes implemented for this experiment were as follows:

1. Heating and probe beam in coaxial alignment. This enables the scattering and hence the scattered light level to be made ten times larger. See Figs A1.1 and A1.2.
2. Probe beam used for scattering changed from a 1.5ns pulse to four 100ps pulses separated by 1ns, hence covering a 3ns period in the plasma parameter evolution. See Fig A1.3 and A1.4.
3. Improved efficiency of the collecting optics. Another factor of about ten was achieved here.
4. In order to investigate the ion-acoustic spectrum a completely separate diagnostic channel was set up capable of looking at light scattered at three different angles (not simultaneously), see Fig A1.5.
5. An attempt was made to measure stimulated Brillouin back scatter using a spectrometer and SI streak camera.

Whilst a full analysis of the results is still in progres it is expected that the following will be obtainable.

1. Measurement of the heating and cooling of the plasma.
2. Measurement of T_e and n_e as a function of space and time; this will give the temperature scale length, electron mean free path and heat flux.
3. The results from (2) will enable us to predict the thermal level and spectral shape of ion acoustic scattering at the various angles at which measurements were taken. This can then be compared with the observed scattering giving an indication of the non-thermal level of ion acoustic waves excited as a function of position and direction.

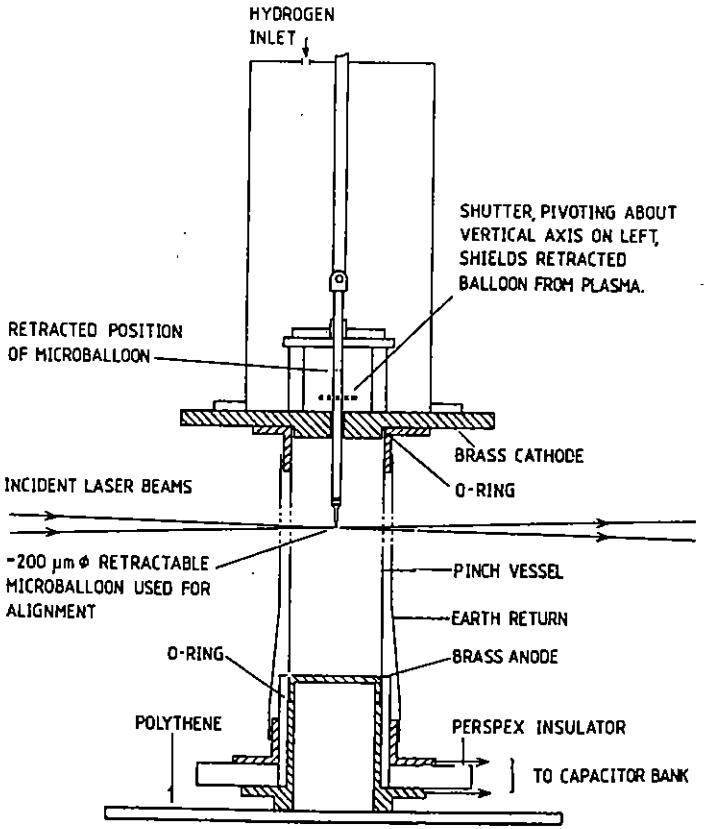

Fig A1.1 Z-pinch plasma assembly and paths of 1.06μm heating and 0.5μm diagnostic beam used for Thomson scattering. Also shown is the retractable microballoon used for alignment of laser beams within plasma.

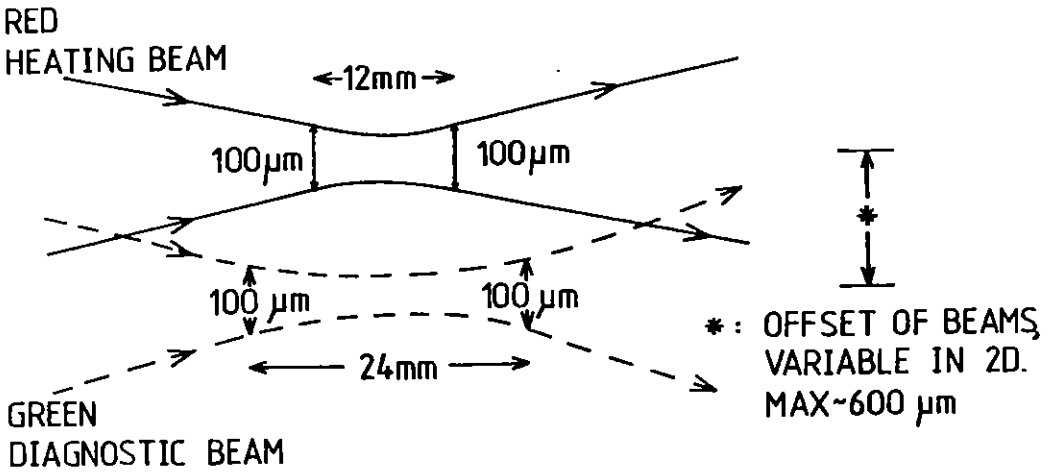

Fig A1.2 1.06μm heating beam and 0.53μm diagnostic beam.

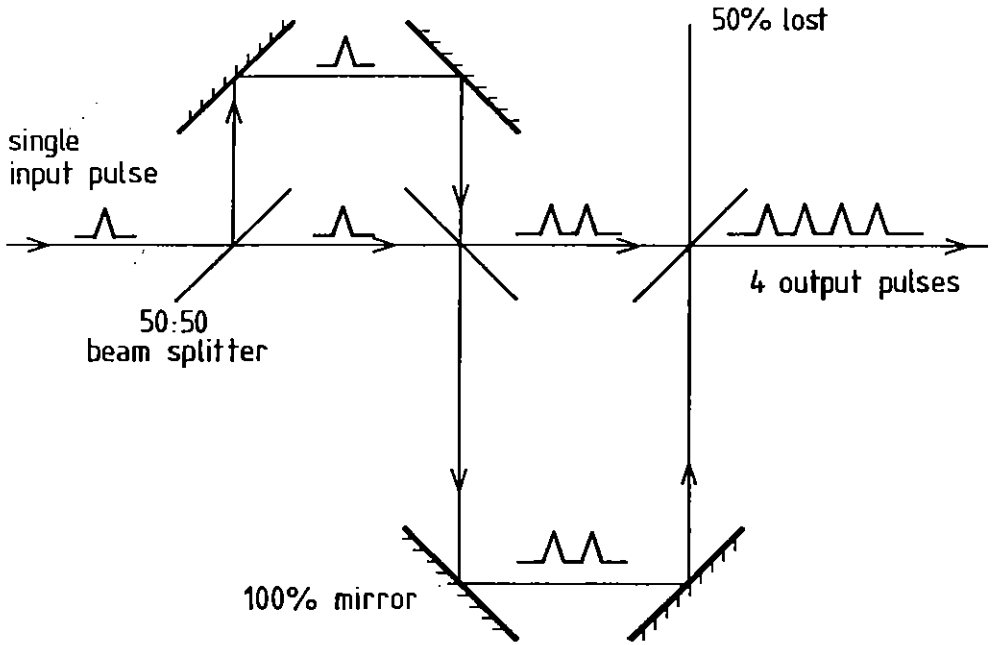

Fig A1.3 Pulse stacker producing four 100ps diagnostic pulses.

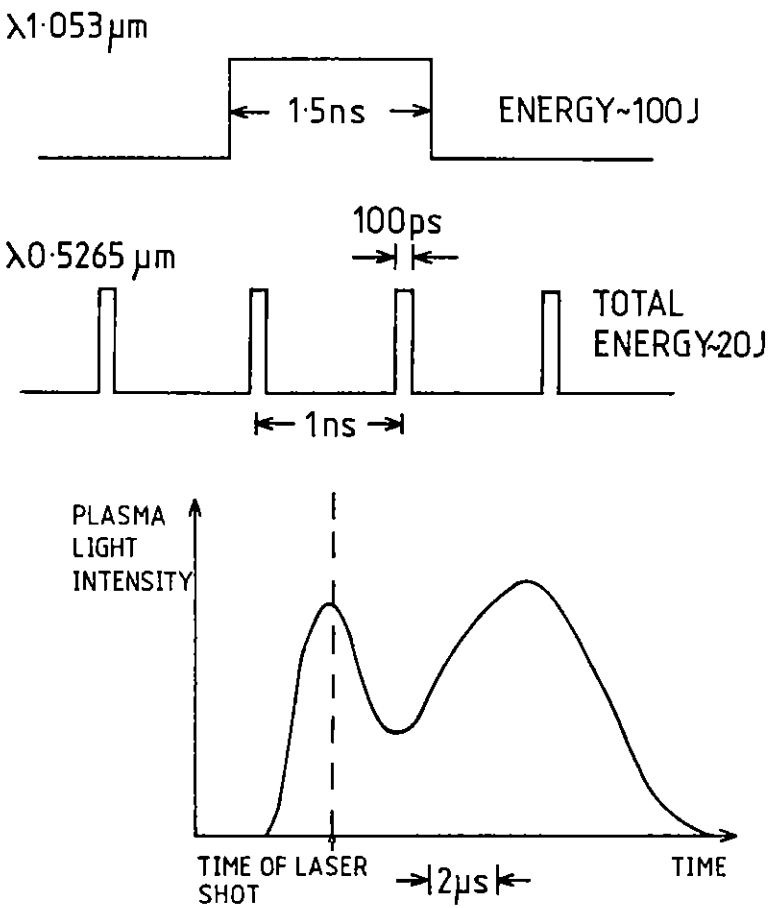

Fig A1.4 Relative timing of heating beams, diagnostic beam and z-pinch plasma.

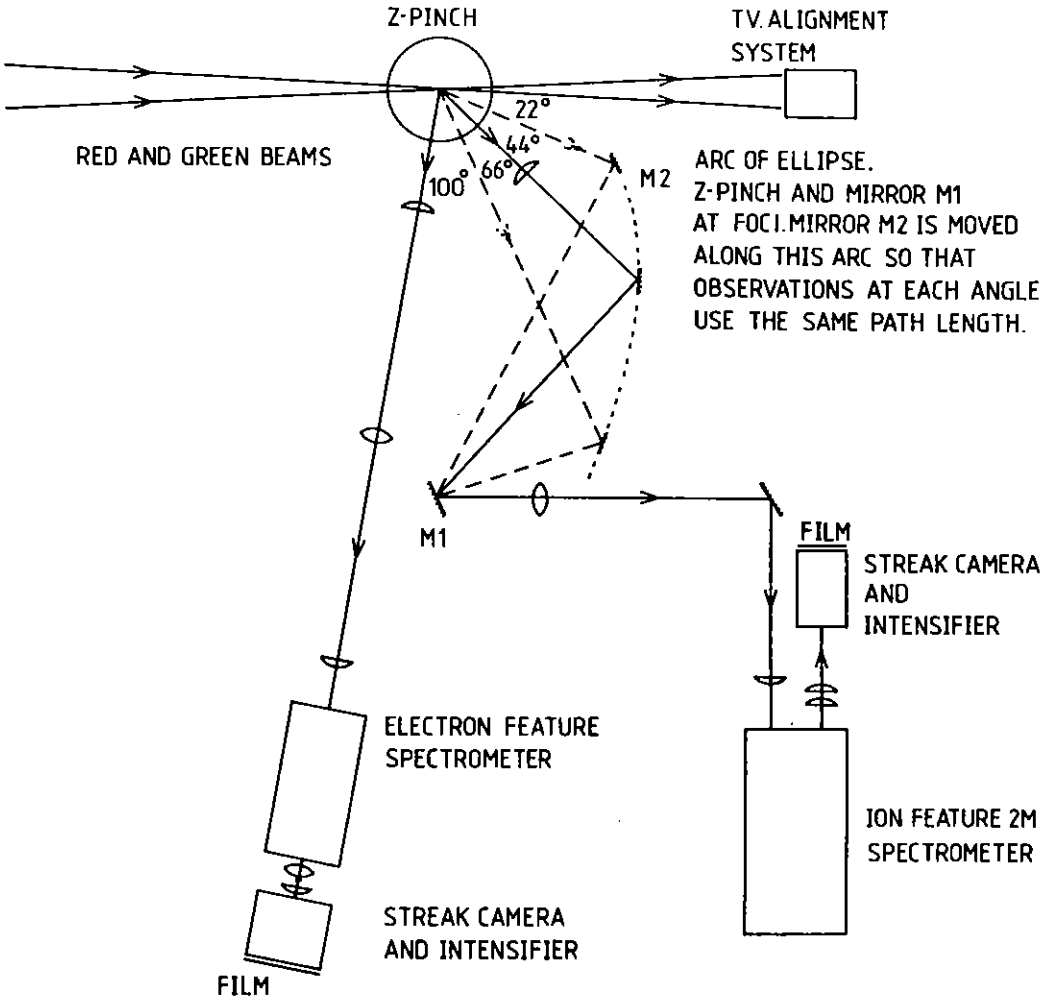

Fig A1.5 Layout of plasma, heating and diagnostic beams and the two Thomson scattering channels monitoring the electron feature at 100° and the ion feature at 22°, 44° or 66°.

In Fig A1.6 some typical results of Thomson scattering are shown. Of the four pulses recorded the earliest gives the initial palsma conditions and the subsequent three show how conditions change in time during and after the heating pulse. The fit of the data of this first pulse to the conventional theory is excellent, demonstrating a thermal plasma and a good signal to noise ratio in the detector. In the subsequent three pulses the fit is not as good. However the signal to noise level should be of a similar level. A degradation of the fit in this manner has been observed by others (A1.2) and linked to the presence of turbulence.

In Fig A1.7 some results of scattering from ion acoustic waves is shown. Again the first pulse gives the initial conditions. It can be seen that the two peaks move apart in time in agreement with the change in the ion acoustic sound speed with increasing temperature. The change in magnitude of the signal has to be corrected for the variation in pulse height of the probe pulses. As this was not monitored directly this information will have to be extracted from the Thomson scattering data which contains the information although it is convolved with collective scattering effects. Once the ion feature results can be normalised the degree of non-thermal scattering can be determined.

The measurements of Brillouin back scattering were hampered by technical difficulties and lack of time. A back scattered signal was eventually detected but with insufficient spectral resolution to be informative.

It is hoped to pursue this experiment further into two main areas. Firstly the apparatus and techniques will be used for the "Beat Wave" project discussed elsewhere in this report (see Sections A5.2.4 and A5.2.5), and secondly we hope to measure the ion and electron waves produced by Brillouin and Raman back scatter directly. This will involve matching the k's of the back scatter waves to the scattering k vector.

Shot "BØ64E
Scattering angle = 100°
Zero displacement between heated and diagnosed volumes

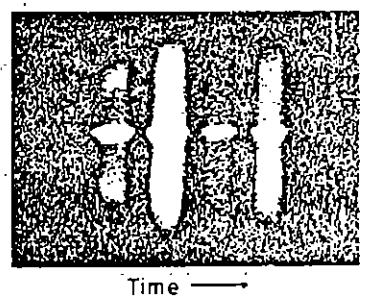

Pulse 1 : T_e ~ 13eV; n_e ~ $3{\cdot}7.10^{17}$ cm^{-3}; α~1·3
Pulse 2 : T_e ~ 29eV; n_e ~ $2{\cdot}7.10^{17}$ cm^{-3}; α~0·7
Pulse 3 : T_e ~ 31eV; n_e ~ $2{\cdot}3.10^{17}$ cm^{-3}; α~0·6
Pulse 4 : T_e ~ 25eV; n_e ~ $2{\cdot}6.10^{17}$ cm^{-3}; α~0·7

COMPARISON OF THEORETICAL AND EXPERIMENTAL DATA

FOR FIRST PULSE OF SHOT BO64E

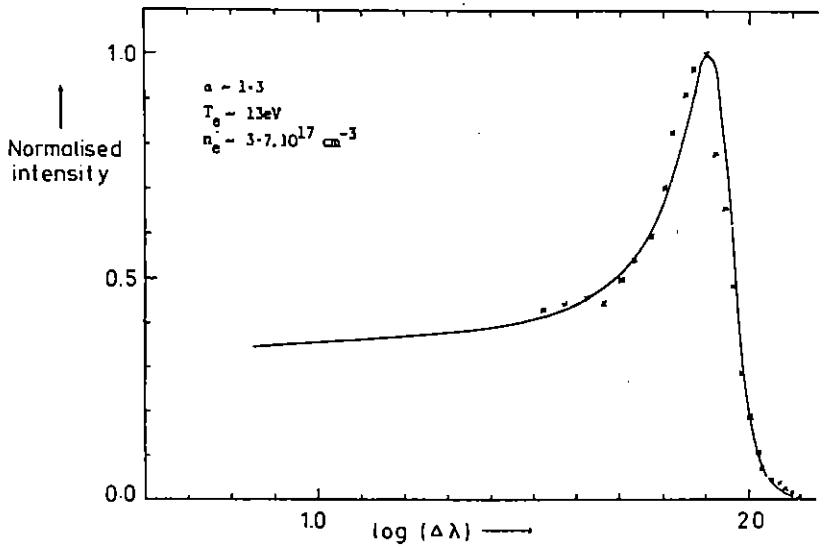

Fig A1.6 Typical electron feature scattering record.

Shot BØ43I
Scattering angle = 22°
Heated volume displaced 400μm
from diagnosed volume

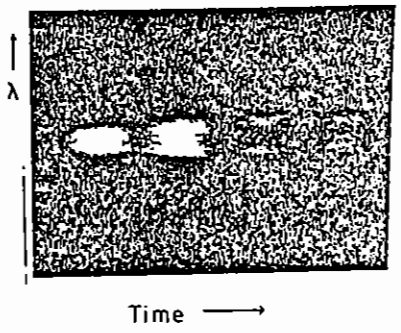

MICRODENSITOMETER TRACES FOR SHOT BO43I

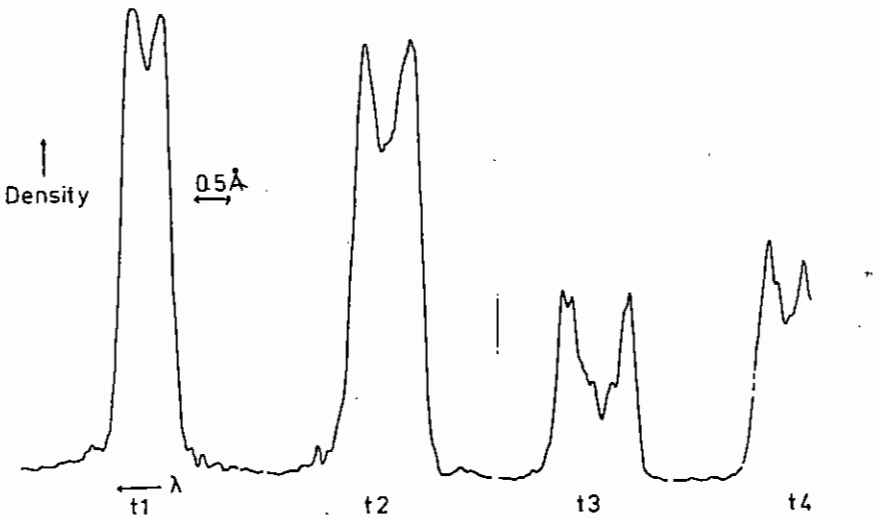

Fig A1.7 Typical ion feature scattering record.

A1.3 MEASUREMENT AND ANALYSIS OF NEAR-CLASSICAL THERMAL TRANSPORT IN ONE-MICRON LASER-IRRADIATED SPHERICAL PLASMAS

A Hauer, W C Mead and O Willi (Los Alamos National Laboratory, USA)
J D Kilkenny, D K Bradley and S D Tabatabaei (Imperial College)
C Hooker (RAL)

In the present experiment we have used a comprehensive set of diagnostics to characterize the plasma conditions and thermal transport in a spherically symmetric plasma. We have made time-resolved spectroscopic measurements (using both low-and moderate-Z radiating ions) of the penetration of the heat front in spherical plasmas. In addition, we have used optical probing to measure simultaneously the density profile of, and the magnetic field in, the underdense plasma. Comparisons with hydrodynamic modeling show that (a) all observables are consistent with a high flux limit and (b) the heat front shows no observable foot.

The targets used in this study consisted of solid glass spheres (~160μm diameter), containing Si and Ca (among other constituents), coated with three layers: (1) CH (0.5 to 2.5μm thick), (2) Al (0.1 μm), and (3) CH (0.5 to 2.5μm). The solid glass ball prevented implosion of the target (and subsequent inward movement of the critical surface).

The targets were uniformly illuminated with the six-beam, 1.06μm, laser facility at the Rutherford Appleton Laboratory. The six beams were focused by f/1 lenses with optical axes along the faces of a cube. Incident irradiance levels were in the range $(1.5\text{-}15)\times10^{14}$ W/cm^2. The laser pulse had an approximately Gaussian temporal profile with 0.83-ns full width at half maximum (FWHM).

The radial intensity profiles of the beams were measured. Small-scale structure results in about 30% rms variation in intensity. The overlap of the six beams and beam-to-beam energy variation resulted in about 50% (peak-to-valley) large-scale variation in incident irradiance across the surface of the sphere.

The primary diagnostic of thermal transport was time-resolved X-ray line spectroscopy. X-ray line emission was observed first from the thin aluminum layer (sensing temperatures of 200-350eV) and later from the silicon (~250-400eV)and calcium (~500-700eV) in the glass ball.

X-ray emission from the target was dispersed (with a thallium acid phthalate crystal) onto the slit of a streak camera covering 1.7 to 2.4 keV. The spectral and temporal resolutions were about 500 ($\lambda/\Delta\lambda$) and 50 ps, respectively. A seventh laser beam with very short duration (~100 ps) was used to generate an X-ray fiducial which references the X-ray spectra to the temporal profile of the laser. The density profile of the underdense plasma ($n_e<n_c$) was measured with a 40-ps, 0.35-μm interferometric probe and the magnetic field was measured with a 20-ps, 0.62-μm Faraday rotation probe (probing densities up to $0.6n_c$).

We adjusted laser focusing to achieve good illumination uniformity while minimizing refraction. Spherical symmetry of the plasma was diagnosed with a Faraday rotation probe (sensing large-scale magnetic fields due to nonuniformity), multi-energy-band X-ray pinhole imaging (as an indicator of plasma heating), and the interferometric probe (indicating uniformity of blowoff). It was found that, for tangential illumination, symmetric uniform X-ray photographs (to within 10%) were obtained with negligible (large scale) magnetic field generation (<100kG in the underdense plasma). Examples of three diagnostics demonstrating the degree of plasma uniformity are given in Fig A1.8 Thermal smoothing (A1.3) of laser irradiance nonuniformities plays an important role in determining the good symmetry seen in Fig A1.8.

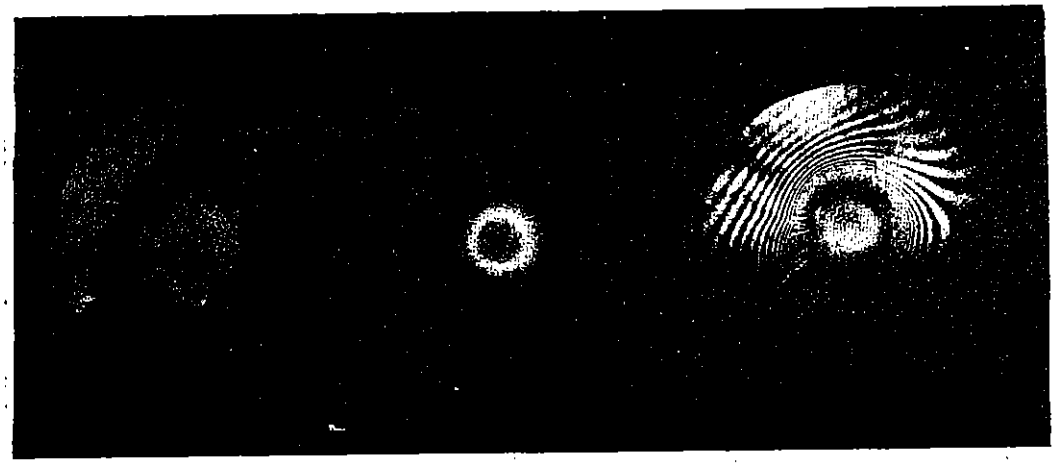

Fig A1.8 Three diagnostics of plasma symmetry characteristics. (a) Faraday rotation probe implies B < 100kG, (b) X-ray pinhold photograph (∿1keV) indicates uniform heating, (c) interferogram indicates blowoff uniformity to ∿ 10-15%.

For uniform illumination, the absorbed fraction measured in these experiments (with ion calorimetry) ranged from 32% to 23% over the incident irradiance range of (1.5 to 15)x10^{14} W/cm^2. For incident irradiance of about 5x10^{14}W/cm^2, the hot-electron temperature, as measured from the X-ray continuum slope (with a seven-channel diode array) was about 3-6keV. Inner-shell (Kα) radiation was observed from solid vanadium targets (of the same diameter as the multilayer targets) coated with various layers of plastic. Faraday-cup ion detection showed immeasurably small energy in fast ions. All these data are consistent with less than 3% of incident laser energy present in hot electrons.

Throughout this work, we have used LASNEX (A1.4) Lagrangian hydrodynamic simulations to predict and analyze the experimental results. The modelling included non-local-thermodynamic-equilibrium atomic physics, multigroup flux-limited radiation diffusion, and multigroup flux-limited diffusion for the suprathermal (and all

laser-heated) electrons, consistent with earlier work (A1.5). Electron thermal transport is modeled by single-group flux-limited diffusion. We used resonance-absorption deposition fractions of 0-10% to explore the sensitivity of the results to hot electrons. Inverse bremsstrahlung was cut off above $0.6n_c$ to account roughly for refraction. With this correction, the calculated absorption agreed well with that measured. The mass ablation rate for a given absorbed intensity was not significantly affected by this correction.

An example of a portion of a time-resolved X-ray line spectrum and a corresponding LASNEX calculation (modeling this specific shot) is given in Fig A1.9. A flux limit of 0.1 was used in this calculation. We are primarily concerned here with the initial penetration of the heat front. The calculations were made for a thin layer near the surfaces of the aluminum and silicon. This predicts the rise of the radiation accurately, but not the full time history. Both theory and experiment show a very rapid rise (<100ps) for the onset of aluminum and silicon emission.

Mass ablation rates can be obtained from the time-resolved spectra by taking the delay between aluminum and silicon emission as the time needed to ablate the plastic layer between them. In Fig A1.10, we plot the specific mass ablation rate versus absorbed irradiance (referenced to the initial surface area). The experimental points on this graph were chosen so that the burnthrough interval occurred within $\pm$ 400ps of the peak of the pulse.

We also show, in Fig A1.10, the results of the simulations for various flux limiters. The bands shown reflect the calculated sensitivity of $\dot{m}$ to time dependent and refractive effects. As shown in the figures, the transport is inhibited over the entire intensity range of this experiment, for values of $f_e<0.1$. The transport and plasma conditions are insensitive to the flux limit for $f_e>0.1$. That is, the transport in this regime is conduction limited. Good agreement is obtained for $f_e \approx 0.08 \pm 0.02$. To determine an upper limit on the effects of hot electrons, some calculations were performed under the assumption that 10% of the energy reaching the critical surface was absorbed into a distribution with $T_{hot} \approx 5$keV. The added hot electrons increases the

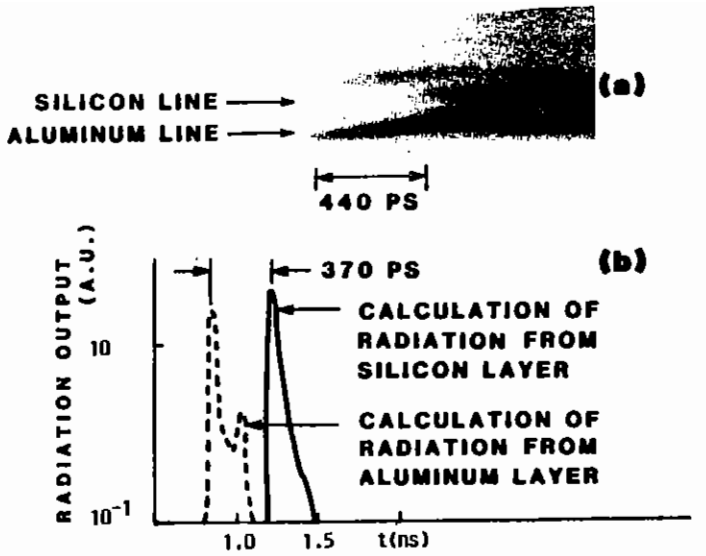

Fig A1.9 Comparison between LASNEX hydrodynamic simulation and experiment. (a) Spectrally resolved X-ray streak; (b) calculated (f_e = 0.1) emission from Al and Si layers. (The aluminium line identified is $1s^2$ - 1s2p.) The calculated emission shown is that of the outer zone of the Al and glass layers, and so decreases more rapidly than that measured.

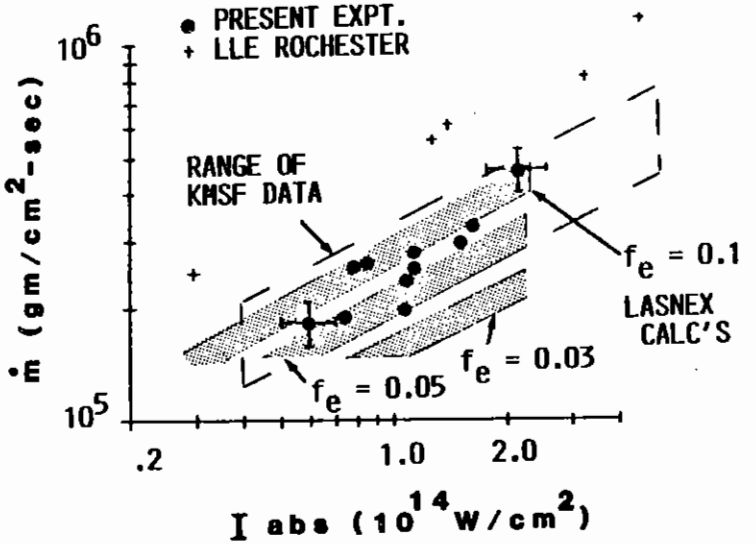

Fig A1.10 Mass ablation rates as a function of absorbed irradiance.

heat front penetration by about 20%, on the assumption of equal thermal and suprathermal flux limits. This would not significantly alter the inferred flux limit.

Also shown in Fig Al.10 is a summary of data in two recent studies of mass ablation performed by Tarvin et al. (Al.6) and points taken by Yaakobi et al (Al.7). The data of (Al.6) agree reasonably well with the present work while those of (Al.7) are somewhat higher. Our calculations (and the measured density profiles) suggest that temperature gradients are steeper in the work of Tarvin et al. because of differences in experimental parameters. This is consistent with their inference of a lower flux limit (f_e=0.03-0.06) from similar mass ablation data. We cannot presently account for the differences between our $\dot{m}$ measurements and those of Yaakobi et al.

Time-resolved measurements of calcium emission from the glass were also made. In Fig Al.11, we show streak traces of a calcium and a silicon line. For the usual tangentially focussed shots, a very small delay (<100ps) was observed between the turnon of silicon and calcium line emission. The rise time between the effective radiating temperatures of silicon and calcium is thus a small fraction of the burnthrough interval. This indicates a relatively steep heat front, and is consistent with the LASNEX non-local-thermodynamic-equilibrium calculations.

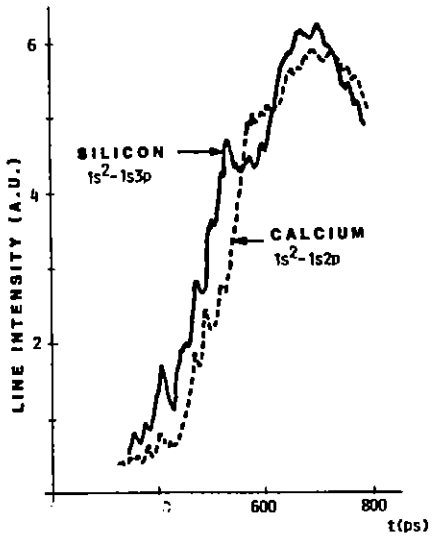

Fig Al.11 Temporal profile of X-ray lines coming from the glass. Nearly simultaneous onset of Si and Ca indicates a steep heat front.

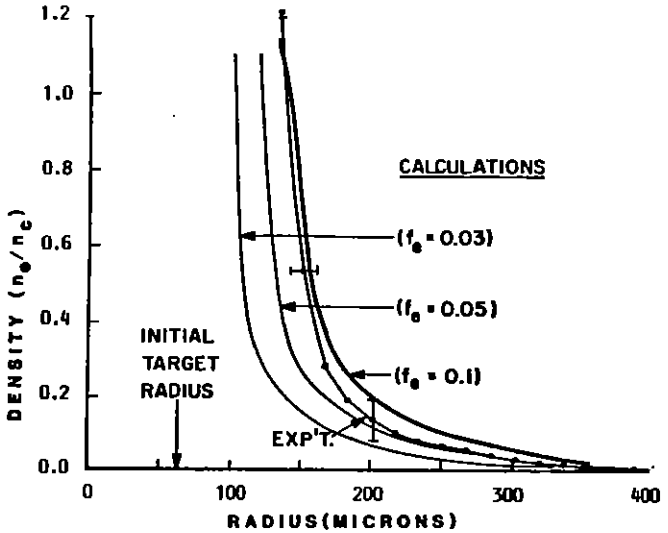

Fig Al.12 Experimental density profile taken at the peak of the laser pulse compared with modelling. Incident intensity $\sim 8 \times 10^{14}$ W/cm^2.

As an additional test of the modeling, we compared the measured and calculated plasma density profiles. The steepness and outward motion of the density contours are indicators of the ablated mass fraction and are thus sensitive to electron energy transport. In Fig Al.12, we show an example of such a comparison. A flux limit f_e=0.05-0.1 gives the best agreement.

In conclusion, we find that the thermal-electron transport in these spherical target experiments is best described by near-classical modeling (f_e=0.08±0.02). Our calculations have shown that a given measured $\dot{m}$ can lead to somewhat different inferred flux limits, depending on experimental parameters such as the temperature gradient. Good plasma symmetry characteristics were established and carefully diagnosed. The effects of coronal magnetic fields were minimized. The observation of little time delay between emission from silicon and

calcium indicates a relative steep heat front and is consistent with the modelling.

A1.4 HOT MATTER STOPPING POWER

P M Evans and A P Fews (Bristol University), S Knight, D Pepler and W Toner (RAL)

A1.4.1 Introduction

An experiment to measure the ratio of the stopping powers of hot to cold materials to alpha particles, protons and tritons has been performed using CR-39 plastic as the major diagnostic. A hot plasma was created by using the laser beams, and it was backlit by thermonuclear products from an exploding pusher implosion. The residual energies of the particles transmitted through hot and adjacent cold material were compared, giving a direct measurement of the induced change in $d\varepsilon/dx$. The method and some preliminary results from the analysis (which is still in progress) is described below.

A1.4.2 Experimental

The experiment was performed in the TA1 target chamber and the layout is shown in Fig A1.13. A 100μm diameter spot in a test foil was heated to plasma temperatures ~ 100eV. The foil was then probed by α-particles generated in an exploding pusher DT-filled microballoon. The 3.5MeV α-particles generated by this implosion passed through the test foil and were recorded in a CR-39 detector. A deflecting magnet was included to sweep plasma ions away from the CR-39, to reduce damage to the plastic surface. A pinhole as placed between the exploding pusher and the test foil, so that the CR-39 contained a pure sample of tracks which had passed through the heated region of the foil. The energy loss of α-particles passing through the foil when cold was determined using a ^{241}Am α-source. Two other CR-39 plates were also used in order to monitor the α-particles directly on leaving the exploding pusher. The time delay between the laser pulses heating the exploding pusher and those heating the test foil was varied, and so was

the beam intensity for each shot. This provided data for comparison with the foil modelling, using MEDUSA simulations. Foils of CH_2, Al, Cu, Au were used to provide stopping power measurements of these materials to α particles, protons and tritons. X-ray emission from the heated foils was recorded on a double pinhole camera.

In the trial experiment, there was no pinhole present and no magnet. The timing of the beams was such that the arrival of the thermonuclear particles probing the foil was simultaneous to the heating of the foil and there was no variation throughout the experiment. It was found that the CR-39 contained intermixed "hot" and "cold" tracks, due to multiple coulomb scattering in the test foil. In order to avoid these complications the layout for the main experiment was improved, as discussed above.

A1.4.3 Calibration

Central to the use of CR-39 for high resoluton energy measurements is the response to a given nuclear species defined by the track etch rate vs range, $V_T(R)$, and etch induction time vs range, $\tau(R)$ relationships (for the full definition of the nomenclature used in this section see ref. (A1.8)). With these data etch, cone dimensions can be precisely predicted under given etch conditions, so the measurable parameters of a given etch cone can be related precisely to the particle range and hence particle energy (A1.9). The $V_T(R)$ and $\tau(R)$ relationships are not universal; CR-39 exhibits fading of track response both with age since manufacture and with exposure in the laser target chamber. These effects are complemented by an increase in the etch induction time. Therefore the complete response of this material is determined for each particular experiment.

For the hot matter experiment a complete calibration was performed for the plastics used. Using a step degrader over a plate of CR-39, DT α-particle tracks of different ranges were registered. Each plate was then etched, so that for a given etch time, a distribution of ranges was obtained. Optimum $V_T(R)$ and $\tau(R)$ response curves were found, for a given absolute range. By means of an iterative process, the difference between the predicted Mi parameter to that measured was minimised by

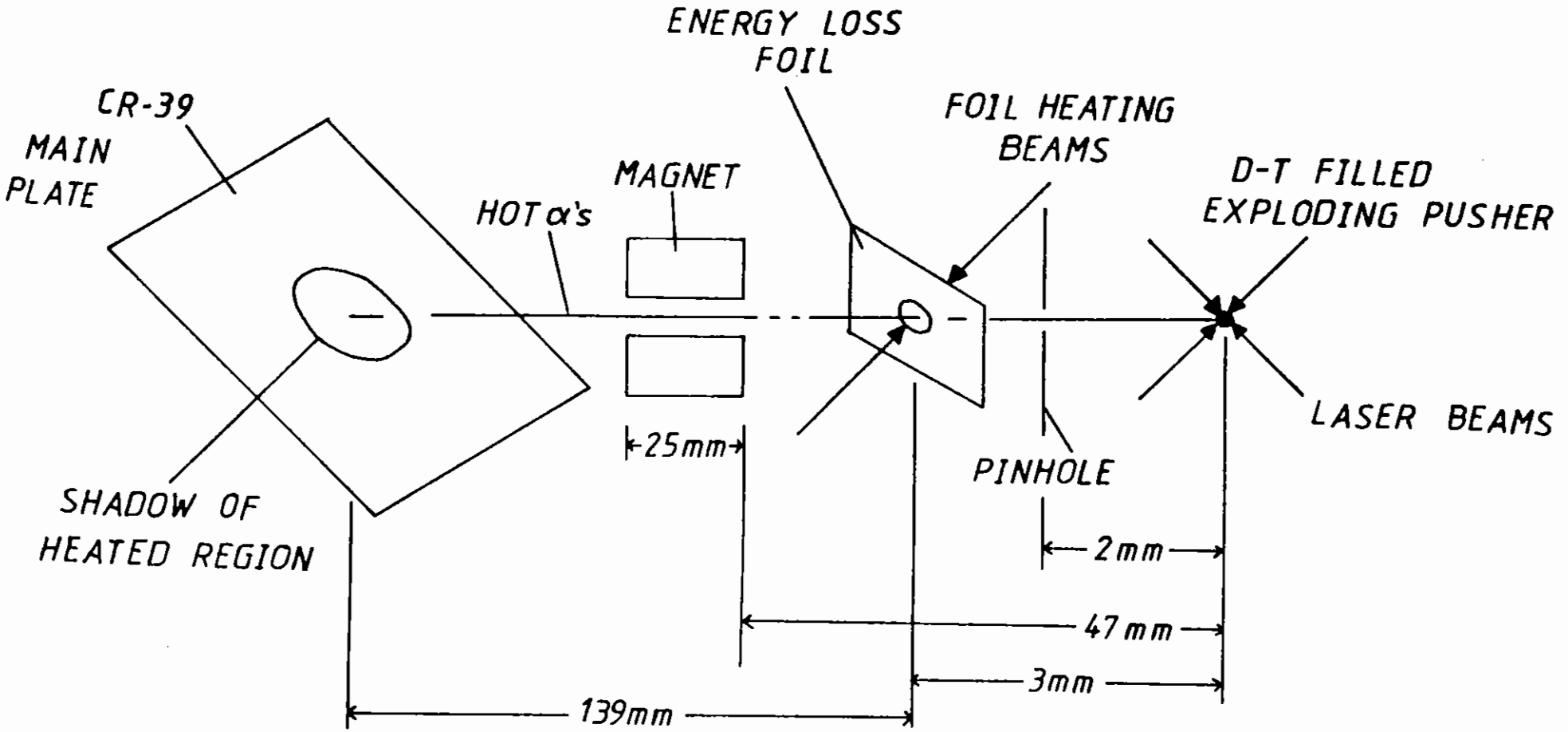

Fig A1.13 Experimental layout of the apparatus for the Hot Matter experiment.

adjusting the absolute range until the best fit as achieved. The self-consistency of the whole calibration procedure was thus guaranteed this can be seen in Fig A1.14.

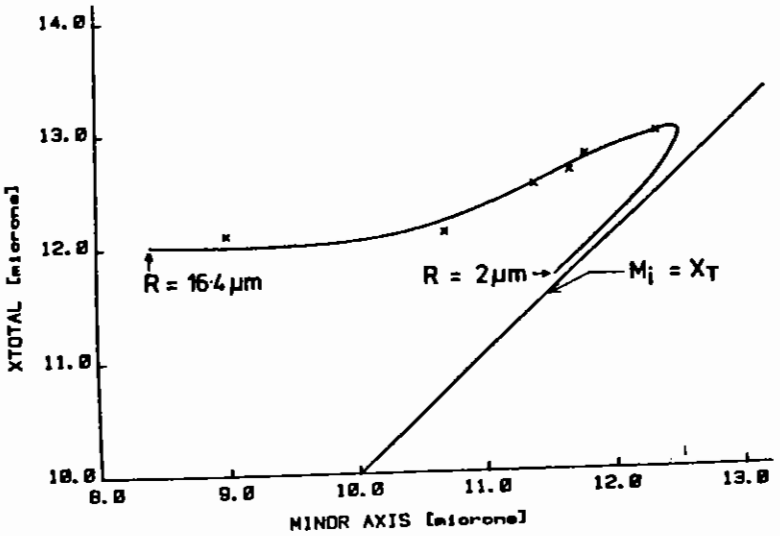

Fig A1.14 Typical trajectory of minor axis versus X_{total}.

Each data point is the average of the measurements of 500-1000 tracks for a given shot. The excellent fit of the trajectory predicted by the calibration, to the measured parameters X_T and Mi is demonstrated. With this etch the point at R = 2μm range is close to the trajectory for X_T = Mi, ie at this range the track is etched to be almost circular.

A1.4.4 Results

The large amount of data yielded from the experient is still being analysed by the automated image analysis system (Section A6.75). However some results have been produced for α particles travelling

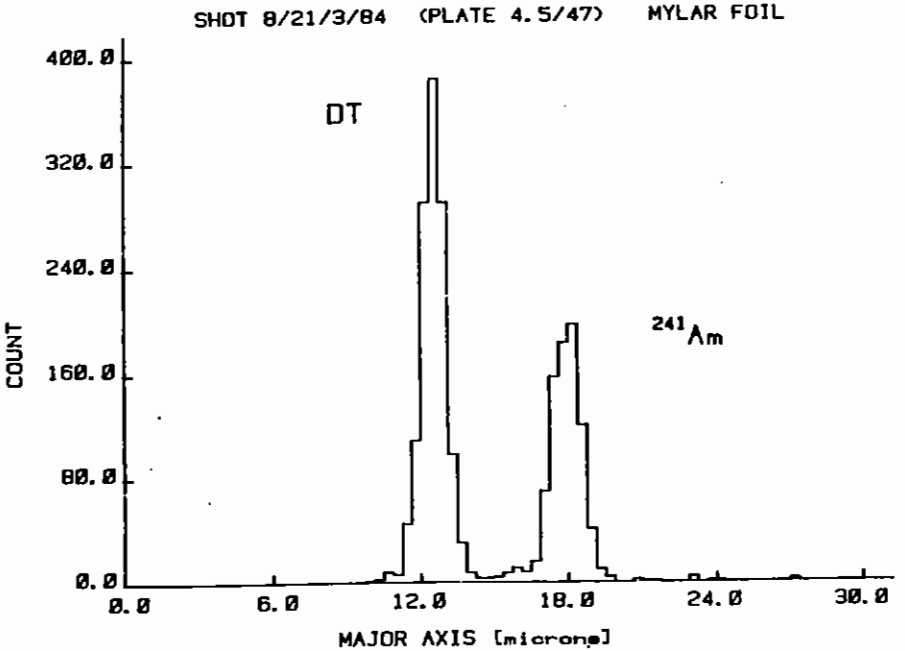

Fig A1.15 Histogram of major axis etch cone parameter showing two peaks; one due to DT α-particles, and the other due to ^{241}Am α-particles.

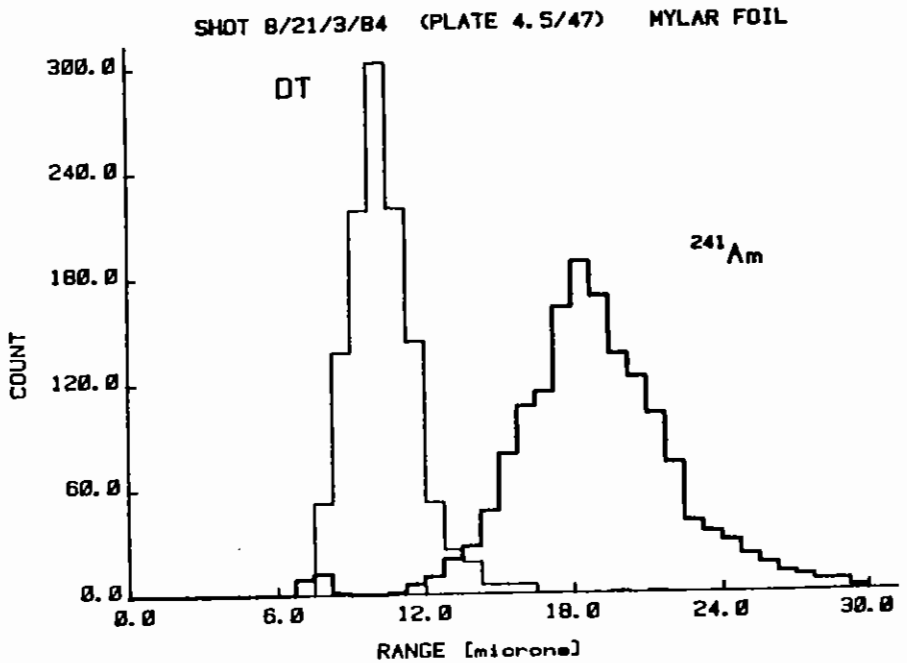

Fig A1.16 Range distribution corresponding to the major axis histogram in Fig A1.15; again the two peaks are distinct.

TABLE 1.1

Shot	Foil	Irradiance $W\ cm^{-2}$	Neutron yield	Time Delay (balloon-foil) ps	Foil Thickness μm in CR-39	
					Hot	Cold
08/21/03/84	mylar	2.3×10^{14}	9×10^{6}	300	6.55	
07/05/04/84	mylar	6.0×10^{14}	7×10^{6}	430	7.80	
09/30/03/84	mylar	5.3×10^{14}	2×10^{6}	450	6.81	5.21
05/29/03/84	Al	3.1×10^{14}	7×10^{6}	150	5.24	3.81
05/21/03/84	Al	4.5×10^{14}	9×10^{6}	300	5.90	
09/20/03/84	Al	9.8×10^{14}	7×10^{6}	370	4.53	

through the foil. Fig A1.15 shows a histogram of the major axis etch cone parameter in CR-39 showing the main peak due to DT α-particles, and a second peak from the ^{241}Am source.

The width of the ^{241}Am peak is broad because of the finite thickness of the source used. The signal, at low range, that may be attributed to fast ions is negligible.

The calibration described above has been used to convert MJ and MI back to measurements of α-particle range Fig A1.16 shows the range distribution corresponding to the distribution shown in Fig A1.15. In this example the path length in the hot foil region is 6.55 ± 0.05μm compared to an initial estimate of 5.21μm in the cold foil. Out of a total of 30 successful data shots 20 have a high enough yield to provide a useful stopping power value. Table 1.1 shows a summary of the hot/cold stopping power data for various foils.

Further analysis of the CR-39 plates continue with parallel analysis of the plasma conditions of the foil at the time of passage of the test particles. Values for the thickness of the heated foils already measured are shown. Only two values have been obtained so far for the actual cold foil thickness although other values are pending. The errors, limited by systematic rather than random causes are estimated at ± 0.1μm for both hot and cold foil thicknesses; improvements on this will be made as analysis continues. To date almost 10^5 tracks have been measured by the automated image analysis system, compared with ~ 4×10^3 in total by previous manual measurements.

A1.5 ANALYSIS OF SRS FROM LONG SCALE-LENGTH UNDERDENSE PLASMA

S J Karttunen (Technical Research Centre of Finland), V Aboites, E McGoldrick and S ML Sim (Essex University)

A1.5.1 Introduction

Near the quarter critical density $n \lesssim 0.25 n_c$ both stimulated Raman scattering and two-plasmon decay excite plasmons with the frequencies close to $\omega_0/2$ where ω_0 is the frequency of the incident light.

Emission of the light at $\omega_0/2$ is generated directly by the Raman process near $0.25n_c$ or indirectly from $2\omega_p$ -plasmons through some conversion or coupling mechanism.

Experimental observations of $\omega_0/2$ harmonic emission have been reported recently by several authors (A1.10-A1.15). A rather narrow line at $\omega_0/2$ with a double peak structure indicates the plasmon decay as the process behind the half harmonic emission (A1.12-A1.15). A much broader emission between $\omega_0/2$ and ω_0 is attributed to stimulated Raman scattering occuring below the quarter critical density (A1.11, A1.14, A1.15).

Experimental arrangement and the results were described in the 1984 annual report (Section A1.3).

A1.5.2 Experimental Results

A typical temporally and spectrally resolved streak record consists of three signals: unconverted 1.05μm light acting as a spectral and temporal marker, forward scattered emission produced by the prepulse and backscattered emission from the main pulse. Results from 0.7μm and 0.3μm foils are shown in Fig A1.17 and Fig A1.18.

The analysis of the temporal evolution of the backscattered signal indicates that for 0.3μm and 0.7μm foils the peak of the stimulated Raman scattering occurs at the peak of the main pulse. For the 0.7μm foils the peak of the forward $\omega_0/2$ emission occurs about 130 ps after the peak of the prepulse.

A1.5.3 Theoretical considerations

Next we consider spectral features of the $\omega_0/2$ harmonic emission assuming that the two-plasmon decay is the dominant process near the quarter critical density.

The coupling between the incident or reflected photon and

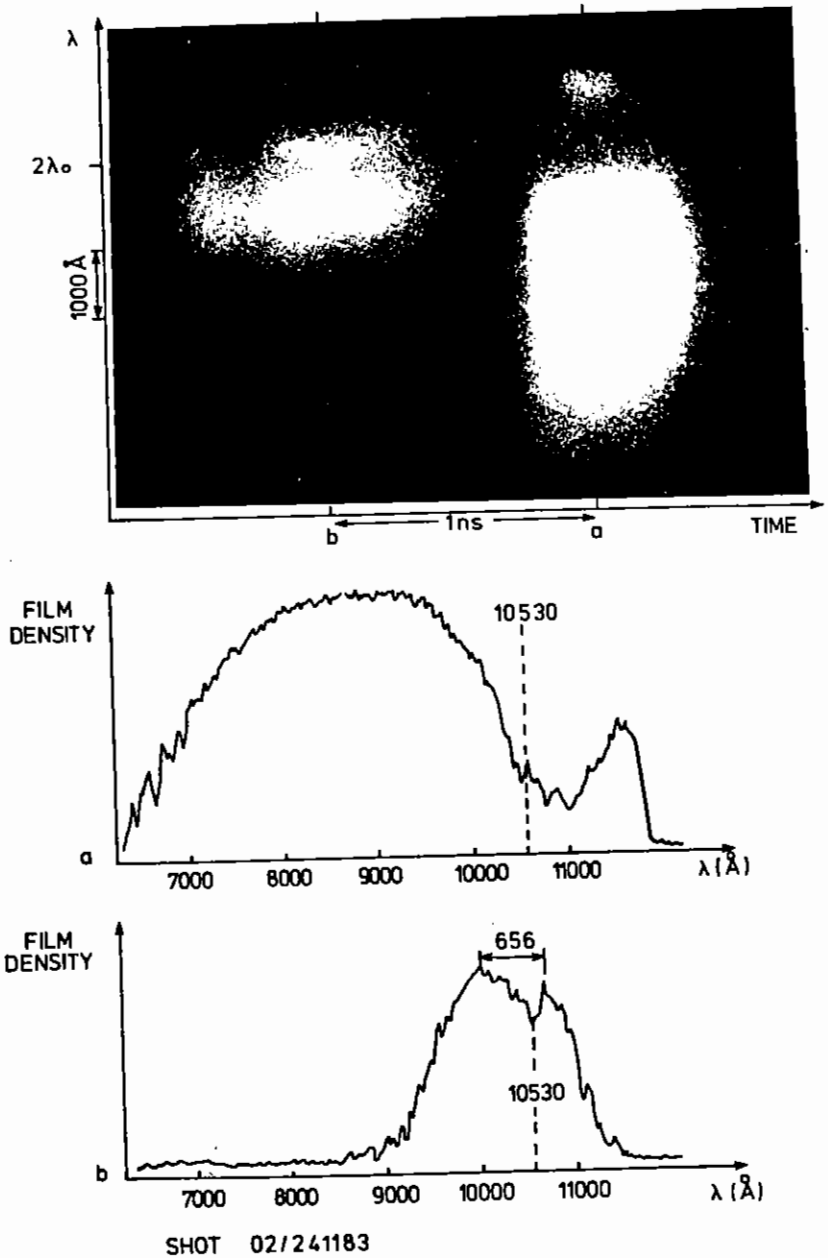

A1.17 Time resolved $\omega_0/2$ spectrum observed with a 0.7μm thick parylene foil target. The microdensitometer traces show a) the broad backscattered emission and b) the much narrower forward scattered emission from the pre-pulse.

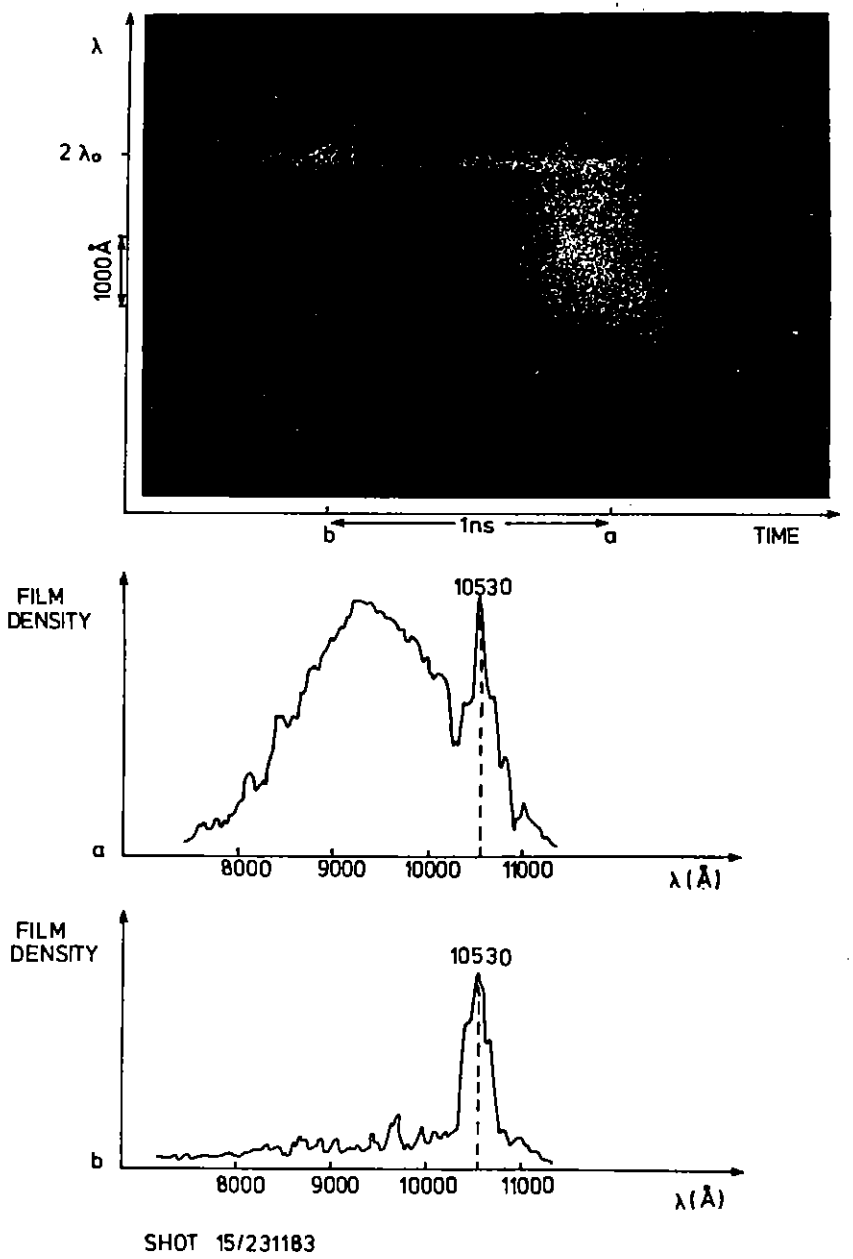

A1.18 Time resolved $\omega_0/2$ spectrum observed with a 0.3μm thick parylene foil target. The microdensitometer traces show a) the broad single peaked backscattered emission and b) the much fainter forward scattered emission from the pre-pulse.

$\omega_0/2$-plasmon from the $2\omega_p$-instability leads to the $\omega_0/2$-emission (similarly to $3\omega_0/2$-emission). When the $2\omega_p$-decay and the $\omega_0/2$ generation take place at the same density, we obtain for the shifts from the nominal $\omega_0/2$ value

$$\Delta\lambda = \frac{9}{2}\left(\frac{v_e}{c}\right)^2 \lambda_L, \qquad (1)$$

$$\Delta\lambda = -\frac{9}{2}\left(\frac{v_e}{c}\right)^2 \lambda_L \left(3+2(k_{\frac{1}{2}}/k_0)\cos\theta\right), \qquad (2)$$

where λ_L is the vacuum wavelength of the incident light and (θ=0 for forward emission and θ = 180° for backscattered emission). V_e and c are the electron thermal velocity and the speed of light, respectively. For the wavenumber $k_{\frac{1}{2}}$ we get approximately $k_{1/2} \approx (k_1\lambda_D)k_0 \approx 2k_0^2\lambda_D$, where λ_D is the Debye length. The coupling to an incident photon ($\bar{k}_0$, ω_0) gives the red shift (1) and the blue shift (2) follows from the coupling to a reflected photon ($-\bar{k}_0$, ω_0). The blue shift (2) is about three times larger than the red shift (1) in the basic case, when the propagation effects of $2\omega_p$-plasmons are neglected.

(a) Forward $\omega_0/2$ emission (prepulse)

The forward $\omega_0/2$ emission during the prepulse must originate in the rear side of the peak density, because the plasma is opaque for the $\omega_0/2$ radiation i.e., $n > 0.25n_c$. On the other hand, the peak density must be less than critical ($n < n_c$) to allow any incident light beyond the density maximum.

At the quarter critical density in the rear side of the target plasma the incident light propagates down the density gradient ($\bar{k}_0 \parallel -\nabla n$). This predicts that the blue shift may increase from the value (2) due to

propagation of the plasmon i.e., the excitation of the plasmon $(\bar{k}_2,\omega_2)$ by the $2\omega_p$-decay may occur at lower density than the resonant $\omega_0/2$ generation. This situation is illustrated in Fig A1.19 which shows the k-diagrams of a $2\omega_p$-decay (at lower density) and the two possible couplings for $\omega_0/2$ generation. For the modified blue shift we find in the limit of small θ (i.e., forward $\omega_0/2$ emission (A1.16).

$$\Delta\lambda = -\frac{9}{2}\left(\frac{v_e}{c}\right)^2 \lambda_L \left[1+2\alpha\left(1\pm\frac{k_\perp}{k_0}\right)\right], \qquad (3)$$

where the "+" sign corresponds to the coupling of the plasmon and the reflected photon and the "-" sign to the coupling between the reflected plasmon and the incident photon. The propagation parameter α is defined by $\alpha=k_2/k_2'$, where k_2 is the plasmon wavenumber at the density of $2\omega_p$-decay and k_2' is the value at the density of $\omega_0/2$ generation (cf., Fig A1.19).

The red shift is modified only slightly in the case of decreasing density $(\bar{k}_0\|-\nabla n)$. Thus the electron temperature can be evaluated from the experimental red shift $\Delta\lambda_{exp} \approx 116$ Å which give $T_e = 2.5$ keV for $\lambda_L=0.53\mu m$.

The experimental blue shift $\Delta\lambda_{exp} \approx -540$ Å is about 4.7 times larger than the red shift indicating that propagation effects must be included.

The asymmetry of the $\omega_0/2$-spectrum is considerably larger than reported earlier (A1.12, A1.13). The spectral analysis (A1.14) gives, in the basic case, a blue shift about three times larger than the red shift.

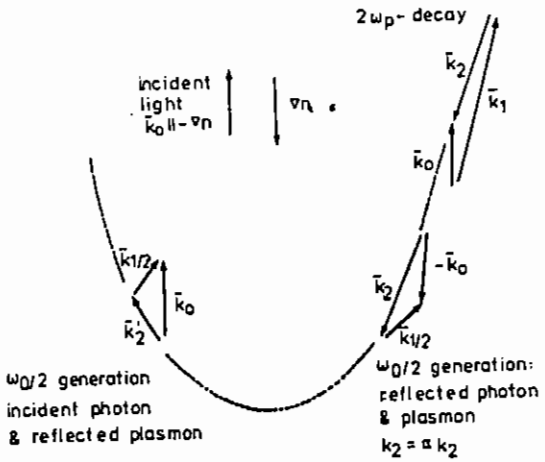

A1.19 Wave vector diagrams for the $2\omega_p$-decay and two possible couplings for the $\omega_0/2$ generation before and after reflection of the plasmon $(\bar{k}_2, \omega_2)$. The situation is at the rear side if the peak density, ie. the incident light travels down the density gradient $(\bar{k}_0\|-\nabla n)$.

However, in the normal case the pump wave travels up the density gradient $(\bar{k}_0\|\nabla n)$. This means that the red shift may enhance due to plasmon propagation making the spectrum more symmetric than in the basic case in agreement with (A1.12) and (A1.13). In the present case, however, the interaction takes place at the rear side of the peak density, where the pump travels down the gradient $(\bar{k}_0\|-\nabla n)$. In this case the asymmetry of the $\omega_0/2$-spectrum is increased as compared with the basic case.

A1.5.3(b) Backscattered emission (main pulse)

The blue-shifted part of the backscattered emission by stimulated Raman scattering is broad, covering the wavelength region from 7000 Å to 10200 Å for the 0.7 μm foils (Fig A1.18). The corresponding density

range can be obtained from

$$\frac{n}{n_c} = \frac{(1-\lambda_L/\lambda_s)2}{(1+3k^2\lambda_D^2)}, \qquad (4)$$

where λ_s is the scattered wavelength and k is the wavenumber of the Raman plasmon, which can be evaluated from the phase matching conditions for the stimulated Raman scattering. Equation (4) gives the density range from $0.04n_c$ to $0.22n_c$ for 0.7μm foils and from $0.11n_c$ to $0.22n_c$ for 0.3μm foils. The upper density is higher than observed in the thick target experiments (Al.11, Al.14, Al.15) in which the backscattering is coming from $n<0.15n_c$. One explanation of this is the nature of the density profile. In thin foil experiments the density gradient scalelength can even increase near the quarter critical surface, particularly if the peak density is close to $0.25n_c$. Under such conditions the stimulated Raman scattering may operate from the maximum density to low densities ($<0.5n_c$), where the Raman process is limited by the Landau-damping.

The backscattered signal has a red-shifted component with the shift $\Delta\lambda \gtrsim 1000$ Å (Fig Al.18). This red shift is too large to be explained by the $2\omega_p$-decay with photon coupling. The argument is that the plasmons, induced by $2\omega_p$-process, which correspond to a shift ~ 1000 Å are too heavily damped to be excited by the two-plasmon decay. This is seen by the following analysis.

Backscattered red-shifted signal must be generated in the front side of the peak density, because the critical density of the scattered light (λ~11500 Å) is about $0.21n_c$. Thus we have a normal situation when the incident light travels up the density gradient (i.e., $\bar{k} \| \nabla n$). In this case the red-shift can be enhanced by plasmon propagation. The red-shift must now be replaced by (Al.17).

$$\Delta\lambda = \frac{9}{2}\left(\frac{v_e}{c}\right)^2 \lambda_L (2\alpha-1), \qquad (5)$$

where α is the propagation parameter defined in the similar way to that

in Eq. (3). With $\Delta\lambda$=1000 Å, λ_L=0.53 μm and $T_e \simeq$ 2 keV we get for the propagation parameter α=5.9. So the wavenumber of the plasmon at the density of the $2\omega_p$-excitation is $k_l = 5.9k_0$, which gives $k_l\lambda_D$=0.74. The Landau-damping with $k_l\lambda_D$=0.74 is approximately Γ_l/ω_l=0.17 which is too heavy for $2\omega_p$-excitation. The damping is also too large to allow any propagation more than few plasmon wavelengths (plasmon wavelength is about $\lambda_p \sim \lambda_L/5.9 \simeq 0.09$μm). The conclusion is that the large red shift ~ 1000 Å can not be produced by the coupling of $2\omega_p$-plasmons with ω_0-photons.

To explain the anomalous red shift, we have to look at Raman excited plasmons. The frequency matching of stimulated Raman scattering predicts that the plasmon is red-shifted from $\omega_0/2$ by the same amount that the Raman scattered light is blue-shifted. From the Raman spectrum in Fig Al.18 we can conclude that there is a broad red-shifted spectrum of Raman plasmons (red shift 500–300 Å from $\omega_0/2$). If these plasmons are converted to photons by some linear or nonlinear process, the conversion leads to the emission of radiation with a large red shift >500 Å from the $\omega_0/2$ frequency. Possible conversion mechanisms are:

(i) inverse resonance absorption (Al.12, Al.17)): $L(\omega) \rightarrow T(\omega)$
(ii) plasmon decay: $L(\omega) \rightarrow T(\omega') + S(\omega_s)$,
(iii) inverse parametric decay: $L(\omega) + S(\omega_s) \rightarrow T(\omega')$,

where L is a plasmon (longitudinal wave), T is a photon (transverse wave) and S is a phonon (ion sound wave). In (ii) and (iii) the frequencies are: $\omega' = \omega \mp \omega_s \simeq \omega$ (the ion sound frequency is small, $\omega_s << \omega, \omega'$).

Al.5.4. Conclusions

Temporally and spectrally resolved $\omega_0/2$ harmonic emission and stimulated Raman scattering has been studied experimentally by irradiating thin foils with two pulses of 0.53μm laser light travelling in opposite directions. The delay between the prepulse and the main pulse was one nanosecond.

During the prepulse the density profile is too steep for stimulated Raman scattering. For 0.7μm foils the forward scattered spectra show a strong asymmetry with respect to the nominal $\omega_0/2$ frequency. The spectral model (Al.16), which assumes the coupling between ω_0-photon and $2\omega_p$-plasmon, explains well the observed asymmetry. The red shift Equation (1) is very insensitive to the emission angle ($k_{1/2} << k_0$), depending mainly on the electron temperature, if the propagation effects of $2\omega_p$-plasmons are neglected.

The main pulse produces a broad backscattered emission due to stimulated Raman scattering . The Raman spectra and the absence of the two-plasmon decay indicate that the peak density of the plasma is below the quarter critical density ($n_{max} \lesssim 0.22 n_c$) during the main pulse. A large red shift ~ 1000Å can not be explained by the $2\omega_p$-instability. It is most likely caused by the conversion of Raman plasmons to photons, for instance by inverse resonance absorption. The large red shift is not observed from the 0.3μm foil targets having longer scalelengths. This supports the inverse resonance absorption as a process responsible for the large red shift from the 0.7μm foils.

The results show that the stimulated Raman scattering is excited at rather low irradiance. A recent model (Al.16), explains the broad spectrum between ω_0 and $\omega_0/2$ by ordinary incoherent Thomson scattering which may occur well below the Raman threshold. The absence of n_c and $0.25 n_c$ layers in our experimental conditions excludes hot electrons from resonance absorption and two-plasmon decay. Hence the present broad Raman spectrum from the main pulse can not be explained by the incoherent Thomson scattering (Al.18).

Al.6 DENSITY AND TEMPERATURE MEASUREMENTS USING DOT-SPECTROSCOPY OF ALUMINIUM IN PLANAR GEOMETRY

S D Tabatabaei, B J MacGowan (Imperial College)

Al.6.1 Introduction:

Emission of X-rays from laser produced plasmas has served as a powerful diagnostic technique, but it is highly desirable to restrict the emitting volume to a small region of space, to minimise effects of inhomogeneity. This is achieved by using the Dot-spectroscopy technique. The unique feature of this technique is the use of tracer materials which are locally embedded into the solid target in finite spot forms. These tracer dots which are highly localized within the focal region of the laser beam, remain localized within the blow-off plasma so that as it moves through the heat front, its emission indicates the local density and temperature. This leads to less ambiguous comparisons between the data and the hydrodynamic computer code models, providing the most direct calibration of these codes because:

(1) All emitted spectral lines, regardless of the ionization state of the emitting ion, must arise in the same volume of plasma. Calculation of plasma parameters such as density and temperature from the ratio of line intensities is then less questionable compared with large target plasmas.

(2) This well defined source volume has circular symmetry, enabling spectral analysis with a 1-D ionisation - radiation model.

(3) If the tracer diameter is made small enough the source-volume homogeneity will be high.

(4) The complicated effects of plasma opacity are reduced by having a smaller, more homogeneous, source volume.

(5) The spectra obtained with this technique have better spectral resolution.

A1.6.2 Experiment

The aims of this experiment were to investigate:

(1) Whether the X-ray emission from thin Al tracer layer spot (0.025μm and 0.05μm thick) was bright enough with respect to the background CH (initially 1μm thick) plasma for spectroscopic measurements.

(2) Whether the tracer layer remained localised as it expanded through the plasma after it was irradiated.

(3) Whether the aluminium recombination continuum emission from the corona from such thin layers could be recorded on the film, yielding the electron tempreature (T_e) measurement from its slope.

(4) Whether electron density (n_e) could be calculated from line ratios of Al-Ly$_\alpha$ (1s - 2p) to Al - He$_\alpha$ ($1s^2$ - 1s2p) and Al-Lyβ (1s - 3p) to Al - He$_\beta$ ($1s^2$ - 1s3p).

The experiment was performed in planar geometry in the single-beam target area of the CLF at RAL, using a neodymium glass laser beam of λ = 0.53μm. The nominal pulse length and focal spot sizes were 1.1ns and 110μm respectively, with laser pulse shape having a Gaussian temporal profile. The typical incident irradiance was ~ 10^{14} Wcm^{-2}.

The experimental set-up is shown in Fig A1.20.

The targets consisted of Al microdots of thicknesses 0.025μm and 0.05μm with measured diameters ranging from ϕ = 20 to 70μm. These dots were vacuum deposited onto a mylar substrate using two overlapping 60μm wide slits. They were then overcoated in vacuum by 1μm of plastic $(CH)_n$. A typical- target is shown in Fig A1.21.

The primary diagnostic was a miniaturised time-resolving crystal X-ray spectrograph (streak camera) equipped with a flat KAP (potassium acid phthalate) crystal (2d = 26.632Å). The photocathode used was a low-density vacuum deposited CsI on 6.5μm Be. Other diagnostics were:

(a) A static minispectrograph with a space resolving slit of width = 10.5μm with a 13.3μm Be filter. The crystal used was ADP

(Ammonium dihydrogen phosphate) (2d = 10.640Å). This instrument was used to obtain time-integrated but space-resolved Al lines for streak camera cross calibration.

(b) A double-pinhole camera with 25μm Be and 6.4μm aluminised mylar filtering. The pinhole substrates were 25μm thick platinum with 10.4μm and 23μm measured circular pinholes. The data from this device gave the focal spot size of the beam and served to ensure a direct and centralised hit by the laser beam, see Fig A1.22.

As the target was irradiated with the laser beam, the Al layer expanded into the corona emitting X-rays characterised by the local temperature and density of the surrounding plastic plasma. A 70μm thick Au wire was stuck across the target to eclipse the dense region of the plastic plasma (high n_e) to ensure streaking the Al-plasma at a region where the dominant n_e contributor from the plastic was the recombination process. The target holder was rotated to ~ 8° to eclipse the correct region of the plasma blow-off from the streak camera see Fig A1.21.

The aluminium electron temperature (Te) was measured from the slope of its recombination continuum measured on a microdensitometer. The results were corrected for the film response using Kodak-RXp film calibration curve produced by exposing the films to a calibrated step-wedge and developing it with the data film, an for reflectivity of the KAP crystal at the spectral region considered.

The result of such measurement is presented in Fig A1.23 and A1.24, together with calculated Te values obtained from 2-D hydrodynamic simulaton code in spherical geometry at two flux limits, f = 0.03 and f = 0.1. The data of shot 11050484 was selected for the anlaysis as it was the best data in which Al recombination continuum dominated the continuum due to the plastic. The onset of Al-continuum emission was recorded on the film of the streak camera as an edge-jump of 5.38Å at the end of the series, see Fig A1.25.

The Hydrogen-like and Helium-like Al line intensities and their time history were measured using time-resolved data, the result is presented in Fig A1.26. Hydrogen-like lines were brighter than

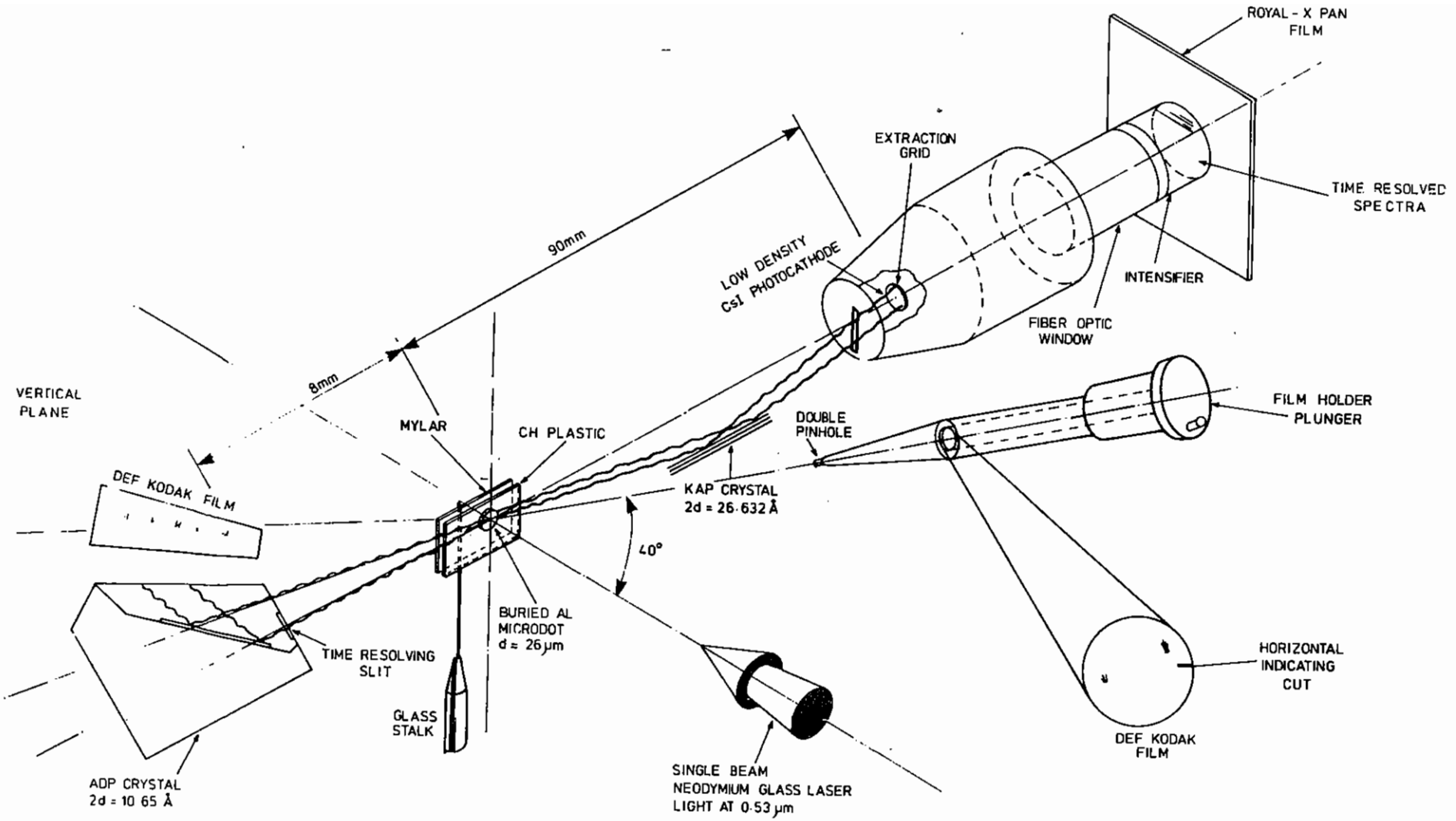

FIG A1.20 THE EXPERIMENTAL LAYOUT OF THE TIME AND SPACE RESOLED DIAGNOSTIC OF ALUMINIUM MICRODOT TARGET EXPERIMENT BURIED UNDER PLASTIC.

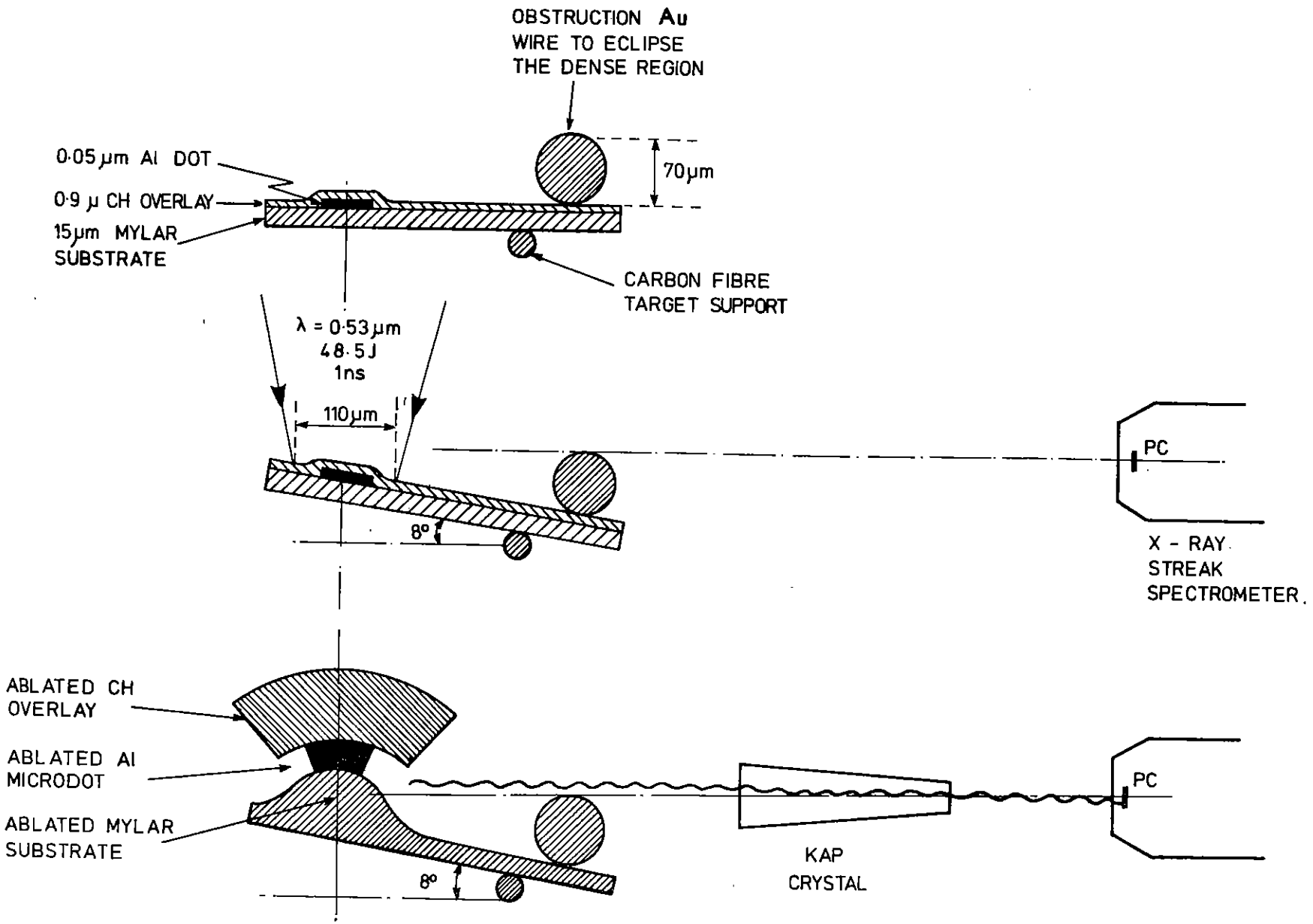

FIG. A1.21 THE TARGET CROSS - SECTION AND TIME RESOLVED DIAGNOSTIC VIEWED FROM TOP OF THE TARGET CHAMBER

Pinhole Camera image of the Al- dot streaming through the background plasma.

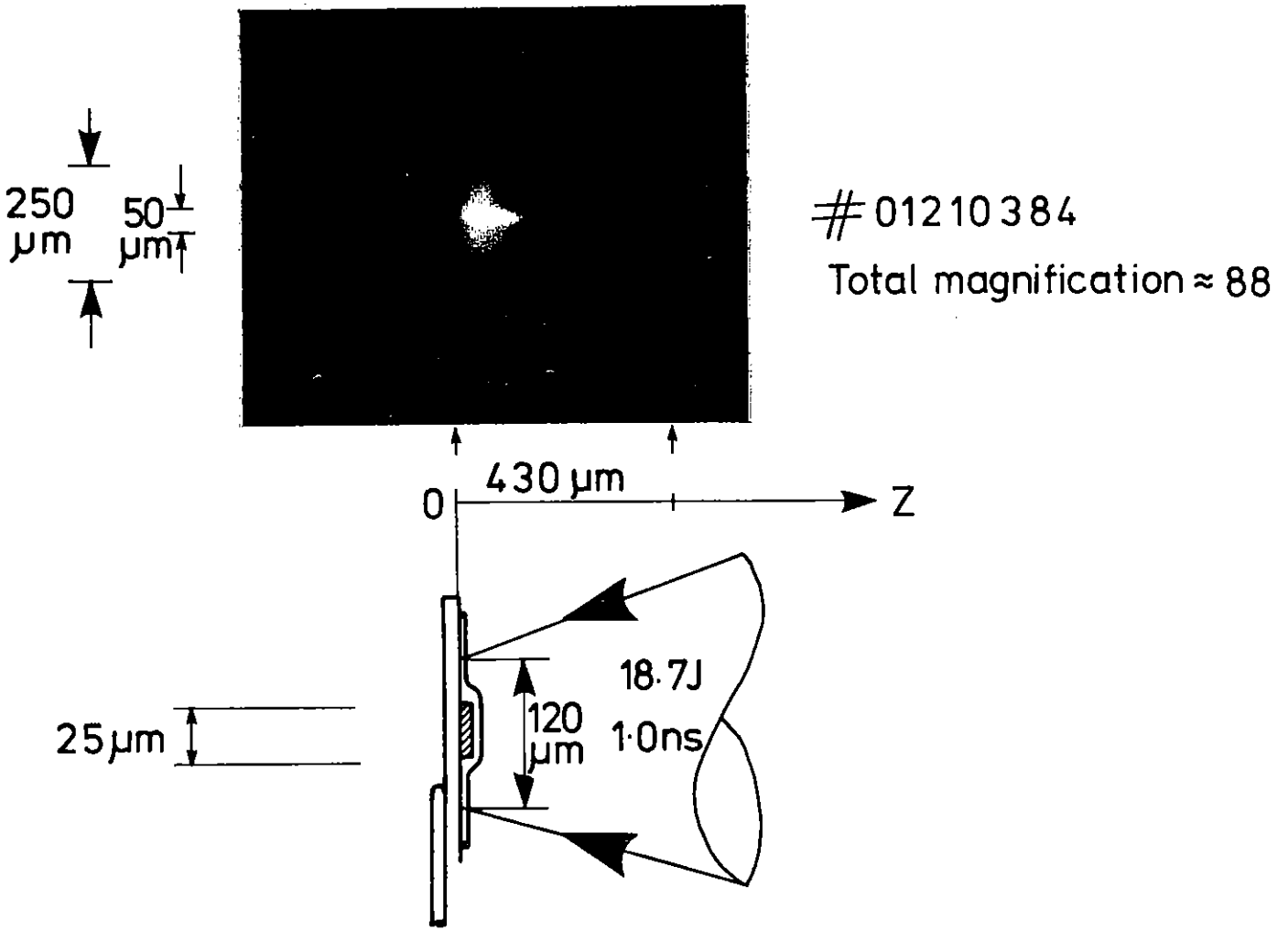

Al.22 Pinhole camera images of the Al-dot streaming through the background plasma.

FIG. A1.23 Time evolution of the Al recombination continuum from a 0.05 μm thick, φ = 70 μm dot buried under 1μm CH.

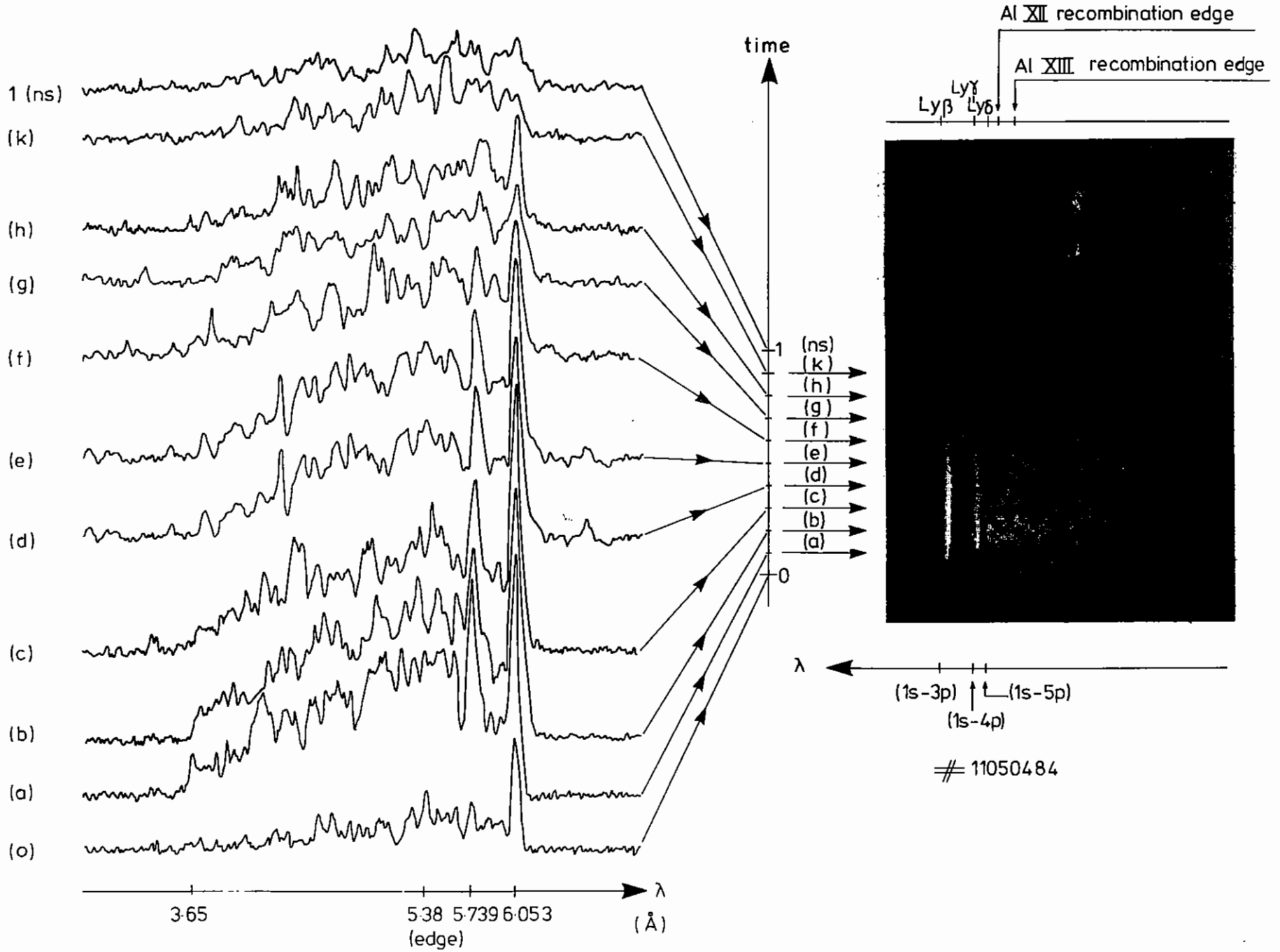

Helium-like lines, all maximising at the same time and varying considerably with time. The peak opacity of Al-Heα($1s^2$-$1s2p$) line was calculated to be 3 with that of Al-Heß ($1s^2$-$1s3p$) much smaller indicating an increased state of ionisation. All Te measurement techniques are based on the existence of steady-state populations in the relevant bound or free states. The experimental indication of violations of the above assumption would be the simultaneous occurrence of lines from more than two subsequent ionisation stages of one element and emitted from the same region of the plasma or the lack of a dip in total line intensities of a lower ionisation stage as a function of time as the intensities of lines from a higher ionisation stage go through a maximum, these lines again being from the same volume element, see Fig A1.26.

The 2-D hydrodynamic simulation code (Lagrangian) used for calculation incorporated:

(a) 28 x 20 zones

(b) flux limited Spitzer conductivity

(c) no Brillouin backscatter, predicting 100% absorption making sure the simulated absorbed irradiance matched the measured absorbed irradiance

(d) no magnetic field.

Calculated and measured Al temperature

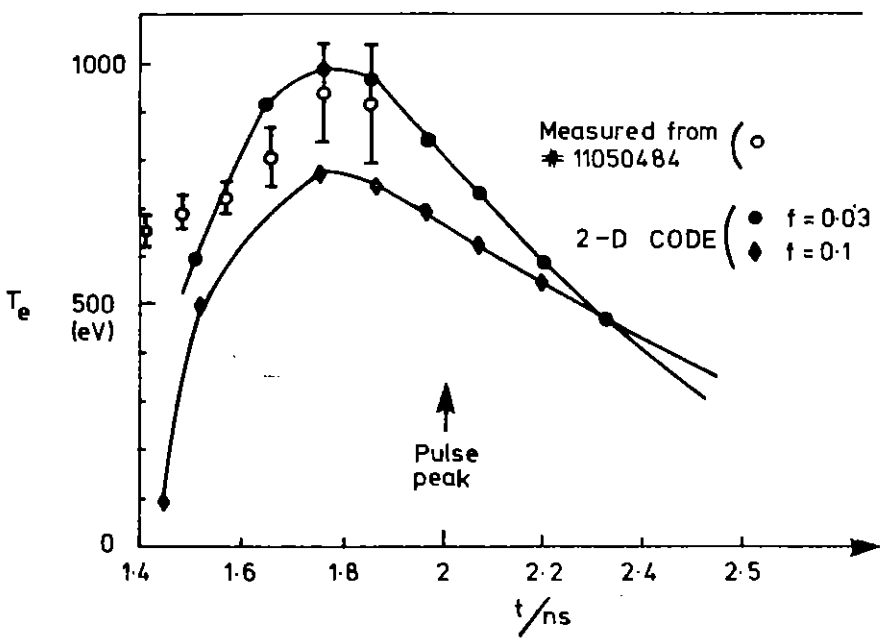

A1.24 Calculated and measured Al temperature.

The Al dot accelerates for ~ 2ns before its expansion reaches a steady velocity of 6.1 x 10^7 cms^{-1} as calculated from the 2-D code outputs. The variation in Al-dot position with time is plotted in Fig A1.27 for two flux limits: f = 0.03 and f = 0.1, giving blow-off velocity of v_p = 6,25 x 10^7 cms^{-1} and v_p = 6.10 x 10^7 cms^{-1} respectively.

The blow-off velocity was measured by measuring the time and positon corresponding to an intensity ratio of $^{Ly\alpha}/_{He\alpha}$ = 1.9 from both time-resolved and space-resolved data. The measured velocity was 6.44 x 10^7 cms^{-1}.

FIG.A1.25 Time resolved aluminium lines and Continuum dominated by the mylar substrate.

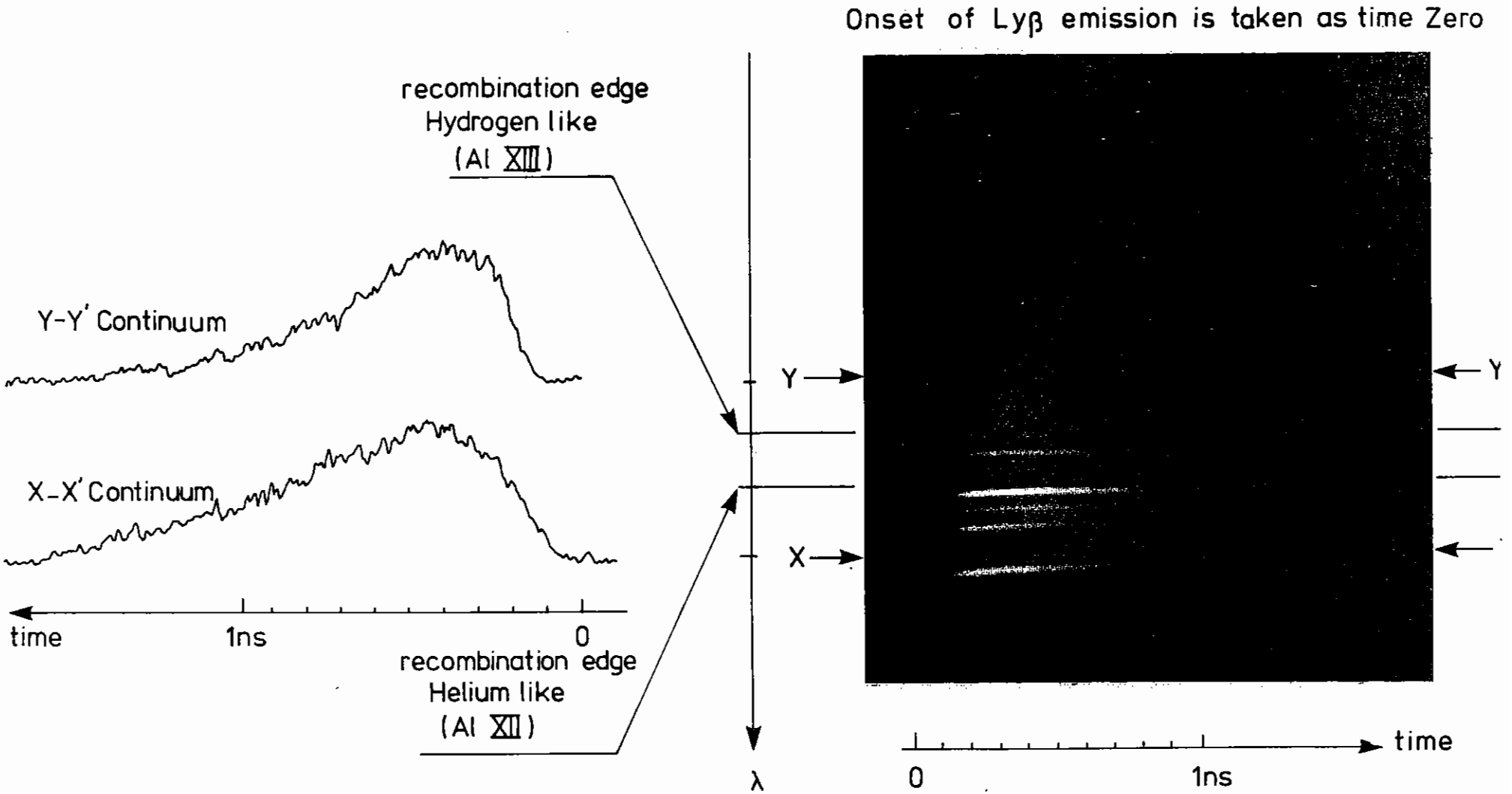

Measured aluminium line intensities

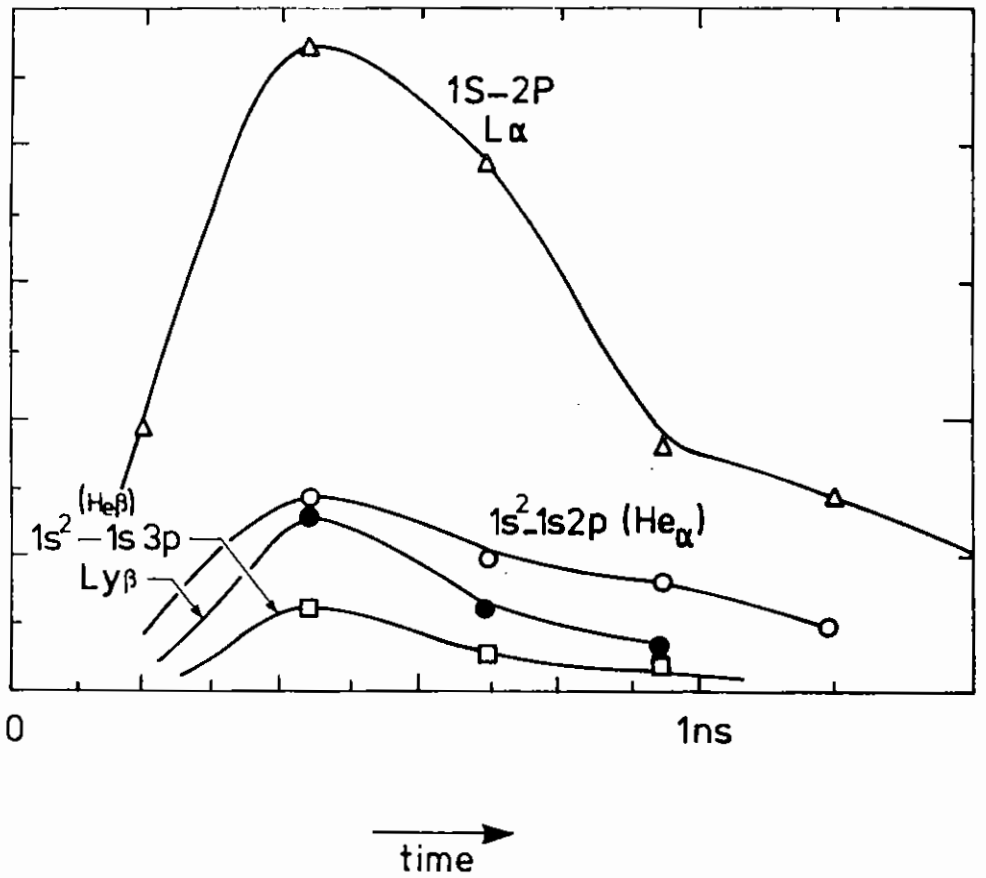

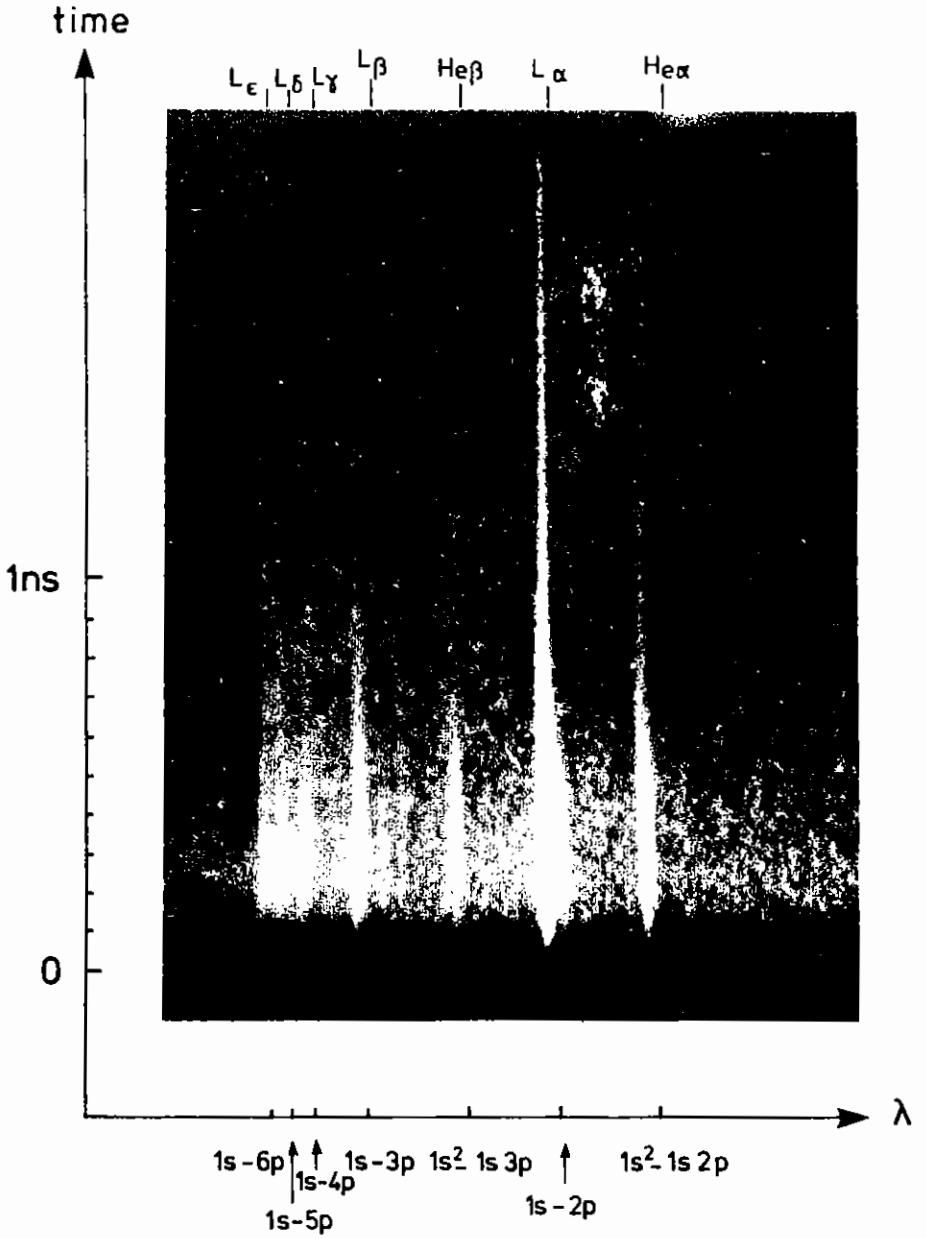

Al.26 Measured aluminium line intensities.

#07060484

A1.6.3 Conclusion

1. Measurement of the Te from the slope of the Al recombination continuum was made. The small emitting volume of the Al eliminated gradient effects.

2. The particle velocity was measured from time and space resolved data.

3. Measured Te from line ratios gave higher values than the above mentioned method.

4. The temperature history of the Al-dot is consistent with calculations from a 2-D Lagrangian simulation code with flux limits in the region of 0.03 to 0.1.

Calculated and measured particle velocity.

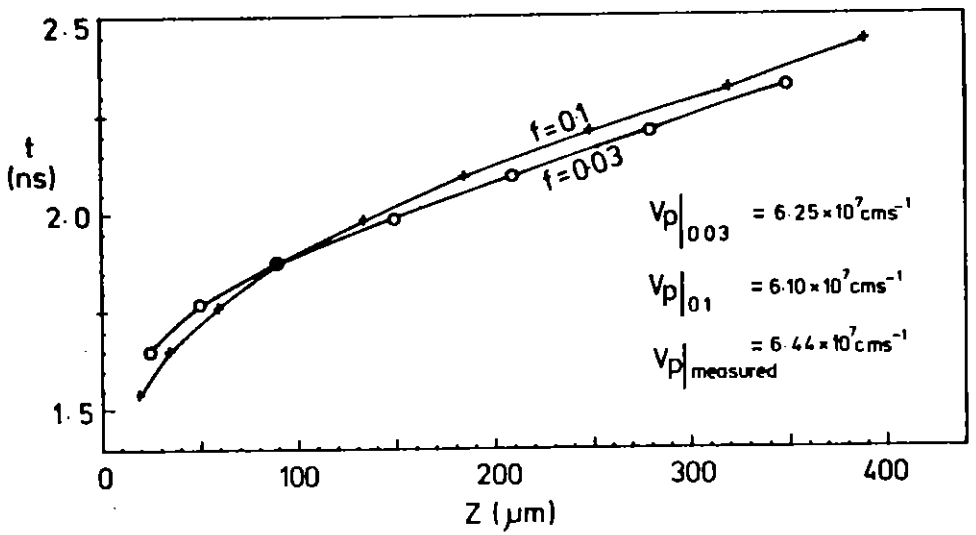

A1.27 Calculated and measured particle velocities.

References

A1.1 CLF Annual Report, RL84049, Section A1-6, (1984)

A1.2 D Ludwig, C Mahn, A Eschluech and P Voight Plasma Physics, 16, 69 (1974)

A1.3 S Obenschain et al., Phys. Rev. Lett. 46, 1402 (1981); A J Cole et al, J Phys. D 15, 1689 (1982)

A1.4 G Zimmerman and W Kruer, Comments Plasma Phys. Controlled Fusion 2, 85 (1975)

A1.5 W C Mead et al., Phys. Fluids 5, 1301 (1984)

A1.6 J Tarvin et al, Phys. Rev. Lett. 51, 1355 (1983)

A1.7 B Yaakobi et al. Phys. Fluids, 27, 516 (1984)

A1.8 CLF Annual Report, RL84049, Section A6.7.2 (1984)

A1.9 A P Fews and D L Henshaw, Nucl Inst Meth, 197, 517-529 (1982)

A.10 J L Bobin, M Decroisette, M Meyer and Y Vitel, Phys Rev Lett, 30, 594 (1973)

A.11 K Tanaka, L M Goldman, W Seka, M C Richardson, J Soures and E A Williams, Phys Rev Lett, 48, 1179 (1982)

A.12 R E Turner, D W Pillion, B F Lasinski and E M Cambell, Phys Fluids, 27, 511 (1984)

A.13 E McGoldrick, S M L Sim, R E Turner and O Willi, Opt Commun, 50, 107 (1984)

A.14 H Figueroa, C Joshi, M Azechi, N A Ebrahim and K Estabrook, Phys Fluids, 27, 1887 (1984)

A.15 W Seka, E A Williams, R S Craxton, L M Goldman, R W Short and K Tanaka, Phys Fluids, 27, 2181 (1984)

A.16 S J Karttunen, Laser and Particle Beams, (to be published) (1985)

A.17 V L Ginzburg, The Propagation of Electromagnetic Waves in Plasmas (Pergamon Press, New York) (1964)

A.18 A Simon and R W Short, Phys Rev Lett, 53, 1912 (1984)

A2 LASER COMPRESSION AND DYNAMICS

Editor A J Cole

A2.1 INTRODUCTION

A J Cole (RAL), T A Hall (Essex)

The experiments performed during this past year under the auspices of this group highlight several major themes of research in the area of laser driven compression.

With the commissioning of the new twelve beam target area a major effort has been applied, both experimentally and theoretically, to ensure the achievement of maximum uniformity of illumination, and also to understand the factors which still limit us in this area.

Also, several exciting new developments in experimental techniques have been tried out during the reporting period. Sections A2.2.6 and A2.4 describe a novel and potentially very powerful technique for diagnosing the structural integrity and stability of laser accelerated targets, both in planar and spherical geometry.

The point-projection X-ray backlighting technique first, reported last year, has been extended to planar target measurements in a rewarding collaboration between Imperial College, RAL and the Naval Research Laboratory.

A2.2 TWELVE BEAM IMPLOSION EXPERIMENTS

A2.2.1 Uniformity and target coupling measurements

C L S Lewis, M J Lamb, P McCavana, J McGlinchey, S Saadat (QUB),
M H Key, W T Toner, A J Cole (RAL), T Barbee (Stanford University)

Preliminary experiments have been carried out to characterize and optimize target irradiation conditions for the new twelve beam geometry. In particular beam timing, beam pointing, beam balance and focussing conditions have been investigated. An 800psec 0.53 μm pulse was used with up to 250J of energy in twelve beams. A thirteenth

100ps, 1.06 μm beam was also available for use in backlighting experiments with up to 35-40J of energy.

Pulse length and relative timing were measured using conventional streak techniques. The twelve driver beams derive from a single long amplified oscillator pulse whose length is measured in the laser area using an infra red Si streak camera. This pulse is split into six each of which pass through a KDP frequency doubling crystal. The six beams are then split in two again and sent to the target chamber. The green pulse length is measured using an optical S20 streak camera.

Each pair of green beams were timed with respect to each other by recording the x-ray emission from a solid metal target on an x-ray streak camera with a caesium iodide photocathode. Then, keeping one member of one pair fixed as a reference each pair was timed with respect to it. The twelve beams were timed to arrive at the centre of the target chamber within about twenty picoseconds of each other. The delay between the main driver pulse and the backlighting pulse was also constantly monitored using the x-ray streak camera as shown in Fig A2.1.

To achieve uniform illumination conditions it is important that the beam pointing be accurate to within about 10% of the target diameter. This was checked by tight focussing onto the surface of a solid glass sphere coated with about 1 μm of plastic. Local burn-through occurrred resulting in bright emission spots and three orthogonally viewing x-ray pinhole cameras were used to simultaneously record the position of the twelve beams on the target surface. The appropriate adjustments to the steering and alignment optics were made and the pointing in Fig A2.2 which shows a 180 μm diameter target is accurate to within 15 μm i.e. <10%.

In compression experiments the driver beams are defocussed to improve illumination uniformity. The defocussing may be either positive or negative as shown in Fig A2.3.

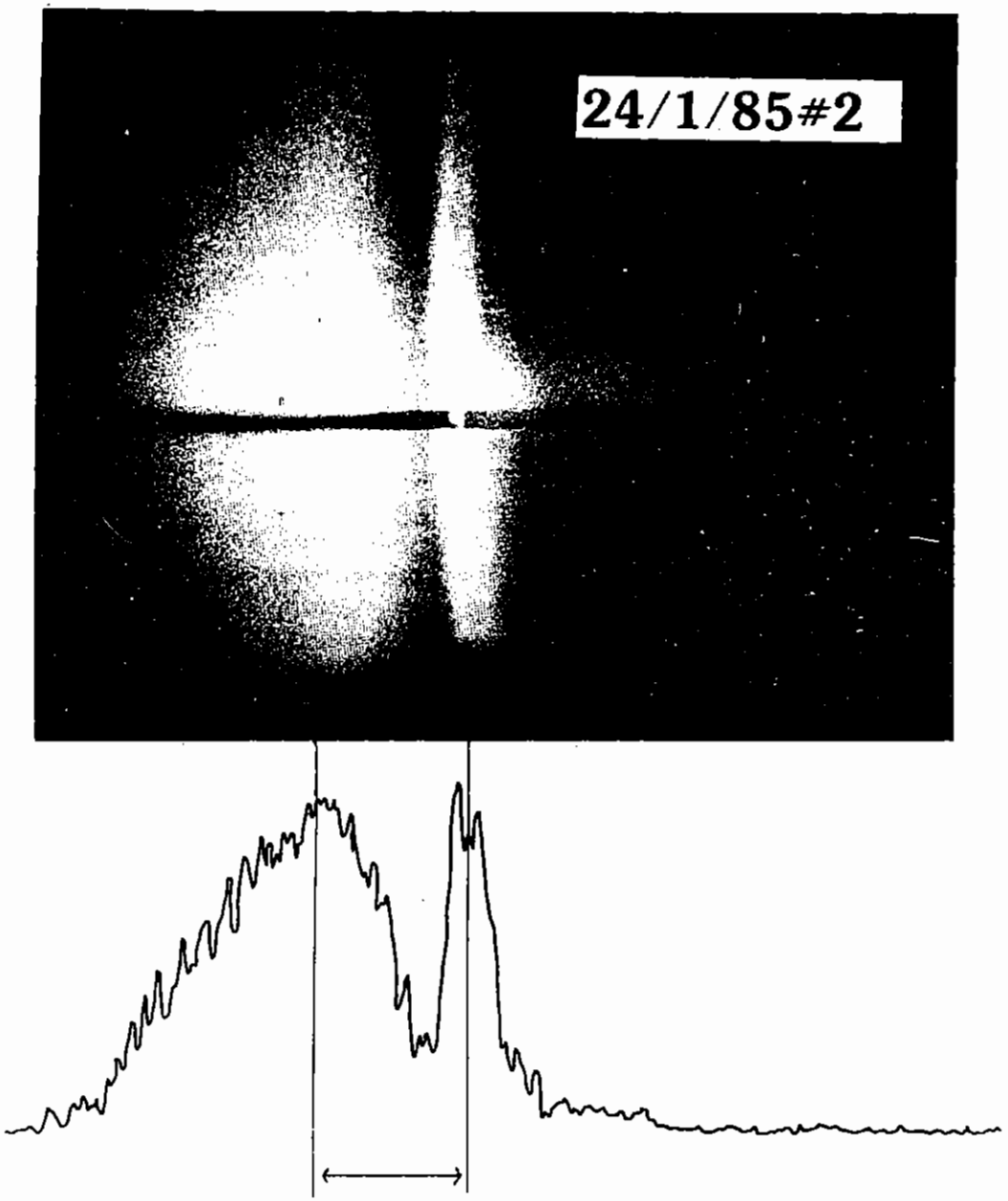

Fig A2.1 Relative timing of long and short pulses

16/1/85#3

12 λ=0.53um BEAMS

E=39 J

R=180 um

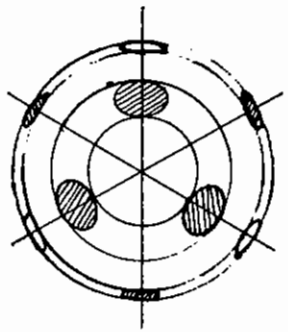

BRIGHT

DIM

Fig A2.2 Pinhole images from 2 almost perpendicular views, for light focussing

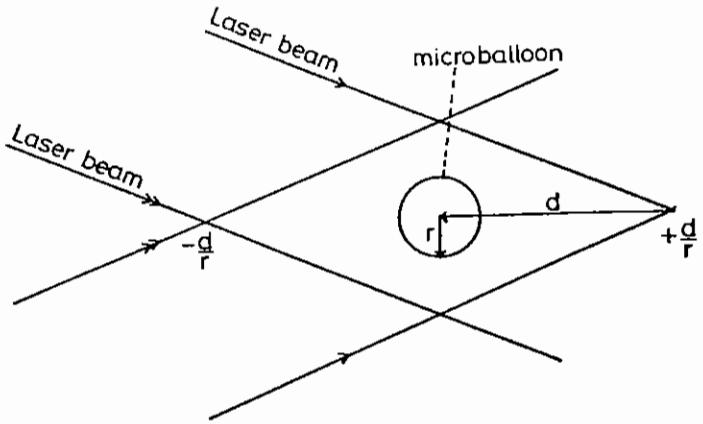

Fig A2.3 Focussing nomenclature

However while increasing the d/r ratio improves the illumination uniformity it reduces the fraction of laser radiation absorbed. Plasma calorimetry was used to measure the absorbed fraction as a function of d/r and the results are shown in Fig A2.5. The plasma calorimeters were placed in random positions in the target chamber since the plasma blow-off from a uniformly irradiated spherical target is believed to be symmetrical.

The illumination uniformity was estimated indirectly from the uniformity of self emission from the plastic shells (Fig A2.4). the more sensitive method of using plastic coated glass targets to observe local burn through at high irradiance points was not used simply due to lack of time. Uniformity was found to be satisfactory for d/r ratios greater than about 8, and 10 was ultimately chosen. It is worth noting that the optimum d/r is expected, from simple geometrical

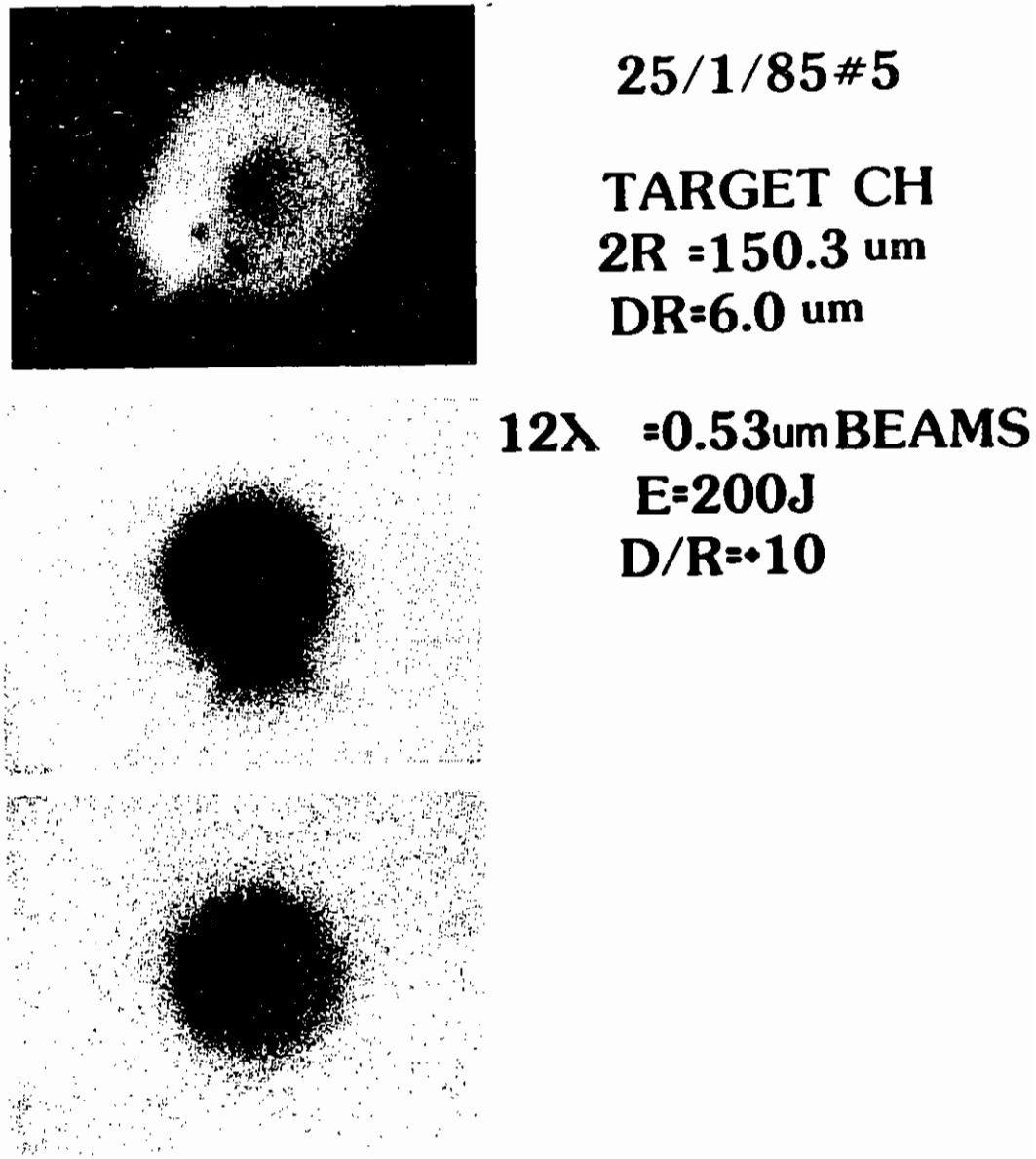

Fig A2.4 Pinhole images from 3 almost orthogonal views (note the bright edge feature is due to the support stalk).

considerations to scale linearly with the f number of the lenses. Hence for 6 beam geometry with f = 1.0 the optimum d/r was around 4.0. The d/r value of + 10.0 for 12 beam goemetry with f = 2.5 is consistent with this.

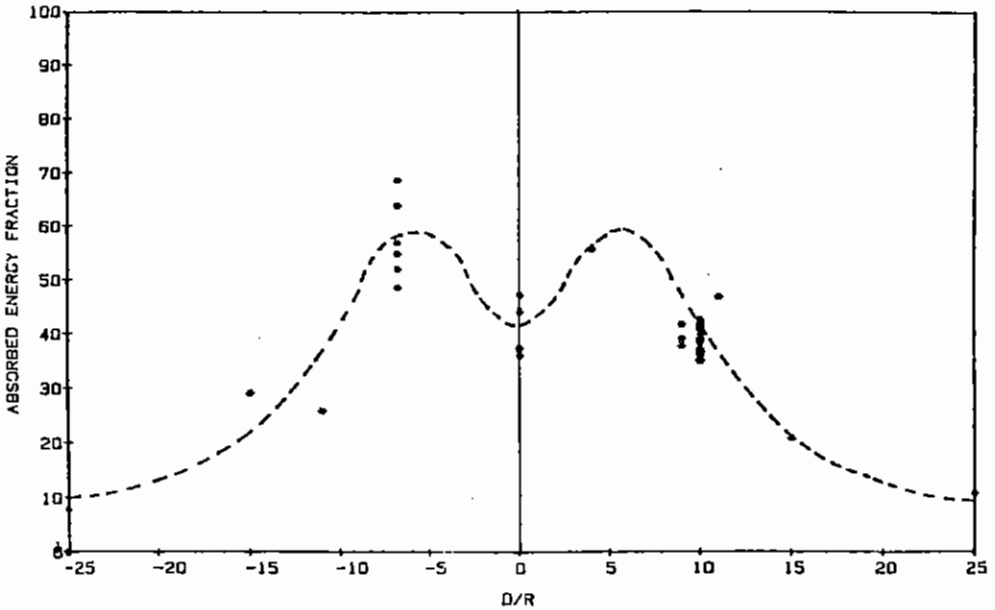

Fig A2.5 Absorbed energy fraction VS D/R for twelve beam irradiation

Finally the energy in each of the twelve beams should be as near as possible equal and this was achieved by a suitable choice of beam splitter and by using the half-wave plates before the frequency doubling crystals to tune the effective conversion effeciency down to that of the poorest crystal. A distribution of energies with a standard deviation of 6% was typical.

A2.2.2 Extended Source Backlighting Measurements

The first phase of the x-radiography exeriments involved conventionaol extended source backlighting. The backlighting sources were either copper or gold foils 7 μm thick and 500 or 350 μm diameter. these 'lollipop' type targets were used rather than large foils because they gave more uniform emission when irradiated by a non-uniform backlighting beam presumably due to the absence of a lateral energy transport loss channel. A pinhole, usually of 6 or 12μm diameter was used to image the backlit microballoon on to the active x-ray detector - a PII phosphor plus image intensifier.

Microdensitometry of the recorded radiograph images yielded optical density profiles which were converted into transmission profiles using a calibration density step wedge printed on each piece of film. This was compared to theoretically calculated transmission profiles generated by converting the mass density profiles from the medusa code into transmission profiles taking into account the recorded spectal distribution in the backlighting source, the filters and the pinhole size used. The data analysis techniques have been previously described in reference A2.1 and yield the essential parameter $r_{\frac{1}{2}}$ which defines the target radius at which 50% transmission of the backlight is observed. Figures A2.6 and A2.7 show typical radiographs with the wall position indicated.

A2.2.3 Point projection radiography using Bragg crystals and multi-layer x-ray mirrors

The standard extended source type of backlighting suffers from the disadvantage that the analysis of results is complicated by the polychromaticity of the backlighting spectrum. A new technique of quasimonochromatic point projection radiography has also been used to diagnose the compressed targets and is described in section A6.7.3 and discussed in reference A2.2. The backlighting point sources were generated by tight focussing the infra-red beam onto the tip of a 10μm wire, which for this experiment was either gold or gold coated with 1 μm of bismuth. A system magnification of 90 was used with the point source 5mm from the target. Figs A2.8 and A2.9 show typical results.

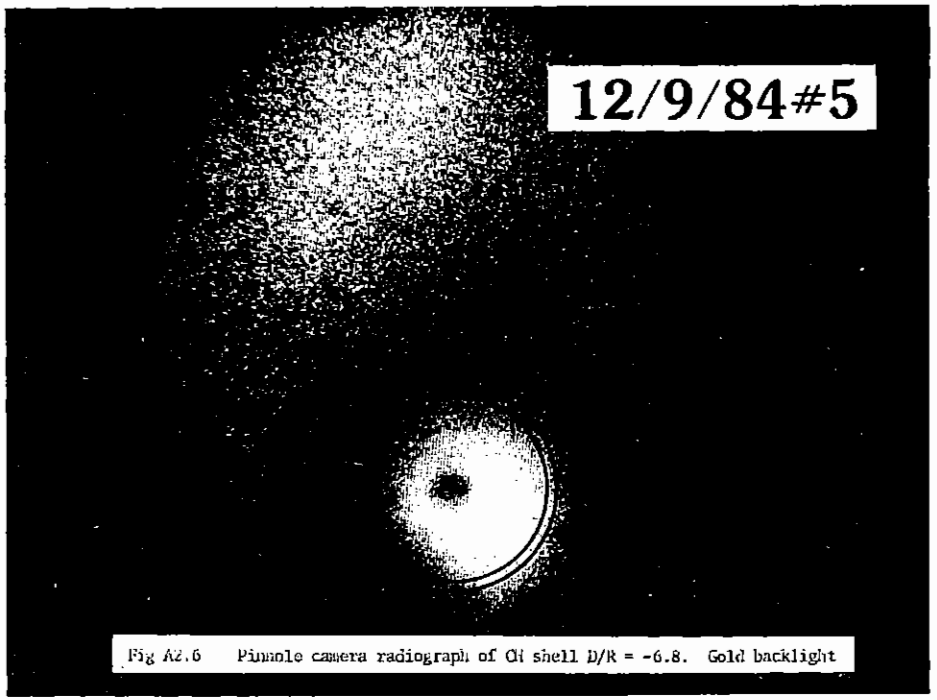

Fig A2.6 Pinhole camera radiograph of Cl shell D/R = -6.8. Gold backlight

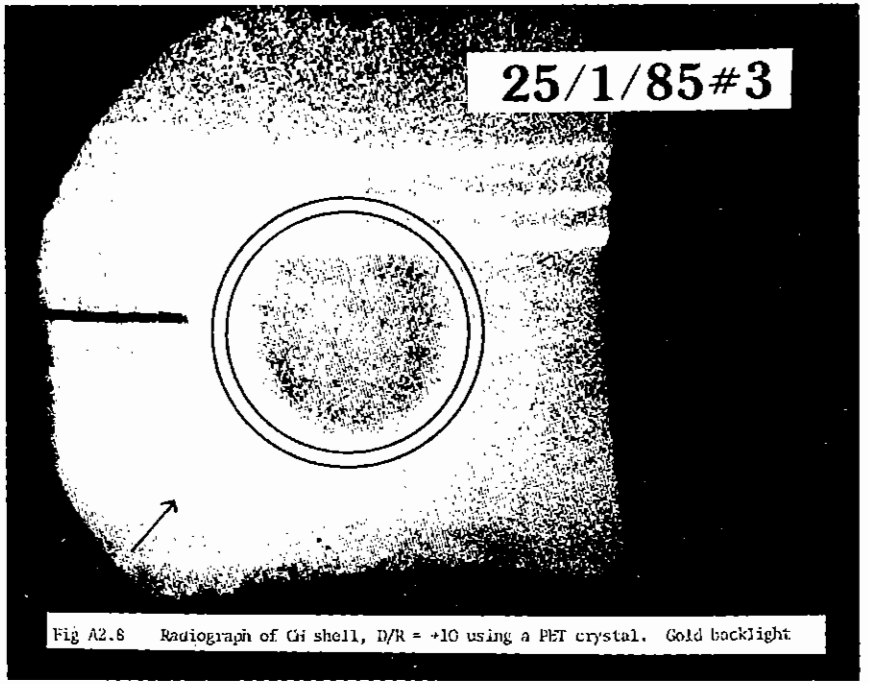

Fig A2.8 Radiograph of Cl shell, D/R = +10 using a PET crystal. Gold backlight

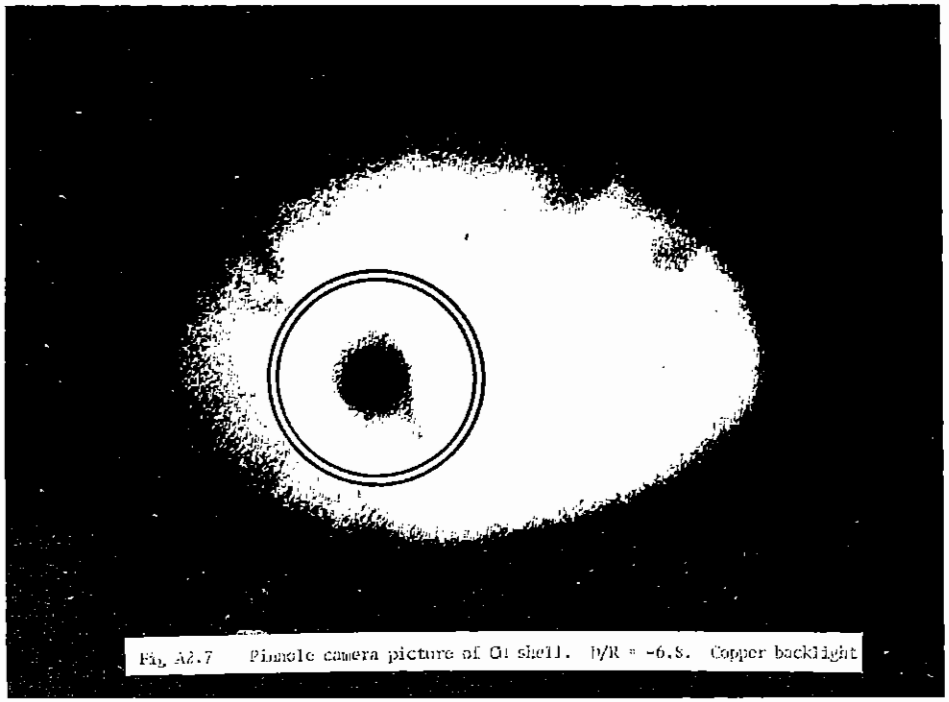

Fig A2.7 Pinhole camera picture of Cl shell. D/R = -6.8. Copper backlight

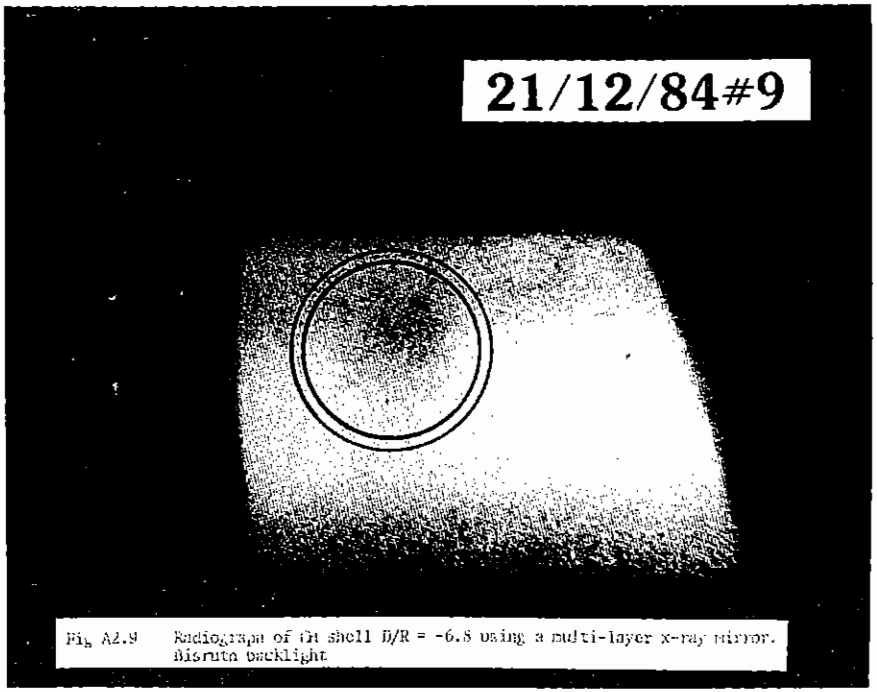

Fig A2.9 Radiograph of Cl shell D/R = -6.8 using a multi-layer x-ray mirror. Bismuth backlight

In Fig A2.8 the dispersing element was a single PET crystal. The resolution of this crystal, as determined from the narrowest spectral feature observed on a recorded Cl spectrum at around 4.4Å was $\sim$ 1000. In Fig A2.9 the dispersing element was a multilayer x-ray mirror (Ref A2.3). This consists of layers of W and C with a periodicity of 20.6Å (effective 2d = 41.2ÅO. This was calibrated as described in section A.7.2 and showed a resolution $\sim$ 50.

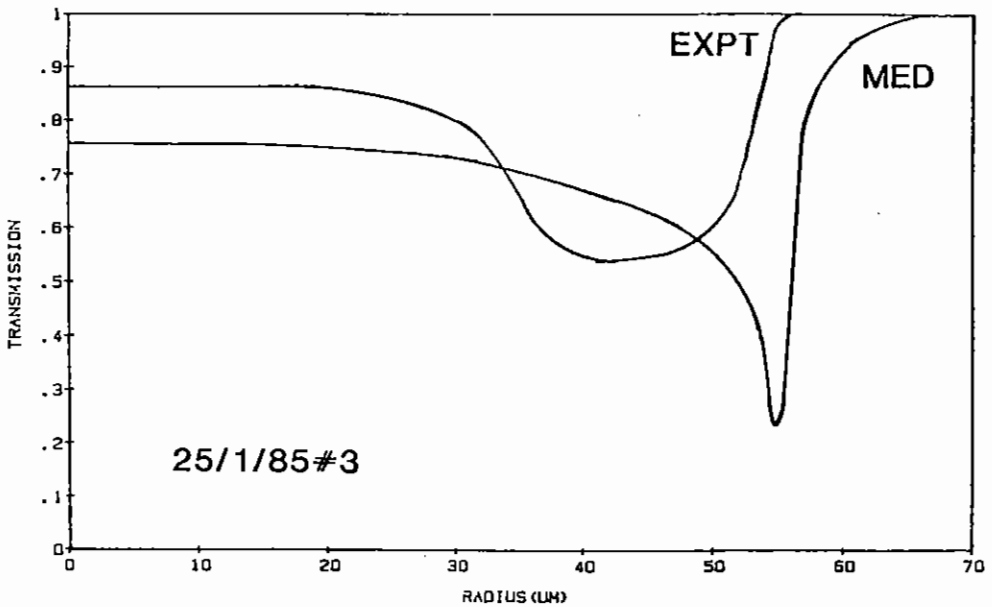

Fig A2.10 Experimental and theoretical transmission profiles

Fig A2.10 shows the experimental and theoretical transmission profiles for shot 3 on 25/1/85. In this case the theoretical profile was calculated directly from the mass density profile generated by the Medusa code assuming a single probe wavelength and does not take into account the backlighting source size or any refractive effects.

Table A2.1 summarizes some of the shots analyzed to date. Fig A2.11 shows the Medusa generated implosion trajectory which should be a good approximation to the trajectories for all the points shown. The experimental points are also indicated. Fig A2.12 summarizes the shots in Table (A2.1). It can be seen that at early times the compressions appear to be better than predicted by the Medusa code. By peak compression however they are significantly worse. The most likely explanation for this can be found in the driver pulse temporal profile which in the code was assumed gaussian. Fig A2.13 shows the assumed and actual pulse shapes. If more energy is being absorbed at early times than the code assumes then one expects the type of discrepancy observed. The target is driven harder at early times with the time to peak implosion τ_{imp} reduced. This will have the effect of making $r_{\frac{1}{2}}(exp)/r_{\frac{1}{2}}(med) < 1$ before compression, > 1 after compression and $= 1$ at some time between the real implosion time and the gaussian pulse predicted implosion time, as observed experimentally. Further analysis with more realistic pulse profiles is currently being carried out. However at this stage a preliminary conclusion which is independant of the exact r-t trajectory simulations is that the overall degree of spherical symmetry in the imploding targets is better than observed under six beam irradiation conditions as discussed in reference (A2.1)

SHOT NUMBER	R_{INIT} (um)	DR_{PLAS} (um)	I_{ABS} x 10^{14} W cm^{-2}	B/L MATERIAL	PINHOLE DIAMETER (um)	PROBE DELAY (ps)	τ_{imp}(MED) (ps)	$\frac{R_{\frac{1}{2}}(MED)}{R_o}$	$\frac{R_{\frac{1}{2}}(EXP)}{R_o}$
(a) 25/1/85 #7	67.7	6.0	0.91	Au	-	-30	1300	0.632	0.081
(b) 25/1/85 #3	71.3	8.2	0.97	Au	-	-30	1500	0.721	0.535
(c) 25/1/85 #1	64.1	7.4	0.96	Au	-	+400	1400	0.210	0.238
(d) 24/1/85 #9	67.9	8.7	1.04	Au	-	+370	1500	0.324	0.587
(e) 23/1/85#13	64.45	9.6	0.83	Au	-	+170	1600	0.602	0.439
(f) 23/1/85 #2	63.55	8.7	0.84	Au	-	+20	1500	0.655	0.484
(g) 22/1/85#20	62.2	7.8	0.85	Au	-	+20	1400	0.615	0.393
(h) 21/12/84#9	66.1	8.7	0.27	BL	-	+1000	2250	0.407	0.434
(i) 6/12/84#18	67.0	7.8	0.54	Au	7.0	+100	1700	0.679	0.555
(j) 6/12/84#13	68.3	8.3	1.33	Au	7.0	+300	1300	0.255	0.274
(k) 19/9/84 #3	83.95	8.5	0.92	Au	10.0	+900	1950	0.239	0.240
(l) 18/9/84#12	66.35	9.0	0.66	Au	12.0	+700	1700	0.323	0.668
(m) 12/9/84 #5	78.35	7.4	0.79	Au	10.0	+300	1750	0.550	0.593
(n) 7/9/84 #3	70.00	6.0	0.72	Au	12.0	+500	1400	0.203	0.382

TABLE A2.1

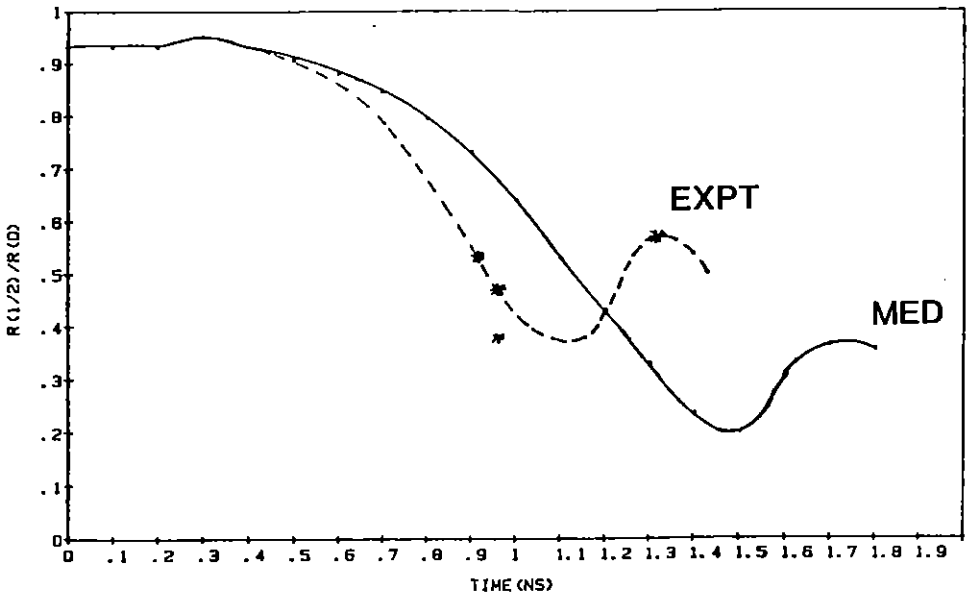

Fig A2.11 Implosion trajectory for shots 22/1/85 2, 23/1/85 2, 25/1/85 3, 24/1/85 9

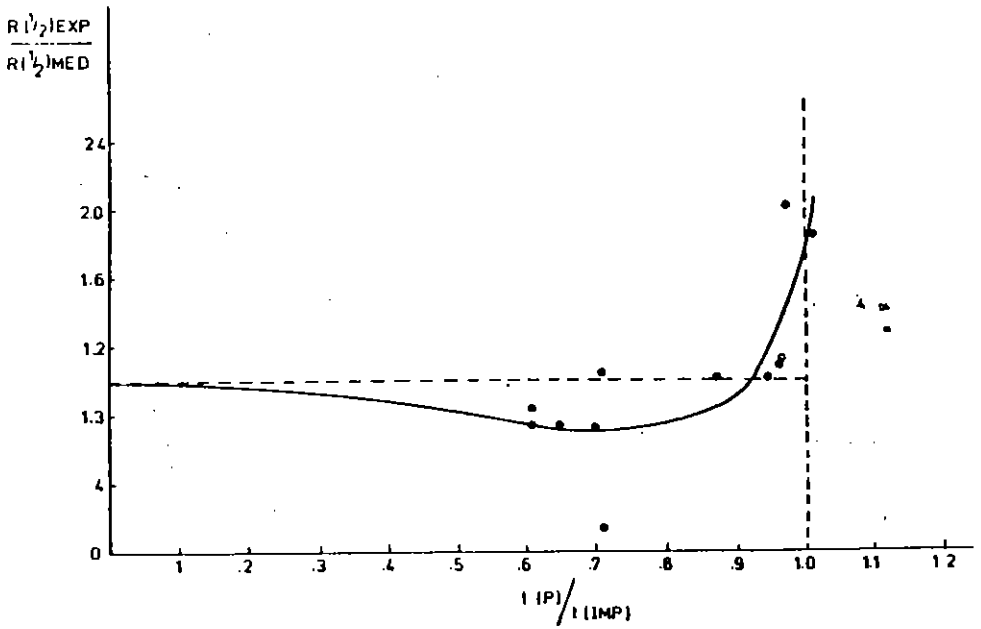

Fig A2.12 Summary of some 12 beam compression shots

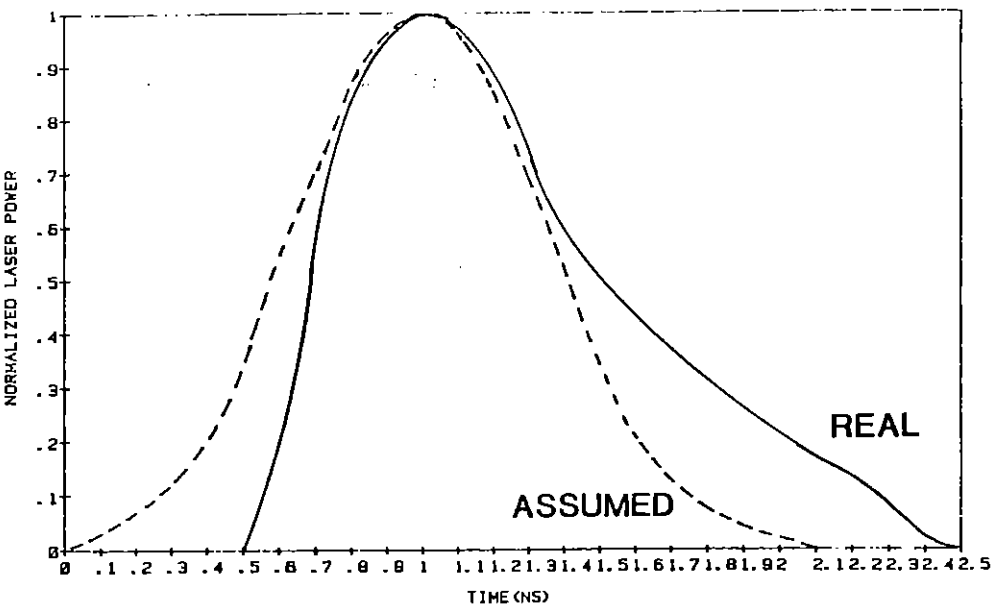

Fig A2.13 Assumed and real laser pulse profiles

A2.2.4 Target emission measurments

Both the radiographic techniques described in preceding sections ideally result in absorption features in a uniformly exposed background which in one case has spectral dispersion in one direction and in the other case is spectrally integrated. However the density recorded on film at any point in the radiography may have contributions from noise at high gain, fluorescence from crystals, filters -and surfaces, and direct exposure to fast electrons or hard x-rays. Most of these effects are believed to be insignificant or else may be minimized or eliminated by various experimental precautions. However there is also the genuine image density contribution due to self emission from the irradiated CH target which is obviously worse in the point projection than in the pinhole imaging case. Self emission images of plastic balloons were shown earlier in Fig. A2.4, and Fig. A2.14 shows a

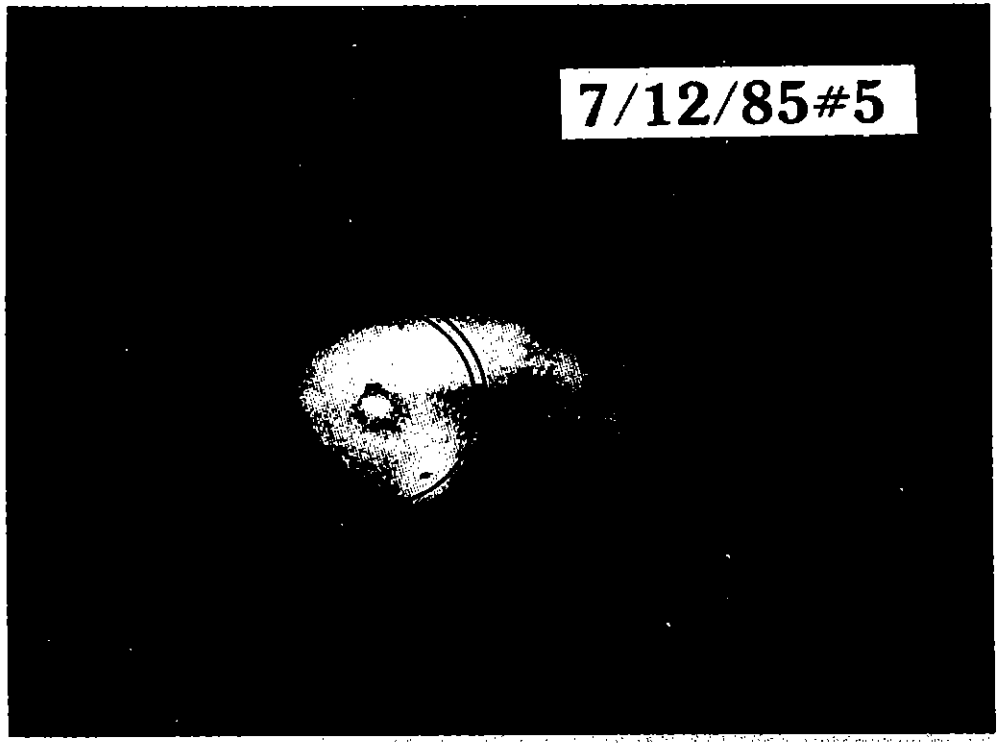

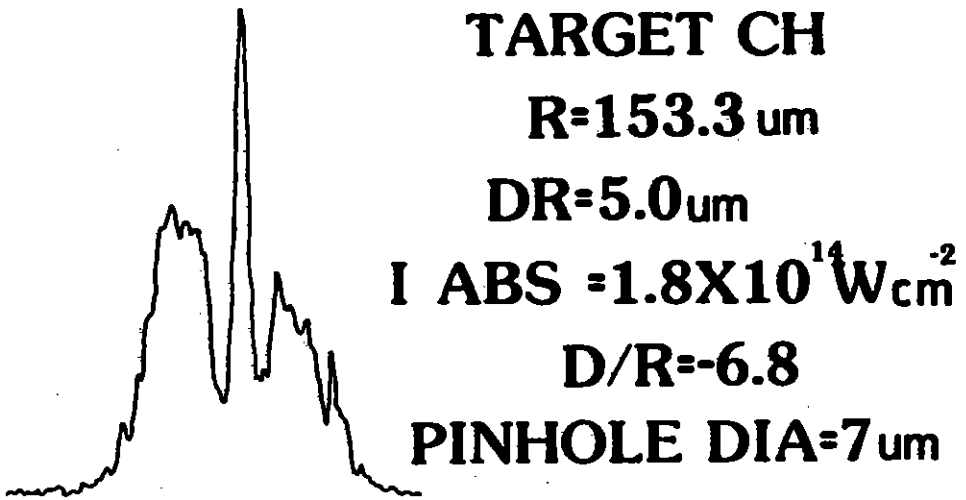

Fig A2.14 Compressed CH shell showing bright core emission

brightly emitting core feature in a compresed microballoon. the absorbed irradiance in this shot was 1.8×10^{14} W cm^{-2} which was unusually high for this experimental run. Unfortunately no space resolving spectrometer was used on this shot but the core emission is probably dominated by Cl emission lines arising from target impurities.

The emission from the plastic plasma has two main components - continuum in the spectral 'window' of the detector and line emission due to impurities in the plastic, and the glue with which the microballoon is mounted onto its support stalk. For low irradiance the continuum emission is negligible compared to the backlighting brightness at around the probe wavelength. However for absorbed irradiances between 0.5×10^{13} and 1.0×10^{14} W cm^{-2} this starts to become significant.

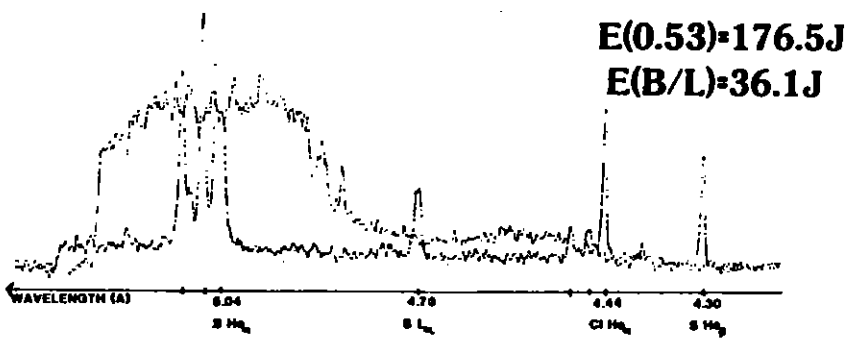

Fig A2.15 Simultaneous spectra of target self emission and backlighting target

Fig A2.15 shows a gold backlight and a plastic target emission spectrum recorded on a minicrystal spectrometer. The sulphur lines arise from sulphur present in the glue and the chlorine lines are at least partially due to chlorine in the plastic of the target. Improved purity in the manufacturing process and the use of unmounted targets (see section A6.7.1) would eliminate this problem.

A2.2.5 Harmonic Imaging Studies of Illumination for twelve laser beams

V Aboites, S M L Sim, E McGoldrick (Essex)
D Bassett, I Ross, A Bell (RAL)

Introduction

Previous work on harmonic imaging studies of illumination uniformity for 0.53μm ablative compressions using the six beams of the RAL. Vulcan laser (A2.4) (A2.5), have shown, in agreement with computer calculations (A2.6), that the best degree of uniformity of illumination is obtained for a D/R focussing parameter of D/R=5 (D is the distance of the focal point beyond the target centre and R is the target radius).

These computer calculations show that the percentage non-uniformity of laser irradiance (defined as (Imax/Imin-1)*100% where Imax and Imin are the maximum and minimum irradiances on the target surface) for a symmetric twelve beam irradiation laser system is approximately 3% (for a six beam system it is ~12%).

In this experiment a study of the uniformity of illumination of imploded microballoons was made when they were irradiated by the twelve beams of the RAL. Vulcan laser under different focussing conditions. This experiment is therefore a continuation of previous work.

Several linear and non-linear processes in the interaction of intense electyromagnetic radiation with plasmas provide us with information about very specific regions of a plasma. Numerous studies (e.g.

(A2.7),(A2.8)) have shown that the critical density region of a plasma n_c can be identified with the region of generation of $2\omega_o$ radiation. Similarly, it has been shown (e.g. (A2.9),(A2.10) that generation of odd-integer half harmonic emission such as $3\omega_o/2$, is due to processes occurring at or near the quarter critical $n_c/4$ region of the plasma.

For this experiment, in order to study the smoothness of the critical (n_c) and quarter critical ($n_c/4$) surfaces of the plasma produced by different irradiation conditions, observations were made of the $2\omega_o$ and $3\omega_o/2$ radiation emitted by the imploded microballoons.

Experiment

Glass microballoons of diameter 170μm to 185μm were irradiated at intensities of 10^{13} to 10^{14} Wcm^{-2} by using twelve laser beams (λ_o= 0.53μm) in a dodecahedral symmetry. The pulse length was 1ns and the beams were focussed using f/2.5 lenses.

The focussing of the twelve laser beams on the microballoon as well as the collection of the harmonic emission emitted and the alignment of the microballoon was identical to that described previously (A2.4) (A2.5).

During this experiment care was taken to fire the laser at time intervals not less than 45 minutes to ensure best possible laser beams profiles (A2.5).

For our experimental conditions the computer simulations show that $2\omega_o$ light which is specularly reflected by an ideal spherical target surface would be observed as shown in Fig A2.16.

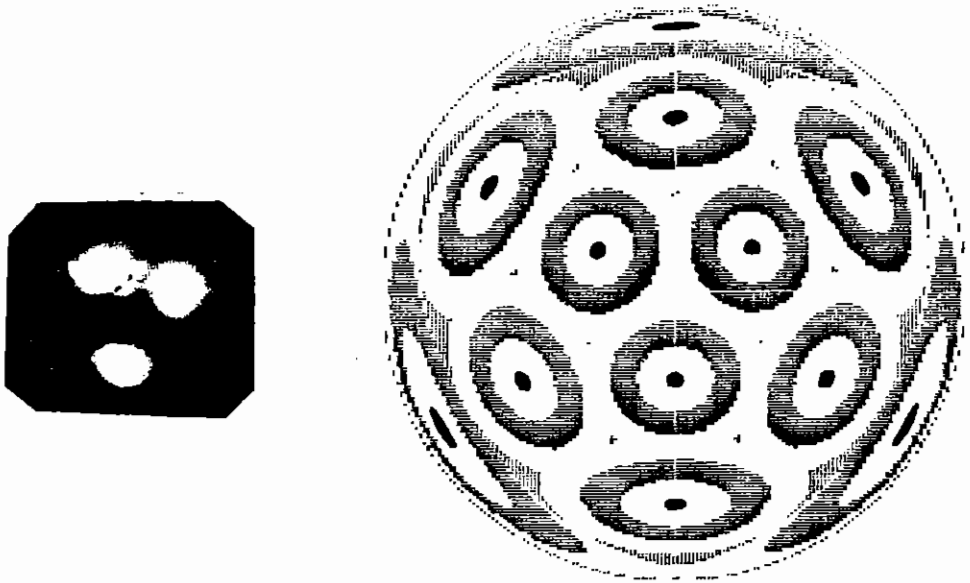

Fig A2.16 Computer simulation of 2Wo emission and experimental result for an inner triangle shot

The three symmetric central spots correspond to light specularly reflected from the three symmetric front laser beams. These three spots are considered the vertices of a triangle which we called 'inner triangle'. In analogous way the next three symjmetric spots consitute the 'external triangle'. Finally, the last set of three laser beams correspond to light specularly reflected from the back laser beams. These spots constitute the 'outer triangle'. When a microballoon is irradiated, irregularities on the critical surface occur due to variations of irradiation uniformity on the microballoon surface. The degree of non-uniformity of illumination is reflected in the deviation of the emission pattern from the ideal shown in Fig A2.16.

Therefore, irregularities on the critical surface are manifest by observation of $2\omega_o$ radiation coming from regions of the target not corresponding to these twelve 'ideal' spots.

Results

In order to check the pointing accuracy of the laser beams, surface focussed shots were obtained for the beams corresponding to the vertices of the 'inner', 'middle', and 'external' triangle. (For a surface focussed shot the beams corresponding to the vertices of the 'outer' triangle are not-observable since they are out of our collection optics). The results for an inner triangle are shown in Fig A2.16.

The computer simulations show that an optimum improvement on the uniformity of irradiation should occur for a D/R parameter of D/R > ~8. Fig A2.17 show the observed pattern for D/R=3, D/R=5 and D/R=8. It can be seen how a significant improvement occurs as the parameter D/R is increased.

Fig A2.17(a) and (c) show a very irregular $2\omega_o$ emission pattern which reflects the poor uniformity of illumination. Fig A2.17(e) shows the expected point-like emission structure characteristic of better uniformity of illumination. In this case the resemblance between the observed $2\omega_o$ emission pattern of Fig A2.17(e) and the computer calculated pattern shown in Fig A2.16 agree in the strucure but differs in the relative positions of the emissions spots. This is probably related to the modifications which atmospheric turbulence introduces in the laser beams on their way to the target chamber. Nevertheless, Fig A2.17(e) shows a clear improvement in the uniformity of illumination as expected from the information provided by the computer simulations.

Conclusions

The optimal condition for uniformity of illumination of imploded microballoons wih twelve laser beams was found for a D/R=8. This is in agreement with computer simulations which predict optimal illumination for D/R>~8.

These results are preliminary and it has not yet been possible to achieve the ideal condition under which 3% uniformity can be obtained

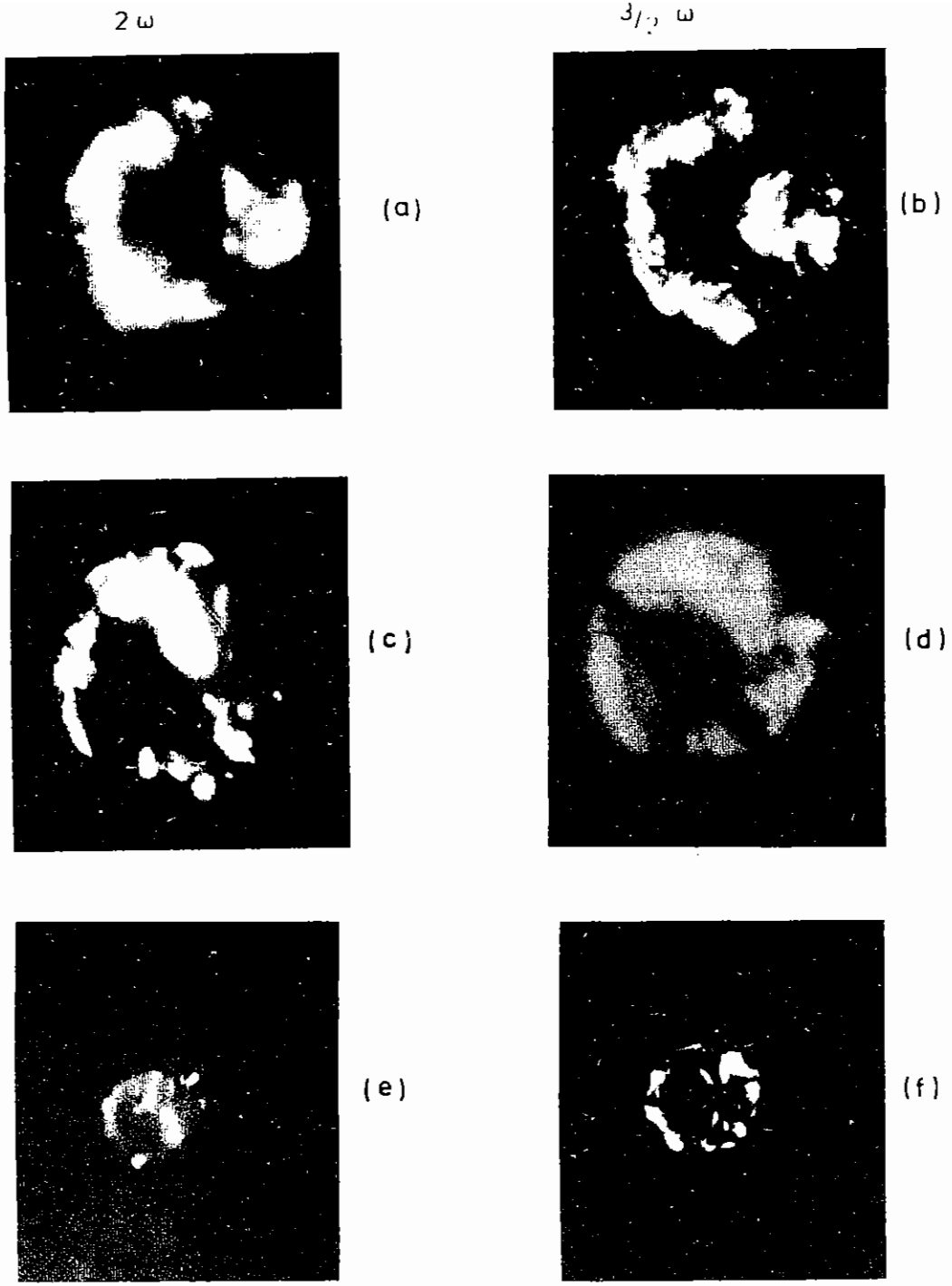

Fig A2.17 Harmonic images for D/R : 3 ((a) and (b)) D/R : 5 ((c) and (d)) and D/R : 8 ((e) and (f))

with 12 beam irradiation. Section A2.3 discusses the criteria which are necessary to achieve this.

A2.2.6 Measurements of target ρR with CR39 plastic

A P Fews, P M Evans Bristol University

An experiment was conducted in November 1984, during the TAW target area commissioning, to measure thermonuclear product distributions from DT filled glass microballoons, which had undergone 12 beam ablative implosions at 0.53μm. The experiment concentrated on thin walled balloons producing "hot ablative" compression and higher thermonuclear yield. The techniques involved have been summarised in earlier annual reports (A2.11). Direct measurements were made of particle energy losses and hence the distribution of (ρR) for particles escaping from the target. The CR-39 was positioned ~30mm from the target with its surface at an angle of ~60° to the line-of-flight. Figure A2.18 shows the measured mean ρR at the time of thermonuclear reaction plotted against the initial ρR (ie target wall thickness). Each point corresponds to a different shot: the crosses show data gathered during 1983 in the 6 beam TA1 target chamber and the two solid points are from this experiment. The final ρR of the target can be seen to vary between ~6 and 10 times the initial wall thickness for measured ρR values of between 2 and 9 x 10^{-3} g.cm^{-2}.

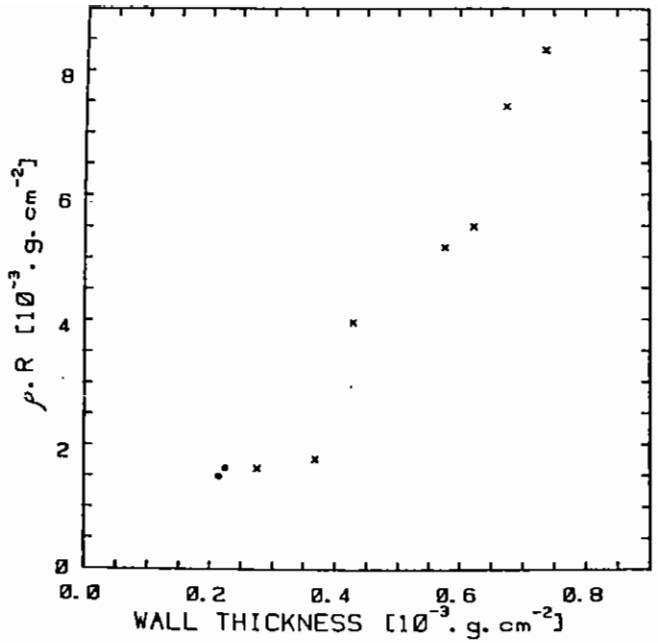

Fig A2.18 Mean compressed ρR against initial target wall thickness

In order to study the uniformity of compression the available solid angle has been used to surround the imploding target with CR-39. As an example of the results obtained Fig A2.19 shows two measured α-particle spectra for shot 04/8/11/84 taken at two positions, 120° apart. The data are plotted in terms of range loss in the target (1 μm in CR39 is equivalent to 1.3×10^{-3} g.cm^{-2}). Two features emerge. The means of the distributions differ by ~5%, illustrating a slight non-uniformity of compression. However both distributions show some 34 tracks with small range loss, < 4μm. This provides evidence of local break up of the imploding shell. This run was carried out at an early stage in the optimisation of the 12-beam illumination system and the data may illustrate the consequences of non-uniform irradation due to beam overlap. This is an important direct observation of the shell condition at the time of thermonuclear reaction. Further shots for

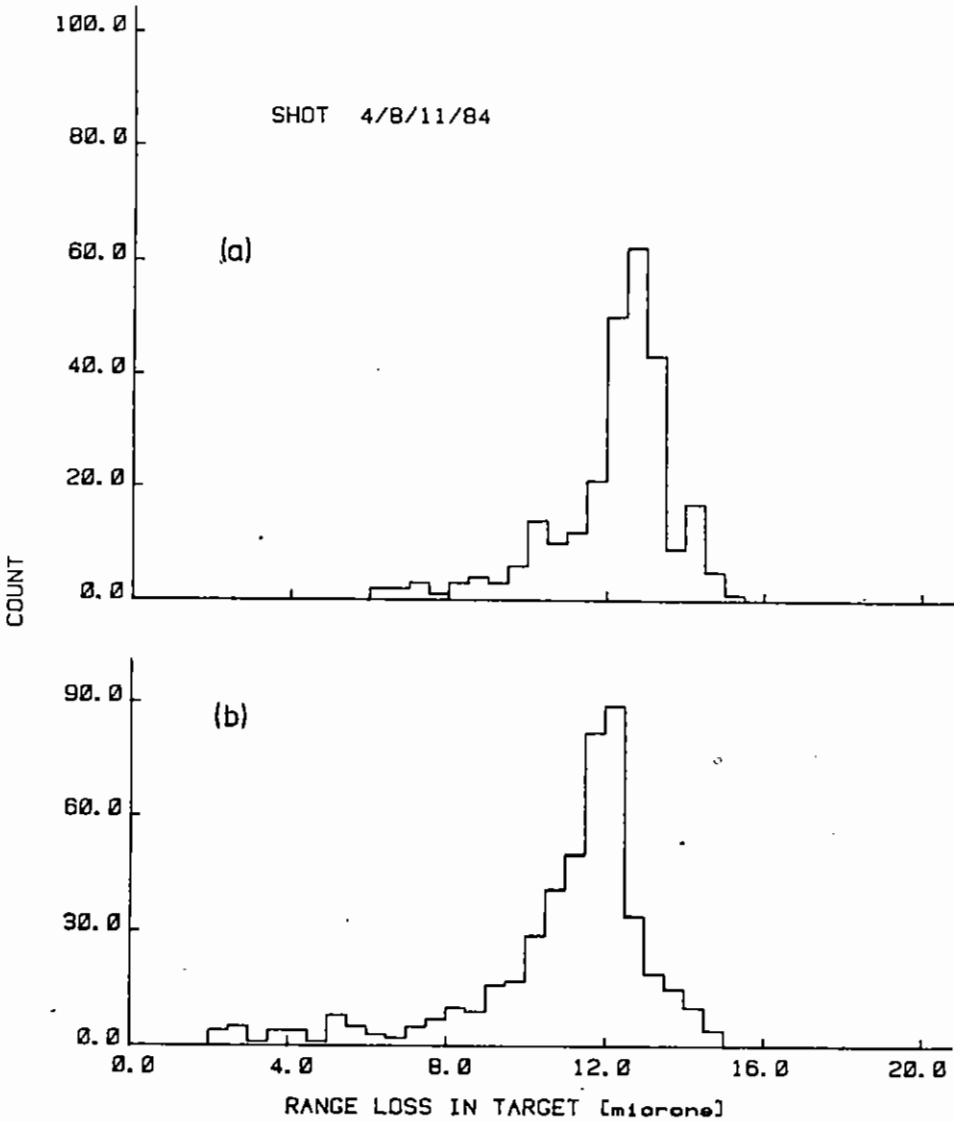

Fig A2.19 Range loss distributions of the same target for two directions 120° apart

this run are currently being analysed and there is clearly scope for continued study of uniformity of implosion using this technique, under optimised illumination conditions.

A2.3 EXPERIMENTAL FACTORS AFFECTING UNIFORMITY OF ILLUMINATION

A R Bell, D J Nicholas, W T Toner (RAL)

In the CLF annual reports of 1982 (A2.12) and 1983,(A2.13) we reported on the analysis of the uniformity of illumination of spherical targets by a limited number (i.e. 6 or 12) laser beams under ideal conditions. We demonstrated the advantages of a 12 beam system under a variety of conditions. The 12 beam system is now in operation and we need to consider the optimisaion of its performance, as regards uniformity of illumination, as influenced by the various experimental and technological constraints which degrade its performance from the ideal. We need to ascertain the dominant factor determining the uniformity of illumination in the practical system, and therefore the point at which improvement should be sought. We have examined deviations from the ideal case of a 12-beam system in which each beam is focussed by f/2.5 lenses, and has an intensity profile which is a fourth-power super-Gaussian dropping to 1/e of its peak at 0.7 times the radius of the focussing lens. We do not take account of the variation of energy absorption as a function of angle of incidence, or of smoothing by redistribution of energy by transport processes in the target. The beams are focussed at a distance beyond the centre of a spherical target with radius R, and D/R is allowed to take one of three values, 8, 10 or 12. The three possible values of D/R are examined because a high value of D/R generally gives better uniformity but gives poor energy coupling to the target because a proportion of the beam misses the target. The choice of D/R is thus determined by balancing high energy absorption against good uniformity. If D/R=8, 76 percent of the energy intercepts the target. D/R=10 gives 54 percent, and D/R=12 only 40 percent intercepting the target.

The errors we consider are treated as being non-systematic. We assume that the errors have a Gaussian distribution with a standard deviation

which is the same for all beams even though the actual errors are uncorrelated between each beam (except in the case of the rat-trap calculation where the error is in the target position). Because the calculations contain a random element we repeat each calculation five times and than calculate the average of the five calculated non-uniformities. We always quote the calculated non-uniformity as Imax/Imin, where Imax is the maximum irradiance on the target, and Imin is the minimum. In one sense, this is a little unfair since the non-uniformities would appear smaller if we quoted the RMS variation in the irradiance over the whole surface of the target. We quote the non-uniformity as a 'maximum over minimum' because target implosion is probably limited by the extremes in the irradiance, rather than the general level of non-uniformity.

We examine each of five types of error separately, as a means of comparing them one with another, although in practice they are present together and add to each other.

a) Errors in the Alignment of the beams on target.

In this case the distance (D) of each beam focus beyond the target centre is correct, but the direction of each beam is incorrect such that the beam axis misses the target centre. The alignment errors of each beam, although uncorrelated, are taken to have the same RMS values of either 10, 20 or 40 micron.

Table A2.2: Beam misalignment, Imax/Imin

RMS error (micron)	D/R = 8	D/R = 10	D/R = 12
0	1.03	1.08	1.10
10	1.17	1.13	1.13
20	1.52	1.27	1.20
40	2.19	1.52	1.33

b) Focussing errors leading to errors in D/R

In this case it is assumed that each beam is aligned correctly such that the beam axis passes through the centre of the target, but that there is a random error in the focussing of each beam leading to errors in the actual D/R of each beam centred about the intended D/R. The RMS value of the error is quoted as a percentage of the intended D/R. For example, a 10 percent RMS error when the intended D/R=8 means that D/R for each beam has a Gaussian distribution with a mean of 8 and a standard deviation of 0.8

Table A2.3: Focussing errors, Imax/Imin

RMS error (percent)	Intended D/R = 8	Intended D/R = 10	Intended D/R = 12
0	1.03	1.08	1.10
2.5	1.07	1.12	1.14
5	1.16	1.19	1.17
10	1.36	1.39	1.43

c) Errors in beam energy

In this case the energy in each beam has a Gaussian distribution with a standard deviation which is either 5, 10, or 20 percent of the mean energy in the beam.

Table A2.4: Errors in the energy balance between beams, Imax/Imin

RMS error (percent)	D/R = 8	D/R = 10	D/R = 12
0	1.03	1.08	1.10
2.5	1.09	1.13	1.15
5	1.15	1.19	1.21
10	1.38	1.40	1.42

d) Beams which are non-circular

Some optical aberrations can result in beams which do not come to a circular focus in the far field. A small spherical target can be close enough to the far field for the non-circularity to become important and we model this by assuming that the beams have a profile which is elliptical instead of circular. The ratio $\varepsilon = r_{major}/r_{minor}$ of the major to minor radius for each beam is taken randomly from a distribution of the form $f(\varepsilon) = \varepsilon \exp(-\text{constant} \times \varepsilon^2)$, which is the distribution function of the magnitude of a two-dimensional vector which has a Gaussian distribution in each dimension. The angular orientation of the major axis is randomly distributed in 2π on the surface of the target. The non-uniformity is calculated for distributions $f(\varepsilon)$ with the mean value or r_{major}/r_{minor} equal to 1.1, 1.2 and 1.4. The beam size is normalised such that the area of the elliptical beam is the same as the undistorted circular beam.

Table A2.5: Non-circular beams, Imax/Imin

RMS r_{max}/r_{min}	D/R = 8	D/R = 10	D/R = 12
1.0	1.03	1.08	1.10
1.1	1.07	1.09	1.10
1.2	1.12	1.11	1.11
1.4	1.16	1.13	1.12

e) Target movement in a rat-trap system

The main problem with the rat-trap as a means of suspending a target is adhesion between the target and its support. This results in a displacement of the target away from the point for which the beams are aligned. The beams are then effectively misaligned but in a systematic manner instead of randomly as assumed in calculation a). The target displacement is assumed to have a Gaussian distribution with a standard deviation of 10, 20 or 40 micron.

Table A2.6: Rat-trap errors, Imax/Imin

RMS target displacement (micron)	D/R = 8	D/R = 10	D/R = 12
0	1.03	1.08	1.10
10	1.19	1.12	1.11
20	1.39	1.18	1.12
40	2.14	1.42	1.20

One of the main problems to be overcome would appear to be the errors in focussing (calculation b)) giving rise to variation in D/R between each beam. A fractional error of δ in D/R produces a fractional error

of approximtely 2δ in the irradiance on target because the energy per unit area in the laser beam decreases as D^{-2} away from the beam focus. Errors in D/R are therefore equivalent to errors in the energy balance between beams. However, it should be noted that the primary parameter is the amount of laser energy intersecting the target, rather than D/R itself, and it may be possible to design alignment procedures which take account of this.

A2.4 MEASUREMENT OF THE RAYLEIGH TAYLOR INSTABILITY USING ALPHA PARTICLE BACKLIGHTING AND CR-39 SPECTROSCOPY

P M Evans, A P Fews (Bristol University), A Cole, C Edwards, C J Hooker, D Pepler and W T Toner (RAL), J Wark (Imperial College)

We have developed a technique to measure the growth of instabilities in laser accelerated targets which has a sensitivity independent of the transverse scale of the mass perturbations, down to transverse scales below 1 µm. Previous measurements of the Rayleigh Tayor instability at the CLF (A2.14) and elsewhere (A2.15) have used back-lighting techniques limited by X-ray diffraction to the measurement of structures with transverse scales > 5µm. Although this is well matched to the acceleration phase Rayleigh Taylor instability, much finer structures have been observed (A2.16) in the corona of laser irradiated targets. Strong local variations in irradiation are inevitable in direct drive experiments using coherent illumination or can be produced by self focusing and may drive these and other instabilities. Measurements sensitive to small transverse scales would be of great value in showing whether or not such fine scale phenomena influence the mass distribution.

The technique is a combination of the method used to study implosion uniformity and that used to meaure the stopping power of hot plasmas. (Sections A2.2.6 and A2.4).

The short pulse (0.1ns) oscillator of the VULCAN laser was used to drive three of its six disc amplifiers to generate an exploding pusher implosion of a D-T filled glass microballoon. The long pulse (1.5ns)

oscillator was used to drive the other three discs whose output was focussed on a lollipop target placed 1 mm from the exploding pusher so as to accelerate the lollipop towards the implosion. The relative timing of short pulse and long pulse beams could be set to any desired values. Alpha particles passing through the accelerated foil were recorded in a CR-39 detector placed a few cm away. Etching the CR-39 reveals etch pits whose dimensions give an accurate measure of the mass distribution of the foil since the fraction of all alpha particles having any particular residual energy is equal to the fraction of the area of the foil having the corresponding thickness. Since the α-particles travel normal to the foil, changes in the energy distribution can be produced by mass re-distribution on any transverse scale down to sub-micron values.

In a short trial experiment, two measurements were made. Fig A2.20 shows the thickness disribution of an Al foil irradiated with 1.05 μm light at an intensity of $\sim 10^{14}$ W cm^{-2}, with the timing set so that the α-particles passed through the foil 1.9ns after the start of the accelerating pulse. The foil was corrugated on a transverse scale of 10μm. The presence of some tracks having essentially no energy loss suggests that the foil had burnt through in places. Fig A2.21 shows the mass distribution of an initially flat, but otherwise similar foil at 1.4ns after the beginning of acceleration. The thickness distribution ranges from amost zero to over 9 μm.

A further series of experiments in which the conditions are better optimised for the study of the Rayleigh Taylor instability (0.53μm radiation at $\sim 10^{13}$ W cm^{-2} with plastic foils) is in progress.

It should be noted that the mass distribution does not contain any information about the actual scale-length. Multiple Coulomb scattering in the foils limits the spatial mapping capability of particle shadowgraphy to > 40μm (though it does not destroy sensitivity of this method to small transverse scales). Auxilliary techniques will be necessary to correlate anomalous behaviour of the mass distribution with perturbation scale-length.

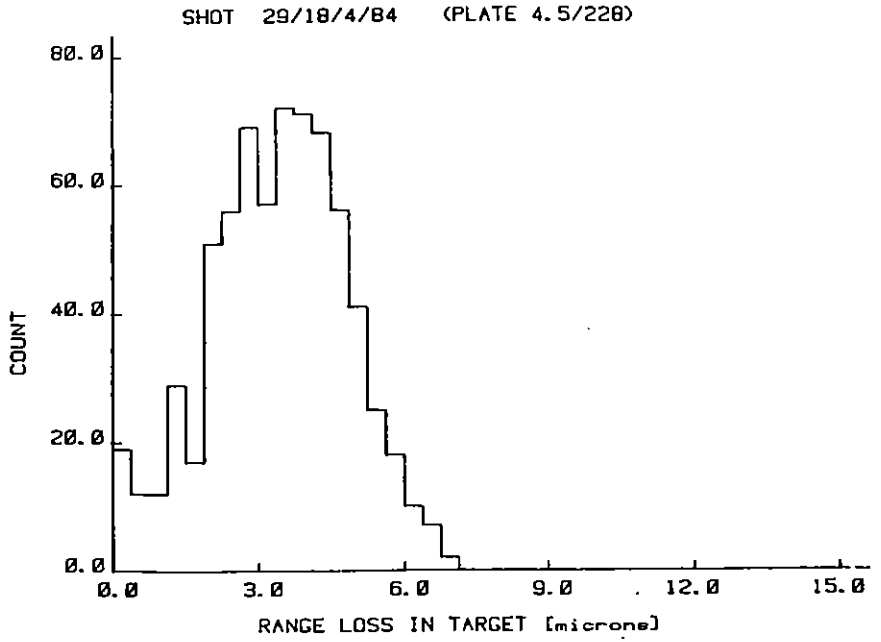

Fig A2.20 Range loss distribution for an accelerated, perturbed target

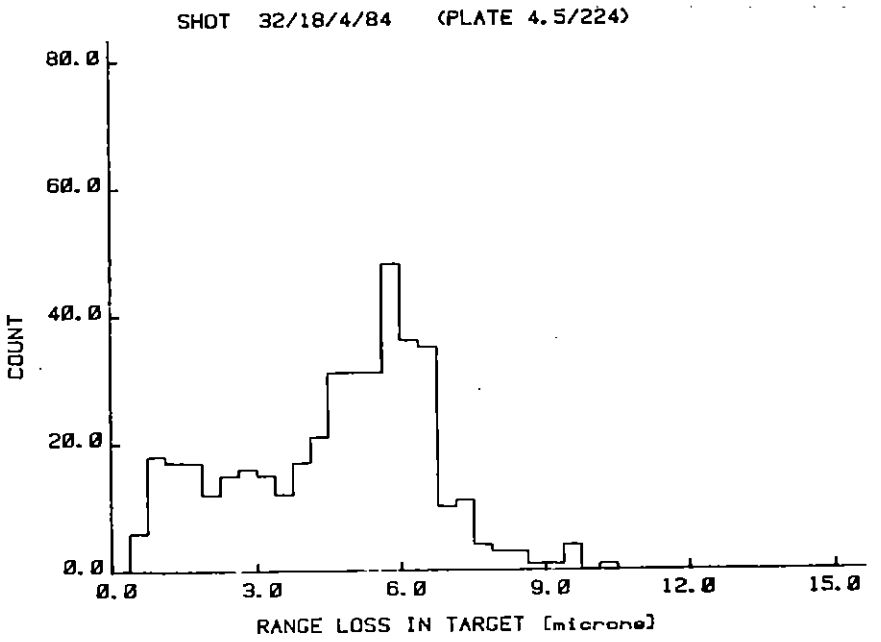

Fig A2.21 Range loss distribution for an accelerated, unperturbed target

A2.5 X-RAY POINT PROJECTION RADIOGRAPHY OF ABOLATIVELY ACCEELERATED FOILS

J Wark J D Kilkenny (Imperial College) A J Cole (RAL) R R Whitlock (Naval Researach Lab. Washington)

This aim of this experiment was to observe laser accelerated foils by point projection radiography; measure the spatial resolution and determine how much of a problem self emission from the target posed.

The point source of X-Rays was produced by focussing 30 J of 0.52 μm light onto the tip of a 10 μm diameter Bismuth wire (see Fig A2.22).

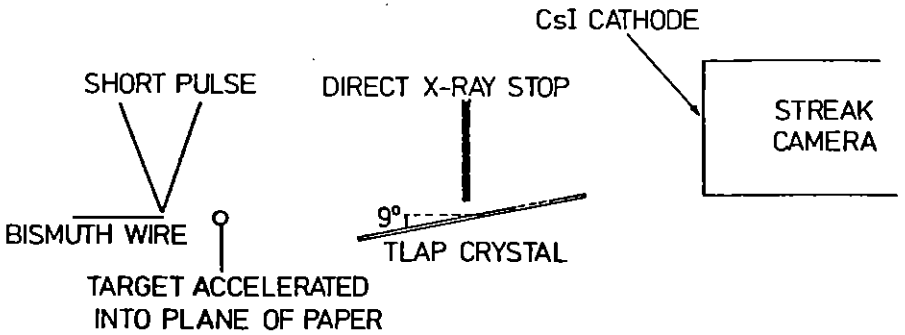

Fig A2.22 Experimental arrangement

The focal spot size was 30 μm and the pulse length 200 ps. The X-Rays produced were spectrally dispersed by a TLAP crystal onto the CsI photocathode of a streak camera in focus mode. The crystal was set

halfway between the point source and the cathode (5 cm from both) at an angle of 9^0 so that the M band of Bismuth (4.4Å) was recorded with a dispersion of 2 Å cm^{-1}. A lead plate was placed 2 mm above the surface of the crystal to block the path of direct X-Rays.

The targets were positioned on a line from the point source to the crystal and were accelerated perpendicular to that line and parallel to the plane of the crystal. The drive beam was a 5ns pulse of 50 J of 1.05μm light.

To measure the resolution of the point source a mesh of 10 μm wires and 15 μm spaces was placed between the point source and the detector at the object position, the result is shown in Fig A2.23.

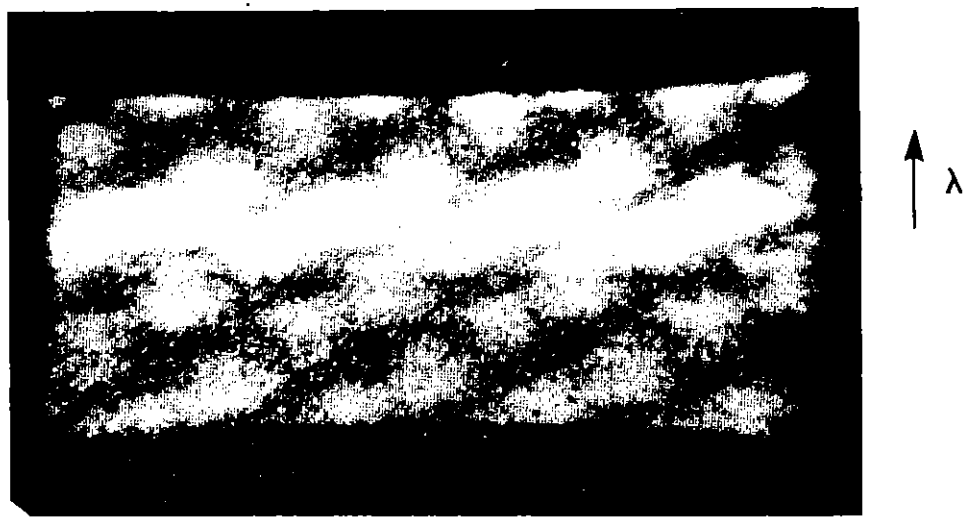

Fig A2.23 Radiograph of mesh

From this we can see that the resolution is certainly better than 10 μm. However, from densitometer tracings it is seen that light does reach the part of the shadow corresponding to the centre of the wire; i.e. part of the source must extend further out than a radius of 5 μm.

Knowing the film response we can convert the density plot to relative intensity above background . Now the opaque wire can be represented as an inverted top hat function in transmission. If we deconvolve the observed intensity distribution with the transmission function of the wire we obtain the relative intensity of the point source as a function of distance, as shown in Fig A2.24. We can quickly check the accuracy of the deconvoluton by calculating the relative intensity at the centre of the shadow. From Fig A2.24 this should simply be the ratio of the areas

$$\frac{A}{A+B} = 0.19$$

compared to the 0.18 observed.

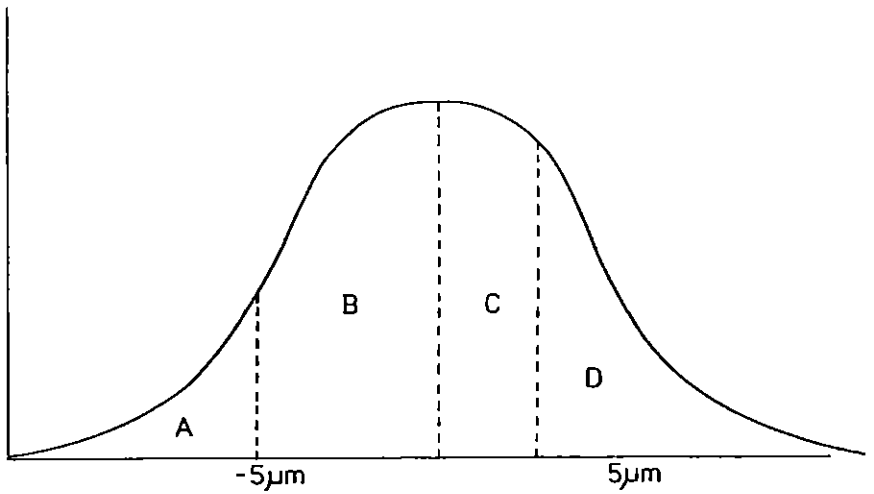

Fig A2.24 Backlighter intensity profile

Also, using Fig A2.24 we can make a formal definition of the resoluton as the width of an opaque wire such that the relative intensity at the centre of the shadow is 0.5 times that far from the shadow. This again can be simply measured from Fig A2.24, it occurs when the two areas C and D are equal. With this definition we find the resolution to be 5μm.

An unirradiated plastic $(CH)_n$ foil was imaged side on as shown in Fig A2.25, there are two things to note. First the transmission of the foil to the 4.4Å x-ryas is 40%, compared to the 25% calculated from the mass attenuation coefficient of the plastic; this is in reasonable agreement with the data found from the resoluton results, ie. some of the source extends beyond a dimater of 10μm. Secondly we see that the shadow of the foil is narrower at 4.4Å than at 3.6Å (where the

resolution was determined). This indicates that the effective source size varies with energy. This is not surprising as the temperature of the source will fall off with radius, and different atomic transitions will have different lifetimes.

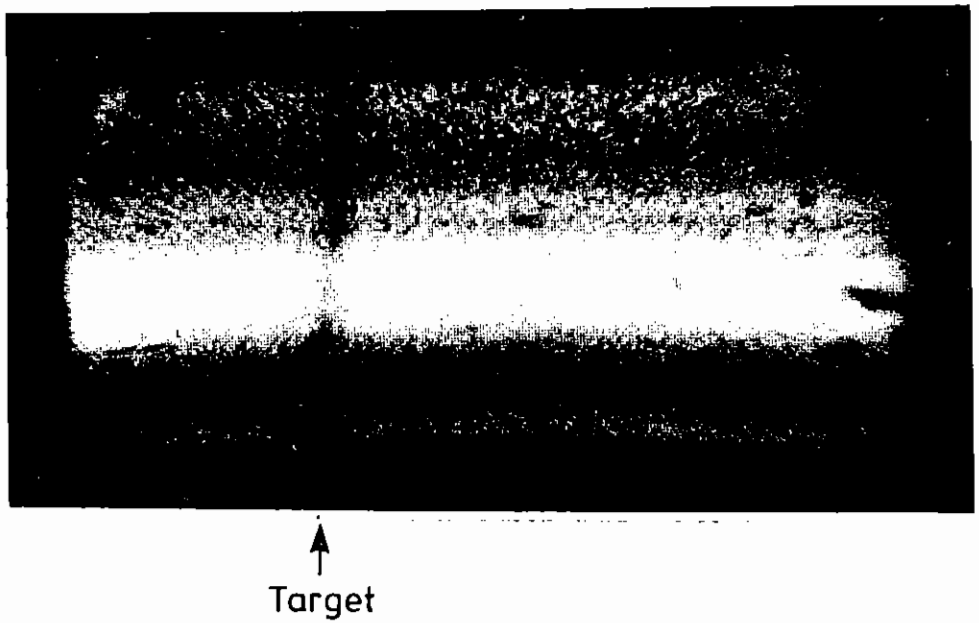

Fig A2.25 Radiograph of unirradiated target

Fig A2.26 shows the image of a plastic $(CH)_n$ foil irradiated with 50 J and probed at 5 ns after the start of the drive pulse. From this picture we can gain some information about the relative magnitude of the self emission from the target. A densitometer tracing through the shadow of the foil in the centre of the Bi m band shows that the transmission is 50%. Now the self emission from the target will contribute a uniform background of light over the whole of the film. Let this background intensity be S, and the intensity of the backlight at 4.4Å be 1; then we have the equation

$$\frac{0.4 + S}{1 + S} = 0.50 \quad \text{ie,} \quad S = 0.2$$

i.e. the backlight is 5 times brighter than the self emission under these conditions.

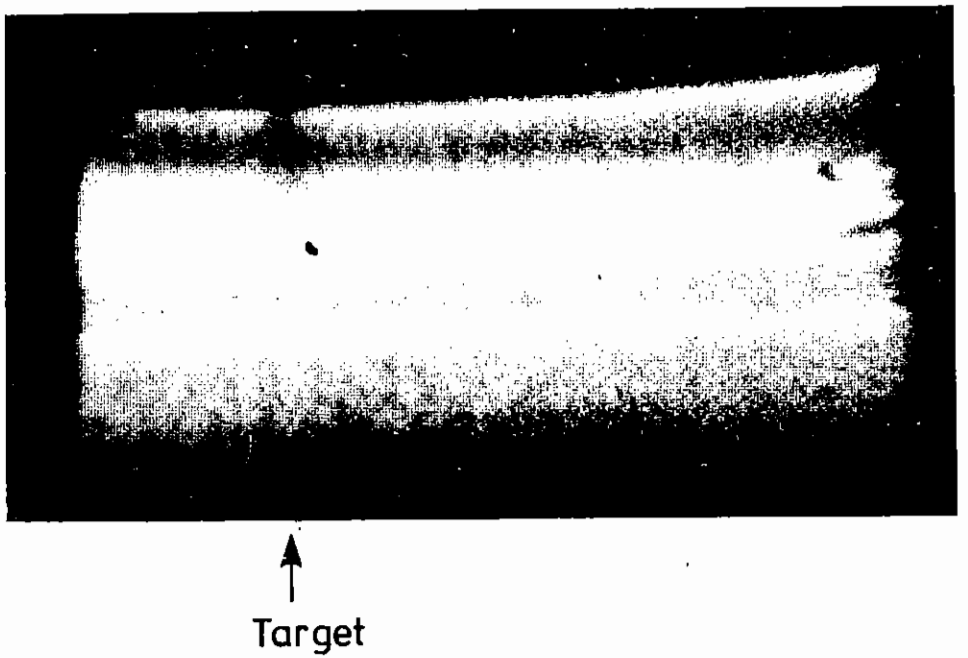

Fig A2.26 Radiograph of accelerated foil

However, the main problem encountered looking side on to a foil is that buckling of the foil may obscure what is happening at the ablation surface. One way of attempting to overcome this was to use a different target design. Here a 10 μm region of KCl absorbs 83% of the light (the total absorption is 95%) just above the Cl K edge at 4.4Å. Thus over half of the m band of Bi the dominant contribution to the shadow will come from the thin KCl region, overcoming the difficulties mentioned above.

However, if such a target is irradiated there is a lot of emission from the Cl He like ions, totally wiping out the shadow of the target, as shown in Fig A2.27. The solution to this may be to cover the front surface of the Chlorine doped target with a layer of $(CH)_n$ type plastic, thus keeping the self emission low but maintaining the thin absorbing region.

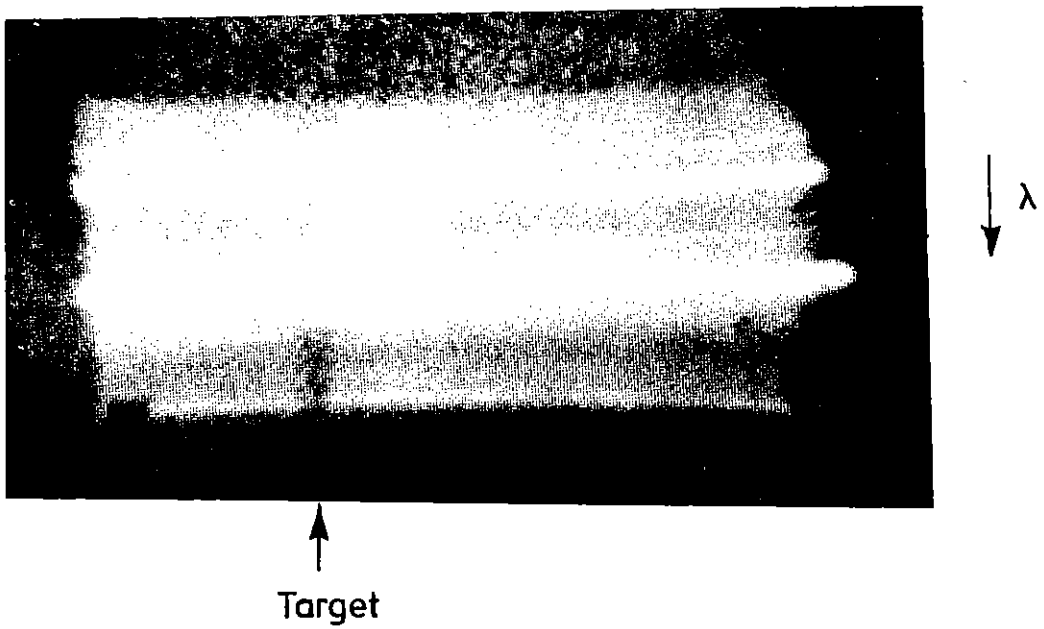

Fig A2.27 Radiograph of KCl doped accelerated foil

A2.6 AN INVESTIGATION OF THERMAL SMOOTHING AT 0.35 μm BY X-RAY SHADOWGRAPHY

A.J. Rankin , J D Kilkenny (Imperial College)
A J Cole, M H Key (RAL)

Thermal smoothing measurements have been made at this lab. using short pulse x-ray backlighting at 1.06 and 0.53 μm (A2.17 (A2.18) and also using a modulated shock transit time technique at 1.06 and 0.35 μm (A2.19). It was intended to extend this study with a combined experiment at 0.35 μm using both approaches simultaneously to accurately compare both sets of data. Due to laser difficulties this was not possible, but new data using shadowgraphy , with a reduced modulation period has been obtained showing some evidence of enhanced smoothing.

The basic experimental arrangement was the same as earlier experiments (A2.17). Shadowgrams were obtained for a drive pulse of 500 psec FWHM duration at 0.35 μm and a fixed delay 100psec FWHM 1.06 μm backlighting pulse. The recording pinhole camera contained a 10 μm platinum pinhole with 3 μm aluminised mylar filtering. This resulted in a 1/e cut off of ~1.2 kev. The targets were 25 and 12.5 μm thick plastic lollipops. The laser beam modulation was strips of neutral density filter.

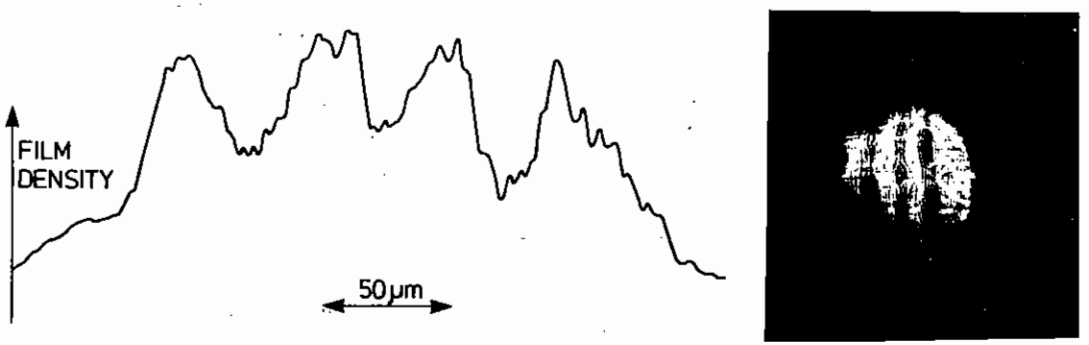

Fig A2.28 Target equivalent plane showing 50μm λp

A typical equivalent plane photograph is shown in Fig A2.28 with microdensitometer tracing showing an Intensity modulation ratio of Imax/Imin of 3.0:1 and period of 50 μm. The backlighting pulse was delayed by 200 psec from the peak of the main pulse so that the targets were shadowed at approximately the end of the drive pulse. This insured that the observation was made during the steady state phase and before the end of irradiation while the target was still being driven.

RESULTS

Two of the shadowgrams obtained are shown in Fig A2.29 as in previous experiments the degree of smoothing is inferred from microdensitometry across the high and low drive regions. The distance modulation parameter is defined as :

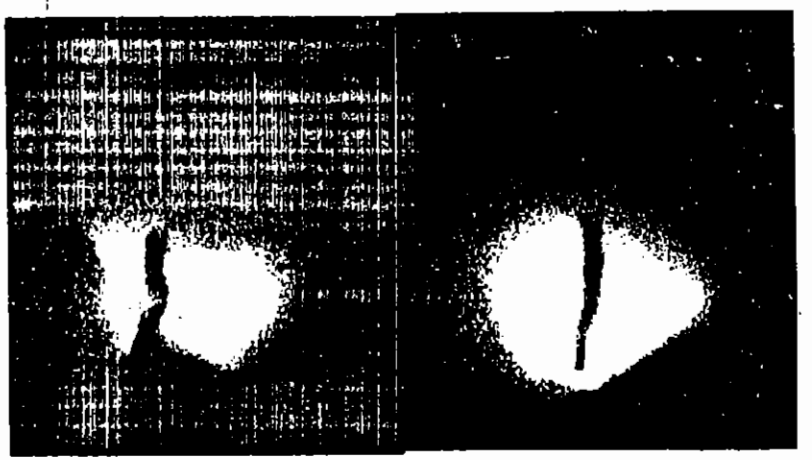

Fig A2.29 Shadowgrams of 20μm accelerated foil at 0.35μm for a modulation of Imax / Imin = 3:1 and λ_p = 50μm

(a) $I_{abs} = 3.2 \times 10^{13}$ Wcm^{-2}, $\Delta = 0.6$

(b) $I_{abs} = 11.2 \times 10^{13}$ Wcm^{-2}, $\Delta = 0.43$

SHOT NO.	TARGET (μm)	DEFOCUS (μm)	ENERGY (J)	ZMAX (μm)	ZMIN (μm)	ZMAX / ZMIN − 1	$I_{abs}/10^{13}$ (Wcm^{-2})
311584	25	75	5.6	9.0	5.6	0.6	3.2
082584	25	100	6.0	12.5	5.6	1.2	8.2
092584	25	100	6.0	9.0	5.6	0.6	8.2
102584	12.0	100	6.4	110.2	83.0	0.33	8.6
063584	25	100	7.2	5.6	2.3	1.4	9.7
073584	25	100	8.2	22.7	15.9	0.43	11.2
163584	12.5	100	4.1	55.6	48.7	0.27	5.6
173584	12.5	100	4.5	62.5	108.9	0.28	6.1
193584	12.5	100	4.2	31.8	11.5	1.76	5.7
203584	12.5	100	4.8	35.2	19.9	0.77	6.6

Table A2.7 X-ray shadowgraphy results at 0.35 μm

$\Delta = \frac{\text{maximum distance travelled}}{\text{minimum distance travelled}} - 1$

The results are tabulated in table A2.7, the energy values have been corrected to compensate for beam modulation absorption, so the calculated irradiances are for the peak drive regions. Absorption fractions were used as Evans et al (A2.20)

The smoothing parameter is plotted as a function of absorbed irradiances in Fig A2.30.

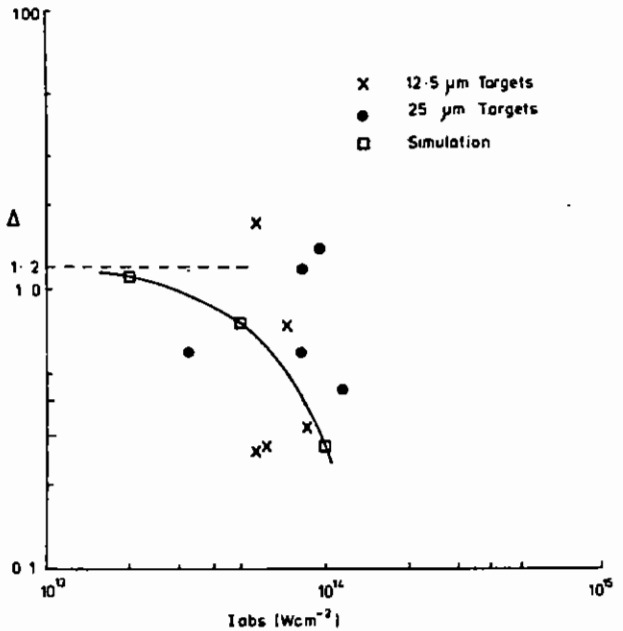

Fig A2.30 Graph of Δ against absorbed irradiance for experimental results and scaled simulation

The wide scatter in the data is probably caused by significant uncertainties in the exact focussing conditions used in the experiment. Axial positioning of the target with respect to the lens focal plane was not known to better than ± 50 μm. This positioning error varied from shot to shot.

This results in the calcualted irradiances being in error by as much as a factor of two. A second consequence is a variation in the exact beam modulation wavelength λp, imposed on the target.

Also shown in Fig A2.30 is an analytical scaling of the 2-D simulations performed at 1.05 μm and 0.53 μm (A2.18), correcting for the different λ_L, λp and Imax/Imin used in this experiment from those used previously. As can be seen, the irradiance regime investigated in this experiment for λL= 0.35 μm is exactly where significant smoothing effects can be expected to start to occur. Therefore the observed smoothing parameter Δ will be sensitive to the exact laser irradiance and beam modulation wavelength experienced by the target.

The fact that some shots do show a significant reduction in Δ from that expected for an unsmoothed drive pressure ($3^{0.7}-1 = 1.2$) indicates that the experiment was successful in demonstrating thermal smoothing for 0.35 μm laser light at asorbed irradiances above approximately 5×10^{13} W cm^{-2} for a beam modulation wavelength of approximately 50 μm. This result supports a laser wavelength scaling for thermal smoothing of $\lambda_L^{2.0} - \lambda_L^{2.5}$, in reasonable agreement with previous results for λ_L = 1.05 μm and 0.52 μm.

References

A2.1 RAL Annual Report to the laser Facility Committee 1984, Section A2.2.4.

A2.2 C L S Lewis and J McGlinchey, 'Quasi-monochromatic projection radiography of dense laser driver spherical targets', Opt Comm (in press)

A2.3 Supplied by Dr Troy Barbee, Stanford University

A2.4 V Aboites, E McGoldrick, S M L Sim, D Bassett, A R Bell and I N Ross, Opt Comm, 52, 108 (1984)

A2.5 V Aboites, S M L Sim, D Bassett and I N Ross, RAL Laser Division Annual Report, Section A2.2.3(b), (1984)

A2.6 A R Bell and D J Nicholas, RAL Report RL-83-127 (1983)

A2.7 R A Cairns, Plasma Physics, 23, 705 (1981)

A2.8 C Yamanaka, T Yamanaka, T Sasaki, J Mizui and H B Kang, Phys Rev Lett, 32, 1038, (1974)

A2.9 A I Avrov, V Yu. Bychenkov, O N Krochin, V V Pustovalov, A A Rupasov, V P Silin, G V Sklizkov, V T Tiokhonchum and A S Shikanov, Sov Phys, JETP, 45, No.13, (1977)

A2.10 H C Barr, RAL Laser Facility Annual Report RL-79-036, 8.12 (1979)

A2.11 A P Fews, Annual Report RAL 84-049, A6.17.2 (1984)

A2.12 A R Bell and D J Nicholas, Annual Report RL-82-039 1.51 (1982)

A2.13 A R Bell, D J Nicholas and I N Ross, Annual Report RL 83-043 1.52 (1983)

A2.14 A J Cole et al, Nature, 299, 329 (1982)

A2.15 R R Whitlock et al, Phys Rev Lett, 52, 819 (1984)

A2.16 O Willi, P T Rumsby, Opt Comm, 37, 45 (1981)

A2.17 A J Cole, J D Kilkenny, P T Rumsby, R G Evans and M H Key, J Phys D, 15, 1689 (1982)

A2.18 A J Cole, R G Evans and J D Kilkenny, Annual Report RL 83-043 5.6 (1983)

A2.19 A J Rankin, J D Kilkenny, A J Cole and M H Key, Annual Report RL 83-043, 5.7 (1983)

A2.20 R G Evans, A R Bell and B J MacGowan, J Phys D, 15, 711 (1982)

A3 Dense Plasmas and Radiation Physics

REFERENCES

Editor S J Rose

A3.1 INTRODUCTION

J Hares (Imperial College)

During the last year, we have seen two new University groups perform experiments on the glass laser in the area of dense plasmas and radiation physics. The first of these is the group from the Spectroscopy Department at Imperial College who investigated the change in X-ray line energy (plasma polarization shift) in plasmas formed in exploding pusher microballoon implosions. The second is the group from Queen's University, Belfast who have performed X-ray brightness measurements from a variety of laser plasma sources. The analysis of these experiments promises to be of great interest from both a theoretical and practical standpoint.

In addition to these experiments, a set of measurements of the chlorine K-edge shift in a dense plasma was performed which showed improved accuracy over previous measurements.

The widening range of experiments performed by the Dense Plasmas and Radiation Physics Group shows increased interest in this new area of physics which has become experimentally accessible with the advent of high-power lasers.

A3.2 COLLIDING-SHOCK EXPERIMENTS IN TAW

J Hares, D K Bradley, A Rankin and S D Tabetabaei (Imperial College)

In this period the colliding shock technique (see CLF annual report 1984) was again used to produce the high Γ conditions required for a K-edge shift measurement. The experiment was improved by:

i) using the full output of the six discs in a double three beam overlap configuration,
ii) increasing the spectral dispersion,
and iii) careful target design.

In all experiments the K-edge of chlorine in C-type parylene was chosen for study, with bismuth providing a bright quasi-continuum backlighting source. The incident laser wavelength was 0.53μm at an intensity of a few x 10^{14} W cm^{-2}.

The experimental layout and target design are shown in Figs A3.1 and A3.2 respectively. The experimental design is similar to that described in the CLF Annual Report 1984 except that the beam splitters in TAW were removed, giving the total energy in six beams. These were overlapped in two groups of three, the two groups being opposed on the two faces of the target.

The streak spectrograph was slightly withdrawn to give an enhanced dispersion of approximately 8eV/mm at the cathode.

The optimum target design was obtained by trading off backlighting intensity against radiative preheat. The Bi backlighting spectrum represents a significant heating source. The brightness was reduced via an overcoat of LiF. The optimum layer thickness was found to be approximately 1μm.

Time resolved absorption spectra of colliding shock compressed C-type parylene were obtained for a variety of irradiation and target conditions. Two of the best shots (i.e. biggest shift) and a calibration shot are shown in Figs A3.3, A3.4 and A3.5.

Fig A3.3 shows a shot with a remote (cold) absorber, the K edge position showing no time dependence. Fig A3.4 shows a shot with no LiF overlay on the Bi backlighting layer. Note the small shift and broadening during the pulse. Fig A3.5 shows a shot with a 1μm LiF overlay. The shift is large (> 10eV) resulting from the reduced radiative preheat from the Bi emission. This is apparent in the reduced continuum intensity on the streak record.

The significant result from these experiments is that the shift is to lower energy. As will be discussed in the theoretical interpretation this helps to check the validity of the various models proposed for continuum depression effects.

The authors would like to thank AWRE for their help with the digitization and colour enhancement of the experimental data.

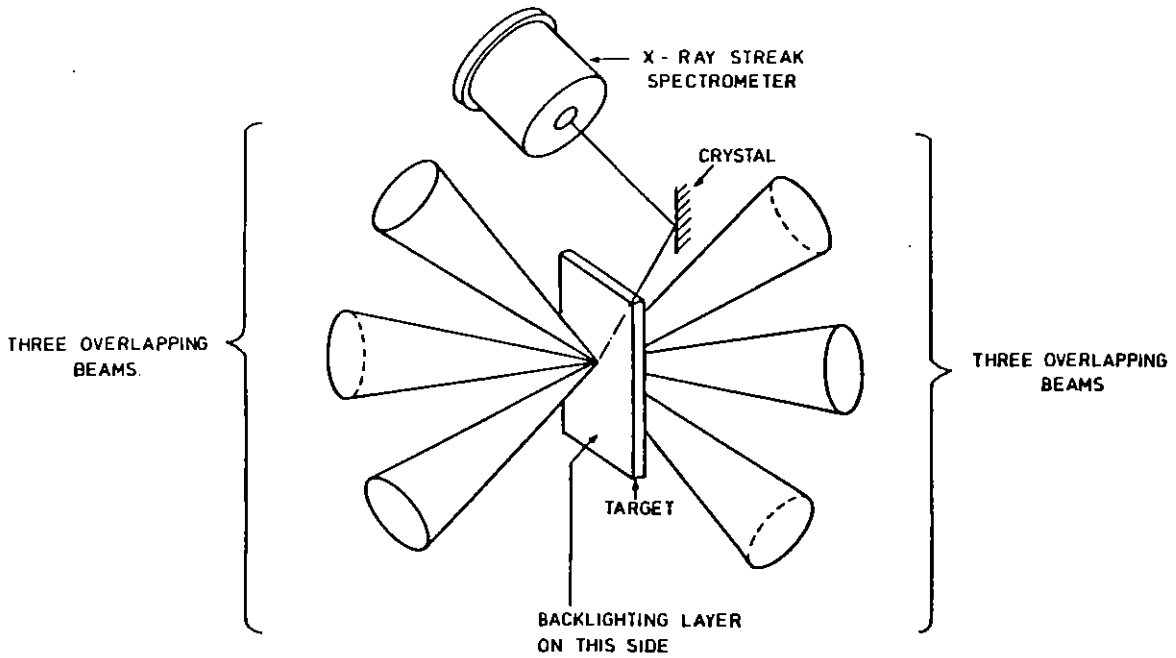

Fig A3.1 Experimental layout of colliding-shock experiment

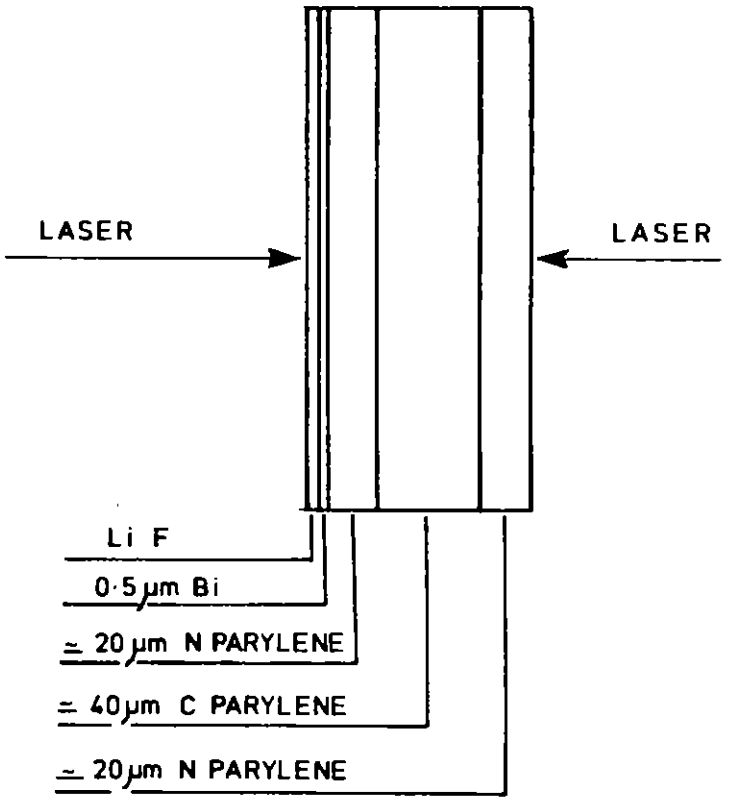

Fig A3.2 Target design for colliding-shock experiment

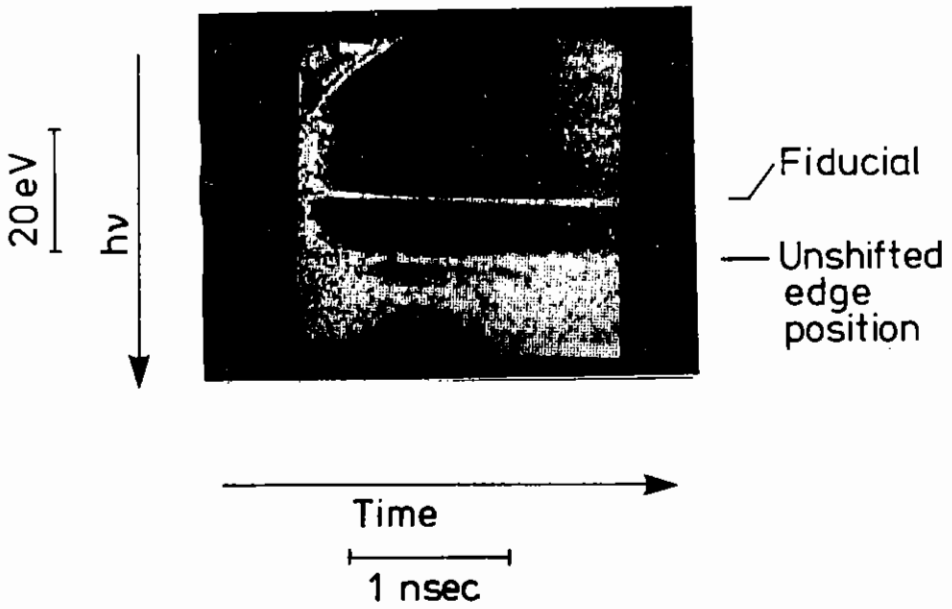

Fig A3.3 Static chlorine K-edge with cold absorber

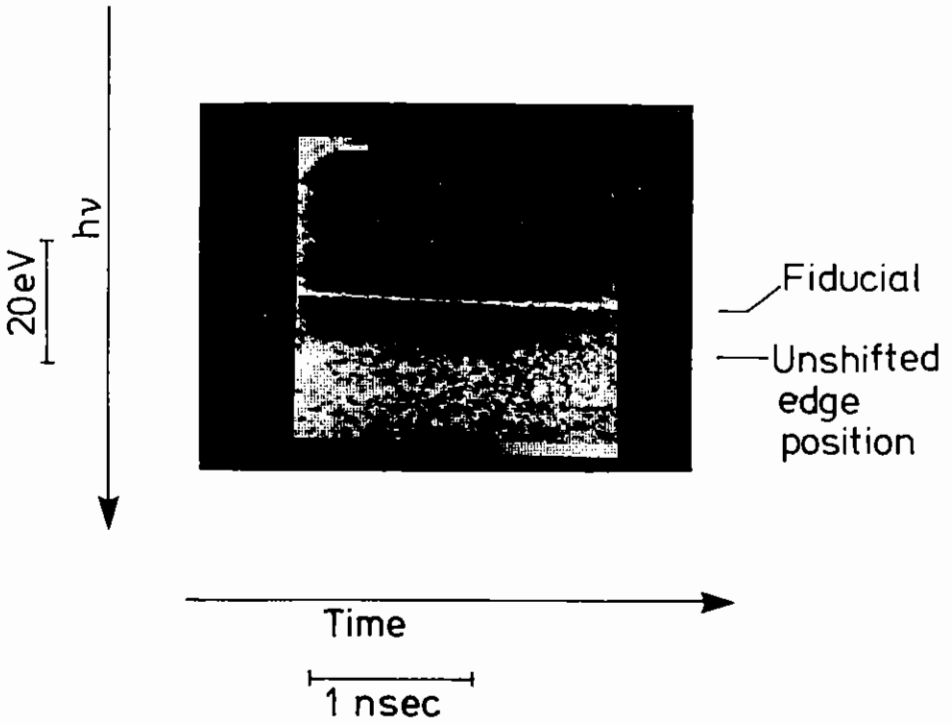

Fig A3.4 Broadening but no shift of chlorine K-edge with strong radiative preheat

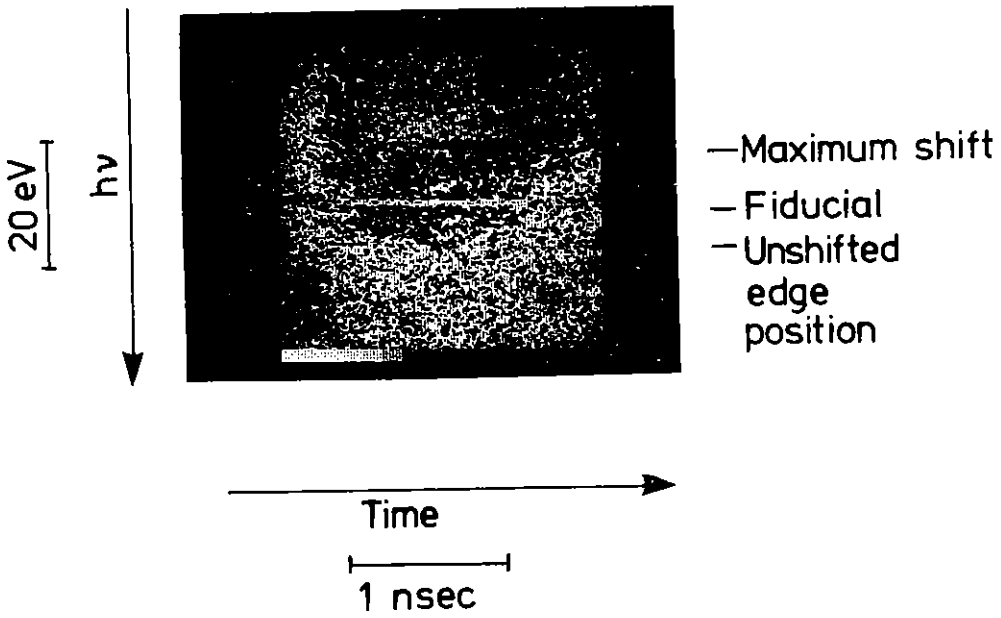

Fig A3.5 Large red-shift of chlorine K-edge with low radiative preheat.
(Note the low backlighting intensity)

A3.3 ANALYSIS OF COLLIDING AND SINGLE-SHOCK EXPERIMENTS

S J Rose (RAL)

A3.3.1 Colliding-shock experiments

In last year's CLF annual report, experiments were described in which time-resolved X-ray radiographic and photoabsorption measurements were made of foil targets under two-sided laser irradiation. The radiographic experiments involved following the compression using streaked radiography of two buried bismuth tracer layers. For the clearest shot (11 14/12/83) a maximum compression of $\gtrsim 6$ was measured, the lower limit being set by resolution. The photoabsorption experiments were the precursors of those described in Section A3.2 of this year's CLF annual report and involved taking time-resolved photoabsorption spectra of the chlorine K-edge, the chlorine being incorporated into the target in a central layer of C-type parylene. For the clearest photoabsorption shot (13 21/12/83) a maximum shift in the position of the K-edge of 10eV was observed.

In the year since those experiments were performed, extensive calculations have been carried out to model both the hydrodynamic behaviour and the atomic physics involved.

The one-dimensional hydrodynamic code MEDUSA (A3.1) was used to simulate the experiments. The calculations did not include the effect of the bismuth backlighter on either the hydrodynamics or the radiative heating of the foil. The calculated time dependence of the average compression for the region between the tracer strips in the radiographic shot 11 14/12/83 is shown in Fig A3.6 and Fig A3.7 shows the average temperature and compression of the C-type parylene region in the photoabsorption shot 13 21/12/83. For the radiographic shot, MEDUSA predicts a maximum average compression of approximately 6, consistent with the experiment. For the absorption experiment a maximum average compression of about 6 is also predicted, together with a peak average temperature of approximatly 15eV.

The Thomas-Fermi method is used to predict the degree of ionization of each of the elements of the C-type parylene plasma (carbon, hydrogen

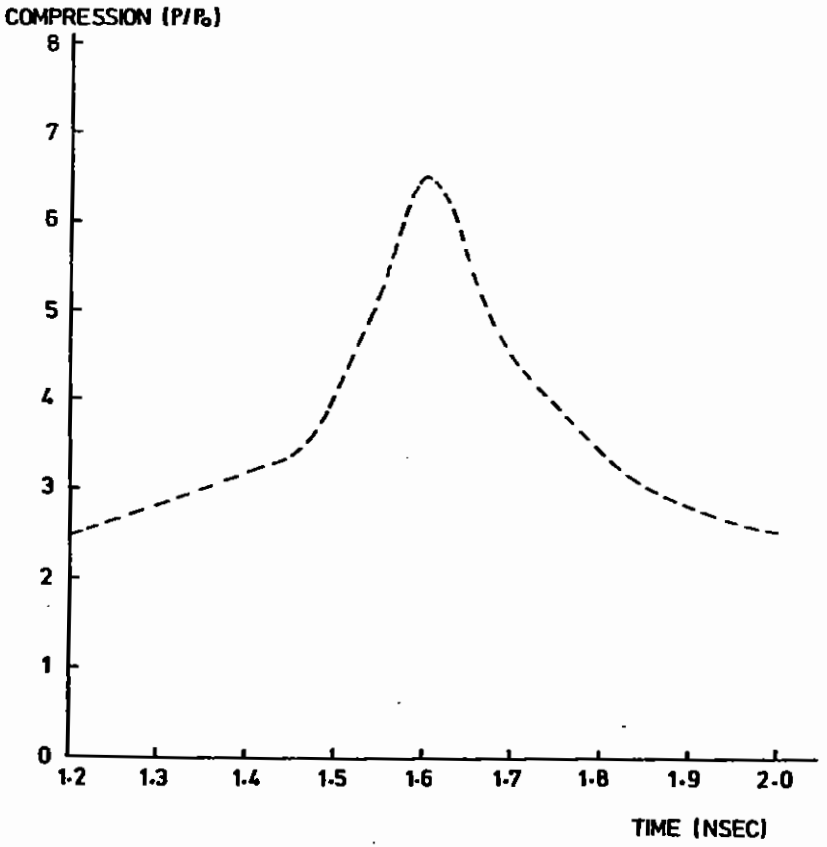

Fig A3.6 Calculated average compression of mylar between tracer strips in the radiographic shot #11 14/12/83

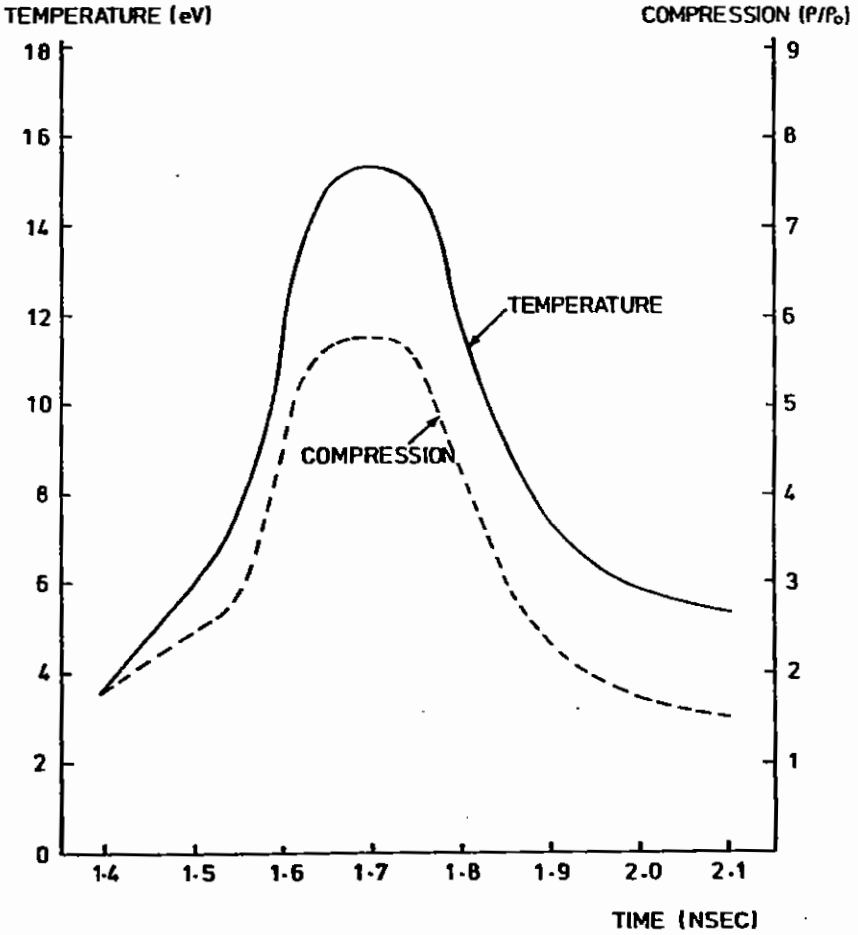

Fig A3.7 Calculated average temperature and compression of C-parylene in photoabsorption shot #13 21/12/83

and chlorine). Thomas-Fermi calculations are performed for each element and the radius of each ion-sphere is adjusted until the electronic pressure at the ion-sphere radius of each element is equal. This procedure ensures that there is a single degeneracy parameter μ for the plasma.

The plasma parameters $Z^*_{C\ell}$ (the average chlorine ionization), Z^*_{mix} (the average ionization for the mixture), Γ_{ii} and Γ_{ee} (the ion-ion and electron-electron strong-coupling parameters) are shown for different temperatures and densities in Figs A3.8 and A3.9.

The shift in the energy of the chlorine K-edge in C-type parylene is given by

$$\Delta E_K(\rho,T)=E_K(\rho,T)-E_K(\rho_o,T_o) \qquad (1)$$

where $E_K(\rho,T)$ is the energy of the chlorine photoabsorption K-edge at temperature T and density ρ, and where T_o and ρ_o are the normal temperature and density of C-type parylene (2.6×10^{-5} eV and 1.29g/cc respectively). $E_K(\rho,T)$ is calculated as the sum of three terms:

$$E_K(\rho,T)=I_K(\rho,T)+\Delta E_{deg}(\rho,T)+\Delta E_{cl}(\rho,T). \qquad (2)$$

The first term (I_K) represents the K-shell ionization energy of a free chlorine ion averaged over the different chlorine ions found in the plasma. For integer $Z^*_{C\ell}$, I_K is approximated as the K-shell ionization energy of the ground-state chlorine ion with the outer $Z^*_{C\ell}$ electrons removed. Calculations are required to obtain the ionization energies as experimental values are not available. Because electronic transitions from the K-shell are involved, relativistic effects must be included for accuracy and the multiconfiguration Dirac-Fock (MCDF) programs of Grant et al (A3.2) and McKenzie et al (A3.3) are used. For non-integer $Z^*_{C\ell}$, I_K is obtained by linear interpolation between the values for integer $Z^*_{C\ell}$. Degeneracy in the free electron system increases the photoabsorption edge energy and this is represented by

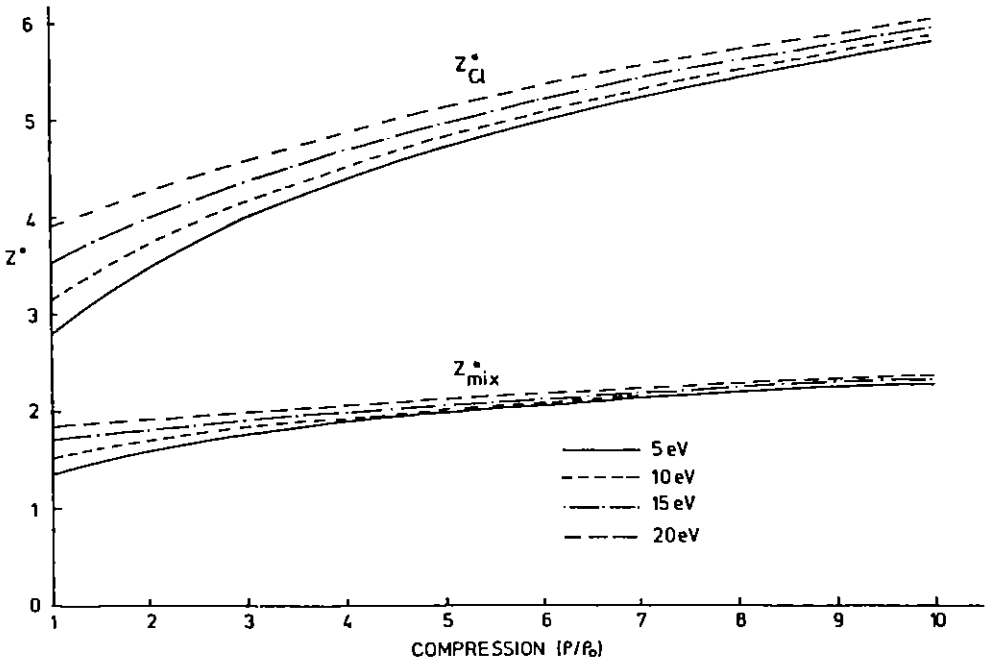

Fig A3.8 Ionization states in C-parylene

the second term in equation (2) (ΔE_{deg}). The probability, p, that a free electron state of energy ϵ is filled is given by

$$p = 1/(e^{(\epsilon-\mu)/kT}+1) \qquad (3)$$

where μ comes from the Thomas-Fermi calculations. For $\mu < 0$ (non-degenerate electrons), $p<1/2$, whilst for $\mu>0$ (degenerate electrons)

$$\begin{aligned} p &< 1/2 \text{ for } \epsilon>\mu \\ p &= 1/2 \text{ for } \epsilon=\mu \\ p &> 1/2 \text{ for } \epsilon<\mu \end{aligned} \qquad (4)$$

showing that

$$\Delta E_{deg} = \begin{cases} \mu & \mu>0 \\ 0 & \mu<0. \end{cases} \qquad (5)$$

Values of μ at different temperatures and densities are shown in Fig A3.10.

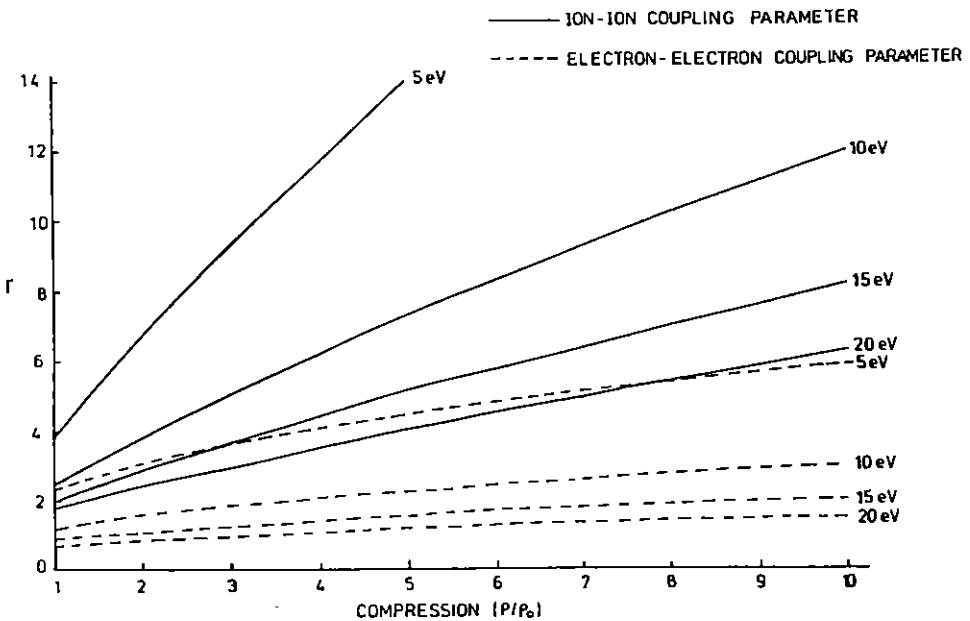

Fig A3.9 Strong coupling parameters in C-parylene

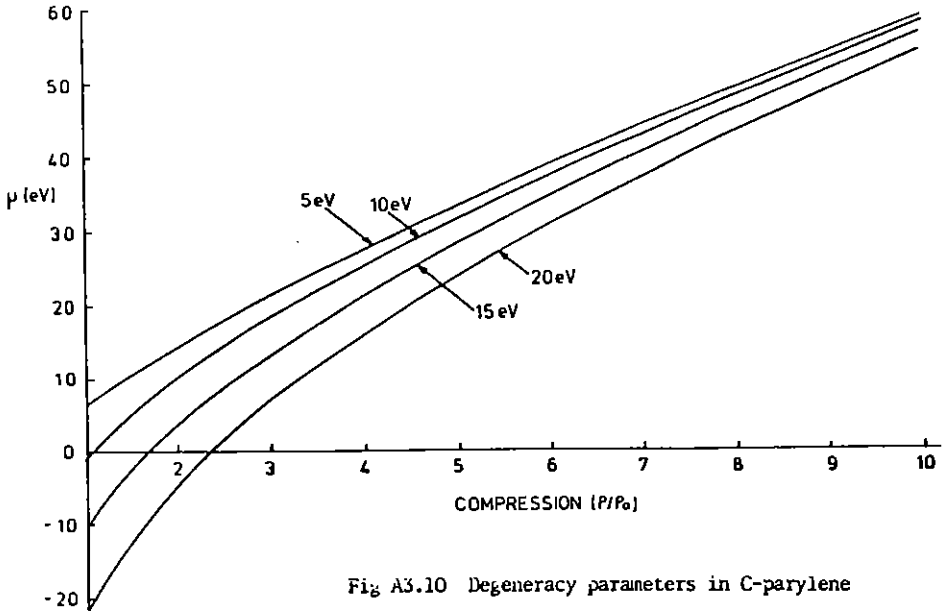

Fig A3.10 Degeneracy parameters in C-parylene

The effect of the plasma neighbours is to reduce the photoabsorption edge energy and this change is represented by the third term in equation 2 ($\Delta E_{c\ell}$). In this work three different models of continuum lowering have been considered.

Model 1 - Ion-sphere

The ion-sphere model in its simplest form has a uniform distribution of free electrons which neutralise the ionic charge and neighbouring plasma particles do not penetrate inside the ion-sphere volume. Continuum lowering arises from a change in the energy of a bound electronic level by the interaction with the free electrons in the ion-sphere. In the model the expression for the continuum lowering is

$$\Delta E_{c\ell} = \frac{Z^*_{C\ell} e^2}{2R_{C\ell}} \left[\frac{\Delta r (Z^*_{C\ell})^2}{R^2_{C\ell}} - 3 \right] \qquad (6)$$

where the second term in the brackets has the largest contribution. The first term represents the effect of orbital relaxation on K-shell ionization.

Model 2 - Augmented ion-sphere.

The second model uses equation (6) with a correction for the interaction energy of the ionised electron with the plasma. The correction is evaluated assuming a uniform ionised electron density interacting with the plasma, described by an ion-sphere model of radius R_{mix} (the average ion-sphere radius) and ion charge Z^*_{mix} and with Z^*_{mix} uniformally distributed free electrons. The modified expression for the continuum lowering is then

$$\Delta E_{c\ell} = \frac{Z^*_{C\ell} e^2}{2R_{C\ell}} \left[\frac{\Delta r (Z^*_{C\ell})^2}{R^2_{C\ell}} - 3 \right] - \frac{3 Z^*_{mix} e^2}{10 R_{mix}} \qquad (7)$$

Model 3 - Neighbouring-ions model.

The modification of the potential experienced by an ionizing electron due to the presence of neighbouring ions allows a different description of the continuum lowering to that in an ion-sphere model; the value of the correction is given by

$$\Delta E_{c\ell} = -\left\{ \frac{Z^*_{C\ell} + 1}{r} + \frac{Z^*_{mix}}{2R_{mix} - r} \right\} e^2 \qquad (8)$$

evaluated at the turning point $\partial \Delta E_{c\ell} / \partial r = 0$.

Using these models estimates of the position of the chlorine K-edge in cold C-type parylene at normal density $\left(E_K(\rho=\rho_0, T=T_0)\right)$ can be made. Continuum lowering models 1,2 and 3 predict 2.853, 2.849 and 2.835 keV respectively, in comparison with an experimental value 2.826 keV.

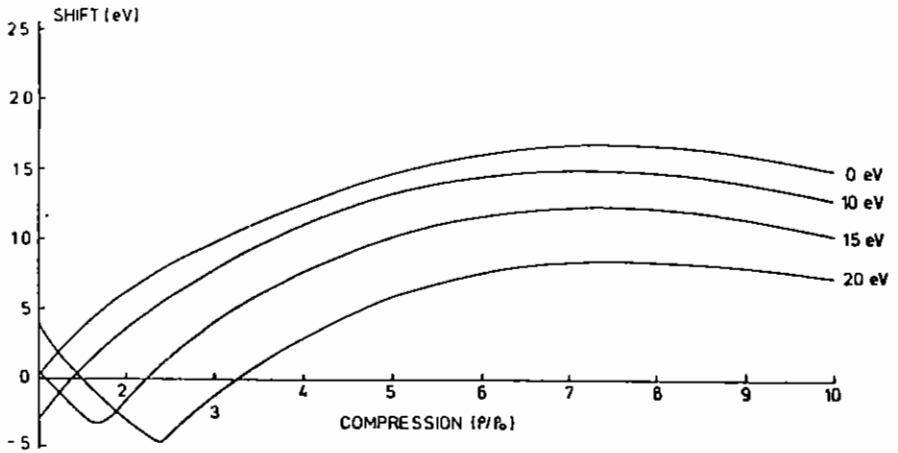

Fig A3.11 K-edge shift calculated using continuum-lowering model 1

Figs A3.11, A3.12 and A3.13 show the values of the shift in position of the K-edge with increasing density and temperature. Neither of the ion-sphere models produce a red-shift under the peak temperature and density conditions predicted to occur in the photoabsorption experiment, whereas model 3 predicts a red-shift of approximately 15 eV in fairly good agreement with the 10 eV observed experimentally.

One of the major uncertainties in the modelling of the photoabsorption experiment is the Thomas-Fermi calculation of the ionization balance. Finite ionization is predicted at zero temperature and normal density. The Thomas-Fermi model does not include chemical effects and calculations have been performed which adjust the Thomas-Fermi

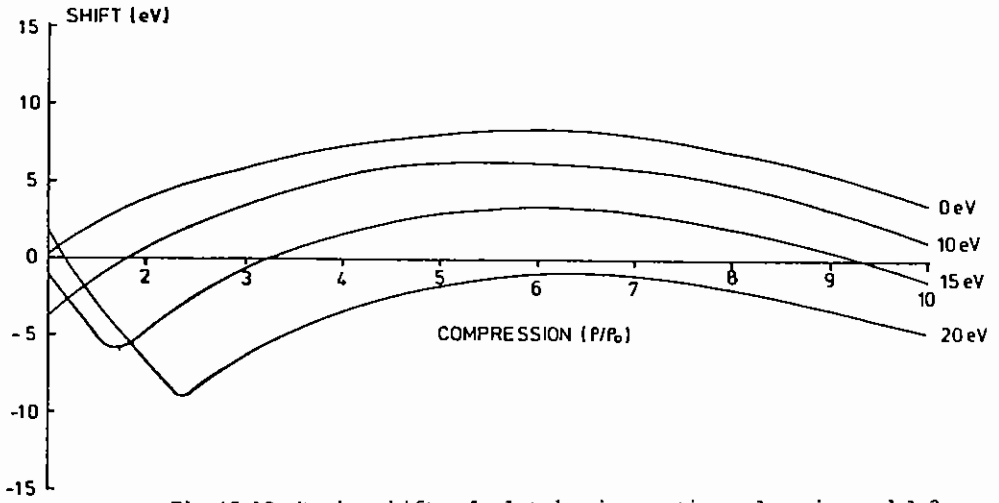

Fig A3.12 K-edge shift calculated using continuum-lowering model 2

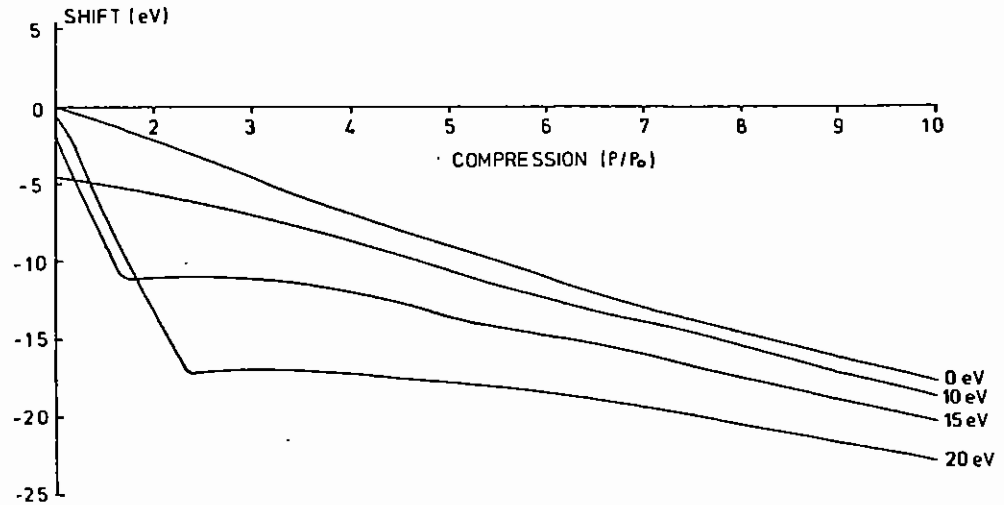

Fig A3.13 K-edge shift calculated using continuum-lowering model 3

ionization to predict at $T=T_o$ and $\rho=\rho_o$, the existence of Cl^- ions in C-type parylene:

$Z^*_{C\ell} \to -1$ $\qquad$ $Z^*_{C\ell} \to 17$

$Z^*_C \to 1/8 \}\ T \to 0$ and $\qquad$ $Z^*_C \to 6 \}\ T \to \infty$

$Z^*_H \to 0$ $\qquad$ $Z^*_H \to 1$

It is believed that this probably gives a more realistic description of the state of ionization. However, although this improves the predicted value of E_K ($\rho=\rho_o$, $T=T_o$) (2.819 keV from models 1,2 and 3), model 3 is still in substantially better agreement with experiment than models 1 or 2 (at a temperature of 15 eV and a compression of 6, models 1,2 and 3 predict shifts of +19.2, +11.8 and -11.7 eV respectively).

A calculation of the observed width of the K-edge has not been attempted. Several mechanisms will contribute, including non-uniformities of temperature and density, and electron degeneracy.

It has been shown that two-sided laser irradiation of a planar target can produce a plasma which is calculated to be both degenerate and strongly-coupled. Ion-sphere models of continuum-lowering do not give good agreement with experiment, whereas this is achieved using a neighbouring-ions model. It appears therefore, on the basis of the calculations reported here, that the experimental data favours one particular formulation of the continuum lowering.

A3.3.2 Single-shock experiments

Experiments involving single-sided irradiation of foil targets were also described in last year's CLF annual report. Using the same radiographic techniques as were employed for the two-sided experiments, both particle- and shock-velocity measurements could be made. A comparison of the experimental results with a theoretical equation of state from the 'SESAME' library has now been attempted.

Unfortunately, the library does not hold data for mylar (the material between the tracer strips in the experiment) and comparison is made instead with the theoretical Hugoniot for polystyrene (A3.4) which is expected to be very similar. The ideal gas Hugoniot is also shown in Fig A3.14 for comparison. Both assume that the material ahead of the shock has not been preheated. With the errors quoted the theoretical values are not in disagreement with the experiment. However the error bars are sufficiently large that the experiment must be considered preliminary and further experiments are planned in which the error in the values of v_s and v_p is reduced. Methods of reducing and estimating the preheat in the material are also being considered.

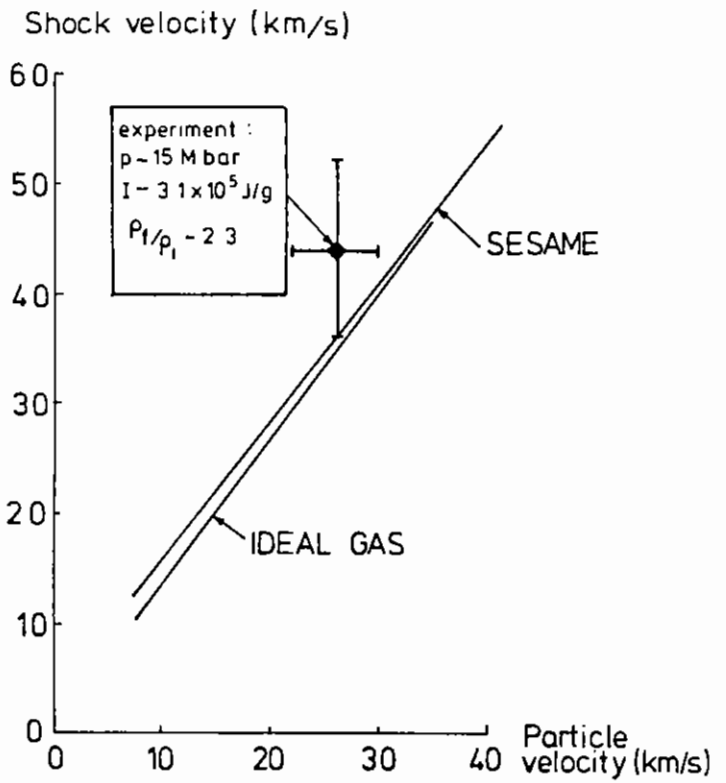

Fig A3.14 Comparison of experimental and theoretical equation of state data

A3.4 NEON LINE SHIFT MEASUREMENTS IN DENSE, LASER-COMPRESSED PLASMAS

K G H Baldwin, J R Liu, J D Kilkenny and D D Burgess (Imperial College)

A3.4.1 Introduction

Shifts in the wavelength of lines emitted from dense, laser-produced plasmas have been the subject of a number of studies in recent years (A3.5-A3.9), which have concentrated in particular on the relative shift of the energy levels of ionised emitters due to polarisation of the surrounding plasma by the emitter (the so called plasma polarisation shift). However, recent experimental observations of carbon, nitrogen and oxygen lines in dense ($10^{21} < n_e < 10^{22}$ cm^{-3} plasmas (A3.11) have failed to confirm the presence of the predicted line shifts, in keeping with the measurement of negligible or very small experimentally observed shifts at lower densities (A3.12, A3.13 and A3.14). In the present experiments we report on the observation of measurable line shifts in hydrogen- and helium-like lines of neon. The lines were observed in dense, laser compressed plasmas produced using VULCAN at the CLF.

A3.4.2 Experiment

Four beams of 0.53μm radiation were tightly focussed onto neon-filled microballoon targets. The total beam energy was 140J and the laser pulse duration 1ns. The microballoons were made of glass (0.75 μm wall thickness and 110 μm diameter) and were filled with neon to a pressure of 2 bar.

The X-ray spectrum from 9 to 14Å was recorded using a flat crystal spectrometer and a mica crystal. The spectra were recorded on DEF film and were integrated both temporally and spatially. To allow a high dispersion and at the same time provide a sufficiently high X-ray intensity, the film plane was located 98 mm from the target at the neon Ly-α wavelength of 12.134Å. The approximate dispersion in the film plane was 0.134 Å/mm, which together with the crystal resolving power

of ~ 1370 (~9mÅ) meant that the spectral resolution was crystal limited for source objects of size < 50 μm. However, careful analysis of the line profiles measured by the crystal spectrometer enabled identification of the line peaks to within several mÅ.

A3.4.3 Results

Two neon spectra were obtained which contained the Lyman series lines (α,β and γ) of hydrogen-like neon as well as the neon He-α line. Also present were a number of lines from silicon (from the microballoon glass shell), as well as impurity lines of sodium and calcium. The non-neon lines were present in first (Na), second (Si) and third (Ca) order. (To enable ready identification of the non-neon lines a further spectrum was taken of a glass microballoon implosion using a deuterium/tritium mixture as the filling gas). The lineshapes of both the Si and Ne lines were used to diagnose the compressed glass and compressed gas plasma conditions respectively. Due to the high spectrometer dispersion the continuum emission spectrum was too weak to provide diagnostic information.

The compressed glass plasma density was determined from the linewidths of the Si Lyman-series lines. For a rigorous and unambiguous determination of the electron density the effects of opacity on the linewidths must be considered (A3.15). However, in experiments (A3.15 and A3.16) using similar laser powers (1.6×10^{11} W), microballoon sizes and neon filling pressures, only the Ly-α line was found to be significantly affected by opacity. Hence the Ly-β line width was used for diagnostic purposes, the Ly-δ line being much weaker and subject to greater measurement errors. When correction was made for the spectrometer resolution, the linewidth Δ was used to determine the electron density using (A3.15):

$$\Delta(\text{eV}) = A \left(\frac{Z}{12}\right)^{B} \left(\frac{n_e}{10^{22}}\right)^{C + (Z-12)D} \qquad (1)$$

where Z is the number charge, n_e the electron density in cm^{-3}, and A, B, C and D are temperature dependent constants. For temperatures of 250-1000 eV equation (1) yielded electron densities of $7.1 - 2.3 \times 10^{22}$ cm^{-3}.

An estimate of the Si temperature can be obtained (A3.17) from the intensity ratio of the Si Ly-α dielectronic satellite ($2p^2$ (^{1}D) - 1s2p) to the He-like 1s4p - $1s^2$ transition. Assuming an electron density of ~ 10^{23} cm^{-3}, the intensity ratio yields a temperature of 300 ± 100 eV, and confirms a self consistent value of the compressed glass electron density of ~ 7×10^{22} cm^{-3}.

Similar diagnostics were used to determine the compressed gas electron density, but due to the absence of a well defined Ly-α dielectronic satellite feature, no reliable temperature diagnostic was available. However, values of $T_e = 300 \pm 50$ and $T_e = 370 \pm 30$ were obtained by two measurements under similar conditions to these obtained in (A3.10). The Ne Ly-β width in the present experiment yielded electron densities of $3.7 - 2.5 \times 10^{22}$ cm^{-3} in the range $T_e = 250 - 500$ eV respectively, and a density of ~ 3×10^{22} cm^{-3} was therefore inferred in the present experiment. This was comparable to the compressed gas density obtained in reference (A3.15) ($2.8 \pm 0.5 \times 10^{22}$ cm^{-3}) under similar conditions.

A3.4.4 Line shift measurements

The positions of the peaks of the spectral lines as a function of distance along the film plane were measured using both a microdensitometer and a Abbe comparator, both yielding similar values within a measurement uncertainty of better than 5 mÅ.

Before the positions of the spectral lines could be fitted to a dispersion curve, the effect of the crystal refractive index on the spectral line positions in the different orders was calculated. The correction to Bragg's law, allowing for refraction of X-rays on entry and exit from the crystal, is given by (A3.18 and A3.19)

$$n\lambda = 2d \left(1 - \frac{\delta}{\sin^2\theta}\right) \sin\theta \qquad (2)$$

where n is the order number, θ the observed glancing angle and δ the unit decrement of the index of refraction (calculated using the Kramers-Kallmann-Mark (A3.18) theory). The angular correction (A3.18) to the observed angle of diffraction is then

$$\theta - \theta_o = \delta \sec\theta \operatorname{cosec}\theta \qquad (3)$$

The wavelengths for all the lines (A3.20) were corrected for refractive index effects in this manner, and the non-neon lines then used as calibration wavelengths to fit a dispersion curve (A3.21). Due to the Z^{-2} scaling of the line wavelengths, there was a close coincidence between the silicon lines in second order with the first order neon lines (as $Z^2_{Si}/Z^2_{Ne} = 1.96$). Hence the silicon lines in particular could be used as a reference point for the neon line shifts, and thereby reduced the sensitivity of the measured shift to small inaccuracies in the determination of the local crystal dispersion.

The deviation of the measured wavelengths from the fitted dispersion curve is shown in Fig A3.15.

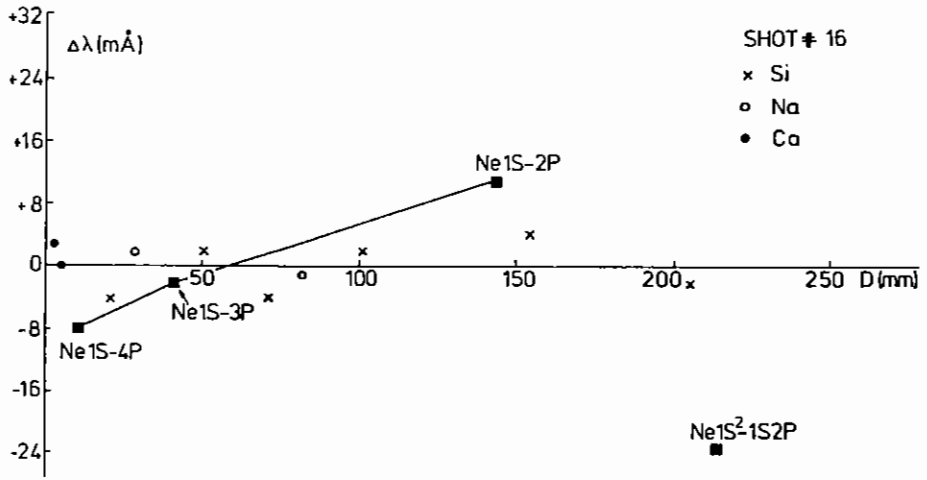

Fig A3.15

Wavelength difference Δλ between the observed and tabulated (A3.20) wavelengths (both corrected for refractive index effects) as a function of distance along the film plane

In spite of the random errors in the averaging of the line position measurements, Fig A3.15 indicates that there is a trend towards a greater red shift for the lower neon Lyman-series members, and a much larger blue shift for the neon He-α line (these trends are apparent even when the refractive index corrections are neglected). The net effect of the refractive index corrections is merely to blue shift all the neon line wavelengths by ~ 9 mÅ on average, and there is a noticeable improvement in the fitting accuracy once the corrections are included (from ± 5 mÅ to ± 3 mÅ). Hence the observed trends in the shift of the neon wavelengths appear not to be a result of instrumental effects arising from measurements in different orders.

A3.4.5 Discussion

The neon line shifts shown in Fig A3.15 do not necessarily represent a measurement of the absolute line shift, since the neon lines are calibrated relative to other lines which may themselves be perturbed. Mechanisms other than emitter-plasma interactions and instrumental effects could also cause a systematic difference in the wavelengths of the neon and non-neon lines.

Spatial separations between the two emitting regions (compressed glass and compressed gas) may produce an apparent shift in the transition wavelengths, although the spherical symmetry of compression experiments usually minimizes such spatial effects. Assuming, however, that the separation of the glass shell and gas core emission regions produced an asymmetry of the order of a typical compressed core diameter (~ 20 μm (A3.15), then under the present geometry the net shift is equivalent to only ~ 3mÅ.

Differential Doppler shifting of the observed lines may have resulted from emission at different stages of the microballoon compression (since the X-ray spectra were not time resolved). In particular, Ly-δ emission is likely to occur at the higher temperatures present in the compressed core when the plasma is stationary, while Ly-α and He-α emission occur over much longer timescales during plasma compression and expansion. Assuming particle velocities (A3.15) of the order of $10^7 cms^{-1}$, this corresponds to a shift of 4mÅ at Ne Ly-α wavelengths.

If it is assumed that only the emission from the imploding shell nearest to the spectrometer is observed while emission from the far side of the plasma is absorbed, the glass shell emission lines will be blue shifted. Assuming then that the neon ions are stationary or are moving towards the spectrometer during the emission process, an apparent red shift of the neon lines will result. However this would not account for the large observed blue shift of the neon He-α line. The He-α line would be expected to be emitted under conditions closer to those for the emission of the more strongly red shifted Ly-α line than for the slightly blue shifted Ly-δ line. Hence it is unlikely that either spatial inhomogeneities or differential Doppler effects can explain the observed line shifts.

A3.4.6 Conclusion

Current theoretical predictions for plasma polarization shifts indicate that the shifts observed are almost an order of magnitude greater than expected. Extrapolation from calculations given in (A3.5) and (A3.7) yield Ly-α red shifts ranging from a lower limit of 0.7 mÅ for the uniform electron model to an upper limit of 1.7 mÅ given by the linearized Debye-Huckel model. By comparison, the observed shift is of the order of + 10 mÅ in the present experiment.

Although calculations for the effect of electron collisions on line shifts (A3.9) have not been performed for hydrogen-like neon lines, the calculations for hydrogen and hydrogen-like helium (A3.9) indicate progressively larger ($\Delta\lambda$) red shifts for higher Lyman series members (blue shift contributions from ion quadrupole effects are in general negligible). This trend is in contrast to the observed smaller ($\Delta\lambda$) red shifts for higher Lyman series members (changing to blue shifts in some cases) which were observed in the present experiments.

A3.5 CHARACTERISATION OF X-RAY SOURCE BRIGHTNESS

M J Lamb, P McCavana, R Corbett, C L S Lewis (Queen's), G Kiehn (Oxford) and M H Key (RAL)

A3.5.1 Introduction

We present here a brief preliminary report of a recent experiment aimed at characterising the X-ray source brightness which can be obtained from a variety of targets irradiated by the VULCAN laser. Such measurements have immediate relevance to other areas of laser plasma studies e.g. in the optimisation of backlighting sources for radiography experiments, and sources for photopumped X-ray laser schemes. They will also be of interest to workers in other areas who may have a requirement for a bright source of X-rays.

A3.5.2 Experiment

We have recorded X-ray spectra in the range 3.5 to 13Å from targets of Cu, Al, Au, Mo, Bi and Cl (saran) for a variety of irradiation conditions using both 1.06μm and 0.53μm laser light.

The experimental arrangement is shown in Fig A3.16 which for clarity shows just one spectrograph. On each shot VULCAN delivered two simultaneous output beams, at wavelengths of 1.06μm and 0.53μm, which were separately focussed on two identical targets positioned adjacent to one another as shown. Except in the case of Mo, when ribbon shaped targets were used, the targets were in the form of 270 μm discs each supported by a thin fibre. Two space-resolving mini crystal spectrographs and X-ray pinhole cameras recorded the X-ray emission from both targets. Each spectrograph recorded spatially separated spectra of the two sources thereby providing a direct comparison between infrared and green irradiation on a single piece of film.

For each of the targets mentioned above a series of shots were taken varying the following irradiation parameters;

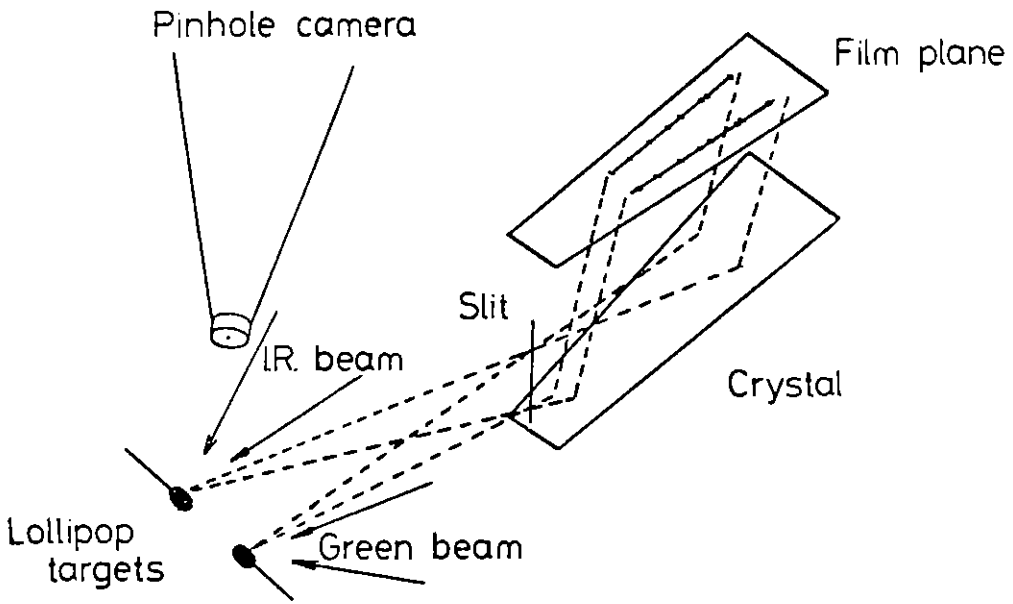

Fig A3.16 Experimental arrangements

(1) laser pulse length - 1ns and 100ps,
(2) focal spot size - tight focus and obscuration focus (all of 270μm disc irradiated),
(3) incident laser energy - high and low.

High laser energies corresponded to 100J (1.06μm, 1ns), 30J (1.06μm, 100ps), 30J (0.53μm, 1ns), and 10J (0.53μm, 100ps). The low energies were typically a factor of 5 to 10 less than the corresponding high energy values.

A complete scan of the above parameters therefore required 8 shots for each target material.

A3.5.3 Results and Conclusions

The choice of targets gave a selection of K,L, and M-shell spectra in the wavelength range 3.5 - 13Å. The dominant spectral features consisted of

(a) Cu L-shell line emission from 10 to 13Å,
(b) Al H-like and He-like resonance lines around 7Å,
(c) Au M-band continuum emission from 4.8 to 5.4Å,
(d) Cl He-like resonance lines around 4Å,
(e) Bi M-band continuum emission from 4.4 to 4.8Å,
(f) Mo L-shell line emission from 3.5 to 5.5Å.

Over 120 spectra were recorded and the results of a detailed analysis will be published later. The following observations may be made after a preliminary analysis.

Table A3.1 summarises some preliminary estimates of the time integrated X-ray emission for a selection of the high energy shots. These refer to the brightest line recorded for Mo, Cl and Al, and the peak of the M-band continuum for Bi and Au.

In all cases X-ray conversion efficiency was larger for green irradiation than for infrared. Hence brighter X-ray sources could be obtained by first coverting the primary laser wavelength to the second harmonic before target irradiation despite the losses involved in the

frequency-doubling process. The increased effectiveness of green irradiation was more noticeable at shorter X-ray wavelengths.

For the laser energies used the time integrated X-ray emission appears relatively insensitive to the laser pulselength, although the instantaneous X-ray power would be greater (up to 10x) for the shorter pulse.

A significant parameter is the focus condition which determines the source size. In the case of obscuration focus (270μm source) the X-ray yield is typically 10x greater than for tight focus (~80μm source). This is consistent with having a larger area source of similar surface brightness, and implies a rather weak scaling of source brightness with incident laser intensity, a conclusion also indicated by the data from the low laser energy shots.

A fuller analysis of all the data obtained is required to confirm and further quantify the trends indicated above. It is hoped to carry out measurements on other target materials and over a wider wavelength range in order to establish a comprehensive database of absolute X-ray yields, and to understand more fully the physics of X-ray production in laser produced plasmas.

		X-ray emission/10^{-5} J ster^{-1} (laser energy/J)			X-ray emission/10^{-3} J ster^{-1} keV^{-1} (laser energy/J)		
		Mo	Cℓ	Aℓ	Bi	Au	
tight focus	G	2.3 (26)	3.1 (33)	2.2 (31)	1.5 (30)	1.2 (47)	1ns
	IR	2.1 (108)	1.7 (94)	1.8 (57)	0.8(105)	0.3(123)	
	G	1.9 (9)	3.2 (9)	1.8 (10)	1.6 (9)	1.0 (14)	100ps
	IR	0.9 (25)	2.2 (25)	1.3 (18)	0.5 (27)	0.5 (30)	
obscuration focus	G	-	17.0 (22)	26.0 (45)	2.0 (20)	17.8 (48)	1ns
	IR	-	14.0 (86)	24.0(105)	6.1 (95)	13.0(123)	
	G	-	8.4 (9)	-	3.2(8.5)	9.2 (14)	100ps
	IR	-	6.2 (24)	17.0 (34)	2.6 (27)	5.3 (30)	

Figure A3.1 Experimental Results

A3.3 References

A3.1 J P Christiansen, D E T F Ashby and K V Roberts, Computer Physics Communications, 7, 271 (1974).

A3.2 I P Grant, B J McKenzie, P H Norrington, D F Mayers and N C Pyper, Computer Physics Communications, 21, 207 (1980).

A3.3 B J McKenzie, I P Grant, P H Norrington, Computer Physics Communications, 21, 233 (1980).

A3.4 B I Bennett, J D Johnson, G I Kerley and G T Rood, Los Alamos Laboratory report LA 7130 (1978).

A3.5 S Skupsky, Phys Rev, A21, 1316 (1980).

A3.6 J Davis and M Blaha, J Quant Spectrosc Radiat Transfer, 27, 307 (1982).

A3.7 R Cauble, J Quant Spectrosc Radiat Tranfer, 28, 41 (1982).

A3.8 V Gupta and A K Rajagopal, Phys Rep, 87, 259 (1982).

A3.9 H R Griem, Phys Rev, A 27, 2566 (1983); 28, 1596 (1983).

A3.10 G V Sholin, Opt Spectrosc, 26, 275 (1969).

A3.11 S Goldsmith, H R Griem and L Cohen, Phys Rev, A 30, 2775 (1984).

A3.12 S Volonte, J Phys D,11, 1615 (1978).

A3.13 E A M Baker and D D Burgess, J Phys B, 12, 2097 (1979).

A3.14 C Fleurier and P Le Gall, J Phys B, 17, 4311 (1984).

A3.15 J D Kilkenny, R W Lee, M H Key and J G Lunney, Phys Rev A, 22, 2746 (1980).

A3.16 B Yaakobi et al, Phys Rev A, 19, 1247 (1979).

A3.17 R W Lee, B L Whitten and R E Stout II, J Quant Spectrosc Radiat Transfer, 32, 91 (1984) - RATION code therein.

A3.18 A H Compton and S K Allison, "X-rays in Theory and Experiment", D van Nostrand, (2nd edition) (1935).

A3.19 Y Cauchois and C Bonnelle, "Atomic Inner-Shell Processes", II, 83, Academic Press (1975).

A3.20 R L Kelly and L J Palumbo, "Atomic and Ionic Emission Lines below 2000 Å", NRL Report 7599, (1973).

A3.21 J W Criss, Applied Spectrosc, 33, 19 (1979).

A4 XUV LASERS AND APPLICATIONS OF LASER-PRODUCED PLASMAS

Editor O Willi

A4 XUV Lasers and Application of Laser Produced Plasmas

A4.1 Introduction

C L S Lewis (Queen's) and O Willi (Imperial College)

In the past year a clear break - through has been achieved in producing a high quality long line focus vital for x-ray laser research. The capability of producing laser heated plasmas with the scale length of centimeters and uniformly heated along the entire length is fundamentally important for any x-ray laser schemes which will show high gain. Experiments with the newly developed aberration free line focus using a lens and off-axis mirror combination proved to be extremely successful. This new configuration is particularly suited to the recombination schemes when thin carbon fibres are used since the narrow dimension in the line focus can approach the diffraction limited spot size of the heating laser beam.

Various measurements of plasma parameters, such as sodium brightness and hydrodynamics, relevant to the sodium-neon photopumped laser scheme yielded extremely valuable information for code developments.

The second major area of activity of the group has been the development of new applications of intense X-rays emitted from hot laser-produced plasmas.

High resolution (better than 200Å) contact micrographs have been produced with exposure times of about a nanosecond. Images of diatoms, muscle and blood cells have been recorded on x-ray resists showing features down to the limit of the SEM used to view the developed resist.

Initial experiments have been carried out to investigate the feasibility of laser reflexafs for studies of metal-silicide formation. An annealing laser beam was used to form specific compounds in the silicide film whereas the reflection EXAFS technique using x-rays produced by a second laser beam examined the temporal evolution of the silicide formation.

Finally an ablating plasma was used to study the behaviour of collisionless shocks created by placing an obstacle in the streaming plasma. Optical probing techniques clearly showed the formation of a bow shock around the spherical obstacle in the absence of magnetic fields.

A4.2 Experimental Assessment of Line Focus Optics for X-ray Laser Experiments

I N Ross, D Bassett (RAL), G Kiehn (Oxford)
O Willi (Imperial College), C Lewis, R Corbett (Queen's)
L Shorrock (Hull)

A4.2.1 Introduction

To achieve considerable gain in X-ray laser experiments, a long line focus with good optical quality is essential. Recently an optical system has been developed to produce a long high quality line focus using a lens and off-axis mirror combination. This system is described in Section A6.6.1. We report here on experimental results of hot uniform cylindrical plasmas obtained with this scheme by irradiating fibre or thin foil targets.

A4.2.2 Experimental Arrangement

Fig. A4.1 shows a schematic of the optical components. An f 2.5 aspheric doubled lens and a spherical mirror are used to generate a 1cm long line focus.

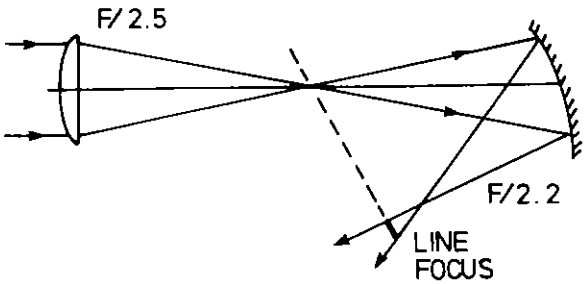

Fig A4.1 Schematic of the optical components to produce an aberration free line focus

The length and the intensity distribution of the line focus are controlled using a shaped aperture in front of the input lens. The width of the line focus was limited by the laser divergence to about 15μm. The plasma was investigated by a)an X-ray pinhole camera to study the uniformity of the emission along the fibre or foil target, b) ion-calorimeters to measure the energy coupled into the plasma and the angular distribution of the plasma blow-off, c) a spectrograph to observe the spectrum in the axial direction and d) a camera to detect the transmitted laser beam through the plasma.

A4.2.3 Experimental Results

The experiments were primarily carried out to investigate the performance of the described line focus scheme. A large number of shots were taken using carbon fibres and thin (1000Å) foil targets.

Parameters such as fibre length, diameter, prepulse levels and total incident energy were varied. The effects of small variations in alignment and focusing were also studied.

X-ray pinhole photography

X-ray pinhole photographs were recorded to monitor the distribution of emission along the fibre in the 1Kev energy band. The diameter of the pinhole was 100μm. Fig. A4.2 shows an x-ray pinhole camera image taken on a fibre target which was irradiated with a 100ps, 10J green laser pulse. As can be clearly seen in Fig. A4.2 no globel non-uniformities were observed.

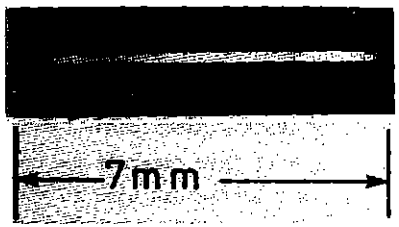

Fig A4.2 X-ray pinhole camera image of an aberration free line focus taken on a 6 μm fibre target

Calorimetry

Three strip calorimeters were used to study the total energy absorption and the plasma angular distribution on fibre targets. According to the quality of the alignment a fraction between 5 to 20% of the incident energy was absorbed resulting in an energy deposition of up to 2j/cm. This is about a factor of two larger than previously achieved with cylindrical optics (Ref. A4.1). Fig A4.3 shows the angular distribution of the plasma blow-off measured on fibre targets. A clear lobed-sided distribution is observed due to the laser beam, single beam irradiation.

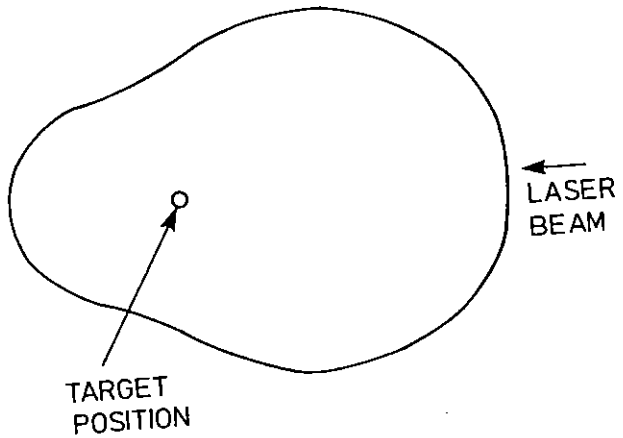

Fig A4.3 Plasma distribution of a single sided irradiated fibre target measured with a series of ion calorimeters

Axial spectrometry

Time integrated spectra were taken along the axis of the fibre and foil targets in the wavelength range from 50 to 200Å. A spectral anomely was observed consisting of a small rectangular intense spot superimposed on the background of the He-like 4-2 carbon transition (see Fig.A4.4). This observation might be an indication of superfluorescent emission with a pain length product of 7. We have however not been able to verify this observation as x-ray lasing beyond any doubt nor have we found any experimental inconsistencies which indicate that this spot is produced by anything else than x-ray lasing.

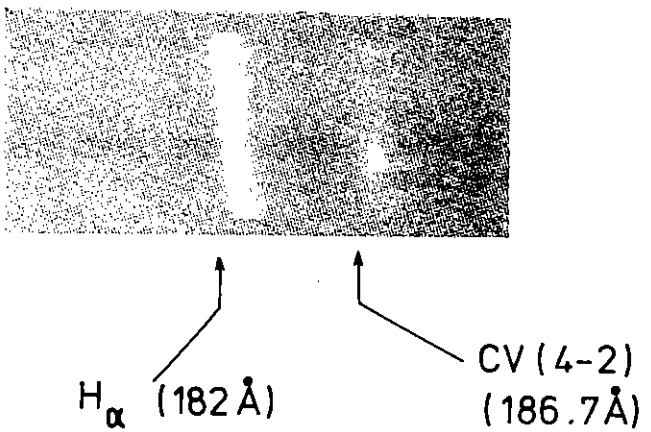

Fig A4.4 Spectrum taken on a carbon fibre showing a small rectangular feature superimposed on the CV (2-4) transition

Small-scale non-uniformity studies

A f/2 lens opposite to the off-axis mirror was used to image the target plane onto burn paper collecting the incident laser light passing through the plasma. As can be seen in Fig. A4.5a small scale non-uniformities with a scale length of 20 to 30 μm were observed along the line focus in the transmitted laser beam. The small scale break-up might be caused by laser beam filamentation. Since a uniform image was obtained (see Fig. A4.5b) when no target was in place proving that the structure was not generated by the off-axis mirror configuration. Further experiments will be carried out to investigate these observations.

A4.2.4 Conclusions

Experiments have shown that, using a new line focus geometry, thin fibres of up to 10mm long can be illuminated efficiently and uniformly. Good coupling of laser energy into plasma energy can be achieved producing a uniformly expanding plasma. Axial spectrometry shows that conditions of X-ray laser action should be achievable with modest laser input energy.

A4.3 Measurements of Plasma Parameters Relevant to the Sodium-Neon Photopumped Laser Scheme

R E Corbett, C L S Lewis, M J Lamb, P McCavana, S Saadat (QUB),
C Deeny, O Willi (ICL), E Fill (Max-Planck Garching), J Lunney (TCD),
D Bassett (RAL)

A4.3.1 Introduction

The sodium-neon scheme involves the pumping of the $1s^2\ ^1S - 1s4p\ ^1P$ transition at 11.0027Å in Ne IX by radiation from the $1s^2\ ^1S - 1s2p\ ^1P$ transition at 11.003Å in Na X, utilising the close wavelength match between the two transitions to give population inversion on the 2-4, 3-4, and 2-3 singlet transitions of Ne IX at 58, 230 and 82Å respectively.

Calculations have predicted that a gain of $100cm^{-1}$ on the Ne IX $1s2p\ ^1P-1s3d\ ^1D$ transition could be achieved for a neon plasma with an electron density of $10^{21}\ cm^{-3}$ and electron temperature of 65 eV pumped by a sodium plasma with a photon flux in the 11Å line equivalent to a 227 eV blackbody (A4.2).

The aim of the experiment was to investigate the conditions under which these plasma parameters might be realised, to measure the absolute pump brightness of the sodium, and to provide a set of data for comparison with hydrodynamic and atomic codes.

A4.3.2 Targets

The targets used were 550 micron diameter, 3 micron thick aluminium lollipops. Neon had been introduced into one side of the foils by ion implantation. Some of the targets had neon implanted at 65 keV, giving neon at a depth of 0.11 microns, while the rest had been implanted at 80 keV, giving neon at a depth of 0.14 microns. The surface dose of neon was 6×10^{16} ions cm^{-2} in both cases. The other sides of the targets were coated with a 0.1 micron thick layer of sodium fluoride.

The essential idea was to irradiate the neon side, allow the neon containing plasma to expand until it had attained the required values of density and temperature, and then to irradiate the side of the foil coated with sodium fluoride to give a bright, optically thick pump plasma (A4.3).

Typical irradiances used were 10^{13} to $10^{14}\ Wcm^{-2}$ at a wavelength of 0.53 microns, with 100ps pulses being used throughout. Focal spot sizes were about 200 to 400 microns.

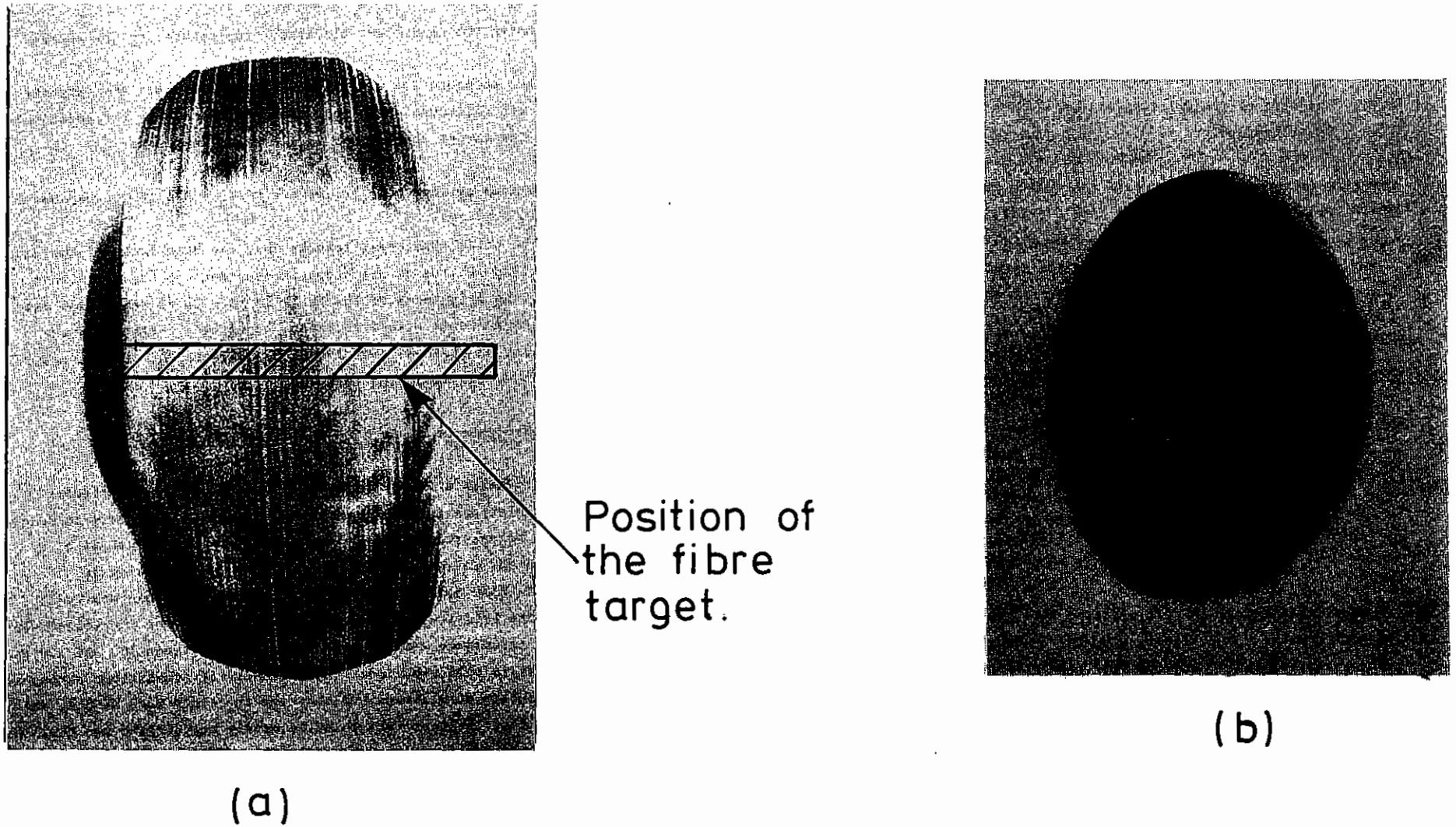

Fig A4.5 Spatial laser beam profile transmitted through the plasma of an irradiated fibre target

A4.3.3 Measurement of Sodium Brightness

To calculate an equivalent blackbody temperature for the 11Å sodium line it was required to know

(i) the total emission in the line
(ii) the duration of the emission
(iii) the size of the emitting region
(iv) the linewidth.

The time-integrated emission from the sodium was recorded using a mini-crystal spectrometer with a TIAP crystal, and an active spectrometer consisting of an image intensifier coupled to a phosphor-coated fibre optic screen on the target chamber wall, with a flat TIAP crystal mounted midway between the target and the phosphor screen, and satisfying the Bragg condition for 11Å radiation.

Another TIAP crystal was used in conjunction with the QUB streak camera to time-resolve the emission. The spectral coverage of both the active devices was about 1.5Å, so that emission from the Na XI $1s\ ^2S - 2p\ ^2P$ line at 10.03Å could also be monitored. A streak camera picture of the two sodium lines is shown in Fig A4.6

Focal spot sizes were measured with a standard pinhole camera. The arrangement of the diagnostics was as shown in Figs A4.7 and A4.8.

The total emission at 11Å was measured from the spectrum recorded on the mini-crystal spectrometer, assuming a value of 2.5×10^{-4} for the rocking curve integral for the TIAP crystal at 11Å. The source was assumed to be a plane surface whose area was determined from the pinhole camera measurement, and the duration of the emission was taken as the FWHM of the streak camera output, the streak speed having been measured as 77 ps per millimetre. The resolution of the active spectrometer was limited to about $\lambda/\Delta\lambda = 450$ by the source size and the crystal rocking angle. This was not sufficient to provide a measurement of the time-integrated linewidth, but allowed an upper limit of 25 mÅ to be placed on it.

From these values, the emission from the source in watts per square metre per unit frequency interval was calculated, and this in turn was used to give a value for the number of photons per mode n_p, where

$$n_p = (\exp(h\nu/kT_B) - 1)^{-1}$$

with T_B being the equivalent blackbody temperature for the source.

The results obtained for six shots are given in Table A4. Figures in brackets are estimates, and it is assumed that 60% of the green energy entering the target chamber was incident on the target.

The calculated optimum pump brightness of $T_B = 227$ eV corresponds to $n_p = 6.9 \times 10^{-3}$.

It is to be noted from these results that the brightness of the Na X $1s^2\ ^1S - 1s2p\ ^1P$ line is not strongly dependent on the irradiance. In contrast, the brightness of the Na XI $1s\ ^2S - 2p\ ^2P$ transition was observed to increase with irradiance, being less bright than the He-like line on 18.10.84 shot 2 and 19.10.84 shot 4, of comparable brightness on the remaining three shots.

A4.3.4 Hydrodynamics of Targets - Interferometry

In order to allow the neon-containing zone to attain the required values of electron temperature and density, it is necessary to delay the laser pulse irradiating the sodium side of the target with respect to the pulse irradiating the neon side. Choosing an appropriate time delay involves the use of hydrodynamic models to simulate the behaviour of the neon-containing side of the target under the given irradiance conditions. Time delays between 300 and 500 ps were chosen in this experiment, on the basis of simulations performed with an average-atom ionisation code run in tandem with MEDUSA, which predicted that the neon ions would be mainly helium-like and that the neon-containing zone would have suitable values of electron temperature and electron density for times in this range.

To provide direct comparison between code predictions and the actual behaviour of the targets, a Nomarski-type interferometer (A4.4) ws used with a red (622 nm) probe beam to probe the plasma expanding from one side of an aluminium target lollipop, at times up to 1 ns after the

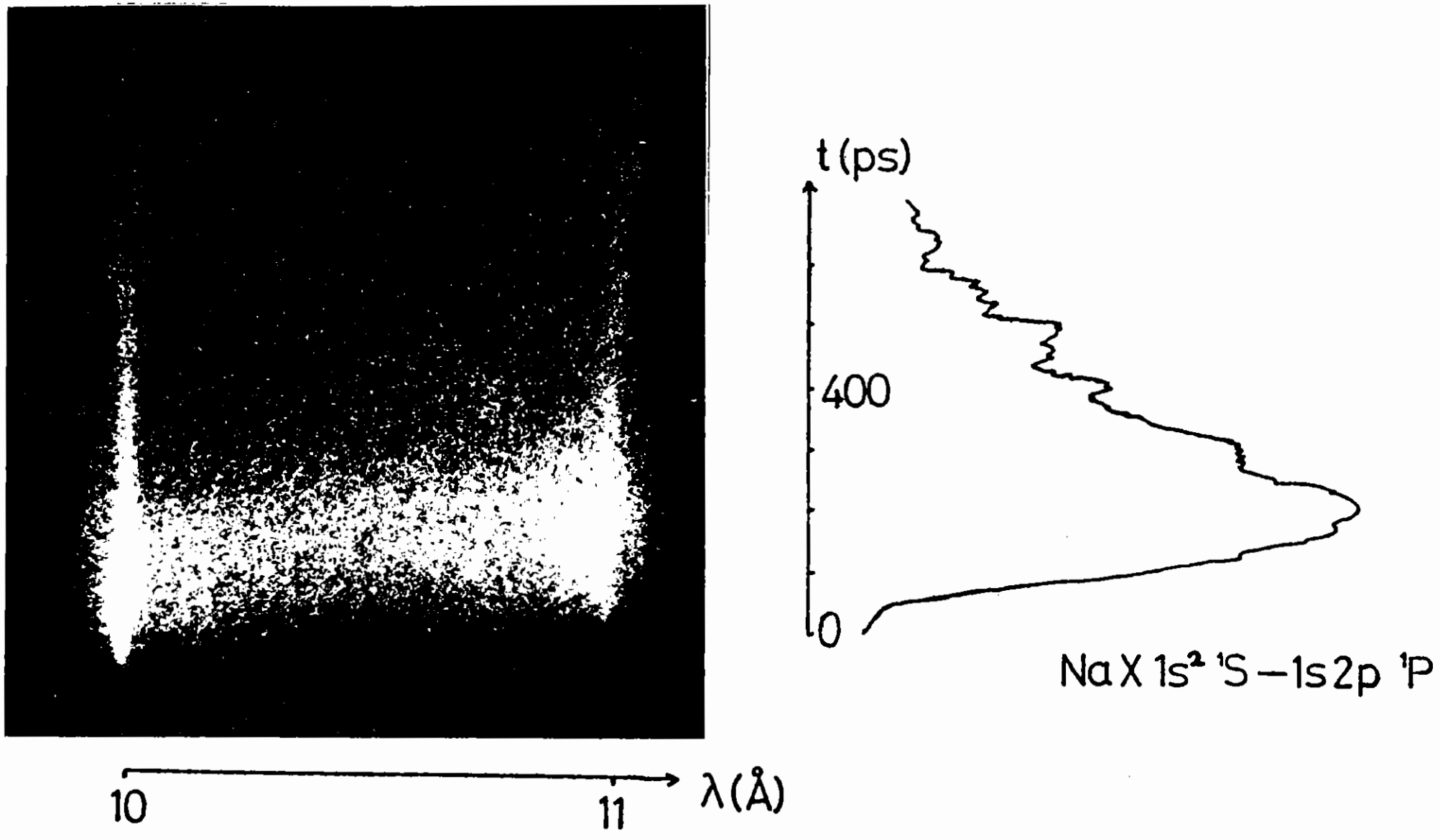

Fig A4.6 Streak camera picture of Na XI 1s ^{2}S - 2p ^{2}P (10.03 Å) and Na X 1s^2 ^{1}S - 1s2p ^{1}P (11.00 Å)

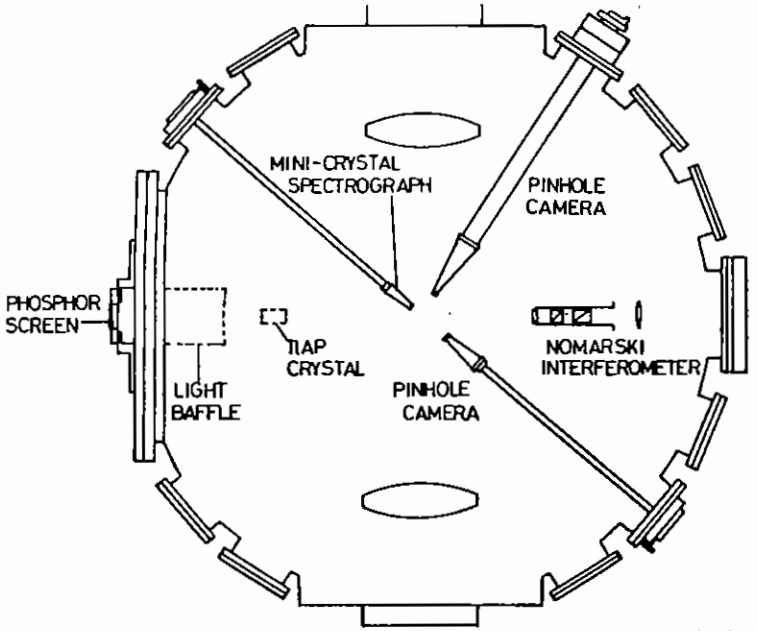

Fig. A4.7 View of diagnostics in equatorial plane of target chamber. The active spectrometer assembly was removed when the interferometer was in use

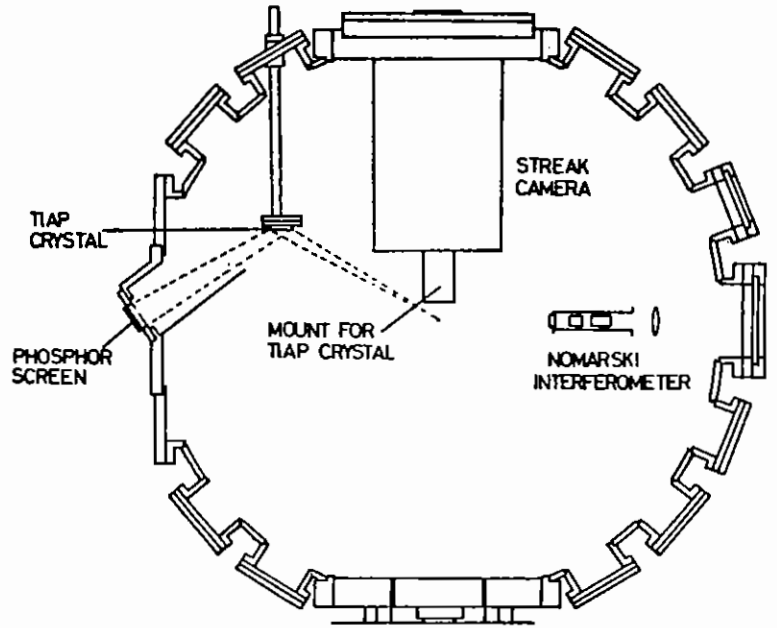

Fig. A4.8 View of diagnostics in E-W vertical plane

TABLE A 4.1

SHOT	GREEN ENERGY (J)	SPOT SIZE (μm)	I_{xe} (Wcm^{-2})	FWHM DURATION OF EMISSION (ps)	n_p	T_B(eV)
18.10.84 2	1.4	367	0.1	(240)	2.2×10^{-6}	106
19.10.84 4	3.9	265	0.4	246	1.1×10^{-4}	124
19.10.84 9	7.9	422	0.3	236	8.3×10^{-6}	120
19.10.84 12	16	(420)	0.7	313	5.4×10^{-6}	135
19.10.84 15	16	306	1.3	246	6.8×10^{-5}	118
19.10.84 20	(16)	340	1.1	293	8.3×10^{-5}	120

target had been irradiated.

The fringe patterns generated were Abel-inverted to give electron density profiles for the plasma. The interferogram from shot 1 of 5.11.84 is shown in Fig A4.9. The probe delay time on this shot was 500 ps. The electron density profiles at various distances from the target surface, as derived from the interferogram, are shown in Fig A4.10. The axial density profile is compared with that predicted by the 2-D hydro-code POLLUX in Fig A4.11, where there is seen to be reasonable agreement between the two.

A4.3.5 Photopumping of Neon

A streak from a photopumped neon target is shown in Fig A4.12. The TlAP crystal reflecting the lines onto the streak camera photocathode was on the sodium side of the target, so that the radiation from the neon was being viewed through the 3 micron thick aluminium target (3 microns of aluminium is 50% transmitting at 11Å). The picture is complicated by the fact that some of the sodium fluoride had found its way onto the neon side of the target during the coating process as evidenced by the presence of emission from the NaXI $1s\ ^2S - 2p\ ^2P$ line before the main pumping pulse. This means that the radiation at 11Å from the neon side of the target is due to both the Ne IX $1s^2\ ^1S - 1s\ 4p\ ^1P$ and the Na X $1s^2\ ^1S - 1s2p\ ^1P$ lines. However, the presence of the neon is clearly indicated by the Ne X $1s^2\ ^1S - 1s4p\ ^1P$ line with no contribution from sodium (Fig A4.13.)

Emission from each side of the target was monitored using two space-resolving mini-spectrometers, with spatial resolutions of 10 to 25 microns. Spectra were also recorded on a 1000 lines per millimetre transmission grating spectrograph, which recorded emission at wavelengths up to 100Å with a spectral resolution of 2Å. By comparing spectra obtained from neon-containing targets with those obtained from the aluminium targets used for the interferometry which did not contain neon, it was possible to identify the neon lines at 58Å and 82Å (Fig A4.14). However, on comparing spectra from pumped and unpumped neon, it did not prove possible to detect any enhancement of the neon lines resulting from photopumping by the sodium.

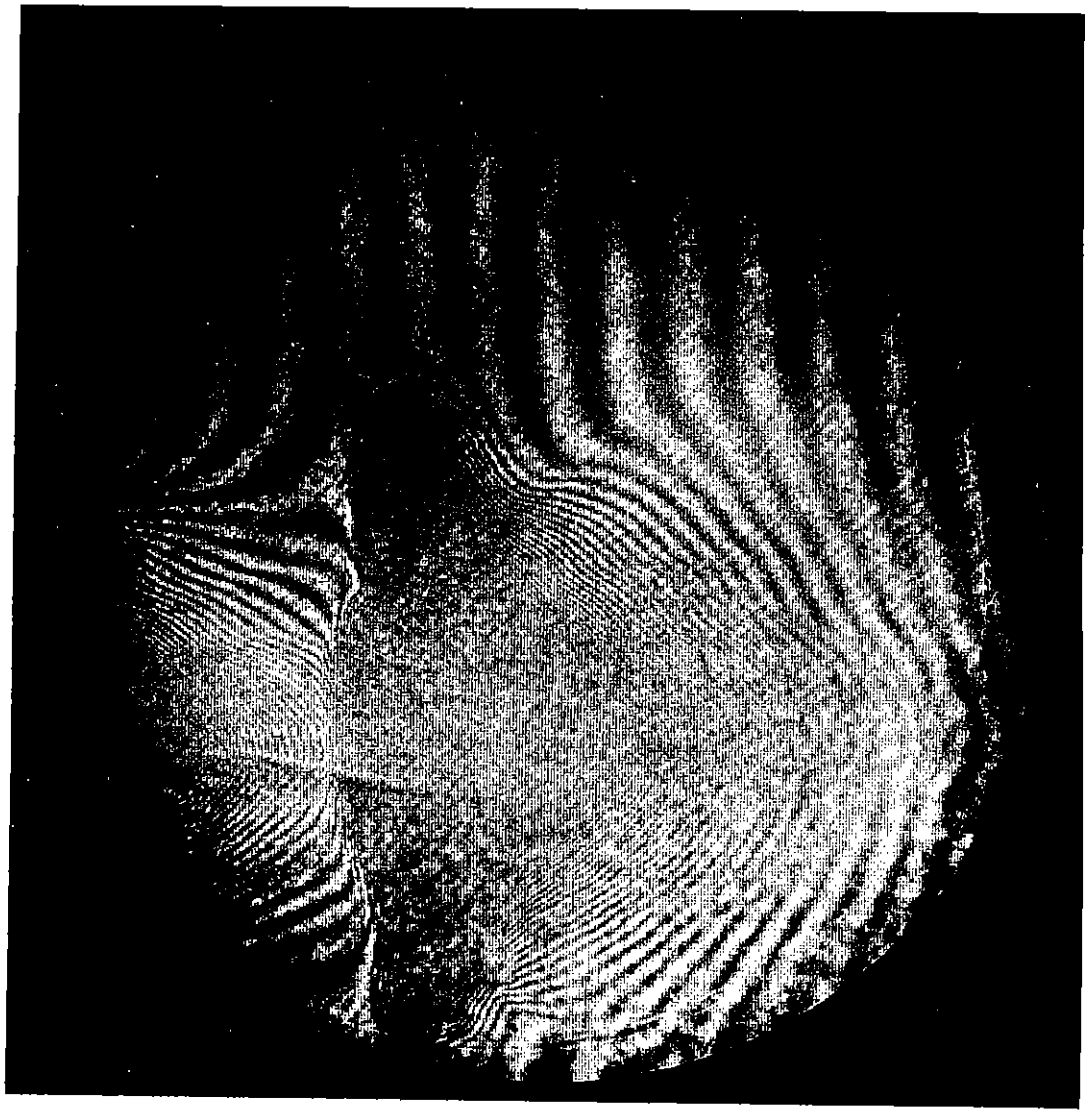

Fig A4.9 Interferograph from 5.11.84 shot 01

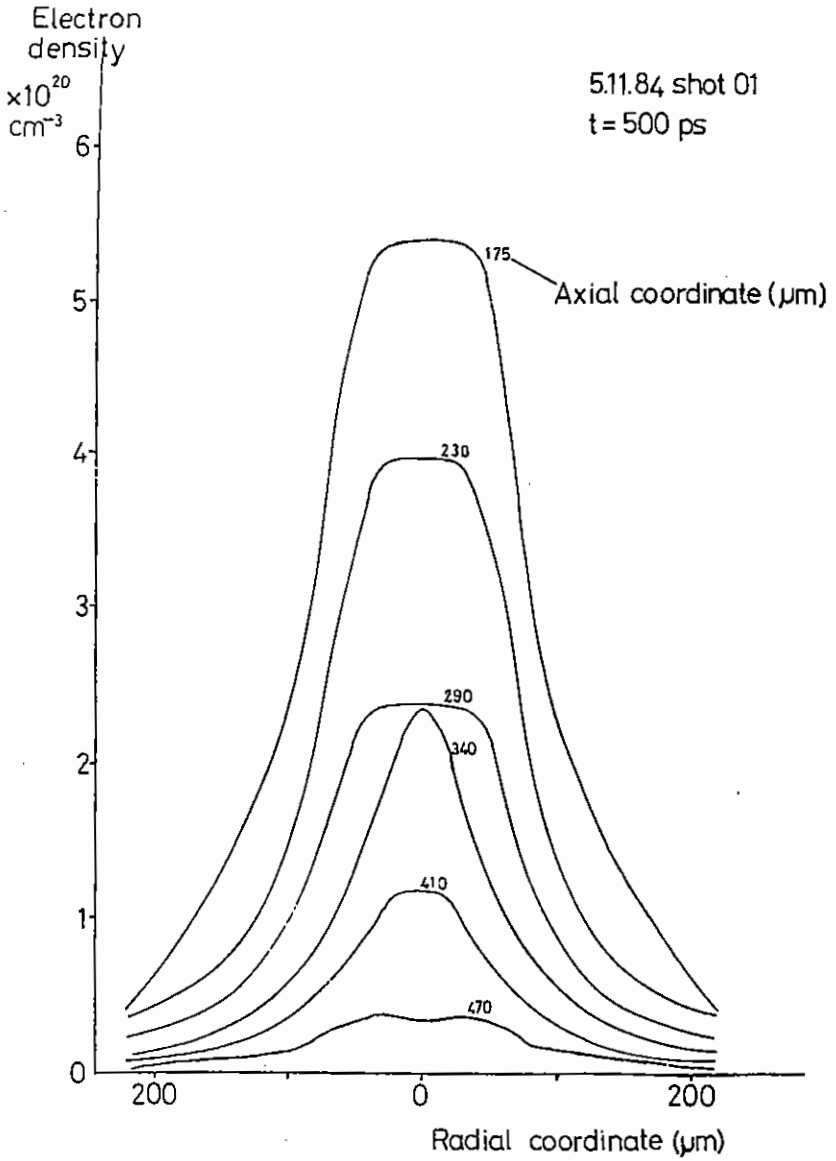

Fig A4.10 Electron density profiles obtained from Abel-inversion of interferograph

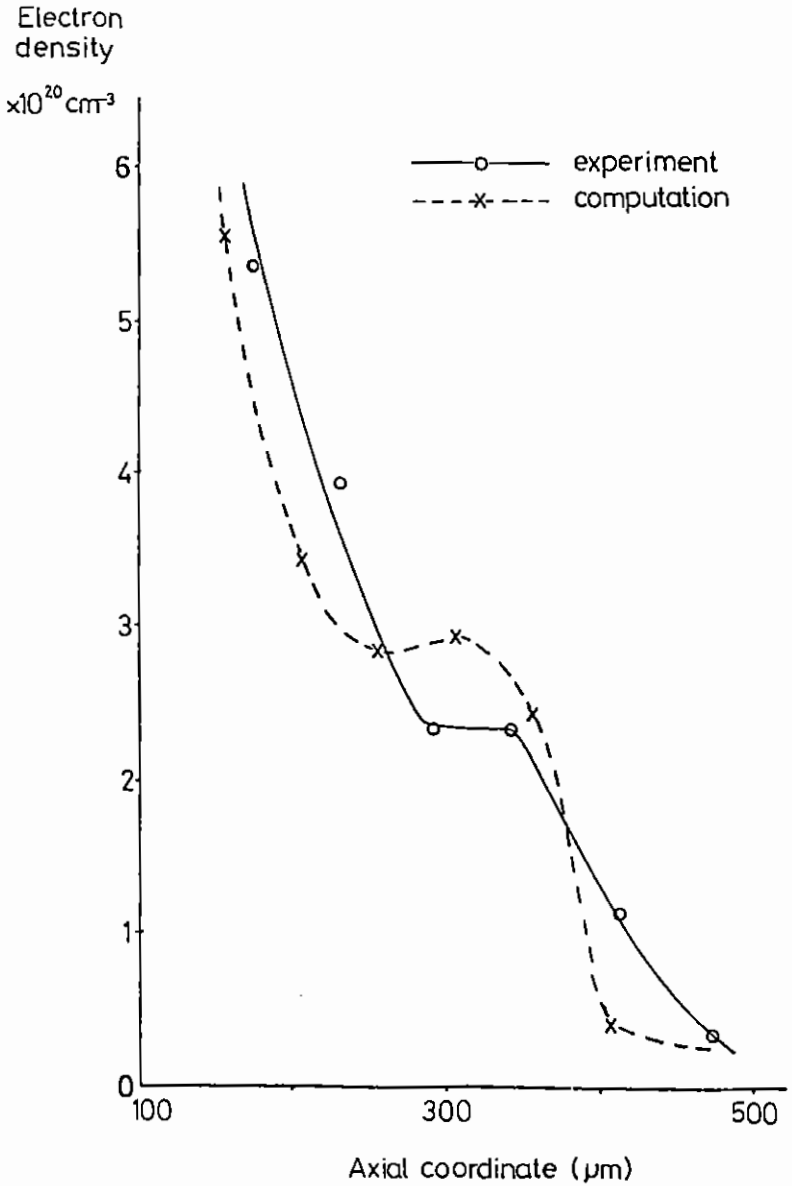

Fig A4.11 Comparison of axial electron density profile with that obtained from the 2-D hydro-code POLLUX

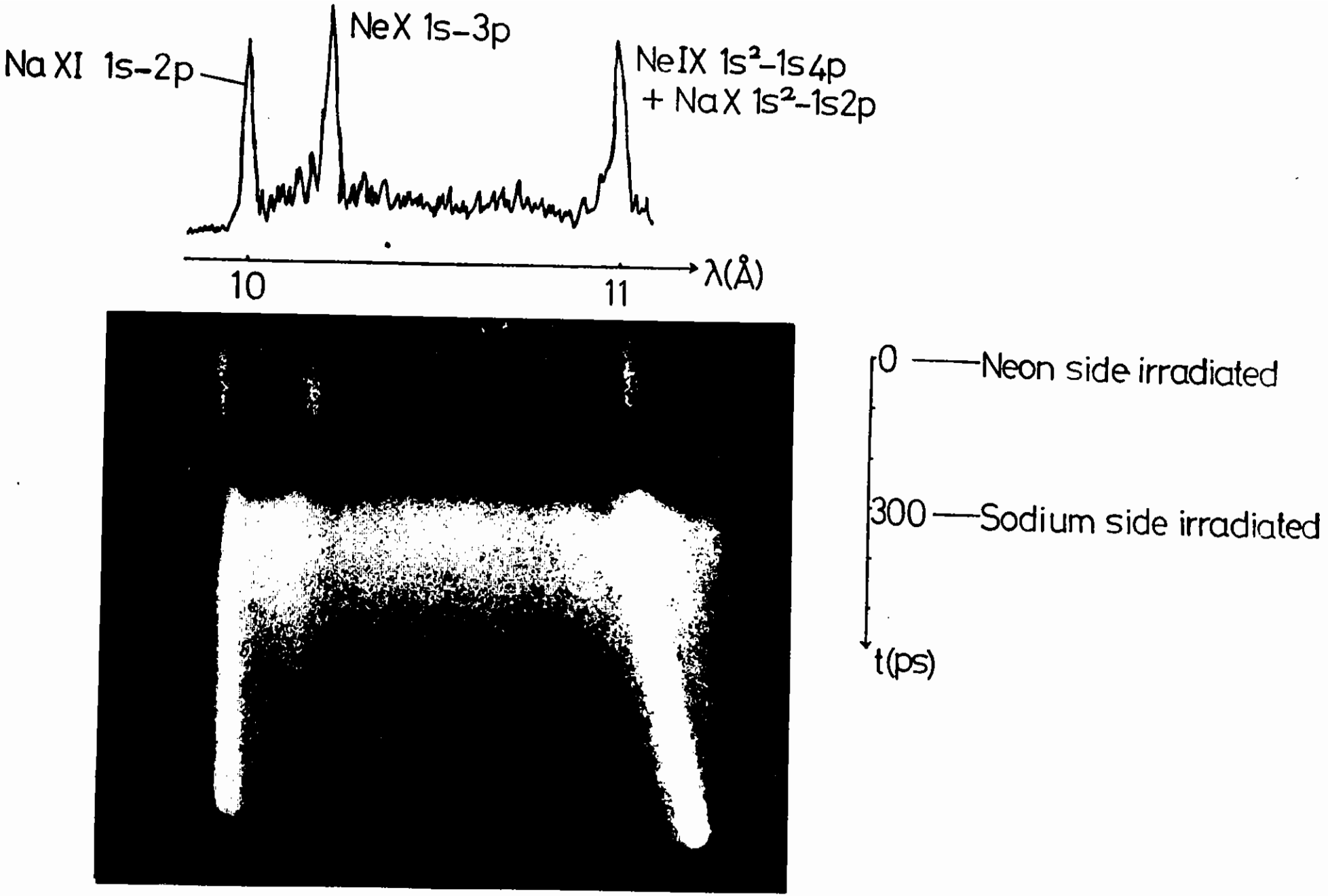

Fig A4.12 Streak camera picture of target under double-sided irradiation

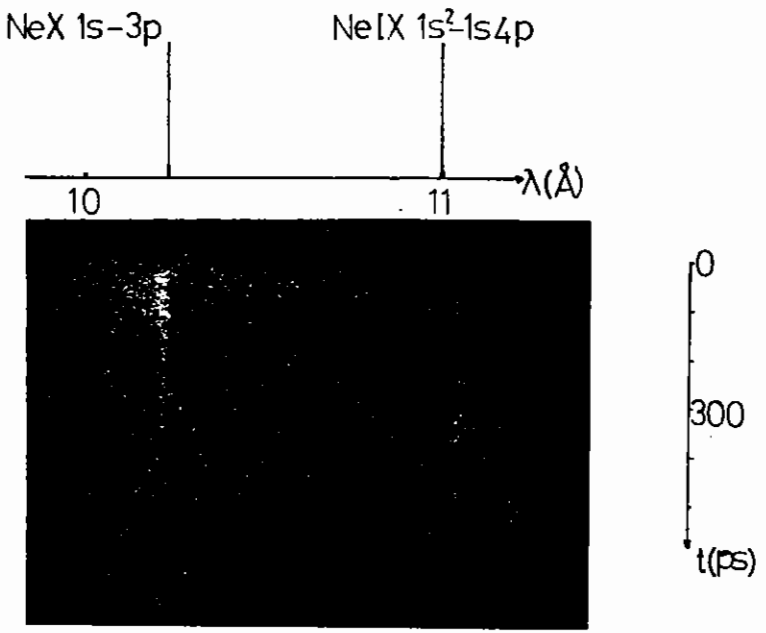

Fig A4.13 Streak camera picture of Ne X $1s\ ^2S - 3p\ ^2P$ (10.24 Å) and Ne IX $1s^2\ ^1S - 1s4p\ ^1P$ (11.00 Å)

A4.3.6 Concluding Remarks

The results of the interferometry give reasonable grounds for confidence in the codes being used to simulate the behaviour of the targets, and the viability of creating pumped and pumping plasmas on opposite sides of a thin aluminium foil is demonstrated by the streak camera pictures of targets under double-sided irradiation.

However, the results of the pump brightness measurements show that the brightness attained by the 11Å sodium line was lower than the calculated optimum, and illustrate the problem of using a He-like ion species as a source of pump radiation. A detailed analysis of the spectra obtained in the course of the x-ray source brightness experiment (reported in Section A3.5), in which the emission from various x-ray sources as a function of irradiance, laser wavelength and pulse length was measured, should given an indication of the best means of achieving a brighter sodium pump.

A4.4 Soft X-ray contact microscopy using a laser-produced plasma X-ray source

R J Rosser, K G Baldwin (Imperial College)
R Feder (IBM, USA)
D Bassett, A Cole, R Eason (RAL)

A4.4.1 Summary

High resolution (better than 200Å) contact micrographs have been produced with exposure times of about a nanosecond. The illuminating source was a short-lived carbon plasma produced by focussing a single short (~1 nsec) 100 Joule pulse from Vulcan to a 300μm spot on a graphite target. This plasma emits strongly in the soft x-ray region, particularly at the CVI (33.7Å) and CV (40.3Å) lines. The specimens were behind a 1000Å thick Si_3N_4 window, at atmospheric pressure in an environmental cell. The images of diatoms recorded on x-ray resist showed features down to the limit of the SEM used to view the developed resist, which was about 200Å.

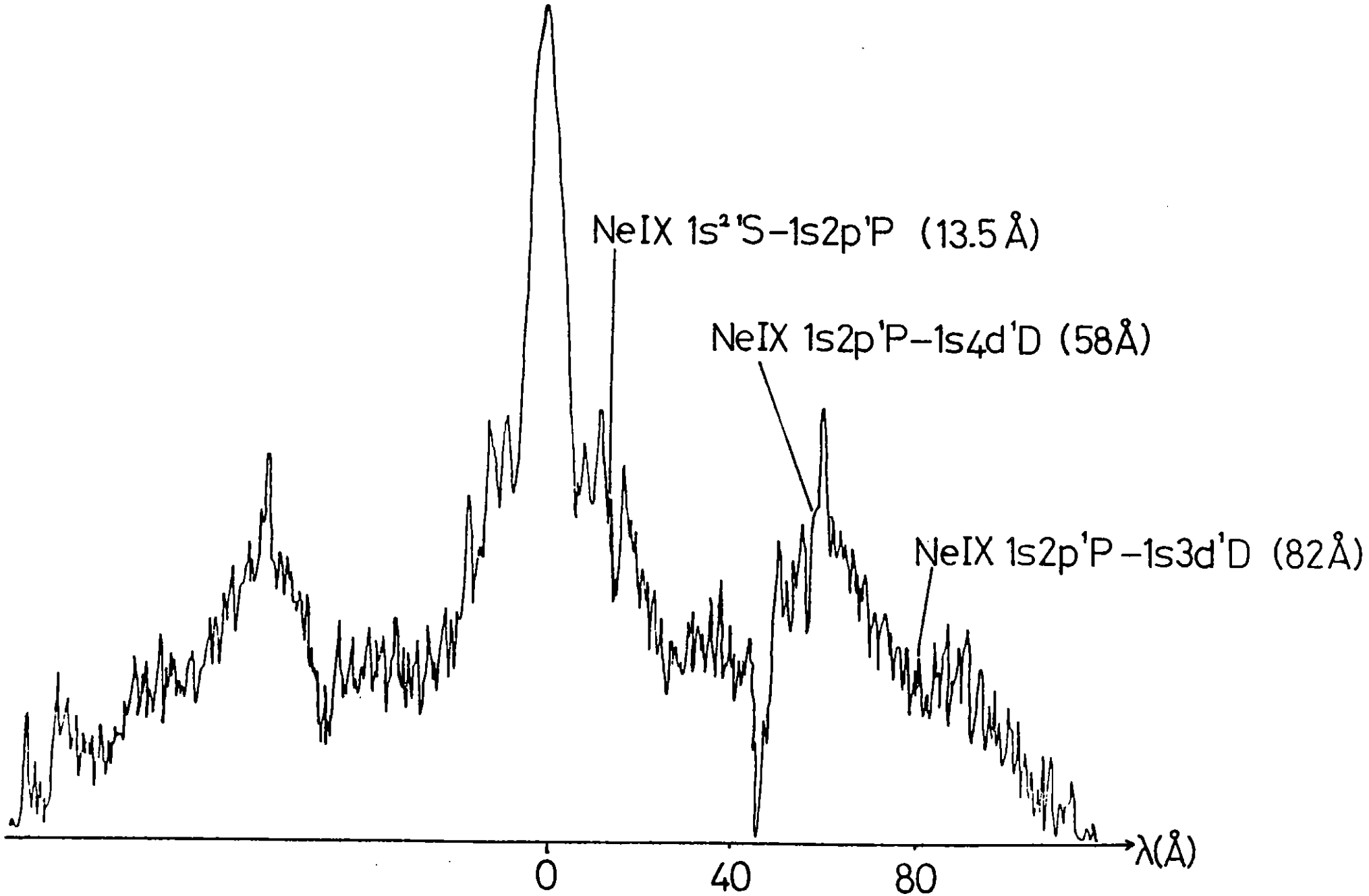

Fig A4.14 Transmission grating spectrum of neon-containing target

A4.4.2 Introduction

High resolution soft x-ray contact microscopy was developed by Feder et al (1977) A4.5, in an attempt to realize the potential advantages of soft (10 to 100Å) x-rays, for imaging biological specimens, namely lower damage and more penetration than electrons and higher resolution than visible light, without the need for difficult to manufacture optics. The technique is analagous to contact printing, consisting of placing the object to be viewed as close as possible to a recording medium (x-ray photo-resist), then making a transmission exposure. The sample is removed from the relief pattern corresponding to the x-ray opacity of the original specimen. This surface can then be viewed by a Nomarksi optical microscope or at higher resolution in an electron microscope. The technique has been gradually refined through better photoresists and specimen preparation and helped considerably by increased availability of synchrotron light, as reported by Sayre and Feder (1981) A4.6.

Recently, Feder et al (1984) A4.7 announced the first suboptical resolution images of a living cell. Using a gas-puff z-pinch as the source of soft x-rays, they took a 100 nsec exposure of a human blood platelet with a resolution of better than 100Å.

In July of 1984, Vulcan was used to produce a soft x-ray source enabling even shorter (~1nsec) exposure time images of specimens in an environmental chamber. This considerably shorter exposure time may be of significance in looking at unfixed biological samples, or in obtaining still pictures of active systems such as muscle.

The laser-plasma source is about a factor of ten brigher than the gas-puff (Rosser, 1984) A4.8, and allows specimens to be placed very near (~10mm) whereas the gas-puff usually has about 50mm source to sample separation. These factors are important as the gas puff source is only just powerful enough for single shot exposure of currently available resists (Feder et al, 1984)A4.7, i.e. it has to be working well.

The laser produced plasma source also allows multiple exposures, either simultaneously but spatially separated or temporally separated by anything from nano-seconds to minutes. Neither of these options are feasible on a gas-puff.

A4.4.3 Experimental Arrangement

The experiments were performed in the target chamber of TA2. The laser was focused onto a graphite target, producing a short lived carbon plasma. This plasma emits a line spectrum, with particularly strong CVI (33.7Å) and CV(40.3Å) features. For absolute calibration, and shot-to-shot comparison purposes, spectra were recorded on Kodak 101-01 film in a Rocket grazing-incidence grating - spectrograph.

1 ns. 100J infra-red (1.06μ) pulses were frequency doubled to give about 30J of green (0.53μ)light, for better conversion to soft x-rays. The beam was focussed to a spot size of about 300μm diameter on the graphite target producing a similarly sized x-ray source.

The specimen, sandwiched between a Si_3N_4 window and a resist coated

silicon wafer, was placed about 54 mm from the source, as shown in figures A4.15 and A4.16. The Si_3N_4 window was 1.0mm by 1.0mm and 1000Å thick, which is sufficient to withstand an atmosphere pressure difference. It had a 40μm period grid of 1.5μ thick Shipley AZ 1350 photoresist on it, to act as wells for the specimens to reside in. The window was destroyed some time after the exposure. Thermal shock waves are suspected, and the time scale involved may be as short as 30 nsec. The resist was a 0.5μ coating of Terpolymer, spun on to a silicon wafer. (Haelbich et al, 1984) A4.9.

After exposure, the resist on the wafer was cleaned for two minutes in an ultra-sonic bath of ethyl alcohol. This removed the shattered window and specimen very effectively. The latent image was then developed for between five and ten minutes in a bath of ethyl cellusolve. Washing in ethyl alcohol completed the preparation for viewing in a Nomarksi microscope. For viewing in a scanning electron microscope, the samples were gold coated.

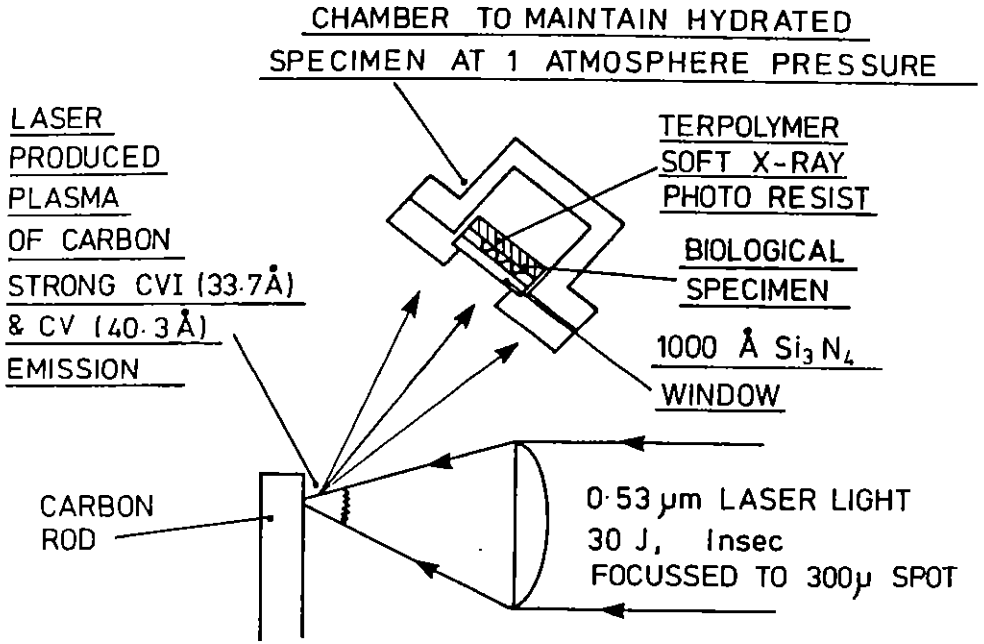

Fig A4.15 The experimental arrangement

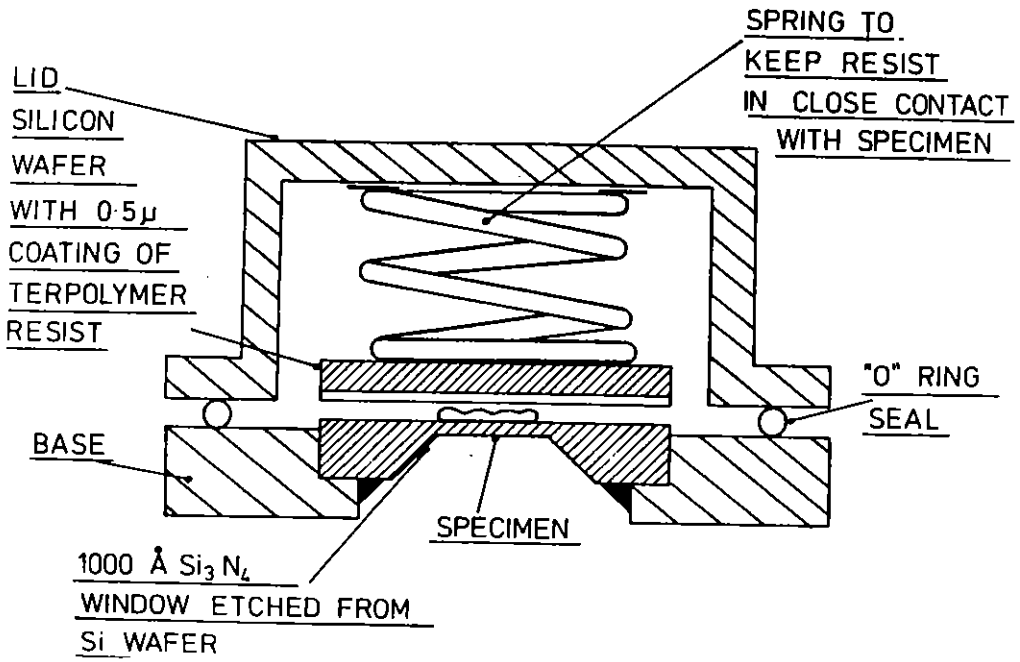

Fig A4.16 A more detailed schematic drawing of the environmental chamber

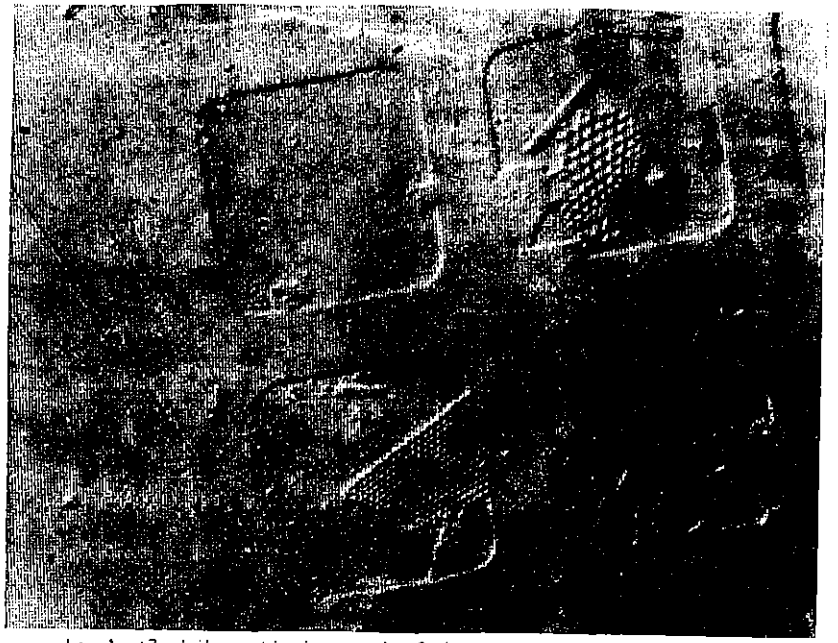

Fig A4.17 A Nomarski micrograph of the developed resist surface. The grid period is 40 μm. The object recorded was a diatom.

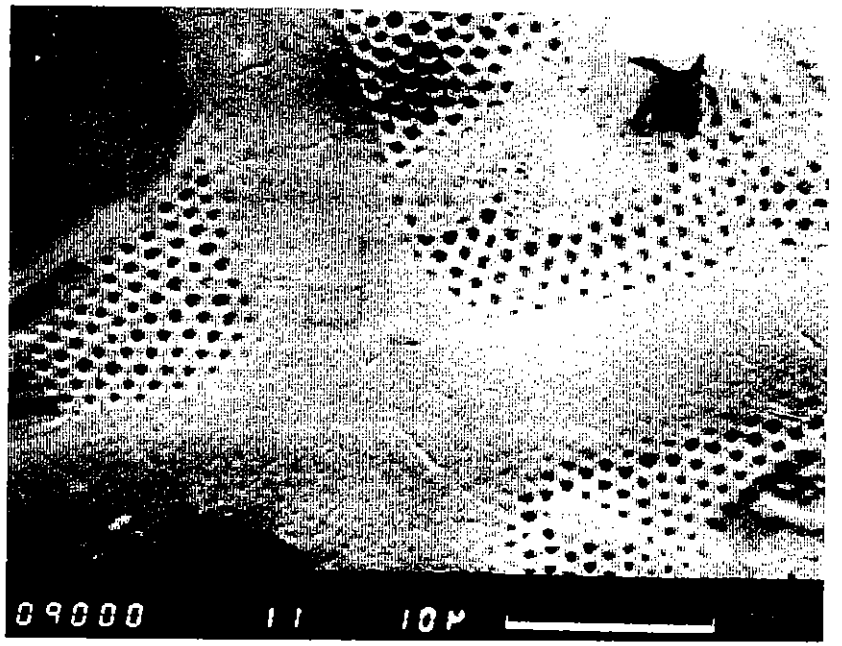

Fig A4.18 A scanning electron microscope view of the resist surface. The object was a diatom

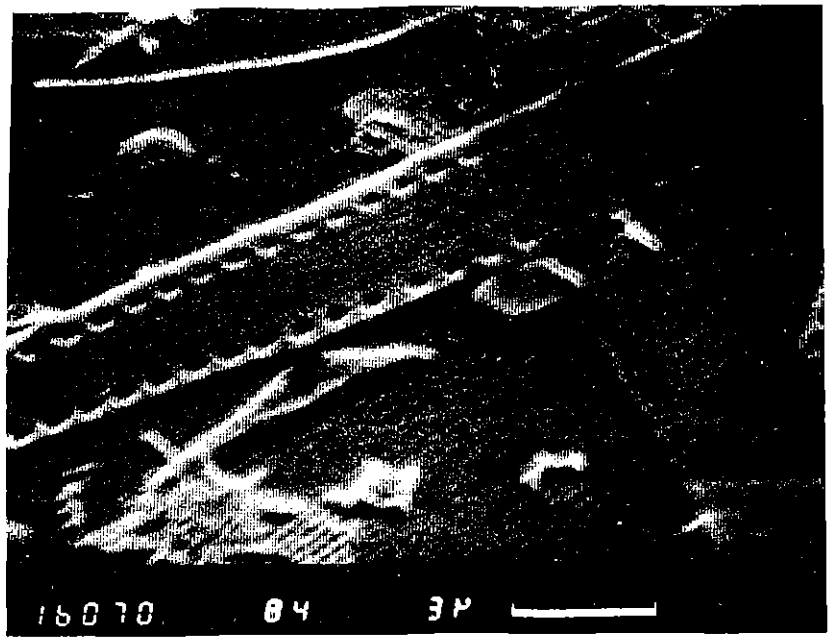

Fig. A4.19 A scanning electron microscope view of the resist surface. The object was a diatom

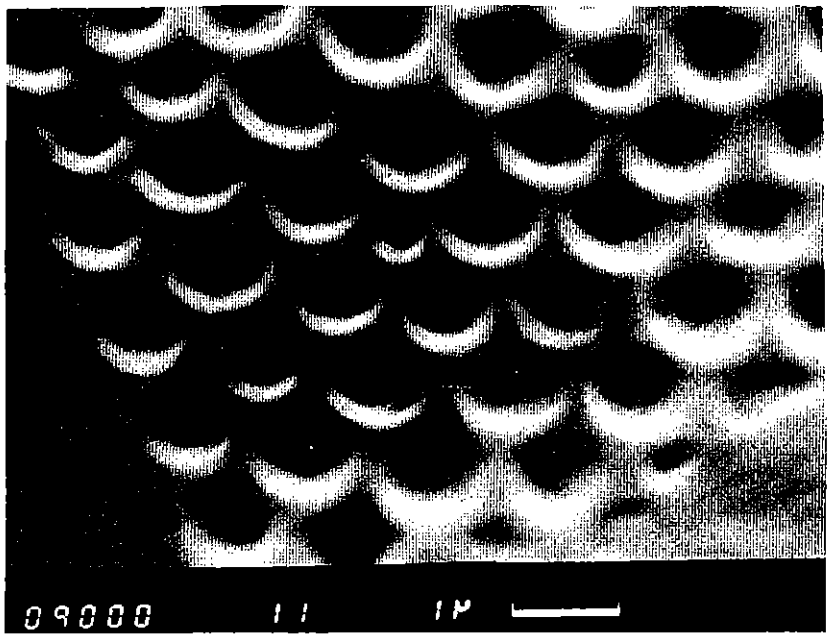

Fig. A4.20 A scanning electron microscope view of the resist surface. The object was a diatom

The results of exposing diatoms, muscle and blood cells, and subsequent resist development, can be seen in figures A4.17 to A4.21.

The highest resolution would be obtained if a transmission electron microscope could be used to look at the developed resist. This can in principle be done by floating off the resist layer, as demonstrated by Cheng et al (1982) A4.10. However, it requires a carbon undercoating for the resist, which had not been put on the wafers used in this experiment. Future work will no doubt use this technique.

A4.4.4 Stereo Images

By splitting the original laser beam into two parts, and focusing them onto different areas of the target, as shown in figure A4.22, a stereo picture can be produced.

Such an image of the grid on the Si_3N_4 windows is shown in Figures A4.23 and A4.24, and consists of two overlapping grids recorded in a single resist. Knowing that the sources were separated by 9 mm and the specimen was 54 mm away, it is possible to calculate the window to resist distance. As can be seen from the picture, this increases from 14μm at the edge to 30.5 μm at the centre, showing the window to be bowed out under pressure.

Having both stereo images recorded overlapping is obviously a severe limitation, but with care (and, one suspects, a great deal of computing) it may be possible to develop this technique to extract sections of thick specimens.

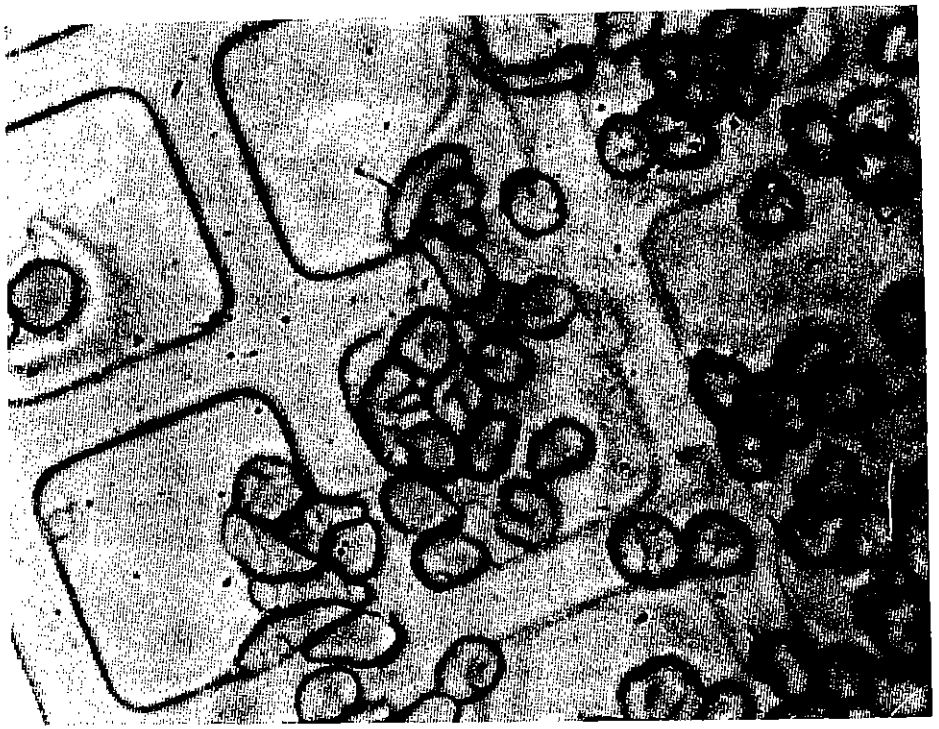

Fig A4.21 A Nomarski micrograph of the resist surface. The grid period is 40 μm. The object was freshly extracted human blood

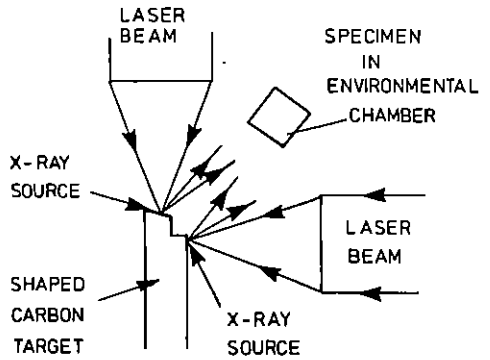

Fig A4.22 The experimental arrangement for recording stereo-micrographs

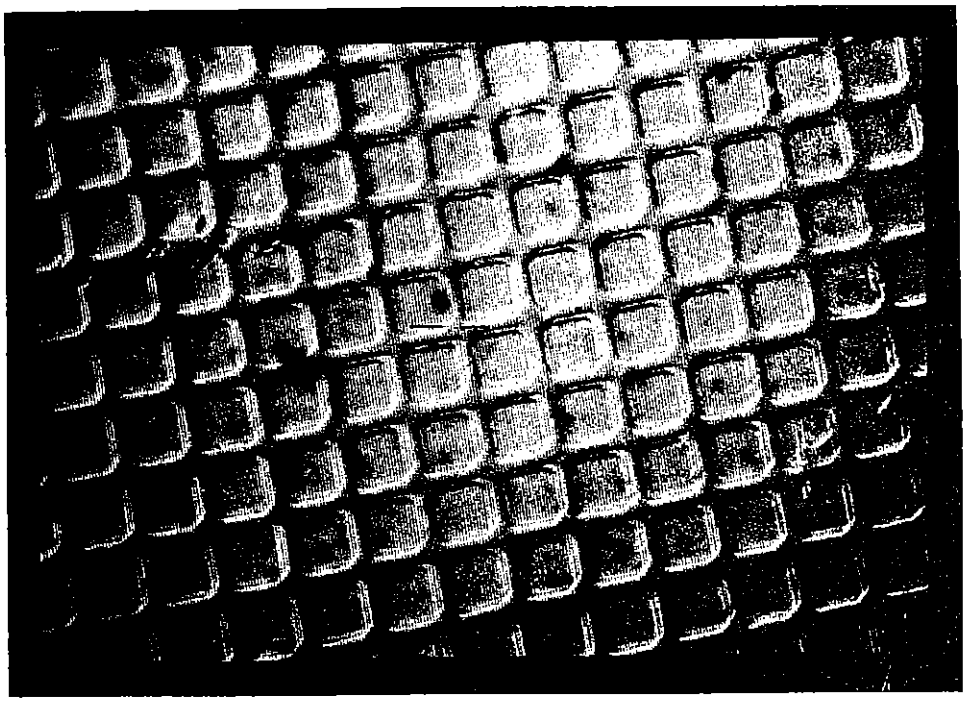

Fig A4.23 A Nomarski micrograph of the resist surface of a stereo-

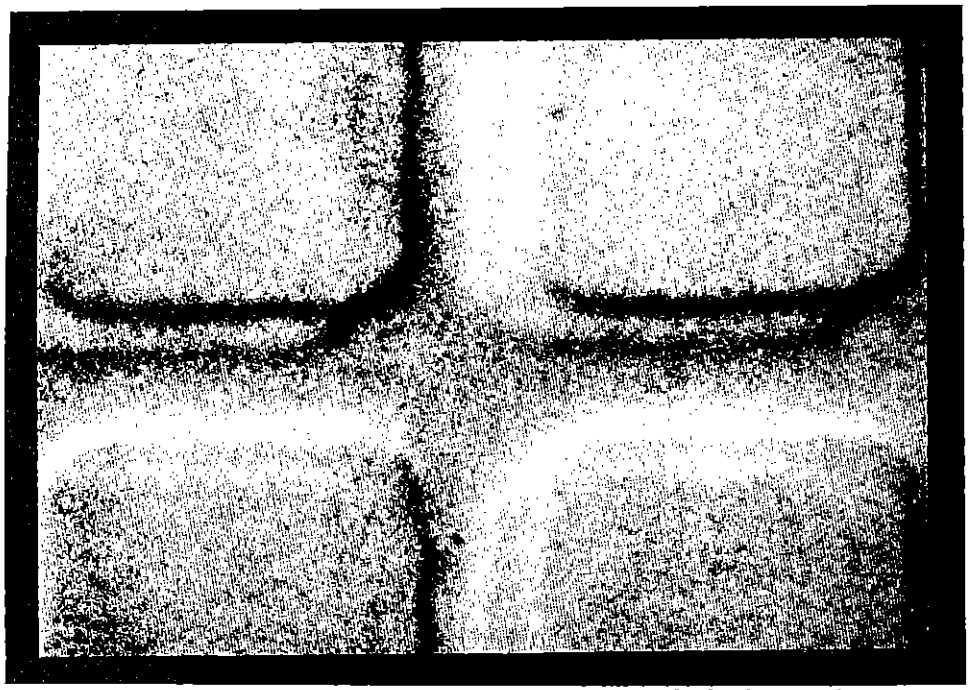

Fig A4.24 A Nomarski micrograph of the stereo-micrograph showing greater detail

A4.4.5 Conclusions

Nano-second exposure soft x-ray contact microscopy of specimens in an environmental chamber has been demonstrated to be practical. The success of these trial experiments has led to a second round of experiments using both the Vulcan (glass) and Sprite (gas) lasers, scheduled for this April/May. The intention is firstly to undertake a survey of materials familiar to people working in the field of electron microscopy, to see how similar or different things look with x-ray microscopy, secondly to use the stereoscopic image technique, and thirdly to image 'live' as opposed to merely hydrated specimens.

A4.5 Laser reflexafs of metal-silicide formation

R W Eason (Essex), D K Bradley, J Hares, A Rankin and S Tabatabaei (Imperial College)

A4.5.1 Introduction

The feasibility of recording extended X-ray absorption fine structure spectra by grazing incidence reflection from flat surfaces has been demonstrated using conventional sources such as synchrotron radiation (A4.11, A4.12) and also recently using laser-produced plasma X-ray sources (A413, A4.14). The intention behind this experiment was to use the reflection EXAFS (reflexafs) technique to examine the temporal evolution of a dynamic process, using a 2-beam configuration. The first beam (annealing beam) would initiate an event, and the second beam (reflexafs beam) would be used to probe the surface structure at various time delays in the range 0-300 nsec after the event. Such a pump-and-probe technique has already been used to look at crystallographic changes occurring to laser annealed crystalline silicon (A4.15). The reflexafs technique however is surface sensitive, as the X-rays only penetrate some tens of Å into the surface, whereas X-ray diffraction reported in A4.15 has a sample depth of ~μm.

The formation of metal silicides was chosen as a suitable study, as the substrate material, silicon, is readily available in large highly polished slices, and experiments on laser-assisted silicide formation have already been successfully performed (A4.16, A4.17). One advantage in laser-assisted surface processing is that alloys and compounds can be formed that are non-stoichiometric, i.e. contain elements in ratios not normally obtainable. The fast quench rates involved can freeze in unusual compounds.

A4.5.2 Experimental

The experimental scenario that was envisaged for the silicide process is shown in figure A4.25. A polished silicon wafer, overcoated with a thin metal overlayer is experimentally determined such that the X-rays are totally reflected from within this overlayer, and do not

penetrate the silicon beneath. A spectrometer set to look at the silicon K-edge spectral region would not therefore show the characteristic absorption edge feature when X-rays of the appropriate energy are reflected from this layer. If an annealing beam is incident on the Ni surface at time t = 0, however, with an energy density sufficient to melt the overlayer, and also some silicon underneath then diffusion, intermixing and subsequent resolidification can occur. For times t>0, if X-rays are reflected from this heated region, then the diffusion process will have brought some silicon atoms to the surface and hence an absorption edge will be seen in the reflected spectrum. The height of the edge is a measure of the amount of silicon present in the surface, and its appearance as a function of time yields information on the dynamics of the process. Finally, analysis of the EXAFS region for shots taken at different time delays will yield details of the specific compounds formed in the silicide film, e.g. for Ni on Si, $NiSi_2$, NiSi, Ni_2Si etc.

While this may sound relatively straightforward, there are several practical constraints which may cause problems.

The critical angle, θ_c, below which X-rays are reflected, is ~0.9° for silicon at the K-edge. This means that firstly everything must be very flat and accurately constructed, and also that the area from which X-rays are reflected has to be large to accommodate a suitable angular range of, for example, 0.2° - 1.1°. If this area is to be annealed, or laser processed then it is very important that the beam uniformity is good over all this area.

In practice the raw output beams from the glass laser show considerable intensity non-uniformity, so that some smoothing must be achieved. The method used is shown in figure A4.26. A 3 x 3 array of 25 mm x 25 mm square mirrors was used to select portions of the original 108 mm diameter beam, for subsequent redirection and spatial overlap on the silicon sample. A 100 ps. 0.53μm pulse was used for the annealing beam and the temporal separation between each mirror was set at > 200ps to avoid interference effects on recombination at the silicon. In practice, a smoother profile was obtained by steering the individual mirrors to achieve overlap on a diffuser, placed in front of the

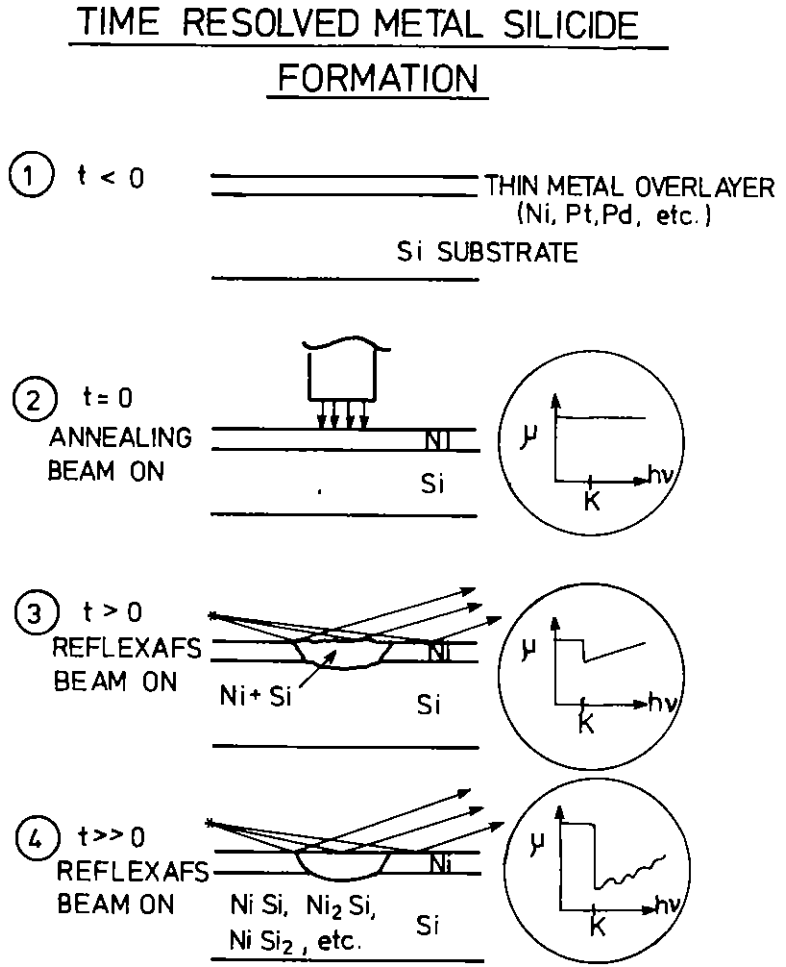

Fig A4.25 Schematic experimental arrangement for time resolved metal silicide formation

silicon.

The overall effect was a considerable smoothing of the intensity profile. Using film to record the spatial distribution, the residual integrated non-uniformity was found to be <10%. The resultant square distribution was also much more suitable for the experimental arrangement, which is detailed in figure A4.27.

A4.5.3 Results

One difficulty in using silicon is the natural surface oxide layer that is present. Before coating with various thicknesses of Ni, the wafers were dipped in HF for ~1 min., to remove the oxide, and then stored in anaerobic conditions, under ethanol, prior to coating.

The thickness of Ni that was just sufficient to suppress the appearance of a Si K-edge was experimentally determined to be 30 Å. For 25 Å, for example, the edge was still faintly apparent in the recorded spectrum.

The results are best summarised with reference to figure A4.28 which shows the various reflexafs spectra recorded.

Shot A was obtained from bare silicon. The curved K-edge, which is characteristic of reflection EXAFS which shows a range of incident angles (A4.14), can be seen, together with the sharp 'white line' absorption feature just after the edge. Also seen is a spectrum of direct X-rays which were incident on the spectrometer without being reflected from the silicon surface. It is desirable to have a simultaneous direct spectrum on each shot for comparison and background subtraction purposes.

Shot B shows the spectrum recorded from a Si wafer which had a 30 A overcoating of Ni. The Si K-edge is not seen here, indicating the sampling depth for reflection to be <30 A. The width of the spectrum in the spatial direction is less than in shot A, and the direct X-ray spectrum is only just visible. This is because of spatial cut-off due to the non-reproducibility of repositioning different silicon wafers,

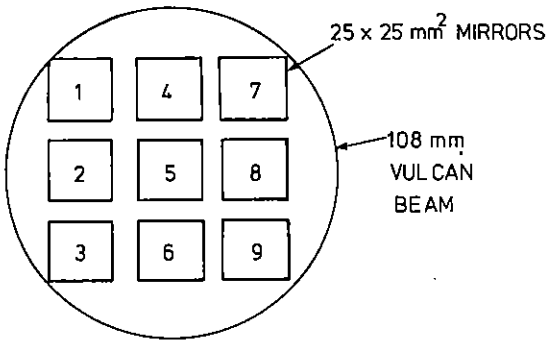

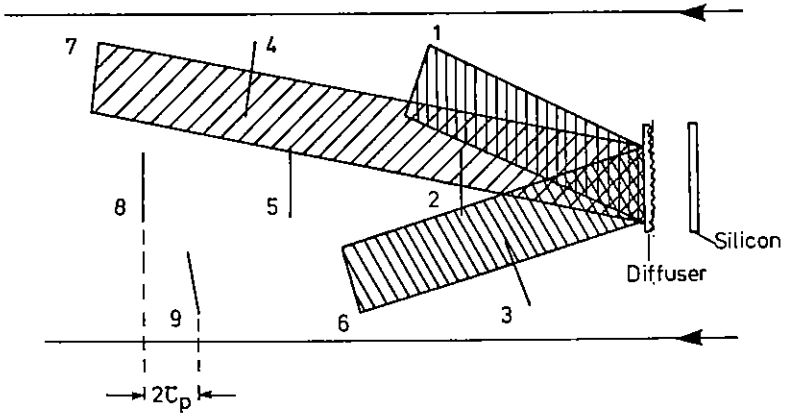

Fig A4.26 Spatial intensity smoothing scheme

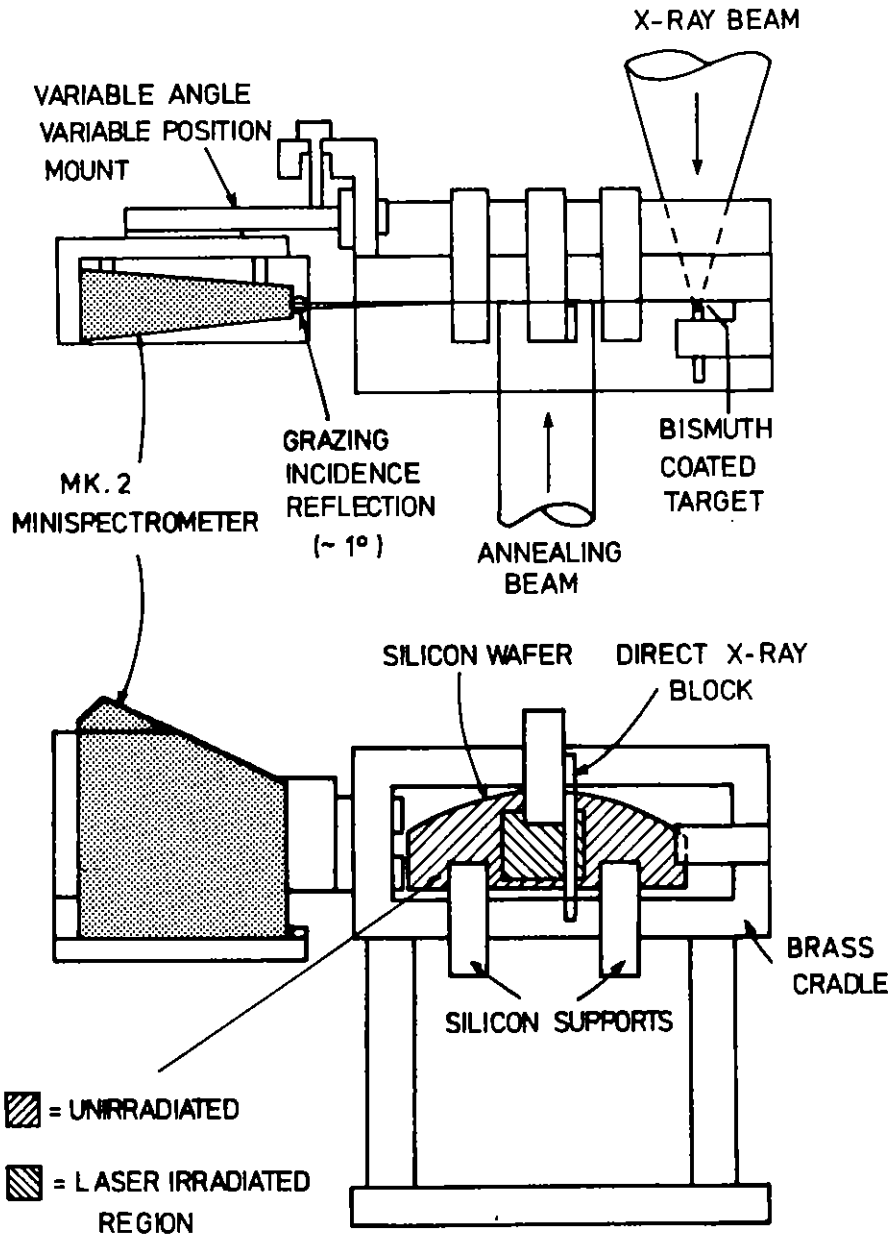

Fig A4.27 Grazing incidence reflexafs rig

from shot to shot.

Shot C was recorded from a nickel silicide which was thermally produced, that is baked in an oven for ~1 hr. (A4.18), at a temperature well below the melting point of either Ni or Si. The edge is clearly seen here, and at the temperature used (~300°C), and for a thin Ni over-layer, a Ni rich silicide should have formed, i.e. Ni_2Si. The intermediate NiSi, and final $NiSi_2$ disilicide phase require temperatures of ~350° and 750°C respectively to form. The defect in this shot in the pre-edge region was due to a hair adhering to the surface, and illustrates some of the problems of grazing incidence geometry. A direct comparison is possible between shots B and C, as they are from the same batch of coated silicon, hence have been prepared in an identical fashion.

Shot D shows the corresponding spectrum from a laser-irradiated sample. A spatially smoothed, diffused, annealing beam was incident on the Ni overlayed silicon slice at a fluence of <1J cm^{-2}, and ~180 nsec later the reflexafs spectrum was recorded. Again the absorption edge is clearly seen, but some structure is also seen running in the spectral direction. This probably corresponds to an area of the sample on which the irradiation conditions were not suitably uniform. It is clearly important to operate within the irradiation window bounded on the low side by insufficient energy density, and on the high side by surface damage.

There is the possibility that the appearance of a K-edge could be explained by merely stripping the surface Ni off the silicon, rather than true compound formation. A K-edge is therefore necessary but not sufficient for realising silicide formation. Electron microscope pictures of surfaces show that for a fluence which is higher than optimum, surface damage occurs, resulting in cratering, and pitting. This can be seen in figure A4.29, which is typical of the cases in which the annealing beam fluence was too high. For shot D, which was laser annealed and showed a K-edge, electron microscope pictures revealed no surface damage at all. A subsequent X-ray fluorescence micro-analysis scan of the area from which the spectrum in shot D was obtained showed the presence of Ni in the surface, in clear contrast to

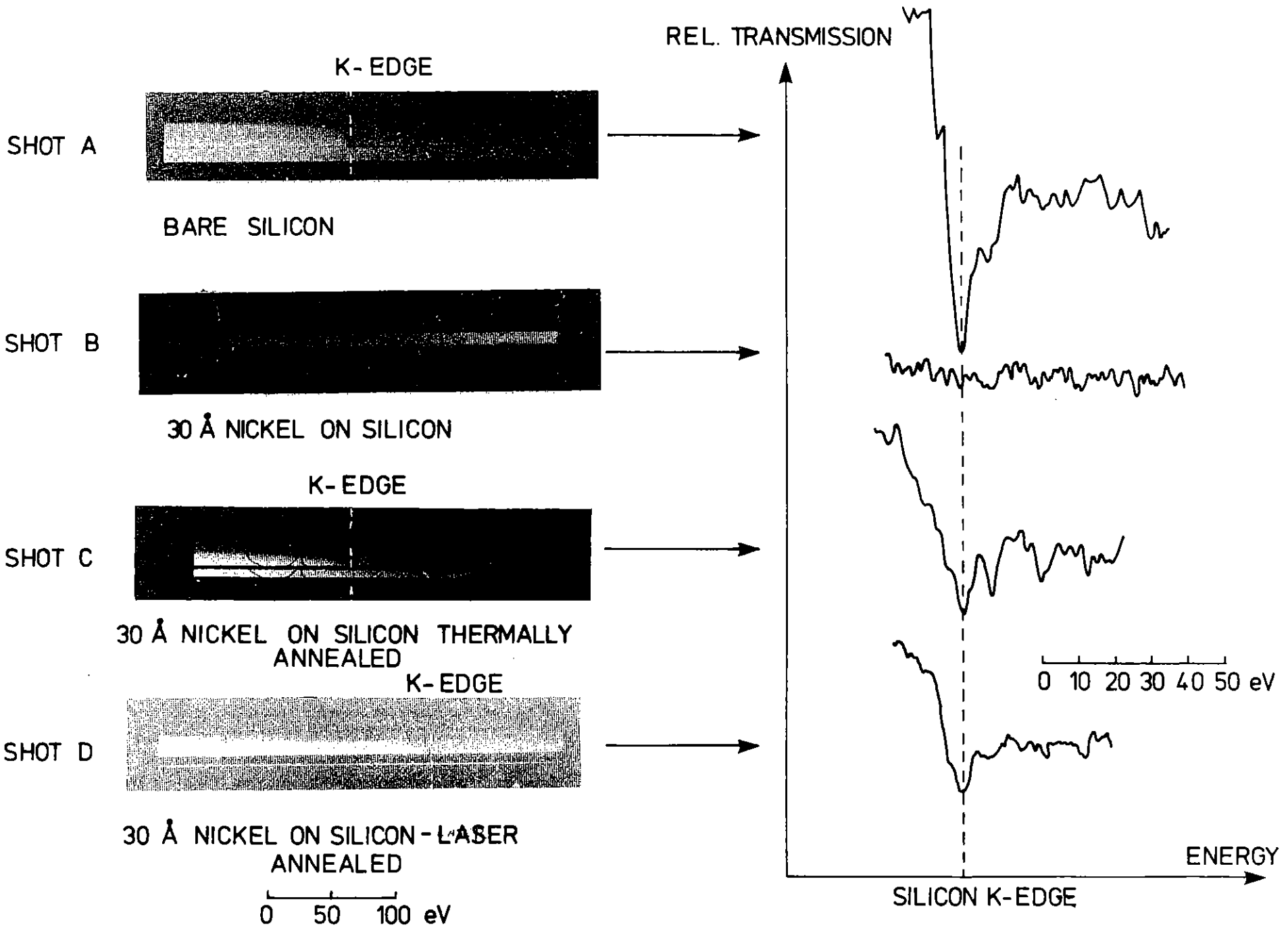

Fig A4.28 Silicon K-edge reflexafs spectra

the result from the middle of the damage spot in figure A4.29, which showed no trace of Ni.

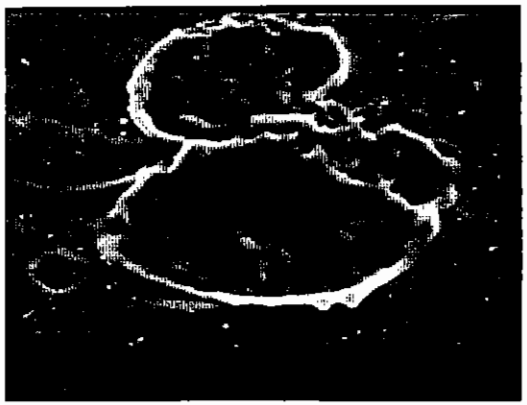

Fig A4.29 Scanning electron microscope picture of damaged Ni on Si surface

A4.5.4 Conclusions

The experiment was a partial success, in that it has been demonstrated that the laser-reflexafs technique can be used to examine surface layers at depth of ≈ 30 Å. It is unfortunate that only the first part of the experiment was performed, and that a time scan was not possible. The difficulties involved in the grazing incidence geometry were not anticiapted, but it is clear that at ~ 0.5°, minor misalignments can prove disastrous, as it is vital that the region being probed by reflected X-rays and the annealing beam are superimposed exactly.

For future experiments, some factors which must be considered are

whether Ni or Si is the most suitable system to study, how to further improve the annealing beam spatial uniformity, what the optimum pulse length is, and whether temporal pulse shaping is desirable.

The EXAFS spectra will be analysed using available EXAFS programs at Daresbury to see if quantitative measurements can be made on the spectra obtained at the + 180 ns time delay.

A4.6 Collisionless shocks in a laser-produced plasma

P Choi, A E Dangor, A K L Dymoke-Bradshaw, M Lewis, O Willi (Imperial College); D J Bassett, A R Bell, C J Hooker (RAL)

A collisionless shock is 'magnetic' when the energy density of the magnetic field is comparable with the kinetic and thermal energy densities. Magnetic shocks are reasonably well understood through laboratory experiments and satellite measurements of the Earth's bow shock. In contrast, the magnetic field is often very weak in astrophysical shocks outside the solar system (A4.19). There is no satisfactory theory of shocks in weakly magnetic plasmas. Such shocks occur only very rarely in the solar wind, and have only been seen in the laboratory at low Mach number (A4.20).

A number of experiments have tried unsuccessfully to create collisionless shocks in the low density plasma ablating from a laser-irradiated target (e.g. A4.21). Although non-magnetic plasmas interstreaming at a high Mach number are stable to small perturbations, there are theoretical indications that a non-linear interaction, once established, is self-sustaining. It is possible that previous experiments have not generated shocks because the interaction would have had to grow from a small linear perturbation in a relatively short time. We have conducted an experiment at the CLF to examine collisionless shocks in a geometry which initiates a shock non-linearly and allows a steady state which lasts longer, by two orders of magnitude, than the characteristic times associated with a shock. Between 100 and 200 J of one micron laser light were deposited in tight focus on the surface of a carbon slab producing a low density, high velocity, ablating plasma which persists for the laser pulselength of

20 nsec. A 250 micron diameter carbon sphere is placed a distance of around 1mm away from the laser spot in the path of the ablating plasma which acts as a wind tunnel. The plasma wind tunnel is probed by Raman-shifted green light for the formation of a bow shock around the spherical obstacle. Figure A4.30 shows an example of a Schlieren image of the plasma flow. A knife-edge Schlieren stop is orientated such that density gradients are only seen if the density rises as it flows away from the laser spot. A shock is clearly seen extending away from the obstacle. The angle made by the wings of the shock is determined by the Mach number of the plasma flow into the shock, but its interpretation is complicated by the non-parallel nature of the flow away from the tight focus laser spot. Fluid calculations show that the angle made by the shock wings in figure A4.30 is indicative of a Mach number of around 2.5 at the obstacle. An ablation velocity of around 5 x 10^7 cm s^{-2} is measured with a Faraday cup placed at the wall of the target chamber. An electron density of around 10^{18} cm^{-3} is measured by interferometry and confirmed by numerical simulation. The ablation velocity, the Mach number and the electron density together determine the various mean free paths in the plasma. The ion mean free paths are of the order of tens of millimetres. The smallest mean free path is the electron mean free path which is around 3mm. In comparison, the apparent shock thickness in figure 1 is only 50 micron, indicating that the shock mechanism is collisionless, especially as regards the all important ion momentum change. The magnetic field was measured by magnetic probes consisting of a single coil, 1mm or less in diameter, placed to intersect a toroidal field 1mm off-axis. The average magnetic field through the coil is always less than 10 KG at the time of optical probing, indicating that the magnetic pressure at the shock is more than two orders of magnitude smaller than the kinetic pressures and therefore dynamically unimportant. The shock shown in figure A4.30 is not seen to be detached from the obstacle at its leading edge where the shock is at its strongest. This point was investigated by also irradiating the obstacle with laser light such that the obstacle was surrounded by a low density plasma which then provides an effectively larger cross-sectional area to the ablating plasma. A clear separation of the shock from the obstacle was then visible. A variety of Schlieren stops were tried, and the presence of density gradients in the opposite direction, consistent with rarefaction waves behind the

Fig A4.30 Schlieren image of the bow shock around an obstacle placed in plasma ablating from a source at the top right. The stalk supporting the obstacle is also visible

shock, was seen. Perhaps the most surprising result, was the occurence of two apparently different types of shock as regards the thickness of the density transition. Figure A4.30 shows a 'thick' shock with an apparent thickness of around 50 microns. In contrast, 'thin' shocks were seen with apparent thicknesses of around 10 micron. Analysis of these thicknesses is complicated by the cylindrical symmetry of the plasma structure and by the nature of Schlieren probing. These complications are in principle removed when the plasma is probed interferometrically and analysed by means of an Abel inversion. Figure A4.31 shows an interferogram, made with a Wollaston prism, of a shock. The interferometer data is not yet analysed, but the shock in figure A4.31 appears to have a thickness between 10 and 20 microns. Other interferograms show much gentler gradients in the fringe shift. The shock thickness is an important parameter which is indicative of the physical processes maintaining the shock. The important scalelength for a purely electrostatic shock is the Debye length which in our experiment is only 0.2 micron. A shock relying upon ion gyration effects would be expected to be many millimetres many thick. A magnetic shock, such as the Earth's bow shock, has a thickness of around ten times the collisionless skin depth, which is 50 micron in our experiment. Interpretation of the observed shock thicknesses must await further analysis of the data.

Fig A4.31 Interferometry of a shock in an ablating plasma. A Wollaston prism is used resulting in a double image. The dominant features of the picture is the double image of the stalk supporting the obstacle. The shock can be seen spreading in a broad angle away from the obstacle at the head of the stalk

References

A4.1 Annual Report to the LFC, RAL-84-049, (1984).

A4.2 J P Apruzese, J Davis and K G Whitney, J Appl Phys 53, 4020, (1982)

A4.3 J G Lunney et al, Optics Communications 50, 367, (1984)

A4.4 Annual Report to the LFC, RL-84-049, A4.2.3.

A4.5 R Feder, E Spiller, J Topalian, A N Broers, W Gudat, B J Panessa Z A Zuduanisky and J Sedat Science 197, 259 (1977)

A4.6 D Sayre and R Feder Status report on contact x-ray microscopy. In: High resolution soft x-ray optics (ed. E.Spiller) pp 56-61, SPIE 316 (1981)

A4.7 R Feder, V Mayne-Banton, D Sayre, B K Kim, M G Baldini and P C Cheng Recent developments in x-ray contact microscopy Science, in press (1984)

A4.8 R J Rosser soft x-ray microscopy at Imperial College. In: X-ray Microscopy (Ed.G Schmahl and D Rudolf) pp 242-250 Springer-Verlag, Berlin (1984)

A4.9 R P Haelbich, J P Silverman and J M Warlaumont Synchroton radiation x-ray lithography. Nuc. Inst. and Phys. Rev. 222, 291-301 (1984)

A4.10 P C Cheng, H B Peng, R Feder and J W McGowan. The use use of Transmission Electron Microscope as a viewing tool for high resolution soft x-ray contact microscopy. In: Electron Microscopy (10th Int. Electron Microscopy Proc),1, pp461-462 (1982).

A4.11 R Barchewitz, M Cremonese-Visicato, G J Onori, Phys. C. 11, p. 4439 (1978)

A4.12 G Martens, P Rabe, Phys. Stat. Sol. (a) 58, p.415 (1980)

A4.13 Chapter A4 section A4.4.4 in Annual Report to the Laser Facility Committee, RAL-84-049 (1984)

A4.14 R W Eason, D K Bradley, J Hares, P Dobson, submitted to Appl. Phys. Letts. Jan. (1985).

A4.15 Chapter A4 section A4.6 in Annual Report to the Laser Facility Committee RAL-84-049 (1984)

A4.16 J M Poate, H J Leamy, T T Sheng, Appl. Phys. Letts. 33, p.918 (1978)

A4.17 T Shibata, T W Sigmon, J F Gibbons, in: Laser and Electron beam processing of Materials, ed. C W White and P S Perry (Acadamic, New York) (1980)

A4.18 G J Ottaviani, Vac. Sci. Technol. 116,p.1112 (1979)

A4.19 C F McKee. Ann. Rev. Astron. Astrophys., 18, 219 (1980)

A4.20 D Biskamp. Nuclear Fusion, 13, 719 (1973)

A4.21 A Y Cheung, R R Goforth and D W Koopman. Phys. Rev. Lett., 31, 429 (1973)

Editor A R Bell

A5.1 Introduction

R A Cairns (St Andrews)

The contributions to this year's report bear witness to the fact that a substantial effort on theory continues to be made, both at the Rutherford Appleton Laboratory and at a number of Universities. As has been the case for the past few years transport theory attracts a lot of attention, with a number of groups tackling different aspects. Work continues on such long-standing interests as Raman and filamentation instabilities and hydrodynamic codes, while the more recently fashionable subject of beat wave accelerators also makes an appearance.

In addition to the work on classical plasma physics and hydrodynamics there is a growing interest in atomic physics processes and dense plasma theory. Section A5.3 presents a number of reports on these topics, together with some work on ion beam fusion.

A5.2.1 Correction of Braginskii's transport coefficients

E M Epperlein and M G Haines (Imperial College)

Significant departures from standard transport coefficients α^c, β^c and κ^c have been found for the electron Ohm's law (A5.1, A5.2).

$$en\underline{E} = -\nabla p + \underline{j}x\underline{B}/c + m\,\underline{\underline{\alpha}}^c\,\underline{j}/e - n\underline{\underline{\beta}}^c \cdot \nabla T,$$

and heat flux

$$\underline{q} = -(nT\tau/m)\underline{\underline{\kappa}}^c \cdot \nabla T - \underline{\underline{\beta}}^c \cdot \underline{j}T/e,$$

in a fully ionized plasma (all symbols have their usual meaning). These have been discovered by carrying out a direct and accurate numerical solution of the linearized Fokker-Planck equation using a Cartesian tensor expansion of the distribution function and a finite difference representation of the velocity variable. The results, which were carried out for plasmas of various atomic numbers, show the presence of major inaccuracies (errors of up to 65%) in Braginskii (A5.3) coefficients $\beta_\wedge^c$, $\kappa_\wedge^c$ and $\kappa_\perp^c$ for Hall parameters $\omega\tau$ in the range $0.3 \lesssim \omega\tau \lesssim 30$. Surprisingly, $\alpha_\wedge^c$ and $\beta_\perp^c$ are found to depend on $(\omega\tau)^{-2/3}$ and $(\omega\tau)^{-5/3}$, and not on $(\omega\tau)^{-1}$ and $(\omega\tau)^{-2}$, respectively, as $\omega\tau \to \infty$. An analytic expansion for large $\omega\tau$ verifies this result, showing that the relatively cold unmagnetised electrons in the distribution function play a dominant role in the cross-field transport.

We have fitted our numerical results to polynomial coefficients in χ ($=\omega\tau$) by the method of least squares. These are identified by:

$$\alpha_\ell^c = \alpha_0 \;(=1-\alpha_0'/a_0'),$$

$$\alpha_\perp^c = 1 - \frac{\alpha_1'\chi+\alpha'_0}{a_2'\chi^2+a_1'\chi+a'_0} ,$$

$$\lim_{\chi\to\infty} \alpha^c/\chi = \alpha_0 \ (=\alpha_0''/a_0''^{8/9}) ,$$

$$\alpha^c = \frac{\chi(\alpha_1''\chi+\alpha_0'')}{(\chi^3+a_2''\chi^2+a_1''\chi+a_0'')^{8/9}},$$

$$\beta_\parallel^c = \beta_0 \ (=\beta_0'/b_0'^{8/9}),$$

$$\beta_\perp^c = \frac{(\beta_1'\chi+\beta_0')}{(\chi^3+b_2'\chi^2+b_1'\chi+b_0')^{8/9}}$$

$$\lim_{\chi\to 0} \beta^c/\chi = \beta_0 \ (=\beta_0''/b_0'').$$

$$\beta^c = \frac{\chi(\beta_1''\chi+\beta_0'')}{(\chi^3+b_2''\chi^2+b_1''\chi+b_0'')} ,$$

$$\chi_\parallel^c = \gamma_0 \ (=\gamma_0'/c_0') ,$$

$$\chi_\perp^c = \frac{(\gamma_1'\chi+\gamma_0')}{(\chi^3+c_2'\chi^2+c_1'\chi+c_0')} ,$$

$$\lim_{\chi\to 0} \kappa^c/\chi = \gamma_0 \ (=\gamma_0/c_0'') \text{ and}$$

$$\kappa_\wedge^c = \frac{\chi(\gamma_1''\chi+\gamma_0'')}{(\chi^3+c_2''\chi^2+c_1''\chi+c_0'')} .$$

In tables A5.1 - A5.3 we tabulate the polynomial coefficients for 15 values of Z. Sufficient numbers of coefficients are used so as to ensure a maximum relative error of less than 15% for any value of Z and $\omega\tau$.

This new set of transport coefficients is particularly suitable for computer simulation of transport in laser produced plasmas.

A5.2.2 The collisional Weibel instability

E M Epperlein and M G Haines (Imperial College)

There have been several recent experimental reports on the occurrence of filamentary structures coupled with strong magnetic fields in the ablation of laser driven targets (A5.4-A5.6). The possibility that they originate at densities higher than critical may have serious consequences on target implosion symmetry by inhibiting lateral ransport and inducing pressure perturbations at the ablation front.

It has been suggested that the origin of these structures can only be explained in terms of an instability mechanism, (A5.4 - A5.6) of which a strong candidate is the one first proposed by Weibel (A5.7) for a collisionless plasma. Experimentally, however, the time and spatial scales of the observed filaments are more appropriately characterized by a collisional type process.

Mochizuki et al (A5.4) developed a collisional version of the Weibel instability by applying perturbation analysis to a quasi-neutral plasma

Table A5.1 The constant coefficients of the rational polynomial used to fit the various components of $\underline{\underline{\alpha}}^{C}$.

Z	1	2	3	4	5	6	7	8	10	12	14	20	30	60	∞
α_o	0.5061	0.4295	0.3950	0.3750	0.3618	0.3524	0.3454	0.3399	0.3319	0.3263	0.3221	0.3144	0.3081	0.3015	0.2945
α'_o	1.37	1.58	1.68	1.74	1.78	1.80	1.82	1.84	1.87	1.88	1.90	3.53	5.49	7.61	9.17
α'_1	3.03	3.21	3.17	3.15	3.14	3.13	3.12	3.11	3.10	3.10	3.09	3.52	3.97	4.41	4.73
a'_o	2.77	2.78	2.78	2.78	2.78	2.79	2.79	2.79	2.79	2.80	2.80	5.14	7.94	1.09x10	1.30x10
a'_1	6.72	6.70	6.47	6.37	6.33	6.29	6.26	6.23	6.21	6.20	6.19	7.97	1.00x10	1.22x10	1.38x10
$\alpha_{o\Lambda}$	0.1989	0.3285	0.4157	0.4794	0.5285	0.5676	0.5996	0.6264	0.6686	0.7004	0.7254	0.7757	0.8209	0.8727	0.9328
α''_o	2.66×10^2	4.91×10^2	6.30×10^2	7.06×10^2	7.23×10^2	7.57×10^2	7.94×10^2	8.17×10^2	8.89×10^2	9.62×10^2	9.88×10^2	1.06×10^3	1.17×10^3	1.30×10^3	1.33×10^3
α''_1	2.53	2.53	2.53	2.53	2.53	2.53	2.53	2.53	2.53	2.53	2.53	2.53	2.53	2.53	2.53
a''_o	3.28×10^3	3.72×10^3	3.79×10^3	3.67×10^3	3.37×10^3	3.28×10^3	3.25×10^3	3.20×10^3	3.27×10^3	3.39×10^3	3.36×10^3	3.36×10^3	3.52×10^3	3.72×10^3	3.54×10^3
a''_1	3.46×10^3	6.69×10^3	8.99×10^3	1.02×10^4	1.06×10^4	1.11×10^4	1.17×10^4	1.22×10^4	1.33×10^4	1.47×10^4	1.51×10^4	1.62×10^4	1.85×10^4	2.08×10^4	2.19×10^4
a''_2	3.66×10^2	5.54×10^2	6.75×10^2	7.35×10^2	7.44×10^2	7.69×10^2	7.93×10^2	8.25×10^2	8.63×10^2	9.25×10^2	9.40×10^2	9.85×10^2	1.08×10^3	1.18×10^3	1.18×10^3

Table A5.2 The constant coefficients of the rational polynomial used to fit the various components of $\underline{\beta}^C$.

Z	1	2	3	4	5	6	7	8	10	12	14	20	30	60	∞
β_o	0.7029	0.9054	1.018	1.092	1.146	1.186	1.218	1.244	1.283	1.312	1.334	1.337	1.414	1.455	1.5
β'_o	1.05×10^3	1.38×10^3	1.55×10^3	1.64×10^3	1.71×10^3	1.74×10^3	1.73×10^3	1.79×10^3	1.92×10^3	1.89×10^3	1.92×10^3	2.01×10^3	2.09×10^3	2.16×10^3	2.20×10^3
β'_1	6.33	6.33	6.33	6.33	6.33	6.33	6.33	6.33	6.33	6.33	6.33	6.33	6.33	6.33	6.33
b'_o	3.71×10^3	3.80×10^3	3.80×10^3	3.74×10^3	3.72×10^3	3.64×10^3	3.53×10^3	3.57×10^3	3.74×10^3	3.58×10^3	3.58×10^3	3.62×10^3	3.68×10^3	3.69×10^3	3.65×10^3
b'_1	4.11×10^3	7.05×10^3	8.75×10^3	9.73×10^3	1.07×10^4	1.11×10^4	1.13×10^4	1.17×10^4	1.29×10^4	1.30×10^4	1.33×10^4	1.43×10^4	1.52×10^4	1.60×10^4	1.68×10^4
b'_2	5.15×10^2	6.42×10^2	6.90×10^2	7.07×10^2	7.31×10^2	7.35×10^2	7.29×10^2	7.34×10^2	7.72×10^2	7.62×10^2	7.65×10^2	7.89×10^2	8.08×10^2	8.22×10^2	8.09×10^2
β_{oA}	0.8831	1.812	2.589	3.236	3.780	4.243	4.640	4.986	5.556	6.007	6.372	7.144	7.874	8.756	9.844
β''_o	2.54	4.40	3.77	3.43	3.20	3.05	2.92	2.82	2.70	2.62	2.55	2.43	2.31	2.26	2.15
β''_1	1.5	1.5	1.5	1.5	1.5	1.5	1.5	1.5	1.5	1.5	1.5	1.5	1.5	1.5	1.5
b''_o	2.87	2.43	1.46	1.06	8.48×10^{-1}	7.18×10^{-1}	6.29×10^{-1}	5.65×10^{-1}	4.86×10^{-1}	4.36×10^{-1}	4.01×10^{-1}	3.41×10^{-1}	2.94×10^{-1}	2.58×10^{-1}	2.19×10^{-1}
b''_1	3.27	5.18	4.34	3.92	3.66	3.48	3.33	3.21	3.09	3.00	2.93	2.81	2.68	2.64	2.53
b''_2	7.09	9.34	8.65	8.27	8.02	7.83	7.68	7.55	7.41	7.30	7.22	7.07	6.91	6.84	6.72

Table A5.3 The constant coefficients of the rational polynomial used to fit the various components of $\underline{\underline{\chi}}^{C}$.

Z	1	2	3	4	5	6	7	8	10	12	14	20	30	60	∞
γ_o	3.203	4.931	6.115	6.995	7.680	8.231	8.685	9.067	9.673	10.13	10.50	11.23	11.90	12.67	13.58
γ'_o	6.18	9.30	1.02x10	9.14	8.60	8.57	8.84	7.93	7.44	7.32	7.08	6.79	6.74	6.36	6.21
γ'_1	4.66	3.96	3.72	3.60	3.53	3.49	3.49	3.43	3.39	3.37	3.35	3.32	3.30	3.27	3.25
c'_o	1.93	1.89	1.66	1.31	1.12	1.04	1.02	8.75×10^{-1}	7.70×10^{-1}	7.22×10^{-1}	6.74×10^{-1}	6.05×10^{-1}	5.66×10^{-1}	5.02×10^{-1}	4.57×10^{-1}
c'_1	2.31	3.78	4.76	4.63	4.62	4.83	5.19	4.74	4.63	4.70	4.64	4.65	4.81	4.71	4.81
c'_2	5.35	7.78	8.88	8.80	8.80	8.96	9.24	8.84	8.71	8.73	8.65	8.60	8.66	8.52	8.53
$\gamma_{o\Lambda}$	6.071	15.75	25.65	34.95	43.45	51.12	58.05	64.29	75.04	83.93	91.38	107.8	124.3	145.2	172.7
γ''_o	4.01	2.46	1.13	6.28×10^{-1}	4.18×10^{-1}	3.19×10^{-1}	2.68×10^{-1}	2.38×10^{-1}	2.25×10^{-1}	2.12×10^{-1}	2.02×10^{-1}	2.00×10^{-1}	1.94×10^{-1}	1.89×10^{-1}	1.86×10^{-1}
γ''_1	2.5	2.5	2.5	2.5	2.5	2.5	2.5	2.5	2.5	2.5	2.5	2.5	2.5	2.5	2.5
c''_o	6.61×10^{-1}	1.56×10^{-1}	4.42×10^{-2}	1.80×10^{-2}	9.63×10^{-3}	6.25×10^{-3}	4.61×10^{-3}	3.71×10^{-3}	3.00×10^{-3}	2.52×10^{-3}	2.21×10^{-3}	1.85×10^{-3}	1.56×10^{-3}	1.30×10^{-3}	1.08×10^{-3}
c''_1	9.31×10^{-1}	3.98×10^{-1}	1.75×10^{-1}	1.01×10^{-1}	7.02×10^{-2}	5.51×10^{-2}	4.65×10^{-2}	4.10×10^{-2}	3.54×10^{-2}	3.17×10^{-2}	2.91×10^{-2}	2.56×10^{-2}	2.28×10^{-2}	2.02×10^{-2}	1.80×10^{-2}
c''_2	2.50	1.71	1.05	7.75×10^{-1}	6.46×10^{-1}	5.78×10^{-1}	5.39×10^{-1}	5.15×10^{-1}	4.97×10^{-1}	4.82×10^{-1}	4.71×10^{-1}	4.61×10^{-1}	4.50×10^{-1}	4.40×10^{-1}	4.30×10^{-1}

composed of hot and cold electron fluids. The pressure anisotropy necessary to drive the instability is provided by postulating an artifical equilibrium whereby the hot electrons carry the inward heat flux from the critical surface and the cold electrons carry the neutralising return current.

A more realistic theory has been subsequently developed by employing a Cartesian tensor description for the electron distribution function in the Fokker-Planck equation (A5.8). Its results were presented in the 1984 Rutherford Report (A5.9), where the predictions of growth rate γ for a given perturbation wavelength λ were shown to be significantly different to that of the 2-fluid theory of Mochizuki et al. Particularly it is found that in the long wavelength limit $\gamma_{kinetic} \propto 1/\lambda^2$ whereas $\gamma_{2\text{-}fluid} \propto 1/\lambda$. Also in this same limit, kinetic theory predicts a maximum ratio of collisionless skin depth to electron mean free path above which no unstable Weibel modes occur.

Here we report on the progress being made towards a more full understanding of the physical processes governing the collisional Weibel instability. We also discuss the possibility of including its effects on the conventional fluid description of the plasma.

In order to investigate the instability we consider the response of an electron travelling in the z direction with a speed v_z when a B-field is applied in the y direction. After a time interval δt the electron acquires an x component of velocity $v_x = \delta t v_z(eB/mc)$, via the Lorentz force. Momentum conservation in the z direction then gives rise to (A5.11).

$$nm\langle v_z\rangle = -\delta t(nm\,\partial_x\langle v_x v_z\rangle - enE_z)$$

$$= -\delta t(nm\,\partial_x\langle v_z^2\rangle\,\delta teB/mc - enE_z),$$

where n is the electron number density, m is the electron mass, e is the magnitude of the electronic charge and E is the induced electric field. The operator <> denotes an average over the electron distribution function. Rearranging the above expression and substituting it into Faraday's and Ampere's laws,

$\partial_t B = c\,\partial_x E_z$ and

$$\partial_x B = -nec\langle v_z\rangle/4\pi,$$

we obtain (using $\partial_x = ik$ and $\partial_t = \gamma^{-1}$)

$$\gamma = k^2 v^2 \delta t - k^2 l_s^2/\delta t, \qquad (1)$$

where $v^2 = \langle v_z^2\rangle$ and $l_s = (mc^2/4\pi ne^2)^{\frac{1}{2}}$ is the collisionless skin depth.

Equation (1) defines an approximate dispersion relation for the Weibel instability. If one is interested in the collisional regime, the characteristic δt for the momentum exchange is assigned to be the mean electron-ion collision time τ and hence

$$\gamma = k^2 v^2 \tau - k^2 l_s^2/\tau.$$

This expression confirms the growth rate dependence on k^2 predicted by the kinetic analysis. It also predicts a critical value of l_s above which γ becomes negative, a phenomenon that is explained by the presence of magnetic diffusion.

It is interesting to note that dispersion relation (1) may also be used to estimate the growth rate of the collisionless Weibel instability. In this case $\partial t = \gamma^{-1}$, and we have (A5.7, A5.11)

$$\gamma = kv(1+k^2 l_s^2)^{\frac{1}{2}}.$$

An essential criterion for describing the Weibel instability lies in an adequate formulation of the electron stress tensor $nm\langle \underline{vv}\rangle$. Braginskii's (A5.3) equations fail to provide such a formulation as they only specify $nm\langle \underline{vv}\rangle$ in terms of gradients in the centre-of-mass velocity. An appropriate expression for $nm\langle \underline{vv}\rangle$ should entail gradients in the heat flow, a work which is currently in progress. A new formulation of the electron stress tensor should enable an approximate description of the Weibel instability by means of one-fluid equations.

A5.2.3 Nernst convection of magnetic field

M G Haines and T H Kho (Imperial College)

One effect of a magnetic field in a heat-carrying plasma is the production of a thermo-electric field in the direction of $\vec{B} \times \nabla T$. This is known as the Nernst effect and arises from the dependence on velocity of the electron collision frequency. This thermo-electric field in turn convects $\vec{B}$ down ∇T through Faraday's law. From linear transport theory, the convection velocity of B by the Nernst effect, $\vec{v}_N = -\tau_e(\beta_1\chi^2+\beta''_0)\nabla T/(m_e\Delta)$ (in Braginskii's notations), turns out to be almost the same as that associated with the heat flow perpendicular to $\vec{B}$, $\vec{v}_T=2\vec{q}/3n_eT_e$ i.e., $v_N/v_T \sim 1$. Thus, the magnetic field appears to be "frozen-in" to the heat-carrying electrons, making the transport of heat and $\vec{B}$ inseparable. This is of particular significance to laser fusion. Here, since (restricting ourselves to a 1-D system with $\vec{B}$ perpendicular to ∇T) the heat flow drives the ablation, $\vec{v}_T$ must be greater than the ablation velocity (except in the immediate neighbourhood of the ablation surface). Therefore, should any magnetic field be created in the overdense plasma, it will be convected towards the solid target instead of being swept out with the plasma.

A 1-D MHD simulation has been performed by ILE Osaka with collaborators from Imperial College (A5.12). A 30-μm thick CH_2 or 15-μm thick SiO_2 foil was irradiated by 1.06 or 0.53μm laser light. A constant source of magnetic field B_o was assumed at the critical point. The laser intensities ranged from 10^{13} to 10^{15} W cm^{-2}.

It was found that B could be amplified by $10-10^2$ times as it was convected inward with the heat flow because $\nabla.\vec{v}_N<0$. In the quasi-steady state, B peaked at a point near the ablation surface where v_N was balanced by the ablation velocity v_A and $v_D=\nabla(c^2\alpha_\perp/4\pi n_e e^2)$ associated with a gradient in resistivity. The amplification factor increased with intensity (because of greater heat flow) but was insensitive to laser wavelength and target material. While the saturated value of the peak magnetic field B_m, depended on the

competing effects of heat flow, ablation and resistivity, and has to be evaluated through a simulation, B near the critical surface where $\lambda_{mfp} >> c/\omega_{pe}$, can be predicted. In the quasi-steady state, an approximate solution of the induction equation gives B/n_i constant. A result of the spatially extended and amplified B would be to inhibit hot-electron transport thereby reducing preheat. It was also found that for $\omega\tau_e >> 1$, the critical and ablation surfaces were brought closer together, improving hydrodynamic coupling.

Recently, we have investigated the Nernst convection with a kinetic (Fokker-Planck) description of electron transport. We considered a 1-D overdense plasma 20μm thick with a fixed source of B at one end. Hydrodynamics was ignored and a fixed exponential density profile with a scalelength of 4μm assumed. The plasma was irradiated by 1.06μm laser light at 10^{14}W/cm^2. The code is described in A5.2.7 in this report.

Fig A5.1 shows the convection and amplification of B over 130ps. The laser energy is deposited in the first spatial cell on the left. Fig A5.2 shows the inward heat flux q, and v_N across the plasma. At the heat front q is about 0.06 of the free streaming heat flux q_{fs}, and both q and v_N are an order of magnitude smaller than the linear transport (Braginskii's) values.

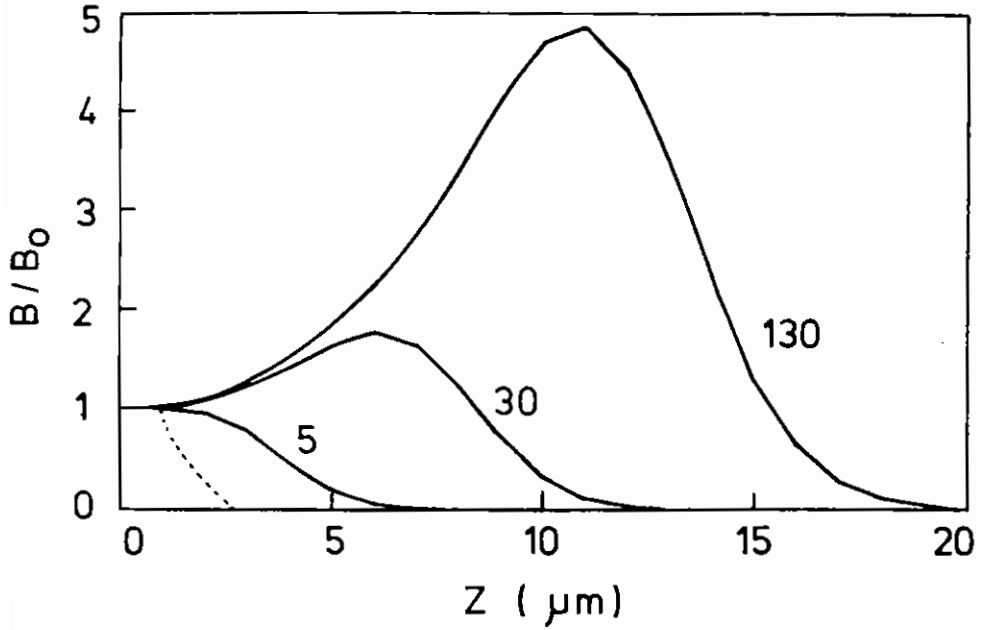

Fig A5.1 The magnetic field at 0 (dotted line), 5, 30 and 130 psec. B_o is the constant source of magnetic field.

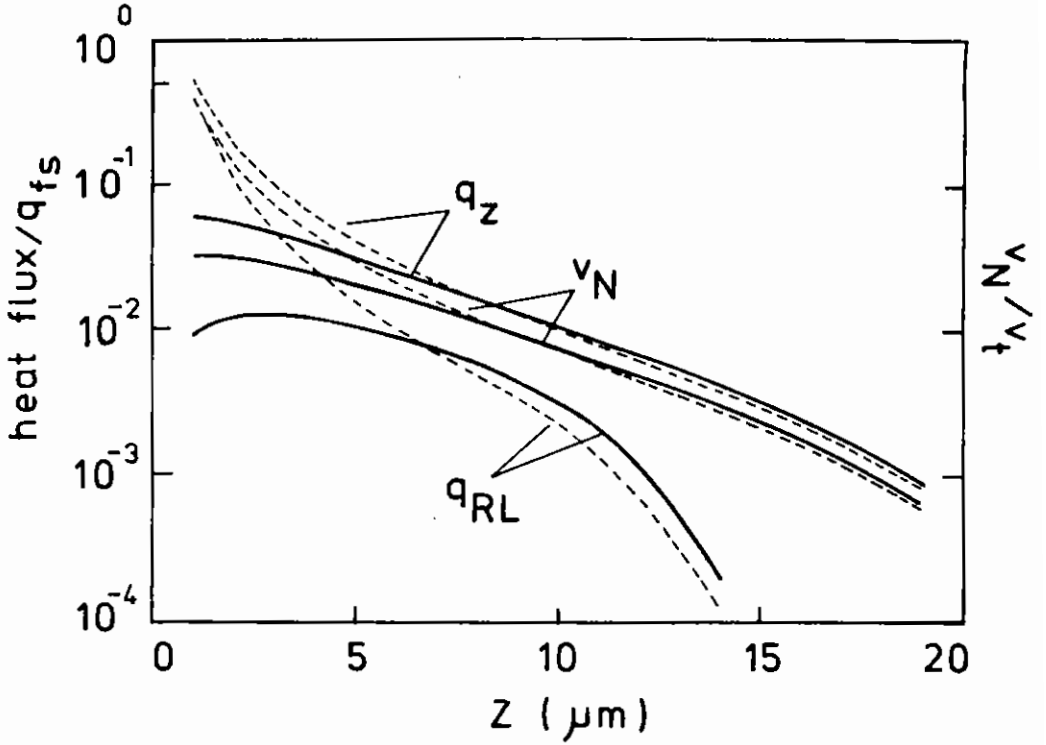

Fig A5.2 Continuous lines show the non linear kinetic, and broken lines the linear transport values of q_z (inward, parallel to ∇T_e heat flux), q_{RL} (Righi-Leduc) and V_N (Nernst convection velocity of B), at 130 psec.

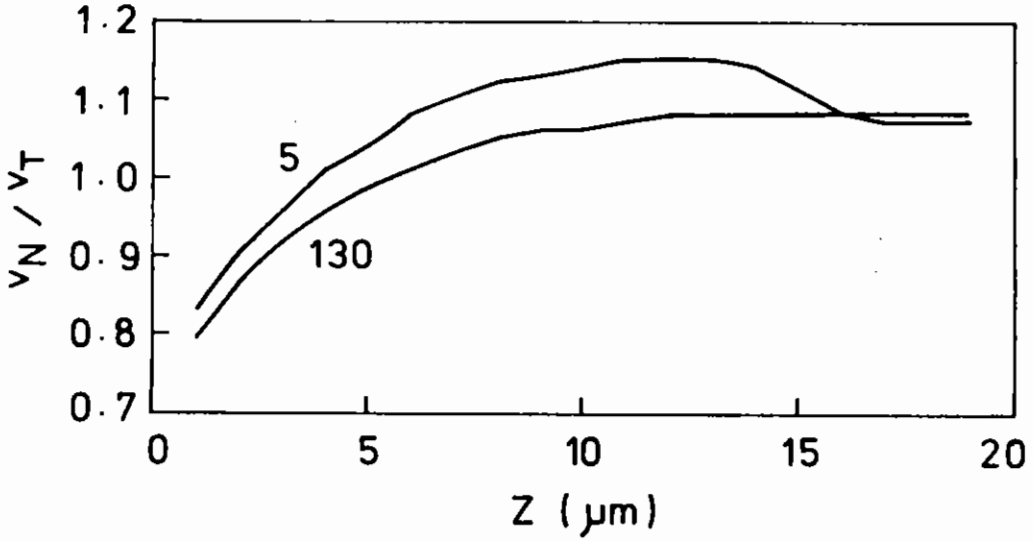

Fig A5.3 Local values of V_N/V_T across the plasma at 5 and 130 psec.

This is due to the depletion of the local Maxwellian tail at the heat front. Fig A5.3 shows v_N/v_T across the plasma at two different times. This ratio is consistently close to unity at all times and over the whole length of the plasma. It confirms the close coupling between B and q, even when the latter is nonlinear (flux-limited). Also shown in Fig A5.2 is a related B X ∇T effect, the Righi-Leduc heat flux. More severe "inhibition" is seen to occur for the Righi-Leduc heat flux than for the inward heat flux (parallel to ∇T).

A5.2.4 Relativistic saturation of plasma beat waves

R G Evans and R Bingham (RAL), R A Cairns (St Andrews)

In the beat wave accelerator (A5.13) two parallel propagating laser waves at frequencies ω_1, ω_2 beat together to drive a resonant plasma wave at $\omega_p = \omega_1 - \omega_2$. The phase velocity of the beat wave is $V_{ph} = \omega_p/k_p \approx c$ and from the general relation $V_{osc}/V_{ph} = \delta n/n$ we see that in the saturated limit ($\delta n/n \sim 1$) both nonlinear plasma effects and relativistic corrections must be considered together.

Taking the relativistic plasma fluid equations.

$$\frac{\partial n_e}{\partial t} + \underline{\nabla}\cdot(n_e \underline{v}) = 0 \qquad 1)$$

$$\left(\frac{\partial}{\partial t} + \underline{v}\cdot\underline{\nabla}\right)\gamma\,\underline{v} = \underline{e}\,(\underline{E} + \underline{v}\times\underline{B})/m \qquad 2)$$

$$\underline{\nabla}\cdot\underline{E} = \frac{e}{\epsilon_o}(n_o - n_e) \qquad 3)$$

and expanding to second order in v/c we obtain the equation for the slowly varying amplitude N of the density fluctuation

$$i\frac{\partial N}{\partial t} + \frac{\omega_p^3}{n_o k_p^2 c^2}\left(\frac{3}{16} - \frac{1}{2}\frac{k_p^2 c^2}{\omega_p^2}\right)|N|^2 N = \frac{n_o e^2 k_p^2}{4m^2\omega_1\omega_2\omega_p} E_1 E_2^* \qquad 4)$$

This is a driven non-linear Schrodinger equation with two contributions to the non-linearity. The first term $-\frac{3}{16}$, is due to the relativistic mass increase of the oscillating electrons, while the second term, is a Doppler shift induced by the plasma drift in the presence of a large amplitude wave. This term has not appeared in previous calculations (A5.14, A5.15) and for $V_{ph} = c$ results in a

non-linear frequency shift of opposite sign to that due to the relativistic effects alone.

The origin of this drift is simply explained and for sound waves is a well known, giving the flow behind a shock wave in the large amplitude limit. If we linearise equation (1) and assume solutions of the form

$$n_e = n_o + \tilde{n}\ e^{i(\omega t - kz)}$$

$$V = \tilde{V}\ e^{i(\omega t - kz)}$$

then $\frac{\tilde{n}}{n_o} = \frac{k}{\omega}\tilde{V} = \frac{\tilde{V}}{V_{ph}}$.

Thus $\tilde{n}$ and $\tilde{V}$ are in phase and the mass flux $(n_o+\tilde{n})\ \tilde{V}$ does not average to zero but gives an effective drift velocity.

$$V_D = \frac{1}{n_o} <(n_o+\tilde{n})\ \tilde{V}> = \frac{1}{2}\ \left(\frac{\tilde{V}}{V_{ph}}\right)^2$$

This is exactly the second non-linear term appearing in Eq.(4). The initial establishment of this drift velocity is due to the transient ponderomotive force as the driving term is applied.

The reason for the non-appearance of this term in earlier work and in some simulations is quite interesting. Poisson's equation (3) is frequently written in terms of the Lagrangian displacement of each electron $E = m\omega_p^2\xi/e$. This result is originally due to Dawson (A5.16) and is rigorously correct only if the plasma under consideration is bounded by undisturbed regions with zero field. In an infinite plasma, or in a simulation with periodic boundaries a uniform translation of each plasma electron through a displacement ξ obviously produces no additional electric field. In a simulation with fixed boundaries, or a real plasma of limited extent then any attempt of the plasma to drift in the direction of the wave will set up a sheath at each boundary, and the resulting DC electric field will prevent further drift.

Numerical simulations have been performed (A5.17) with a 1D relativistic particle in cell code and have confirmed the sign of the frequency shift given by Eq.(4). Fig A5.4 shows a particle phase space plot calculated by the PIC code showing the strong anharmonic nature of the large amplitude wave and the average velocity in the direction of wave propagation ($V_{ph} > 0$: $V_D > 0$).

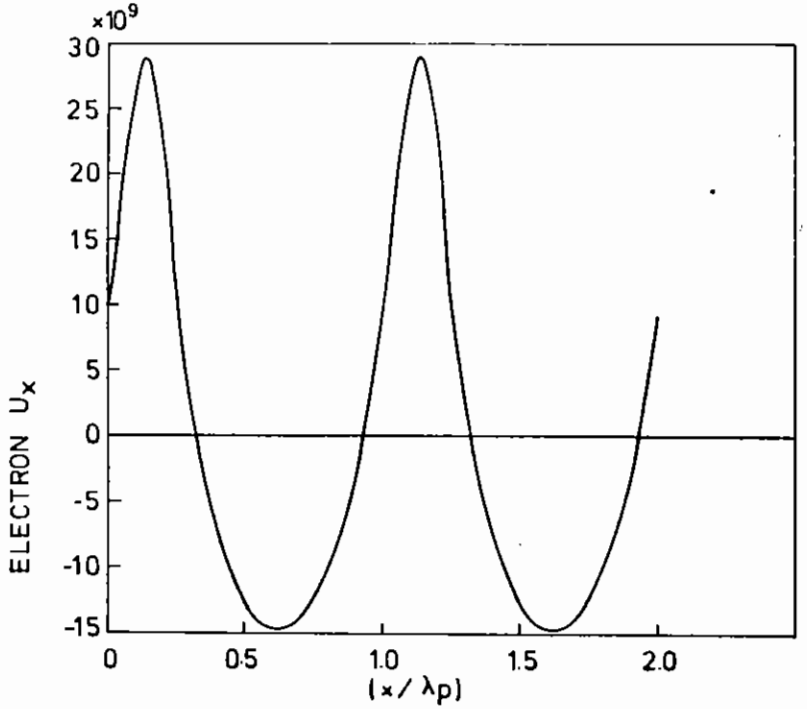

Fig A5.4 Electron phase space plot from the 1D relativistic PIC code.

A5.2.5 Efficiency factors in the beat wave accelerator

R G Evans (RAL)

The plasma beat wave accelerator as proposed by Tajima and Dawson (A5.13) offers the possibility of producing accelerating fields of many GeV m^{-1}. Its ultimate usefulness as a practical particle accelerator will depend on the efficiency of the overall process including the

laser efficiency, the coupling of laser energy to the beat wave, and the extraction of energy from the beat wave by the particle beam.

The fundamental parameters of the beat wave accelerator are: laser frequencies ω_1, ω_2, wavevectors k_1, k_2 plasma frequency $\omega_p = \omega_1 - \omega_2$, plasma wavevector $k_p = k_1 - k_2$, laser pump strengths $a_1 = eE/m\omega c$. The plasma wave is driven up to some fraction $\varepsilon = \delta n/n$ of the wavebreaking limit giving an electrostatic field

$$eE_p = m c \omega_p \varepsilon$$

The phase velocity of the beat wave is $v_{ph} = \omega_p/k_p$ corresponding to a Lorentz factor $\gamma = \omega_1/\omega_p$. This phase velocity is generally less than the velocity of GeV electrons so that the length of one stage is limited by phase slip to $L = 2\gamma^2 c/\omega_p$ giving an energy gain per stage of $\Delta\gamma = 2\varepsilon\gamma^2$.

The simplest estimate of the efficiency of energy transfer between the lasers and the plasma wave is given by Ruth and Chao (A5.18). The growth rate of the beat wave is $d\varepsilon/dt = \omega_p a_1 a_2/4 = \frac{1}{4} a^2 \omega_p$ for equal intensity pumps. If the laser pump duration is τ then the final beat wave amplitude is $\varepsilon = \frac{1}{4}a^2 \tau \omega_p$. The total beat energy in stage length L is then $u_{wave} = \varepsilon^2 mc^2 n_e AL$, where A is the cross-sectional area of the beat wave and the laser beams (assumed equal). The energy in the laser beams is $u_{light} = \frac{E^2}{4\pi} c\tau A$
giving an efficiency $u_{wave}/u_{light} = \varepsilon/2$

If the laser frequencies can be "chirped" to avoid detuning the plasma resonance at large amplitude then at first sight it appears possible to couple up to 25% of the laser energy into the plasma before exceeding the cold plasma trapping limit $\varepsilon = \frac{1}{4}$.

If however the beat wave is viewed as composed of elementary scattering events

$$\text{photon } (\omega_1) + \text{photon } (\omega_2) + \text{plasmon}(\omega_p)$$

then the Manley Rowe relations show that the energy transfer efficiency is ω_p/ω_1. A full treatment of the non-linear plasma equations shows

that as the beat wave is generated there is a second scattering process

$$\text{photon } (\omega_2) + \text{photon } (\omega_3 = \omega_2 - \omega_p) + \text{plasmon } (\omega_p)$$

giving rise to a new electromagnetic wave at ω_3. As the pump at ω_1 diminishes, ω_3 grows, and the process repeats giving rise to $\omega_4 = \omega_3 - \omega_p$ etc. This "Raman cascade" is limited in ultimate efficiency for the following reasons.

a) The phase velocities of the pumps at ω_2, ω_3, ω_4 are not equal giving rise to a dephasing of the pump waves.

b) If the pump waves ω_1 and ω_2 have a diffraction limited Rayleigh waist then because of the non-linearity of the generation mechanisms ω_3 etc will be spatially narrower. They will have a larger diffraction angle and will propagate out of the beat wave volume.

Both of these processes need to be analysed in detail because of the 'phase locking' inherent in all coupled wave interactions. Normally only the driven mode is phase locked but in the case of strong pump depletion the phase of the pump waves is also modified. Depending on the sign of the phase pulling this may give rise to self-focussing or defocussing. Also the phase of the beat wave will drift as the pumps cascade to lower frequencies and this will modify the effective phase velocity of the beat wave.

In a conventional RF cavity a beam of vanishingly small cross-section is able to extract energy from a large volume by virtue of its wake field partially cancelling the RF field in the cavity. In the same way the wake field of a small beam of particles in a plasma extends out to radii of at least c/ω_p by virtue of the fringe fields from the perturbed charge density in the plasma (A5.19, A5.20). We thus obtain the extremely important result that an arbitrarily narrow beam is able to extract a large fraction of the beat wave energy over an area of order $(c/\omega_p)^2$.

The energy per unit length in the beat wave is $u = \varepsilon^2 n_e mc^2 A_{wave}$.

The energy gain per unit length by a beam containing N_b particles is $\Delta u = eEN_b = \varepsilon mc\omega_p N_b$. If the beam area is A_{beam} and occupies a length $\ell = \delta\theta c/\omega_p$ then the extraction efficiency is $\eta = (n_b/n_e)\,(A_{beam}/A_{wave})\,\delta\theta\varepsilon^{-1}$ where n_b is the number density in the beam. If it is argued that $n_b \ll n_e$ to avoid instabilities such as the Weibel instability, and $\delta\theta \ll 1$ to give a small energy spread then the extraction efficiency is obviously very poor. However we can have $n_b \gg n_e$ so that the plasma becomes a weak perturbation on the beam particles. The growth rate of the Weibel instability is then more usefully thought of in terms of the plasma density of the beam particles $\omega_{pb}^2 = 4\pi n_b e^2/m$. In the rest frame of the beam the instability has a growth rate which is some fraction of ω_{pb}, but in the laboratory frame this is reduced by a factor of γ_b, which is 2×10^6 for a 1TeV beam.

In this case it is more useful to express the beam loading as the number of beam particles that extract all the beat wave energy from an area $A = \pi\,(c/\omega_p)^2$

$$N_b = \pi\varepsilon\; n_e\;(c/\omega_p)^3$$

We note that since $\omega_p \propto n_e^{\frac{1}{2}}$, $N_b \propto n_e^{-\frac{1}{2}}$, ie lower densities accelerate more particles. For a typical density $n_e = 10^{17}$ cm^{-3} and $c/\omega_p = 2.10^{-3}$; $N_b = 2 \times 10^9\,\varepsilon$.

If the emittance requirements of the accelerated beam force the beam radius in the beat wave region to be much less than c/ω_p then the effective radius of the beat wave is about $2c/\omega_p$ and wave energy outside this region cannot be extracted by the particle beam. If the laser beams are focussed by diffraction limited optics to a Gaussian waist then the Rayleigh length $R = 2\pi\,a^2/\lambda$ where a is the waist radius and λ the laser wavelength. If we put $a = 2c/\omega_p$ then $R = \gamma c/\omega_p$, but

the optimum stage length for energy coupling is $L = 2\gamma^2\,c/\omega_p$. If the Rayleigh length is matched to the depletion length then the beat wave is too large in cross-section for efficient extraction while if matched to the optimum beam waist the stage length is too short for efficient coupling of the laser energy to the beat wave. If $\gamma \gg 1$ then Rayleigh optics are inevitably limited to a maximum efficiency $< 1/\gamma$.

In conclusion, the efficiency of the beat wave accelerator is probably limited to 10% - 20% in coupling laser energy to the beat wave, and a high efficiency of extraction of beat wave energy to particle beam energy would occur with 10^8 particles per bunch. The behaviour of wake fields and Weibel instabilities in this limit is unknown and needs to be calculated.

A5.2.6 Simulations of Raman Scatter in a Rippled Density Profile

H C Barr and G A Gardner (Bangor)

Experiments in which stimulated Raman scattering (SRS) is observed usually also exhibit stimulated Brillouin scattering (SBS). Particle simulations show how the presence of SBS generated ion waves inhibit the growth of the Raman instability while giving rise to added structure in the emission spectrum.

A series of particle simulations, using a 1 1/2D fully relativistic electromagnetic particle code, were performed in which a laser beam was launched into a plasma homogeneous but for an imposed fixed ion density ripple of wavenumber $2k_0$ appropriate to SBS:

$$n_i(x) = n_0\;(1 + \varepsilon\;\cos\;2k_0\;x) \qquad (1)$$

k_0 is the local laser wavenumber. The parameters for the runs were $v_0/c = 0.1$, $V_e/c = 0.035$, $L = 57c/\omega_0$ and, for the figures shown below, $n_0 = 0.15n_c$ where n_c is the laser critical density. The ripple amplitude ε varied from 0 to 15%.

The effect of the ripple is primarily on the electron plasma waves which are no longer sinusoidal but composed of linear combinations of

the Fourier modes $k \pm 2nk_0$ (A5.21). Landau damping is increased by coupling into higher k modes. Independent of this, Raman growth is reduced since energy is distributed between the driven k and undriven quasiresonant idlers at $k \pm 2nk_0$. In addition, the possibility of new decay instabilities arise. By frequency matching with any normal mode which contains the driven Fourier mode at a finite amplitude, it is possible that a whole hierarchy of plasma waves may be driven unstable and appear as sidebands in the Raman emission spectrum.

A simple fluid theory illustrates the main effects. Plasma wave propagation in a sinusoidal density profile is described by the Mathieu equation (A5.22). A mode coupling approach yields

$$(a - \kappa^2)\, y(\kappa) = q(y(\kappa + 2) + y(\kappa - 2)) \qquad (2)$$

where $\omega^2 = \omega_p^2 + 3k_0^2 v_e^2 a$, $\kappa = k/k_0$, $y(\kappa) = n_e(k)/n_0$ and $q = \varepsilon/6k_0^2\lambda_0^2$. The parameter q quantifies the coupling efficiency between modes. The frequency being fixed, small q means that electron pressure can compensate density changes due to the ripple allowing the plasma wave, although nonsinusoidal to exist everywhere. Then (2) may be truncated, keeping only modes κ, $\kappa \pm 2$ to give the normal mode frequency correct to order q^2:

$$a(\kappa) = \kappa^2 + \frac{q^2}{2(\kappa^2 - 1)} \qquad (3)$$

Thus, if mode κ is directly driven by the laser and Raman scattered wave, then to order q^2, three normal modes contain this driven mode κ. The first is given by (3) with the driven mode κ as its main component (ω_1 say) and two other modes (ω_3 ω_2 say) obtained from (3) by letting $\kappa \to \kappa \pm 2$ in which the driven mode is one of the idlers of the normal mode. When q is large, electron pressure can no longer compensate the change in density and the wave is increasingly trapped in the ripple troughs. Then the normal modes are made up of many Fourier modes $\kappa \pm 2n$ and a numerical solution of (2) is required. In practice, only a few modes have $k\lambda_D < 1$ the others being heavily damped as is apparent in the simulations where q lies between 0 and 3.53 ($\varepsilon = 15\%$).

The laser coupling requires the inclusion of the term $-\kappa^2 v_0 v_s/3v_e^2$ on the right of equation (2) but only for that κ directly driven by the laser and scattered light waves. v_s is the oscillatory velocity of electrons in the scattered wave given as usual by

$$(\omega_s^2 - \omega_p^2 - k_s^2 c^2)v_s = \omega_p^2 v_0\, y(\kappa) \qquad (4)$$

where $\omega_s = \omega_0 - \omega$, $k_s = k_0 - k$. Solving between (2) and (4) to order q^2 determines the growth rates corresponding to ω_1, ω_2, ω_3:

$$\nu_1 = \nu_0 \left(1 - \frac{q^2}{32(\kappa - 1)^2} \right) \qquad (5)$$

and

$$\nu_{3,2} = q\nu_0/4\left|\kappa \pm 1\right| \qquad (6)$$

where ν_0 is the homogeneous growth rate. As q increases, ω_1 has its growth reduced while ω_2 and ω_3 emerge more strongly. In the simulations where $\kappa = 1.5$ we have $\nu_1 > \nu_2 > \nu_3$

Fig A5.5 shows the time evolution of the total electrostatic energy in the simulation plasma for three ripple amplitudes. The 5% ($q = 1.2$) ripple shows little change from the homogeneous case with the scattered spectrum showing a single peak at $\omega = \omega_1$ with no evidence of sidebands (see Fig A5.6). At 10% ($q \simeq 2.53$) there is a substantial reduction in growth with the appearance of a peak corresponding to $\omega \simeq \omega_2$. With the 15% ripple ($q \simeq 3.53$) the waves barely emerge from noise in the time span of the run (chosen to be the time to saturation by wavebreaking in the unrippled case) although there is now evidence of four peaks in the emission spectrum. It is not feasible to make a precise comparison between this simple theory and the simulation spectra. The simulations are a time dependent problem which includes sloshing of energy back and forth between modes leading to modulational frequency shifts as well as shifts due to electron trapping. These effects were minimised by analysing signals for times before they came into play.

The main conclusion of these simulations is clear, that the presence of ion waves leads to a substantial reduction in Raman emission.

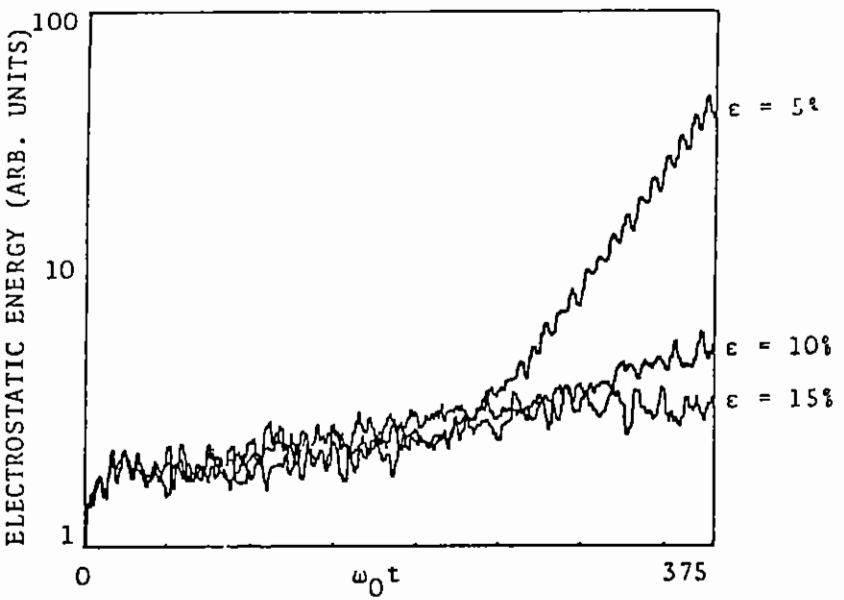

Fig A5.5 Time evolution of the total electrostatic energy for three ripple amptitudes.

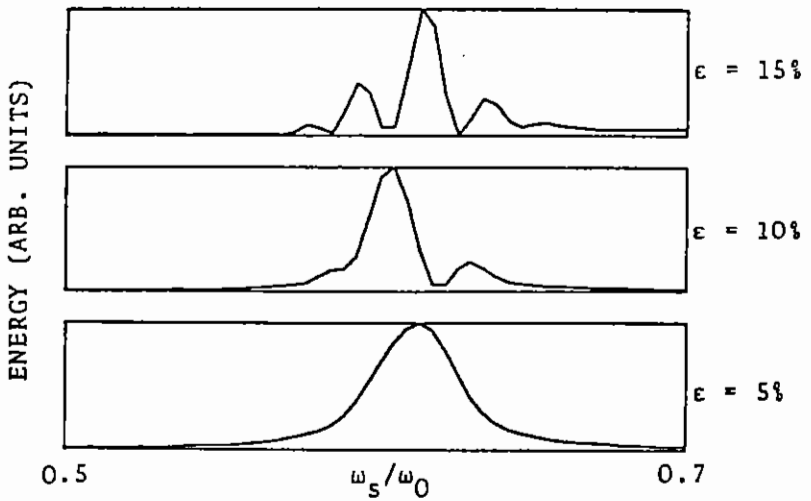

Fig A5.6 Scattered light spectrum.

A5.2.7 Non-linear heat flow with magnetic field

T H Kho (Imperial)

A 1-D kinetic code for electron transport with self-consistent E and B fields has been developed. Inverse bremsstrahlung absorption is included. The governing equations are

$$\frac{\partial f}{\partial t} + \vec{v}.\nabla f - \frac{e}{m}(\vec{E} + \vec{v}\times\vec{B}).\nabla_v f = C_{\text{Fokker-Planck}} + H_{\text{Inverse bremsstrahlung}}$$

$$\frac{\partial \vec{B}}{\partial t} = -\nabla\times\vec{E}$$

$$\nabla\times\vec{H} = \vec{j}$$

The inclusion of a magnetic field is a new development in electron kinetic codes. To satisfy Faraday's and Ampere's laws, the 1-D problem i.e., where spatial variation is allowed in one direction only, in fact requires E and the particle flux to be two-dimensional. The electron distribution function is approximated by a first order expansion in Cartesian tensors,

$$f(r,\vec{v},t) = f^0(r,v,t) + (\vec{v}/v).\vec{f}^1.$$

This expansion provides a simple expression for the multi-dimensional nature of the flux ($\vec{f}^1$). Substitution of this expansion into the kinetic equation yields a coupled set of equations for f^0 and $\vec{f}^1$,

$$\frac{\partial f^0}{\partial t} + \frac{v}{3}\nabla.\vec{f}^1 - \frac{e}{3mv^2}\frac{\partial}{\partial v}(v^2\vec{E}.\vec{f}^1) = C^0 + H^0$$

$$\frac{\partial \vec{f}^1}{\partial t} + v.\nabla f^0 - \frac{e}{m}\vec{E}.\frac{\partial f^0}{\partial v} - \frac{e\vec{B}}{m}\times\vec{f}^1 = \vec{C}^1$$

In the second equation $\partial\vec{f}^1/\partial t$ is neglected as it is small compared with the rest of the terms for the bulk of the electron population.

A finite difference scheme which preserves conservation of energy and

number density (A5.24) is applied to the $\partial f^0/\partial t$ equation. Testing of this scheme on the problem of thermalisation of a system of charged particles has led to the discovery that some classic features of the thermalisation process are in fact, numerical artefacts (A5.25).

Implicit time integration in previous kinetic codes (A5.26,A5.27) involved the use of fractional time steps ("time-splitting") to avoid large matrices. This could lead to difficulties in some circumstances (A5.24). By eliminating f^1 from the $\partial f^0/\partial t$ equation, it is found that the resulting large, sparse (non-diagonal) matrix can be solved very rapidly by the IDCG method (A5.28). The E and B fields are obtained by an iterative scheme.

Some of the results from this code are described in A5.2.3.

A5.2.8 Calculations with a fully implicit Fokker-Planck Code

S Jorna and L Wood (St Andrews)

We have developed a differencing scheme, which can be rendered fully implicit, for solving the Fokker-Planck equation for anisotropic systems of spherical geometry. The angle-dependent part of the distribution function is solved by differencing rather than by assuming an expansion in Legendre polynomials. We can therefore assess directly the accuracy of the frequently made assumption that the distribution function varies linearly with the expansion parameter (μ). A further advantage of this approach is that extension to higher spatial dimensions is straightforward.

The scheme selected is three-level in which optimum compromise between stability and accuracy is achieved by varying a parameter, which adjusts the admixture of terms at each time level in the Fokker-Planck equation (a la Douglas-Rachford). The scattering and diffusion terms are obtained from the most recently available distribution function. The electric field is obtained from Poisson's equation also using the updated distribution function. Facility for allowing ion motion is incorporated, but in all calculations to date the ion density has been kept fixed. There is also a facility for including a particle

conserving scheme [a la Chang and Cooper (A5.29)] in the velocity dependent level, but for diagnostic reasons this has not been implemented. We have found so far that imposing a neutrality condition on the plasma is sufficient with an 80 point velocity mesh extending to 12 thermal speeds.

At the radial boundaries the distribution function is made to conserve current at each time step in a manner similar to that employed by Matte and Virmont (A5.30).

Cubic spline fits are used where they improve particle and energy conservation. In particular, it has proved necessary to use a spline fit in the calculation of the heat flow to produce zero heat flow in a single-temperature system.

Initial calibration tests were similar to those adopted by Bell, Evans and Nicholas (A5.26). First, the code was run without collision terms to reproduce Landau damping. Accuracy on both the plasma period and the damping decrement was adequate (Fig A5.7). Second, relaxation of a Gaussian hump on a Maxwellian background was studied (Fig A5.8) and yielded relaxation times in agreement with those obtained by Dolinsky (Fig A5.8). Third, the full code was run for a spherical system with the boundaries kept at equal temperature. The original Maxwellian was maintained throughout the region to an accuracy better than 0.1% after 100 time steps, corresponding to $2000/\pi$ plasma periods.

The problem studied was that of heat conduction between two spherical shells, one kept at a fixed temperature, T_0 say, the other ramped up over 20 time-steps to $2T_0$.

Fig A5.9 shows the radial temperature variation for a system with inner radius 20μm and outer radius 24μm. This is to be compared (Fig A5.10) with the planar case. It will be noted that the temperature in the case with curvature rises less rapidly than in the planar case. Bell has suggested that this may be a geometrical effect in which the higher temperature electrons have mean free paths sufficiently long to miss the core. For the present case this would apply to electrons with a

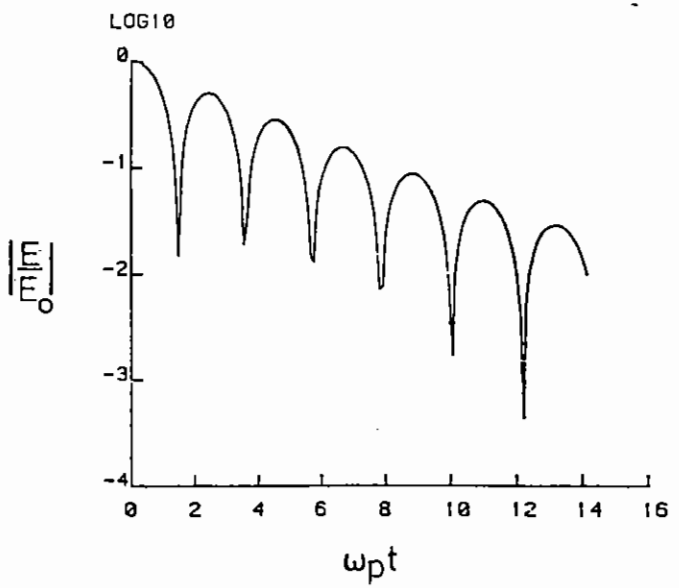

Fig A5.7 Electric field plotted against $\omega_p t$ in the absence of collisions

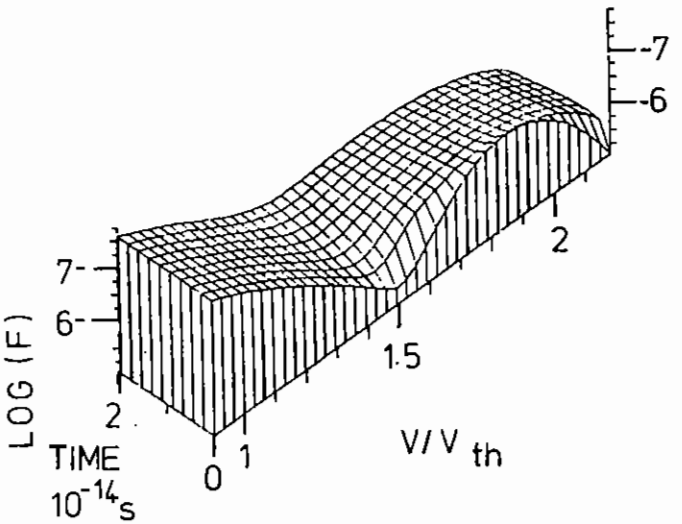

Fig A5.8 Relaxation of humped distribution plotted against speed and time

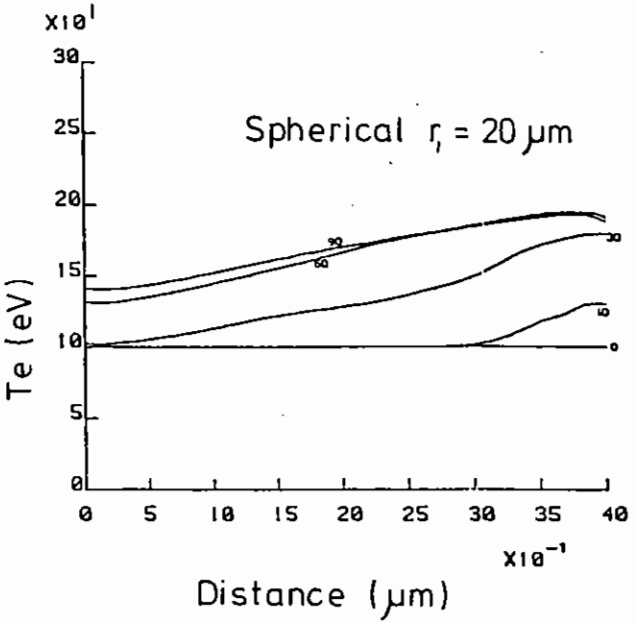

Fig A5.9 Variation of temperature with distance at different times in spherical geometry (r_1 = 20μm, r_2 = 24μm)

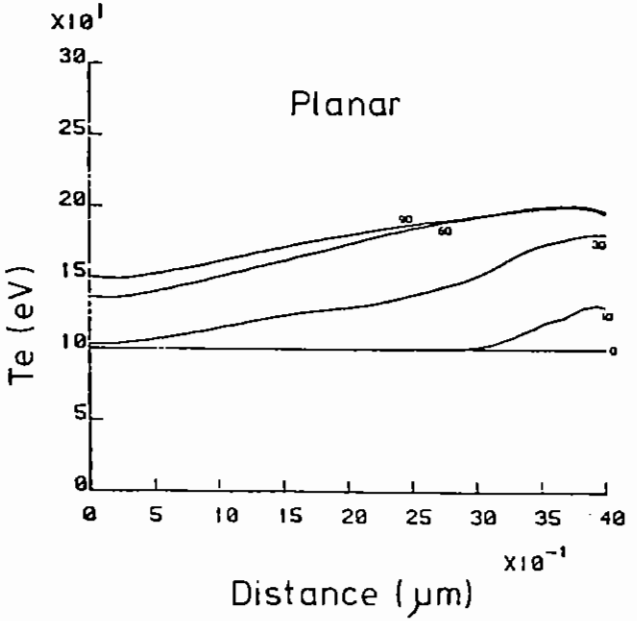

Fig A5.10 Variation of temperature with distance at different times in planar geometry

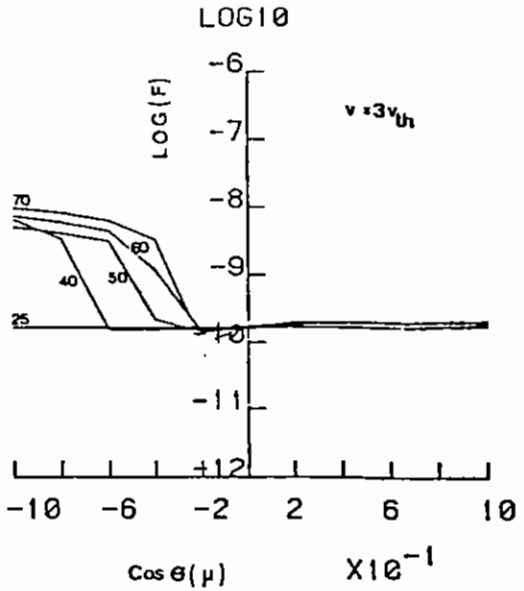

Fig A5.11 Angular variation of distribution function for $v = 3v_{th}$ near cold boundary at different times

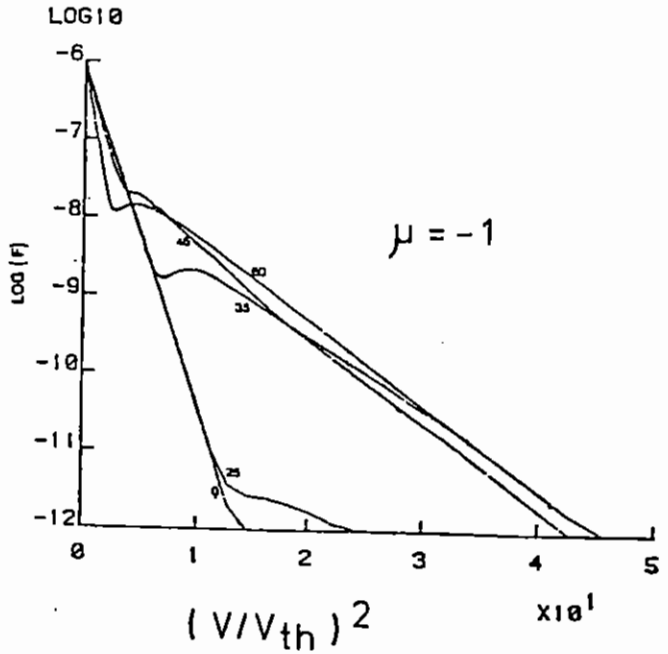

Fig A5.12 Variation of distribution function against $(v/v_{th})^2$ for $\mu=-1$ near cold boundary at different times

velocity exceeding five times the thermal speed, emitted from the boundary outside a cone or apical half-angle 56^0.

In Fig A5.11 we show the dependence near the cold boundary of the distribution function on μ ($\equiv \cos\theta$) at a velocity three times the thermal speed at different times. There is significant curvature in the distribution function at thirty time steps, which seems to indicate that a linear approximation for f in μ is inaccurate especially near the hot boundary (where this effect is even more pronounced) at speeds exceeding several thermal speeds.

Fig A5.12 shows the dependence of the distribution function on velocity near the cold boundary for $\mu=-1$. The Maxwellian distribution develops a two-temperature profile.

Calculations are presently underway to compare heat flows at various thermal gradients with the Spitzer-Harm results. We will then investigate the effect of transverse conduction on the smoothing and of initial temperature (and density) ripples as the conduction front moves in. This will necessitate extending the code to two spatial dimensions which is straightforward with the differencing method adopted here.

A5.2.9 Thermal Smoothing of Non-Uniform Laser Illumination of a Planar Target

A R Bell (RAL) and E M Epperlein (Imperial)

We examine the thermal smoothing of pressure non-uniformities produced by non-uniform laser energy deposition. In the calculation, a massive planar target is driven by a temporally uniform laser beam for a time which is much longer than the hydrodynamic flow time between the solid and critical surfaces. It is assumed that the laser energy is dumped at the critical surface and has a small time-independent variation about the mean which varies sinusoidally in one direction while being constant in the other. The equations are linearised in the small perturbation, and two-dimensional steady-state ablation structures are calculated. These calculations are similar to those published by Manheimer, Columbant and Gardner (A5.32) but differ in the following

ways: 1) the zeroth order uniform ablation structure is calculated without their neglect of the kinetic energy of bulk plasma flow in the energy equation, 2) the ablation structures are calculated here in the underdense (density less than critical) plasma, 3) we include the magnetic field generated by the grad(n)xgrad(T) term. The first of these differences is probably not particularly important, only making a small numerical difference to the results, but the lack of treatment of the underdense plasma in A5.32 leads to a false boundary condition at the critical surface which omits an important part of the smoothing process. Their equations 30 and 31 state that an excess of laser energy deposited at a certain point on the critical surface and transported to higher density is then convected out as plasma enthalpy flow through that same point, whereas in actuality the energy transported inwards is spread laterally by thermal conduction and is subsequently convected out over a surface area of the critical surface surrounding that point, thereby contributing to the smoothing process. A further effect neglected by their choice of boundary condition is that excess laser energy deposited at one point not only results in increased energy flow towards higher density but also leads to an energy flow into the underdense plasma where thermal conduction can add to the smoothing. The Braginskii transport coefficients are used throughout this calculation. It has been shown (A5.33) that for steady-state planar ablation the temperature gradients are relatively gentle and that the Braginskii conductivity is a good approximation at least for the zeroth order uniform ablation. The assumption of planar geometry is a more serious approximation since it is only realistic at low irradiance and short laser wavelength.

The boundary conditions at the critical surface are that the mass flow, momentum flow, lateral velocity, and temperature are continuous. The energy flow is discontinuous since energy is injected at this surface. The position of the critical density can be perturbed away from its zeroth order position.

Curve (a) of Fig A5.13 is a plot of the mass flow perturbation at the critical surface as a function of perturbation wavelength for a given amplitude in the perturbation of the laser energy input. It shows that smoothing becomes important at relatively long wavelengths, kD=0.03

where D is the distance between the critical and solid surfaces, and k is the spatial frequency of the perturbation. Excess energy deposited at one point on the critical surface is transported laterally, thus spreading it over a larger area and reducing the amplitude of the perturbation flowing through the critical surface. At long wavelengths, kD<1, most of the excess energy is conducted outwards into the underdense plasma, where smoothing occurs reducing its effect on the mass flow. Curve (b) of Fig A5.13 plots the amplitude of the perturbation at a point close to the base of the temperature front as a function of kD. The perturbation is more strongly smoothed at the solid surface then at the critical surface showing that the transport of the non-uniformities from the critical to the solid surface is reduced by smoothing processes, but the effect is not as large as the reduction in the non-uniformities already present at the critical surface. The difference between the comparable curves for momentum flow, instead of mass flow, is not as marked (Fig A5.14). The perturbed momentum flow is less strongly smoothed than the mass flow at long wavelengths.

The 2-D profiles described above have density and temperature gradients which are perpendicular to the zeroth order density and temperature gradients. Consequently, grad(n) x grad(T) is non-zero and magnetic field is generated. The magnetic field produces transverse Righi-Leduc heat flow which feeds back onto the temperature and pressure thereby influencing the hydrodynamics. The magnetic field is therefore an integral part of the hydrodynamics and should be included in the calculation. Beside the grad(n)xgrad(T) source term and the Righi-Leduc heat flow it is also necessary to include transport of the magnetic field by the Nernst effect and collisional damping of the magnetic field. The Nernst term is important because it transports magnetic field against the bulk plasma flow towards the solid surface (A5.12). Collisional dissipation is important where the plasma is dense and cold, and dominates very close to the solid surface. We make the approximation that dissipation takes place only at the solid surface and need not be included in the equations for the plasma between the critical and solid surfaces. We use the Braginskii coefficients for Z=3.

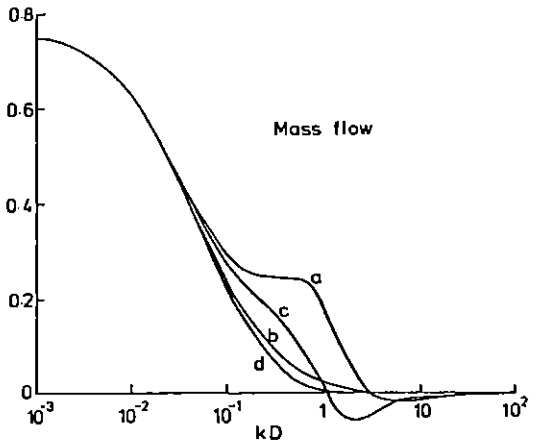

Fig A5.13 A plot of amplitude of the mass flow perturbation for a given fixed amplitude sinusoidal perturbation in laser irradiance. The amplitude is plotted as a function of kD whre k is the spatial frequency of the perturbation and D is the zeroth order distance between the critical and solid surfaces. Curves (a) and (b) are the results for calculations which neglect the magnetic field. Curves (c) and (d) include the effect of the magnetic field. Curves (a) and (c) give the perturbation amplitude at the critical surface, curves (b) and (d) at a point close to the solid surface

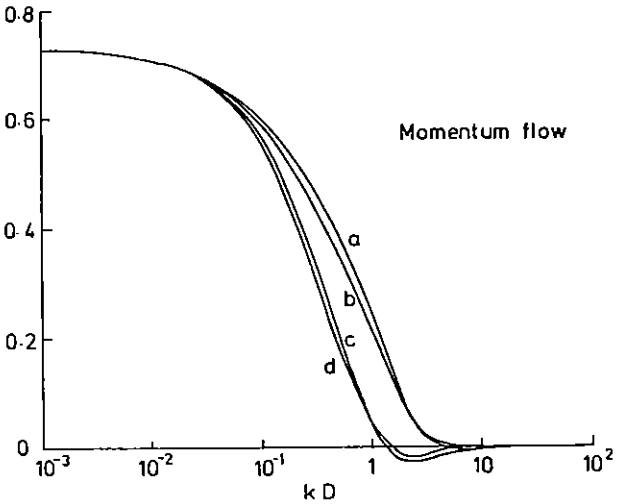

Fig A5.14 Same as Fig A5.13, but for momentum flow instead of mass flow

Curves (c) and (d) of Figs A5.13 and A5.14 show the magnitude of the perturbations at the critical and solid surface respectively when the magnetic field is included in the calculation. The magnetic field produces an increase in smoothing which is consistent with the positive stability of these equations at densities greater than critical (A5.34, A5.35). Smoothing of the momentum flow takes place at wavelengths which are approximately twice as long when the magnetic field is included.

A5.2.10 Hydro-Code Development

G J Pert, J D Crossland, M J Henshaw (Hull University)

The detail which can be resolved in a finite difference calculation, is obviously limited by the mesh spacing. In the course of a typical laser-plasma interaction the mesh spacing in a Lagrangian code varies markedly throughout different regions of the problem, on the other hand in an Eulerian grid the spacing is roughly constant and determined by the overall dimensions of the problem. Non-uniform meshes in Eulerian schemes can be used to give improved resolution over fixed regions in space, and Lagrangian ones to a specific zone of fluid. Neither approach in this simple form can cope with a moving zone requiring high resolution. This difficulty is inherent in modelling laser-plasma interaction, particularly if detailed study of the ablation zone is required, for example, in an analysis of Rayleigh-Taylor instability. To this end effort has been made to use the quasi-Lagrangian rezoning techniques in POLLUX as adaptive grid generators.

The specific problems for which these methods have been developed have been thermal smoothing and the development of Rayleigh-Taylor instability. In these we have been able to identify an "ideal" set of mesh points to which we require the mesh to conform. In the case of thermal smoothing this is based on the average ablation surface defined by the change in sign of the flow velocity averaged across the mesh. Parallel to the axis from this point to a point downstream of the average critical surface a grid with linearly increasing cell size is used. For the regions upstream of the ablation surface and downstream

of the critical surface a coarse uniform mesh suffices. A uniform mesh is used transverse to the asymmetry axis.

The Rayleigh-Taylor studies are examining the flow in spherical geometry. For this a simple von Neumann-Richtmyer one dimensional code is used to generate the ideal mesh points and the mesh boundaries: the normal quasi-Lagrangian mesh boundary conditions (A5.36) are relaxed.

The "ideal" mesh is imposed on the actual mesh by means of the slip device previously used (A5.37) to maintain a well-structured mesh in rezoning. Thus, considering one dimension, if x_i is the "ideal" mesh and z_i the actual mesh the quasi-Lagrangian mesh velocity, V_i, has an additional component to give a total:

$$V_i^1 = \beta\ V_i + (1-\beta)\ \text{Min}\left[0,\ (x_i-z_i)/(z_f-z_b)\right]\ \text{Sign}\ (V_i)/Dt \qquad (1)$$

where z_b and z_f are the mesh boundaries. In normal applications we set

$$\beta = \text{Min}\left[1,\ 10(dz/dx)_i\right] \qquad (2)$$

which keeps the mesh well ordered. More generally if we set:

$$\beta = \text{Min}\left[1,\ \alpha(dz/dx)_i,\ \alpha(dx/dx)_i\right. \qquad (3)$$

the mesh pulling term in (1) will operate as soon as the mesh cells are either too large or too small, ie $\Delta z_i > \alpha\ \Delta x_i$ or $\Delta z_i < 1/\alpha\ \Delta x_i$. Thus as $\alpha \to 0$, the mesh pulling term dominates the quasi-Lagrangian movement. In order to allow some slippage we have found it advantageous to set α to about 1.

In these calculations we have found it necessary to either relax the quasi-Lagrangian mesh boundary conditions, or to ensure that the "ideal" mesh also maintains these same conditions, preferably with the "ideal" and actual meshes having the same boundary velocity.

A5.3 ATOMIC AND RADIATION PHYSICS

A5.3.1 The calculation of line coincidences in helium-like ions: The sodium-neon and strontium-bromine line coincidences

S J Rose (RAL)

The possibility of using resonant photopumping to achieve far-UV laser action has been considered by many authors (A5.38-A5.41). Recently Alley et al (A5.42) considered using line coincidences between ions of higher Z to produce laser action in the X-ray region. It is the purpose of this work to assess the importance of the different contributions to line coincidences in both high- and low-Z schemes.

Two proposed photon-pumped laser systems are considered. The first scheme involves the NaX $1s^2\ ^1S_o$ - $1s2p\ ^1P_1$ line pumping the NeIX $1s^2\ ^1S_o$ - $1s4p\ ^1P_1$ transition. The two line positions have been measured experimentally (A5.43) to lie at 11.0027 Å and 11.0003 Å respectively and the scheme is designed to produce laser action in the NeIX 3-2, 4-2 and 4-3 singlet lines lying in the far-UV. The second scheme involves one of the coincidences listed by Alley et al (A5.42); the Sr $1s^2\ ^1S_o$ - $1s2p\ ^3P_1$ transition pumps the Br $1s^2\ ^1S_o$ - $1s3p\ ^1P_1$ line, resulting in laser action in the $1s3s\ ^1S_0$- $1s2p^1P_1$ and $1s3d\ ^1D_2$ - $1s2p\ ^1P_1$, transitions which lie in the X-ray range.

In this work, these coincidences have been studied theoretically by calculating the electronic structure using the multiconfiguration Dirac-Fock programs of Grant et al (A5.44) and McKenzie et al(A5.45).

Table A5.4 shows the calculated and experimental energies of the NaX $1s^2\ ^1S_o$ - $1s2p\ ^1P_1$ and NeIX $1s^2\ ^1S_o$ - $1s4p\ ^1P_1$ lines. Although the inclusion of the dynamic part of the interelectron interaction and of quantum-electrodynamic effects are found to worsen the agreement with experiment, resulting in a discrepancy for each line of just over 1eV, for the difference in energy between the two transitions (the important quantity in resonant photopumping) the inclusion of these effects is found to improve agreement bringing the calculated energy difference between the two lines to within 0.2eV (less than 2mÅ) of

Table A5.4

Notes	$E(Ne;1s^2\ ^1S_0-1s4p\ ^1P_1)$	$E(Ne;1s^2\ ^1S_0-1s2p\ ^1P_1)$	$E(Ne;1s^2\ ^1S_0-1s2p\ ^1P_1)$ $-E(Ne;1s^2\ ^1S_0-1s4p\ ^1P_1)$
(a)	1126.29	1126.40	0.11
(b)	1125.96	1125.95	-0.01
(c)	1125.85	1125.79	-0.06
(d)	1127.11	1126.86	-0.25

(a) MCDF single-manifold calculations.

(b) As (a) but including dynamic part of electron-electron interaction.

(c) As (b) but including quantum-electrodynamic corrections.

(d) Experimental data.

Table A5.5

Notes	$E(Br;1s^2\ ^1S_0-1s3p\ ^1P_1)$	$E(Sr;1s^2\ ^1S_0-1s2p\ ^3P_1)$	$E(Sr;1s^2\ ^1S_0-1s2p\ ^3P_1)$ $-E(Br;1s^2\ ^1S_0-1s3p\ ^1P_1)$
(a)	14584.5	14593.5	9.0
(b)	14569.3	14574.4	5.1
(c)	14559.6	14561.5	1.9
(d)	14559.4	14561.1	1.7

(a) MCDF single manifold point-nucleus calculations.

(b) As (a) but including dynamic part of electron-electron interaction.

(c) As (b) but including quantum-electrodynamic corrections.

(d) As (c) but using finite nucleus.

experiment. The remaining discrepancy between theory and experiment is thought to arise mainly because single-manifold calculations do not completely include the effects of electron correlation. For each ion the ground state is expected to be least well described resulting in the larger experimental than theoretical transition energy. However, the energy difference between the two lines is more accurately predicted because the nuclear charge of each ion is very similar and each transition is between a $1s^2$ ground and a 1snp excited state resulting in some cancellation of error.

Table A5.5 shows the energy of the Sr $1s^2\ ^1S_0$ - $1s2p^3P_1$ and Br $1s^2\ ^1S_0-1s4p\ ^1P_1$ lines together with the energy difference between them. The effects of the dynamic part of the interelectron interaction and of quantum-electrodynamic effects are much larger for the strontium-bromine than the sodium-neon system and each effect alters the energy difference by several eV. The effect of using a finite nuclear charge distribution in place of a point nucleus is also not negligible.

Neither line position has been measured experimentally. However for the same reasons as in the sodium-neon case it is expected that the calculated energies will lie somewhat below the true values but that the error in the energy difference between the lines will be smaller. Because multimanifold calculations to include the remaining contribution from electron correlation would involve substantial computational work, these have not been attempted here.

The efficiency of resonant photopumping is critically dependent on the energy difference between the lines. Single-manifold multiconfiguration Dirac-Fock calculations, including the effects of the dynamic part of the interelectron interaction and quantum-electrodynamic effects, are able to predict the line energies in the sodium-neon scheme to within 2eV and the line energy difference to within 0.2eV. The discrepancies are thought to arise mainly from an inadequate description of electron correlation.

Calculations of the higher-Z strontium-bromine system (for which there is no experimental information on line positions) show that the effects

of the dynamic part of the interelectron interaction, quantum-electrodynamic effects and the finite nuclear charge distribution each make a significant contribution to the difference in energy between the lines. Each of these effects needs to be included for reliable predictions of line coincidences for such ions.

A5.3.2 Modelling of single pass ase XUV laser beam characteristics

M H Key (RAL)

The development of XUV lasers has progressed rapidly via spectroscopic evidence for population inversion eg (A5.46), measurement of high gain coefficient 'g' in small plasma length 'l' ($1 < g < 10cm^{-1}$, $l \sim 0.1cm$), eg (A5.47) to most recently demonstration of high single pass exponential amplification exp (gl) with $gl \sim 6$, exp (gl) ~ 500 (A5.48).

The final step on the road to a single pass amplified spontaneous emission laser will be to produce sufficient values of gl to reach the saturated output condition where, at the ends of the plasma column (Fig A5.15), excited ions are de-excited predominantly by stimulated emission and the laser produces its most collimated output beam and maximum beam brightness. (The output increases only linearly with 'gl' beyond the saturation limit, which is insignificant relative to the dramatic exponential increase in output with gl, below the limit).

In this report we discuss how the near field and far field characteristics of such lasers depend on gl for gl values less than the saturation limit, motivated by the need to diagnose and interpret experiments such as those reported in Section A4.2.

Saturated ASE Laser Characteristics

A simple two-level model suffices to show the main features of the saturated laser characteristics. The upper and lower levels have population density N_u and N_l and degeneracy g_u and g_l, the transition photon energy is $h\nu$ the wave length is λ, the radiative lifetime of the upper state is A_{ul} and the stimulated emission cross section is σ_{ul}.

The gain coefficient in the medium, for line width $\Delta\nu$ is,

$$g = \left(n_l \frac{g_u}{g_l} - n_u\right) \frac{A_{ul}\,\lambda^2}{8\pi\,\Delta\nu} \qquad (1)$$

and it is convenient to write this as

$$g = \eta\, n_u\, \sigma_{ul} \qquad (2)$$

where η is the inversion fraction.

In most cases of interest the transition is Doppler broadened and the ion temperature is related to the transition photon energy so we can write

$$kT_i = \xi\, h\nu \qquad (3)$$

and

$$\Delta\nu = \frac{2\nu}{c}\left(\frac{2\,\ln 2\,\xi\,h\nu}{M_i}\right)^{\frac{1}{2}} \qquad (4)$$

Finally in deducing the saturation limit it is necessary to know the lifetime τ_u of the upper state, which is typically less than A_{ul}^{-1} because of collisional processes, so we can write

$$\tau_u^{-1} = m\, A_{ul} \qquad (5)$$

If we now consider a simple geometry with length L and square cross section of width w, the flux density of photons (n_ν cm^{-2} sec^{-1}) at either end is obtained by simple integration (assuming $gL \gg 1$),

$$n_\nu = (1/4\pi)(w/L)^2 \exp(gL)\, A_{ul}/(n\sigma_{ul}) \qquad (6)$$

The saturation condition for $(n_\nu)_s$ is,

$$(n_\nu)_s \sigma_{ul} > m A_{ul} \qquad (7)$$

which leads directly to

$$(gl)_s > \ln\left[4\pi\, mn\, (L/w)^2\right] \qquad (8)$$

Typically $m \sim 10$, $n \sim 0.1$ and $L/w \sim 300$, giving $(gl)_s > 14$ for saturation. Changing the assumed numbers within a realistic range makes little difference to $(gl)_s$.

The saturated output $(n_\nu)_s$ can be derived from the above equations in the form,

$$(n_\nu)_s = 4\,(2\ln 2)^{\frac{1}{2}} \frac{1}{c^3} \left(\frac{h}{m_p}\right)^{\frac{1}{2}} \left(\frac{\xi}{\eta^2 A}\right)^{\frac{1}{2}} \left(\frac{w}{L}\right)^2 \exp\left[(gL)_s\right] \nu^{7/2} \qquad (9)$$

where A is the atomic mass number and m_p the mass of a proton. There is a strong frequency dependence (which is $\nu^{9/2}$ if expressed in terms of output power density I_s). For a wavelength of 20nm and assuming parameters typical of the Se 3p-3s laser scheme (ref 3) [viz $\xi = 1$, $A = 80$, Eq (4)] then, with other parameters as before, $I_s = 4 \times 10^8$ watts cm^{-2} showing the considerable near field power density of saturated XUV lasers.

It is interesting to note that this result is insensitive to the atomic physics parameters of particular laser schemes and depends mainly on the frequency and the geometry. The geometrical angular divergence of the output is w/L and the brightness in the far field, B_s, follows directly from Eq (9). The magnitude of B_s is proportional to w^2 if the other ratios are left as before, so assuming $w \sim 10^{-2}$ cm we obtain a total power output of 4×10^4 watts with a brightness of 3×10^{13} watts/steradian in the far field or 3×10^{13} watts cm^{-2} $sterad^{-1}$ in the near field.

Finally it is useful to note that in the far field the ratio of the amplified spontaneous emission along the axis of the system to the spontaneous emission is $[(\exp(gL)-1)]/gL$ for any value of gL.

Numerical Modelling of the Near and Far Field Beam Characteristics

Fig. A5.15 shows how a simple numerical model was used to calculate the distribution of emission in the near and far field for values of gL below the saturation limit.

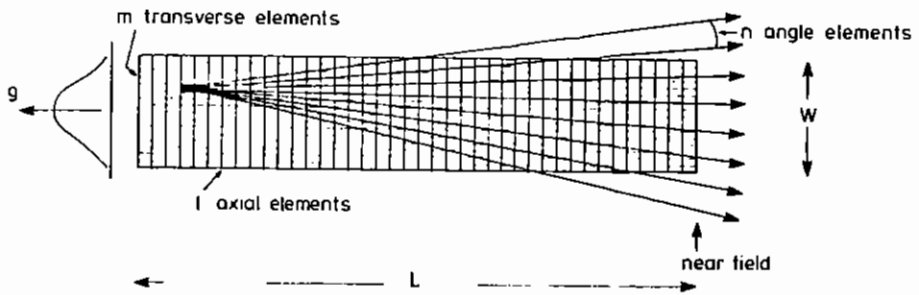

Fig A5.15 Numerical model uses L X M source elements and N rays from each element to compute amplified spontaneous emission in far and near field. The gain coefficient varies transversely but is constant axially.

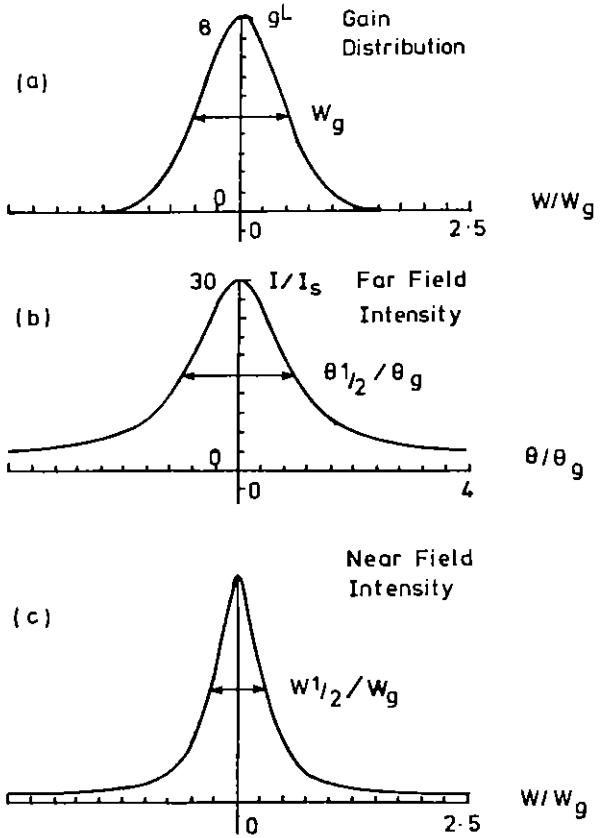

Fig A5.16 (a) Gaussian transverse distribution of gain assumed in the model with maximum gl = 8 in this example. W_g is the full width at half maximum, and the plasma is assumed to extend to a maximum width of 2.5 W_g with uniform source brightness but variable gain.

(b) Calculated far-field intensity distribution showing full width at half maximum θ_j normalised to the geometrical angle W_g/L. The intensity I is normalised to the spontaneous emission intensity I_s.

(c) Near field intensity distribution showing full width at half maximum W_j/Wg

The transverse spatial distribution of gain was assumed to be gaussian, Fig A5.16a and all spontaneously emitted photons were assumed to experience the same amplification coefficient [ie spectral narrowing of the output was neglected.

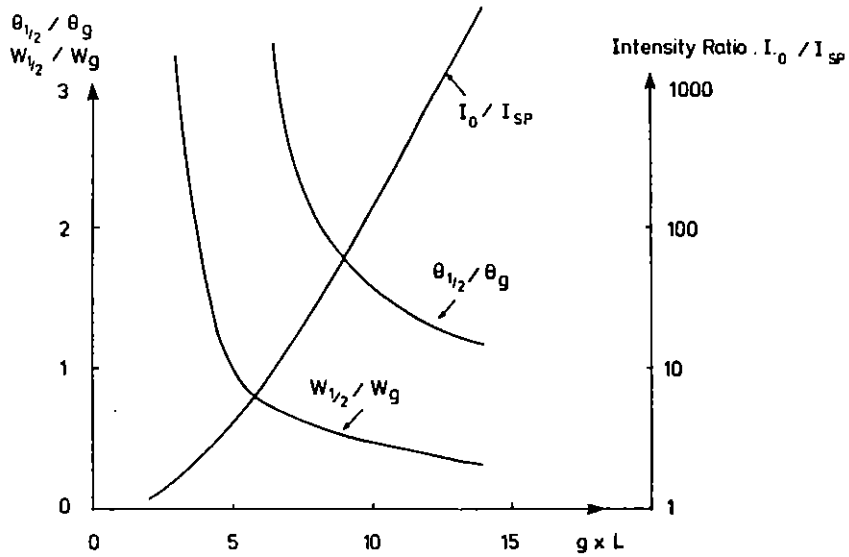

Fig A5.17 Model results (a) far-field beam divergence (FWHM) intensity θ_j) normalised to the geometrical angle $\theta_g = W_g/L$, where W_g is the FWHM gain in Fig A5.16 and L is the length. (b) Near-field FWHM intensity W_j normalised to W_g. (c) Ratio of peak intensity in the far-field on axis I_o to the spontaneous background I_{sp}.

Its inclusion would reduce the calculated output somewhat but would not significantly affect the main conclusions presented below].

The calculation shows the distribution of output in the near field, Fig. 5.16c and far field, Fig A5.16 b, assuming straight line propagation. The results are expressed in dimensionless fashion with the output normalised to the spontaneous background and the spatial and angular scales in the near and far field being normalised to the width of the gaussian distribution of gain w_g and to the geometrical angle w_g/L respectively.

The results are summarised in Fig A5.17 which shows how the beam narrows sharply in the near and far field as gl increases and the ratio of the output intensity to the spontaneous background increases exponentially.

Diagnostics based on direct observation of the laser "beam" become possible for $gL > 8$. This model has been used to analyse the experiment reported in Section A4.2 leading to the conclusion that the apparent output power and beam angle in the far field are consistent with $gL = 9$ but would require a source size at the diffraction limit $[w_{\frac{1}{2}} < 6\ \mu m]$, which is difficult to explain.

A5.3.3 The solution of Benchmark Problems for Radiative Transfer Methods

J M Salter (Imperial College), R W Lee (Livermore)

The radiative properties of hot dense matter, eg. opacities and emissivities, are central to the study of radiative transfer (RT) (A5.49). Historically, astrophysicists have performed the most sophisticated RT work: however, recent interest in the radiative properties of hot dense matter has been spurred by work on laboratory plasmas and thus, there is a mismatch between numerical development (astrophysical) and application (laboratory). For the purpose of correcting this, data has been proposed which can be used to construct a benchmark radiative transfer calculation for laboratory plasmas.

On the one hand, astrophysicists have developed techniques that will satisfy the requirements of laboratory systems but without necessarily taking account of the special nature of laboratory plasmas. On the other hand, the study of laboratory plasmas has moved toward ever more detailed simulations, detailed in both the amount of data on radiative properties included and in the hydrodynamic complexities; however, the RT problem has been treated approximately. Two questions arise:

1. Can one find, in the restricted regime of hot dense plasmas, RT techniques that are efficient and robust while producing solutions of the required accuracy?

2. Can one define a set of techniques which have predefined accuracy for various laboratory sources?

In addition, a large number of groups work on the characterisation of the radiation from different laboratory plasma sources and there has been a tendency to have no cross-reference or cross-calibration for various RT techniques. Therefore, it is of interest to provide a basis for cross-comparison. To do this, we propose a set of simple benchmarks.

To resolve the questions about relevant RT techniques and to provide a basis for cross-referencing, we present two benchmark problems which are an outgrowth of work from a CECAM workshop. In each case, we have chosen a laboratory system which is schematic in that it represents a fictitious atom in a plasma, with atomic rate coefficients, that can reasonably be assumed to test the RT in the hot dense plasma regimes of interest. The first difficulty is that the label "hot dense" is not inclusive enough but to overcome this we have chosen two cases which we believe will span the region. The cases are time independent and in planar geometry. The characteristics of the solution which can be compared are the source function and the intensity as functions of frequency, together with the level populations which are self consistently determined.

The benchmark is defined by a temperature and atomic number density, ie. total density of all ion stages present, together with a geometric slab thickness. Since we are interested in having everything defined but the RT schemes which are to be tested, we have specified all the variables necessary; rates for the rate equations and all the cross-sections for the free-free, bound-free and bound-bound transitions. Further, we suggest that the use of a published Voigt profile generator will eliminate extraneous errors (A5.50).

a. Hydrogen Slab

We take a hydrogen plasma in a steady state, which is attainable in the recombination phase of a hydrogen filled Z-pinch. The major problem here is the relatively high optical depth, for a laboratory plasma, in the Lyman alpha transition. Any linking of line transitions is likely to happen in this case.

b. K-Shell Argon Slab

To go to the other limit of hot dense plasmas, we treat a schematic "Argon" ion with multiple ion stages, spin "allowed" and "forbidden" transitions in the helium-like ion stage and autoionising levels in the lithium-like ion stage. This should introduce in a schematic model the added complexities found in highly stripped ions.

The derivation of a spatial distribution function for the radiation in an optically deep medium is complicated by the fact that the source function, from which all the parameters of the radiation field can be obtained, is dependent on the level populations which in turn depend on the radiation from other positions, and it is this non-locality that necessitates the use of sophisticated methods of solution.

To provide an initial solution to the benchmark, we have formulated a generalised RT model. The principle behind the solution is to solve the rate equations connecting the atomic levels and the Radiation Transfer Equation (RTE) self consistently so that changes in the one are reflected in changes in the other. In practice, this means iterating between the two halves of the problem until there is convergence. The difficulties introduced by non-local contributions to the source function are dealt with in the solution of the RTE by using a method related to the Feautrier method (A5.51).

The model which has been built by the authors is based on the outline described above. In detail, the atom being treated can contain up to 10 ion stages, each with up to 10 levels. The levels are connected by collisional and radiative transitions, and there are also hydrogen and

helium-like continua with collisional ionisation and recombination. Up to 30 line and another 30 continuum transitions can be dealt with.

Results have been obtained in a fully self consistent manner and work is continuing to establish the feasibility of various approximate methods of solution.

The benchmarks as described above are a first attempt to organise a set of multi-level RT calculations which can answer the needs of researchers into the radiative properties of hot dense matter. The two benchmarks are simple and should be considered a first step toward more exciting tests.

Numerous difficulties, which face those researchers interested in laboratory plasmas, have been ignored. Firstly, there are gradients which are present in most plasmas. The fact that these have been ignored indicates that a RT method which produces a solution to these problems, though accurate, may suffer when gradients are introduced. Secondly, there are the difficulties of time dependence which arise in all dynamic systems. However, dynamic coupling of the RT and rate equations to the hydrodynamic equations is outside the scope of this simple set of problems. Further investigation may be needed to determine whether, in laboratory plasmas, detailed RT is necessary to perform the correct hydrodynamics. It is conceivable that the hydrodynamic history can be obtained by recourse to simple RT models which provide the correct energy transfer while the details of the emission could be reconstructed afterward.

A5.3.4 Integral Transport of Radiation in Dense Plasmas

T D Beynon and A Djaoui (Birmingham)

The simulation of the hydrodynamic and thermodynamic behaviour of a fusion target can be very sensitive to the modelling of radiative phenomena. Energy transfer by photons is generally more important than energy transfer by electrons in the range of temperature and density of interest to fusion.

In Fig A5.18 the ratio of the radiation heat conductivity K_R to the electron heat conductivity K_e, is shown where K_R is calculated from the Rosseland mean free path l_R as

$$K_R = \frac{16\sigma T_e^3}{3} l_R \qquad (1)$$

where σ is the Stefan-Boltzmann constant and T_e is the electron temperature. K_e is adapted from the Spitzer-form and is given by

$$K_e = 1.83 \times 10^{-10} T_e^{5/2} (\log \Lambda)^{-1} Z^{-1} \qquad (2)$$

where Z = 82 is the number of electrons in lead and

$$\Lambda = 1.24 \times 10^7 T_e^{3/2} n_e^{-\frac{1}{2}} Z^{-1}$$

n_e is the electron density.

The modelling of radiation transport in an ICF target is a difficult problem; the presence of shock waves induces high discontinuities in temperature and density, the state of the target varies considerably during the heating, compression and burn phase. Methods based on the diffusion approximation are only applicable if the target is fairly thick to radiation. If the mean free path of radiation is of the order of the mesh size used in the finite difference of the hydrodynamic equations a transport treatment is necessary. In spherical geometry however, even the discrete ordinate code ANISN (A5.52) leads to incorrect results, especially in the central region. A ray-by-ray solution of the radiative transfer equation is presented. This is to be used as a standard calculation with which to compare less accurate but faster calculations.

Assuming that the plasma is a purely absorbing medium, the general form of the integral transport equation for photons of frequency ν emerging from a slab with a thickness Δx, in direction ψ is

$$I_\nu(x,\psi) = \int_0^{\Delta x/\psi} j_\nu(x',\psi) \exp\left[-\alpha_\nu(x')(x-x')\right] dx' + I_\nu(0,\psi) \exp\left[-\int_0^{\Delta x/\psi} \alpha_\nu(x') dx'\right]$$

(3)

where α_ν is the total absorption cross section. If LTE holds we have

$$j_\nu(x',\psi) = \alpha_\nu(x') B_\nu \left[T(x')\right] \qquad (4)$$

where B_ν is the Planckian function. From the solution of Eq 3 the net energy absorption from radiation per unit volume E_R can be calculated as

$$E_R(x) = -\nabla . F_R(x) \qquad (5)$$

where $F_R(x) = 2\pi \int \psi d\psi \int d\nu \; I_\nu \; (x,\psi)$

and the force per unit volume f_R resulting from the absorption of radiation is

$$f_R(x) = \frac{2\pi}{c} \int \psi d\psi \int d\nu \; \alpha_\nu(x) \; I_\nu \; (x,\psi) \qquad (6)$$

Equations 5 and 6 can be coupled to the hydrodynamic equations for a simulation of targets.

For its solution Eq 3 is integrated over discrete frequency intervals $[\nu_g, \nu_{g+1},]$ g = 1, ..., G where G is the number of intervals or groups. The group form of Eq 3 for the group intensity I_g is

$$I_g(\tau_g,\psi) = \int_0^{\tau_g/\psi} \alpha_g(x^1) \; B_g \left[T(x^1)\right] \; e^{-\tau^1} d\tau^1 + I_y(0,\psi) e^{-\tau_g/\psi} \qquad (7)$$

where $d\tau^1 = \alpha_\nu \; (x^1) dx^1$ and B_g is the fraction of the black body spectrum in group g, which is calculated using the tabulated Debye function. The group cross sections α_g are predetermined using a suitable weighting scheme. The ray-by-ray solution of Eq 7 in spherical geometry proceeds in the following way:

(i) define a spherical mesh structure r_k, K = 1,...,N (cf Fig.A5.19) and split the energy domain into G groups.

(ii) divide the sphere into sections using the rays tangent to the mesh boundaries.

(iii) in each section and for each surface choose a set of 1-gaussian weights and discrete directions ψ_1. Follow each ray 1 from the outside to the surface in consideration and continue through to re-intersect the same surface, applying Eq 7 at each boundary interface.

(iv) compute Eq 5 and 6 on each surface, for each angular interval and for each energy group and then sum over angle and energy.

Unlike ANISN the ray-by-ray solution will always lead to the correct value for the angular intensity, but it has no knowledge of particle conservation. On the other hand, as there is more than one set of angular intensity values which satisfy the transport equation, ANISN adjusts the angular intensities in order to achieve particle conservation and in doing so can lead to the wrong angular information.

In Fig A5.20 the heating profiles for an iron target configuration is shown. ANISN predicts the wrong sign in the low temperature (LT) region.

The algorithm is insensitive to the order of the quadrature used. A two point Gauss integration of moments is adequate. It is however very sensitive to the multigroup data used. 'Convergence' seems to be achieved at about 20 energy groups as the differences between the heating profiles are only reduced slightly when doubling the number of groups (cf Fig A5.21).

This is not necessarily true for a target with a different composition. The running time is about 10 times the ANISN running time but the accuracy is much higher.

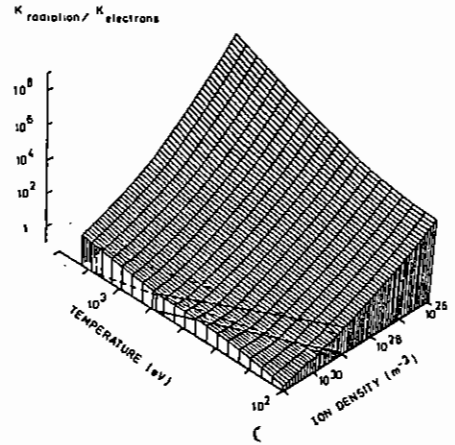

Fig A5.18 $K_{radiation}/K_{electrons}$ for lead (Z = 82)

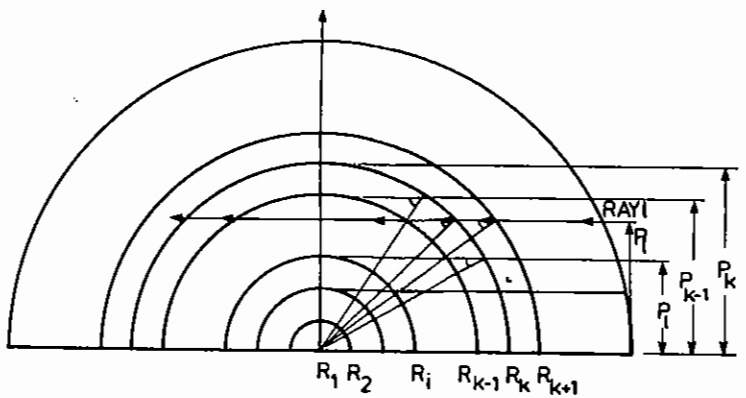

Fig A5.19 Space-angle mesh structure in spherical geometry

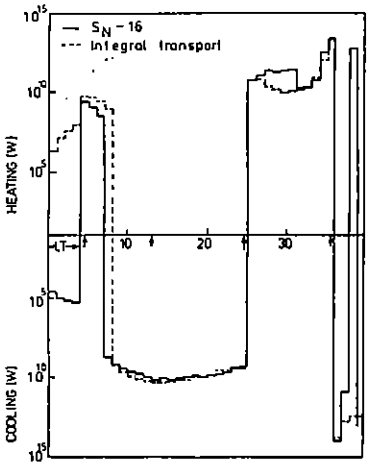

Fig A5.20 Heating profile

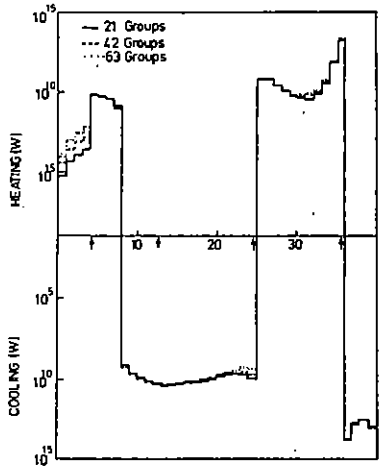

Fig A5.21 Heating profile using integral transport

A5.3.5 Effects of Ion Beam Widths on Rayleigh-Taylor Instabilities

T D Beynon and D P Edwards (Birmingham)

Ion beam spot size has been shown (A5.53) to be an important consideration in the coupling of beam into the target to produce an inward moving pusher. The compression is sensitive to the radial energy deposition profiles and to the effect of the beam missing the target. In the present work we investigate the effect of beam spot size on Rayleigh-Taylor (RT) instability growth at the ablator-pusher interface during implosion and later as the pusher is decelerated by the fuel. According to the classical linear theory (A5.54) the growth of amplitude η is given by

$$\eta = \eta_0 e^{\gamma t} \qquad \gamma = \sqrt{\frac{2\pi}{\lambda}\alpha a} \qquad l \equiv \frac{2\pi r}{\lambda} \tag{1}$$

where η_0 is the initial perturbation which is assumed periodic with wavelength λ, a is the interface acceleration and α is the Atwood number, $\alpha = (\rho_+ - \rho_-)/(\rho_+ + \rho_-)$, ρ_+ and ρ_- being the densities in the two Lagrangian cells either side the interface: l is the harmonic of the perturbation which is likely to be dependent on non-symmetric illumination. The instability growth is calculated using the above linear treatment incorporated in the 1-D hydrodynamics code MEDUSA, modified to include a full radiation treatment and a detailed $d\varepsilon/dx$ description for the plasma.

The standard target design shown in Fig A5.22 is used for the study. The central structure is a 0.8mm DT gas-filled void surrounded by a 0.225mm shell of solid DT and a 0.75mm lead pusher (giving it an aspect ratio of 14, consistent with reasonable RT stability).

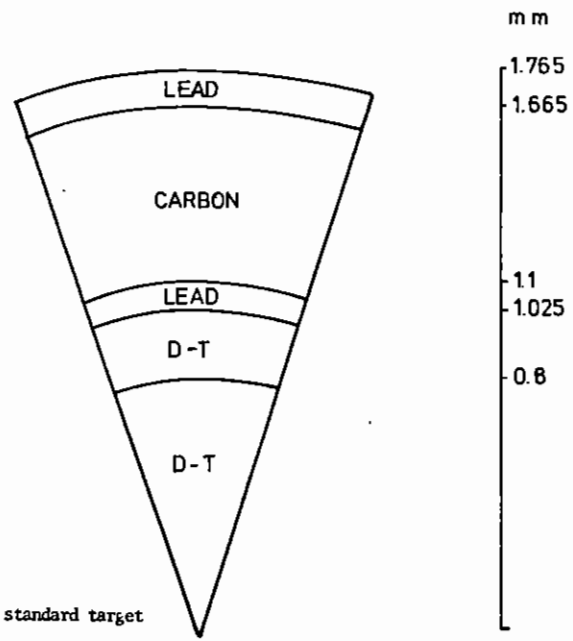

Fig A5.22 The standard target

This in turn is surrounded by 0.565mm of carbon ablator and a 0.1mm lead tamper. This target is not intended to represent an optimised ICF target but is chosen rather to illustrate the beam width effects on RT growth.

The heavy ion beams are assumed to consist of Uranium ions of such energy as to just be able to penetrate the carbon layer (about 15GeV). The focussed beam spot is assumed to have a gaussian shape of the form $\exp(-x^2/2\sigma^2)$, x being measured from the centre of the cylindrical beam. The beam spot size is defined as σ, the standard deviation. The pulse shape of the beam consists of a pre-pulse at 0.5% of the main power pulse of 10^{15} W. The pre-pulse lasts until either the shock wave has reached the inner edge of the solid DT or 20ns has elapsed.

Fig A5.23 shows the time-averaged energy deposition profiles for the different beam spot sizes. At the target surface the deposition is greater for the wider ($\sigma \sim 1$, $\sigma \sim 2$mm) beams compared with the narrow ($\sigma \sim 0$) beam. This is due mainly to ions entering the target obliquely. Further into the target the deposition profiles of the wider beams peak and fall whilst that of the narrow beam continues to rise. This is because only ions in the centre of the wider beams contribute to energy deposition in this region compared to all of the ions in the narrow beam.

For the wider beams total energy deposition takes place in the carbon layer, whereas the deposition profile for the narrow beam peaks at the end of the ion range and energy is deposited inside the lead pusher itself. This high energy deposition and beam 'tunnelling' at the ablator-pusher interface has important consequences for instability.

The perturbation amplitudes were calculated for these different beam spot sizes and are shown in Fig A5.24 as a function of time.

The initial displacement was taken as 5×10^{-8}m and the largest value of the harmonic ($l = 20$) consistent with the linear treatment was used.

The use of a narrow beam as a driver results in maximum instability growth. Greater beam coupling to the target and higher energy deposition density in the carbon layer just before the pusher results in a rapid implosion and high interface acceleration. This also results in a reduction in the carbon density and an increase in the Atwood number during the prepulse period. However as the beam switches to full power substantial beam tunnelling through the interface takes place so reducing the density gradient and Atwood number during the period of maximum growth (see Fig A5.25).

Energy deposition in the pusher just after the power switch also accounts for the small plateau of 'stability' in the amplitude growth. The temperature and internal pressure of the pusher rise while the density on the carbon side of the interface is falling. This effectively causes a deceleration of the interface for a short period,

and hence stability. As the beam deposits more energy in the carbon and ablation increases, the inward acceleration is resumed and there is a sharp instablity growth until the interface is again decelerated due to the rebounding shock.

In the case of the medium width beam the flatter energy deposition profile results in a less rapid interface acceleration. The Atwood number however is still considerably reduced during the period of maximum growth. These two factors result in a small instability amplitude.

In the wide beam case the interface acceleration is reduced even more. However, since the total energy deposition is in the carbon layer there is a small drop in the Atwood number as the beam switches to full power (Fig A5.25). The density gradient at the materials interface is thus left substantially intact and instability growth is increased.

The instability of the fuel-pusher interface takes place during the final stages of the implosion whilst the pusher is being decelerated by the fuel. To achieve reasonable gains the standard target had to be tailored to suit the beam spot size of the driver. This optimisation is performed by reducing the depth of the carbon layer for use with the intermediate beam so that the peak in the energy deposition occurs just before the pusher, the beam energy remaining constant thoughout. In this way gains of about 10 were achieved and the modified targets were then used with their respective beam spot sizes to investigate the fuel-pusher interface instability.

Perturbations grow initially as described by the linear theory. However, for $\eta > \lambda/2\pi$ Eqn 1 is no longer valid. Simulations with 2D-codes (A5.55) show that the perturbations continue to grow as spikes with the maximal pusher velocity. Fusion is assumed to cease when the spike reaches the target centre. This is known as the free-fall model.

In Fig A5.26 is plotted the fuel radius (solid line) for the standard target driven by the narrow beam. The free fall line (dashed) and the

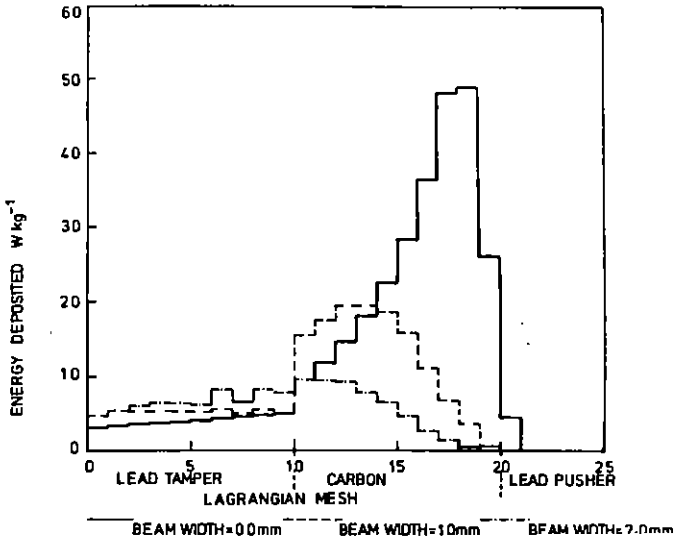

Fig A5.23 Radial energy deposition profiles. The beam is travelling left to right

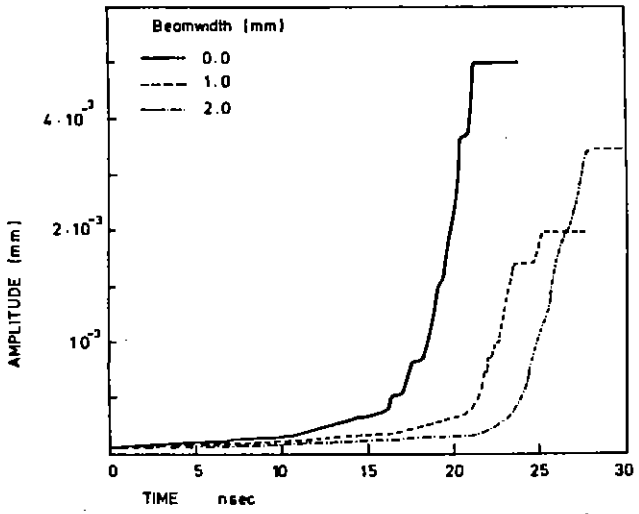

Fig A5.24 Rayleigh-Taylor instability amplitude as a function of time

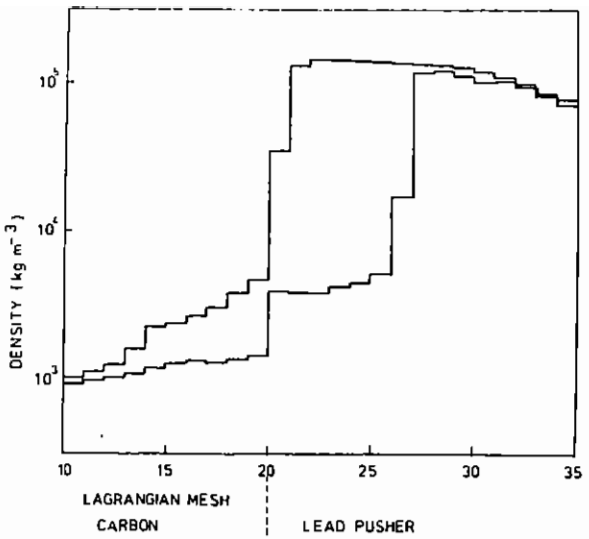

Fig A5.25 Density profile in region of ablator-pusher interface

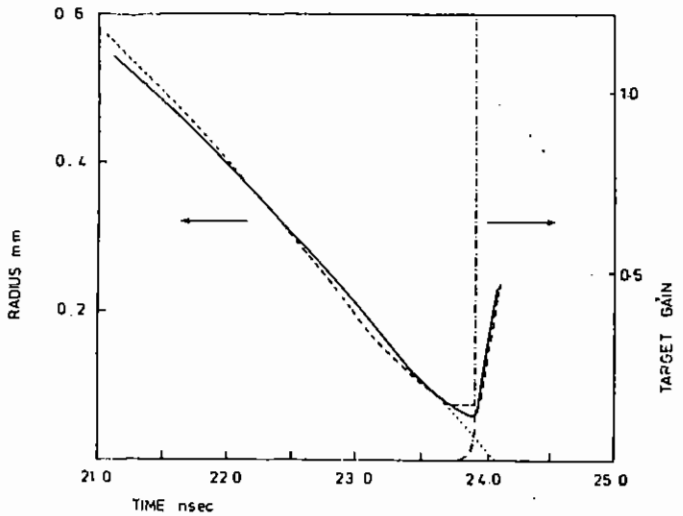

Fig A5.26 Radius of fuel boundary (solid line) and target gain (-.-.-.-.) as a function of time for the standard target and narrow beam. The dotted line represents free fall. The dashed line gives the radius of the fuel boundary for the modified standard target

fraction of fusion yield (dash-dotted) are also shown. Similar results for the modified target driven by the narrow beam are also shown.

In both cases it is seen that fusion has 'taken off' before the spike reaches the target centre. In this case the target is assumed to be successful.

A5.3.6 Fission Fragmentation Effects on Heavy Ion Beam Inertial Fusion Targets

T D Beynon and E H Smith (Birmingham University)

The possibility that intense beams of ions could be used to heat and compress targets containing deuterium-tritium mixtures to produce thermonuclear ignition has led to an increased interest in the theory of the interaction of ions in hot, dense plasma. Of particular importance for the design of such targets is the modelling of the slowing down power for ions of energy E, $S(E) = -dE/dx$, in order to compute the energy deposited by the beam. An important non-plasma effect which may contribute significantly to the energy deposition process, and hence to the details of the target design, is due to the fissioning of the incident ion with a nucleus in the target particularly if the incident beam is composed of heavy ions.

An ideal way to examine the consequences of fission is to consider a beam of uranium ions (^{238}U) at a characteristic energy of 10 GeV on targets with various outer ablative regions such as hydrogen, carbon or gold. In each case the interaction energies in the centre of mass (CM) coordinate system are 42 MeV, 480 MeV and 4.5 GeV, respectively. At 40-50 MeV the (p,^{238}U) fission reaction is well described by the rotating liquid drop model (A5.56) whilst the heavy ion fission for (^{12}C, ^{238}U) and (^{197}Au, ^{238}U) is reasonably well understood, experimentally at least.

Two approximations are made for our present study. Firstly, the fission cross section, σ_f, can be approximated by the geometric form

$$\sigma_f = \pi(1.07 \times 10^{-15}[A_1^{1/3} + A_2^{1/3}])^2 \ m^2$$

where A_1 and A_2 refer respectively to the heavy ion and target nucleus mass numbers. This form of σ_f agrees well with measured data for those nuclei with significant fission cross sections. Secondly, the fission fragments are assumed to be emitted with zero transverse momentum. Measurements of fission fragment angular distributions for both light ion and heavy ion induced reactions indicate this to be an acceptable approximation.

We consider the reaction $A_1(E_1) + A_2(0) \rightarrow A_3(E_3) + A_4(E_4)$ where subscripts 1, 2 refer respectively to incident and target particles, 3, 4 refer to fission fragements. A_n is a mass number and E_n is a kinetic energy measured in the laboratory (L) system. Simple dynamics yields

$$E_{3(4)} = A_1 E_1 [A_{3(4)} - A_{4(3)}]/[A_3 + A_4]^2 + A_{4(3)}E_T/[A_3 + A_4]$$
$$-(+)2[A_1A_3A_4E_1([A_3+A_4]E_T-A_1E_1)]^{\frac{1}{2}}/[A_3 + A_4]^2 \qquad (1)$$

where A_4 is defined to be that fragment which, in the CM system, moves in the direction of the incident beam: $E_2 = \epsilon_F + E_1$ where ϵ_F is energy released in the fission reaction and $E_3 + E_4 = E_T$. In all subsequent calculations $\epsilon_F = 200$ MeV.

At these large values of excitation energies nuclear shell effects are negligible in the sense that equipartition of mass and charge may be assumed in the fission fragments. Thus putting $A_2 = A_3$ in (1) produces the simplified relationship

$$E_{3(4)} = E_T/2 -(+) [A_1E_1(2A_3E_T - A_1E_1)]^{\frac{1}{2}}/2A_3 \qquad (2)$$

We see that the incident ion beam, undergoing fission as it slows down in the target plasma, produces two fission fragments of equal mass and charge but different energies. Generally these fragments will be moving in the same direction as the beam in the L system but with different (Z^2/E) signatures and hence different ranges. As the

primary beam slows down an energy $E_1 = [A_3(A_1-A_3)]\epsilon_F \equiv E_c$ is reached for which $E_3 = 0$. For $E_1 < E_c$ this fission fragment (A_3) now moves in the opposite direction to the primary beam to further enhance the already heated region of the plasma. Note that for $A_1 >> A_3$, $E_c \rightarrow 0$ whereas $E_c \rightarrow \infty$ for the case of $A_1 = A_3$, eg. uranium ions incident on a uranium ablator region.

Thus, as a parallel beam of ions traverses the plasma we shall have two heating mechanisms, one due to the primary beam with an associated slowing down power of $S_\rho(E)$, and another due to the slowing down of the fission fragments.

To explore these effects in a target configuration a spherical single shell target of outer radius 2.23mm has been considered. The target has a LiD ablator region of thickness 1.13 kg m^{-2} covering a Pb region of thickness 11.3 kg m^{-2} and a D-T zone of thickness 4.48×10^{-2} kg m^{-2}. The central zone has a D-T gas fill of density 2.24×10^{-2} kg m^{-3}. The target has been analysed with a heavy ion version of the one-dimensional hydrodynamics code MEDUSA (A5.57) which has a corrected Thomas-Fermi equation of state (A5.58) and a complete radiation package which handles high and low Z materials (A5.56). The target is uniformly irradiated with 10 GeV U^{+1} ion beams where each beam has a cylindrical geometry with a particle intensity distributed radially as $\exp(-y^2/2\Delta^2)$ where y is measured form the centre of the beam, orthogonally to its direction of propagation. The beam spot size is defined as Δ. The pulse shape of the incident ion beam consists of a prepulse followed by a main pulse, both at constant power levels wit the main pulse either at 2.5×10^{14}W or 1.0×10^{15}W. The prepulse power is set to 0.5% of the main pulse.

Fig A5.27 shows the maximum value of the density-radius product, ρr, attained by the D-T as a function of power level and beam spot size, both with and without fission fragmentation included. The dependence of target performance on Δ and power level has been discussed in detail elsewhere (A5.53) and is a complicated function of the effects of ion range shortening, thermal conductivity and energy deposition distributions at various beam widths. The preheating of the inner regions of the target by fission fragmentation at each of the two

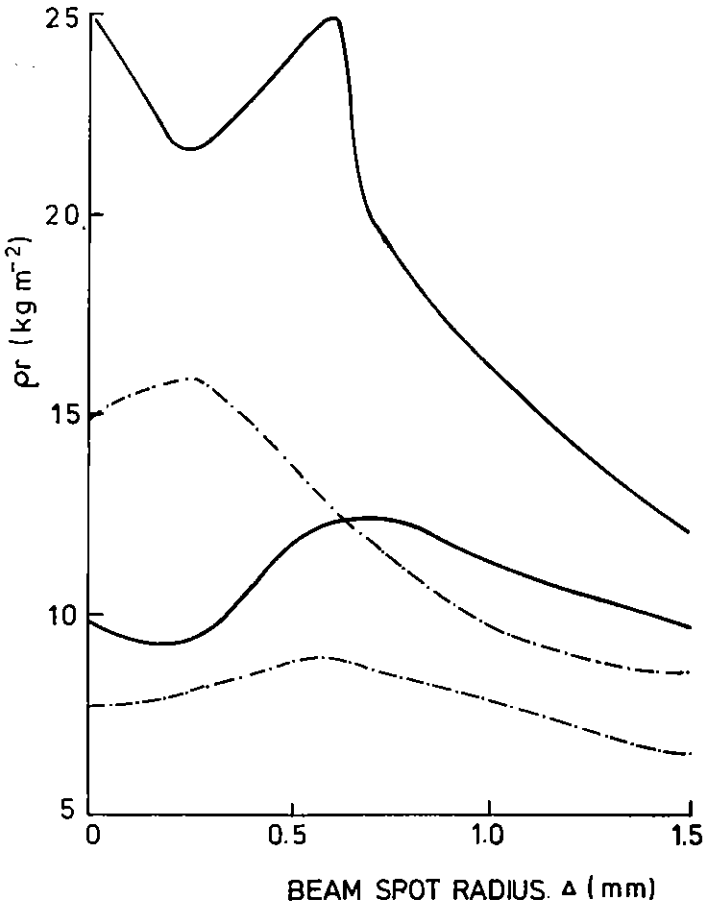

Fig. A5.27 Maximum ρr values attained by D-T at various beam widths Δ. The solid curves are avaluated at an incident power of 1.0×10^{15}W, and the dashed curves at 2.5×10^{14}W. For each pair the upper curve has been obtained with no fission fragmentation effects included.

power levels is seen to have a deleterious effect on the target performance, reducing the ρr-values by about a factor 2. The effect, at a given beam size, is larger at the higher power level when the preheat is larger in comparison with the Fermi energy of the cold material. At a given power level, the effect is lessened with increasing beam size as a larger fraction of the primary beam trajectories does not point towards the central region of the target. This suggests that the use of a hollow beam could provide a method of preheat reduction (A5.59). Generally, the condition $\rho r \geq 20$–30 kg m^{-2} is required for a minimally-acceptable target. In the case considered here fission effects make that condition attainable. One concludes that considerable caution should be exercised in designing fusion targets driven by heavy ions with significant σ_f-values unless a full analysis of the fission effects is included.

References

A5.1 E M Epperlein, J Phys D: Appl Phys, 17, 1823 (1984)

A5.2 E M Epperlein and M G Haines, Plasma Transport Coefficients in a Magnetic Field by Direct Numerical Solution of the Fokker-Planck Equation, (submitted to Phys Fluids) (1985)

A5.3 S I Braginskii, Sov Phys JETP, 6, 358 (1958)

A5.4 T Mochizuki, T Yabe, K Mima, K Yoshikawa, H Azechi, A Kikuchi and C Yamanaka, Jpn J Appl Phys, 19, L645 (1980)

A5.5 O Willi, P T Rumsby, C Hooker, A Raven and Z Q Lin, Opt Comm, 41, 110 (1982)

A5.6 G Thiell and B Meyer, Laser and Particle Beams, 3, 51 (1985)

A5.7 E S Weibel, Phys Rev Lett, 2, 83 (1959)

A5.8 E M Epperlein, PhD Thesis, Imperial College London (1984)

A5.9 E M Epperlein, RAL Report, RL-84-049 (1984)

A5.10 A Comparison of the Kinetic and 2 Electron Fluid Models of the Collisional Weibel Instability in Laser-Plasma (submitted to Plasma Phys Controlled Fusion) (1985)

A5.11 B D Fried, Phys Fluids, 2, 337 (1959)

A5.12 A Nishiguchi et al, Phys Rev Lett, 53, 262 (1984)

A5.13 T Tajima and J M Dawson, Phys Rev Lett, 43, 267 (1979)

A5.14 M N Rosenbluth and C S Liu, Phys Rev Lett, 29, 701 (1982)

A5.15 C M Tang, P Sprangle, R N Sudan, Appl Phys Lett, 45, 375 (1984)

A5.16 J Dawson, Phys Rev, 113, 383 (1959)

A5.17 R G Evans, RAL Report RAL-84-086 (1984)

A5.18 R D Ruth and A W Chao, Laser Acceleration of Particles, Los Alamos AIP Conference Proceedings No 91 New York (1982)

A5.19 P Chen, J M Dawson, R W Huff and T Katsouleas, SLAC Report SLAC-PUB-3487, submitted to Phys Rev Lett (1984)

A5.20 R D Ruth, A W Chao, P L Morton and P B Wilson, Stanford University Report SLAC-PUB-3374, submitted to Particle Accelerators (1984)

A5.21 P K Kaw, A T Lin and J M Dawson, Phys Fluids, 16, 1967 (1973)

A5.22 H C Barr and F F Chen, Anomalous Absorption Conference, Santa Fe, NM, USA (1982)

A5.23 H C Barr and G A Gardner, Proc International Conference on Plasma Physics, Lausanne, 2, 265 (1984)

A5.24 A B Langdon, Workshop report on The Flux-Limiter and Heat Flow Instabilities in Laser-Fusion Plasmas, Centre European de Calcul Atomique et Moleculaire (1981)

A5.25 T H Kho, Relaxation of a System of Charged Particles, Phys Rev A (in press)

A5.26 A R Bell, R G Evans and D J Nicholas, Phys Rev Lett, 46, 243 (1981)

A5.27 J P Matte and J Virmont, Phys Rev Lett, 49, 1936 (1982)

A5.28 D S Kershaw, J Comp Phys, 26, 43 (1978)

A5.29 J S Chang and G Cooper, J Comp Phys, 6, 1 (1970)

A5.30 J Matte and J Virmont, Electronic Heat Transport Down Steep Temperature Gradients, CECAM Report (1983)

A5.31 A Dolinsky, Phys Fluids, 436 (1965)

A5.32 W M Manheimer, D G Colombant and J H Gardner, Phys Fluids, 25, 1644 (1982)

A5.33 A R Bell, Phys Fluids (in press) (1985)

A5.34 D A Tidman and R A Shanny, Phys Fluids, 17, 1207 (1974)

A5.35 M Ogasawara, A Hirao and H Ohkubo, J Phys Soc Japan, 49, 322 (1980)

A5.36 G J Pert, J Comp Phys, 49, 1 (1983)

A5.37 G J Pert, Central Laser Facility Annual Report, RL-83-043, 86 (1983)

A5.38 A V Vinogradov, I I Sobelman and E A Yukov, Sov J Quantum Electron, 5, 59 (1975)

A5.39 B A Norton and N J Peacock, J Phys B, 8, 989 (1975)

A5.40 P Hagelstein, The Physics of Short Wavelength Laser Design, Lawrence Livermore National Laboratory, unpublished

A5.41 J P Apruzese, J Davis and K G Whitney, J Appl Phys, 33, 4020 (1982)

A5.42 W E Alley, G Chapline, P Kunasz and J C Weisheit, JQSRT, 27, 257 (1982)

A5.43 J G Lunney, R E Corbett, M J Lamb, C L S Lewis, P McCavana, L D Shorrock, S J Rose and F Pinzhong, Opt Comm, 50, 367 (1984)

A5.44 I P Grant, B J McKenzie, P H Norrington, D F Mayers and N C Pyper, Computer Phys Comm, 21, 207 (1980)

A5.45 B J McKenzie, I P Grant and P H Norrington, Computer Phys Comm, 21, 233 (1980)

A5.46 M H Key, C L S Lewis, M J Lamb, Opt Comm, 28, 331 (1979)

A5.47 D Jacoby, G J Pert, L D Shorrock, G J Tallents, J Phys B, 15, 3557 (1982)

A5.48 D L Matthews et al, Phys Rev Lett, 54, 110 (1985)

A5.49 D Mihalas, 'Stellar Atmospheres', publ W H Freeman and Co. New York (1978)

A5.50 S R Drayson, JQSRT, 16, 611 (1976)

A5.51 D Mihalas, Stellar Atmospheres, Chapter 6 (Freeman, New York) (1978)

A5.52 W W Engles (Jnr), Computer Technology Centre, Union Carbide Corp Report No K-1693 (1967)

A5.53 T D Beynon and E H Smith, Proc 1984 International Symposium on Heavy Ion Accelerators and their Applications to Inertial Fusion, 537, Institute of Nuclear Study, Univ of Tokyo (1984)

A5.54 G Taylor, Proc Roy Soc, A207, 192 (1950)

A5.55 J R Freeman, M J Clauser and S L Thompson, Nuclear Fusion, 17, 223 (1977)

A5.56 T D Beynon and E H Smith, Proc 2nd International Conference on Radiative Properties of Hot Dense Plasma, Sarasota, Florida (1983)

A5.57 J P Christiansen, D E T F Ashby and K V Roberts, Comp Phys Comm, 7, 271 (1974)

A5.58 A R Bell, Rutherford Laboratory Report No RL-80-091 (1980)

A5.59 P Krejcik, Proc Symposium on Accelerator Aspects of Heavy Ion Fusion, GSI Darmstadt Report No GSI-82-8, 255 (1982)

A6 GLASS LASER FACILITY OPERATIONS AND DEVELOPMENT

Editor J E Boon

A6 GLASS LASER FACILITY OPERATIONS AND DEVELOPMENT

A6.1 INTRODUCTION

P T Rumsby (RAL)

Operation of the glass laser system over the past year has once again been reliable and intensive with over 1800 full power shots being delivered to 2 target irradiation chambers. Many minor improvements have been made to the laser system during the year to improve operational reliability and efficiency, to extend the range of pulse lengths and beam options available to experimenters and to improve beam quality. Diagnostic instrumentation development has been active and a major impact has been made on the X-ray laser programme at the CLF with the development of novel high quality line focus optics. All these developments are discussed below.

Glass laser facility development has completed one more stage of the Phase I upgrade programme approved in 1973. The completion and commissioning of the new 12 beam compression area (Target Area West) in August 1984 and the transfer of compression experiments from the old 6 beam area (TA1) has led to major improvements in irradiation uniformity and quality of implosions. Laser beams arriving at this area have been improved significantly in quality with the installation of vacuum spatial filters at the output of the laser system. Design work on the new multi purpose target irradiation facility (Target Area East) has now been completed and installation is proceeding rapidly.

A6.2 GLASS LASER OPERATIONS

N Allen, C Danson, C Edwards, B Espey, D Rodkiss, P Rumsby, R Wellstood and R Wyatt (RAL)

Vulcan has performed with outstanding reliability over a period which has seen the closure of the 6 beam compression area (TA1) in May and the commissioning and operation of the new 12 beam compression facility (TAW) in June. Only 44 target shots were fired into TA1 before it shut down while 660 full shots on target have been delivered to the new TAW since its start up. In addition over 1000 target shots have been delivered to the 2 beam target area (TA2) during the year. Of the 52 weeks in the year 35 were used for target area shots and the remainder for laser maintenance and development.

Much time has been devoted to both on and off line developments of all aspects of the laser system. Major improvements to short pulse oscillator reliability have been achieved by using a smaller diameter YLF rod to reduce pumping requirements and by installing a new stabilised long pulse (ms) power supply from JK lasers. Reproducibility of selection of a single pulse from the mode locked train has been considerably improved by fitting new drive electronics from Kentech Instruments while installation of a variable length charged line to the silicon switched long pulse selector system now means that the pulses length can be readily varied from shot to shot from 0.5 to 5ns by the laser operator. In addition the full 20ns half width Q-switched pulse from the long pulse oscillator can now be switched to bypass the switch out Pockel cells. Two sets of experiments have already been performed with 20ns pulses on target. Considerable success has been achieved in developing a mode locked oscillator containing both an YLF and a YAG rod to give synchronous pulses at 1.052 and 1.064 μm. This novel oscillator will be used for scheduled laser beat wave experiments. A novel pulse stacker arrangement has been built which enables 4 mode locked pulses of equal amplitude and separated by 1ns to be produced and amplified by the laser for diagnostic purposes.

Beam quality has been improved by two major changes to the system. The method used to cool the 108mm diameter disc amplifiers has been dramatically improved with the result that no significant degradation in beam quality can be seen even when a 20 minute shot rate is sustained. In the 6 beam system vacuum spatial filters have been installed at the end of the rod system and also at the output. These filter the beams significantly and also partially relay the beam towards the target plane.

Most of the above items of development are discussed in detail in section A6.3.

The versatility and flexibility of the VULCAN glass laser system was well demonstrated in the year by the rapidity with which a highly non standard target irradiation geometry was set up. The six beam output disc amplifier array was fed with a mixture of short (70ps) and long (4ns) pulses derived from the independent rod amplifier chains and synchronized oscillators. With this system experiments were conducted in which some beams imploded D T filled shells with short pulses to produce α particles to probe foils accelerated with long pulse beams.

A6.3 GLASS LASER DEVELOPMENT

A6.3.1 Oscillator Development

C Danson, C Edwards, P Rumsby (RAL)

During the past twelve months oscillator development has been aimed primarily at improving both the long and short term stability of the on-line equipment. This has meant the replacement of most of the electronics associated with the mode-locked oscillator, which included the r.f. amplifier which drives the mode-locking crystal and the high voltage switching electronics which provide Q-switching electronics to both cavities.

One severe problem has been the limited lifetime of the flashlamps in the short pulse oscillator. Typical lamp lifetimes of less than 10,000 shots had been experienced which was approximately two operational weeks. During this period the stability of the oscillator would steadily decline. The flashlamp manufactures (Noblelight Ltd) embarked on a series of electrode modifications to the lamps which were then tested in the on-line oscillator. Significant improvements in flashlamp lifetime were measured with more than 40,000 shots being achieved with the final design. This number of shots was still well below the 3×10^6 quoted by J.K.Lasers with their AML systems. Consequently it was decided to replace the prototype power supply

system in use with a new J.K.Lasers AML power supply. This has facilities to shape the current pulse to provide optimum pumping. In conjunction with this the ¼" diameter YLF rod in the short pulse cavity was replaced by a new 5mm diameter rod. The smaller rod requires lower pumping and therefore extends lamp lifetime. When these modifications were completed very stable short pulse operation was achieved. Although only recently completed initial results indicate that lamp lifetime will not be a serious problem in the future.

A major experimental activity in the coming year will be the investigation of longitudinal waves driven in a low density plasma by the beating of two e.m. waves from the laser system. To achieve this the glass laser will be reconfigured to amplify pulses of 2 wavelengths, 1.064 and 1.052μm. To drive this system a new mode locked oscillator is being developed that has both YLF and YAG rods in the cavity to produces 100ps pulses at both wavelengths. Equipment loaned by J K Lasers has allowed such a double wavelength oscillator to be constructed. Preliminary results indicate that such a double wavelength output oscillator can be run with sufficient stability.

A6.3.2 Pulse Length Improvements

(a) Variable Long Pulse

One of the constraints in the scheduling of experiments has been that both target areas have been required to operate with the same long pulse length. This was because the high voltage pulse-forming line to the Austen switch which set the pulse length could only be changed on a daily basis. Kentech Ltd have now designed and built a variable length pulse-forming line which allows the pulse duration to be changed from shot to shot (Ref A6.1). The device consists of a series of conductive inserts set in a vertically mounted PTFE tube. Each insert contains a magnet which can be raised to make contact with a charging resistor by energising coils set on the outside of the tube. The pulse length is determined by the number of inserts raised. At present the device is operated manually but it is planned to modify the control electronics to operate via the 4080 computer. Fig A6.1 shows the pulse widths available.

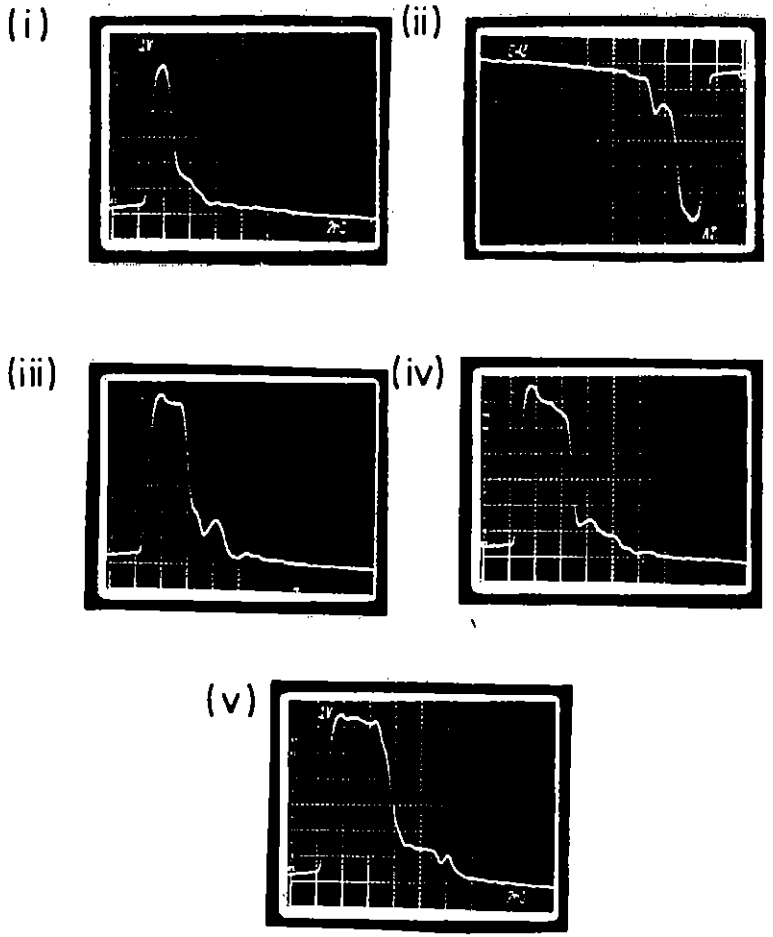

THE RANGE OF PULSEWIDTHS AVAILABLE USING THE KENTECH HIGH VOLTAGE VARIABLE LENGTH STUB.

(i) Kentech control on position 3ie: 3stub lengths raised ≃ 1·2ns (detector limit) (ii) Position 4 (ii)Position 5 (iv) Position 6 (v) Position 7

FIG. A6.1

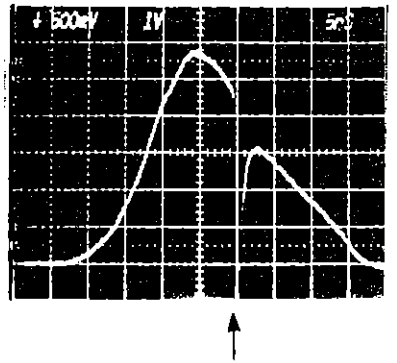

Probe pulse Superimposed on long pulse signal

THE PULSE GENERATED FOR THE COLLISIONLESS SHOCK EXPERIMENT

FIG.A6.2

(b) 20ns pulse generation

The "Collisionless shock" experiment required the full width of the long-pulse Q-switched envelope to be propagated. A pair of remotely insertable mirrors have now been installed so that the long pulse oscillator output can bypass the switchout Pockels Cells. The optical pulse propagated is slightly modified by an isolation Pockels cell, situated in the laser rod chain, which has a gate width of 25ns. The pulse generated for the experiment is shown in Fig A6.2. This 20 ns pulse option is now available for all experiments.

(c) Pulse stacker

A high energy multi-pulse probe beam was required during the year for the Z-pinch experiment to investigate ion-acoustic turbulence in low-density plasmas. This improvement would allow coarse time resolution to be achieved on a single shot and would also increase the rate of data aquisition. The requirements were for four 100ps pulses to be generated separated by 1ns and each containing at least 10J. An etalon device would be

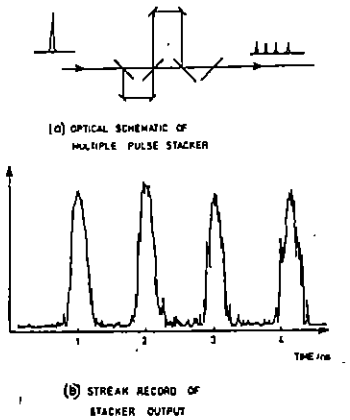

Fig A6.3

unsuitable for this application because of the high efficiency and pulse to pulse uniformity which was needed for the experiment. The final design of the splitter system used (Ref A6.2) is shown in Fig A6.3(a). The only energy loss in the system occurs at the third splitter making the device 50% efficient. The compensator plate was used to ease alignment in preventing lateral shear of the output when placed in the beam line. The whole splitter device is mounted on a base plate and can be located in the short pulse beam line on a kinematic mount making changes from single to pulse operation simple. A streak record of the splitter output is shown in Fig A6.3(b).

The device with simple modifications can be made available with various inter-pulse spacings, limited only by available space, and can also be modified to provide eight pulses relatively easily.

A6.3.3 ϕ108 Disc Amplifier Cooling

J Boon, C Danson, M Mead (RAL)

The design of the ϕ108 disc amplifiers in use at present in the Vulcan laser system are based on the original Lawrence Livermore B75 disc amplifier technology released in 1975. The original amplifiers were designed and constructed by I.L.C., subsequent amplifiers have been constructed in this country, but have been unchanged to maintain interchangability of components.

Users of the facility have recently been pressing for an increased repetition rate of full beam shots, and at the same time expressing concern regarding beam quality, especially when comparing the quality of shots early in the day to shots after long periods of operation. From the information originally given by Lawrence Livermore, the maximum recommended repetition rate was every 60 minutes but even at this rate of operation there, appeared to be some long term thermal effect on beam quality.

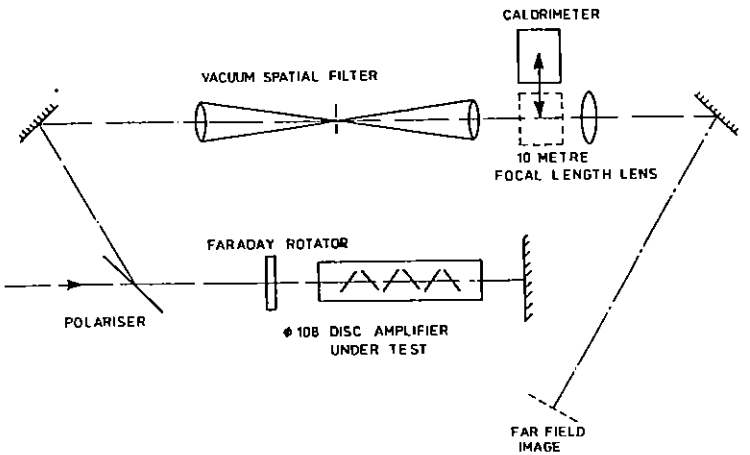

Fig A6.4 Equipment arrangement for investigating the thermal effects on beam quality in ϕ108 disc amplifiers.

To investigate these thermal effects on beam quality, a ϕ108 disc amplifier was set up as shown in Fig A6.4, such that a probe beam from the rod amplifier chain could be double passed in the disc amplifier, then passed through a vacuum spatial filter with a pin hole, and the total emerging beam pulse energy measured with a calorimeter.

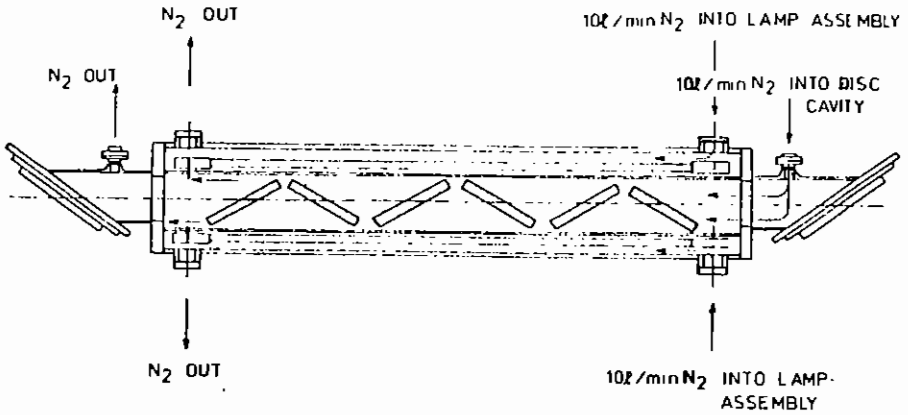

Fig A6.5 Existing Ø108 disc amplifier system.

A lens was also included to enable a far field image to be obtained. Two sets of measurements were taken using an unmodified ϕ108 amplifier with a nitrogen gas system as shown in Fig A6.5.

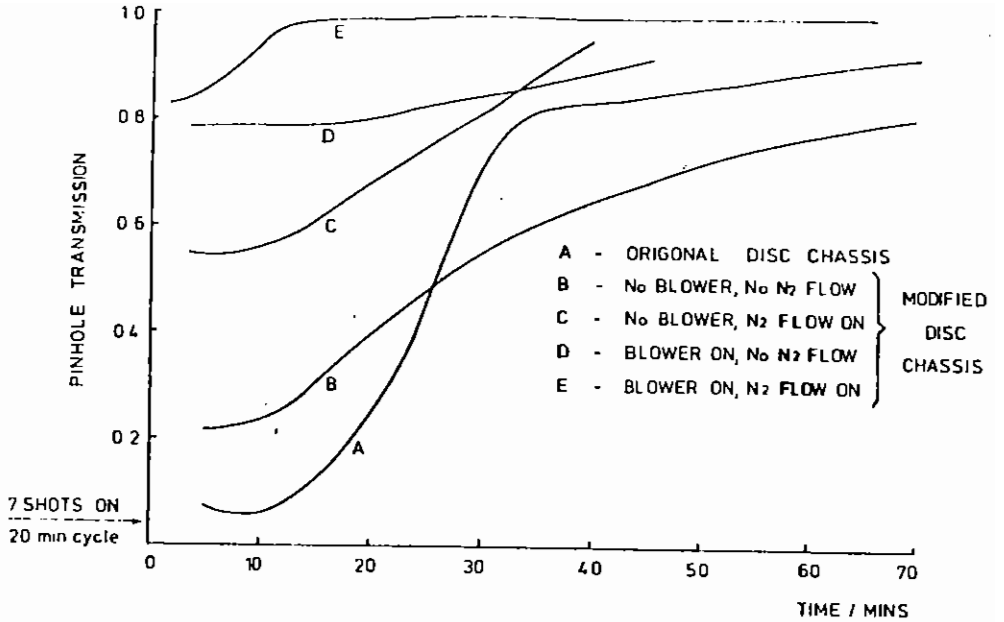

Fig A6.6 Results of transmission tests after varying the thermal conditions in a Ø108 disc amplifier.

Firstly the test beam was passed through the system before the amplifier lamps had been fired to establish the normal pinhole transmission. The amplifier lamps were than fired at 20 minute intervals, in the first test four times and in the second 6 times. Between firing the amplifier lamps, measurements of the probe beam transmission through the pinhole were taken, the results being plotted in Fig A6.6.

These measurements demonstrate conclusively how the thermal characteristics of the original ϕ108 amplifier caused beam distortions unless sufficient time was allowed between shots, and that if a high repetition rate was continued the distortion increased. This meant that unless a radical increase in amplifier cooling could be accomplished, the original shot rate of once per hour would have to be

followed. The existing ϕ108 amplifier gas system, Figure A6.5 besides providing cooling, preasurised the amplifier to resist entry of dirt and contaminents, and excluded oxygen from the system, which are all important factors in operation.

Measurements carried out during the testing of the new ϕ150 amplifier (see Section A6.3.4) showed that the majority of the thermal energy after an amplifier shot was retained in the flash lamps, the flash lamp reflectors and the disc shields, and that these components should be efficienctly cooled immediately after a shot. The amount of nitrogen being used at present only created a laminar flow of gas around these components, and to provide sufficient gas to increase the Reynolds number and achieve turbulence for efficient cooling was not economically possible. Also the nitrogen supplied to the disc cavity, whilst cooling the face of the first disc, formed a laminar flow in the clearance between the disc holders and the disc shield tubes, the hot gas in between the discs being hardly disturbed.

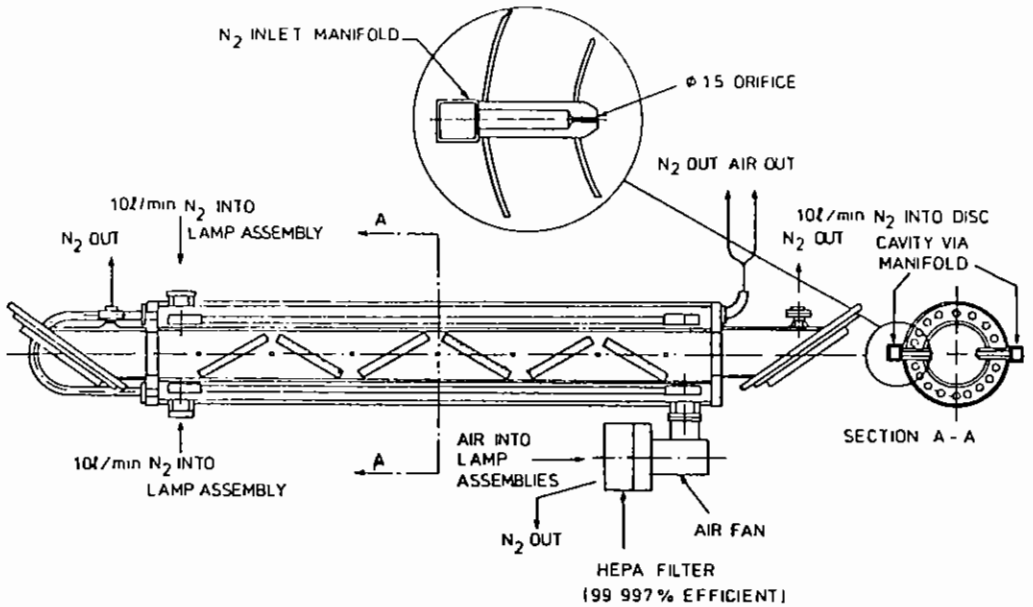

Fig A6.7 New arrangement of gas and air flow for cooling Ø108 disc amplifier.

The new ϕ108 amplifier cooling system is as shown in Fig A6.7. The nitrogen is fed into the disc cavity by way of two manifolds running the length of the amplifier and attached to the disc support rails.

The rails are drilled to create small orifices which jet the gas into the dead spaces between the discs causing turbulence, and the gas then exits from the amplifier at both ends. This has advantage of giving even cooling over the whole length of the amplifier, and encouraging any debris to be swept to the ends away from the disc surfaces.

Additionally a high efficiency air fan is fitted to blow air into one lamp assembly, the air being drawn from the laser clean room which has humidity and temperature control, via a 99.997% HEPA filter. The two lamp assemblies are coupled together at the opposite end with two pipes, and the air is freely discharged from the other end of the lamp

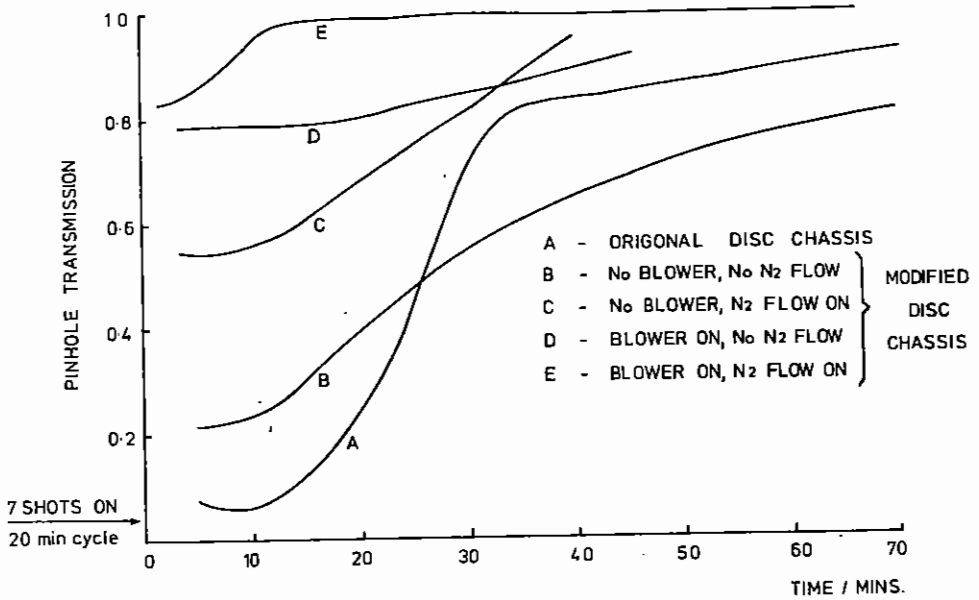

Fig A6.8 Results of transmission tests carried out on the modified Ø108 disc amplifier.

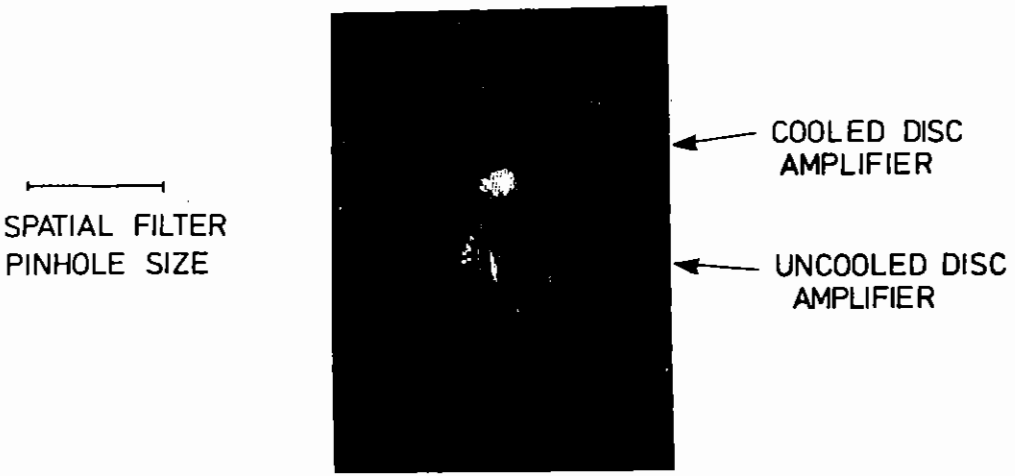

FIG A6.9 FAR FIELD IMAGES RECORDED 30 mins. AFTER 7 SHOTS FIRED ON A 20min CYCLE.

assembly. Nitrogen is fed into the lamp assemblies at the coupled ends to achieve efficient oxygen purging.

In operating the amplifier, all nitrogen supplies are stopped one minute before a shot. Immediately following a shot, the fan and all the nitrogen supplies are turned on, the fan being turned off after 10 minutes to allow the nitrogen to purge the system of oxygen before the next shot.

The modified amplifier was then installed in the apparatus described in Fig A6.4 and similar measurements of probe beam transmission through a pinhole with varying cooling parameters were taken after the amplifier had been fired seven times on a 20 minute cycle. These results are shown in Fig A6.8. The difference between curves A and B can only be due to the static mechanical modifications.

These results clearly show that both the modifications to the disc cavity cooling, and the lamp assembly cooling are necessary and complimentary, and that a 20 minute shot rate may now be maintained without beam distortion. Fig A6.9 shows a far field image recorded 30 mins. after the 7 shots fired on a 20 min. cycle which also confirms these results. All the ϕ108 disc amplifiers, and subsequent designs of ϕ150 and ϕ208 amplifiers will have these features incorporated.

A6.3.4 Design and Performance of a ϕ150mm Neodymium Glass Box Amplifier

I Ross, J Boon, E Hodgson, M Mead (RAL)

Introduction

Upgrade plans for the VULCAN laser require either increasing the number of beams or increasing the aperture of each beam; they require increased energy in the back lighting beam preferably in a single beam, and they require a high quality high energy large aperture beam for single beam experiments. From these requirements comes the need for a larger aperture glass disc amplifier. Since the first stage upgrade involves a doubling of the laser energy (requiring a doubling

of the backlighting energy) an amplifier with twice the energy capability of our existing ϕ 108 mm diameter amplifier is required. Since also the energy limit of an amplifier is restricted by damage to a particular energy per unit area, the area must increase in proportion to the energy requirement and our new amplifier must then have twice the area of the existing amplifiers in order to be capable of giving twice the energy. A ϕ150mm diameter clear aperture was chosen as it is close to a factor of two increase in area and matches that of one of the LLNL amplifiers (leading to less expensive discs). The appropriate design of amplifier was determined by the desire to make it as simple and efficient as possible while maintaining sufficient gain to produce the required energy. A subsiduary but important factor in the design has been to minimise and if possible eliminate dynamic optical distortion of the transmitted beam.

Design

The design is based on a large number of measurements at the Lawrence Livermore National Laboratory (LLNL) on different types of disc amplifier (A6.3). From analysis of this data, scaling laws have been developed (A6.4) to enable us to predict the performance of any particular design and hence to find the optimum design. Our starting point was the LLNL ϕ150mm 'Y' disc amplifier; a 'cylindrical' amplifier designed for maximum gain (having a small signal gain of 4.6) 24 lamps and a total energy storage of about 300 KJ. The approach taken was to make a number of desirable improvements, calculate the expected gain and check this against the minimum gain necessary to achieve the required energy performance.

Gain requirements

We assume that the ϕ150mm amplifier amplifies the output pulse from a ϕ108 amplifier as indicated in A6.10.

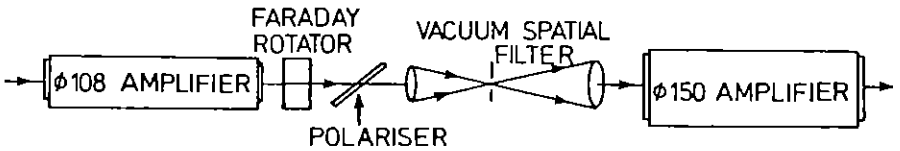

Fig A6.10 Ø150mm disc amplifier optical arrangement.

The gain of the ϕ 150 amplifier must be sufficient to amplify a 150 joule beam from the ϕ108 amplifier to an output of about 400 joules allowing for some loss, say 16%, in the intervening optics. This requires a saturated gain of 3.2 from the ϕ150 amplifier. Using the Franz-Nodvik equation with a saturation intensity of $3J/cm^2$ and assuming a 65% 'fill' factor, we calculate a required small signal gain of 4.2. This we regard as the minimum gain necessary for our ϕ150 amplifier.

Proposed improvements

i) Change from a 'cylindrical' to a 'box' design. An improvement of 40% in coupling efficiency is expected but for a fixed lamp loading the input energy capacity is down by $33^1/_3$% because of a reduction in the number of lamps from 24 to 16. Using this scaling a 'box' ϕ150 'Y' disc amplifier would have a gain of 4.15 for an input energy of 200KJ.

ii) Increase the lamp bore from ϕ15mm to ϕ20mm , and reduce the number of lamps from 16 to 12. The scaling laws suggest that $\ell n\ G \sim Nd^{9/8}$ for an energy input of $E \sim d$, where N = number of lamps, d = lamp bore. This predicts for the modified ϕ150mm box amplifier a gain of 4.37 at an input energy of 200KJ.

iii) The LLNL 'Y' disc amplifier has laser glass with 2% Nd concentration. The scaling laws suggest that this is not optimum for highest gain. Calculation suggests that a concentration of about 3% will give higher gains but the actual increase in gain is not easily predicted in this case due to the complicated interdependence of gain, neodymium concentration, other material parameters and losses due to amplified spontaneous emission.

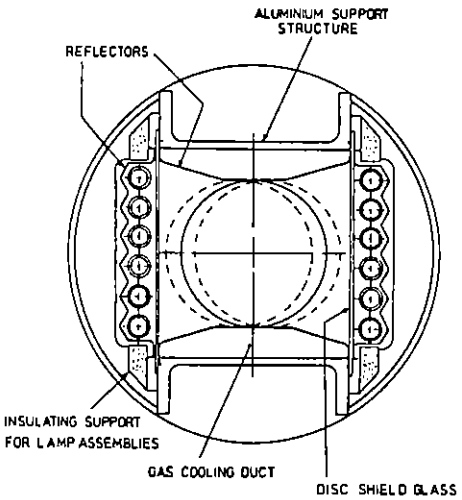

Fig A6.11 Cross section of Ø150mm disc amplifier showing arrangements of components.

Final optical design

Figure A6.11 shows a cross-sectional optical schematic for the modified ϕ150mm amplifier. Analysis of the performance of different reflector shapes, together with LLNL data, have resulted in the choice of the 'V' geometry lamp reflector. This gives close to optimum coupling while being simple and inexpensive to manufacture. An important aspect of pump cavity design is to minimise the pump cavity volume, since the coupling efficiency is directly related to the fraction of this volume filled with laser material. For this reason the mechanical design seeks to squeeze up all components as much as possible within the requirements of reasonable tolerances.

Mechanical Design

Figure A6.11 also shows the main features of the mechanical construction which are:

i) Because the disc shields in a 'box' design are flat sheets of glass, rather than a slit silicon tube as in the existing ϕ108 amplifier which entails large mechanical tolerances, the clearances between the disc holders and the flash lamps can be very small thus keeping the pumped volume to a minimum.

ii) All internal surfaces of the amplifier are reflectors, thus no major parts of the structure are directly exposed to the lamp light. This has enabled the main structure to be made of aluminium rather than stainless steel resulting in reduced cost of both raw material and machining, and overall weight (important in handling, cleaning and assembling amplifiers).

iii) Both lamp assemblies are mounted on insulators to electrically isolate them from the rest of the amplifier assembly. This enables them to be separately earthed with the flash lamp circuit, preventing circulating currents and high voltages appearing outside the amplifier, particularly as a result of flash lamp failure.

iv) An improved disc cooling and purging system is possible with the 'box' design, similar to the modifications being incorporated in the existing Ø108 amplifiers to overcome beam distortions (see Section A6.3.3). This is achieved by using the reflectors on the unpumped sides of the box, which also support the discs, as gas manifolds. The nitrogen is fed into the centre of both top and bottom of the amplifier, which forces it to blow into the disc cavity via clearance slots between the discs and the reflector, thus cooling the discs, ensuring mixing throughout the amplifier, and discharging the gas at both ends.

Forced air cooling of the lamp assemblies is about to be tested, but should be as effective in removing the heat as has been shown in the Ø108 improvements .

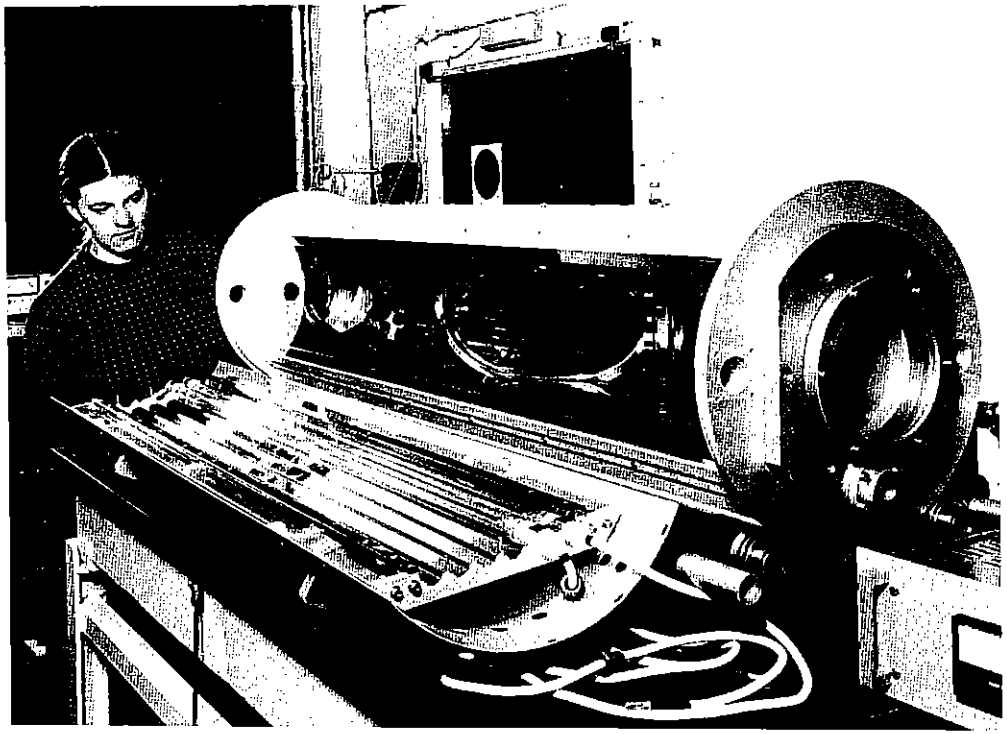

Fig A6.12 Preliminary mechanical assembly of Ø150 disc amplifier.

A photograph of the assembled amplifier is shown in Fig A6.12 prior to final coating of reflectors.

Performance

Gain measurements

Fig A6.13 shows the measurement scheme. A Q-switched phosphate glass oscillator producing 3 Q-switched pulses separated by ~ 25μs injects a small (~ 1cm) beam through the amplifier in double pass. The input and output energies are monitored with photodiodes and a storage oscilloscope. The oscillator was fired and traces recorded both before and after the disc shot as well as on the disc shot, the nett gain (independent of passive losses) being calculated from these recordings. On each disc shot three gain measurements corresponding to three different probe pulse timings were obtained using all three oscillator pulses. An external delay box enabled the probe pulse timing with respect to the amplifier discharge to be varied at will to maximise the gain. Translation of the amplifier allowed gain measurements to be taken at various positions in its aperture and so map out the gain distribution across the aperture. Since we were measuring small signal gain the probe beam energy was adjusted to ensure that the amplified pulse intensity (J/cm^2) << the saturation intensity ($3J/cm^2$).

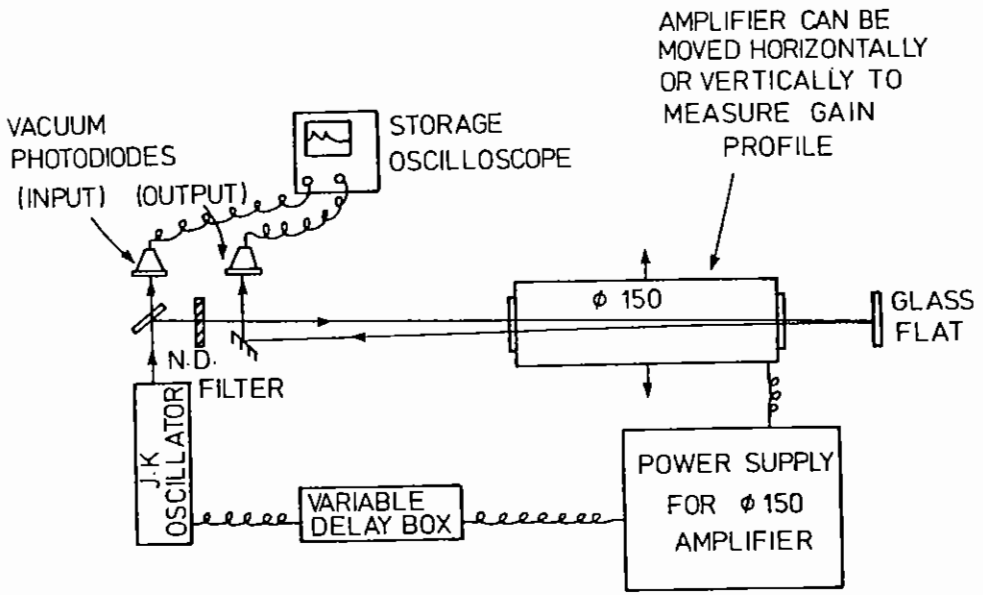

Fig A6.13 Schematic of gain measurement layout.

The principal inaccuracies of these measurements resulted from interference effects in the amplifier windows which varied their transmission slightly from shot to shot and from the use of 'chopped mode' on the oscilloscope to record both photodiode signals simultaneously. Some gain measurements were made with improved accuracy by expanding the probe beam to large size (10cm) and by recording the two photodiodes on separate oscilloscopes.

Reduction of the data gives the curves of Figs A6.14a and A6.14b, showing the single pass small signal gain variation with pumping energy and the map of gain across the disc aperture. The gain at full bank energy (190KJ) is seen to be ~ 4.3, in excess of our requirements of 4.2.

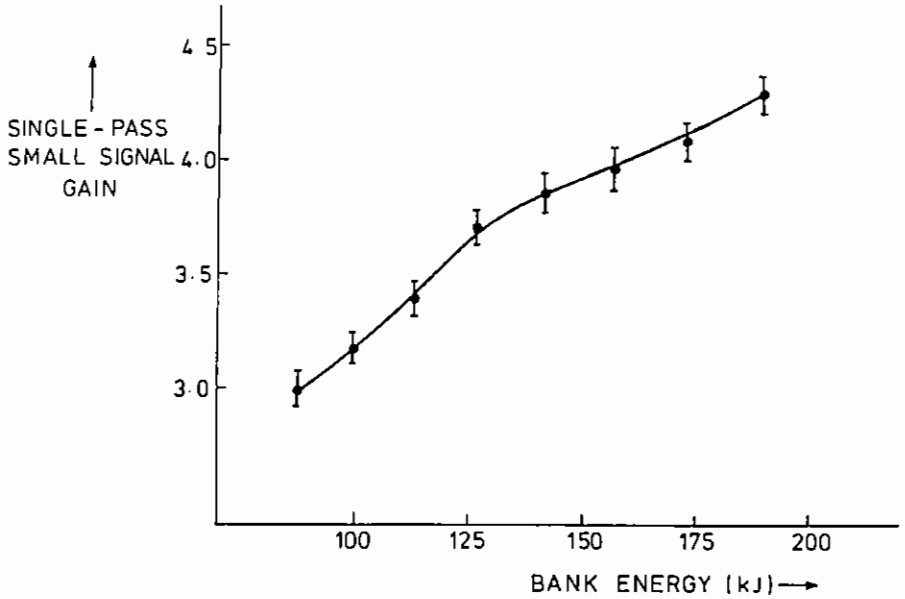

Fig A6.14 (a) Single pass gain as a function of capacitor bank energy.

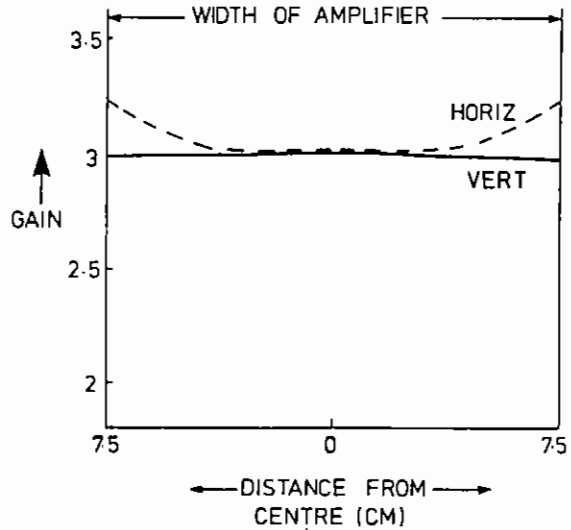

Fig A6.14 (b) Gain distribution across aperture of Ø150 disc amplifier.

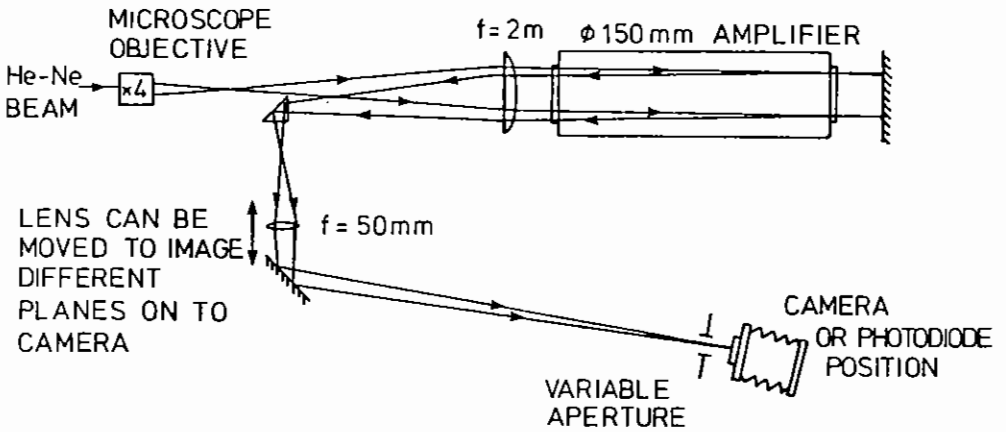

Fig A6.15 Schematic of layout used for beam distortion measurements.

Beam distortion measurements

The arrangement used for beam distortion measurements is shown in Fig A6.15. Far field or equivalent plane measurements were possible by a focussing adjustment of the x5 imaging objective. Care was taken to ensure as good optical quality as possible in the optics of this arrangement. It should be noted that all measurements are for double pass operation-single pass gives much better beam quality. Far field and equivalent plane pictures of the system without the amplifier are shown in Fig A6.16a. The far field distribution shows a small residual spherical aberration (as expected with the F/15 singlet lens used) but, more important, shows very little asymmetrical error. All 'equivalent' plane pictures were standardised to be equivalent to a plane 300m downstream of the amplifier which corresponds to 600μm inside the focus of an F/2.5 lens.

(a) WITHOUT ϕ 150 mm AMPLIFIER

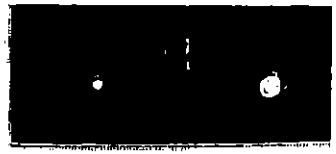

FAR-FIELD (AT TWO EXPOSURES)

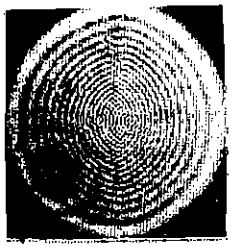

EQUIVALENT PLANE

(b) AMPLIFIER COLD

FAR FIELD

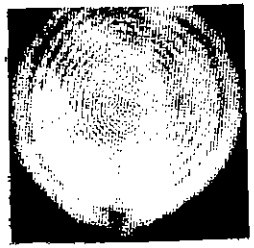

EQUIVALENT PLANE

(c) 15 MINUTES AFTER AMPLIFIER SHOT

FAR FIELD

WITH NITROGEN COOLING

EQUIVALENT PLANE

WITH HELIUM COOLING

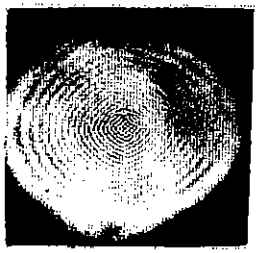

Fig A6.16 Far field and equivalent plane photographs for various amplifier conditions.

PASSIVE INTERFEROGRAM OF ϕ150 AMPLIFIER

Fig A6.17

function of time while firing the amplifier several times. Fig A6.18 plots some of these measurements.

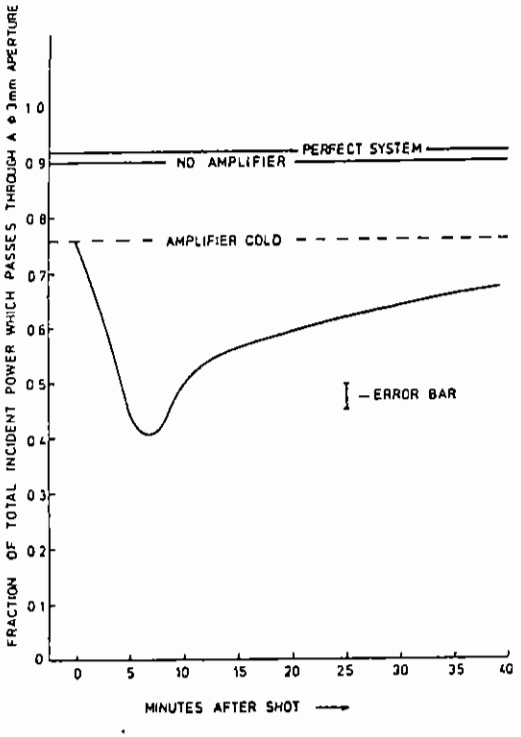

Fig A6.18 Transmission of a pinhole as a function of time.

The pinhole size (~ 2 x diffraction limit) or ~ 30 μ rad is chosen to be sensitive to small changes in beam quality. The measurements indicate that the beam deterioration is modest with over 60% of the energy within 25μ rad. This represents a large improvement over the performance of the existing φ108mm amplifiers.

Temperature measurements

Before attempting to find ways of improving the beam quality, some tests were carried out to find out how the heat is distributed within the amplifier head after a shot and how this distribution changes with time. This knowledge is necessary before deciding how to efficiently cool the amplifier without distorting the transmitted beam.

(i) Lamp cavity measurements

The lamp half-shell was opened immediately after firing the lamps and a touch thermometer used to measure the temperature distributions as a function of time. The results are shown in Fig A6.19. We conclude that most of the thermal energy is deposited in the lamps and reflectors and thereafter is redistributed on about a 10 minute time scale with a considerable long term heat flow inwards towards the discs. The long term temperature rise indicated a very slow and inadequate cooling rate for the lamp cavity.

(ii) Disc Holder Measurements

A temperature probe contacted onto the top of a disc holder measured its temperature variation after firing the amplifier (Fig A6.20). We note in particular that a) the initial temperature rise of 1.5°C occurs in a relatively short time of 3 min due, we think, to a redistribution of heat in laser discs b) there is a long term temperature rise of 1.8°C even after 40 mins which is not sufficient to give a large optical distortion in the laser glass (which is nearly athermal), but which is sufficient to lead to distortion from temperature gradients in the cooling gas.

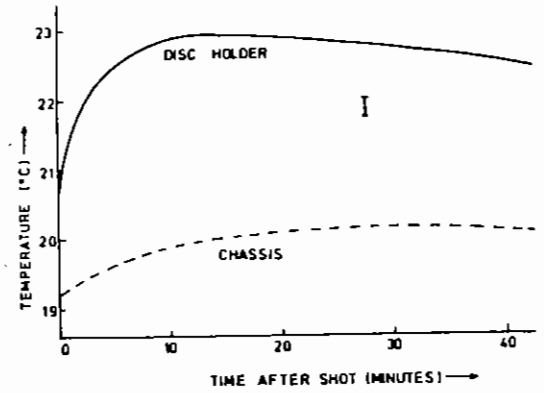

Fig A6.19

Temperature variation of various Ø150 amplifier component with time.

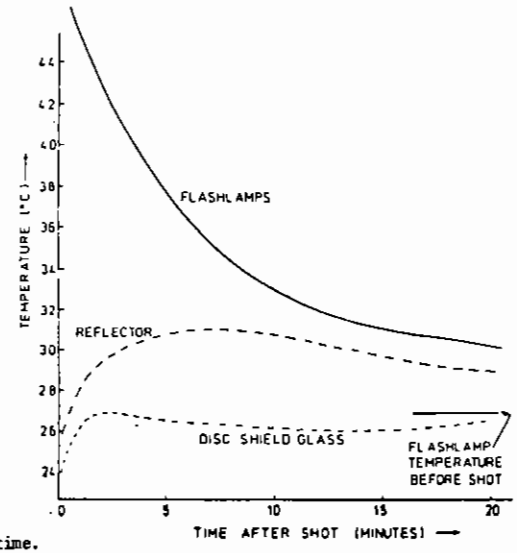

Fig A6.20

Temperature variation of Ø150 amplifier component with time.

A significant long term temperature rise of 0.9°C of the chassis after 40 min is also measured, again suggesting an inadequate cooling rate for the amplifier as a whole.

Beam quality improvements

i) Thermal distortion in the laser discs results from heat directly deposited in the discs by absorption of lamp light and from heat conducted into the discs from the lamp cavity where most of the heat is deposited. The second of these sources of heat can be arrested by inserting insulating material between the disc holders and chassis. This has the added advantage that any non uniform heating or cooling of the discs due to their non uniform contact with the holders will be reduced. PTFE spacers were made and inserted to provide this thermal insulation. Subsequent beam quality tests showed that any improvement was small. We concluded that residual distortion of the type seen is probably due to distortion in the cooling gas resulting from temperature gradients in the gas. This hypothesis correctly predicts the poor regions of the beam which are in close proximity to relatively warm metallic reflectors.

ii) A possible solution to reduce the beam distortion caused by thermal gradients in the cooling gas is to replace the nitrogen in the disc cavity by helium which has an 8 times lower refractivity than nitrogen. This is possible in the ϕ150mm amplifier in which a reasonable seal is possible between the disc and lamp cavities. It is not cost effective to blow the helium without a closed circuit system but could be useful for cooling purposes. Helium has a 6 times higher thermal conductivity than nitrogen so that even stationary it may provide more effective cooling than flowing nitrogen. Helium was flowed through the disc cavity until it displaced the nitrogen. Optical distortion tests were carried out as before. Fig A6.16(c) shows 'cold' amplifier and 'hot' amplifier equivalent plane pictures with helium. These show a dramatic improvement in the 'hot' amplifier beam distortion, recorded only 15 minutes after the third consecutive 20 minute amplifier shot. These suggest that a shot firing rate as high as 4 shots per hour is possible if a more efficient heat extraction is

available for the lamp cavities to prevent long term build up of temperature over several hours.

Also shown in Fig A6.16c is the effect of replacing the helium fill by a nitrogen fill when the amplifier is 'hot'. The immediate return of optical distortion similar to that earlier recorded in Fig A6.17 is a good demonstration of the advantage of using helium.

iii) A more efficient heat extraction system for the lamp cavities has been successfully tested on the ϕ 108mm amplifiers and will be fitted to the ϕ150 amplifier for further tests.

Conclusions

The amplifier development programme has resulted in an efficient ϕ150 disc amplifier giving a small signal gain of 4.3 at 190KJ energy storage with only 12 lamps and a simple mechanical design. The design, together with subsequent improvements suggest that a near diffraction limited optical quality output beam is possible even at repetition rates as high as 4 shots per hour.

The performance of this amplifier meets the needs of the laser upgrade programme and may also lead to similar box designs for the smaller ϕ108mm amplifier and a possible new larger aperture ϕ206 amplifier.

A6.3.5 Vacuum Spatial Filter Installation

C Edwards, S Hancock (RAL)

Major efforts have been made this year to improve the quality of beam delivered to target areas. The transfer of compression experiments to TAW has led to major increases in air propagation path lengths between the end of the laser system and the target chamber and this, together with limited spatial filtering and relaying, has given rise to poorer quality beams than desirable.

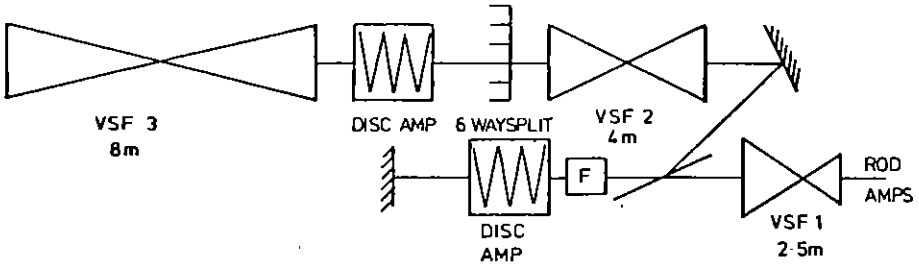

Fig A6.21 Layout of 6 beam system.

To start to overcome this problem a first stage of vacuum spatial filter (VSF) installation has just been completed. Fig A6.21 shows the new layout of the 6 beam system beyond the end of the rod amplifier chain with 6 new 8m long VSFs at the output and one additional expanding VSF before the first disc amplifier. At this stage relaying from the rod output plane is only partial but the full image relay scheme for the 6 beam system will be completed when the length of VSF 2 is doubled to 8m later in the year.

VSFs 1 and 2 use lenses with dielectric AR coatings whereas the 6 output VSFs contain lenses which have been processed by the Schott neutral solution technique. Experience with this type of coating has indicated that oil contamination can be a problem and consequently totally oil free pumping system based on triode ion pumps have been designed and built.

Operating experience of the new system is limited at present but first results indicate considerable improvements in beam quality at the output of the VSF array, particularly for short pulse operation.

A6.3.6 Computer Control and Data Acquisition

C J Reason, B Espey and P Gottfeldt (RAL)

This has largely been a year of consolidation and improvements to existing facilities. The GEC 4080 computer and CAMAC equipment has been reliable and the serial CAMAC branch, installed last year, has run successfully.

Control

The dump system for the Quantel driver described last year, has been fully implemented in software. Work has also progressed on the ability to fire shots from the south control room via the serial branch. This has reached the stage of firing shots for test purposes and is now being extended to give further control to the experimenters. This concept has also been extended to allow shots to be fired on a similar basis from within the laser room. The wave plates that are controlled by the "Essex Tiny Basic Computer" had a response time that was significantly slower than any other part of the system and this has PROM.

Diagnostics and data acquisition.

A number of detailed changes have been made to the diagnostics including reading the pre-lase signal from a Philips digital 'scope via an IEEE 488 interface in CAMAC. All LeCroy 12 channel ADCs have been removed from the system and all energy monitoring is now done using the CAMAC CEM module described in previous years. The software for a graphics plotter has been developed and this is now being installed in the south control room to provide hard copy output. The laser program now keeps statistics on the types of shots that have been fired and how many times each amplifier has been triggered. A project was initiated to monitor the pulse length and beam quality of the laser using several

commercially available frame stores. The initial results proved disappointing but have given the information and experience needed to specify a new system and this will be developed and installed during the year.

A6.4 TARGET FABRICATION AND DEVELOPMENT

C Brown, B Child, T le Roux, N Prior, P Rumsby and S Whittaker (RAL)

The last year has involved the production of a large number of standard foil, shell and lollipop targets for the experimental programme. In particular 1984 has seen the completion of the new 12 green beam compression facility (TAW) and consequently a major activity of the target fabrication group has been the provision of targets for the commissioning experiments. Many solid glass spheres have been selected, characterized, mounted and coated with up to 3μm thick layers of parylene for initial irradiance uniformity and energy coupling measurements. Following this, high quality polystyrene shells with aspect ratios of about 8 have been manufactured, selected, mounted and gas filled for compression experiments. X-radiography of these events has required the production of quantities of backlighting targets. Copper and other metal foil lollipops of 500μm diameter have been punched and mounted for pinhole imaging experiments while wires of 10μm diameter have been mounted and coated with a variety of materials for point source radiography. To produce small X-ray sources for this later type of radiography reactive plasma etching techniques have been used to reduce the diameter of commercial carbon fibres to below 1μm.

Much of the research and development work carried out during the year by the group has been associated with X-ray laser experiments. Techniques have been developed for making, measuring and handling a wide variety of plastic foils in the thickness range from 100nm to 400nm. Foils of 150nm thickness have been mounted as substrates for collisionally excited X-ray laser experiments, as filters for XUV spectrometers and as bases for XUV sensitive photocathodes for streak cameras. In all cases techniques have been established for applying

coatings without damaging the fragile foils. Stripes of selenium 60nm thick, 50μm wide and 10mm long have been applied to foils for line focus irradiation for X-ray laser experiments.

Work has continued on UV laser photo-ablative etching of polymer targets. Production work has involved supplying 270μm diameter polystyrene lollipops of 5μm thickness modulated by photo-ablative etching with a 0.5μm amplitude of periodity 20μm together with similarly modulated shell targets of 150μm diameter for Rayleigh-Taylor growth rate experiments. Development activities have involved studying in detail the etch rate variation with laser fluence and wavelength of a wide variety of polymers.

A6.5 TARGET AREAS

A6.5.1 Target Area West Commissioning

C J Hooker, C J Reason, W T Toner, P Gottfeldt, R W Eason, S P Knight, D L Collins and S G Appleton (RAL)

On Wednesday 18 April 1984 the last laser shot was fired into Target Area One, and the area was shut down. In the weeks that followed the target chamber, beam towers, frameworks and tables were stripped out. Many of the components were moved to new locations in Target Area West, where installation of beam lines, television viewing systems and alignment optics was proceeding. During the same period the control system evolved rapidly, as the control electronics were tested and integrated with the area components and the computer program that was to drive them. The South Control Room was prepared for occupation and the dark-rooms on the mezzamine floor were fitted out.

The first full shot was fired into the new area on 6 June, exactly seven weeks after the shutdown of TA1. However, a further month of beam timing, optics alignment, calorimetry calibration and diagnostic checking was needed before the first twelve-beam 2ω implosion shot on 3 July. The active and static X-ray pinhole cameras, plasma calorimeters and harmonic imaging system were all functioning; data from these and

from the beam calorimeters, streak camera and equivalent-plane camera were obtained on every shot. In early August the backlighting beam was installed, and short-pulse X-ray backlighting of the implosions began, using lollipop targets and the active X-ray pinhole camera for imaging.

The energy distribution between the beams was uneven at first, due to the poor quality of some of the green beam-splitters. In one case the split ratio was 60:40 rather than 50:50, and this imbalance was clearly seen in the asymmetry of the early implosions. Replacement beam-splitters were obtained in September, after which the energy variation was reduced to less than five percent over the twelve beams. A timing error in one beam was corrected at the same time, and subsequent implosions were greatly improved. Good data were obtained from all diagnostics in a parameter scan through different defocusing conditions, with total green energies on target of up to 150 Joules in 700ps.

The remainder of the year saw a gradual shakedown in operating practice, and the discovery and correction of a number of problems. Chief of these were some slight differences in collimation and pointing between the local alignment lasers and the main CW YAG beam, which were found to have a serious effect on the illumination uniformity. They were traced to wedge effects in some of the mirrors, and new alignment procedures were adopted to solve the problem. T A West is now fully commissioned and operating well.

The computer-based control system described in last year's report (A6.5.4) has proved to be highly satisfactory. A practised operator can align twelve beams onto target, and prepare the area to receive a shot, well within the 20-minute cycle time of the laser. Given a few minutes' instruction, even inexperienced personnel can perform routine alignment jobs.

The T A West control program has changed considerably since experiments began. Many new features have been added to keep pace with evolving operating practice and to control additional equipment. The flexibility of the Micropower Pascal program-development package has

greatly simplified the making of these changes, and the program has reached a stage where requests for new features are rare. The LSI-11/23 development system used for editing and compilation has been enhanced by adding a 128K memory board and a 20Mbyte Winchester disk, so changes to the program can now be made in a third of the time previously needed.

In recent weeks a new Camac-crate housing for the Falcon microcomputer in T A West has been received from Hylec, a UK supplier. A version of the control program incorporating new Camac driver software to run in this housing is being debugged at present, and when ready will be burned into EPROMs and installed in the housing. The Falcon will then be a stand-alone system, and the LSI-II will be freed for other applications.

A6.5.2 Target Area East Design

C Hooker, A Damerell and P Gottfeldt (RAL)

Target Area East is intended as a versatile multi-beam irradiation facility for experiments not requiring spherically symmetric target illumination. It will thus complement T.A. West and provide features similar (but superior) to those of T.A. 2, which is due to close down at the end of May 1985. The seven beams from the laser area will all be available in T.A. East, and several different beam layouts (Fig A6.22) will make possible a wide range of experiments on X-ray lasers and laser-plasma interactions. The target chamber has two 600mm apertures onto which various 'top-hat' flanges can be fitted to accommodate different experimental configurations; in addition, a large space is available on the East side of the area for experiments such as the Z-pinch, or for extra diagnostic equipment. Other features of the area have been designed for maximum compatibility with T.A. West: the target chambers are the same diameter to allow interchange of diagnostics, and much of the control electronics, software and alignment system hardware will be identical.

The key feature of T.A.East is its range of possible beam configurations, two of which are shown in Fig. A6.23. Fig. A6.23(a)

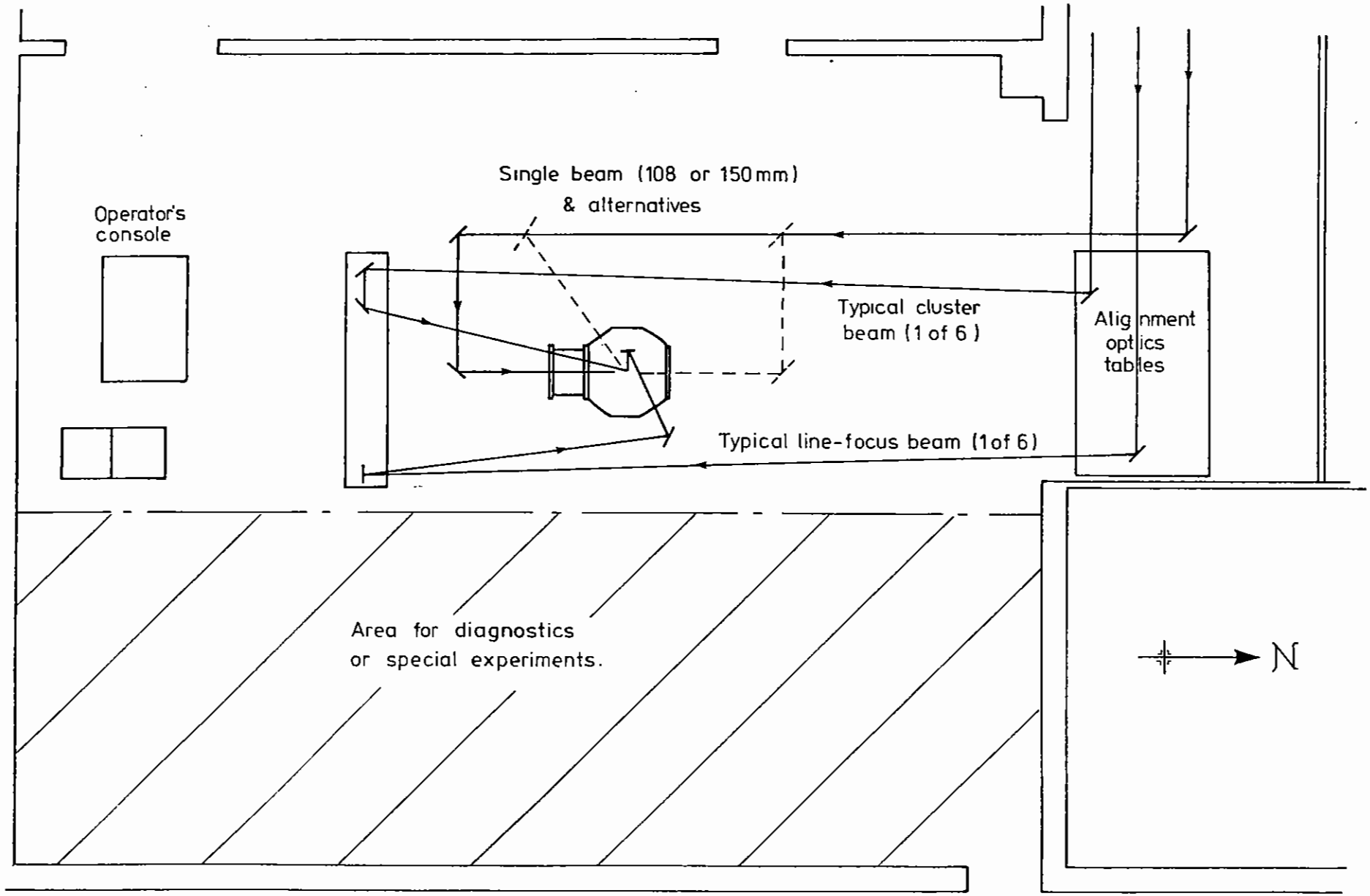

Fig A6.22 Proposed layout of Target Area East.

spherical mirror scheme developed by Rose and Hodgson (see Section A6.6.1). The six beams can be arranged either symmetrically around the target axis, or in two clusters of three beams each, depending on whether fibre or foil targets are being irradiated. The focal line runs horizontally N-S and is roughly 8mm long.

Fig. A6.23 (b) shows the six-beam cluster configuration, which will allow high-intensity single-spot, multiple-spot or sequential shot irradiation, depending on the focusing and timing of the beams. The individual cluster lenses will be approximately f/10, arranged in a cone with an apex angle of about 30°. The seventh beam will be available for backlighting, and the axis of the cluster cone could be used for diagnostic access.

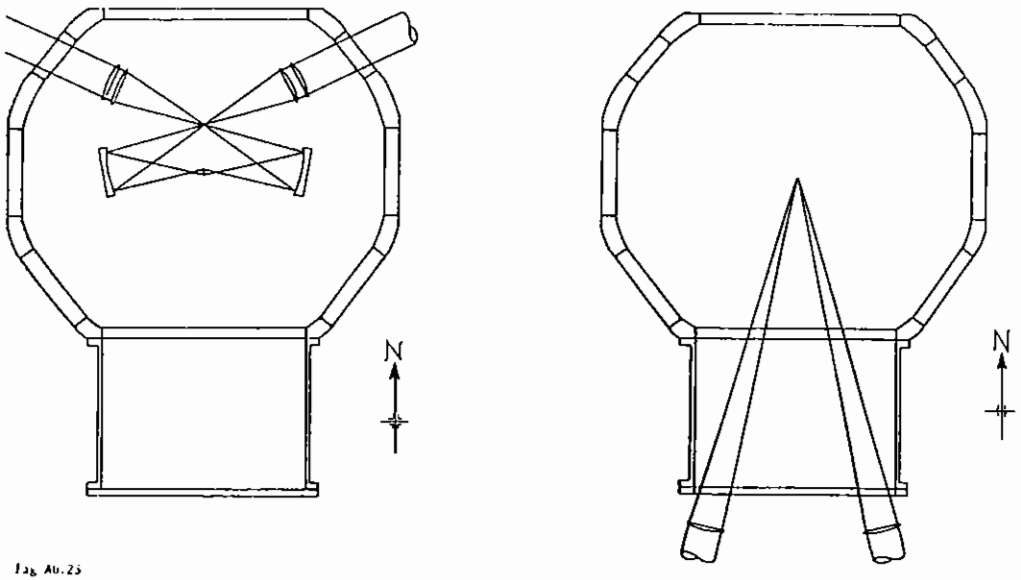

Fig A6.23

(a) Proposed layout in target vessel for line-focus experiments. (b) Proposed layout in target vessel for six beam cluster configuration.

this beam will be available in T A East with energies up to 400J in 1ns, for experiments needing the very highest intensities.

These are the configurations planned at present; operations will commence in September with the line-focus set-up, and the cluster beam will be commissioned after 2-3 months, subject to demand. The design emphasis is on versatility, however, and other configurations could be introduced later. Among those considered are two opposed clusters, each with three beams, and a longer line focus derived from the 150mm single beam.

The hardware of the control system for TAE is identical to that for TAW which was described in last year's report. However, an additional feature has been introduced which allows equipment common to both areas to be controlled from either TAE or TAW. A secondary multiplexer has been built which allows standard crates to be addressed from either TA. Each common crate requires one of the 15 outputs from each of the crate multiplexers situated in the TAs. Arbitration between the two sources of command is governed by the GEC 4080 computer. A watch-dog circuit is incorporated in the secondary multiplexer to prevent operation of common equipment if the GEC 4080 is not working.

Optical path lengths to TAE may be changed using 6 variable delays driven by D.C. Motors. Each motor moves a pair of mirrors set at 45° to the optical path using a lead screw 2m long. An incremented encoder on the motor shaft allows the relative optical delay introduced into the path length to be determined. The multiplexer structure is not adapted to provide the positioned control required for the delays and it is proposed to use an independent micro-processor controlled system for this purpose. The TAE controls will operate on this system using a V.24 link via CAMAC.

A6.6 FOCUSING OPTICS

A6.6.1 Line Focus Optics

I Ross, E Hodgson (RAL)

Experiments aimed at establishing the feasibility of X-ray laser action in materials such as carbon and selenium demands a target illumination which is a line focus of length of order 10mm and width a few microns. Earlier experiments were limited by a line focus which was only narrow over a length of a millimetre or so. In consequence, since the gain of a laser is exponential with length, any inversion produced had only a marginal and inconclusive effect on the axial intensity. To overcome this difficultly an improved design of line focus optics has been developed and is described more fully elsewhere (Ref A6.5).

The design is based on the simple principle illustrated by the spherical mirror reflection shown in Fig A6.24. Any axi symmetric optical system such as this spherical mirror, when illuminated with a parallel beam down the optical axis, will focus the beam with aberration. Since all rays must remain in the plane defined by the incident ray and surface normal (plane of Fig A6.24), all rays must pass through the optical axis. Since the optical system has rotational symmetry about the optical axis this is true for all rays in the beam, resulting in a line focus distribution along the optical axis. The transverse extent of the line focus is diffraction limted for a perfectly spherical mirror.

Other requirements have been considered in arriving at our chosen design, illustrated in Fig A6.25. For good coupling efficiency of incident light into the target plasma we require that rays are all nearly normal incidence to the target (situated at the line focus). We require that the deposition distribution along the line focus be easily controllable and in particular it will normally need to be as uniform as possible. We also require that the beam size on all optics be at least as large as the incident laser beam to minimise the chance of optical damage.

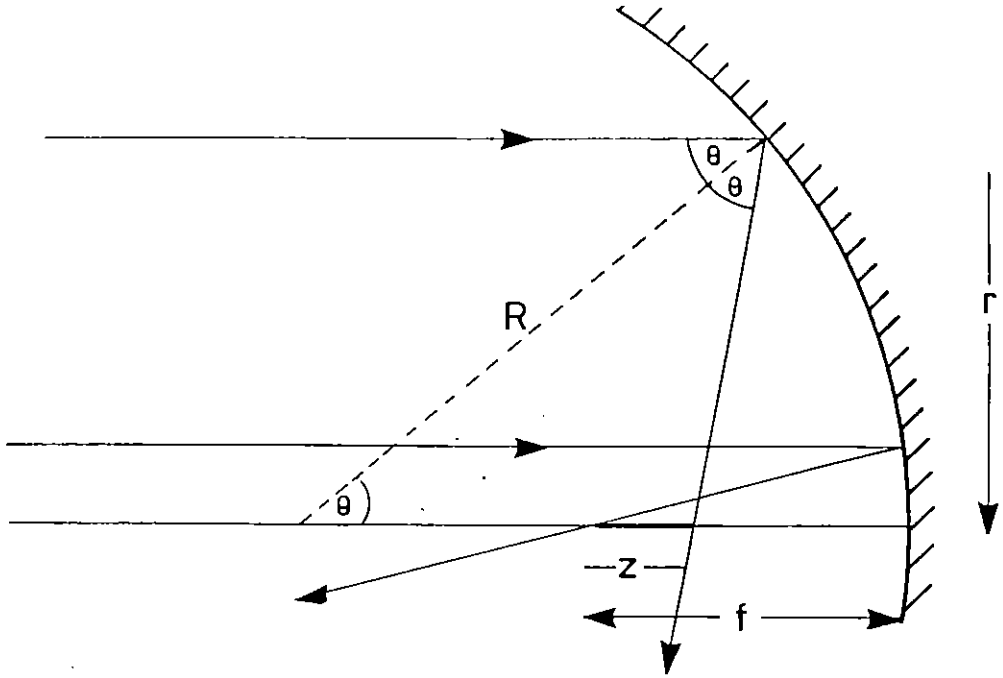

Fig A6.24 Ray diagram for a spherical mirror.

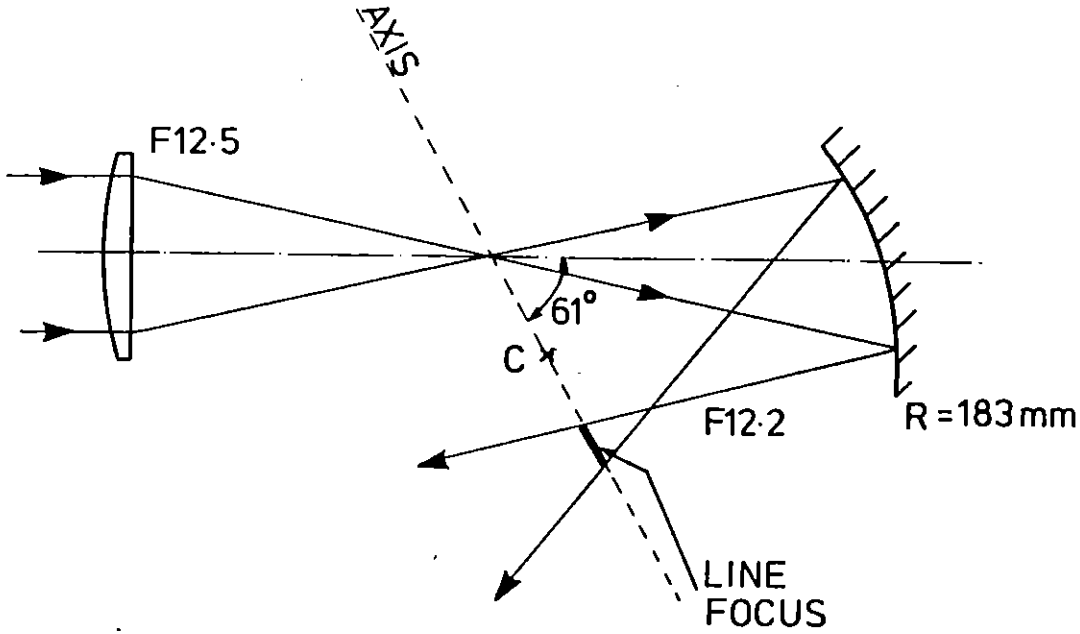

Fig A6.25 Design of Off-Axis line focus mirror giving a 10mm line focus.

The design illustrated in Fig A6.25 is an extension of the axi-symmetric system of Fig A6.24, the principle still being valid if the incident beam has a focus on the optical axis and if that beam only illuminates a small off axis area of the mirror. This off-axis region is the mirror depicted in Fig A6.25.

One or two properties of this design are worthy of comment:

i) The length of the line focus can be varied by either varying the input beam size or by changing the tilt of the mirror. The length goes approximately as the input beam size and as the square of the mirror tilt angle.

ii) The quality of the line focus is only dependent upon the quality of the primary beam focus. Changes in tilt or translation of the mirror merely move or stretch the line focus without introducing transverse aberrations.

iii) Multibeam multidirectional illumination of the target is straight forwardly achieved using several identical lens/mirror pairs set up with a common axis. This axis contains all primary foci, mirror centres of curvature and, of course the line focus. In particular the coincidence of all primary foci makes alignment of the system that much easier.

iv) Alignment onto target can be achieved relatively simply with independent adjustments of the lens and mirror.

v) An appropriately shaped aperture in the incident beam can give excellent uniformity along the line focus with very sharp cut off at each end.

vi) The mirror is of course achromatic.

Initial tests on the line focus optics were carried out using an expanded HeNe laser beam. Fig A6.26 show photographs of the line focus over a length of 9mm. The transverse extent of the line was demonstrated to be close to diffraction limit of the F/2 mirror.

Fig A6.27 shows the measured distribution along the line focus using a shaped aperture as shown. Better than ± 5% uniformity is measured with end cut-off regions considerably less than the instrumental resolution.

Experiments have now been carried out on VULCAN with second harmonic pulses focussed onto carbon fibres of 7μm diameter and onto thin foils of selenium. These experiments are reported in Section A4.2.

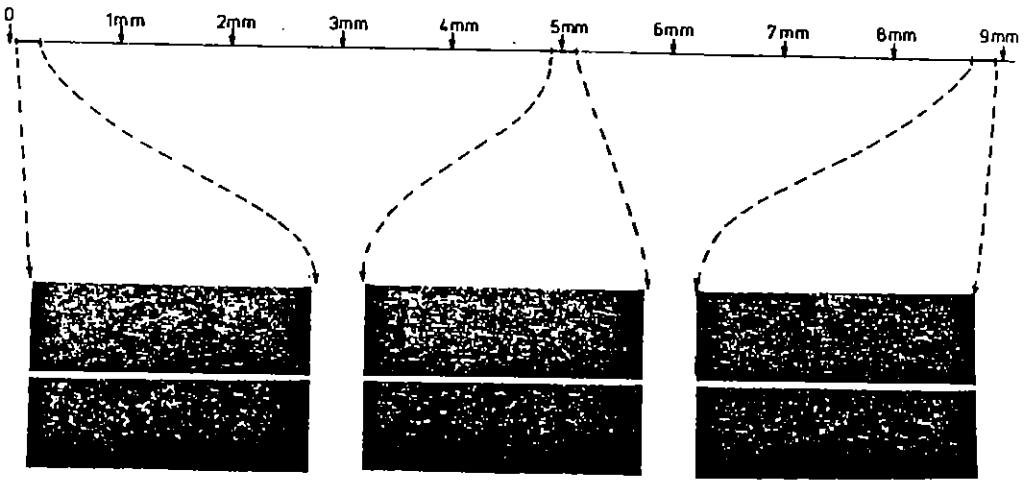

Fig A6.26 Line focus to scale showing segments photographed.

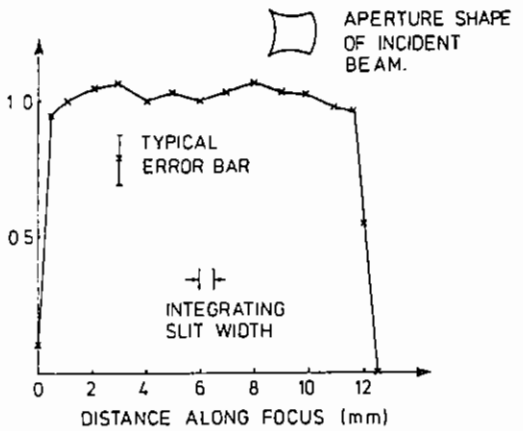

Fig A6.27 Intensity variation along line focus.

A6.6.2 Aspheric Lens Manufacture

Following the successful manufacture last year of fourteen f2.5 Aspheric Doublets for the ϕ108 beams in TAW, a further 8 are now being manufactured for use in TAE.

Also two sets of spare optical components for the Apodisers, at present in use on the glass laser, are being manufactured. The Apodisers are vital components used for shaping the beam to a modified gausian distribution in the rod amplifier stages. The original and only suppliers of these components have stopped manufacture, owing to the difficulties encountered in shaping such a steep aspheric. Manufacture

will also start this year two f2.5 Aspheric Doublets for the new ϕ150 single beam. These will be based on a similar design to that of the ϕ108 doublets, and similar techniques of manufacture will be used.

A6.7 DIAGNOSTIC INSTRUMENTATION

A6.7.1 Inertial Positioning System for Stalkless Spherical Targets

G Tsakiris, J Bayerl (MPIQ Garching) J McGlinchey, C L S Lewis (Queen's), A R Damerell and C J Hooker (RAL)

As a result of work carried out at the Max-Planck Institute, Garching, Munich, RAL and QUB a device has been developed for the accurate positioning of stalkless targets and their release. The current device is the third version and has been designed to be compatible with the RAL twelve beam target chamber. It is commonly called a 'Rat Trap'.

The Rat Trap is shown schematically in Fig. A6.28. The plastic shell target is placed by means of a very fine glass capilliary on an airline on top of the pin. The hammer is forced against three springs up to the position shown by a pneumatic bellows requiring a differential pressure of two atmospheres. It is locked in this position and the bellows are withdrawn. A solenoid releases the hammer which synchronizes the laser pulse and near the bottom of its travel the hammer makes contact with the pin which starts to move down almost instantaneously with a velocity of 20 m s^{-1}. The target remains in its position and starts to accelerate under gravity.

The main difficulty with previous versions was cohesion between the microballoon and rod surface. However extensive testing of various surfaces carried out at Queen's University Belfast and investigation of the effects of moisture, electro-static charge, chamber pressure etc. has resulted in the reduction of this effect to an acceptable level. Fig. A6.29 shows curves of balloon displacement vs time for two different chamber pressures along with the reference $s = {}^1/_2 gt^2$ curve. The best surfaces tested were certain highly polished metals.

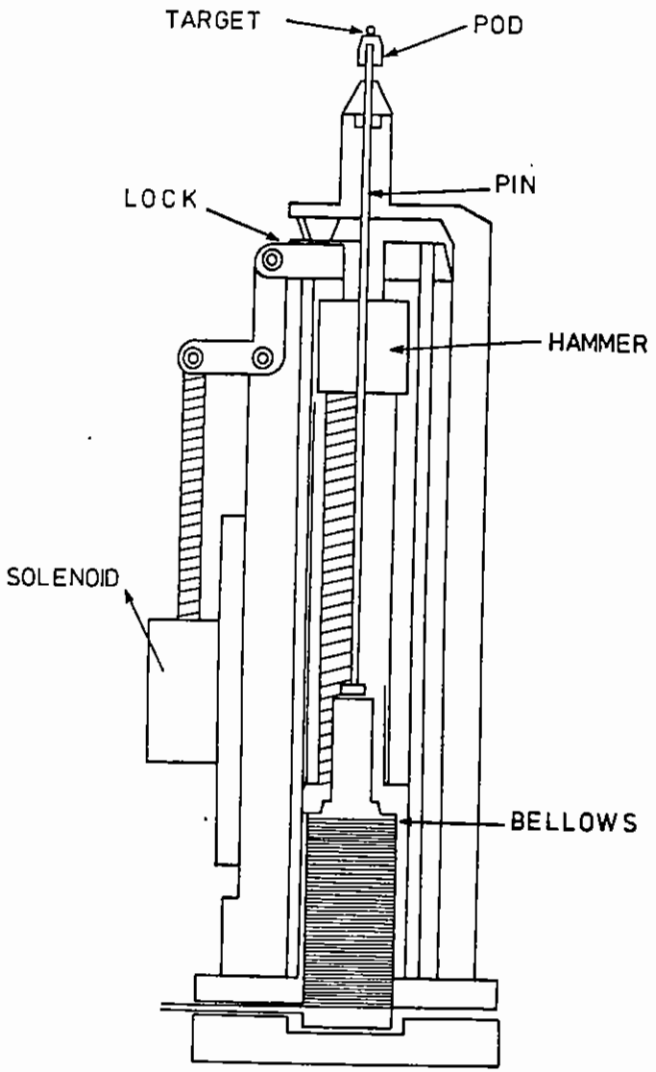

Fig A6.28

Schematic diagram of the inertial positioning device for use in the twelve beam target vessel.

Graphite also gave good release of the microballoons but not in its polished form. At low pressures (0.1 torr) there is little adhesion and since the delay between the Rat Trap firing and the laser pulse can be made 0.5ms or less the microballoon does not move significantly before it is irradiated (Fig A6.29).

The only remaining difficulty with the device is that due to the considerable internal momentum developed after the hammer release. The entire device, unless rigidly clamped to a massive object, will move. This results in a displacement of at best several tens of microns before release. However the Rat Trap must also be mounted in such a way as to allow accurate x, y and z positioning of the target and a mounting mechanism which will satisfy both sets of requirements is currently being designed. Testing is due to resume in June 1985.

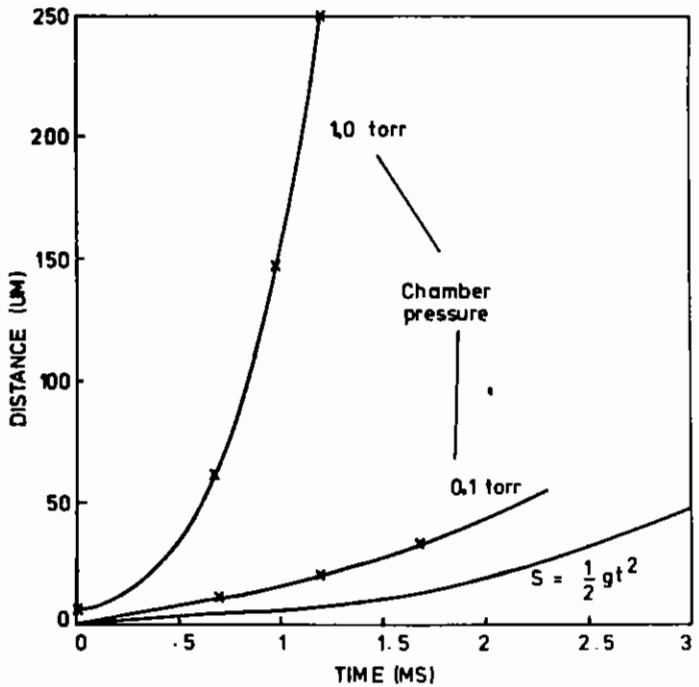

Fig A6.29 Distance VS time for targets released from a graphite surface.

A6.7.2 Point-Projection Diagnostic Development

C L S Lewis, J McGlinchey (QUB) and T Damerell (RAL)

Apparatus designed to facilitate the application of point projection of X-rays as a diagnostic in backlighting experiments has been constructed and successfully tested. The layout of the equipment is shown in Fig A6.30 and the degrees of freedom available for alignment, spectral range selection and crystal positioning illustrated. These include pointing and positioning of a thin wire target ($\sim$ 10 μm ϕ) through θ, X_B, Y_B, Z_B and angular and spatial positioning of a given crystal to allow radiography in a specified energy bond through ψ , p and q. All parameters are written in to the same software used to align the main target and lenses.

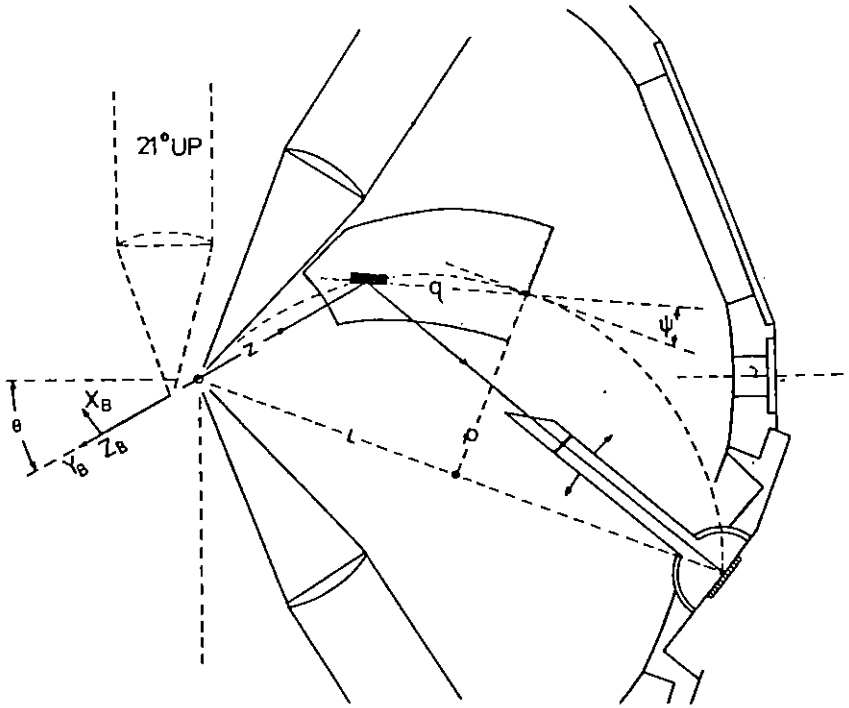

Fig A6.30 Geometrical layout for Bragg crystal used in point projection radiography. The target to phosphor screen detector distance is < 58cm.

The crystal mounting is arranged such that for a given probe energy the crystal can be tracked along an arc of a circle which passes through the source and the detector while maintaining the appropriate Bragg matching angle. This is illustrated in Fig. A6.30 where p, q and ψ are related to the mean probe wavelength λ and the source to crystal separation z by

$$p = \frac{\lambda}{(1-\lambda^2)^{\frac{1}{2}}}$$

$$q = z\left[\left(\frac{1}{z^2(1-\lambda^2)} - \lambda^2\right)^{\frac{1}{2}} - (1-\lambda^2)^{\frac{1}{2}}\right]^{\frac{1}{2}}$$

and $\sin\psi = z\lambda\left(\left({}^{1}/_{z^2} - \lambda^2 + \lambda^4\right)^{1/2} + \lambda^2 - 1\right)$

Here $\lambda < 1$ is in units of the crystal 2d spacing and p, q and z are in units of the distance between the point source and the detector. The p, q and ψ adjustments are engineered onto a single stand-alone base plate and the crystal can be located anywhere within the hatched region of Fig A6.30. For a 40 x 30 mm PET crystal this corresponds to a probe wavelength region of ~ 4-6 Å with a spectral range at any setting $\Delta\lambda \sim \lambda/10$ and a closest approach distance of the crystal to the target of $\lesssim$ 15 cm. The 50 mm diameter phosphor plate (fibre optically coupled to an image intensifier) which acts as detector is angled in the chamber wall flange so that incident rays from any crystal position are $\lesssim$ 10° off normal.

Light baffling of the phosphor is achieved with an extendable, sliding tube turret which can be swung around to point at the crystal and which carries an alluminised mylar filter.

This geometry has been chosen as a means of aligning the crystal close to the target as it allows a future option of locating the phosphor screen much closer to the crystal in a re-entrant flange. This will be advantageous when the point source is moved closer to the main target to minimise distortion of the projection through refraction with

a resultant very high magnification (Ref A6.6). At present this separation is typically 5 mm with a magnification of ≈ x 100.

A6.7.3 X-Ray Pinhole Camera with Multilayer X-Ray Mirror

A Cole and E Madraszek (RAL)

The X-ray pinhole camera with phosphor/intensifier recording has been routinely and successfully used on many experiments since its introduction (Ref A6.7).

A modification has now been made to incorporate a multi-layer X-ray mirror (A6.7.2) into this device. The arrangement is shown in Fig. A6.31). The axial displacement of the mirror can be varied by using different spacers, the mirror tilt is controlled by the micrometer. Typical ray angles on the mirror are 1.5°-3.5°.

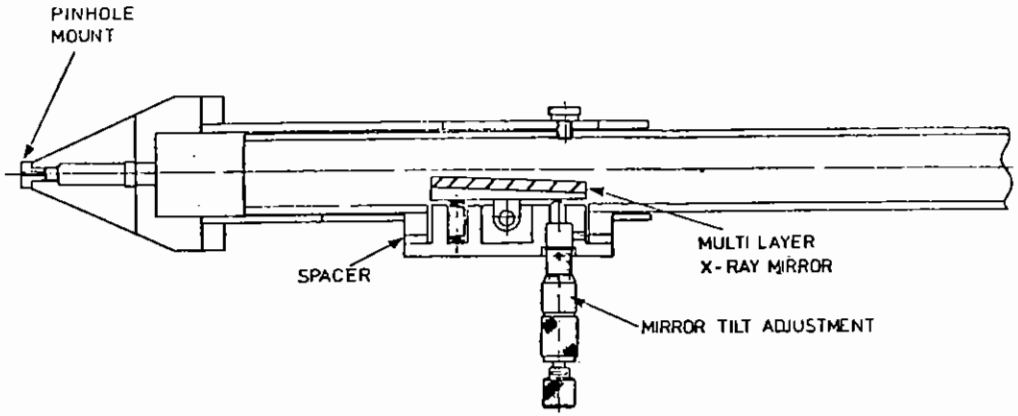

Fig A6.31 Arrangement of X-ray pinhole camera with multilayer X ray mirror.

By using two pinholes, correctly seperated and orientated on a single substrate, made by the laser drilling technique (A6.8), it is possible to project two images onto the phosphor. One is a direct pinhole image, the other undergoes reflection at the mirror and is therefore monochromatic.

A6.7.4 Fully Automated Image Analysis of Alpha- Particle and Proton Etched Tracker in CR-39 plastic

A P Fews, (Bristol University)

An image analysis system has been developed which is capable of fully automated scanning, identification and measurement of etched nuclear particle tracks in plastic. It is here applied to α-particle and proton tracks in CR-39 plastic.

The operational system described here differs in several important respects from the prototype described previously (1984 Annual Report). The system described here became operational in December 1984 and has been used since then to analyse several experiments at the CLF using CR-39.

Summary

The surface of the CR-39 is scanned on a microscope stage capable of stepping in 1μm steps over 10 x 10 cm. An autofocus system positions the microscope objective to ~ 1μm of the plastic surface. Images of the CR-39 surface (containing etch pits and plastic defects) are produced by a T.V. camera. The images are read by a PDP 11/73 computer into a 512 x 512 pixel 8 bit deep frame buffer. The computer analyses these images, as outlined below, to produce measurements of the track etch pits. These measurements enable accurate determination of the energy and position of the α-particles (or protons) incident on the CR-39. The scanning algorithm in the computer moves the microscope stage and selects the appropriate portions of the image such that all events are analysed once and only once.

Typically the system scans with an optical magnification of ~0.5μm/pixel, giving a measurement resolution of ~0.2μm by interpolation along a line of pixels.

Track Selection

A variety of selection criteria are applied in sequence to candidate events. This enables reliable discrimination between etch cones, with well defined geometries, and non-track defects which appear on the plastic surface. The most effective of these criteria are

i) the symmetry of the event about its longest axis
ii) the convexity of the event perimeter
iii) the average grey land of the track

Track Measurement

Some typical geometries of etch cones are shown in Fig A6.32 which shows a 17.5μm -track (3.5MeV) at a dip angle of 35 degree, for etch times of 0.4 0.48 and 0.80 hours. The measurable parameters of the etch pit are also shown: these are the major and minor axes M_j and M_1 the total projected length X , the depth Z , and the radius of the etched out end $\frac{m}{2}$.

The system is now capable of categorising an event into the following types:

i) Shallow tracks where $M_i \leq X_T$ (as shown for 0.40 and 0.48 hr etch times in Fig A6.32). Here the parameters M_j, M_i, X_T and m are measurable. The parameters M_i, X_T and m are on the outer perimeter of the event, but the parameter M_j is inside the perimeter and its measurement depends on knowledge of the grey level distributions inside the event.

The only parameter that is not measurable in this case is Z_t.

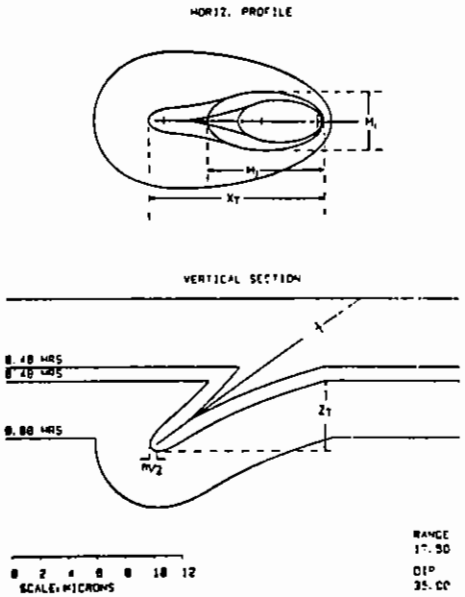

Fig A6.32 Typical geometries of etched cones in CR39 plastic

This contains little extra information however since the measurement error would depend on the depth of field of the microscope, which is clearly larger than its horizontal resolution.

ii) Steep tracks, where $M_j > X_T$. The measurable parameters in this case are M_j and M_i. The other parameters, X_T, m and Z_T are not observable because they are blocked from view by other parts of the etch cone. This will always happen when the tracks are viewed on the upper surface of the plastic.

iii) Short range tracks whose range $< \Delta$, where Δ is the bulk etched layer of the CR-39, such that $M_i = m$, and consequently $M_j = X_T$. This is shown in the 0.80 hr etch time in Fig A6.32. The parameters M_j and M_i may or may not be equal. In this category the parameters (M_j, X_T) and $(M_i, m/2)$ are measurable. The parameter Z_T is not directly measurable.

These measurements are all obtained from the image, when the microscope is focussed on the (upper) surface of the CR-39. There are no plans at present to measure the depths of the tracks, from a stepping motor on the Z drive, for the reasons outlined above. However, in category (iii) above, for round tracks where $M_j = M_i = X_T = m$ only one independent measurement can be made. In this case a Z_T measurement would be desirable. This may be achievable from information present in the grey land distribution around the track when focussing on the plastic surface, without the need for taking image frames at other focal positions.

Track Analysis

The data from the image analysis program are passed to the track analysis program for the compilation of the input particle parameters. These parameters are:

1) The particle range at the plastic surface (and hence its energy).
2) The particle dip angle with respect to the plastic surface.
3) The characteristic bulk etching rate of the plastic, V_B.
4) The scale factor for the track etch rate range relationship that best fits the measured track parameters.
5) The etch induction time.

The analysis can cope with any arbitrary set of measured etch pit parameters and calculated any arbitrary combination of the input particle parameter listed above (provided a sufficient number of track parameters were measured).

Calibration of the CR-39

Sets of measured tracks are taken on CR-39 plates exposed through a step degrader to α-particles, and etched for different times.

The program can use this data to build up a new V_T-range curve, etch induction time-range curve even if the total range of the α-particles is not known. The new V_T-range and τ-range relationships can be compared with the previous curves, and iteration can be performed if necessary. This is the first time that a semi-automatic calculation of the V_T-range and τ-range curves has been accomplished (as compared to merely calculating scaling factors, as described earlier).

To date, the automated scanning image analysis system has measured ~10^5 α tracks compared to ~ 4 x 10^3 tracks by manual measurement in the whole history of the Track Analyiser group at Bristol, and is now an essential part of experiments using CR-39 at the CLF. In this report see Sections A1.4 - (Hot matter stopping power), Section A2.4 - (Rayleigh-Taylor instability) and Section A2.2 - (ablative compression).

A6.7.5 Barbee Mirror Characterisation

K Evans (Leceister University), A Cole (RAL)

The sample studied consisted of 75 periods of alternating W and C sputtered (by Professor Barbee, Stanford) on to a polished metal core (supplied by Astron) with nominal period 21Å. The full face area was some 9mm by 35mm. Assessment was required of the Bragg reflection behaviour exhibited at glancing angles 2° to 10°. Assessment was also needed of specular reflection at these angles to the extent that these

effects will reduce the signal/noise ratio in use of the Bragg reflections.

The sample was mounted to table 2 of the Leicester machine. Pairs of slits set a pencil beam of aperture 0.3mm by 2.00mm, collimated to 8.4 mins of arc. The X-ray tube was loaded to generate Moseley lines (by electron bombardment) at (among others) λ 9.89, 7.13, 6.99, 5.73, 3.74. A scan from 10° 00' to 5° 40' is shown in Fig A6.33. The scan was made with the beam passing a 25μm Be high-pass filter. From the predefined spectral content of the beam, an identification can be made of the lines observed. These are indicated on Fig A6.33 together with the literature value of the wavelength of that transition. The chart is accurately linear in glancing angle of the beam to the reflector; the end points are known to within a few arc minutes. Therefore any one of the lines recorded may be used as reference to make a first calculation of the grating period. The best recorded, and least ambiguous, line of the set is S K_α at λ 5.37. This gives an estimate of the grating period at 2d ≈ 43.8Å. Using this nominal value of the grating period the wavelengths of all the other lines recorded on Fig A6.32 could be calculated as a check on the identifications of the whole set, and therefore (importantly) on that of the S K_α line upon whose correct identification the calculated value of 2d depends. There can be no doubt that the identifications are correct; the spread of the differences between the calculated and literature values of the line wavelengths suggests an uncertainty on 2d of no more than 1 part in 200, so 2d = 43.8 ± 0.2Å. We note from Fig A6.33 that the two lines at λ 6.99 and λ 7.13 may be said to be just resolved. This requires a resolution $\Delta\lambda/\lambda \leq 1$ part in 50. Scans covering the range 5° → 2° show that the device is capable of strong specular reflection of softer radiations.

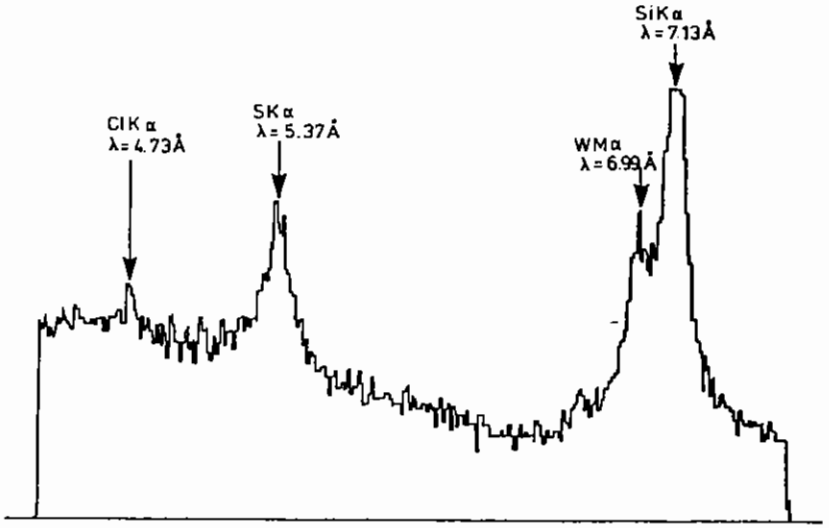

Fig A6.33 Reflection spectrum for W/C multilayer $10^{o} \rightarrow 5^{o}$

CHAPTER A6 REFERENCES

A6.1 C Danson, C Edwards, R Wyatt. The Vulcan Pulse Generating System. RAL Report 84-124 (1984)

A6.2 C Danson, C Edwards, I Ross A Pulse Stacker for time resolved plasma diagnostics. Optics and Laser Technology April (1985)

A6.3 W E Martin et al Solid State Disc Amplifiers for Fusion - Laser Systems IEEE. J. Qu. ElECT. QE17 1744 (1981)

A6.4 I N Ross. Design of Neodymium Glass Disc Amplifiers RAL. Report RL82-044 (1982)

A6.5 I Ross and E Hodgson. Some Optical Designs for the Generation of High Quality Line Foci. J. Phys. E. Sci Inst.18 169 (1985)

A6.6 C Lewis and J McGlinchey Quasi-monochromatic projection radiography of dense laser driven spherical targets Opt. Comm. (in press).

A6.7 Annual Report to the LFC RL-83-043 1.35 (1983)

Introduction

J Szechi, M J C Smith, G Hogg, F O'Neill (RAL)

The Ultraviolet Radiation Facility (UVRF) continued to provide laser radiation from the vacuum ultraviolet to the near infrared together with a range of diagnostic equipment. During the reporting year the facility was used for fundamental research in biology, chemistry and physics by groups from 13 Universities. Demand for use of the facility was very high and experiments proposed by five first-time users were incorporated in the year's schedule.

Studies involving resonance Raman spectroscopy accounted for a substantial fraction of the scheduled time and much progress was made in this area. A notable success in the application of Raman techniques in the biological field was the measurement of vibrational frequencies in an enzyme-substrate intermediate providing information on the hydrogen bonding in the intermediate. Important results were obtained in other areas of spectroscopy and photochemistry. The purchase of new equipment provided the experimenters with better diagnostic facilities. A new Innova argon ion laser has proved a useful aid in resonance Raman studies, and the new Ultraspec spectrophotometer is a useful aid in sample preparation.

While the lasers provided by the UVRF were maintained in operable condition for over 90% of the scheduled time, the need for a major overhaul became apparent. Arrangements were made at the end of the reporting year for service of the EMG 101 and EMG 150 lasers by Lambda Physik in Germany and improved performance is expected after they return from the manufacturer.

Towards the end of the reporting period a lot of effort was put into the development of new laboratory space and on the purchase of new lasers for the planned Laser Support Facility (LSF). From the end of April 1985 the UVRF will be incorporated into the LSF and this new facility will provide additional laser systems such as picosecond lasers and YAG pumped dye lasers.

B1 CHEMISTRY

B1.1 RESONANCE RAMAN SPECTROSCOPY

B1.1.1 Time-Resolved Resonance Raman Spectroscopy

J N Moore, D Phillips (The Royal Institution). P M Killough and R E Hester (York University).

a. Sulphonated anthraquinone derivatives

Investigations have continued into the resonance Raman spectroscopy of intermediate species observed in the photochemical reactions of several sulphonated anthraquinone derivatives. These molecules are of interest because of their high photochemical reactivity, applications as photosensitising agents, and possible use in the field of solar energy storage. The scheme for reaction following absorption of a photon, as obtained from transient absorption studies, is given in Fig B1.1. The singlet state is too short-lived to be observed in these experiments, but the triplet, transients B and C, the semiquinone radical anion and its protonated form, the neutral radical, have lifetimes which allow study with the nanosecond time resolution available here. The experimental arrangement is given in Fig B1.2.

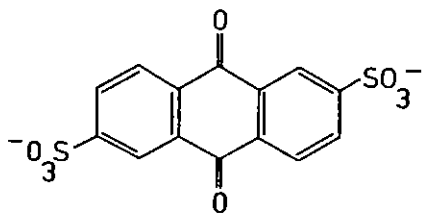

Anthraquinone-2,6-disulphonate

The sample is pumped into the excited state by excimer 1 using XeF to give output at 351 nm. The dye laser, delayed by a suitable time from

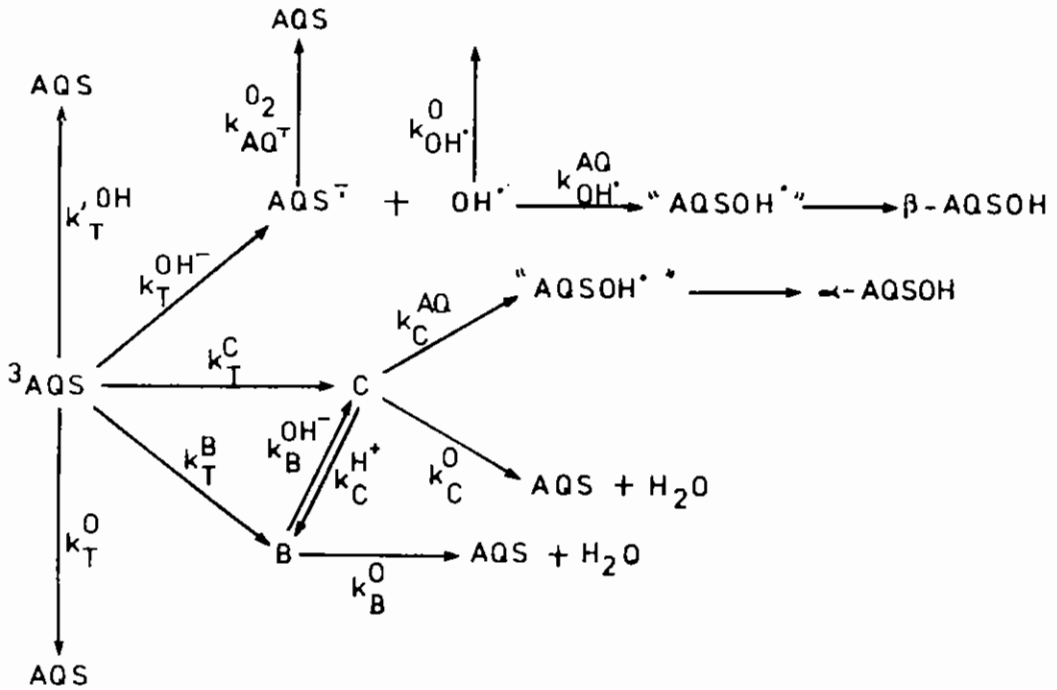

Figure B1.1

the pump pulse, is then used to probe the resonance Raman spectra of the various species formed following photolysis. By varying the time delay between the two lasers the time dependence of the transients may be studied. Changing the probe laser wavelength in the range 400-560 nm allows the various absorption bands to be tuned into, thereby giving resonance enhancement of the species associated with each absorption band selectively.

Spectra have been obtained for all five species stated above as suitable candidates for observation. The radical anion, $AQ^{-\cdot}$, has produced the highest quality spectra and the time dependence of this anion is shown in Fig B1.3. Here, the species is produced by electron transfer from nitrite ion to the triplet and the decay is due to quenching by oxygen. This spectrum is observed at 480 nm, but by tuning the probe laser to wavelengths shorter than 425 nm and adjusting the pH of the sample to less than 2, the protonated form, $AQH^\cdot$, may be detected. The other species have proved more difficult to characterise because of two photon effects encountered using the high power densities of the focussed dye laser, but nevertheless their spectra have been obtained and kinetic properties studied. Polarisation studies are presently underway to determine the symmetry properties of the vibrations observed.

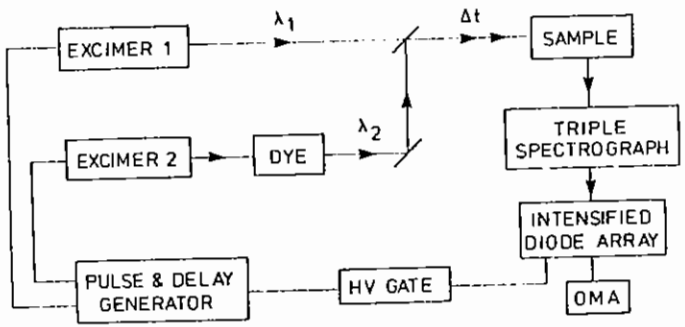

Figure B1.2

b. 7-Hydroxyflavone and related compounds

Proton transfer reactions in electronically excited states are important in understanding the nature of those excited states, and are of widespread photochemical importance. Frequently the reactions, involving singlet states, are rapid and require observations on the picosecond timescale. However, 7-Hydroxyflavone and several related compounds have been studied recently by transient absorption and fluorescence techniques and have been found to produce tautomers by excited state proton transfer which in their ground state have lifetimes in the nanosecond to microsecond regime. These studies have tentatively assigned the structures of the tautomers, but without any observation of the vibrational bands needed to confirm such

assignments. Hence time-resolved resonance Raman studies have been undertaken to achieve this.

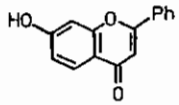

7-Hydroxyflavone

7-hydroxyflavone has been excited at 351 nm, and probe wavelengths of 370-425 nm have been used to observe the resonance Raman scattering. Despite the strong methanol solvent bands present in the region of observation, spectra due to both ground state tautomers have been observed and their time dependencies studied. These seem to correlate well with the lifetimes reported in the transient absorption studies, and work is continuing to assign the bands and determine the structures of the species.

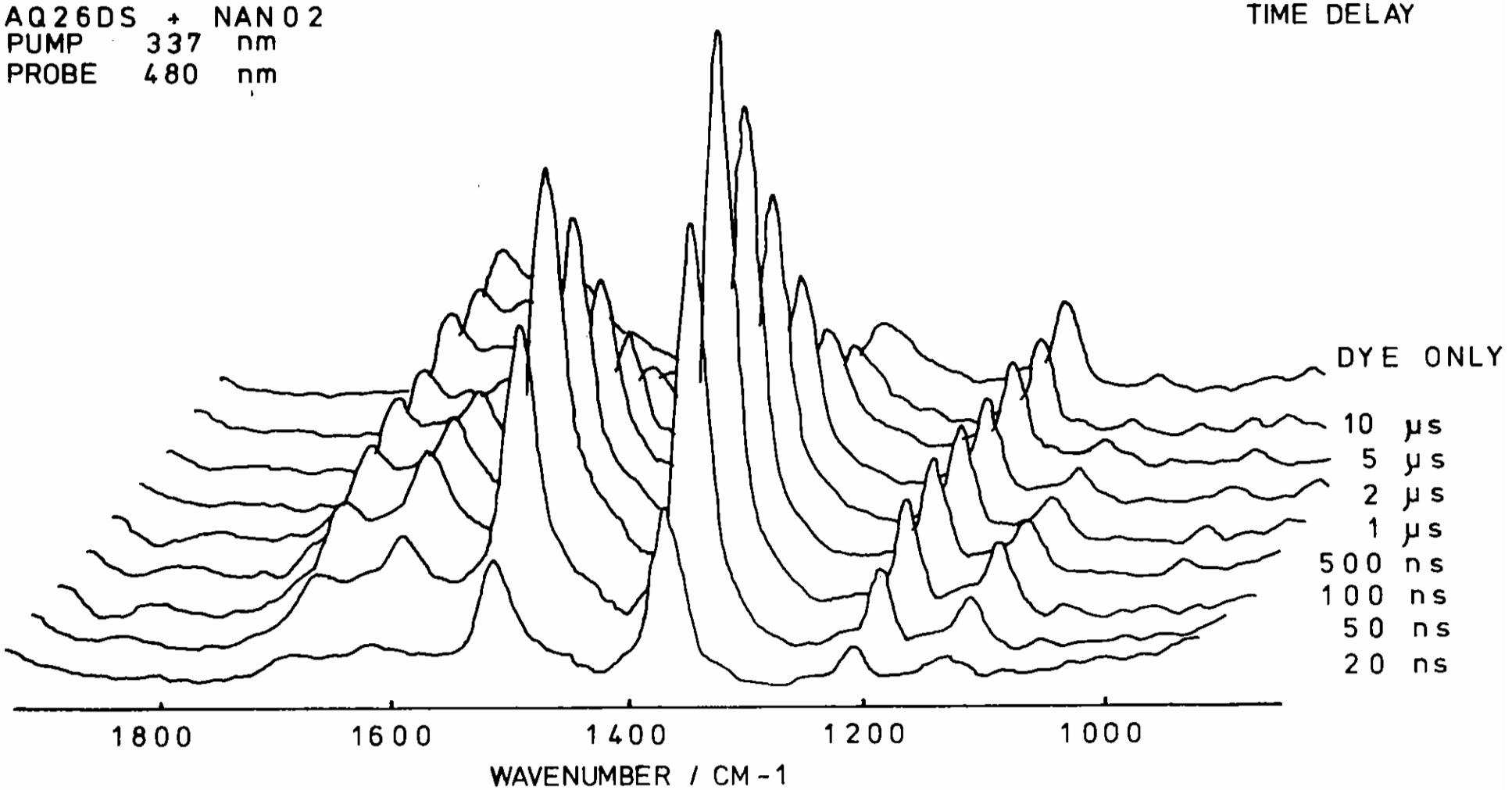
AQ26DS + NAN02
PUMP 337 nm
PROBE 480 nm
TIME DELAY
DYE ONLY
10 µs
5 µs
2 µs
1 µs
500 ns
100 ns
50 ns
20 ns
1800
1600
1400
1200
1000
WAVENUMBER / CM-1

Figure B1.3

B1.1.2 UV Surface Enhanced Resonance Raman Spectroscopy (SERRS)

R E Hester, A C Gorvin, J de Groot and R B Girling (York University)

Surface Enhanced Raman Scattering (SERS), has been used in many recent investigations to further understanding of surface chemistry and alsc as a means of obtaining spectra from very small quantities of material. The effect has been shown to be strongest for silver and gold sols and electrodes illuminated with red laser light. However, it has been shown recently that if the material absorbed to the metal surface has an absorption band in the short-wavelength visible spectrum, then the maximum of the excitation profile moves from the red to the approximate position of the absorption peak of the adsorbate. This is the SERRS effect.

Many molecules absorb light in the UV, and if this shift of the excitation profile applied to the UV as it does to the visible then many molecules would become available for study. A study of UVSERRS effects could help to elucidate the fundamental mechanisms of this new phenomenon.

The colloids which formed the main part of our first set of experiments were examined using the jet and pump which has been described in previous reports. The colloids remained stable in this system provided the flow rate was maintained a a minimum compatible with an even flow from the jet. It was found that too high flow rates caused aggregation of the sol with consequent loss of the SERRS effect. The laser power was reduced to approximately 3mJ (measured before the sample illumination optics) and the beam was focussed below the jet.

The experiments on electrode surfaces were carried out using an electrochemical cell illustrated in Fig B1.4.

The laser was focussed above the electrode surface to avoid damage to the cell window. The electrode was aligned by using an argon ion cw laser before switching to the line narrowed KrF laser.

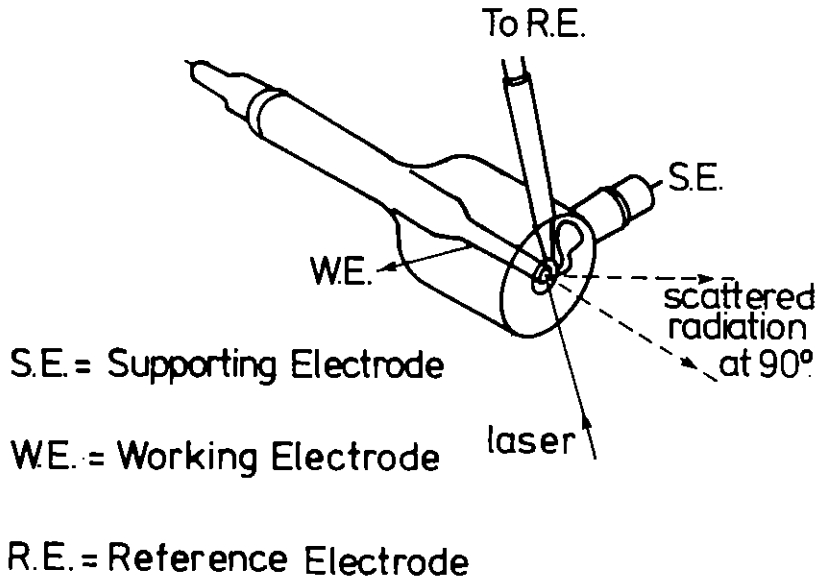

Figure B1.4 The electrochemical cell used for SERRS experiments and the study of chemically modified electrodes

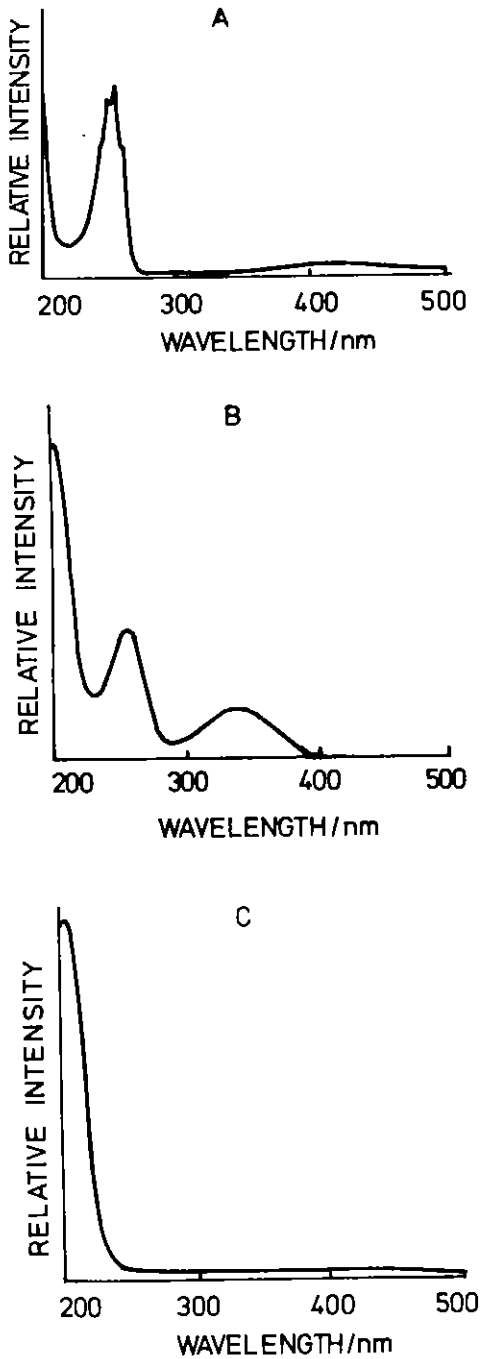

Figure B1. 5 UV/vis. absorption spectra of A- pyridine; B- NADH; C- pyrrole.

Pyridine was selected as the first molecule to be studied as it is well documented in the literature and has been used as a standard in SERS experiments. Pyridine has a strong absorption band in the region of the 248 nm laser line (Fig B1.5), indicating that the SERRS effect should work well for this molecule.

Initially a RRS was sought from the pyridine. An aqueous solution of 1 x 10^{-3} M pyridine was prepared and aligned without a RRS from pyridine being observed. The concentration of the pyridine was then varied between neat and 1 x 10^{-6} M without observing a RRS from any of these solutions.

A small quantity of pyridine was added to a sol in an attempt to observe SERRS despite the lack of a resonance Raman spectrum, but again without success.

NADH was selected as the next molecule to be studied. It has an absorption maximum at 260 nm (Fig B1.5) and adsorbs on silver quite readily.

In addition its RRS had already been obtained with 248 nm excitation (see last year's report). The RRS was obtained at first in a repeat of the previous experiment. On addition of the silver sol to the NADH solution the RRS was observed to decrease in intensity slightly, rather than increase in intensity as expected if the SERRS effect was in operation. The decrease in intensity can be explained by the dilution of the sample upon addition to the silver sol.

The experiment was repeated with a gold sol, when the same effect was observed.

Tests were carried out for SERRS with pyrrole as the adsorbed molecule; this molecule adsorbs weakly in the region of the laser (Fig B1.5) and a RRS was obtained from a 10^{-1} M solution. However, upon addition of the sol no enhancement was observed; in fact a decrease in the quality of the spectrum was noted similar to the effect observed with NADH.

Finally an experiment was carried out to try to obtain a SERRS spectrum from pyrrole adsorbed onto a silver electrode suitably prepared to generate surface enhancement. This experiment also proved to be fruitless.

From these experiments we have established that the SERRS effect cannot be seen in the UV when excited with high peak power excimer lasers. It is a matter of concern that we could not see a RRS for pyridine and, since the gold and silver sols used absorb strongly in this region, as does pyridine, it is possible that the samples are being "burnt out". Two further experiments are therefore suggested before this set of negative results can be completely analysed. First, a system known to give SERRS in the visible region with cw lasers should be illuminated with the excimer/dye laser in an appropriate spectral region. Secondly, if possible, a low peak power UV laser should be used to try to obtain a RRS of pyridine and SERRS spectra.

B1.1.3 Raman spectra from modified electrodes

R E Hester, A C Gorvin, J de Groot and R B Girling (York University)

Little progress has been made on this area of research this year. However, we have managed to gain some valuable experience in the use of the electrochemical cell and we are now confident that useful results could be achieved next year.

When we first started to use the cell we found that we very easily damaged the silica window by focussing the laser incorrectly. We then tried focussing the laser above the electrode rather than below it (as is normally done with capillary tubes or with the jet). This had the effect of defocussing the laser beam at the electrode surface and also giving a low power density at the cell window.

At first we were unable to see any scattering from the electrode surface or reflections from the cell window collected by the ellipsoidal mirror and focussed onto the spectrometer entrance slit. This was probably due to the very low laser powers used, for fear of damaging the cell window. With the new focussing arrangement we were

able to increase the power of the laser to about 3mJ and were then able to see the pattern of reflected light and scatter from the electrode that we had expected.

We also found that we were able to align the scattered light collection optics by observing the intense water band at about 3200 cm^{-1}. Although the amount of light scattered by the water between the electrode surface and the cell window is very small, giving only weak Raman spectra, it is nonetheless sufficient to correctly align the cell and collection optics.

We reached this stage on our last visit to the Laboratory. We made no further progress due to the instabilities of the KrF laser at that time. We feel confident now though that it is possible to examine an electrode surface, modified by an organic polymer, without damage to the surface or the cell. Over the next year we should obtain some useful results from this line of research.

B1.1.4 Resonance Raman spectroscopy of change-transfer excited states of Copper (I) complexes.

S E J Bell, J Lawthers and J J McGarvey (Queen's University Belfast)

a. Introduction

Resonance Raman (RR) spectroscopy has recently been employed in several instances as a structural probe of the excited states of transition metal complexes (B1.1), notably of polypyridyl complexes of Ruthenium (II) which are of interest in relation to solar energy conversion schemes. Also of interest in this respect are the metal-to-ligand charge-transfer (MLCT) excited states of Copper (I) complexes, $Cu(L)_2^+$, with ligands such as 1,10 phenanthroline (P), 2,9-dimethyl-1,10 phenanthroline (DMP) and 2,9-diphenyl 1,10-phenanthroline (DPP) which

appear to have considerable potential application in photoelectrochemical systems (B1.2). Using a pulsed Nd^{3+}/YAG laser at QUB we have recently recorded the MLCT excited state absorption (ESA) spectra of $Cu(DMP)_2^+$ and Cu $(DPP)_2^+$ and we now report the results of preliminary investigations at RAL of the RR spectroscopy of these two complexes and also of Cu $(P)_2^+$.

b. Experimental

The RR spectra were generated by means of the FL2002E pulsed dye laser using excitation wavelengths in the regions of 390 nm and 460nm. The pulsed laser beam (rep. rate 10Hz)was brought to a focus slightly above a quartz capillary sample-tube, typical pre-focus laser energies being in the range (3-8)mJ/pulse. Solutions of the complexes (ca.10^{-3}mol dm^{-3}) in dichloromethane or chloroform were purged with argon and injected from a syringe through the capillary generally at flow rates > 10ml/min. to minimize heating and/or photodecomposition of sample. The 90° Raman scattered radiation was dispersed by the Triplemate spectrograph (600 lines/mm grating) onto the diode array OMA2. Gating of the array was imperative in order to achieve acceptable spectral resolution. Raman spectra of indene and cyclohexane, recorded on static samples under the same optical condition as the complex solutions, were used for frequency (cm^{-1}) calibration.

c. Results and Discussion

Due to the relatively small amounts of samples available and the necessity to use fast flow rates, the number of spectral scans on each sample was kept to a minimum. In some instances this amounted to the accumulation of as few as sixty laser shots per sample. The three complexes display strong MLCT absorption bands in the visible region and the RR spectra of $Cu(P)_2^+$ and $Cu(DMP)_2^+$, both excited at λ_{EX} = 457.9nm, are shown in Fig B1.6 (a),(b). They exhibit substantially

the same pattern of peaks as published ground electronic state (g.s.) RR spectra of $Fe(P)_3^{2+}$(B1.3) and $Ru(P)_3^{2+}$in which the bands have been assigned to skeletal stretching vibrations of the ligands. The most prominent feature in all of the spectra is a peak in the region of 1430cm^{-1}. RR spectra of $Cu(P)_2^+$ and $Cu(DPP)_2^+$ identical to those in (a) and (b) (within the uncertainties of the cm^{-1} measurements) have also been observed under cw excitation (at QUB) with an Ar^+laser at 488nm. It therefore appears that the spectra in Fig B1.6 (a) and (b) recorded under pulsed dye laser excitation are g.s. spectra, with no features attributable to the MLCT excited state. This is not unexpected, particularly in the case of $Cu(P)_2^+$ where the lifetime of the MLCT state in short (<1ns) in comparison with the dye laser pulse duration. Furthermore, λ_{EX} = 457.9nm is well removed from λ_{max} in the ESA spectrum so that negligible resonance enhancement of the Raman scattering from this state should be expected. The RR spectrum in Fig B1.6(c) is that of $Cu(DPP)_2$ generated at λ_{EX} = 385nm. A striking difference compared to the spectra in (a) and (b) is the absence of the feature at 1430cm^{-1} and the emergence of new features at ca.1413cm^{-1}. The reproducibility of the spectra is demonstrated by the two traces in (c) recorded in separate runs on fresh samples. The significant point about the spectrum is that λ_{EX} is almost coincident with λ_{max} in the ESA spectrum (shown in Fig B1.7) of the MLCT state of $Cu(DPP)_2^+$.

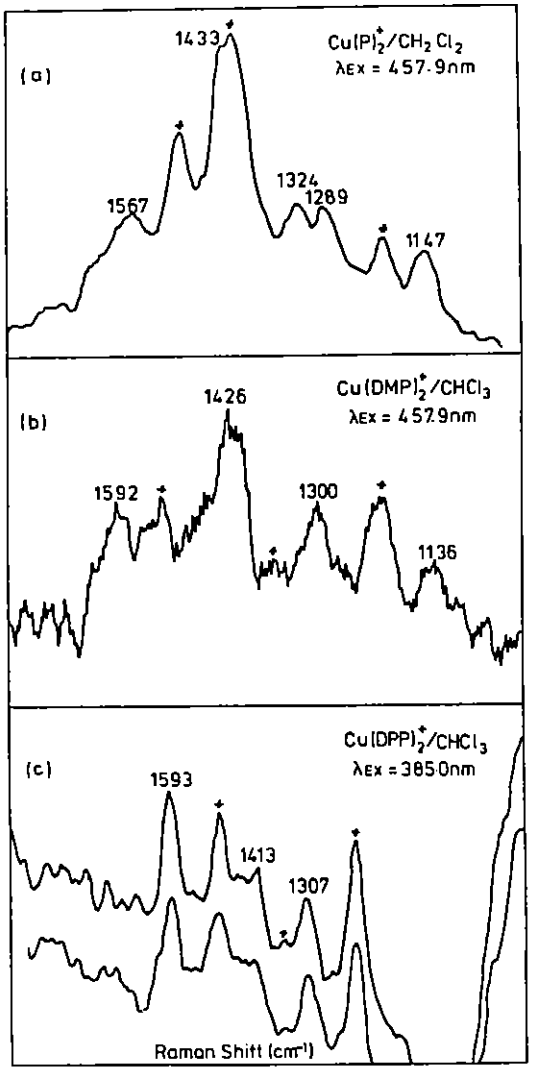

Figure B1.6 Dye laser-generated resonance Raman spectra of $Cu(L)^+_2$ complexes in solution. (#denotes solvent peaks)

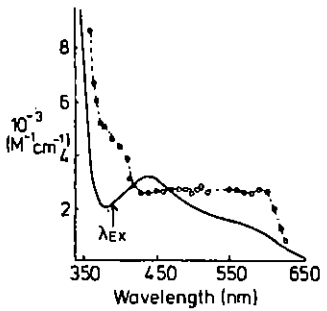

Figure B1.7

Ground (_____) and MLCT excited state in CH_2Cl_2. (↑ marks dye laser excitation (----------) absorption spectra of $Cu(DPP)^+_2$ wavelength for RR spectrum in Fig 1(c)).

Although two of the peaks in the RR spectrum are close to those in the g.s. spectrum (b) of $Cu(DMP)^+_2$ their intensities suggest that they are unlikely to be due to g.s. scattering since substantial depletion of the g.s. occurs under the excitation conditions used for the generation of spectrum (c) where the number of photons is estimated to exceed by a factor of (2-3) the number of absorbing species in the irradiated volume. The lifetime of the MLCT state of $Cu(DPP)^+_2$ in $CHCP_3$ is >200ns so that a considerable concentration can be created during the laser pulse. We tentatively suggest that the spectrum in Fig B1.6(c) may be attributable to RR scattering from this MLCT state i.e. the same laser pulse serves both to populate and to interrogate the excited state. If this tentative assignment is correct (see below) then the persistence in spectrum (c) of frequencies characteristic of the neutral DPP ligand would suggest that the MLCT excited state may be formulated as $Cu^{II}(DPP)(DPP)^{\bullet-}$, with the 'transferred' electron localized on one of the ligands. The evidence for the assignment is obviously far from complete and to substantiate it, studies are in progress on the electronic absorption and Raman spectroscopy of the radical anions $(DMP)^{\bullet-}$ and $(DPP)^{\bullet-}$. A 'true' g.s. RR spectrum of $Cu(DPP)^+_2$, generated by cw excitation at 385nm, should also be recorded to rule out the possibility that spectrum (c) may arise from selective enhancement of different g.s. vibrational modes when λ_{EX} is altered from 457.9nm to 385nm. Further support for the proposed

assignment should be provided by measuring Raman excitation profiles of the MLCT excited state and by two-laser pump-probe experiments. It is hoped to initiate such studies in future visits to RAL.

B1.2 NON LINEAR SPECTROSCOPY

B1.2.1 Two-Photon Spectroscopy of Uranyl Compounds

R G Denning, J R G Thorne and T J Barker (Oxford University)

The covalent bond in actinide chemistry is seen in its simplest and most striking form in the actinyl ions MO_2^{2+}. These centrosymmetric ions provide a straightforward test of our understanding of the covalent bond in these elements. The metal-oxygen bond is exceptionally short and strong; the half-life for oxygen exchange in aqueous solution is greater than 4×10^4 hours. Any analysis of the bonding requires an understanding of the role of 5f, 6d and 6p metal orbitals, as well as the oxygen orbitals. The optical spectrum is very helpful in assessing the nature of the first excited configurations, and has been the subject of a series of polarised single-photon studies in a number of different symmetries (B1.4). The visible spectrum is highly structured and complex and is composed of vibronic structure originating from as many as six doubly degenerate states of the cylindrical ion, split to differing degrees by the equatorial field. Those pure electronic transitions which are directly observed have polarisations, in centrosymmetric sites, indicating that they are parity forbidden. Taken together with the angular-momentum properties of the excited states it appears that the excited states have a configuration $\gamma_u\gamma_u'$, where γ_u is an oxygen based molecular orbital and γ_u' is an f-orbital. The exact nature of γ_u and γ_u' has been the source of some controversy, with the possibilities that γ_u is either σ_u or π_u. The latter choice predicts twice the number of excited states within the same region of the spectrum, and the question inevitably arises as to whether all the excited states have been observed and their symmetries correctly assigned. In a spectrum with considerable vibronic complexity this question cannot be answered conclusively. In $Cs_2UO_2C\ell_4$, a total of twelve electronic excited states are inferred from the vibronic structure, but only seven no-phonon transitions are

directly observed, the location and symmetry of the remainder being deduced from subtleties of the vibrational structure.

We have studied single crystals of $Cs_2UO_2C\ell_4$ by two-photon luminescence excitation at 4.2K, with 0.2A resolution in the range of photon energies between 10,400 cm^{-1} and 14,400 cm^{-1}, giving access to most of the region where the single-photon spectrum has been studied precisely (B1.4). It was necessary to use a large range of dyes; IR-140, Dibenzocyanin, Oxazine-750, Styryl 9, Hexacyanine-3, Nile Blue, DCM and Sulpharhodamine B. In the approximate D_{2h} site symmetry, four distinct polarizations are expected with excited state symmetries $A_{1g}(xx,yy,zz)$, $B_{1g}(xy)$, $B_{2g}(xz)$, $B_{3g}(yz)$, where the brackets indicate the polarisations of the two-photons creating the transition. Our experiments have concentrated on the yy,xy, and yz polarisations.

Figure B1.8 contains a survey of a small portion of the yy polarisation showing its comparison with the same region in single-photon absorption. The two-photon spectrum excludes most of the vibronic structure. The most intense features in the spectrum are pure electronic transitions (and progressions thereon) most of which have not been observed previously.

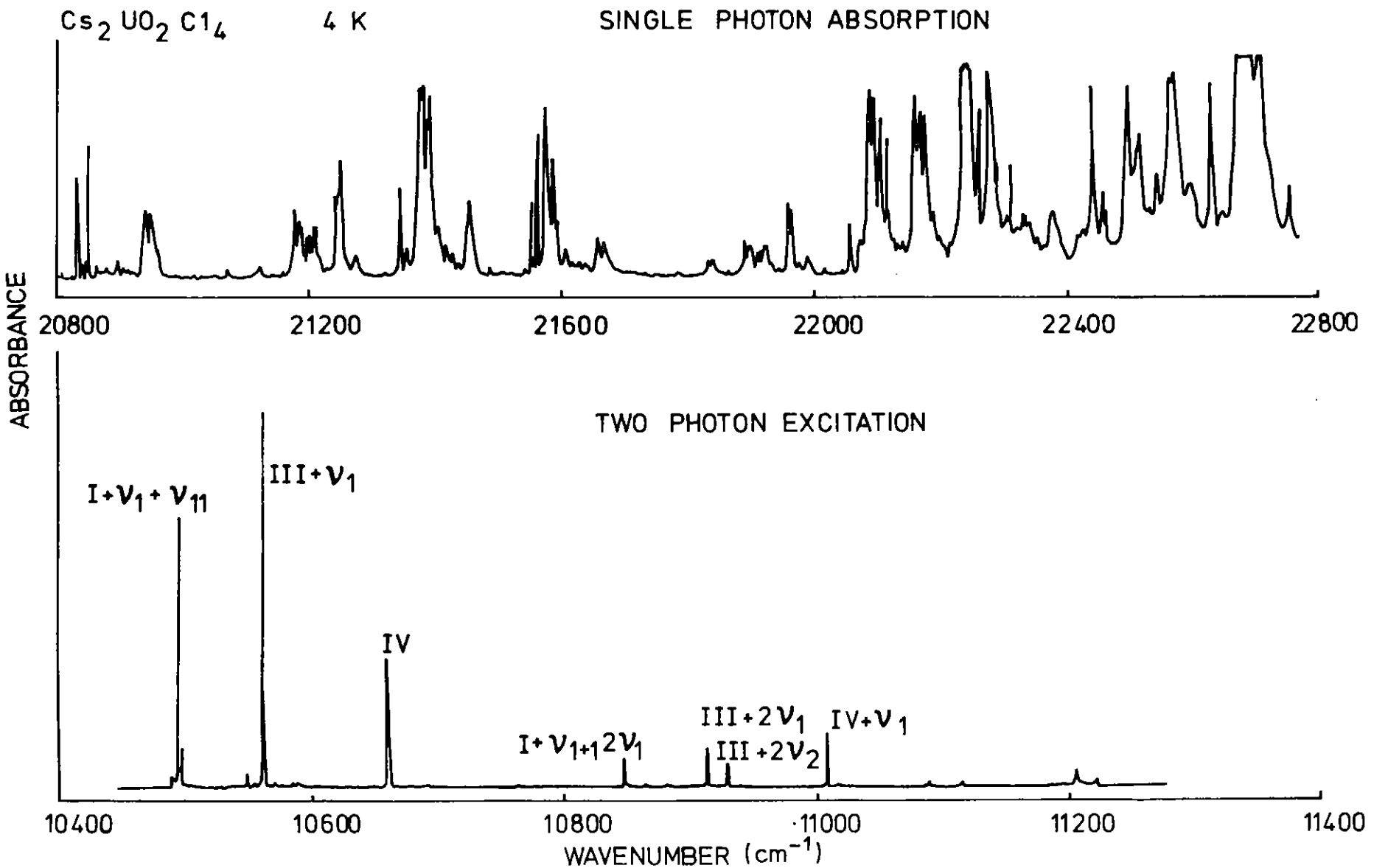
$Cs_2UO_2Cl_4$
4 K
SINGLE PHOTON ABSORPTION
ABSORBANCE
20800
21200
21600
22000
22400
22800
TWO PHOTON EXCITATION
I+ν1+ν11
III+ν1
IV
I+ν1+1 2ν1
III+2ν1
III+2ν2
IV+ν1
10400
10600
10800
11000
11200
11400
WAVENUMBER (cm−1)

Figure B1.8

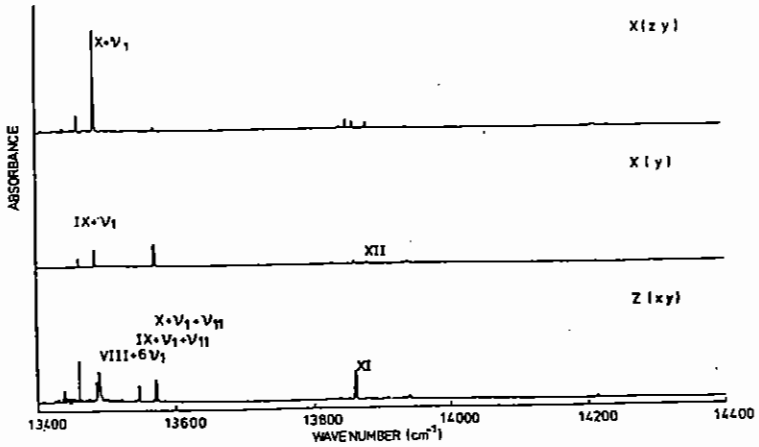

Figure B1.9

Figure B1.9 shows an example of the three polarisations, from which the symmetry of the transitions is readily inferred. Table B1.1 summarises the energies, symmetries and polarisation of the various excited states.

Table B1.1

Origin	D_{2h} Symmetry	Wavenumber	Single-photon	Transition Mechanism Obs	Two-photon	Obs
I	B_{2g}	20,095.7	μ_y	/	xz	/
II	B_{3g}	20,097.3	μ_x	/	yz	/
III	B_{1g}	20,406.5	θ_{xy}	/	xy	/
IV	A_g	21,313.8	$\theta_{x^2-y^2}$	-	yy	/
V	B_{2g}	22,026	μ_y	/	xz	-
VI	B_{3g}	22,076	μ_x	-	yz	-
VII	A_g	22,410	$\theta_{x^2-y^2}$	-	yy	/
VIII	B_{1g}	22,755	θ_{xy}	-	xy	/
IX	B_{2g}	26,197.3	μ_x	/	xz	/
X	B_{3g}	26,247.6	μ_x	/	yz	/
XI	B_{1g}	27,721	μ_z	/	xy	/
XII	A_g	27,758.0	$\theta_{x^2-y^2}$	-	yy	/

The observations in the two-photon spectrum, confirm the symmetries of the excited states, and give important support to the theoretical model we have developed to interpret the energies of the states (B1.5). There is much additional detail in the spectrum, on account of its sharpness and relative simplicity.

There are four major points which the two-photon spectrum clarifies. First, the anharmonicity in the progression is easily measured, and the anharmonic coupling between the symmetric and asymmetric stretching frequencies of the uranyl group is obvious, but differs in magnitude between the various electronic states, promising an electronic interpretation of the anharmonicity. Second, the role of the uranyl rocking mode, is very pronounced. The polarisation of those features due to it suggests that the vibration provides intensity via the virtual intermediate state. Third, the energy ordering of origins VII and VIII and origins III and IV, which is confirmed by the two-photon

selection rules, reflects the influence of the tetragonal field on states with $\sigma_u \delta_u$ configurational parentage. The relative order actually fixes the predominant spin configuration of the parent states and is valuable in defining the ordering of the possible configurations. Fourth, the totally symmetric uranium chlorine stretching frequency can be identified coupled to the excited states. Its frequency is within $1cm^{-1}$ of the value in the ground state. It follows that the excitation has a negligible influence on the primarily ionic uranium-chlorine bond. If the excitation has a strong charge-transfer component the change in charge on the uranium would lower this frequency, so the result implies a strongly one-centre transition - a result which supports the most recent theoretical models of the bonding (B1.6).

We wish to acknowledge support from the SERC as well as the invaluable assistance of UVRF staff.

B1.2.2 Multiphoton Ionisation of H_2O and D_2O

M N R Ashfold and J M Bayley (University of Bristol)

The water molecule has long been popular as a model system for testing our understanding of the dynamics of molecular photofragmentation processes. Within the past year, the predissociation of its $\tilde{C}^1B_1$ Rydberg state has been investigated in a fully quantum state specific manner (B1.7). .The success of that study - the first to achieve such full quantum state selection in both the fragmenting parent molecule and in the resulting photoproducts - was dependent upon a number of factors, not the least of which being the availability of the suitably intense, tunable narrow band laser required for the multiphoton preparation of the water molecules in the selected quantum levels of the C electronic state. A detailed prior knowledge of the excited state energy levels was vital also. In the case of $H_2O(\tilde{C})$ this information was available from conventional vacuum ultraviolet (vuv) absorption spectroscopy (B1.8) and from more recent multiphoton

ionisation (MPI) studies involving the water molecule (B1.9) . In the latter studies, the $\tilde{C}$ electronic state.

The water molecule possesses numerous higher energy Rydberg states, many of which predissociate at a rate that is sufficiently slow ($k < 10^{12}s^{-1}$) to suggest that they should show up as rotationally structured three photon resonances in four photon MPI spectra. In this way the $\tilde{D}'^1B_1$ and $\tilde{D}^{-1}A_2$ electronic states, and their respective predissociation behaviours, were characterised (B1.11). These studies were extended to slightly higher energies at the Rutherford UVRF through use of an excimer laser (KrF, 248 nm) pumped tunable dye laser (Lambda-Physik EMG 150 and FL 2002 rspectively) operating on the dye p-terphenyl. This system produced tunable dye laser light of adequate intensity down to $\lambda \geq 330$ nm with which it proved possible to obtain the MPI spectrum of D_2O displayed in Fig B1.10. Details of the experimental technique has been presented previously (B1.9), (B1.11).

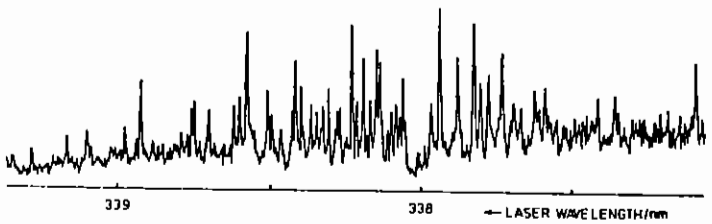

Figure B1.10 MPI signal from 5 Torr D_2O as a function of laser excitation wavelength, obtained using linearly polarised 2 mJ dye laser pulses.

The resonances apparent in Fig B1.10 correspond to three photon

excitations to individual rotational levels of the vibrational origin of the $\tilde{E}^1B_1$ ($3da_1 + 2b_1$) Rydberg state of D_2O. Analysis yields the following spectroscopic constants (in cm^{-1}) for the excited state: ν_o = 89717.8± 0.5, A' = 16.09 ± 0.05, B' = 5.41 ± 0.04, C' = 4.27 ± 0.02. As with the lower energy $^1B_1$ electronic states of H_2O and D_2O (B1.9),(B1.11) the rate of predissociation from the $\tilde{E}^1B_1$ state is seen to depend sensitively upon the parent rotational quantum state and, in particular, upon the amount of a-axis rotational angular momentum associated with that level. $\tilde{E}$ state rotational levels for which $\langle J_a^2 \rangle$ >>0 predissociate so fast that transitions involving these levels fail to show up as resonances in the MPI spectrum; conversely, those with $\langle J_a^2 \rangle$ = 0 show particularly intensely. The observation may be rationalised in terms of a heterogeneous predissociation of the $\tilde{E}^1B_1$ state brought about via Coriolis coupling to a dissociative electronic state of A_1 symmetry.

B1.3 PHOTOCHEMISTRY

B1.3.1 Energy Disposal in Simple Chemical Reactions

N J Dutton, I W Fletcher and J C Whitehead (Manchester University)

The reactions

$$I(^2P_{3/2}) + F_2 \rightarrow IF(v,J) + F$$

$$I^*(^2P_{1/2}) + F_2 \rightarrow IF(v,J) + F$$

are important steps in the iodine/fluorine system that is used as source of IF for the IF chemical laser. We have commenced a study to determine the IF vibrational and rotational state distributions under collision free conditions. The iodine atoms are generated by excimer photolysis

$$C_6H_5I \xrightarrow{193\pm nm} C_6H_5 + I(^2P_{3/2})$$

and

$$C_2F_5I \xrightarrow{248 nm} C_2F_5 + I^*(^2P_{1/2})$$

in a flowing system containing about 10 m Torr RI, 15 m Torr F_2 and 300 m Torr He. The IF internal state distributions are determined by laser-induced fluorescence using the tuneable output of an excimer-pumped dye laser. The dye laser is triggered about 240 ns after the photolysis laser to ensure that the IF product is detected before any relaxing collisions have taken place.

Fig B1.11 shows a portion of the (5,0) band of IF produced by the reaction $I + F_2 \rightarrow IF + F$. The spectrum indicates a rotational temperature of 250K.

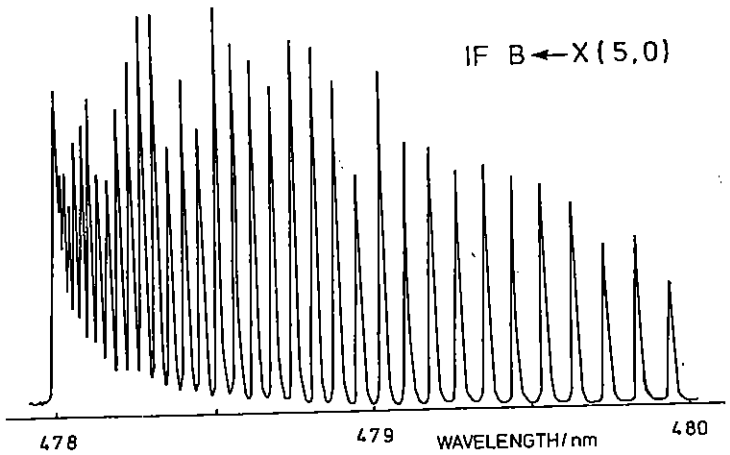

Figure B1.11

Continued work is required to completely characterise the IF vibrational and rotational distributions from each reaction.

B1.3.2 Colloidal Photochemistry

G T Brown and J R Darwent (Birkbeck College, London)

Electrostatic fields at solid/liquid interfaces can be used to catalyse or direct competing chemical reactions. This property has been exploited in a number of novel systems for Solar Energy conversion. The phenomenum is also important in electrochemistry and interface science. The photochemistry of semiconductor colloids has only attracted attention in recent years and represents a rich area for new chemical studies.(B1.12) The colloids are transparent and well suited to time-resolved techniques such as flash photolysis and resonance Raman spectroscopy.(B1.13) As a result, they can provide unique information about the parameters which control interfacial electron transfer.

Our preliminary experiments at the UVRF were designed to exploit the time and spectral resolution available with the EMG 101E XeCl excimer laser. The emission wavelength (308 nm) is particularly suitable for exciting colloidal TiO_2 and the 20 ns time resolution was a significant improvement on our microsecond equipment at Birkbeck. Consequently we were able to extend our studies on interfacial electrons and begin to explore the effect of surface charge when there is a large overvoltage for the reaction. A simple test reaction was chosen that involves electron transfer from TiO_2 to the cation methyl viologen (N,N'dimethyl-4,4' bipyridine).(B1.14)

Previous work in our laboratory has shown that for TiO_2 in the pH region 2 - 6 the rate is controlled by the thermodynamic driving force (Taffel Equation) and electrostatics.(B1.14) Since the surface charge on the colloidal particles changes from positive to negative in this region there can be dramatic changes in the electrostatic forces. Indeed we find that the electrochemical rate constant (k_{et} cm/s) is sensitive to pH and ionic strength (I dm^3 mol^{-1}) so that

1) $\log k_{et} = \log k^{\Theta}_{et} + \alpha\,(pH - PZZP)$

and

2) $\alpha = \alpha_o + \beta / \sqrt{I}$

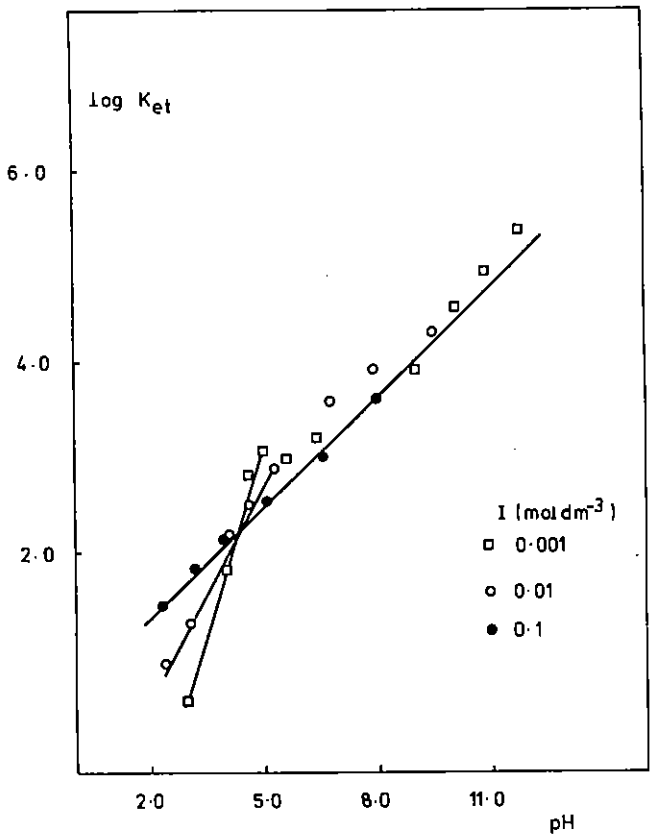

Figure B1.12 Variation in pseudo first-order rate constants for reduction of methyl viologen with pH and ionic strength.

where α_o and β are constants and $k^{\ominus}_{et}$ is the electrochemical rate constant when the surface charge is zero, i.e. at the point of zero zeta potential (PZZP). The experiments at the UVRF were designed to test the validity of equations (1) and (2) at high pH when the thermodynamic driving force and surface charge are large.

The work was very successful and the results are summarised in Figure B1.12.

Both ionic strength and pH have charge transfer so that the rate can change by a factor of 10,000. Whereas the rate is sensitive to ionic strength in between pH 2 and 6, it has little effect above pH 7. In this region the reaction is dominated by the thermodynamic term. This may result from variations in the number of ions adsorbed in the Helmoltz layer on the surface of the particles. For example if more ions are adsorbed at low ionic strengths this will reduce the electrostatic attraction and moderate the ionic strength effect. Further experiments will be needed to test this hypothesis.

B1.4 LASER INDUCED FLUORESCENCE

B1.4.1 Oscillatory continuum emission from IBr, Br_2, I_2 and other work

J P T Wilkinson, R J Donovan, D Austin, M MacDonald (Edinburgh University) and A Hopkirk (Keele University)

The studies on the oscillatory continuum emission from bound-free transitions in the molecular halogens and interhalogens were pursued with particular regard to improving the resolution of spectra. Studies of the spectra of both I_2 and IBr were carried out by using the line-narrowed ArF laser in an attempt to reduce spectral congestion which can result in the simultaneous pumping of a number of vibrational levels when using a broad-band ArF laser. In both cases no significant change in structure was discernable. However, for IBr the spectra

obtained were of much higher quality than those produced with broad-band ArF excitation. Also, the use of the tunability of the line-narrowed source led to a better understanding of the nature of the IBr transition which gives rise to the bound-free fluorescence since the tuning range of the ArF laser encompasses three prominent Rydberg features in its absorption spectrum. Tuning the laser over the entire line-narrowed range did not lead to any significant change in the fluorescence yield and this reaffirmed our conclusion that the transition leading to the bound-free fluorescence is to a weak ion-pair state absorption which underlies the much stronger Rydberg state absorption.

The studies of Br_2 used fluorine laser radiation at 157nm to excite fluorescence. Previous studies had shown unexpected spectral complexity (in comparison to that found for I_2) and this had been tentatively ascribed to the presence of three different isotopic variants, $^{81,81}Br_2$, $^{81,79}Br_2$ and $^{79,79}Br_2$. We thus carried out experiments on an isotopically pure sample of $^{81,81}Br_2$ and the results obtained clearly demonstrated that the mixed isotope spectra were indeed complicated by emission from different isotopic variants. Analysis of the $^{81,81}Br_2$ spectra using the Edinburgh computer codes is presently being undertaken.

Further study of the $CN(A^2\pi)$ emission following photodissociation of ICN at 157nm (F_2 laser), has been greatly facilitated by the use of the Oxford Lasers EX-1 laser. The much higher powers available have enabled the recording of well resolved spectra using far fewer laser shots than in previous experiments. The recording of the emission system using a mixture of ICN with a large excess of helium has enabled us to make a more definitive assignment of the vibrational distribution for the $CN(A^2\pi)$ photofragment due to the easing of the problems associated with rotational congestion, see Fig B1.13. A more detailed report on this work is in preparation.

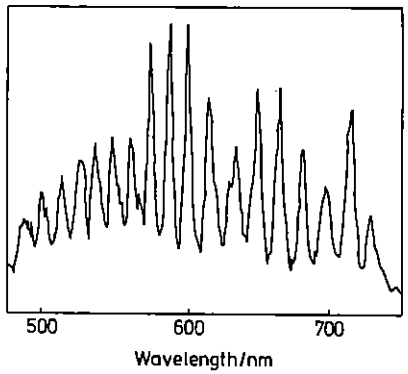

Figure B1.13 $CN(A^2\Pi_i)$ emission from 157.6 nm photolysis of a mixture if 4 $mTorr^{-1}$ if ICN and 400 $mTorr^{-1}$ of He.

B1.4.2 Absorption and Laser-induced fluorescence excitation spectra of $^{12}CH_2O$ and $^{13}CH_2O$ over the wavelength range of the XeCl Laser

C G Cureton and D M Goodall (York University)

a. Introduction

Formaldehyde is the best candidate molecule for a single-stage ^{13}C-enrichment scheme using laser excitation of an electronic transition (B1.15, B1.16, B1.17). Irradiation in the carbonyl $n\pi^*$ band covering the region 360-270 nm leads to simple products upon predissociation:

$$H_2CO \xrightarrow{h\nu} H_2 + CO$$

The mechanism is predominantly molecular at longer wavelengths, but with an increasing component proceeding by a radical pathway for shorter wavelength (λ_{ex}<330 nm) excitation (B1.17, B1.18). Using a variety of laser sources (frequency-tripled YAG (B1.19), ion lasers (B1.17, B1.20) or tunable dye lasers (B1.16, B1.20) with linewidths ~0.1 cm^{-1} to allow discrimination between rovibronic lines for $^{13}CH_2O$ and $^{12}CH_2O$ (natural linewidth = 0.06 cm^{-1} at room temperature) enrichment factors over 30 have been obtained.

RGH lasers are the most powerful UV laser sources commercially available. If a suitable wavelength could be found within the XeCl range for selective absorption by $^{13}CH_2O$, an enrichment scheme viable on the grounds of scale and cost might be devised. The objective of this experiment was to use the tunable dye-laser at the UVRF to measure the fluorescence excitation spectra (and hence the relative absorption) of $^{12}CH_2O$ and $^{13}CH_2O$ at high resolution over the range 307.8-308.3 nm chosen to correspond to the expected output of a line-narrowed, tunable XeCl laser.

b. Experimental

Cylindrical gas cells constructed of quartz with silica windows were filled with 2.0 torr of formaldehyde, $^{12}CH_2O$ or $^{13}CH_2O$, which was obtained by heating the corresponding paraformaldehyde under vacuum. Paraformaldehyde with 90% ^{13}C isotopic purity was a gift from Amersham International plc. Low resolution (0.4 nm; 42 cm^{-1}) absorption spectra of the same samples were measured using a UV spectrophotometer (Varian 2300).

Fluorescence excitation spectra were measured at the RAL. The radiation source was the FL2002E dye laser with the dye sulpharhodamine-B tuned around 616 nm and frequency-doubled using a KDP crystal. The laser was step-tuned over the range 307.8-308.3 nm with a linewidth of 0.4 cm^{-1} (0.004 nm), the pulse energy being around 1 mJ. For 2 spectra a wider range of 305-310 nm was examined. Broadband fluorescence emitted in the range 350-480 nm was detected at right-angles to the laser beam using a side-window photomultiplier tube with a filter to reject scattered laser radiation. A "boxcar" averager

was used to provide a 100 μs gate synchronized with the laser pulse (10 Hz) for data collection.

c. Results

From the absorption spectra obtained at York, it appears that the XeCl laser range 307.8-308.3 nm lies near the minimum between the $2^3_0 4^3_0$ and $2^1_0 5^1_0$; $1^1_0 2^1_0 4^1_0$ bands for both of the isotopic forms.

Fig B1.14 shows the fluorescence excitation spectrum of $^{12}CH_2O$ at 0.4 cm^{-1} resolution.

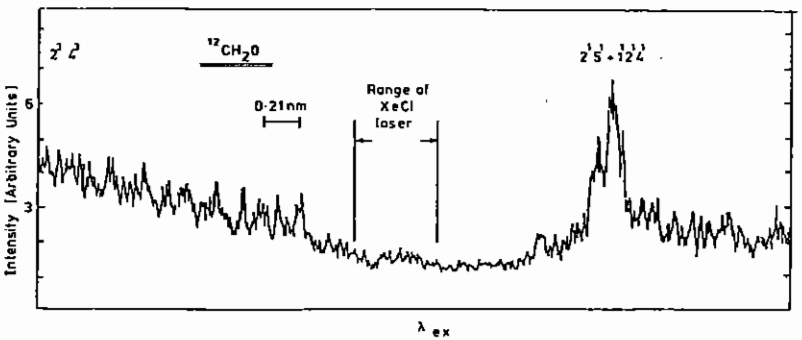

Figure B1.14 Fluorescence excitation spectrum of $^{12}CH_2O$ (2 torr) in the region of 308 nm.

The C^{13} sample taken to the RAL was subsequently found to give an unsatisfactory absorption spectrum, so no fluorescence information was obtained for $^{13}CH_2O$.

d. Discussion

The absorption spectrum of $^{13}CH_2O$ shows that the maximum of the $2^3_0 4^3_0$ band occurs at 307.1 nm, shifted 0.9 nm to the red of the corresponding band for $^{12}CH_2O$ centred at 306.2 nm. The ratio of $^{13}C/^{12}C$ absorption coefficients was found to be 1.3 at 308.0 nm, and 1.7 at 307.8 nm. To effect a viable ^{13}C enrichment, $^{13}CH_2O$ must have an absorbance greater than $^{12}CH_2O$ in order to generate ^{13}C-enriched CO as a photo-product. Taken alone, the low resolution absorption spectra therefore seem promising.

The fluorescence spectrum of $^{12}CH_2O$ (Fig B1.14) shows a minimum at 308 nm, as found in the absorption spectrum. The fluorescence intensity ratio I_F (λ peak)/I_F (λ trough), used to compare the $2^1_0 5^1_0 + 1^1_0 2^1_0 4^1_0$ peak with the 308 nm trough, has a value of 5. This corresponds closely with the value 4.3 obtained by comparing absorbance ratios at the same wavelengths in the low resolution absorption spectrum. (Since the quantum yield of fluorescence should not vary significantly over a narrow wavelength range, the excitation spectra should also give a measure of the relative intensities of absorption).

At the bandwidth of 0.4 cm^{-1} used in obtaining Fig B1.14 the fluorescence excitation spectrum is seen to have a substantial contribution from an underlying continuum, with sharp features corresponding to individual rovibronic lines. The linewidth of a line narrowed XeCl RGH laser is given as 0.01 nm (~ 1 cm^{-1}), which is a factor 2 greater than in the present experiment. It follows that no greater discrimination between peak and trough absorbance values could be achieved using XeCl RGH laser excitation than is evident in Fig B1.14.

A comparison of peak heights in the excitation spectrum for lines in

the $2^3 4^3$ band with the fluorescence intensity in the 307.8-308.3 region suggests that a $^{13}CH_2O$ red shift of 0.9 nm would give a maximum absorbance ratio A (λ,^{13}C)/A(λ,^{12}C) of 3. It would probably not be worthwhile measuring the fluorescence spectrum of $^{13}CH_2O$ at 0.4-1cm^{-1} resolution, since an absorbance ratio in excess of 10 is required to warrant more detailed consideration of a line narrowed XeCl RGH laser for ^{13}C isotope enrichment. Evidently high enrichment factors are only achievable with laser sources having linewidths comparable to the 0.06 cm^{-1} natural linewidth of $^{13}CH_2O$ and $^{12}CH_2O$.

References

B1.1 Y C Chung, N Leventis, P J Wagner and G E Leroi, J.Amer.Chem. Soc., 107, 1414, (1985) and references therein.

B1.2 V A Vante, V Ern, P Chartier, C O Dietrich-Buchecker, D R McMillin, P A Mannot and J P Sauvage, Nouv.J.de Chimie, 7, 3, (1983)

B1.3 R J H Clark, P C Turtle, D P Strommen, B Streusand, J Kincaid and K Nakamoto, Inorg.Chem., 16, 84, (1977).

B1.4 R G Denning, T R Snellgrove and D R Woodwark, Mol Phys, 32, 491, (1976);
R G Denning, D N Foster, T R Snellgrove and D R Woodwark, Mol Phys, 37, 1039, (1979).

B1.5 R G Denning, T R Snellgrove and D R Woodwark, Mol Phys, 37, 1109, (1979).

B1.6 R L DeKock, E J Baerends, P M Boerriger and J G Snijders, Chem Phys Lett, 105, 308 (1984).

B1.7 A Hodgson, J P Simons, M N R Ashfold, J M Bayley and R N Dixon, Chem Phys Lett, 107, 1 (1984); Mol Phys XX, XXX, (1985).

B1.8 J W C Johns, Can J Phys, 41, 209, (1964)

B1.9 M N R Ashfold, J M Bayley and R N Dixon, Chem Phys, 84, 35, (1984)

B1.10 R N Dixon, J M Bayley and M N R Ashfold, Chem Phys, 84, 21, (1984)

B1.11 M N R Ashfold, J M Bayley and R N Dixon, Can J Phys, 62, 1806, (1984)

B1.12 M Gratzel, D Dounghong and J Ramsden, J Amer Chem Soc, (1982) 104, 2977; A Henglein, Ber Bunsenges Phys Chem, 86, 241, (1982)

B1.13 R Rossetti, S M Beck and L E Brus, J Amer Chem Soc, 106, 980 (1984); K Metcalfe and R Hester, J Chem Soc Chem Comm, 133, (1983)

B1.14 G T Brown and J R Darwent, J. Chem Soc Comm, 1985, 98; ibid, J. Amer Chem Soc, submitted for publication; W J Albery, P N Bartlett, C P Wilde and J R Darwent, J Amer Chem Soc, to appear March 1985.

B1.15 E S Yeung and C B Moore, Appl. Phys. Lett. 21, 109 (1972)

B1.16 J H Clark, Y Haas, P L Houston and C B Moore, Chem. Phys. Lett. 35, 82 (1975)

B1.17 J B Marling, J.Chem. Phys. 66, 4200 (1977)

B1.18 J H Clark, C B Moore and N S Nogar, J.Chem. Phys. 68, 1264 (1978)

B1.19 J B Marling, U S Patent No. 4,029, 558 (1977)

B1.20 C B Moore, J H Clark, Y Haas and P L Houston, U.S. Patent No. 4, 212, 717 (1980)

B1.21 C G Cureton and D M Goodall, Advances in Infrared and Raman Spectroscopy, 10, 307 (1983)

B1.22 Lambda-Physik brochure for EMG 150 ET

B2 BIOLOGY

B2.1 ULTRA-VIOLET RESONANCE RAMAN SPECTROSCOPY OF A HIGHLY SPECIFIC ACYL-PAPAIN

P J Tonge, C W Wharton, R J Szawelski (Birmingham), P J Killough and R E Hester (York)

B2.1.1 Introduction

The cysteine proteinase papain catalyses the hydrolysis of esters, peptides and polypeptides via the formation of transient thiolacylenzyme intermediates:

$$\text{E-SH} + \text{RC(=O)-OR'} \rightarrow \underset{\text{Thiolacylenzyme}}{\text{E-S-C(=O)-R}} \rightarrow \text{E-SH} + \text{RCOOH}$$

or -NHR' +ROH or $R'NH_2$

The formal covalent bond changes are well documented (B2.1) but little is known about the factors, such as geometric distortion and non-bonding interactions that promote catalysis. Such effects will result in a perturbation of the vibrational signature of the bond(s) involved and can thus be studied using vibrational spectroscopy.

In order to obtain information regarding the conformation of the acyl group and its interactions with the enzyme's active site Carey and coworkers (B2.2) have used the resonance Raman (RR) approach to monitor the vibrational spectrum of the bonds undergoing transformation during the catalytic cycle. Their method relies on the formation of a transient dithioacylpapain (λmax 315 nm) intermediate during the enzyme catalysed hydrolysis of a thionoester substrate (E-S-C(=S)-R). By using laser irradiation at 324 nm they have observed RR bands characteristic of the dithioester group and its immediate covalently bound neighbours.

Although the dithioester chromophore is constructed by only a single atom substitution, sulphur for oxygen, it would obviously be of more value to study the 'natural' oxygen thiolester acylenzyme.

Simple thiolesters absorb maximally at about 230 nm, 20-40% of the maximum absorption persisting at 248 nm in aqueous solution. Using KrF excimer laser radiation (248 nm, line narrowed) we have been studying a series of thiolester model compounds as well as the acylenzyme formed between papain and a specific oxygen ester substrate, N-Acetyl-L-Phe-Gly methyl ester (kcat = 5 s^{-1}, Km = 32 μM).

B2.1.2 Materials and Methods

a. Enzyme Preparation

The enzyme is isolated from a crude latex obtained from the fruit of the tropical pawpaw using a series of ammonium sulphate and sodium chloride precipitations which sequentially enrich the precipitate in the desired protein. Papain prepared in this manner consists of three components characterised by the oxidation state of the active centre thiol group. For activity this thiol group is required in its reduced form and this constitutes approx. 50% of the preparation. The remaining 50% consists of reversibly oxidised papain which is converted to active papain in the presence of a reducing agent and irreversibly oxidised thiol. Active papain is separated from the irreversibly oxidised contaminant using affinity chromatography. In this procedure activated-thiol enzyme is allowed to react via a disulphide bond with a low molecular weight thiol group attached to an insoluble matrix. Irreversibly oxidised thiol cannot form such a disulphide and is washed straight through the matrix leaving the bound active component behind. Enzyme containing 1 active thiol/molecule can then be separated from the matrix by reductive cleavage of the disulphide (B2.3).

b. Acylenzyme Formation

For the RR experiments acylenzyme is generated using the substrate N-Acetyl-L-Phe-Gly methylester. A titrimetric procedure is used to ensure that the enzyme is continuously saturated with substrate during the course of the reaction; the so-called 'steady-state'. Reaction yields 1 proton/substrate molecule hydrolysed and can be followed using a pH meter, the pH being maintained at a constant value by additions of

equal amounts of alkali. A linear relationship between alkali added and time of addition is indicative of the steady state.

c. Flow System

For presentation to the laser the enzyme and substrate are continuously mixed in a flow system. Since it is known that the deacylation step (breakdown of the acylenzyme) is rate-limiting we know that the enzyme is completely acylated in the conditions we used. It is thus possible to achieve a situation in which a metastable species (half-life ~ 100 ms), the acylenzyme, remains at a stable concentration for the 8-10 seconds required for passage through the sample capillary. The flow system was accurately calibrated using coloured dyes and air bubbles. That complete mixing occurs at the flow rates used, was ensured by observing the mixing of coloured dyes. It was found necessary to include a capillary flow accelerator after the mixing chamber to ensure complete mixing.

The acylenzyme is pumped through a Spectrosil quartz capillary which, in turn, is translated through the path of the pulsed laser beam to avoid optical aberration from denatured protein. The rate of mixing is arranged such that each laser pulse (10 ns, 5 mJ, 10 Hz) impinges upon a fresh sample of mixed enzyme and substrate which is in the steady state for the whole (10 cm) length of the sample tube. The enzyme is, as expected, subject to damage by the high intensity laser pulses and loses some 30% of its activity in a single pulse. A notable and surprising feature of all the spectra we gathered was the very low level of fluorescence interference; only the substrate showed any significant fluorescence.

B2.1.3 Results and Conclusion

Thiolester carbonyl stretch has been observed at 1-50 mM in a number of model compounds and has been found to vary from 1685 cm^{-1} for ethyl thioloacetate Fig. B2.1 (IR (MECN) 1688 cm^{-1}) to 1687 cm^{-1} for the thiolester analogue of the substrate (5% MECN/H_2O or ^2H_2O). As shown in Fig.B2.2 a feature is seen at 1690 cm^{-1} in the resonance Raman spectrum of flow-mixed enzyme and substrate which is absent in the

control spectra. We propose that this is the thiolester carbonyl stretching vibration in the acylenzyme. This indicates that there is no hydrogen bonding interaction between the carbonyl oxygen atom and the protein backbone, the so-called 'oxyanion hole' (B2.4). Such an interaction would be expected to lower the thiolester carbonyl stretching frequency relative to the model compounds.

A notable feature seen in Fig. B2.2 is the marked pre-resonance enhancement of amide I carbonyl vibrations (λmax 195 nm) in both the enzyme (1640 cm^{-1}) and the substrate (1667, 1643 cm^{-1}).

We believe the present result represents the first direct observation of an acylated thiol intermediate during the papain-catalysed hydrolysis of a specific oxygen ester substrate (B2.5).

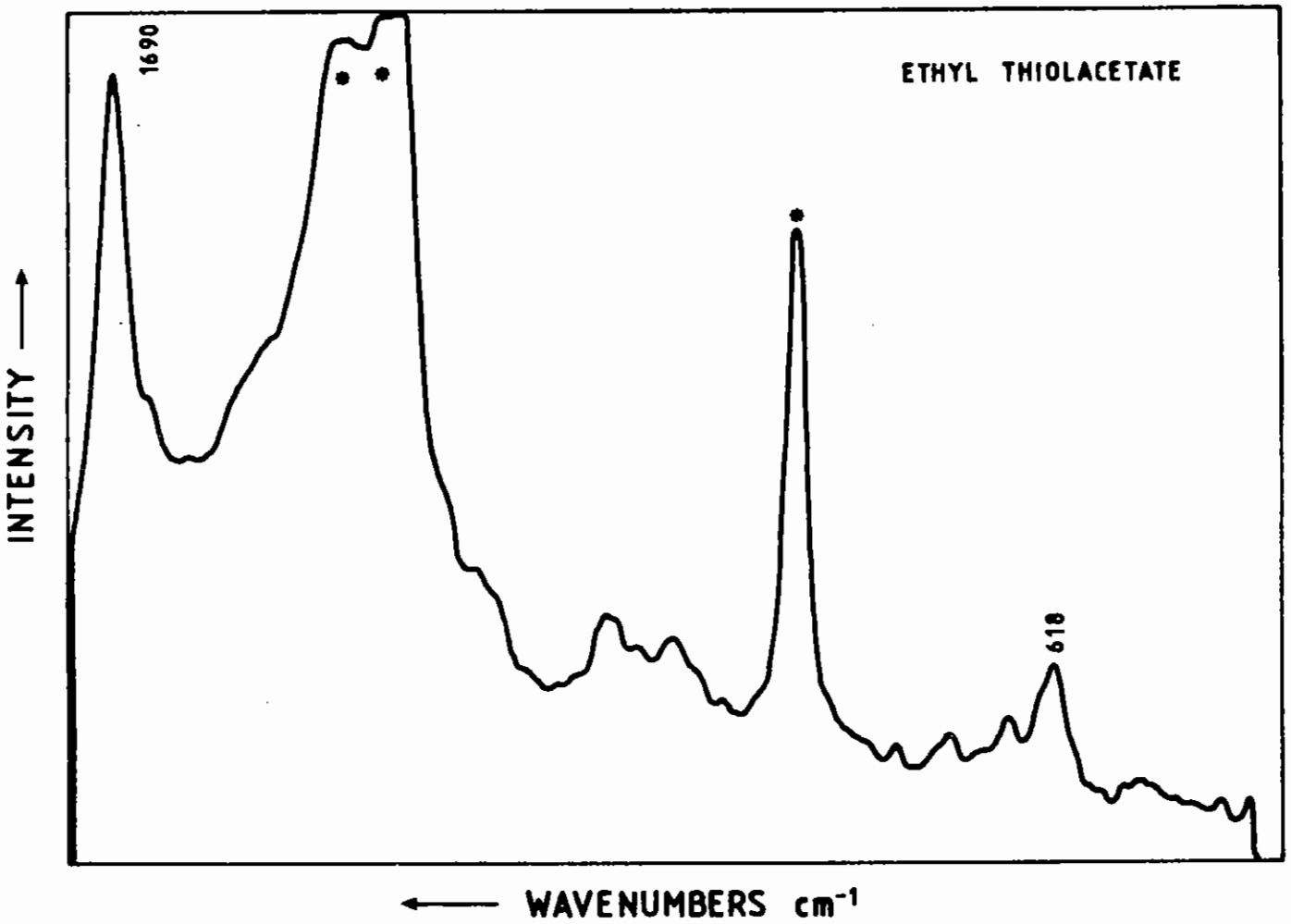

Fig B2.1 Ultra-violet resonance Raman spectrum of Ethyl thiolacetate 18 mM in acetonitrile. 1600 scans (50 delays/scan, 16000 laser pulses) coadded and smoothed. * = solvent peaks

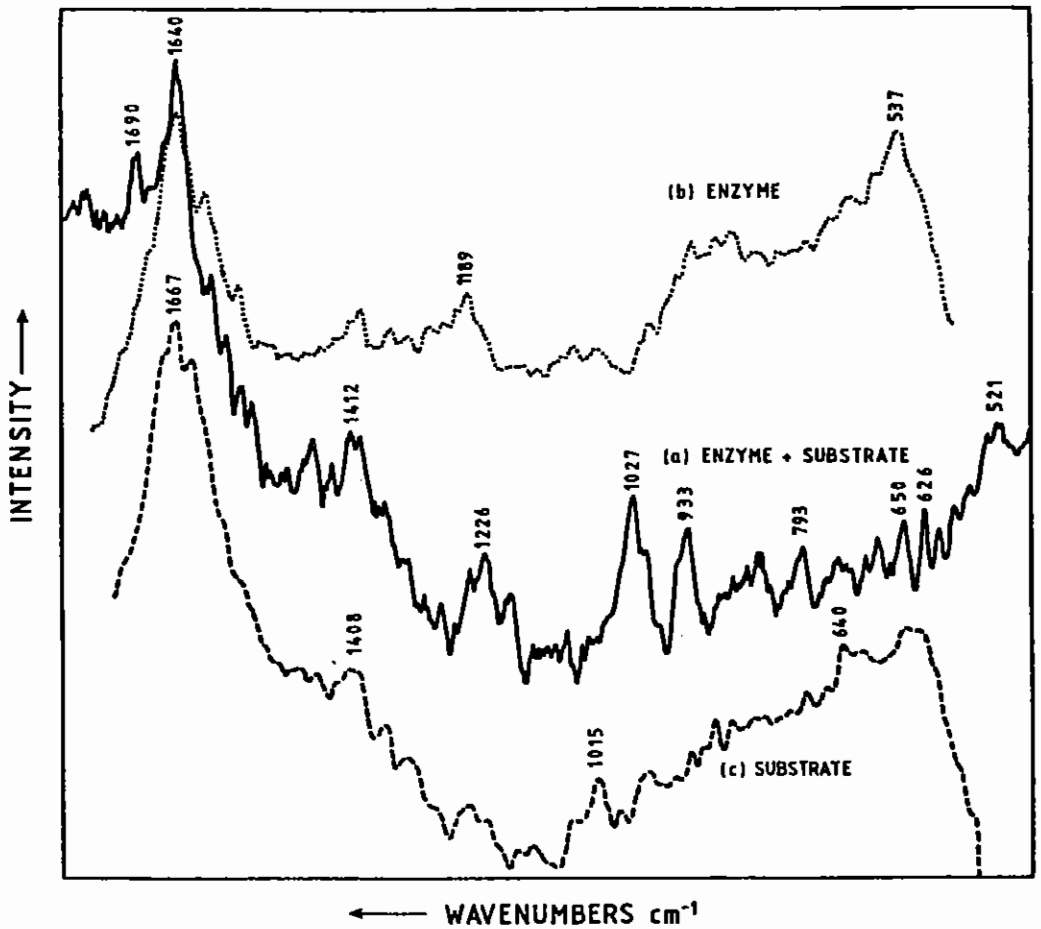

Fig B2.2 Ultra-violet resonance Raman spectrum of N-Acetyl-L-Phe-Gly-papain (a), papain (b), and substrate (c). Note the abscissa scales of (a), (b) and (c) are different. The acylenzyme (0.1 mM) was prepared by continuous mixing of 20 mM substrate in 10% acetonitrile (MECN), 90% 0.3 M phosphate buffer pH 7, 1 mM EDTA, and 0.2 mM papain in 0.1 M KCl, 1 mM EDTA at RT such that the steady state was maintained for 8-10 s. For each spectrum 2000 scans were coadded and smoothed.

B2.2 INTERMEDIATES IN CHLOROPHYLL FORMATION

W T Griffiths (Bristol)

B2.2.1 Introduction

Chlorophyll a synthesis by plants is a light requiring process since one of the enzymes involved in the pathway is a photoenzyme with an obligate requirement for light. This enzyme, protochlorophyllide reductase, catalyses the penultimate step in chlorophyll synthesis viz. the light dependent reduction of protochlorphyllide using NADPH as hydrogen donor. (Fig.B2.3). In this reaction the product, chlorophyllide, (λ max. 672nm) is formed within approx. 0.5μs of the illumination. Recent studies however (B2.6) using crude preparations of dark grown plant tissues have identified at least one transient with λ max. around 690nm involved in the process. This was formed instantly upon illumination with its decay coinciding with the formation of chlorophyllide. In the present study we have used purified enzyme preparations and added substrates (protochlorophyllide + NADPH) to reconstitute the process of chlorophyll synthesis. The 690nm absorbing transient has been detected in this in vitro reconstituted system.

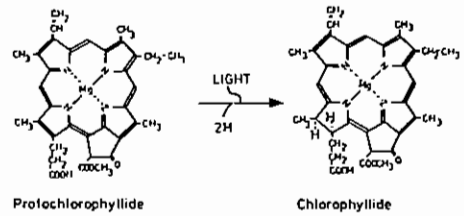

Fig B2.3 Photoreduction of protochlorophyllide catalysed by protochlorophyllide reductase

B2.2.2 Materials and Methods

Purified preparations of etioplasts, etioplast membranes and cholate solubilised protochlorophyllide reductase were prepared from dark grown tissues of wheat or oat plants as previously described (B 2.7). NADPH was a product of Boehringer (Mannheim). Protochlorophyllide was isolated from etiolated tissues as before (B 2.7).

Flash induced absorbance measurements were carried out on samples (approx. 0.3mg protein ml^{-1}) resuspended in buffer. Samples were placed in 3.0ml plastic cuvettes of 1cm pathlength. Exciting light was provided by an excimer (Lambda Physik 101E) pumped Rhodamine dye laser (Lambda Physik FL2002E) tuned to 652nm with pulse energy of approx.

12mJ. The laser beam was expanded to fill the 1cm length of the cuvette. The measuring light was provided by a 250 W pulsed Xenon arc lamp (Applied Photophysics). This was passed through a 692nm transmitting interference filter and focussed to fill the cuvette at right angles to the exciting beam. The emergent beam was detected by a screened photomultiplier (EMI type 9698QB) and the signal displayed on an oscilloscope. The data was transferred through a transient recorder (Datalab model 9502) for storage on a floppy disc for subsequent processing.

B2.2.3 Results and Discussion

Biological material, particularly that from plant membranes is invariably highly light scattering and contains large quantities of coloured and fluorescent material. As a consequence measurement of small absorbance changes in such samples is often very difficult. In the present work, after several preliminary attempts, an experimental arrangement suitable for monitoring small (less than 1%) flash absorbance changes at 690nm in etioplast membranes was achieved. Fig B2.4 shows typical traces obtained on flash illumination of etioplasts isolated from dark grown wheat tissues. Illumination (trace a) causes an instantaneous increase in absorbance at 690nm with a rise time faster than the resolution of the instrument. After the flash this absorbance decayed with an estimated $t_{\frac{1}{2}}$ of approx. 12μsec. This value agrees almost exactly with a similar figure for the 690 → chlorophyllide reaction recently published (B 2.8). Confirmation of the identity of this transient as the 690nm absorbing intermediate of chlorophyll formation is provided by the fact that after 3 flashes (trace b) no further illumination induced change is observed, indicating depletion of the endogenous substrates of the preparation.

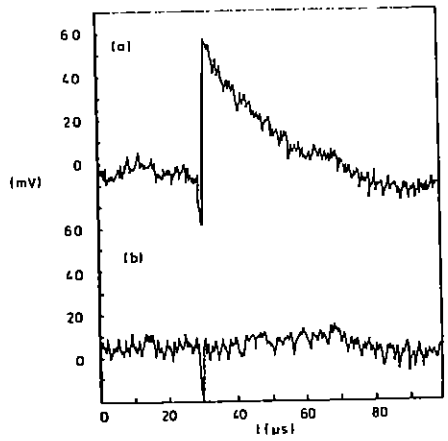

Fig B2.4 Fast absorbance changes at 690 nm in flash illuminated etioplasts. Wheat etioplasts (0.3mg protein ml^{-1}) were flash illuminated (actinic light - λ 652nm, 10ns, 12mJ) and absorbance changes at 690nm measured. Curve (a) represents the change induced by the first flash, Curve (b) the response to a third flash on the sample.

For further proof of this identification we will need to

1) show that it is possible to reconstitute the change in flash depleted membranes (B2.2 - trace b) by addition of endogenous substrates

2) monitor product, i.e. chlorophyll formation at 675nm under otherwise identical conditions and show that the chlorophyll appears on a time scale identical to the 690nm decay.

These preliminary results demonstrate that it is possible to observe intermediates of chlorophyll formation in an in vitro system. Such a system can be readily manipulated experimentally in such a way as to provide information on the chemical nature of the intermediates thereby leading to a mechanism for the photoreduction.

References

B2.1 L Polgar and P Halasz (1982) Biochem. J. 207, 1-10

B2.2 P R Carey and A C Storer, (1984) Ann. Rev. Biophys. Bioeng. 13, 25-49

B2.3 K Brocklehurst, B S Baines and M P J Kierstan, (1981) Topics in Enzyme and Fermentation Biotechnology, 5

B2.4 B Asboth and L Polgar (1983) Biochemistry 22, 117-122

B2.5 P J Tonge, C W Wharton, R J Szawelski, P J Killough and R E Hester (1985) Biochem. Soc. Trans. In Press

B2.6 F Franck and P Mathis (1980) Photochem. Photobiol. 32, 799-803

B2.7 W T Griffiths (1978) Biochem. J. 152, 623-635

B2.8 J Iwai, M Ikeuchi, Y Inoue and T Kobayashi (1984) In "Protochlorophyllide Reduction and Greening" (C Sironval, and M Brouers eds.) W Junk Publishers. Amsterdam, pp 99-112

B3 PHYSICS

B3.1 LYMAN α SPECTROSCOPY

K G H Baldwin*, D D Burgess, D A Evans, J Marangos and M G Nicholson
(Imperial College)

Groundstate hydrogen populations have been measured as a function of time in a recombining hydrogen z-pinched plasma by obtaining Lyman-α absorption lineprofiles. The tunable coherent VUV radiation at around 1216Å was generated by four wave mixing of F12002 dye laser radiation in Krypton gas as described previously (B3. 1-3). By varying the delay between the peak of the pinch current and the firing of the laser, plasma conditions at four different times were studied. At the delay times used, the electron density was in the range $10^{14} < n_e < 6 \times 10^{15} cm^{-1}$ and electron temperature was in the range $0.3 < Te < 1.4eV$.

Measurements were made both along the axis of the pinch (March/April 1984) and perpendicular to the axis (November 1984), in order to gain data about possible colder end zones existing in the plasma. Complimentary Ly-α emission measurements were also made. Groundstate hydrogen populations were calculated from the measured opacities at known wavelength detunings from line centre using the equation;

$$\tau = \frac{e^2}{4\pi\varepsilon_o mc} NfL \quad \frac{\Delta\nu_{\frac{1}{2}-\frac{1}{2}}}{(\Delta\nu)} \qquad (B3.4)$$

Here it is assumed that measurements are in the Stark broadened wing of the profile where the form of the profile is Lorentzian.

* Now at The Research School for Physical Sciences, Canberra, Australia

B3.1.1 Experimental

The VUV output from the tripling cell was passed through the plasma vessel and was then incident upon the entrance slit of a 1 metre VUV monochromator. The plasma vessel was fitted with re-entrant MgF_2 windows to eliminate the effects of end-zones. The monochromator was used with wide slits (approximately 1mm) since the plasma emission was negligible. The use of wide slits in the monochromator gave a high throughput and considerably eased tuning problems in the detection system. The Lyman-α signal was detected by a solar blind photomultiplier fitted with an additional Lyman-α interference filter to discriminate against untripled light.

The absorption measurements were carried out by measuring the coherent VUV intensity over several shots before and after each plasma transmission measurement. Accuracy was limited by the shot-to-shot fluctuation in the coherent VUV intensity.

B3.1.2 Results

The profiles for delay times T = 10, 30 and 45μs are plotted in Figs B3.1-3. Only opacities below τ = 4 are measurable with this technique. A best fit Lorentzian is drawn on each set of data. Populations are derived from equation 1 using Griems (B3.5) ½ - ½ widths and the τ = 1 point wavelength detunings of the graph. Ground state hydrogen populations are plotted as a function of time in Fig B3.4. The population shows a monotonic rise with time.

The result for axial and transverse measurements agree well except for the T = 60μs result, where the transverse result shows a substantially higher groundstate hydrogen population than the axial result. This may be due to colder end zones, developing by 60μs, which reduce the opacity of the axial measurement and hence gives a population lower than the true value.

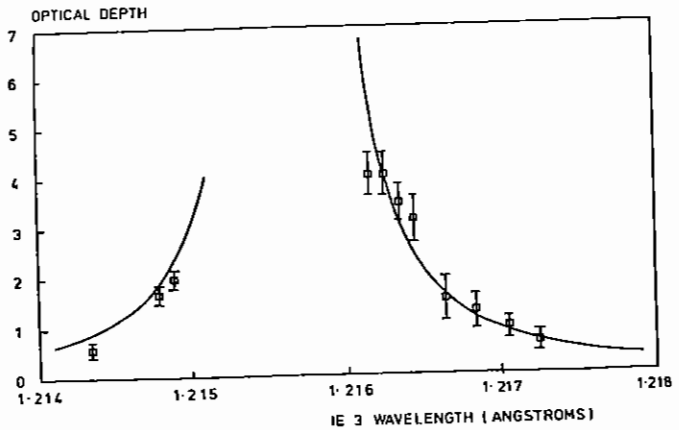

Fig B3.1 Lyman-Alpha absorption in a hydrogen plasma, 10 μS delay

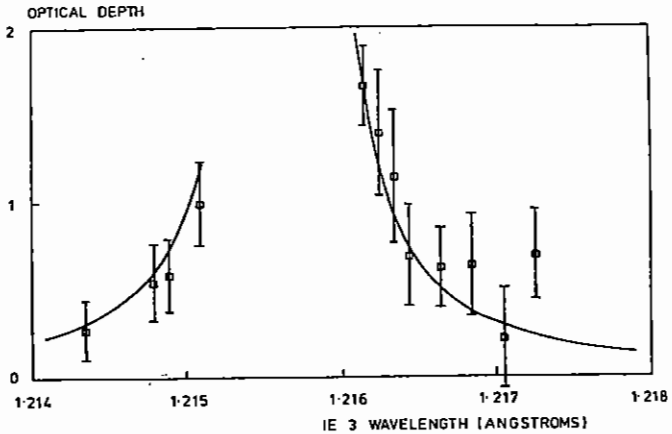

Fig B3.3 Lyman-Alpha absorption in a hydrogen plasma, 45 μS delay

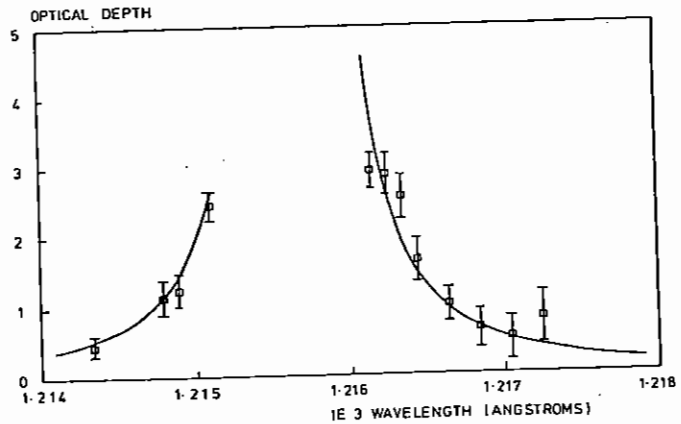

Fig B3.2 Lyman-Alpha absorption in a hydrogen plasma, 30 μS delay

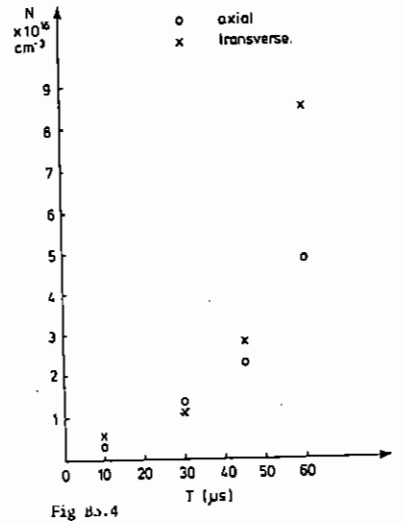

Fig B3.4 Ground state hydrogen population as a function of time

B3.2 THE APPLICATION OF UP-CONVERTED VUV SOURCES TO RADIATION TRANSFER STUDIES IN NEUTRAL ATOMIC HYDROGEN

D D Burgess, C D Heryet and R C M Learner (Imperial College)

The aim of this investigation is the use of the up-converted laser already developed by Dr K Baldwin and Professor D D Burgess (Imperial College) at CLF for the study of fundamental processes involving atomic hydrogen in the 122nm region. The primary interest is in the propagation of radiation (absorption, scattering, trapping, quenching, etc) over a wide range of atomic number densities and detuning frequencies.

This year's work has concentrated on the design and testing of PTFE-coated cells suitable for the containment of the necessary large atomic number densities; and preliminary results from the last scheduled period (March 1985) suggest that the production and containment are now sufficiently well understood to reach the ultimate target of 10^{12} - 10^{16} atoms per cm^3, corresponding to line centre opacities ranging from less than one to 10^4, in the cell now under construction.

The experimental data will initially be related to well understood parameters such as the Rayleigh cross-section (at large detunings) and the absorption cross-section (at low densities). The results of an earlier run (December 1984) at around 10^{13} atoms per cm^3 are shown in Fig B3.5. The experimental configuration is shown schematically in Fig B3.6. The function of the VUV monochromator is the removal of radiation of the fundamental (ie untripled) frequency. The preliminary analysis of results from the scheduled period in March 1985 suggests that a substantially-increased opacity has now been obtained and, perhaps more importantly, even higher opacities can be obtained in future cells.

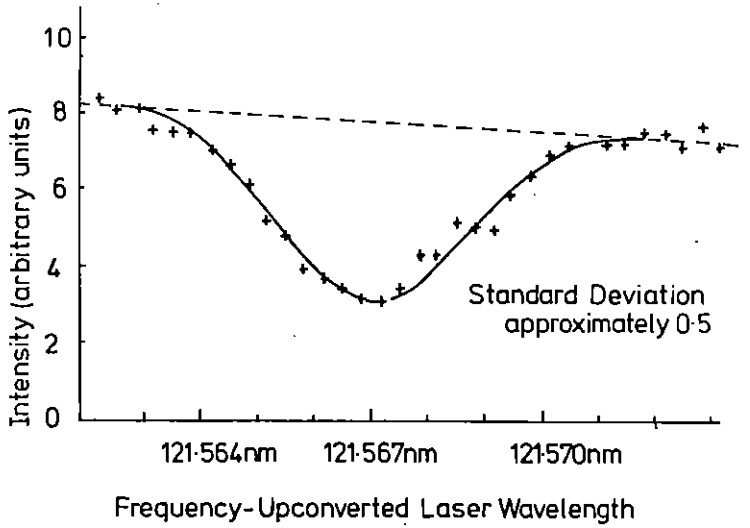

Fig B3.5 Lyman-α absorption profile (not corrected for detector response and window transmission) obtained in neutral atomic hydrogen at around 10^{13} atoms per cm^3. The Doppler width (3.8pm) corresponds to a temperature of 1900K.

Now that a well-diagnosed experimental configuration has been established, the study will proceed to the case of very high opacity, for which there is as yet no satisfactory theoretical model. Close to line centre the interest is not so much in the line shape but in the time-dependence of the laser pulse shape. The tunable up-converted source will be used to study the diffusion processes that affect radiation trapping at large optical depths (up to 10^4) by monitoring the time evolution of the input pulse as a function of tuning through the line core.

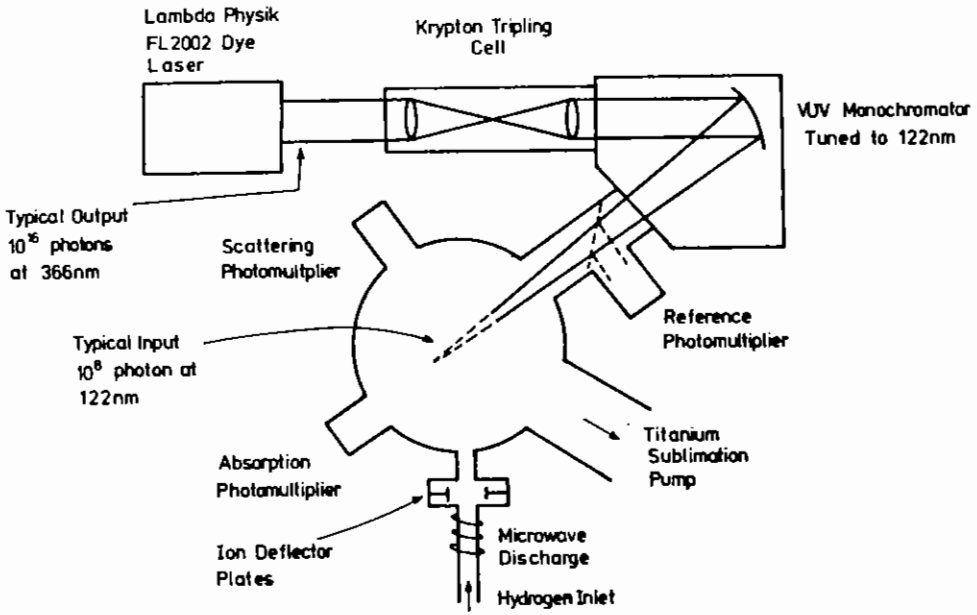

Fig B3.6 Schematic layout of apparatus for radiative transfer studies in neutral atomic hydrogen using a frequency up-converted VUV source at 122nm.

B3.3 STIMULATED RAMAN SCATTERING AND STIMULATED COLLISIONAL INDUCED FLUORESCENCE IN ATOMIC THALLIUM-NOBLE GAS MIXTURES

D G Cunningham, D Denvir, I Duncan and T Morrow (Queen's Belfast)

B3.3.1 Introduction

In the 1984 annual report to the Laser Facility Committee we described preliminary experiments on stimulated anti-stokes Raman and collisional induced resonance lasers in atomic thallium-argon mixtures. During the past year this work has been extended to other atomic thallium-noble gas systems and attempts have been made to obtain optical gain on the thallium-xenon exciplex bands.

B3.3.2 Theoretical Considerations

The stimulated electronic Raman scattering (SERS) process may be used to efficiently frequency shift high power laser outputs. In such experiments it is usual for the Raman pump laser frequency ω_p to be tuned close to a resonance frequency $\omega_{2\ 3}$ of the Raman medium to take advantage of the greatly enhanced scattering cross-section and the Raman output may be tuned over a limited frequency range by tuning the pump laser in the vicinity of the resonance frequency $\omega_{2\ 3}$.

However when the Raman medium is collisionally perturbed and the Raman pump laser frequency ω_p is such that $h(\omega_{2\ 3} - \omega_p) < kT$, then the resonance level 3 may be populated by inelastic (or quasi-elastic) collisions. These collisions can be considered to provide the energy required to transfer part of the 'population' associated with the laser induced virtual state to the resonance atomic state as shown in Fig B3.7. This process may also be viewed from a quasi-molecular viewpoint as illustrated in Fig B3.8. Interaction with the Xe perturber causes the $Tl(7^2S^1/_2)$ level to come into resonance with the laser pump frequency ω_p at some internuclear separation R, allowing absorption of a pump photon and creating an excited Tl-Xe quasi-molecule which may have enough internal kinetic energy to break up into a ground state Xe atom and an excited $Tl(7^2S^1/_2)$ atom, resulting in population inversion and laser action on the atomic thallium resonance at high pump powers and high collision rates. This collisional induced process is generally referred to as SCF i.e. stimulated collisional induced fluorescence (B3.8).

In the quasi-static theory of line broadening, developed by Hedges et al (B3.9), the radiation absorbed or emitted by the quasi-molecular system at a frequency ω (R) is identified with the electronic transition at internuclear separation R such that $\hbar\omega(R) = V_u(R) - V_l(R)$ where $V_u(R)$ and $V_l(R)$ are the potential energies of the upper (u) and lower (l) quasi-molecular states. This relation may be used to relate the probability distribution of inter-nuclear separations to the absorption and emission profiles.

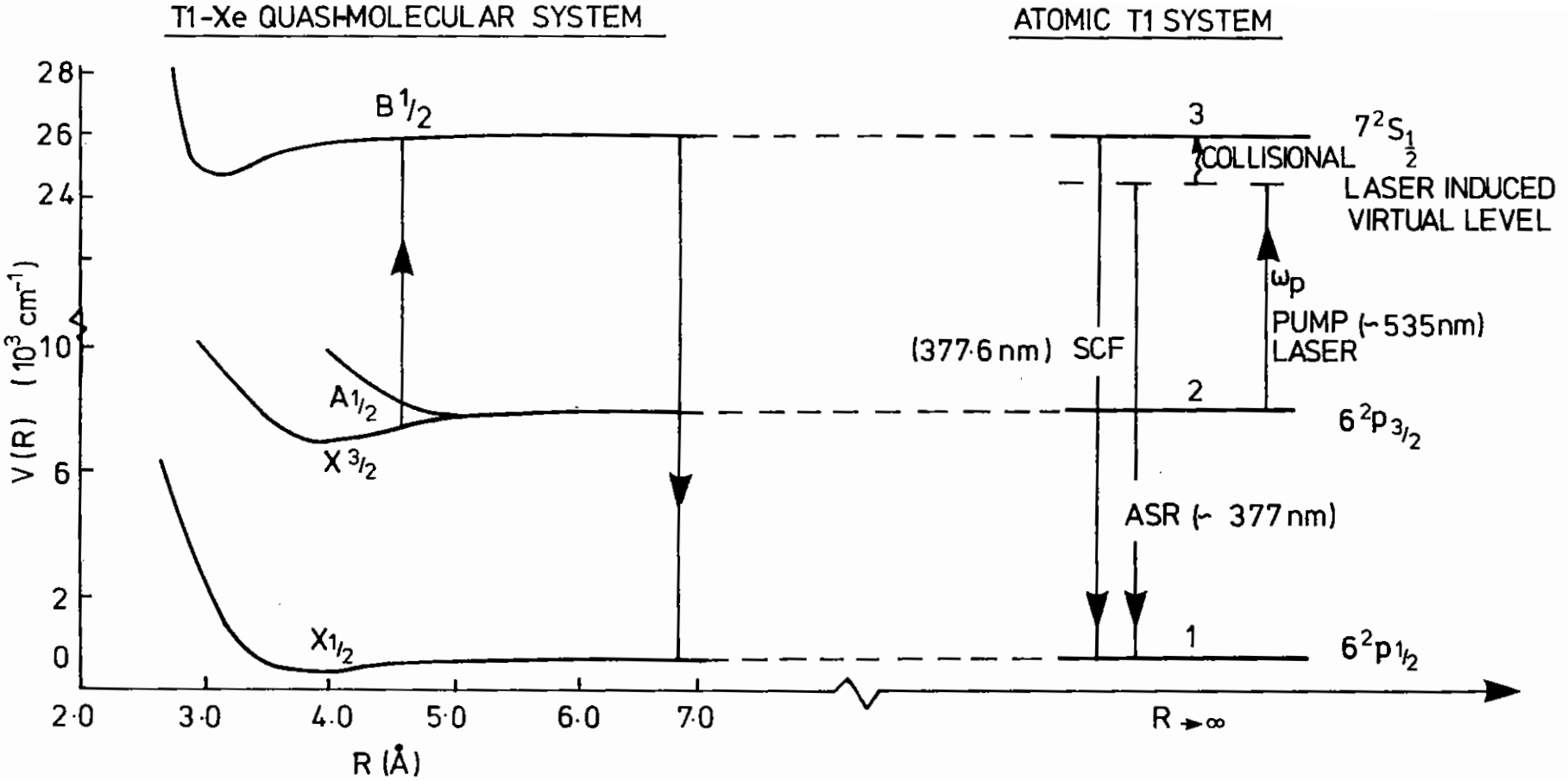

Fig B3.8 Tl-Xe quasi-molecular potentials from ref B3.7 showing the scheme for the SCF resonance laser.

Fig B3.7 A schematic of the atomic Tl anti-stokes raman laser (ASR) and the stimulated collisional induced fluorescence laser (SCF).

Cheron et al (B3.6-7) have measured the normalised emission line shape $I_J(\nu,T)$ of the bands associated with the Tl-noble gas quasi-molecules and determined the potential energy curves for the quasi-molecular states correlating with the $Tl(7^2S^1/_2, 6^2P_J)$ states. Using quasi-static theory, they showed that the absorption cross-section $\sigma_A(\nu,T)$ at frequency ν and temperature T for the quasi-molecular transitions are given by expressions 1 and 2 where $A_o(J)$ is the Einstein coefficient for the $Tl(7^2S^1/_2 - 6^2P_J)$ transition at frequency ν_o and noble gas number density n_o.

$$\sigma_A(\nu,T) = n_o \left(\frac{gu}{gl}\right) \left(\frac{\lambda^2}{8\pi}\right) . I_J(\nu,T) . A_o(J) . \exp\left(\frac{h\nu(R) - h\nu_o}{kT}\right) \qquad (1)$$

$$\sigma_S(\nu,T) = n_o \left(\frac{\lambda^2}{8\pi}\right) . A_o(J) . I_J(\nu,T) \qquad (2)$$

The resultant net gain (or absorption) coefficient $\alpha_J(\nu,T)$ for the quasi-molecular system may be calculated from 5 using individual absorption coefficients $K(\nu,T)$ and gain coefficients $G(\nu,T)$ given in 3 and 4.

$$K_J(\nu,T) = \left(Tl(6^2P_J)\right) \sigma_A(\nu,T) \qquad (3)$$

$$G(\nu,T) = \left(Tl(7^2S^1/_2)\right)\sigma_S(\nu,T) \qquad (4)$$

$$\alpha_J(\nu,T) = G(\nu,T) - K_J(\nu,T) \qquad (5)$$

Since the Tl-noble gas quasi-molecules are only weakly bound (binding energy ~ few kT) it may be assumed (at least to a first approximation) that all the excited quasi-molecules formed dissociate to form free $Tl(7^2S^1/_2)$ atoms. The resultant gain coefficient on the atomic resonance transition α_J may be estimated from the normal atomic stimulated emission cross-section σ using 6.

$$\alpha(\nu_J) = \sigma_{ST}(\nu_T).\left(\left(Tl(7S^1/_2)\right) - \left(Tl(6^2P_J)\right)\right) \qquad (6)$$

The above expressions may be used to model both the quasi-molecular absorption from the pump dye laser beam and the resulting gain of the

atomic resonance lasers. Since SERS effects are neglected in the above considerations this model would only be valid for conditions where the SERS is below threshold.

The absorption and stimulated emission cross-sections in the exciplex wings, calculated for a xenon number density of 5.5×10^{19} cm^{-3} using equations 1 and 2, are shown in Figs B3.9a and B3.9b. Since σ_S is considerably larger than σ_A over a wide wavelength range to the red of the atomic resonance the Tl-Xe quasi-molecular system has potential as a viable tunable exciplex laser medium. Previous attempts to obtain optical gain in the Tl-Xe system using e-beam and discharge pumping have been unsuccessful however due to the relatively low $Tl(7^2S^1/_2)$ number densities obtained using these techniques. Wavelength selective photo-dissociation of Tl halides in conjunction with optical pumping via the quasi-molecular absorption in the exciplex wings of the $Tl(7^2S^1/_2\text{-}6^2P_J)$ absorptions could however provide a means of producing the high densities required to obtain appreciable optical gain in the exciplex bands. The lower operating temperatures employed with Tl halides as atomic Tl donors is also advantageous due to the temperature dependence of $I_J(\nu,T)$. A Tl-Xe exciplex laser based on flashlamp photo-dissociation of Tl-halides by the UV output of the lamp and optical excitation via the Tl-Xe quasi-molecular absorption from the visible output of the lamp could be envisaged.

An attempt to observe optical gain in the Tl-Xe exciplex bands is described in the present report. Observable optical gain on the exciplex bands would be expected in high pressure xenon mixtures under conditions where the $Tl(7^2S^1/_2)$ number density is high ($\sim 10^{16} - 10^{17}$ cm^{-3}) but where no net population inversions exist within the atomic resonance transitions. Obviously these conditions could be best satisfied if the number densities in the thallium $7^2S^1/_2$ and 6^2P_J states are approximately equal and of the order of $10^{16} - 10^{17}$ cm^{-3}. Wavelength selective laser photo-dissociation of thallium halides in conjunction with laser pumping in the quasi-molecular absorption bands provides a convenient technique for initial investigation of such well-defined population distributions at high number densities.

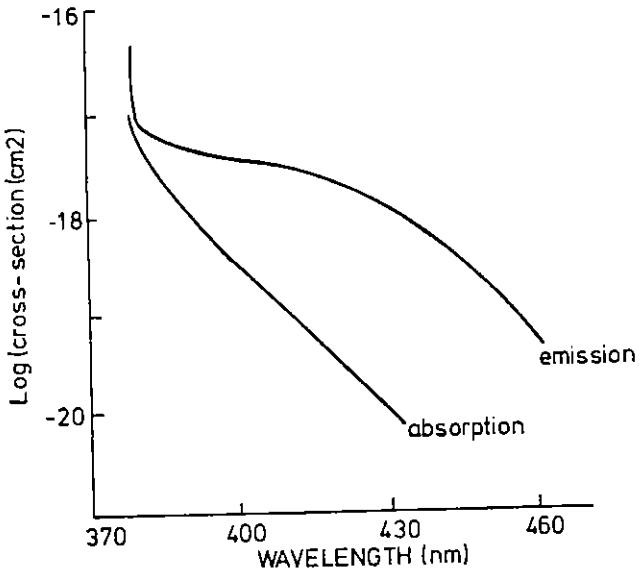

Fig B3.9a Calculated absorption and stimulated emission cross-sections for Tl-Xe violet exciplex band (Xe) = 5×10^{19} cm^{-3}.

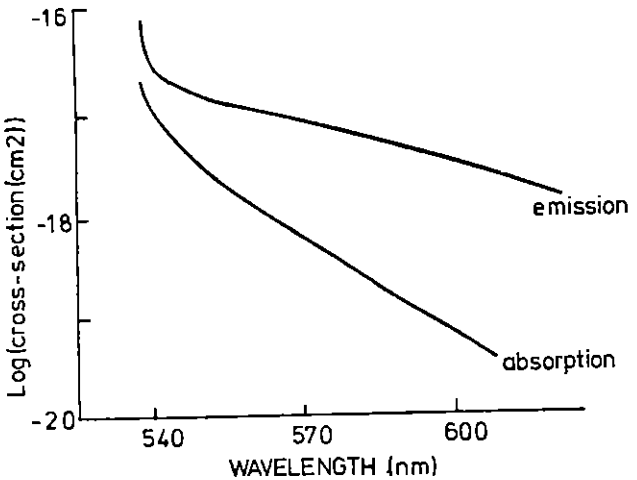

Fig B3.9b Calculated absorption and stimulated emission cross-sections for Tl-Xe green exciplex band (Xe) = 5×10^{19} cm^{-3}.

The experiment attempted is illustrated schematically in figures B3.10a and B3.10b. High number densities of Tl($6^2P^1/_2$) and Tl($6^2P^3/_2$) atoms are created in the ratio of ~ 3:7 by photo-dissociation of TlCl (B3.10) using a high power 248 nm KrF laser. A high power dye laser at ~ 535 nm pumps, via the quasi-molecular absorption, an appreciable fraction of the Tl($6^2P^3/_2$) population into the quasi-molecular state correlating with the Tl($7^2S^1/_2$). This scheme (figure B3.10a) would produce a tunable 'up-converted' exciplex laser at ~ 450 nm. In contrast to normal frequency up-conversion processes, such as anti-Stoke's Raman generation, this exciplex 'up-conversion' process would be possible with broad-band pump lasers of poor beam quality and would provide tunable up-converted outputs. Several other schemes based on atoms of groups I,III, VI and VII, which have been used or proposed as ASR media, merit investigation as potential up-converted UV and VUV exciplex lasers in collisionally perturbed environments.

B3.3.3 Experimental

The experimental arrangement used for up-conversion experiments was identical to that described previously (B3.11). Thallium ($6^2P^3/_2$) atoms were produced by photodissociation of TlCl (B3.10) with the 193 nm output from a Lambda Physik (E.M.G. 201) ArF laser.

$$\text{is TlCl} \xrightarrow{193\ \text{nm}} \text{Tl}\ (6^2P^3/_2) + \text{Cl(or Cl*)} \qquad (7)$$

Approximately 30 mJ of the 193 nm laser output, in a ~ 10 ns pulse, was focused into the TlCl vapour cell with a lens of 0.5 m focal length. The tunable optical excitation source was a XeCl excimer pumped dye laser (E.M.G. 101 and FL 2002) with a pulse length ~ 7 nm, a line width ~ 0.2 cm^{-1} and an output pulse energy of ~ 3 mJ near 535 nm. The dye laser was focused with a separate lens of focal length 0.5 m and combined with the ArF laser using a flat with a small central aluminised spot; the aluminised spot was protected from the ArF laser by a solid shield. The temporal delay between the two laser beams was controlled by a delay generator and monitored using a fast photodiode and oscilloscope. In this experimental configuration maintaining fixed delays to a required accuracy of ± 5 ns proved to be a particular

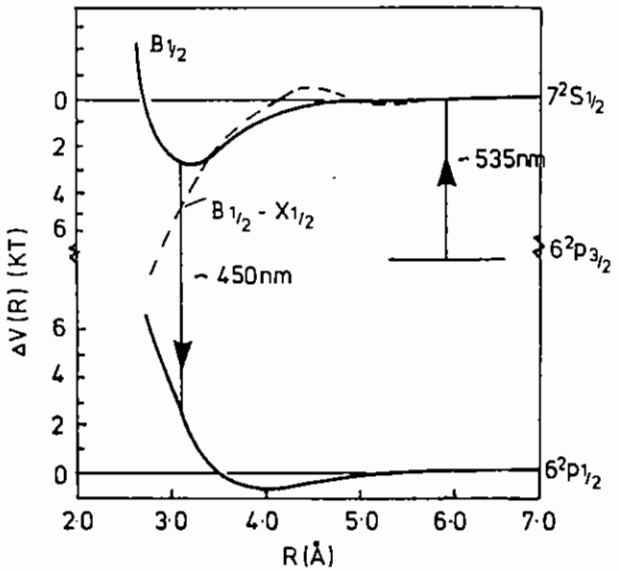

Fig B3.10a Potential energy curves for the Tl-Xe quasi-molecular system showing a possible optical pumping scheme which can result in a tunable exciplex laser output.

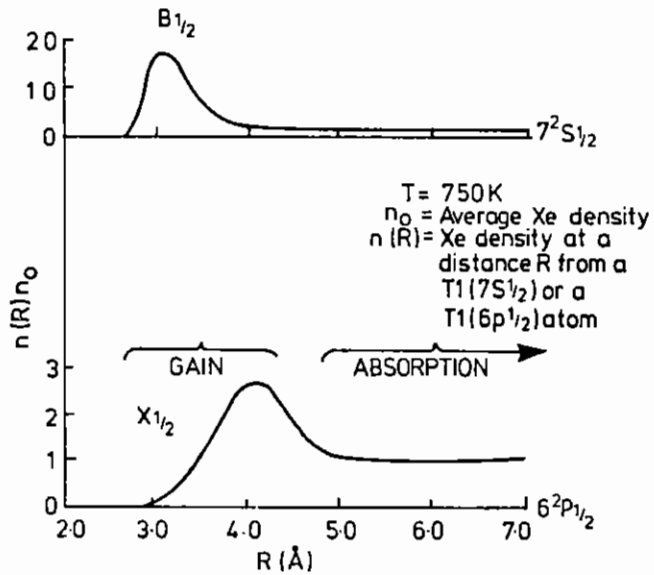

Fig B3.10b The solid $n(R)/n_o$ lines are the classical equilibrium distributions (29) for the $B_{1/2}$ and $X_{1/2}$ quasimolecular states.

problem due to the inherent temporal jitter in the switching circuits of both excimer lasers.

The experimental arrangement for the down-conversion and exciplex gain experiments is shown in figure B3.11. In the down-conversion experiments TlCl (B3.10) using the 308 nm XeCl excimer laser, part of the output of which also pumped the tunable ~ 377 nm dye laser.

i.e. $TlCl \xrightarrow{308\ nm} Tl(6^2P^1/_2) + Cl\ (or\ Cl^*)$ (8)

Approximately 10 mJ of XeCl laser energy was used to pump the dye laser. The pulse was ~ 10 ns and the dye laser had an output pulse energy of ~ 0.25 mJ and a bandwidth ~ 0.2 cm^{-1}. The dye laser output was either directed as a parallel beam (of area $\sim$ 0.25 cm^2) or focused into the TlCl vapour cell.

In the exciplex gain experiments both $Tl(6^2P^1/_2)$ and $Tl(6^2P^3/_2)$ atoms were produced (in the ratio 3:7) by photodissociation of of TlCl (B3.10) using the 248 nm KrF laser with unstable resonator optics. Part of the 248 nm output also pumped the tunable (~ 378 nm or ~ 535 nm) dye laser. For both the down-conversion and exciplex gain experiments the temporal delay between the photo-dissociation excimer laser and dye laser pulses was adjusted by varying the optical path difference of the two laser beams. This particular experimental configuration was chosen in order to eliminate the temporal jitter inherent in using two separate excimer lasers as photo-dissociation source and dye laser pump. Unfortunately the 248 nm Krf output proved to be a particularly inefficient pump for the dye laser and the maximum dye laser output obtained, for a KrF input pulse energy of ~ 300 mJ, was ~ 2 mJ.

The TlCl vapour cells (spectrosil 'B' grade quartz, length 14 cm) were enclosed in an oven and the TlCl vapour pressure controlled by varying the temperature of a cold finger reservoir. The spectral profiles and intensities of the SERS and atomic resonance laser outputs were studied with a 0.5 m Hilger-Watt grating spectrograph and either an image

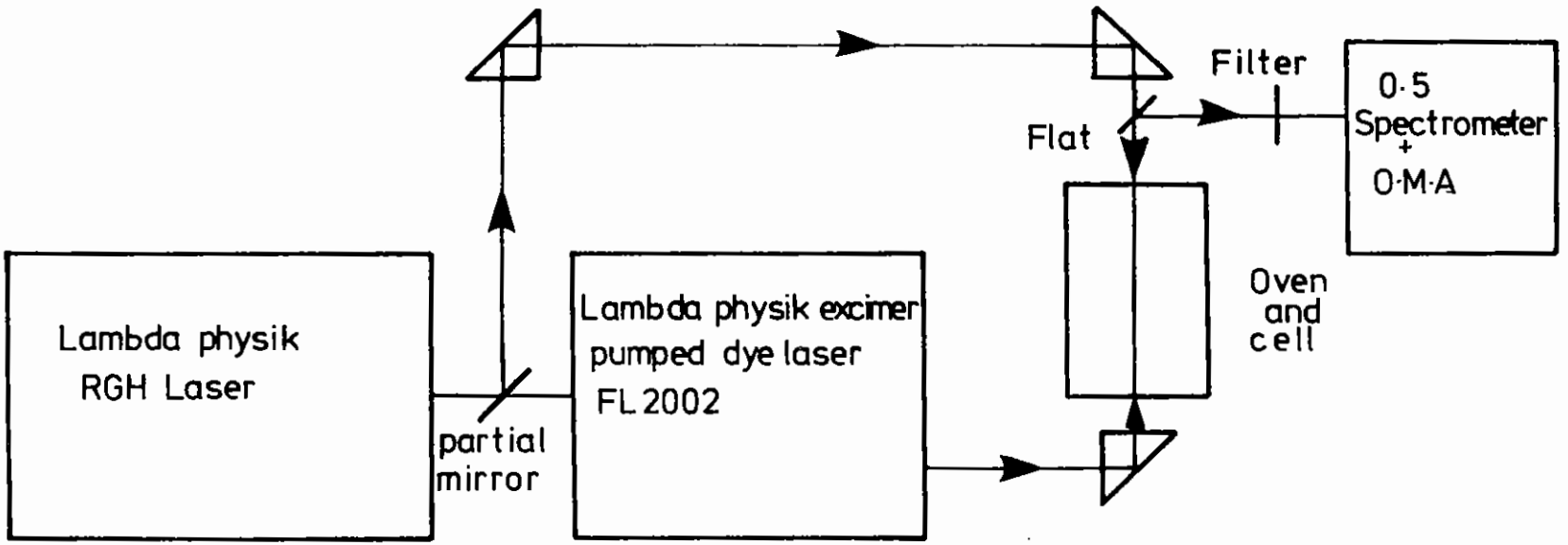

Fig B3.11 Experimental arrangement used for down-conversion and exciplex gain experiments.

intensified diode array or a vidicon detector, O.M.A. system (P.A.R). A TlCl density of ~ 10^{16} molecules cm^{-3} and an inert gas density of 2 x 10^{19} cm^{-3} was used throughout the experiments described.

B3.3.4 Results and discussion

With only the 308 nm photodissociation radiation incident on the thallium-xenon mixture no atomic lasers were observed in the wavelength region (300-600) nm. When the wavelength of the exciting dye laser was tuned to within ± 0.1 nm of the atomic resonances (i.e, $7S_{1/2}$ + $6P_{3/2,1/2}$) both SERS and SCF resonance laser outputs were easily obtained for both up-conversion and down-conversion experiments. The SERS could be distinguished from the SCF resonance output since it tuned with the dye laser wavelength. For dye laser detunings greater than 0.3 nm only the SCF resonance laser outputs were observed.

In the upconversion experiments the ASRL and/or SCF resonance laser outputs were critically dependent on the delay between the photolysis excimer laser pulse and the exciting dye laser pulse. Reproducible upconverted outputs were only observed when both pulses were synchronised to reach their peak intensities within ± 5 nm. The results of the up-conversion, down-conversion and exciplex gain experiments are discussed in (a) - (c) below.

a. Up-conversion experiments

Fig B3.12 shows the variation of upconverted output pulse energies as a function of dye laser wavelength for both the 377.6 nm atomic resonance (SCF) and ASR lasers. Close to resonance the SCF laser output drops due to competing processes such as Raman scattering, self focussing etc (B3.12). The tuning curve of the ASR laser was found to be much narrower than that previously observed for zero or low buffer gas pressures (B3.11-12). The reduced tuning range of the ASR laser can be attributed to a decrease in the stimulated anti-stokes Raman cross-section due to broadening of the atomic resonance and to the decrease in the pump power due to quasi-molecular absorption from the dye laser beam. The output pulse energies of both the SCF and ASR

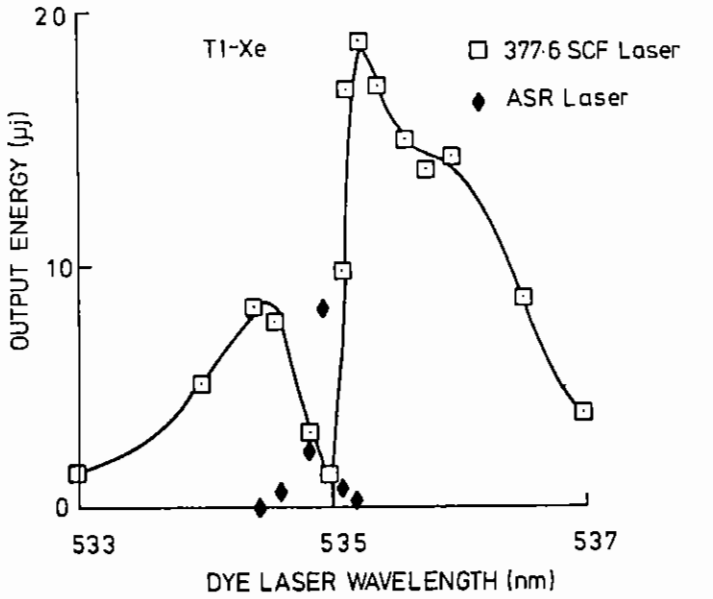

Fig B3.12 ASR and 377.6 nm SCF laser output pulse energies as a function of dye laser pump wavelength (the dye laser pulse energy was 3 mJ).

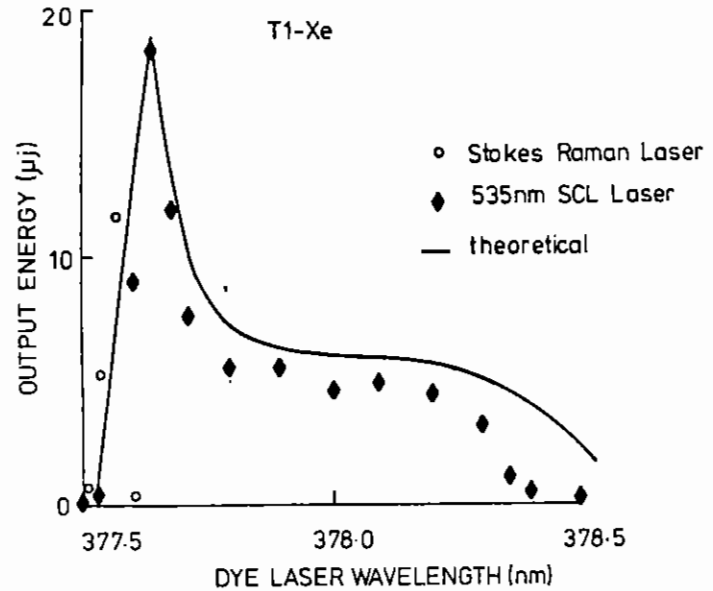

Fig B3.13 Stokes Raman and 535 nm SCF laser output pulse energies as a function of dye laser pump wavelength (the dye laser pulse energy was 250 μJ).

lasers were found to be saturated (i.e. independent of dye laser power) over most of the dye laser tuning range shown in figure B3.12.

b. Down-conversion experiment

Fig (B3.13) shows the variation of down-converted output pulse energies as a function of dye laser wavelength for both the 535 nm atomic resonance SCF and Stokes Raman lasers in Tl-Xe mixtures. The wavelength profile of the Tl-Xe quasi-molecular absorption, shown in Fig B3.14, was obtained by measuring the absorption from the dye laser beam as a function of dye laser wavelength. The absorption from the dye laser beam at fixed wavelength was found to be a function of dye laser pulse energy indicating bleaching of the Tl-Xe quasi-molecular absorption at high dye laser pulse energies (Fig B3.15). The pulse duration of the SCF laser was a maximum of ~ 5 ns when the dye laser was tuned close to the 377.6 nm resonance and decreased with detuning from resonance.

The solid lines shown in Fig B3.13 were calculated from the quasi-static theory taking into account the temporal dependences of the $Tl(7^2S_{1/2}, 6^2P_J)$ number densities (i.e. including gain saturation and bleaching of the quasi-molecular absorption at high dye laser pulse energies). Excellent agreement was observed between theory and experiment for the Tl-Xe quasi-molecular absorption from the dye laser beam (Fig B3.14). The experimentally measured SCF laser output as a function of dye laser input wavelength (Fig B3.13) is similar to the predicted dependence but is somewhat lower particularly for $\lambda > 378.25$ nm where the SCF laser is not operating in the gain-saturated regime. This deviation is not unexpected since the theoretical model used neglects optical losses (including stimulated Raman generation) and is based on a σ_{ST} measured (B3.13) for a lower inert gas pressure. The theoretical dependence therefore represents the upper limit attainable experimentally.

The maximum conversion efficiency obtained, in terms of SCF laser output energy to dye laser energy absorbed, was 17% for the single pass super-fluorescent system investigated. The latter figure is equivalent to 50% of the maximum possible down-conversion efficiency in

this process. Higher efficiencies are possible under resonant cavity conditions. Fig B3.16 shows the variation of the down-converted 535 nm SCF resonance laser output energy as a funcion of pump dye laser wavelength for Tl-He mixtures. The wavelength profile in Fig B3.16 reflects the unbounded nature of the Tl-He quasi-molecular potentials correlating with the $Tl(7^2S_{1/2}, 6^2P_J)$ states.

c. Exciplex gain experiment

Attempts were made to observe optical gain in the Tl-Xe exciplex bands using the 248 nm KrF laser as both photo-dissociation source and synchronous pump for the 535 nm dye laser. Due to the limitations of this configuration (discussed above) the pulse energies incident on the vapour cell were limited to ~ 20 mJ in the 248 nm photo-dissociation beam and ~ 1 mJ in the 535 nm dye laser beam. Focused geometry was therefore required in order to create the high number density conditions favourable for observation of optical gain in the exciplex bands. However with only the focused (~ diffraction limited) 248 nm laser incident on the vapour cell an intense super-fluorescent 535 nm ($7^2S_{1/2} - 6^2P_{3/2}$) resonance laser was observed. Since single photon photo-dissociation of TlCl at 248 nm produces only $Tl(6^2P_J)$ atoms this effect can only be explained on the basis of either two photon absorption by TlCl or a sequential single photon absorption process in atomic thallium to produce higher excited Tl states.

Under unfocused conditions the super-fluorescent resonance laser was absent but weaker fluorescence from higher excited states of thallium was observed. Unfortunately the atomic number densities obtainable under unfocused conditions (~ 5×10^{14} cm^{-3}) were too low (by ~ 100) to produce observable optical gain on the Tl-Xe exciplex bands.

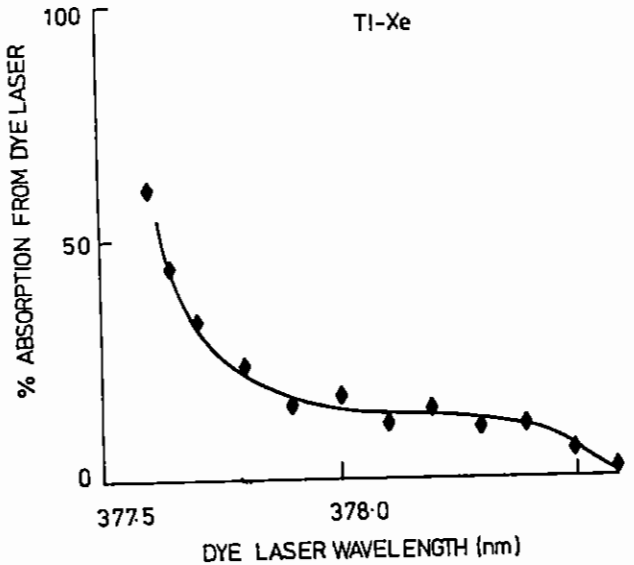

Fig B3.14 Tl-Xe Quasi-Molecular absorption from the pump dye laser beam versus dye laser wavelength. The incident dye laser pulse energy was 235 μJ. The Solid line calculated from the quasi-static theoretical model.

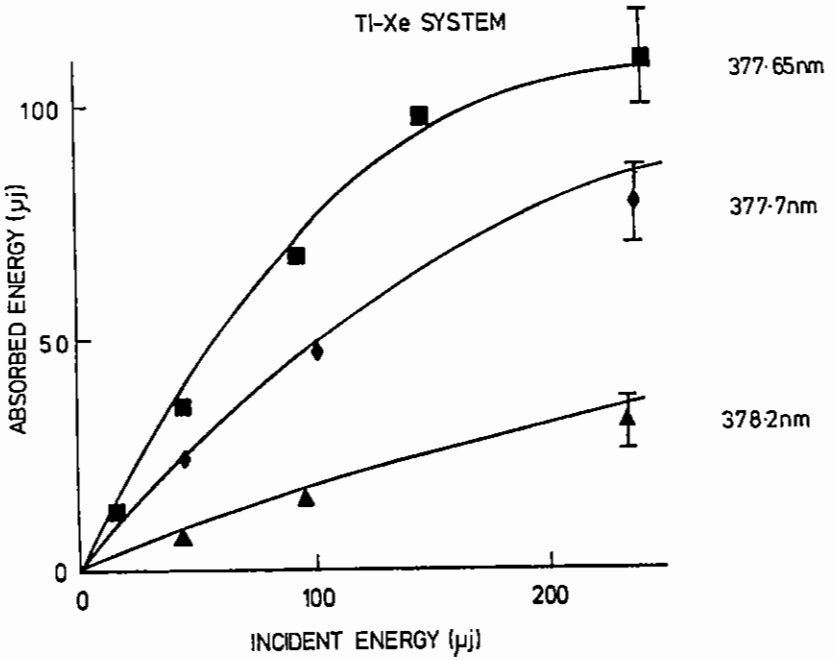

Fig B3.15 Absorbed dye laser energy versus incident dye laser energy for three dye laser wavelengths within the violet Tl-Xe quasi-molecular band. The solid lines are calculated from the quasi-static theoretical model.

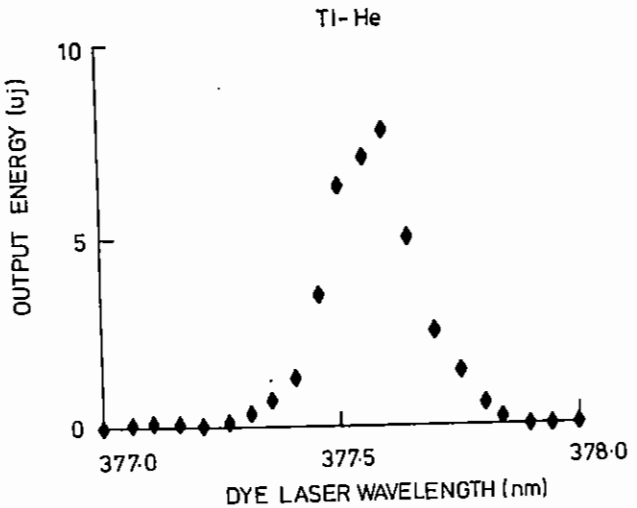

Fig B3.16 535 nm SCF laser pulse energy versus pump dye laser wavelength. The pump dye laser energy was 250 μJ.

B3.3.5 Conclusions

We have demonstrated that wavelength selective photo-dissociation by high power excimer lasers in conjunction with optical pumping in quasi-molecular absorption bands provides a convenient technique for production of high number densities and specific population distributions in excited atomic and exciplex systems. This technique has considerable potential for efficient production of new frequency up-converted SCF resonance lasers and optically pumped exciplex lasers in the UV and VUV regions.

B3.4 STIMULATED ANTI-STOKES RAMAN GENERATION IN POPULATION INVERTED HIGHLY VIBRATIONALLY EXCITED MOLECULAR SYSTEMS

I Gillan, D Denvir, J Bechara, H Cormican, I Duncan, W D McGrath and T Morrow (Queen's Belfast)

B3.4.1 Introduction

During the past year a programme on possible stimulated anti-stokes Raman (SASR) up-conversion (Fig B3.17) in inverted highly vibrationally excited molecules was initiated.

Due to the proliferation of closely spaced electronic-vibrational-rotational lines in the UV-visible spectra of such molecules they have considerable potential for providing continuously tunable up-converted laser outputs in the UV and VUV. Vibrationally excited NO($X^2\pi$) produced by direct UV photodissociation of NOCl provides a convenient candidate for initial studies (B3.14-16).

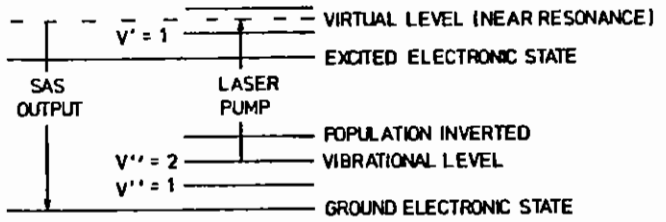

Fig B3.17

Results obtained by previous workers (B3.17) indicated that photodissociation of NOCl at 193 nm results in the direct production of highly vibrationally excited NO $X^2\pi$(v'' = 1-16) with the vibrational population distribution peaking at v'' = 7-10. The latter workers based their conclusions on low pressure (< 300 m torr) IR emission measurements and their results therefore provide no direct evidence on the temporal dependence of the population inversion of the higher vibrational levels w.r.t. the v'' = 0 level. The exact relaxation kinetics of the different vibrational levels are not yet fully understood nor the relaxation times known, particularly under high number density conditions.

Our initial experiments therefore concentrated on confirming the vibrational population inversion w.r.t. the v'' = 0 and determining the optimum experimental conditions for producing high number densities in

the higher v'' levels. The vibrational relaxation of the higher vibrational levels (in particular the $X^2\pi$, v'' = 9)and the subsequent build up of population in the v'' = 0 level were investigated at specific delay times in the range 10 ns - 1 ms after direct photodissociation of NOCl at 193 nm.

B3.4.2 Experimental

The vibrational relaxation of the NO($X^2\pi$) state was investigated by tuning the dye laser into resonance with appropriate absorption lines in the β and γ systems of NO and measuring the subsequent fluorescence from either the $B^2\pi$ or $A^2\Sigma^+$ states respectively (Fig B3.18). The photolysing ArF laser (EMG MSC 103) was focused through the CaF_2 window of the flowing gas cell (Fig B3.22) by a cylindrical lens (f = 20 cm). Complete photodissociation of NOCl pressures up to 60 torr could be achieved for ArF laser pulse energies of ~ 100 mJ. The delayed dye laser probe beam was passed through the nascent $NO^{\ddagger}$approximately 1 mm behind the excimer entrance window. The resulting β/γ fluorescence was collected and imaged on the entrance slits of two separate spectrometers. One spectrometer was fitted with the intensified diode array system (OMA) and provided direct recording of the complete fluorescence spectrum. The second spectrometer was fitted with a photomultiplier (RCA 1P28) which monitored the fluorescence intensity in one particular vibrational band. A record of the photomultiplier output as a function of dye laser input wavelength provided an excitation (absorption) spectrum of the $NO^{\ddagger}$ ($A^2\Sigma^+ \leftarrow X^2\pi$ or $B^2\pi \leftarrow X^2\pi$) vibrational bands. The photomultiplier output was fed, via an A/D converter, to an Apple microcomputer which provided software sample-hold and signal integration over a number (generally 10) of events, resulting in an improved signal/noise ratio. The dye laser pulse energy was monitored with a pyroelectric detector and the excitation (absorption) spectrum of $NO^{\ddagger}$ was corrected directly by the microcomputer for variations in the dye laser pulse energy with wavelength. The Apple microcomputer also controlled the tuning steps of the dye laser and the firing sequence of the photodissociation and probe dye lasers.

B3.4.3 Results and discussion

An excitation (absorption) spectrum of NO $A^2\Sigma^+$(v' = 0) ← NO $X^2\pi$(v''=0) band (Fig B3.19) was recorded in order to accurately calibrate the detection system, in terms of both wavelength and NO v'' = 0 number density. A limited region of the latter is shown at higher dispersion in Fig B3.20 and the same excitation spectrum of NO v'' = 0 observed at 150 ns after the photolysis of an NOCl mixture is shown for comparison in Fig B3.21.

The nascent $NO^{\ddagger}$ was probed by the dye laser at various delay times after the initial photodissociation. With the dye laser tuned to selected rotational lines in the γ(0,0)band the build up of the v'' = 0 population was monitored. Fig B3.23 shows the results obtained when the dye laser was tuned to J = $11^1/_2$ of the Q22 + R12 system. The peak fluorescence (corresponding to maximum NO v'' = 0 population) observed was 75% of the value obtained when the same pressure (0.98 torr) of pure NO was passed through the flow system. The apparent reduction of the ground state population at long delays (> 100 μs) is probably due to diffusion and gas flow reducing the NO density in the detection region. Similar results were obtained for lines of low (i.e. $3\frac{1}{2}$) or high (i.e. $15\frac{1}{2}$) J-values within the γ(0,0) system showing that the observed temporal variation of population was not influenced by rotational relaxation.

The temporal dependance of the v'' = 9 was investigated in detail for various NOCl pressures in the range 0.4 - 20 torr. The half-life of the v'' = 9 decreased markedly with increase in initial NOCl pressure (i.e. total number density of $NO^{\ddagger}$) from ~ 7 μs at 0.4 torr to ~ 25ns at 20 torr. Since the kinetics of the v'' = 9 relaxation are complex and the results are not yet fully processed these will be discussed in detail at a later stage.

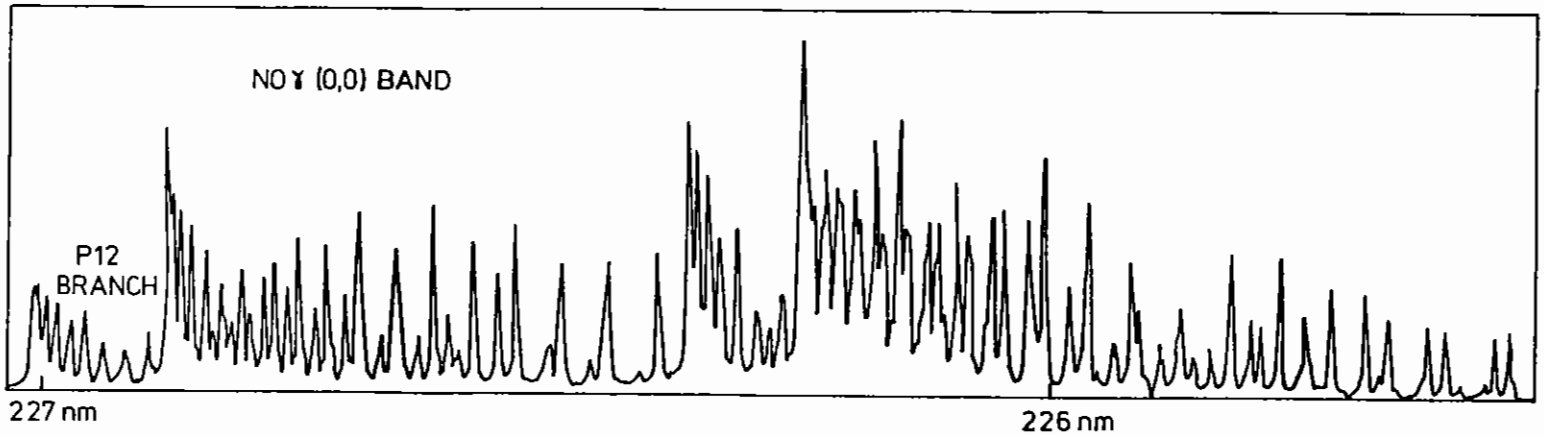

Fig B3.19 Excitation spectrum of NO γ(0,0) band recorded at NO pressure of 0.98 torr

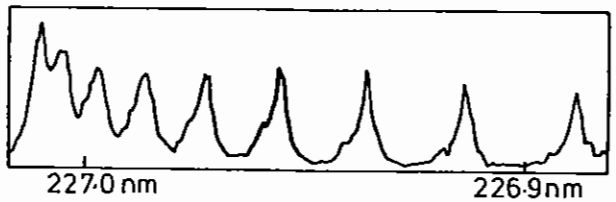

Fig B3.20 The P12 branch in Fig B3.19 at higher dispersion

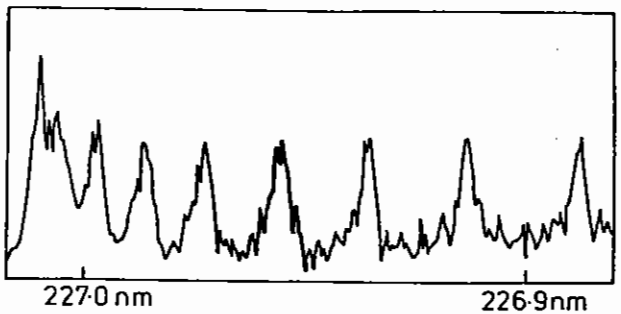

Fig B3.21 Excitation spectrum of the P12 branch of NO γ(0,0) band observed at 150 ns after 193 nm photodissociation of 0.98 torr NOCl

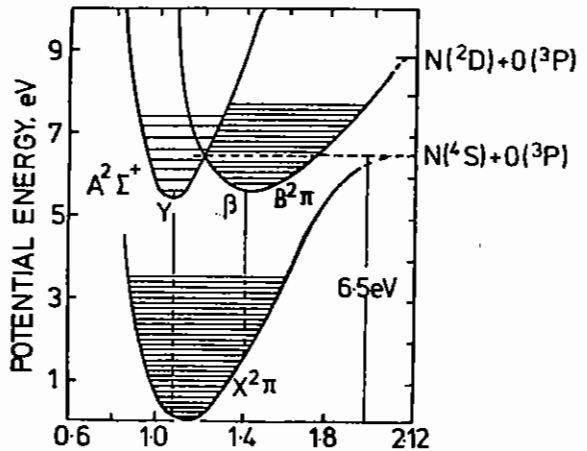

Fig B3.18 Potential curves of the lower lying states of NO

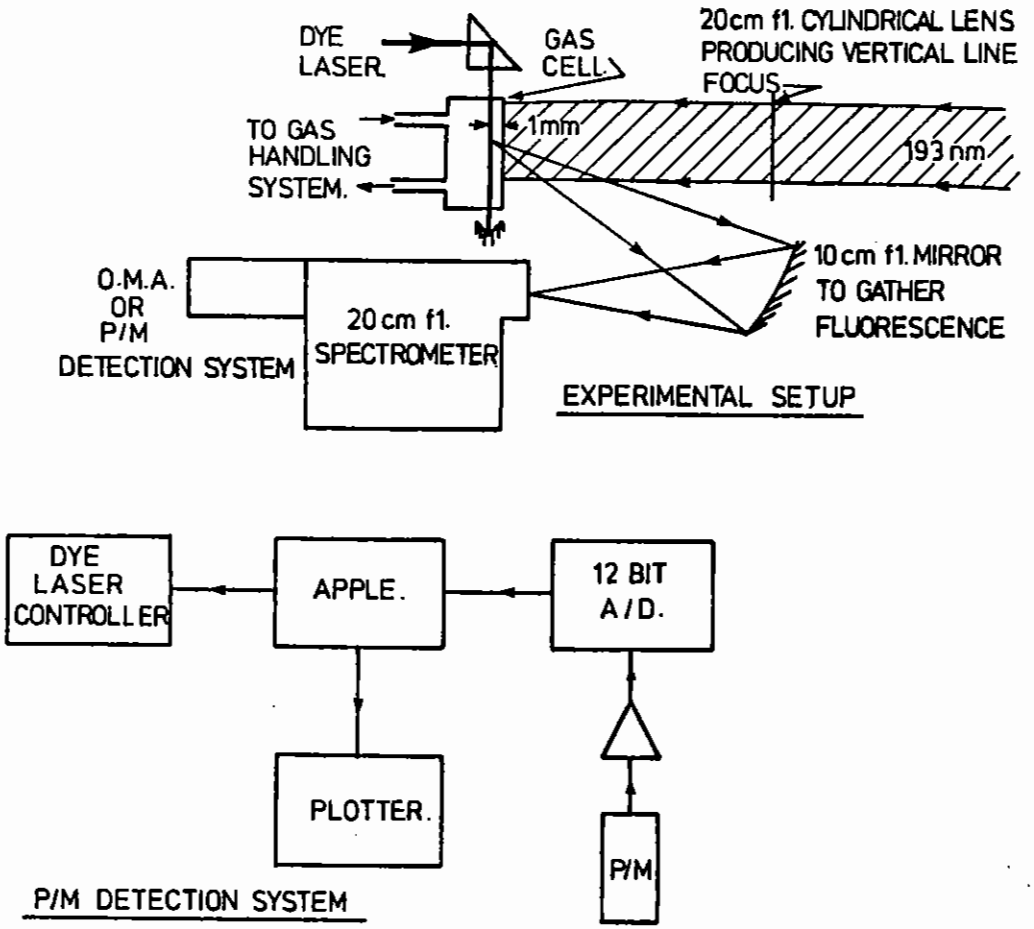

Fig B3.22 Schematic diagram of the experimental set-up

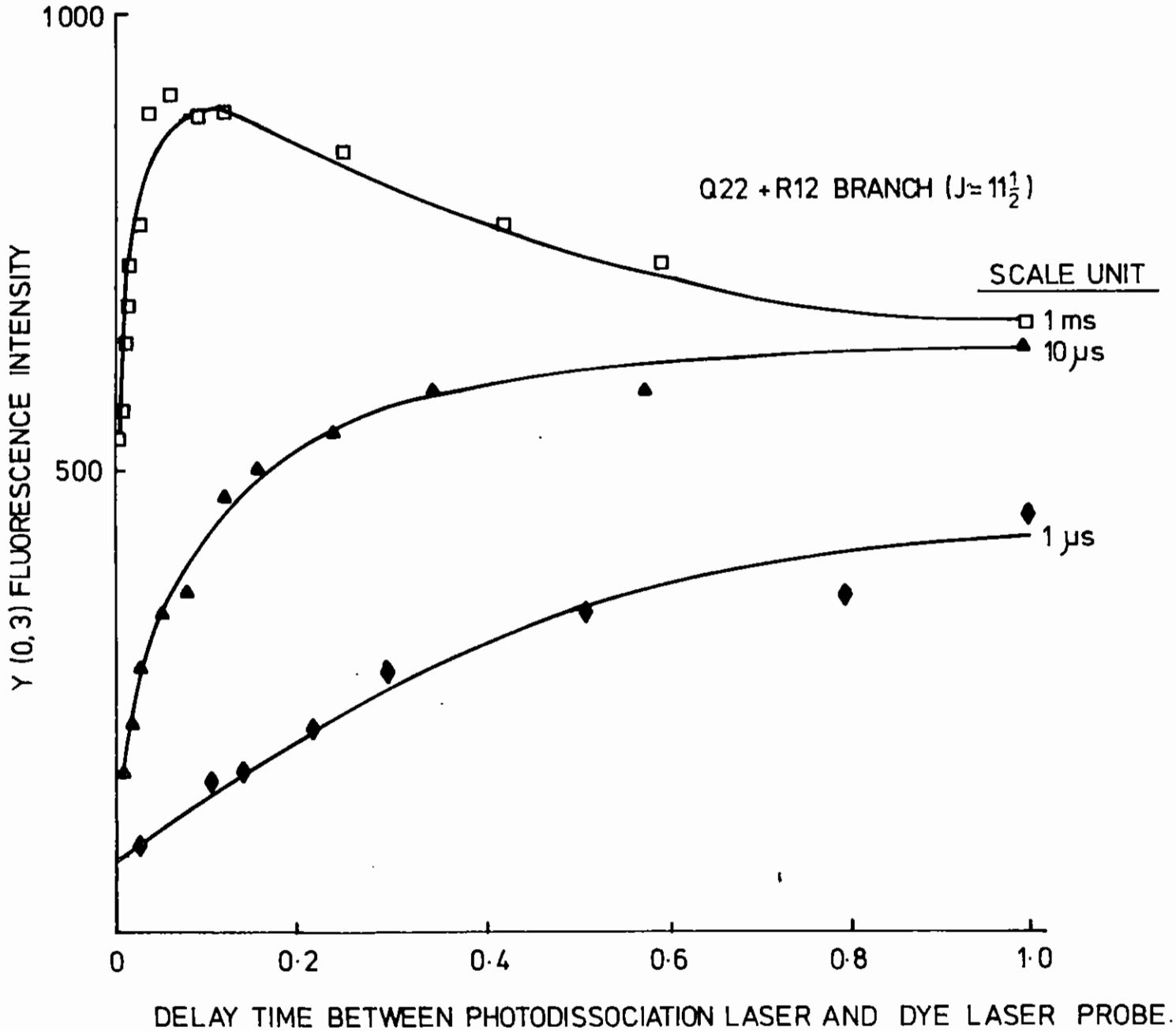

Fig B3.23 Build up of $X^2\pi v'' = 0$ population as a function of time after initial photodissociation of NOCl at 193 nm.

B3.4.4 Conclusions

We have demonstrated that high number densities of inverted high vibrational levels of NO are produced by direct photodissociation of NOCl at 193 nm. For the first time it has been possible to show that the NO fragment is produced exclusively in higher vibrationally excited states and to follow the decay of these vibrational levels and the subsequent build up in the v'' = 0. As expected the NO(v'' = 9) lifetime shows a marked dependance on initial NOCl pressure (i.e. overall $NO^{\ddagger}$ concentration after photolysis). At high $NO^{\ddagger}$ number densities however the v'' = 9 lifetime is sufficiently long (e.g. > 25ns at 20 torr) to enable SASR frequency up-conversion experiments to be attempted.

B3 REFERENCES

B3.1 1983 } RAL Annual Reports
B3.2 1984
B3.3 J Phys D, 17, No 11, L169 (Nov 1984)
B3.4 A P Thorne, Spectrophysics, Academic Press
B3.5 Griems, Spectral Line Broadening in Plasmas (1974)
B3.6 B Cheron, R Scheps, A Gallagher, J Chem Phys, 65, 326 (1976)
B3.7 B Cheron, R Scheps, A Gallagher, Phys Rev A, 15, 651, (1977)
B3.8 M G Raymer, J L Carlsten, Phys Rev Lett, 39, 1326, (1977)
B3.9 R M Hedges, D L Drummond, A Gallagher, Phys Rev, 6, 1519 (1972)
B3.10 N J A Van Veen, M S De Vries, T Baller, A E Vries, Chem Phys, 55, 371, (1981)
B3.11 D G Cunningham, D Denvir, I Duncan, T Morrow, Optica Acta, 31, 249 (1984)
B3.12 K Ludewigt, K Birkmann, B Wellegehausen, Appl Phys, B33, 133 (1984)
B3.13 P Burkhard, W Luthy, T Gerber, Opt Lett, 5, 512 (1980).
B3.14 N Basco and R G W Norrish, Proc. Roy. Soc. London, A268, 291 (1962)
B3.15 A J Grimley and P L Houston, J. Chem. Phys., 72, 1471 (1980)
B3.16 G E Busch and K R Wilson, J. Chem. Phys., 56, 3655 (1972)
B3.17 M D Moser, E Weitz and C Schatz, J.Chem. Phys., 78, 2757 (1983)

B4 FACILITY DEVELOPMENT

B4.1 GENERATION OF TUNABLE COHERENT VUV RADIATION BY ANTI-STOKES SCATTERING OF EXCIMER PUMPED DYE LASER RADIATION

K G H Baldwin, J P Marangos and D D Burgess (Imperial College)
M C Gower (RAL)

Coherent radiation in the vacuum ultraviolet has important applications in plasma diagnostics, spectroscopy, and photochemistry. One method of generating tunable coherent VUV radiation has been to employ four-wave mixing processes in rare gases and metal vapours (B4.1). Another method uses stimulated Raman scattering coupled with a four-wave parametric mixing process (B4.2). In this process, the pump, stimulated Stokes and anti-Stokes radiations mix together to produce coherent radiation at ω_{ASn} which is resonant with the anti-Stokes frequencies of the scattering molecule, such that $\omega_{AS1} = 2\omega_L - \omega_{S1}$ and $\omega_{ASn} = (\omega_L + \omega_{ASn-1} - \omega_{S1}) = \omega_L + n\omega_{10}$. Here ω_L and ω_{S1} are the pump and first Stokes frequencies, while ω_{10} is the vibrational frequency of the molecule (4155 cm^{-1} for H_2). The wavevector diagrams for the phase matching of these four-wave processes are shown in Figs. B4.1(a) and (b). Schomburg et al. (B4.2) have reported coherent VUV generation by this method using hydrogen as the Raman shifting and four-wave mixing medium. A high energy (>100mJ), high beam quality (TEM_{oo} mode) relatively complex frequency doubled,Nd:YAG-pumped dye laser was employed in their experiment to generate coherent radiation down to 1380 Å.

By contrast, the present work employs a simple, low power (<10mJ), transversely pumped commercial dye laser system to generate radiation down to 1362 Å (the 11th anti-Stokes line in H_2). To our knowledge this is the shortest wavelength generated to date by anti-Stokes (AS) shifting of dye laser radiation, and was achieved by employing UV dyes rather than the visible dyes that have been used in previous work. The H_2 pressure dependence of the intensity of the AS_5 to AS_{10} lines was also investigated. Using the known response of the detection system at 1640 Å the energy of the radiation in the AS_8 line was further

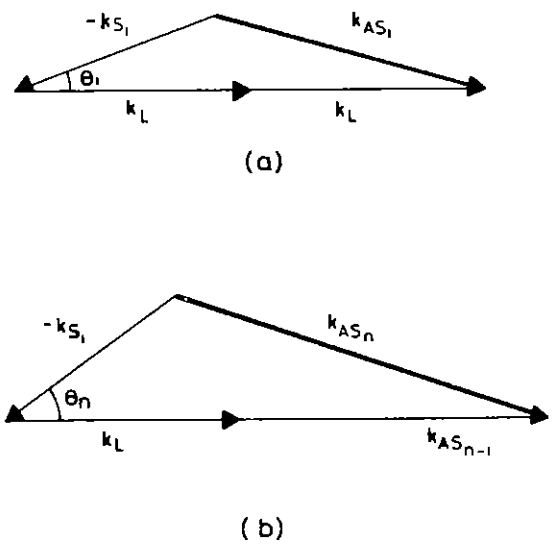

Fig B4.1 (a) Phase matching diagram showing the mixing of two pump photons having wavevectors k_L with a photon at the first Stokes frequency ω_{S_1}. (b) Phase matching diagram showing the mixing of the pump and first Stokes radiation with the radiation at the previous anti-Stokes frequency to produce radiation at ω_{AS_n}.

estimated. Finally, a comparison was made of the relative efficiency in generating radiation at 1640 Å using two different pump wavelengths obtained from butyl-PBD (3600 Å) and Coumarin-47(5149 Å) dyes.

The experimental arrangement used to generate and detect the VUV radiation is shown in Fig. B4.2.

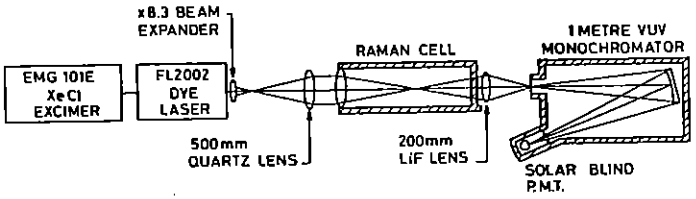

Fig B4.2 The commercially available excimer-pumped dye laser system and hydrogen-filled Raman cell used to produce the coherent VUV radiation, which was detected using a 1 m monochromator and solar blind photomultiplier.

It employed a commercially available, 3-stage dye laser (Lambda Physik FL2002) pumped transversely by a XeCl excimer laser (Lambda Physik EMG 101E). The dye laser produced a 7.4 mJ pulse of 4 ns duration with a linewidth of ~0.2 cm^{-1} when operated at 3606 Å using butyl-PBD dye. The beam profile was oval in cross-section with minor and major axis dimensions of 2 mm and 3 mm, and measured divergences of 0.8 mrad in the vertical direction and 0.5 mrad (with a gaussian profile) in the horizontal direction.

By using a telescope, the dye laser output beam was expanded by a factor of 8.3 in order to enhance the Raman conversion efficiency. telescope allowed the higher-order anti-Stokes components to be ph. matched over a wider range of angles. Without the telescope the dispersed emission from only the AS_1-AS_4 lines was visible as fluorescence on a white card, whereas all the AS_1-AS_6 lines outsi.. VUV were visible when the telescope was in place. The expanded dye laser output was focussed using a 0.5 m focal length spectrosil l. le. into the 1.04m long hydrogen filled Raman cell which was originally designed for the Raman shifting of excimer laser radiation (Lambda Physik EMG 75). The lens also acted as Raman cell entrance window, and a 5 mm thick CaF_2 window was used on the output side.

For observation of generated wavelengths down to 1899 Å (AS_6), a quartz prism disperser in air was employed. A Gen-Tec joulemeter (ED100)was used to measure the energies of the AS_1 to AS_3 components of the generated radiation. For observation of wavelengths shorter than 1899 Å (AS_7 to AS_{11} , the generated VUV radiation was focussed by a 0.2 m focal length LiF lens to a spot several centimetres in front of the entrance slits of a 1 m VUV monochromator. The VUV radiation was dispersed by a MgF_2 coated, 1200 lines/mm grating blazed at 1200 Å. Detection of the radiation was performed photoelectrically using a Hamamatsu photomultiplier and a Tektronix 7904 oscilloscope.

The VUV detection system enabled ovservation of generated radiation down to the AS_{11} line at 1362 Å. Observation of shorter wavelength radiation was limited by a combination of the poor transmission of the CaF_2 optics, and the increasing dispersion of the hydrogen in the Raman cell at shorter wavelengths so that the phase matching condition $k_L + k_{ASn-1} - k_{S1} = k_{ASn}$ can no longer be satisfied.

The measured energies of the first three AS lines are shown in table B4.1. As can be seen, the energy decreases by a factor ~3 between successive AS components of the generated radiation. In a similar experiment using Coumarin-2 dye at 4400Å and a comparable laser system, Brink and Proch (B4.3) found a similar ratio for generating radiation at anti-Stokes frequencies in the ultraviolet spectral region.

Table B4.1
ENERGIES OF THE FIRST THREE ANTI-STOKES COMPONENTS AT A HYDROGEN PRESSURE OF 9 BAR.

AS_n	WAVELENGTH (Å)	ENERGY (μJ)
n = 1	3136.0	150 ± 20
n = 2	2774.5	50 ± 10
n = 3	2487.7	20 ± 5

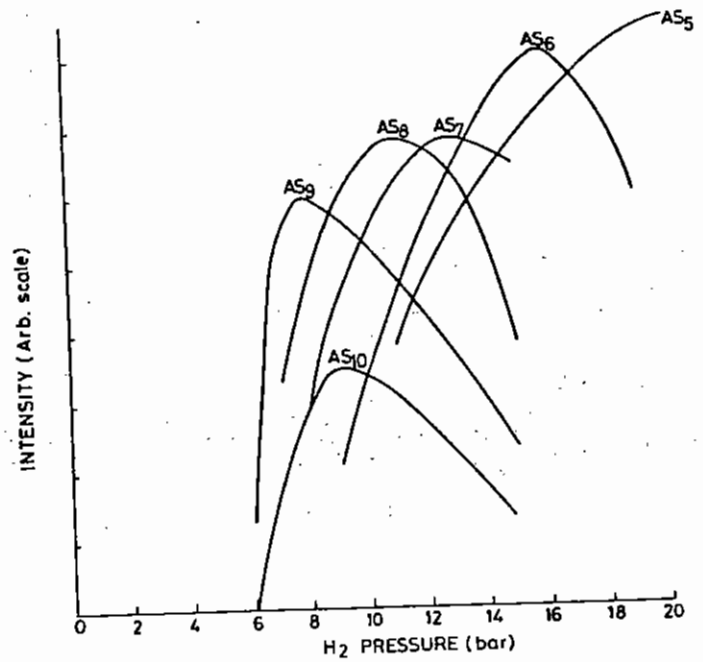

Fig B4.3 VUV output vs hydrogen pressure in the Raman cell for the AS_5-AS_{10} lines. The curve for each line is on an arbitrary linear intensity scale and is not related to the intensity scales for the neighbouring curves.

Physical Laboratory (B4.4), the response of the monochromator and photomultiplier was measured at 1640Å. This calibration was then used to calculate the energy in the AS_8 component at 1640Å using the known slit widths of the monochromator. In order to obtain a rough estimate of the energy, it was assumed that the size of the AS_8 beam was of the same order as the dye laser beam at the monochromator entrance slits. This assumption yielded a value of ~20nJ at 1640Å (5 W peak power), which is consistent with a factor of ~ 3 reduction in energy with each successive higher AS component.

The measured pressure dependences of the AS_5- AS_{10} lines is shown in Fig. B4.3. A decrease in the pressure at which the signal is optimised can be seen for higher order AS lines. This trend is in agreement with the results obtained using longer wavelength dye laser radiation. (B4.3, B4.5).

A comparison between the efficiency of generating 1640-Å radiation using the AS_8 line from a pump laser containing butyl-PBD dye (3606Å), and the AS_{10} line from a pump laser containing Coumarin-47 dye (5149Å) was carried out. When using butyl-PBD, the energy of the dye laser 3606Å was measured to be 7.4mJ. The hydrogen pressure in the Raman cell was then adjusted to optimise the signal at 1640Å. With the detection system unaltered the dye was changed to Coumarin-47, and the dye laser energy was then measured to be 15mJ at 5149Å. However, no signal was detected at the AS_{10} line at 1640Å, even though the dye laser output was twice that obtained when butyl-PBD was used. Only when the gain in the photo-multiplier was increased by a factor of ~12 was some signal detected, and only then after optimization of the hydrogen pressure in the Raman cell.

It is evident that the generation of coherent VUV radiation by stimulated Raman scattering is enhanced by the use of shorter wavelength dye laser pump radiation. As well as the stimulated Raman gain for first Stokes generation being larger at shorter wavelengths, we expect the phase matching requirements to be less severe when fewer frequency shifts are involved in the four-wave mixing process. We have shown that the increase in efficiency obtained when using ultraviolet

pump wavelengths means that even relatively simple, commercially available dye laser systems can be used to generate coherent VUV radiation down to 1360Å in a hydrogen-filled Raman shifting Cell.

B4.2 Improved stability of line-narrowed excimer lasers

I N Ross, F O'Neill, E Madraszek, D Baker, G Hogg and E M Hodgson
(RAL)

Considerable time has been devoted to facility development on the line-narrowed excimer laser based on the EMG150 system which has shown that its spectral performance is limited by mechanical and thermal instabilities of its optical components. To largely remove these problems the optical mounting system has been redesigned. All the optics, except one oscillator end mirror which has been given a more rigid support, have been decoupled from the laser head by mounting kinematically from a surface table, and temperature stable optical mounts with differential adjustments and rigid supports have been introduced. Early tests on the new layout using KrF have indicated a wavelength stability better than 0.5 cm^{-1} with single shot linewidth of less than 0.5 cm^{-1}. Figure B4.4 demonstrates that short term stability with the laser running at 10 Hz.

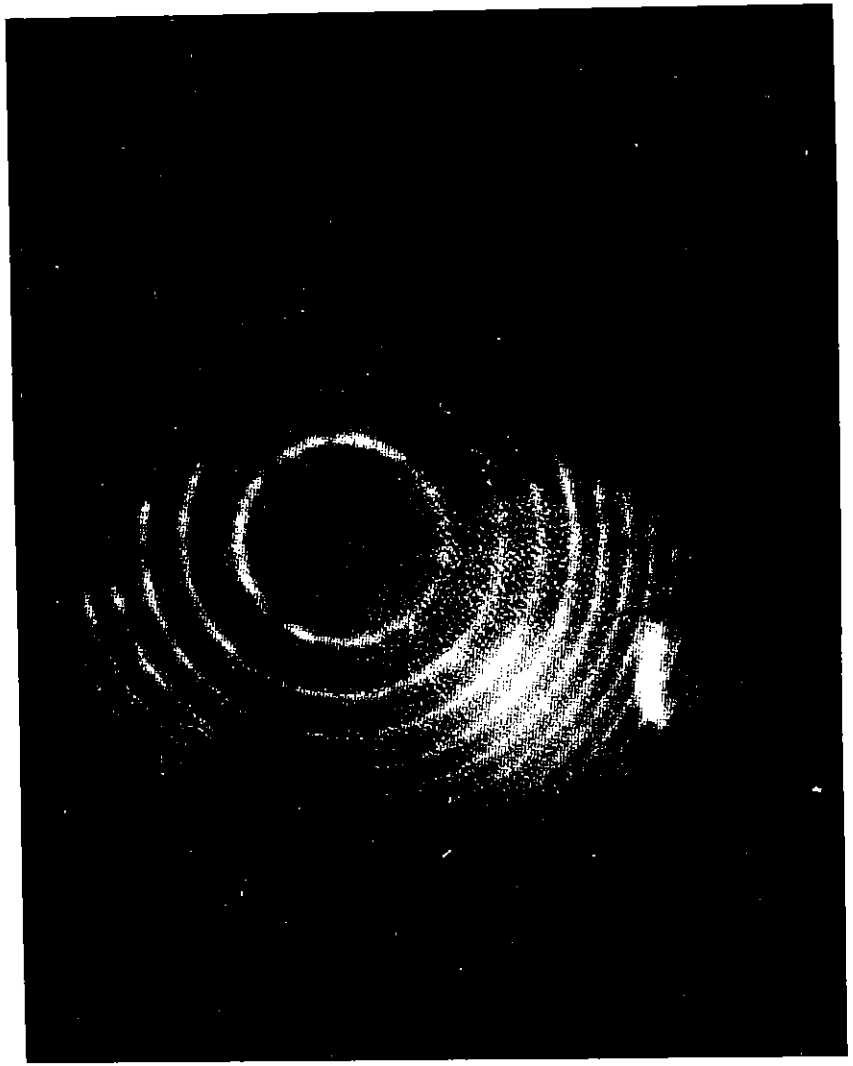

Fig B4.4 Fabry Perot interferogram of line-narrowed output of stabilised EMG 150 running at 10 Hz. Free spectral range of interferometer = 2 cm^{-1}.

In practical terms the laser is now much easier to run for experiments such as those described above in Sections B1-B3. As an example in a recent experiment on resonance Raman spectroscopy using the improved line narrowing arrangement it was found that the EMG150 operating on KrF could run at high repetition rate for 2-3 days without optical adjustment. Previously using the system as delivered by the manufacturer, adjustments to the optical alignment had to be carried out every 1-2 hours to maintain the narrowest line-width.

B4.3 New Ancillary Equipment

J Szechi and F O'Neill (RAL)

There have been several major purchases of UVRF equipment during this reporting year. A 5-watt INNOVA-90-5 Argon ion laser from coherent is now available and is used to generate cw Raman spectra as an alignment aid for the Raman spectrometer. A pulsed Xenon Arc lamp from Applied Photophysics Ltd has been purchased and has been used in flash photolysis experiments, both as an analyzing beam and a photolysing source. An LKB Ultraspec 4050 vis/uv scanning spectrophotometer has also been purchased. The UVRF has also reclaimed a transient recorder, made up of a Biomation 8100 100 MHz 8 bit waveform recorder and a Tracor Northern digital signal analyzer NS-570A which had been on loan to a University, and this is now available for experimental use.

Last year we reported on operational problems due to a lack of spare parts, particularly thyratrons, for the lasers. In spite of the increasing age of the equipment, less experimental time has been lost this year, as we now carry most of our own spares.

During the course of this year, the capabilities of the FL2002E dye laser have been considerably expanded by the provision of a second set of dye circulators and a new set of pump optics to enable it to be pumped by a KrF laser. A monitor etalon has also been purchased to facilitate installation of the intra-cavity etalon for line-narrowed operation. A full set of SHG crystals is now available for this laser, extending the wavelength coverage down to 217 nm.

Other items purchased during the year include new calorimeters, pulse generators, a pH meter, HeNe lasers and a Jobin Yvon H20UV monochromator. A Hewlett Packard HP7090A plotter has been purchased which can be connected to the existing OMA II system to produce high quality graphical and alpha numeric output.

B4.4 The New Laser Support Facility

F O'Neill (RAL)

Since the UVRF first started operations in 1982, its work has concentrated on the applications of excimer lasers and excimer-pumped dye lasers in various areas of physics, chemistry, biology and engineering. Whilst the high rate of usage of UVRF facilities indicated that it was satisfying a definite demand from University research teams it became obvious that there was a growing requirement to provide a broader range of laser facilities in particular picosecond lasers, Nd:YAG pumped dye lasers, CW argon ion and CW dye lasers etc. In addition it was thought desirable that lasers could be used in University laboratories, through a loan pool, as well as at the Central Laser Facility as had previously been the case with the UVRF.

It was out of this situation that a new Laser Support Facility (LSF) has been established with a formal start up date set to be the 1st May 1985. The overall aim of the Laser Support Facility is to give University users access to the widest possible range of lasers and advanced instrumentation and that where possible these facilities should be available for use either at the Central Laser Facility or in University laboratories. There will be three fairly distinct elements to the LSF:-

(1) Loan pool lasers consisting initially two of two Nd:YAG pumped dye lasers but with other lasers added over a period of two years (1985/86). The discussion on which lasers to buy in the future will depend on user demand but possible systems are an excimer-pumped dye laser, a CW dye laser and perhaps a third Nd:YAG pumped dye laser.

(2) A high energy picosecond dye laser delivering sub-millijoule (50-500μJ), 5psec pulses at 10Hz repetition rate at various wavelengths from the UV to the red. This laser will initially satisfy a considerable demand from the photo-biology community and although formally part of the loan pool equipment will most likely, because of its complexity, be used at the CLF.

(3) All the lasers (excimer + excimer pumped dye lasers) and ancillary equipment that is presently in the UVRF will be transferred into the LSF and will continue to be available to University researchers for use at the CLF.

The start up of LSF operations will entail some changes in the usage of laboratory space. New laboratory space will be made available to house the picosecond laser and the excimer lasers(which will be moved out of the old UVRF laboratories). The old UVRF laboratories will be used for loan pool operations a purpose for which they are very suitable since they have double door access to a truck loading area. The complete layout of the new LSF laboratory area as it will be from the 1st May 1985 is shown in Fig B4.5.

SECTION B4 - REFERENCES

B4.1 R Hilbig and R Wallenstein, Appl Optics, 21, 913 (1982).

B4.2 H Schomburg, H F Döbele and B Rückle, Appl Phys, B30, 131 (1983).

B4.3 D J Brink and D Proch, Optics Lett, 7, 494 (1982).

B4.4 D H Nettleton and R C Preston, NPL Report Qu 60, (1980).

B4.5 V Wilke and W Schmidt, Appl Phys, 18, 177 (1979).

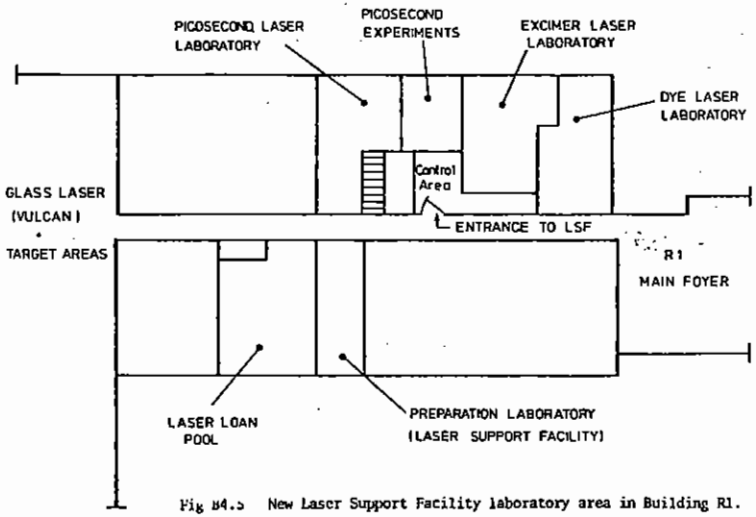

Fig B4.5 New Laser Support Facility laboratory area in Building R1.

Editor F O'Neill

C INTRODUCTION

F O'Neill (RAL)

The research and development programme on the high power KrF laser has progressed very rapidly in this reporting year and two very significant milestones have been reached. We have for the first time used the Sprite KrF laser for target experiments using 249 nm laser light. Secondly we have used the Sprite KrF laser to perform a high energy experiment to study the conversion of the KrF laser to a Raman output from CH_4 and H_2.

The target experiments are significant in that they represent the first ever performed with a high power KrF laser. We have demonstrated that the beam quality of the Sprite laser is sufficiently good to generate high temperature laser plasmas. The target experiments have also been valuable as they have highlighted deficiencies in the laser system (all of which have now been rectified) and have identified ways in which the laser could be improved for future target work.

The Raman conversion experiments are of crucial importance for the future development of the KrF laser. Our future work will concentrate on increasing the intensity of the KrF laser by using optical multiplexing and Raman amplification. The success of this programme was crucially dependant on being able to demonstrate a conversion efficiency from the KrF laser to Stokes output, - from CH_4 or H_2, of >50%. A lower efficiency would render the use of Raman amplifiers unviable. In fact efficiencies well in excess of 50% have been observed and thus our future programme involving the use of Raman conversion has been given a boost - this work is now being vigorously pursued.

The target experiments and Raman experiments are described in sections C1 and C2 below and the work related to the KrF optical multiplexer is reported in section C3.

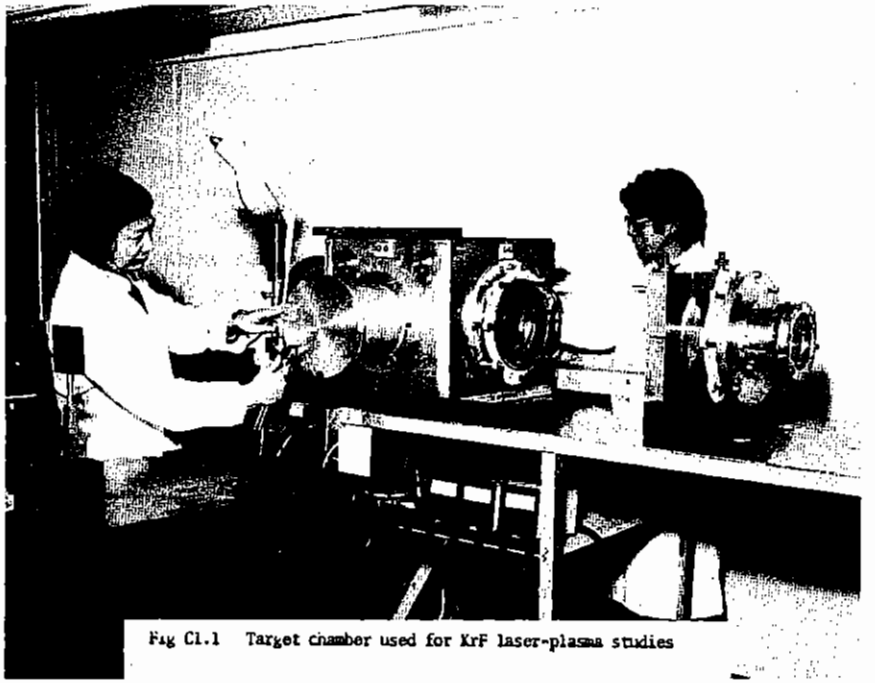

Fig C1.1 Target chamber used for KrF laser-plasma studies

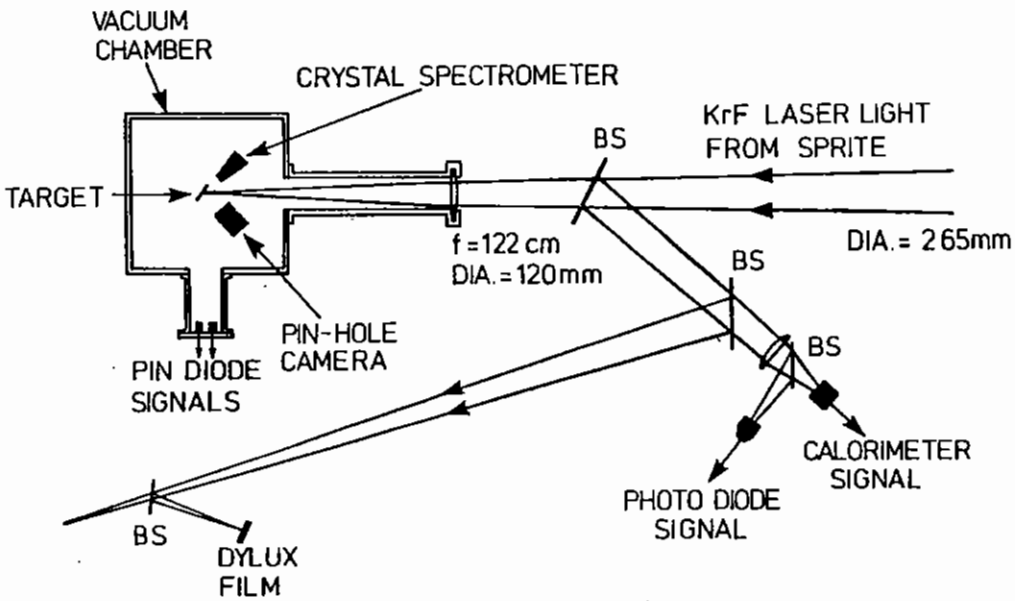

Fig C1.2 Experimental arrangement for KrF laser plasma studies

C1 TARGET EXPERIMENTS WITH THE SPRITE KrF LASER

Y Matsumoto, M J Shaw, F O'Neill, J P Partanen, M H Key, I N Ross, E M Hodgson (RAL), R Eason (Essex), Y Sakagami (Oxford)

C1.1 DESCRIPTION OF THE TARGET AREA SET-UP AND LASER PERFORMANCE

Early in this reporting year it was decided to use the Sprite KrF laser for preliminary target experiments. The experiments were mainly aimed at using the laser to generate high intensity X-ray pulses from laser produced plasmas. An increasingly large proportion of the activity of the CLF is devoted to the investigation and application of laser plasma X-ray sources and the Sprite KrF laser should be well suited for application to this type of work because of its high repetition rate, short wavelength and low running expenses. From the Sprite laser development point of view an early start up of target experiments is highly desirable even with the present 50ns pulse because it encourages work on improvements in areas such as laser beam quality, machine reliability, optics survivability, etc.

Target experiments were carried out during April and May 1984 using a simple box target chamber which is shown in Fig. C1.1. The layout of the experimental apparatus is shown in Fig. C1.2.

The e-beam-pumped KrF laser, Sprite, produces a single beam of 265mm diameter from an injection locked unstable resonator cavity. The separation of the resonator optics was adjusted so that the output beam converged to a diameter of 120 mm after propagating the 13-m distance to the target chamber. A plano-convex fused silica lens of 1.22-m focal length formed the input window of the evacuated target chamber (10^{-4} Torr) and focused the laser beam onto target. Target alignment was accomplished using low-energy pulses from the Sprite injection laser (Lambda Physik, EMG 101E) after they had passed through the Sprite optical cavity. When the Sprite laser was fired, up to 110J in 50ns was available on target in a lasing bandwidth of approximately $80cm^{-1}$. Injection locking was needed to obtain a low divergence output of high energy from Sprite (C1.1).

To estimate the focal spot size on target we have measured the divergence of the laser by taking Dylux film photographs (C1.2) of the laser pattern in the focal plane of the convergent output beam at a distance of 26m from the laser cavity. These measurements showed the angular distribution of the laser light to have a double-lobed structure an effect which was traced to being caused by pressure-induced distortion of the rear laser mirror which also served as the closure plate of the two-atmosphere laser cell. For future experiments we plan to use external laser mirrors which will avoid this problem and produce close to diffraction limited laser beams.

The overall divergence angle of the laser (containing 90% of the energy) was approximately 70μR. With the present focusing arrangement (convergent laser beam and f=1.22 m lens) we calculate that the intensity profile on target will have two spots, one strong and one weak, separated by approximatley 100μm within an overall spot diamter (containing 90% of the energy) of 190μm. Spherical aberration of the focusing lens contributes approximately 50μm of transverse aberration to the spot size. The intensity on target at the peak of the strong spot (containing ~ 50% of the laser energy within a circle of 100μm diameter) is estimated to be 3×10^{13} W/cm^2 for a laser energy on target of 110J.

The performance of the Sprite laser during the two month period of target operations is summarised in Fig C1.3 and Fig C1.4. These figures give information on the number of laser and target shots achieved per day and the laser energies on target. It can be seen that there were typically ~ 5 target shots per day with most laser pulse energies being in the range 40-100 J. The number of target shots per day was determined mainly by the time required for analysis of results between shots and also the time spent on alignment of target and diagnostic equipment preceeding shots. The firing rate of the laser presents no limitation as it could fire every 5-10 minutes if necessary.

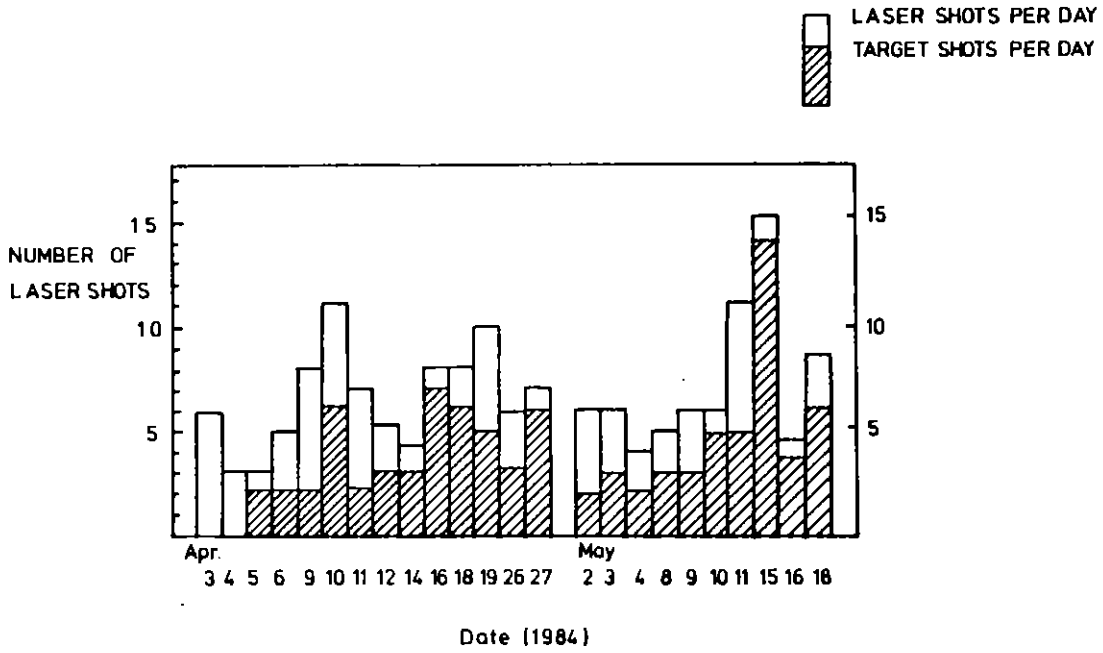

Fig C1.3 Histogram showing the number of laser shots and target shots per day achieved with KrF laser during the two month running period

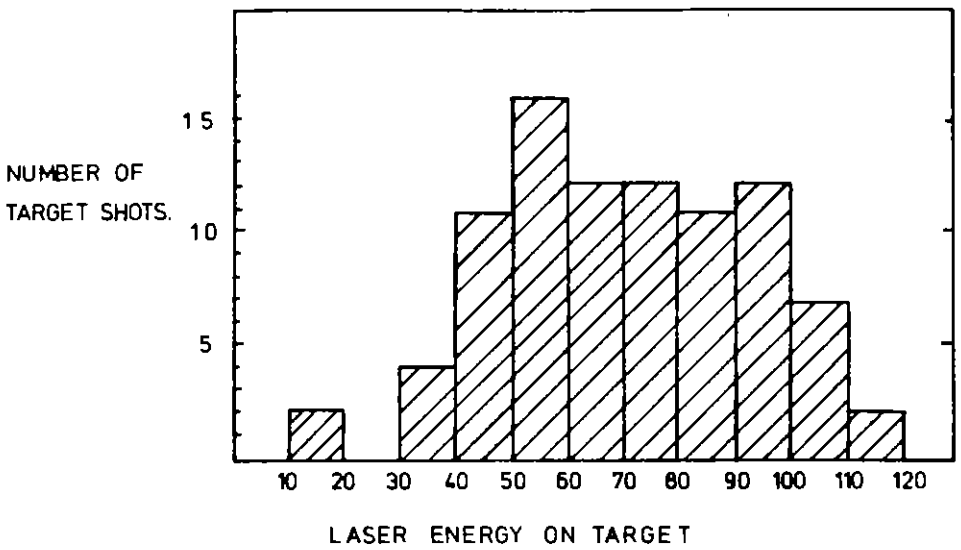

Fig C1.4 Histogram showing the spread of KrF laser pulse energies on target

C1.2 X-RAY EMISSION FROM KrF LASER-PRODUCED Al PLASMAS

The first target experiments consisted of a rapid survey of X-ray emission from a number of target materials. X-rays were detected using a pinhole camera for spatial information, a crystal spectrometer for spectral information and X-ray diodes for temporal information. It quickly became apparent that Al was the highest Z material that reliably gave high intensity hard X-ray emission ($h\nu > 1$ keV). Our experiments therefore concentrated on the use of Al targets with the aim of obtaining as much quantitative information as possible on the Al plasmas.

In these experiments the angle of incidence of the laser beam on target was in the range 25°-45° from the normal to the surface and an x-ray pinhole camera viewed the plasma at 60° to the laser axis. An X-ray image of the laser-produced plasma taken with a 10μm pinhole and a 24μm aluminized mylar filter (e^{-1} transmission for 2.7-keV photons) is shown in Fig. C1.5. The X-ray image has two spots spaced by 100 μm corresponding to the calculated double peaked laser profile on target. The overall size of the X-ray source is 225 μm which is slightly larger than the calculated size of the laser spot of 190 μm.

X-ray spectra in the range 0.53-0.92 nm were recorded using a miniature flat crystal spectrometer (C1.3) with an ammonium dihydrogen phosphate (ADP) crystal with 2d=1.065nm. The spectrometer slits were protected from target debris by a 12-μm-thick sheet of aluminized mylar (e^{-1} transmission for $h\nu$=1.9 keV). Spectra were recorded on Kodak DEF X-ray film and Fig C1.6 shows a single shot spectrum with strong emission of the resonance lines of Al XII (He-like) and Al XIII (H-like) and the recombination continuum of Al XII. The absolute brightness of the emission was deduced from the densitometer trace of Fig C1.6 using a crystal reflectivity value of 10^{-4} (C1.4) and using the measured sensitivity of the film(C1.5). The most intense line, Al XII, 1^1S_0-2^1P_1 at 0.776 nm, emitted 2.8×10^{14} photon sterad^{-1} (after subtraction of the background due to scattered light). The temperature of the plasma is calculated from the slope of the recombination continuum to be 200 eV and from the H-like to He-like line intensity ratios to be 400 eV. This temperature difference has been seen in

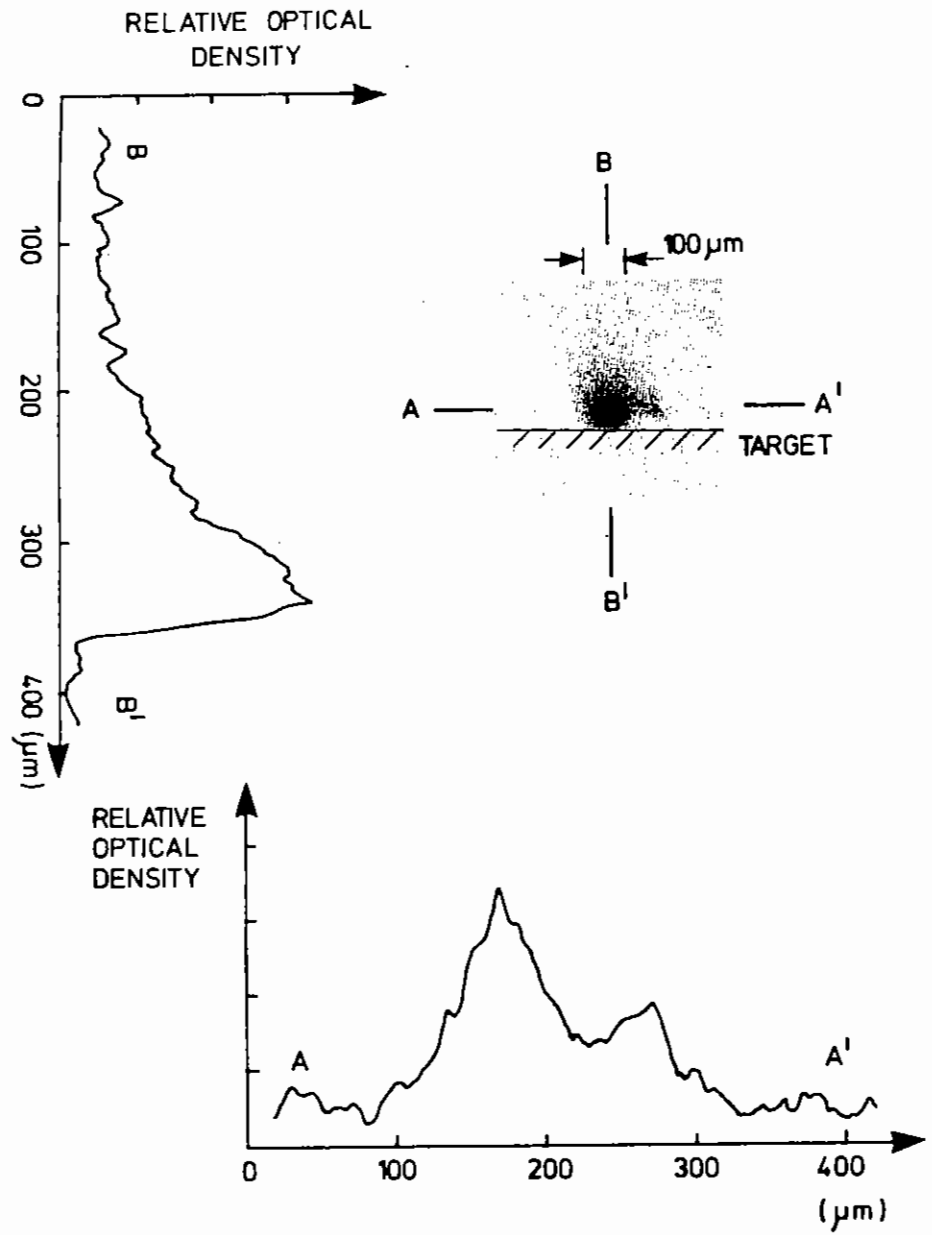

Fig C1.5 X-ray pinhole camera image and microndensitometer traces of KrF laser-produced Al plasmas

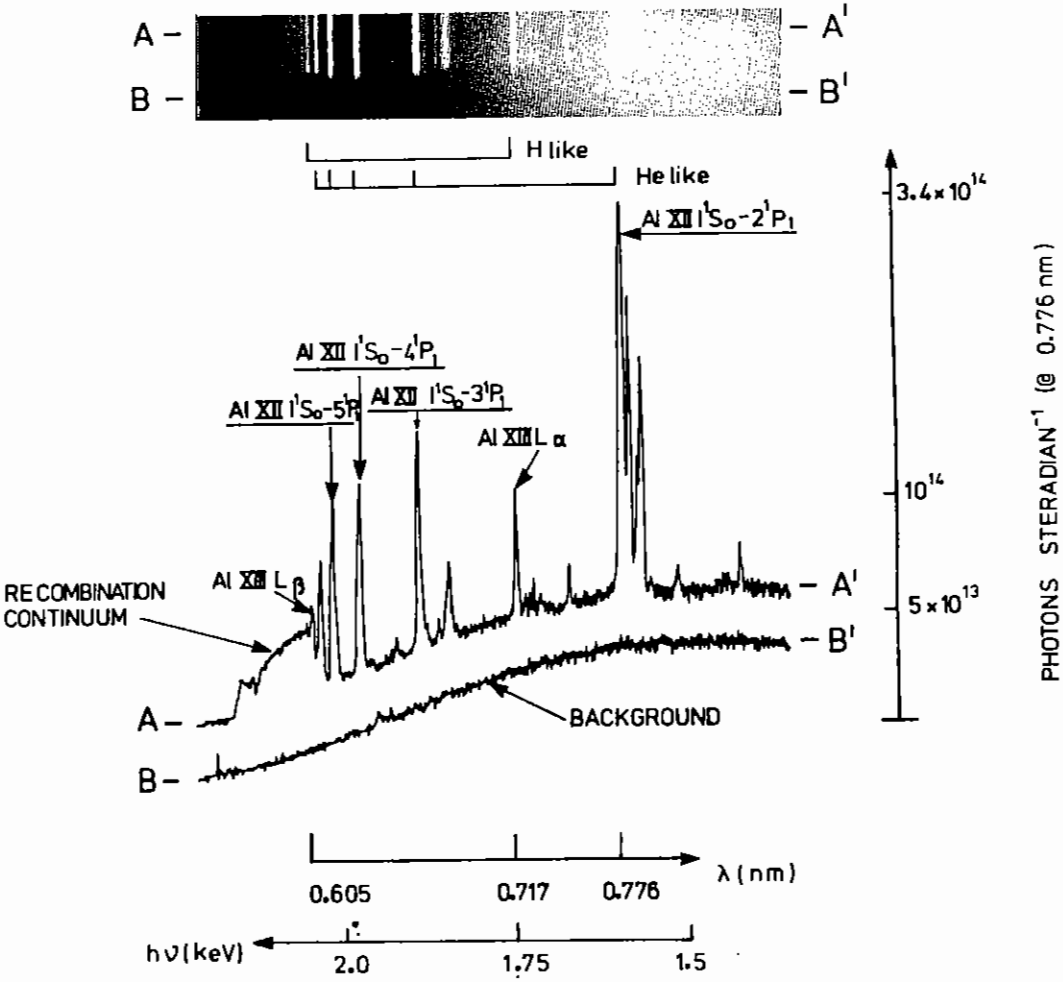

Fig C1.6 X-ray spectrum from Al plasma (upper) and microdensitometer trace of x-ray film (lower)

previous work with Nd:glass lasers (C1.6) where the effect was explained as being due to the temperature profile of the plasma.

The temporal characteristics of the X-ray emission were measured with a PIN diode filtered with 74 μm mylar (50 μm mylar plus 24 μm aluminized mylar) with e^{-1} transmission for $h\nu$ = 3.8keV (Fig C1.7).

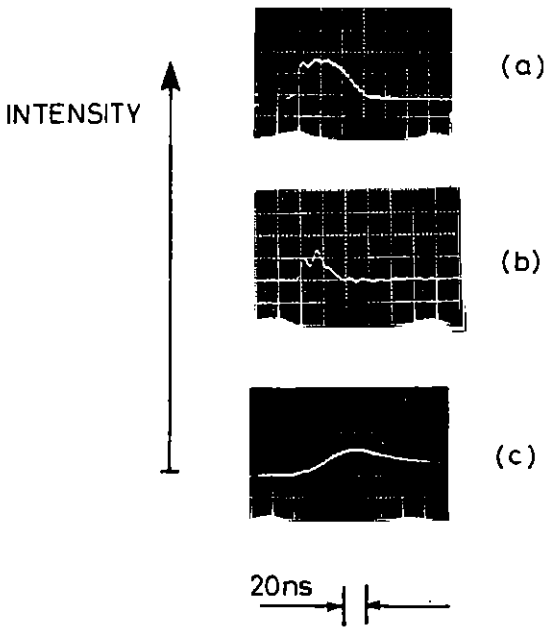

Fig C1.7 Temporal history of (a) laser pulse, (b) x-ray emission from the target, (c) visible light emission from the target

The PIN diode signal is generated by the X-ray emission in the range 1.5-2.5keV because the mylar filter strongly absorbs softer X rays. The notable feature is that the X-ray emission rises rapidly following the shape of the 2-ns rising edge of the laser pulse but then falls during the laser pulse with a full width at half-maximum of 20ns. This premature termination of X-ray emission can be attributed to the growth of the effective area of energy deposition during the laser pulse (C1.7). Also shown in Fig C1.7 is a signal from a PIN diode monitoring visible light. This signal has a duration of > 100 ns as a result of the long-lived recombining plasma.

It is possible to calculate the spectral brightness of the X-ray source from the above spectroscopic and temporal data. Assuming a uniformly emitting circular source of 200 μm diameter we obtain a maximum spectral brightness of 1.1 x 10^{17} erg cm^{-2} s^{-1} $sterad^{-1}$ in $\Delta\nu/\nu = 10^{-3}$. This can be compared with the single pulse brightness of a typical high power synchrotron radiation source (C1.8) and is 10^4 times brighter.

The efficiency of conversion from laser power into X-ray power (η_x) can be estimated from the above PIN diode data. We can write.

$$\eta_x = E_x \tau_l / E_l \tau_x ,$$

where E_x, E_l are the X-ray and laser energies and τ_x, τ_l are the corresponding pulse durations. Assuming optically thin emission (constant energy $steradian^{-1}$) into 2π steradians and estimating the sensitivity of the PIN diode (C1.9) the efficiency of conversion into x-rays in the range 1.5 keV < hν < 2.5 keV is estimated to be 0.2% for E_l=90J. For this calculation we have assumed the PIN diode filter to have an average transmission of 1.2% for photons in the range 1.5-2.5 keV. The conversion efficiency increases with laser power as shown in Fig. C1.8.

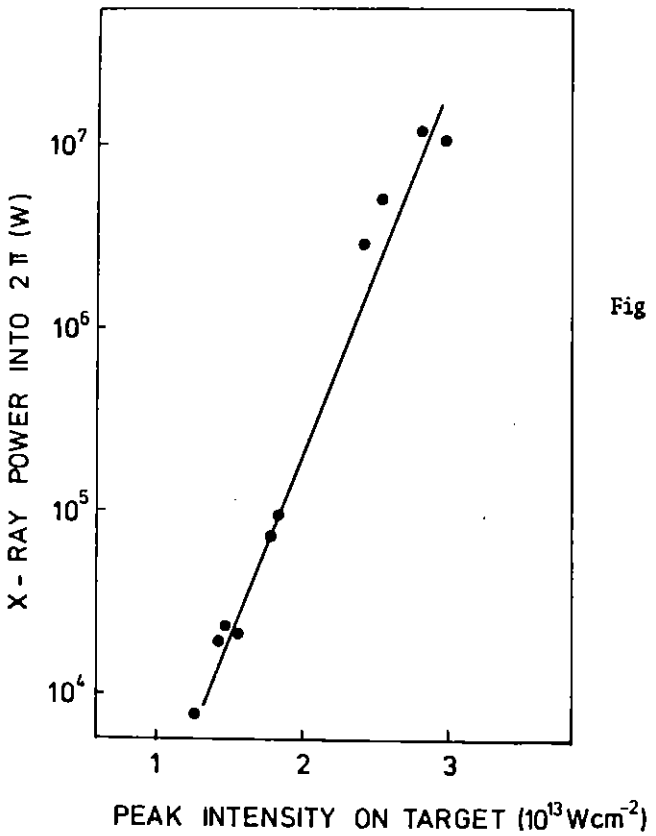

Fig C1.8 Integrated X-ray power (into 2π steradians) from Al plasma source as a function of incident laser intensity on target

Clearly the source brightness increases rapidly with laser irradiance in this range of irradiance and similar results have been seen with a Nd:glass laser (C1.7). Other work has shown a saturation in the conversion efficiency in the limit of high irradiance (C1.10).

These experiments represent the first ever reported observation of hard X-rays from a KrF laser produced plasma. It has also been shown that KrF lasers can be operated at sufficiently high power and with sufficiently low beam divergence to be highly competitive with Nd:glass lasers in producing soft X-ray radiation sources. The target experiments have given us information on the focussing properties of the Sprite laser beam and have led to the following conclusions: (1) A simple f/10 spherical lens contributes too much spherical aberration distortion to the target spot, (2) the reflective laser optics must be mounted outside the laser pressure vessel to avoid optical distortions due to pressure loading and (3) it is crucial to use injection locking with the short pulse Sprite laser to obtain a low divergence laser beam. To overcome problems (1) and (2) above we will in future use aspheric focussing optics and the laser mirrors will be mounted outside the laser pressure cell.

C1.3 X-RAY EMISSION FROM KrF LASER-PRODUCED C PLASMAS

When a high power laser beam is focussed onto carbon targets at intensities $>10^{12}$ W cm^{-2} the temperature in the resultant laser-produced plasma is high enough for carbon ions to be highly stripped of their electrons. Under these conditions some of the X-ray line emission from the plasma results from radiative transitions of electrons in H-like (CVI) and He-like (C-V) carbon and a number of these line emissions fall within the 2.3 - 4.4 nm spectral range which is termed the "water-window" for biological X-ray microscopy applications (C1.11). Previous experiments at the CLF(C1.12) have used the 1ns pulse from the Nd:Glass laser Vulcan to generate carbon laser-plasma X-ray sources for biological microscopy applications. For these applications it is perhaps not necessary to have such short duration X-ray pulses and we have therefore used the 50ns KrF laser pulses from Sprite to produce X-ray sources for comparison with the VULCAN work. The target illumination set-up was as is shown in Fig.

C1.2 except that the crystal spectrometer was replaced with a grazing incidence grating spectrograph (Rocket-type) to observe soft X-rays. Also the pinhole camera was no longer used.

The KrF laser was focussed onto polyethylene or graphite targets at a power density ~6 x 10^{12}W/cm^2 in a spot size of 200μm. The soft X-ray pulse duration measured with a PIN diode was 30ns. Fig. C1.9 shows a microdensitometer trace of a section of the X-ray spectrum recorded from the carbon laser-produced plasma using the Rocket spectrograph. The spectrum consists of three strong lines from CVI and two from CV in the 2.7 - 4.0 nm wavelength range (i.e. within the "water window") lying on an intense background. The cause of the back-ground is not completely clear but it is thought to be due to scattered laser light. The total energy into 2π in the five spectral lines shown in Fig. C1.9 is estimated to be ~ 2 joules. This is similar to the energy observed from carbon plasmas produced using the VULCAN laser and thus this KrF laser-plasma source should be usable for X-ray microscopy applications in the same way as the Nd: laser source.

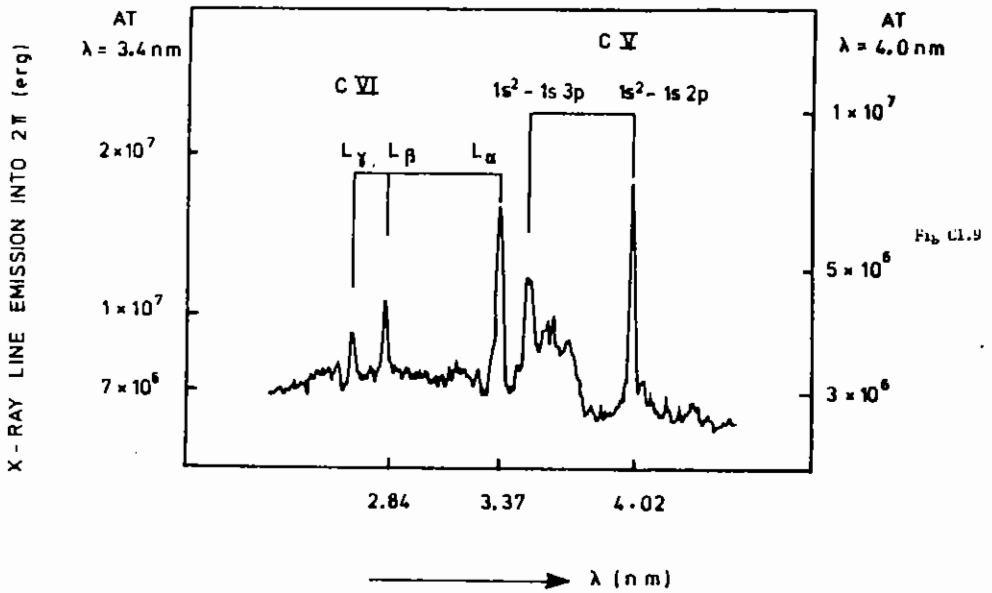

Fig C1.9

Microdensitometer tracing of x-ray spectrum from KrF laser produced carbon plasma recorded on Kodak 101-01 film. Target material was polyethylene although similar spectra were obtained with graphite targets

C1.4 LASER PLASMA EXPERIMENTS WITH OTHER TARGET MATERIALS

Some X-ray measurements have been made with target materials of higher Z than described above. In general the intensity of X-ray emission from higher Z laser plasmas was too low to achieve successful recording of X-ray pinhole photographs or X-ray spectra. Signals generated by hard X-rays were however detected with the PIN diode detectors and in Fig. C1.10 we have plotted the peak voltage of the PIN diode signal versus Z. For each target a 50μm thickness of Aluminised Mylar (e^{-1} transmission for hν = 3.0 keV) was placed in front of the PIN diode except in the case of Aℓ where a 75μm thickness (e^{-1} transmission for hν = 3.5 keV) was used.

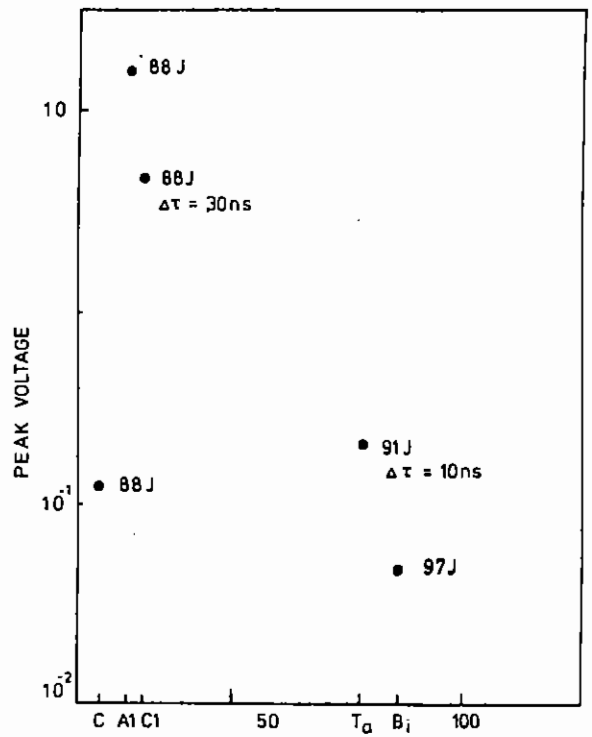

Fig C1.10 Peak voltage of PIN diode signals for various target materials

It can be seen that there is strong hard X-ray emission observed with Aℓ targets due to the high temperatures (200-400eV.) achieved in the laser produced plasma. The hard X-ray emission falls off rapidly with target Z. This effect is thought to be caused by the KrF light being more strongly absorbed in the plasma blow-off from the target as Z increases. Thus while at higher Z the overall conversion of laser light to X-rays may be high, the plasma temperature is lower (laser energy absorbed in a larger plasma volume) and thus hard X-rays are not produced. This hypothesis is supported by the fact that the observed duration of the hard X-ray pulse gets shorter as Z increases e.g. Δτ = 30ns for Cℓ and Δτ = 10ns for Ta.

CALIBRATION OF THE DUST PARTICLE SENSOR ON BOARD THE GIOTTO SPACECRAFT

A Ridgeley (RAL)

The Sprite laser has been used to calibrate the dust impact detection system (Didsy) on board the Giotto spacecraft which will intercept Halley's comet in March 1986.

The Giotto spacecraft will encounter the comet at a relative speed of 68 km/s, at which speed even very small dust particles can mortally damage an unprotectd spacecraft. Giotto is protected from dust particle damage by means of a dual shield comprising a 1 mm thick aluminium bumper shield and a 25 mm thick kevlar and plastic form rear shield mounted 250 mm behind the bumper shield. Particles lighter than about 10^{-6}g are expected to be stopped by the bumper shield. Heavier particles will penetrate the bumper shield but will generate a diverging cloud of debris which will impact the rear shield over a large area with much reduced penetrating ability.

The Didsy experiment is a collaboration between the University of Kent at Canterbury and several other groups, with J A N McDonnell at Canterbury the Principle Investigator. The experiment will detect particle impacts on the two shields using various technique including piezo-electric sensors to detect the elastic wave motions induced in the shield by the particle impacts (C1.13).

The calibration of the Didsy experiment has presented a problem because particles in the mass range of interest cannot conveniently be accelerated to 68 km/sec in the laboratory. This is particularly unfortunate as it is believed that for impact speeds of greater than 10 km/sec crater formation becomes the dominant effect in the collision (C1.14).

Lasers provide a means of simulating hypervelocity particle impacts as the timescale of energy transfer is comparable to that of a hypervelocity impact, and focussed laser pulses do produce craters very similar to those produced in hypervelocity impacts (C1.15).

The Sprite laser had been observed to form hemispherical craters up to 2 mm diameter in aluminium targets, and was therefore expected to produce a good simulation of nearly penetrating events in the Giotto bumper shield.

An experiment was performed in which one flight-type piezo sensor was mounted on a 1 mm thick aluminium plate, and another on a rear shield sample mounted 125 mm behind the aluminium target plate. The front plate was bombarded with focussed laser shots in the energy range 20 - 80J and the response of the sensors measured.

Penetration of a 1 mm thick plate was not observed in this energy range but energies in excess of 35J produced spallation from the back of the target plate, causing stimulation of the rear sensor.

Penetration was observed at about 30J energy when a 0.5mm target plate was used.

By identifying the sensor response to a nearly penetrating event the experiment has gone a long way towards putting the Didsy calibration onto an absolute scale, and has given an estimate for the response of the rear shield sensor to a just penetrating event.

C2 KrF RAMAN CONVERSION STUDIES IN CH_4 AND H_2

M J Shaw, Y Owadano, J P Partanen, I N Ross, F O'Neill and E M Hodgson (RAL)

C2.1 SUMMARY

In the past year significant progress has been made on the KrF Raman amplifier experiment. In CH_4 at 3 bar pressure power conversion efficiencies of 75% with a simultaneous gain of 300 have been obtained. The experiments have been extended to H_2 at 1 bar pressure. In this case the laser linewidth was considerably larger than the Raman linewidth. Nevertheless conversion efficiencies in the region of 65% were obtained at power gains of 500x. In H_2 the small signal gain

coefficient has been determined and found to be equal to the single mode value once a certain phasing distance is allowed for. The results are in agreement with "phase locking" theories.

C2.2 EXPERIMENTAL ARRANGEMENT USED TO MEASURE ENERGY EXTRACTION FROM A FORWARD RAMAN AMPLIFIER IN A LIGHT GUIDE

The experimental set up is shown in Fig C2.1. The Raman generator is used in the forward mode with H_2 giving typically 10mJ in a 15 to 20ns pulse on the $Q_1(1)$ line at 277nm and as a backward generator with CH_4 producing a highly modulated 6ns pulse of typically 30mJ energy at 268nm.

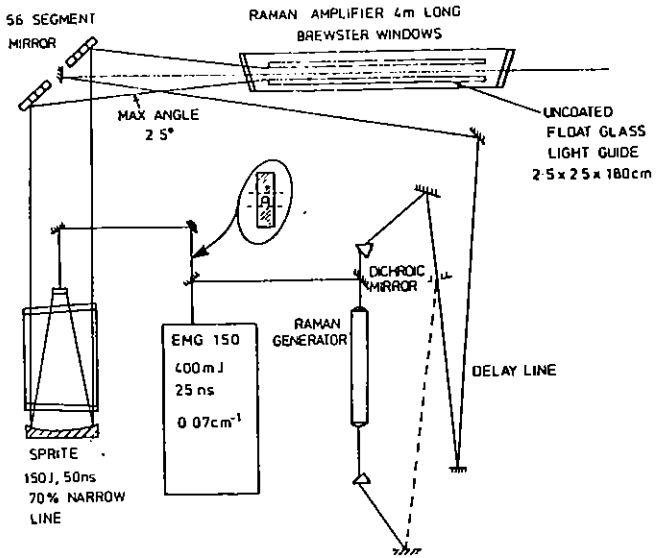

Fig C2.1 Experimental arrangement for investigating the light guided forward Raman amplifier. The Stokes generator is used in the backward direction for CH_4 and in the forward direction for H_2 (dotted).

The diagnostic layout is shown in Fig C2.2. Photodiodes and calorimeters measure the pulse shapes and energies of both pump and Stokes beams both before and after the light guide. An additonal joulemeter measured the polarization of the pump by the reflection from the Brewster angled window at the entrance to the guide.

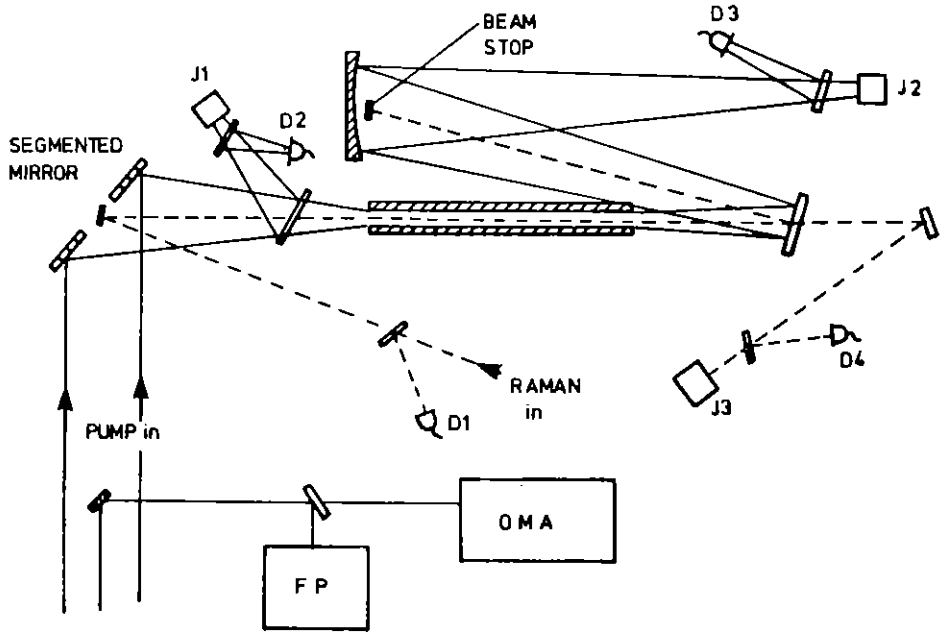

Fig C2.2 Diagnostics used on the Raman experiment. J = joulemeter, D = photodiode, FP = Fabry-Perot interferometer, OMA = Optical multi-channel analyser

The transmission of the guide fell short of its calculated value of 90% being typically in the region of 70 to 80% the lower value occurring at higher laser power.

The locking efficiency of Sprite was determined by taking spectra with an optical multichannel analyser situated some 20 m from the output window. The locking was found to depend strongly on the tuning of the oscillator as shown in Fig C2.3.

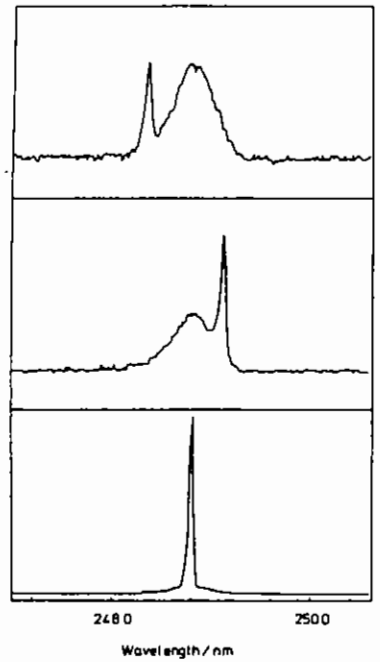

Fig C2.3 Spectra from the OMA showing Sprite locking efficiency. The fraction of the total energy in the narrow line was a = 11%, b = 21%, c = 78%.

In these spectra the narrow line is not resolved but the natural unlocked linewidth of 2.6Å FWHM is. The oscillator needed to be tuned to line center for best locking and in this case the fraction of output energy in the narrow line varied from shot to shot in the region of 60 to 75%. The unlocked output is not polarised and the energy reflected from the Brewster window was consistant with the spectral measurement.

The width of the useful narrow line component of the pump was measured with a Fabry Perot etalon and was found to vary from shot to shot. At best the linewidth was 0.07 cm^{-1} FWHM however the output was sometimes wider than this and occasionally on two or more lines. At its narrowest the oscillator is oscillating on typically 20 longitudinal modes which gives rise to substantial mode beating in the output pulse.

C2.3 LIGHT GUIDED CH_4 RAMAN AMPLIFIER

Results from the forward amplifier in CH_4 were all taken at 3 bar pressure. Fig C2.4 a b c show respectively the pump and depleted pump pulse and the input and output Stokes pulses from a typical shot. The effect of saturation shows in the output Stokes pulse which has less modulation and is of longer duration than the input.

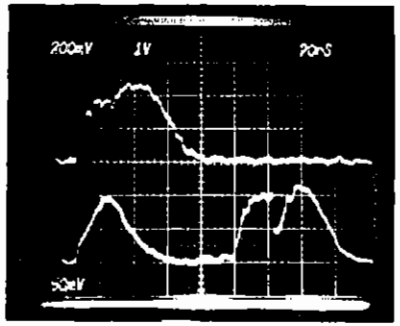

a)

(b)

(c)

Fig C2.4 Oscillograms for forward Raman amplification in CH_4 at 3 bar pressure. a) shows the input pump pulse (top trace) and depleted pump pulse (second pulse on bottom trace), b) is the input Stokes pulse and c) is the amplified Stokes pulse. In this shot the total incident pump energy was 52J in 55ns. The total transmitted energy (pump and Stokes corrected for loss in photon energy) was 36J. The input Stokes energy was 10mJ and the output Stokes energy was 3.7J. 73% of the pump energy was in a narrow line.

The strong depletion of the pump is also evident. The total Stokes output energy in this case was 3.7J. The power extraction efficiency was determined by the quantity:-

$$\eta = \frac{(E_s / t_s)}{(E_p F_n T) / 0.9 t_p}$$

where the numerator is the Stokes output power and the denominator is the useful pump power at the input to the light guide taking account of T, the Raman cell measured transmission, 0.9 the calculated guide transmission and F_n the fraction of pump in the narrow line.

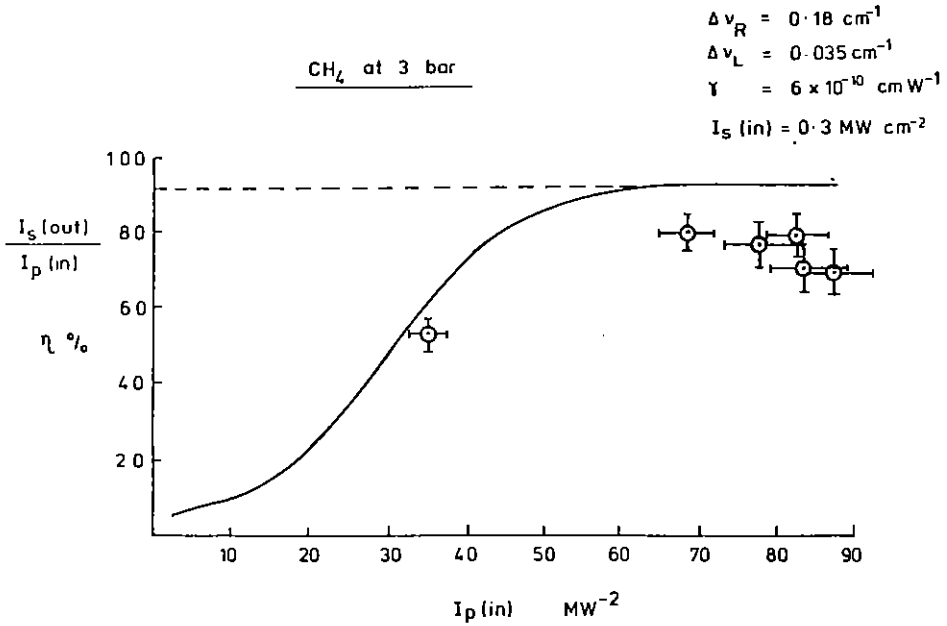

Fig C2.5 Power conversion efficiency in CH_4 at 3 bar as a function of pump intensity. Solid curve is the prediction of the simple 1D model

Extraction efficiency data for a number of shots are plotted in fig C2.5 and are compared with the simple 1D model which for the case of a << 1 is:

$$\eta = \frac{a \exp(\gamma I_p \ell)}{a\,(\omega_p/\omega_s)\exp(\gamma I_p \ell) + 1}$$

where a is the Stokes input power divided by the pump input power. The Raman gain coefficient γ is taken from Goldhar Taylor and Murray (C2.1) which at 3 bar pressure and a laser linewidth of 0.07 cm^{-1} is 6 x 10^{-10} cm W^{-1}.

Simple estimates of the beam quality of the Stokes beam were made using dylux film. The input Stokes beam was about 4 x diffraction limited and the amplified output beam was found to be little changed from this

value. At the same time observations of the second Stokes component of the output beam were made and approximately 10% of the output was found to be at the second Stokes wavelength for the highest pump powers.

During these measurements a major difficulty of using CH_4 in Raman amplifiers came to light. It was found that the output energy of the oscillator in particular and to a lesser extent the amplifier, deteriorated with number of laser shots. Full performance could be restored by changing the gas. Apparently the CH_4 is being decomposed to form some absorbing impurities. If the gas is subjected to very many laser shots then carbon deposits are easily seen on the windows. It is not clear whether or not breakdown is necessary to produce these effects.

C2.4 LIGHT GUIDED H_2 RAMAN AMPLIFIER

Partially to overcome the above effects it was decided to investigate H_2 in the light-guided amplifier. The Raman generator was changed to a forward generator since very little energy (and then only in a single subnanosecnd pulse) was available from H_2 in the backward direction. The problem with forward generation at 1 bar pressure is that very many rotational and vibrational Stokes orders are produced as shown in fig C2.6. The first vibrational Q(1) line was selected for amplification. Typically about 10mJ in a 20 ns pulse was produced giving less than 100 kW cm^{-2} Stokes input intensity compared with typical pump powers of 50 MW cm^{-2}. Thus saturation would require gains of about 500X. Initial results showed that this was quite easy to achieve even with the gas pressure at 1 bar. Fig C2.7 shows the pump depletion and amplification of the Stokes input beam.

These results suggested that the gain was considerably greater than that expected for uncorrelated pump and Stokes waves. In this case the gain should be given by

$$\gamma = \gamma_o \Delta\nu_R/(\Delta\nu_R + \Delta\nu_p)$$

Where $\Delta\nu_R$ is the HWHM of the Raman line which for H_2 at 1bar and 300K is 0.0057 cm^{-1} (C2.2) and $\Delta\nu_p$ is the HWHM of the pump laser

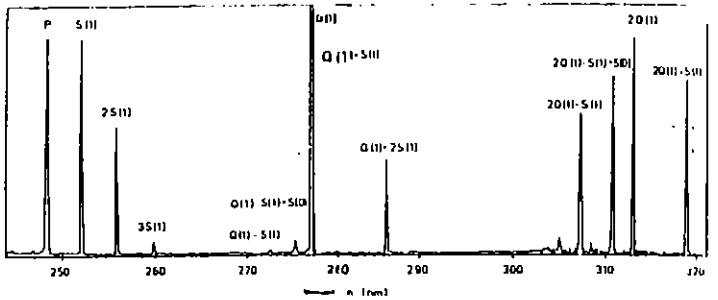

Fig C2.6 High resolution Raman Spectrum from a KrF pumped forward Raman generator at 1bar pressure. Pump energy was ~ 100mJ in 25ns and a 1m lens was used. The Raman frequencies in H_2 are S(0) = 354.4cm^{-1} S(1) = 587.1cm^{-1} and $Q_1(1)$ = 4155.2cm^{-1}. Note 1. The S(0) line from para H_2 only occurs as an intercombination line associated with S(1) and Q(1). Apart from P, S(1) and Q(1) all of the lines shown are generated from the above by four wave mixing processes. Note 2: the relative amplitudes between the pump, Q(1) and 2Q(1) groups are not to scale. They also vary significantly from shot to shot.

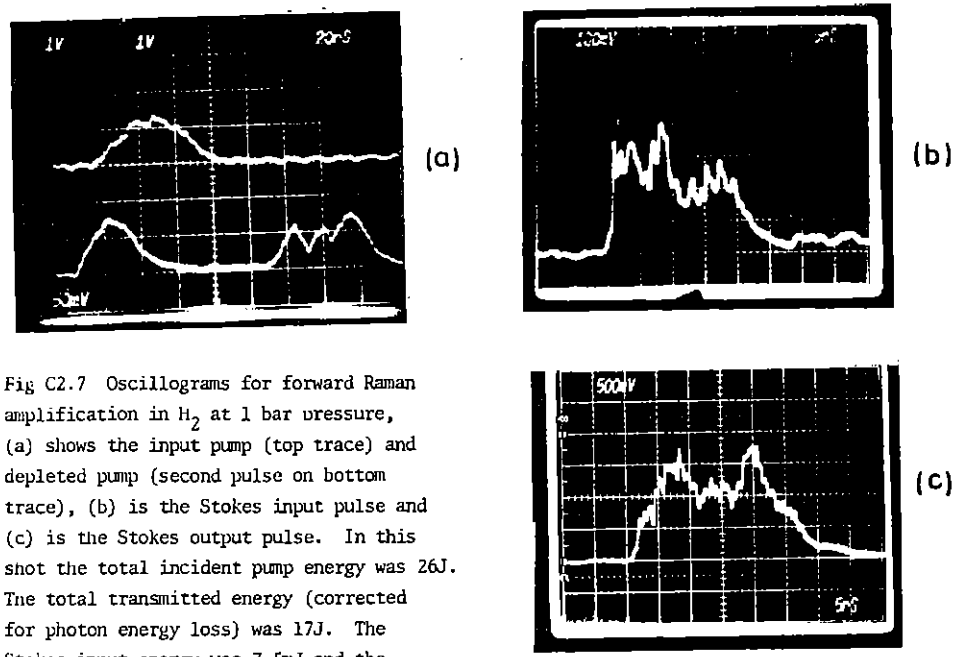

Fig C2.7 Oscillograms for forward Raman amplification in H_2 at 1 bar pressure, (a) shows the input pump (top trace) and depleted pump (second pulse on bottom trace), (b) is the Stokes input pulse and (c) is the Stokes output pulse. In this shot the total incident pump energy was 26J. The total transmitted energy (corrected for photon energy loss) was 17J. The Stokes input energy was 7.5mJ and the Stokes output energy was 4.3J. 75% of the pump energy was in a narrow line.

(~ 0.035cm^{-1}). The uncorrelated gain should thus be a factor of 7 less than the line center gain. The line center gain in H_2 is easily calculated from the expression

$$\gamma_o = \frac{\lambda_s^2}{h\nu_s} \frac{f_o N}{\pi \Delta\nu_R} \left(\frac{(\delta\sigma)}{\delta\Omega}\right)_{248}$$

Where $(\delta\sigma/\delta\Omega)$ is the differential scattering cross section at 248nm recently determined by Bischel and Black (C2.3) to be 48 x 10^{-30} cm^2 St^{-1}. N = the scatterer density and f_o is the fraction of ortho H_2 at 300K which is 0.66. Thus at 1 bar pressure and 300K with forward scattering γ_o = 1.55 x 10^{-9} cm W^{-1}.

Gain measurements were carried out at low pump power so as not to be in the depletion region and were done as a function of laser linewidth which was changed from its 0.07cm^{-1} FWHM by removing the tuning etalon from the oscillator which gave a linewidth of 0.7 cm^{-1} FWHM and to very broadband operation by removing the tuning prisms to give ~40cm^{-1} linewidth.

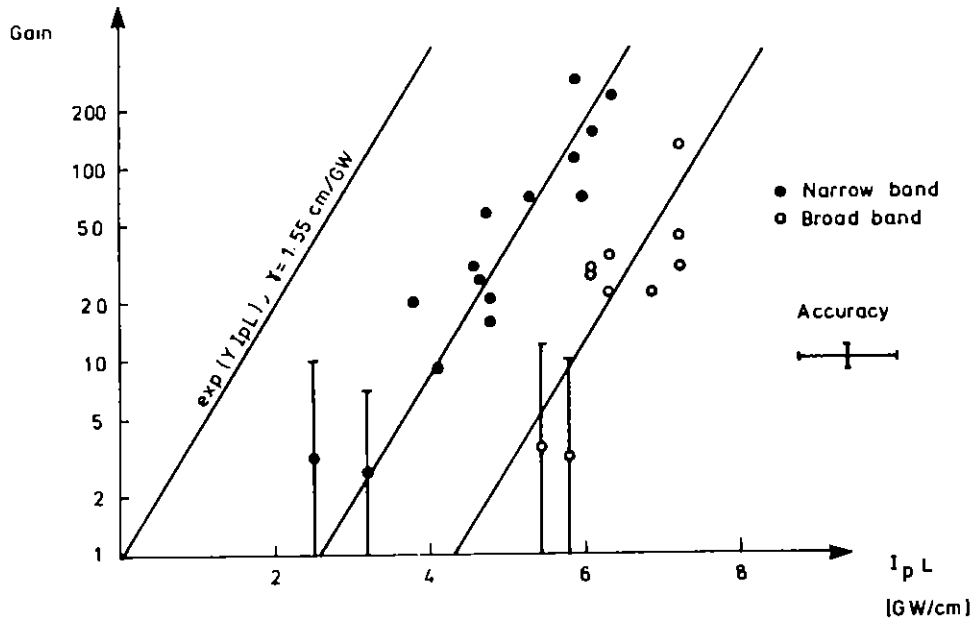

Fig C2.8 Small signal gain measurements in H_2 at 1 bar pressure as a function of $I_p L$. For the narrow band points the laser linewidth was $0.07cm^{-1}$ FWHM and for the broadband case $\Delta\omega_L = 0.7cm^{-1}$ FWHM. The solid lines are drawn for the calculated small signal gain coefficient at 1 bar of 1.55×10^{-9} cm W^{-1}

The results are shown in Fig C2.8 and come from only five laser shots. Each 20ns laser pulse is divided into 5ns intervals and the mean input and output power estimated from the photodiode traces to give the data points plotted. No gain could be observed for the case of 40 cm^{-1} laser linewidth. The interesting point is that after an initial amplification length the gain becomes equal to the single mode value. The effect of laser linewidth is to change the initial gain length required. These results are in agreement with the "phase-locking" theory (see for example (C2.4) and (C2.5)) which gives a small signal amplification following the law

$$I_s = I_s(in)\ (1 + \frac{1}{M}\ (e^{\gamma I_p \ell} - 1))$$

which for large gains is approximated by

$$I_s(out) = \frac{I_s(in)}{M}\ e^{\gamma I_p \ell}$$

where M is the number of modes in the pump (and Stokes) spectrum. The stokes intensity thus grows as though initiated by the intensity of a single mode.

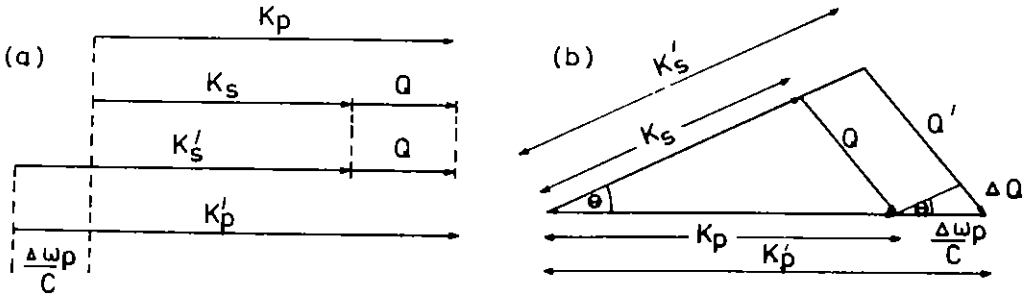

Fig C2.9 a) Shows how with no dispersion and co-propagation, wave vectors from different ends of a broad band Spectrum $\Delta\omega_p$ can scatter from the same Raman excitation, Q. b) Shows the effect of having the pump and Stokes wave vectors at an angle θ. In this case a spread of Q is given by $\Delta Q \simeq \Delta\omega_p\, \theta/C$ is produced for small angles θ

The reason that this can be so is illustrated in Fig. C2.9a which shows a single pump mode k_p scattering from the phased array in the medium Q to give a single Stokes mode k_s. Provided they are phased correctly other modes in the pump spectrum can scatter from the same Q. Q can only grow from the initial intensity of a single mode viz:- $I_s(in)/M$. As it grows other modes scatter from the same Q. After they are phase-locked in this manner amplification proceeds as though all of the pump intensity were concentrated in a single mode.

Akhmanov et al (C2.6) were the first to point out the complication that dispersion adds to this picture. In this case modes at different ends of the pump and Stokes spectrum will not interact via the same Q but the pump spectrum $\Delta\omega_p$ will produce a range of Q vectors of width ΔQ. The effects of dispersion will however be small if the critical gain length in the medium $L_{gain} \approx (\gamma_o I_p)^{-1}$ is shorter than the dispersion length $L_{dis} \approx \pi(\Delta Q)^{-1}$. In the case of co-propagating waves in a dispersive medium the dispersion results in differing group velocities V_p and V_s and the inequality $L_{gain} < L_{dis}$ defines a critical pump intensity I_c such that if

$$I_p > I_{cr} = 4\left(\frac{1}{V_p} - \frac{1}{V_s}\right)\frac{\Delta\bar{\nu}_L}{\gamma_o}$$

then dispersion may be neglected

In our case the normal dispersion of the medium(H_2 at 1 bar) is very small but the effect of pumping the medium at an angle is similar to that of dispersion in the co-propagating case. This is shown in Fig. C2.9b. If the angle between pump and Stokes, θ is small then the pump spectrum of width $\Delta\omega_p$ gives rise to a $\Delta Q \approx \Delta\omega_p\theta/c$ and the component of ΔQ along the axis is $\theta\Delta Q$. In this case the critical intensity is given by

$$I_{cr} \approx 4\Delta\bar{\nu}_L\theta^2/\gamma_o$$

where $\Delta\bar{\nu}_L$ is the laser linewidth in cm^{-1}. For the three linewidths tested 0.07, 0.7 and 40cm^{-1} the critical intensities are 0.07, 0.7 and 40 MW cm^{-2} respectively. The pump intensity greatly exceeds the first two cases but not the third which was where no gain was observed.

Finally the H_2 results are plotted in Fig C2.10 to show the conversion efficiency as a function of pump intensity. Data are compared to the simple 1D model as used in CH_4 however in this case I_s(in) was set to I_s (in)/M where M is the number of oscillator modes (about 20 at 0.07cm^{-1}) and the gain is set equal to γ_o.

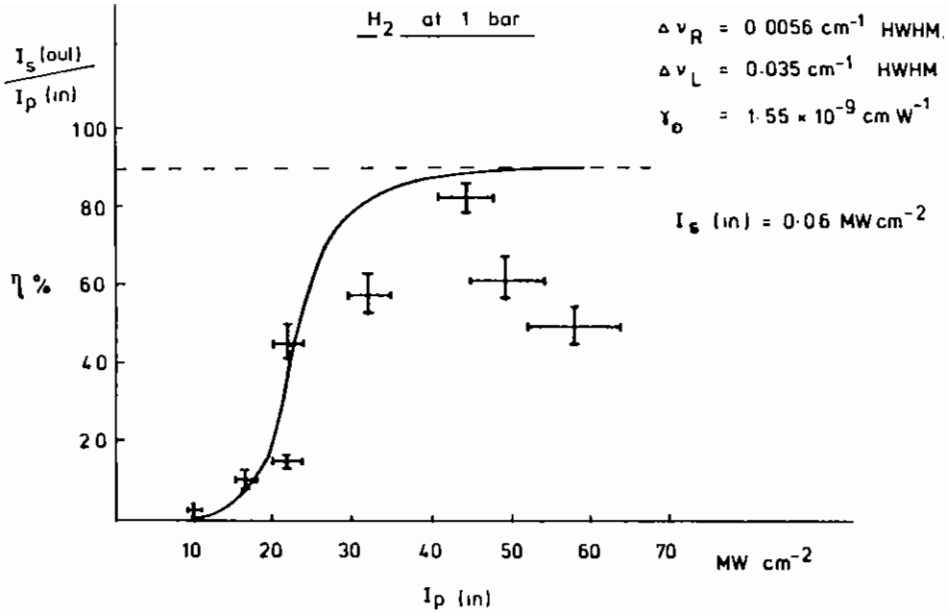

Fig C2.10 Extraction efficiency as a function of pump intensity of a forward Raman amplifier in H_2 at 1 bar pressure. Solid curve is from the simple 1D model using single mode input intensity and gain coefficient

The drop in efficiency above 40 MW cm^{-2} is due to self Raman generation in the pump. At this intensity and due to substantial pump beam overlap in H_2 outside the guide, the gain exponent $\gamma_o I_p L$ for self generation is in the region 20-30.

C2.5 IMPLICATIONS FOR THE SPRITE MULTIPLEXER SYSTEM

The above results are useful in indicating the best approach for applying Raman amplifiers to the Sprite multiplexer system. The most likely scenario in the short term is as follows:-

1) A forward Raman beam combiner pumped by 8 x 8ns pulses from the Sprite multiplexer to produce a single high quality Stokes beam of energy 150-250 J in 8ns.
2) Use rotational (252nm) or vibrational (277nm) shift in H_2 at

atmospheric pressure or below.

3) Use window loading ≈ 1 J cm^{-2}.
4) Use a light guide with dielectric coatings for high R at ≈ 10° grazing angle. (Such coatings have already been tested and found to have R ≈ 99.5% and damage levels equivalent to a beam fluence ≈ 10 J cm^{-2}.)
5) Final amplifier to run at 100 x gain or less for best conversion efficiency.
6) Use single mode pumping to maximise gain and eliminate mode beating effects.

Construction of such a system now appears to be perfectly feasible within a reasonable time scale and will greatly enhance the target shooting capabilities of Sprite.

C3 PROGRESS ON THE SPRITE KrF OPTICAL MULTIPLEXER

F O'Neill (RAL)

C3.1 ASSEMBLY OF MULTIPLEXER HARDWARE

The Sprite KrF laser fitted with an injection locked unstable resonator cavity is now being used as a target irradiation facility and the first experiments have been described in section C1 above. Based on these experiments we have now operational a fully dedicated KrF target facility capable of providing on target irradiances of $>10^{13}$ W cm^{-2} in 50ns pulses at 249nm. Establishment of this facility represents the achievement of our first major goal in the KrF laser project. The next aim is to increase the power on target by pulse compression using some combination of optical multiplexing and Raman conversion.

While the design of the end stages of the KrF pulse compressor have not yet been finalised it is clear that the front end will consist of a X8 optical multiplexer as was described in the 1984 Annual report. The multiplexer has been designed to produce an output of 200J in 8ns in 8 beams using the Sprite laser as the final amplifier stage. In this past year the construction of the room for the multiplexer optics has

been completed and all optics and hardware (e.g. beam pipes, mirror mounts, etc.) have been purchased. A UV Pockels cell has also been purchased and will be used to switch an 8ns pulse from the Lambda Physik EMG 150 laser to provide the input to the KrF multiplexer. The other major component of the multiplexer is the Goblin e-beam-pumped pre-amplifier which as described below is now operational.

Thus all the components necessary to produce a 200J, 8ns, 8-beam output from Sprite are now available and it is planned to have the optical multiplexer system operational before the end of the next financial year.

C3.2 PROGRESS ON THE E-BEAM-PUMPED GOBLIN PRE-AMPLIFIER

F Kannari, H T Medhurst, M J Shaw (RAL)

C3.2.1 Goblin Pulsed Power Performance

The routine checking on the electric performance of the Goblin e-beam generator has been satisfactorily carried out. During the reporting year approximately 150 e-beam shots were fired.

The 10-stage marx generator has been successfully triggered by a newly developed magnetic-switch-driven trigger generator with a low jitter (1σ of <20ns). The measured voltage gain from the marx to line is 0.95 and the energy transfer efficiency, which is limited mainly by the relatively large series resistance of marx of 16Ω, is 0.47.
To date the output gap has been operated in the self-break mode. The charging time of the pulse forming line is 400ns. Fig. C3.1 shows the self breakdown voltage versus pressure curve.

The e-beam diode consists of the old ELF diode chamber and the new cheese-grater-type cathode with an emitting area of (5x50)cm^2. Fig. C3.2 shows the typical time history of the PFL voltage, the diode voltage, and the diode current.

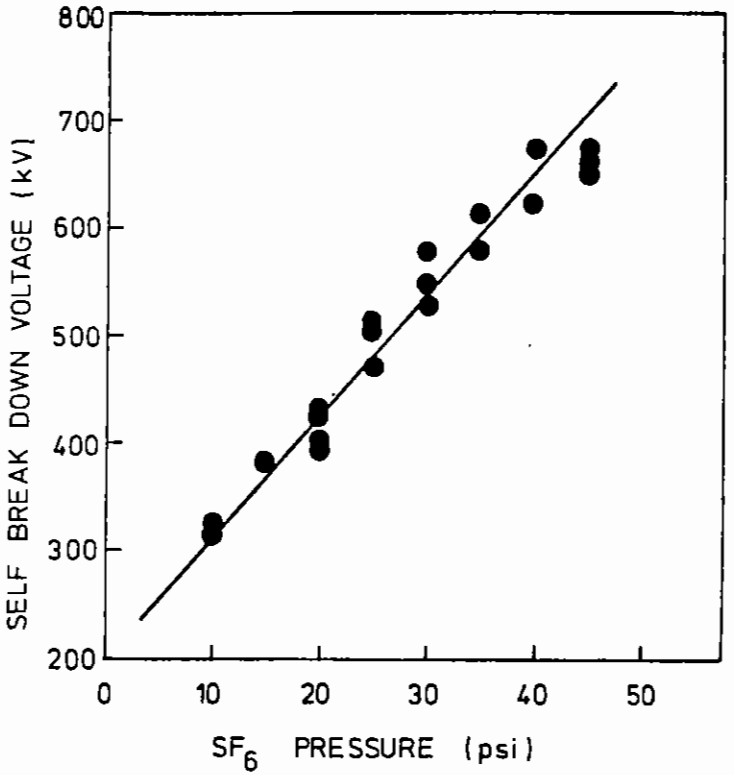

Fig C3.1 Self breakdown voltage versus SF_6 pressure for PFL output gap

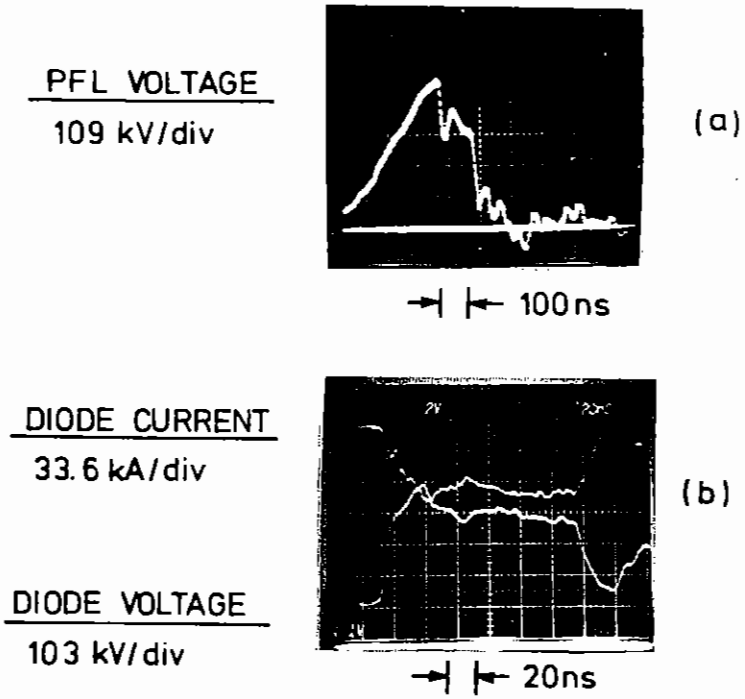

Fig C3.2 a) Timehistory of PFL voltage
b) Upper trace diode current
Lower trace diode voltage

The risetime of the current is approximetry 20ns. The pulse width is 120ns, FWHM. The maximum output obtainable at ± 80kV marx charging is 450KV and 70KA.

The e-beam transmission efficiency was measured by an Al-plate Farady-Cup and an e-beam calorimeter placed after the pressure foil. Through these measurements, the best combination of anode and pressure foils was decided. These were 12.5μm-Ti for the anode and 75μm-Kapton for the pressure foil. Figs. C3.3 and C3.4 show the measured transmitted current and total e-beam energy as a function of diode voltage, respectively.

The maximum current transmission efficiency and the maximum available e-beam energy are 80% and 1.4kJ, respectively. The e-beam deposition

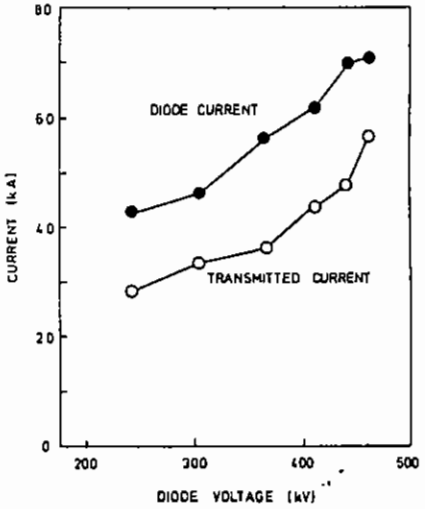

Fig C3.3 Dependence of e-beam current transmission upon diode voltage

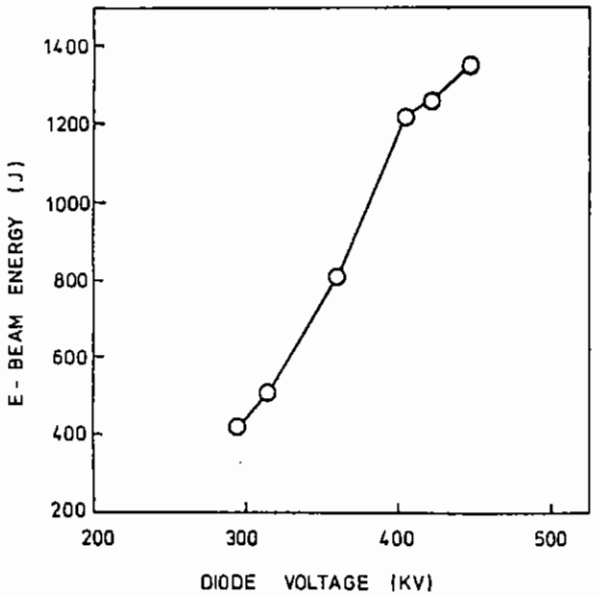

Fig C3.4 Dependence of available e-be. energy measure. by a calorimet. upon diode voltage

energy was also measured by filling the old ELF laser cell with Freon 12 and measuring the pressure jump. Fig. C3.5 shows the e-beam deposition energy versus diode voltage. In this case, the deposition efficiency was limited by the relatively small gas volume of laser cell. The maximum deposition energy obtained is 0.9kJ at a equivalent KrF laser gas pressure of 3 atm.

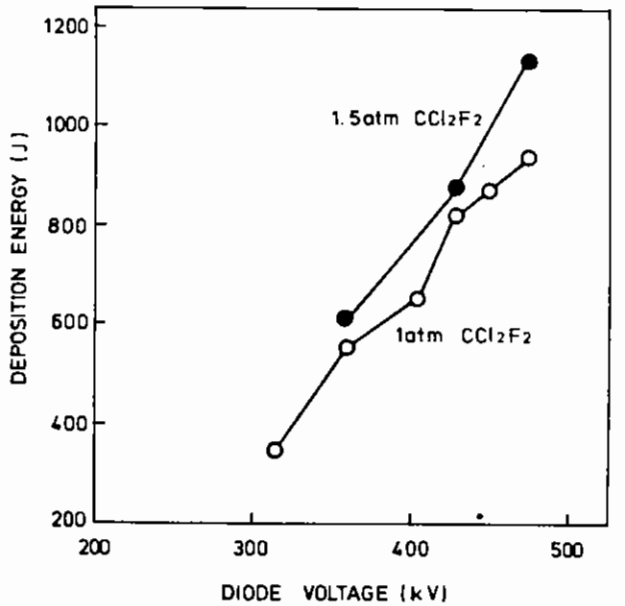

Fig C3.5 Dependence of e-beam deposition energy measured by pressure-jump upon diode voltage

Goblin has been operated as a KrF oscillator. In spite of very low transmission windows (the only ones available at the time!) an output of 4J was obtained at a total laser gas pressure of 1.5atm. The other factor which limited the laser energy was the significantly large dead-volume behind the pressure foil in which the most of e-beam energy has been deposited. A low-pressure drift region which has been currently installed will improve the volumetric laser extraction efficiency.

C3.2.2 Goblin Marx Triggering

A novel high-voltage trigger generator has been developed to fulfil the requirement of low jitter and reliable triggering for Goblin. The generator comprises two parts, a d.c. charged capacitor switched by a tetrode thyratron situated outside the marx oil tank and an air-cored pulse transformer driven by a magnetic switch in close proximity to the marx generator inside the tank. Fig C3.6 shows the basic circuit.

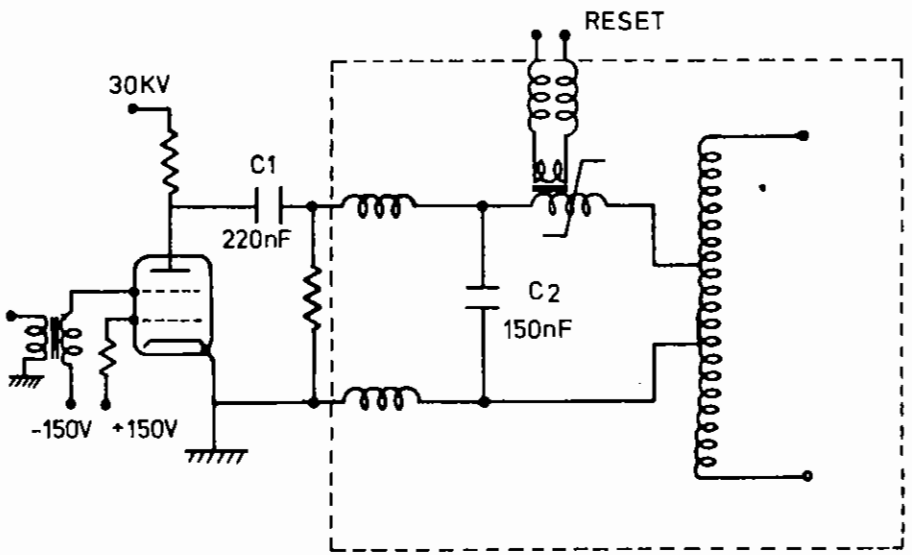

Fig C3.6 Basic circuit of a magnetic switch driven high-voltage trigger generator

There are several factors which have to be considered in the design in order to obtain high switching voltage and the high transformer gain thus resulting in high dV/dt at the output:-

1) The ratio of the saturated inductance of magnetic switch, L_{sat} ($\alpha\ \mu_{sat}\ N^2A$, where N is the number of turns and A is the cross sectional area), to the primary inductance of transformer, L_p, must be small for high transformer gain.

2) Magnetic switch must saturate at close to the peak of charging voltage of C2 ($NA\Delta\beta \sim V_p \tau/2$, where $\Delta\beta$ is saturation flux, τ is charging time of C2, and V_p is peak voltage of C2).

3) The ratio of unsaturated inductance, L_{unsat} ($\alpha\ \mu_{unsat}\ N^2A$), to L_p must be large to reduce the prepulse level induced during the charging of C2.

4) Large isolation inductance is necessary between C2 and the thyratron if operation of the transformer with one of output ends at the earth is required.

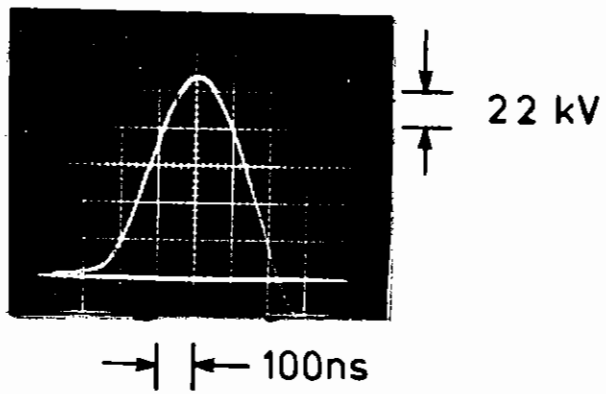

Fig C3.7 Typical output voltage of trigger generator

Because these constraints can not be fully satisfied by a single design parameter, we must find the best compromise between them.

Specifically, sufficient reduction of the pre-pulse level (which directly affects the marx triggering performance) can be attained only at the sacrifice of transformer gain.

As a result, we have used two magnetic cores in series with 2-turn-windings. In this case, the saturation time of the magnetic core is 1.6μs and the switching voltage is 19kV. The half transformer gain is about 7. Fig. C3.7 shows the output waveform of half the transformer measured by a 4kΩ $CuSO_4$ probe as a load. The peak voltage is 118kV and the 10%-90% risetime is 150ns.

By floating both ends of the output from the earth, a bi-polar output around ± 110kV is obtained and is used with opposite polarities triggering alternate midplane gaps in the Goblin marx. We have compared the triggering performance between bi-polar triggering and single-polar triggering.

Figs. C3.8 and C3.9 show the delay as a function of the percent of self-breakdown voltage (V_{sB}) for dry-air and an SF_6 filled gap respectively. Delay and jitter were determined by measuring the time between the voltage rise at the trigger electrode and at the 800Ω-$CuSO_4$ dummy load. In spite of a low dV/dt value of triggering voltage, triggering was controlled down to about 50% of V_{sb} for dry air and 60% of V_{sb} for SF_6 respectively. Comparison between single-polarity and bi-polar triggering shows much shorter delays for the former. However, there is no significant difference on the jitter performance. Because the performance of marx triggering depends not only on the dV/dt of the triggering voltage but also on the inter-connections in the marx generator itself, these jitter results may be explained by the prescence of sufficient capacitive and resistive - coupling between stages to over-volt the gaps.

In conclusion, using bi-polar triggering the Goblin marx can be successfully triggered down to 50% V_{sb} for dry air and to 60% V_{sb} for SF_6 with a jitter of 20ns or less which is only 5% of charging time of the water line.

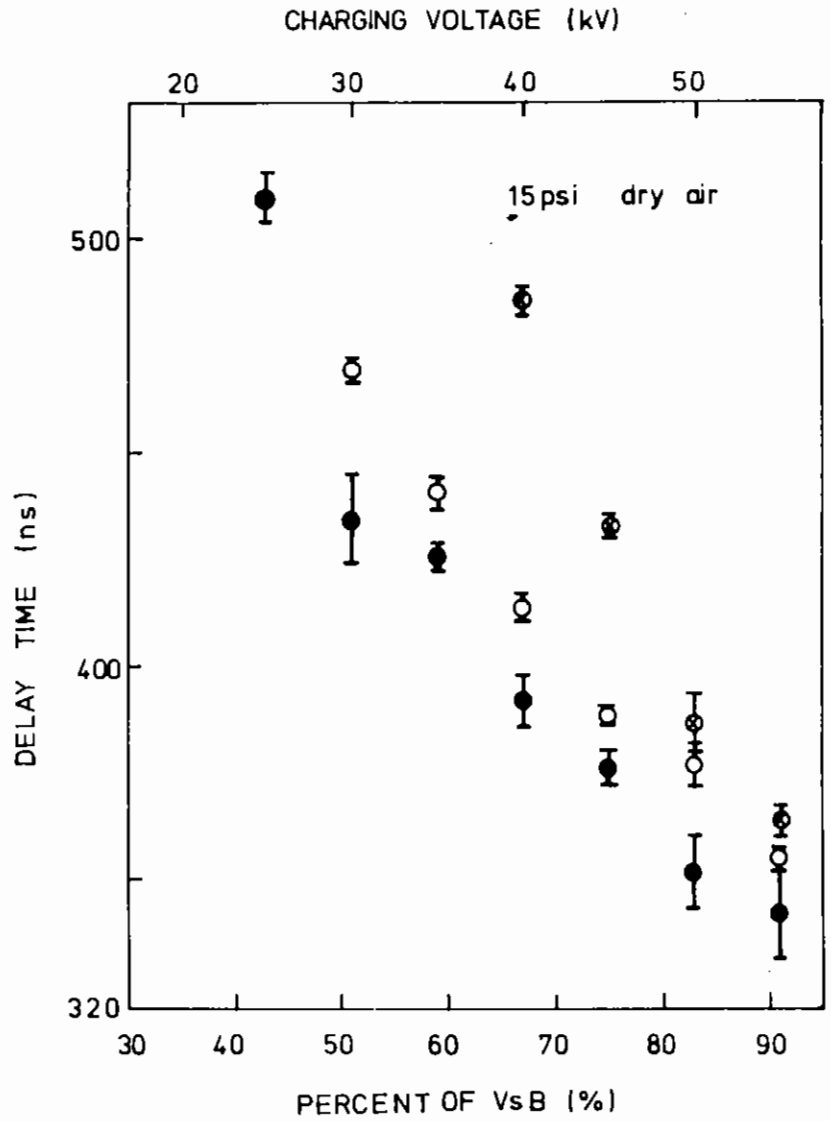

Fig. C3.8 Delay time of marx triggering versus percent self-breakdown voltage for dry-air filled marx

a) ● single (negative) - polar triggering

b) ○ bi (negative voltage to odd stage gap) - polar triggering

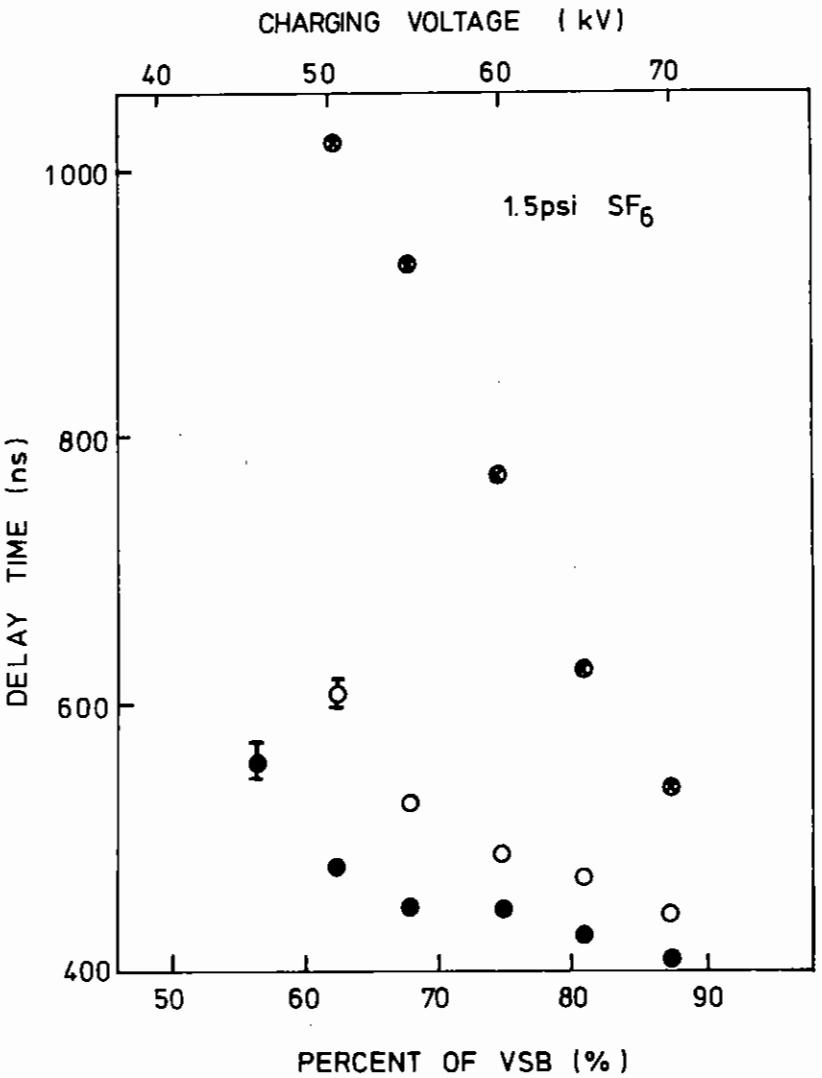

Fig C3.9 Delay time of marx triggering versus percent self-breakdown voltage for SF_6 filled marx. Symbols are similar to ones of Fig C3.8

References

C1.1 Rutherford Appleton Laboratory, Laser Division Annual Report Report No. RAL-84-049 1984.

C1.2 M W Taylor, J Goldhar and J R Murray, Appl. Opt. 21, 4 (1982)

C1.3 J D Kilkenny, R W Lee, M H Key and J G Lunney, Phys. Rev. A22, 2246 (1980)

C1.4 Crystal reflectivity calibration performed by K Evans, University of Leicester (private communication)

C1.5 P D Rockett (private communication)

C1.6 B Yaakobi, P Bourke, Y Conturie, J Delettrez, J M Forsyth, R D Frankel, L M Goldman, R L McCrory, W Seka, J M Soures, A J Burek and R E Deslattes, Opt. Commun. 38, 196 (1981)

C1.7 K Eidmann, M H Key and R Sigel, J Appl Phys, 47, 2402 (1976)

C1.8 European Science Foundation, edited by Y Farge (unpublished) (1979)

C1.9 PIN silicon photodiodes manufactured by Quantrad Corp Los Angeles, CA 90064

C1.10 D L Matthews, E M Campbell, N M Ceglio, G Hermes, R Kauffman, L Koppell, R Lee, K Manes, V Rupert, V W Slivinsky, R Turner and F Ze, J Appl Phys, 54, 4260, (1983)

C1.11 R McCorkle, J Angieello, G Coleman, R Feder and S J La Placa, Science, 205, 401 (1979)

C1.12 Rutherford Appleton Lab., Laser Division Annual Report RL-84-049, 1984.

C1.13 J A M McDonnell, E Grun, G C Evans, R F Turner, J G Firth, W C Casey, H Kuezera, W M Alexander, D H Clark, R J L Grand, M S Hanner, D W Hughes, E Igenbergs, B A Lindblad,J C Mandeville, G Lebehan, Z Lekanina, ESA SP-169 (1981)

C1.14 A P Stanysikovich, J Exptl Theoret Phys (USSR), 36, 1605, (1959)

C1.15 W M Burton, Rutherford Appleton Labortaory Report, RL-82-030.

C2.1 J Goldhar, M W Taylor and J R Murray. IEEE JQE QE20, 772 (1984)

C2.2 A Owyoung, Optics Letts 2, 91, (1978)

C2.3 W K Bischel and G Black in "Excimer Lasers - 1983" AIP Conference Proceedings No 100 pages 181-187 (1983)

C2.4 I G Zubarev and S I Mikhailov Sov. J.Q. Elec 8, 1338 (1978)

C2.5 E A Stappaerts, W H Long and H Komine Optics Letts 5, 4, (1980)

C2.6 S A Akhamov, Y E D Yakov and L I P Pavlov Sov Phys JETP 39, 249 (1974)

PART II

PART II

LASERS FOR MICROCIRCUIT FABRICATION

Section Editor M C Gower

Part II LASERS FOR MICROCIRCUIT FABRICATION

1. INTRODUCTION

M C Gower (RAL)

This section of the Laser Division annual report covers the progress of work undertaken by Laser Division staff working on the 'Microcircuit Fabrication using Lasers' project. This project, which officially began in November 1983, is a 3 year programme and is jointly funded on a 50:50 basis by the Engineering Board of the SERC and the Department of Trade and Industry (DTI) to a total of £780K. It involves a collaborative effort between the Laser and Technology Divisions of RAL.

The aims and scope of the programme are to carry out an investigative study of the potential novel uses of lasers in microcircuit fabrication with particular emphasis being placed on the use of laser sources in photolithography. More specifically, it is hoped that results arising from the programme will eventually show that laser sources can provide cheap, high-throughput photolithography for device sizes down to 1-2μm.

This report covers only that part of the project undertaken in the Laser Division, namely, investigations of novel methods of high - resolution image projection using lasers. This activity involves 2 man years of RAL Laser Division staff effort supplemented by research sandwich student and consultative support. A parallel effort, which studies the behaviour of photoresist materials to exposure by excimer laser radiation, is being undertaken by staff from Technology Division and is not included in this report.

The three techniques for image projection which are being studied all involve the use of either 'real' or 'lapsed time' phase conjugate mirrors (PCM's). The first method makes use a of thermally-induced optical nonlinearity in liquid solutions to produce real-time phase conjugate reflections by degenerate four-wave mixing of ultraviolet excimer laser radiation at 249nm in the type of arrangement shown

schematically in Fig. 1. Initial studies of image projection with a 355nm laser using this technique were first reported by Levenson[1] although, because of the low reflectivity of the PCM and the ensuing optical damage to mask and beamsplitter components, his minimum exposure time of the photoresist was limited to approximately 30 seconds which is much too long for any practical device. To circumvent these damage problems we plan to incorporate a small KrF laser amplifier between the beam splitter and phase conjugate mirror. This amplifier is being developed under an extra-mural research (EMR) agreement with Oxford University. Progress in this activity is described in the second section of this report.

In the third section there is a brief description of an investigation of the use of holographic techniques to high-resolution image projection. Although such techniques were first investigated some 17 years ago[2] there are few subsequent reports of further work in this field. A patent application arising from the work in this field is currently being filed.

In the final section we report progress on the use of photorefractive media in particular $BaTiO_3$ crystals for generating dynamic holograms to project high-resolution images. Although the group at IBM[3] have used photorefractive $LiNbO_3$ crystals to project speckle-free images with a resolution of > 800 line pairs/mm using a CW 413nm Kr^+ laser, the phase conjugate reflectivity of the crystal was so low (<0.001%) that the photoresist exposure time was unacceptably long (8-20min). The high reflectivity obtainable from simple self-pumped $BaTiO_3$ crystals (up to 30%) have enabled us to reduce this exposure time to approximately 5 sec.

One of the main objectives of the project is to feed into UK industry for possible future commercial exploitation the more promising results of the research. Commercial rights are held by the DTI. With this in mind, the project management committee is currently actively engaged in consulting a number of U.K. companies with a view to commercial exploitation. From the research carried out so far on novel methods of image projection, the British Technology Group (BTG) on behalf of the

project is preparing three patent applications. The possibility of future commercial exploitation of the results arising from the project necessitates that some of the work should remain proprietry. It is recognised that this is somewhat of a new departure for the Laser Division where 'open research' is usually carried out.

IMAGE PROJECTION

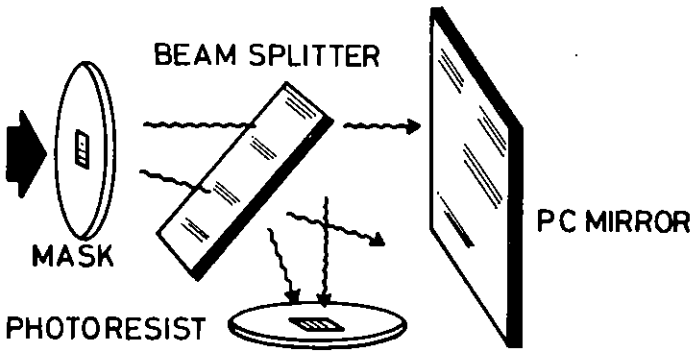

Fig 1 Schematic of image projection using real-time phase conjugate mirrors.

2. (a) PHASE CONJUGATE IMAGING AND PHOTOLITHOGRAPHY BY FOUR WAVE MIXING AT 249nm WAVELENGTH

M Golombok, R Harris, M C Gower (RAL) and A F Gibson (Consultant)

Phase conjugation by four-wave mixing was first demonstrated at 249nm by Caro and Gower[4] in a joint project between RAL and Oxford University. The essential features of their technique were (i) The interference of a probe and pump ("write") beam in an absorbing liquid resulting in the formation of a phase hologram due to the resultant

spatially non-uniform heating and (ii) the subsequent "reading" of the hologram by a second pump beam which generates, by diffraction from the hologram, the phase conjugate of the probe beam. Gower and Caro did not examine the ability of their technique to generate images though Levenson,[1] using the same mixing method, generated images in a photoresist using the third harmonic of Nd-YAG as his ultra-violet source (355nm). His results were not very encouraging. In particular Levenson found he required unacceptably long exposures (greater than 30sec) to generate patterns in commercially available photoresists and damaged both mask and beam splitter.

Taking the problems encountered by Levenson into account we are studying alternative optical arrangements to generate images of masks on photoresist layers, while still using Caro and Gower's original four-wave mixing method. Experimental work began in November 1984 with the delivery of a Lambda-Physik 150 KrF laser designed to deliver pulses of over 700mJ energy in a 20 x 20mm^2 beam though we have not, as yet, been able to use its full capability. For our initial studies the laser is being used to feed an optical arrangement of the type shown schematically in Fig 2, except that delivery of the quarter-wave plate, shown in front of the mirror(M2) which generates the read beam, is still awaited. This, in conjunction with the polarisation gate, will protect the laser from feedback via mirrors M1 and M2 and allow the laser to operate at full power. The quarter-wave plate also rotates the plane of the polarisation of the conjugate beam relative to the probe beam.

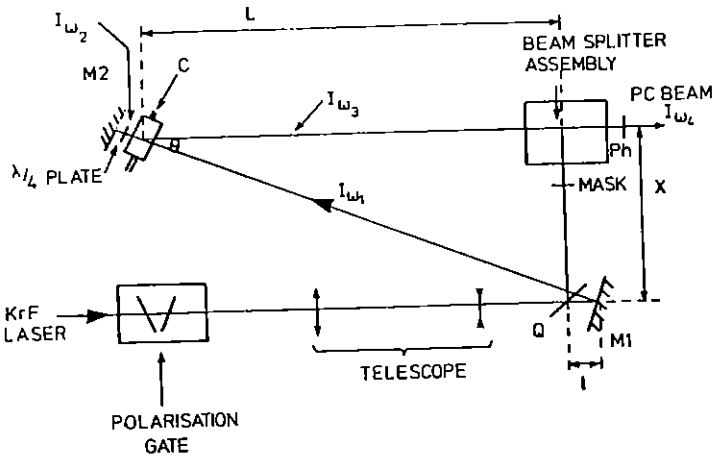

Fig 2 An experimental arrangement for the observation of phase conjugation by degenerate four-wave mixing in an absorbing liquid. M1, M2 100% dielectric mirrors. C is a flowing dye cell. Q splits off the probe beam: $I_{W_3} \sim .01\, I_{W_2}$, $I_{W_2} \sim \frac{1}{2} I_{W_1}$ Ph. Photoresist on substrate.

Interference between probe (W_3) and pump (W_1) beams in the cell C requires equal path lengths to an accuracy set by the coherence length of the laser, in our case about 3cm. In the set up shown, the equal path length condition is met if

$$\ell = \frac{XL}{2L+X}$$

and the angle between W_1 and W_3, which must be kept small, is given by

$$\tan\Theta = \frac{X}{L+\ell} .$$

As ℓ increases, the alignment of the write and read beams becomes more critical (as sin Θ) and, if the angular alignment tolerance becomes

less than the irreducible divergence of the pump beams, the intensity ratio Iw_4/Iw_3 falls. For our laser, this requires $\Theta < 10°$.

At the present time, as shown in the figure, we are using "front pumping" i.e. beams W_1 and W_3 are incident on the interaction cell from the same side. This, together with the need to keep Θ small, places undesirable constraints on the system. A back pumped cell has been designed and is under test. The beam splitter assembly is currently the subject of patent action. Finally it should be noted that a relatively low-gain amplifier (see section 2(b)) is under construction to enhance the power of the conjugate beam.

Though incomplete, as indicated above, the structure shown in Figure 2 has been used to generate images of a mask on a photoresist layer and a resolution better than 10μm obtained. This does not, of course, represent the limit of the technique but the limit set by the currently available components.

2(b) WIDE-APERTURE AMPLIFIER DEVELOPMENT FOR 249nm PHASE CONJUGATE MIRROR PROJECTION

G J Hirst, V Rivano and C E Webb, (Clarendon Laboratory)

Ideally a laser photolithography system should be able to expose the photoresist on a semiconductor substrate in a single short pulse, thus avoiding the problems associated with substrate vibration and pulse repetition rate which may limit the processing speed. Discharge pumped rare-gas halide excimer lasers, particularly the KrF laser at 249 nm, produce appropriately short pulses (typically 20 ns long) with sufficient energy (hundreds of millijoules) to carry out this task, but simple mask-projection is not possible in a single pulse because the intensity required to expose the resist is too high to put through conventional masks. These are damaged unless the incident intensity is held below about 10% of the value required for exposure.

One solution to this problem is to install a laser amplifier in the path between the mask and the substrate so as to raise the intensity to

the level required. The amplifier can be double-passed using a beam splitter and if a phase conjugate mirror is used as the retro-reflector any phase variations in the amplifier medium will be corrected automatically. To retain a large numerical aperature the complete optical train also includes a lens between the beam splitter and the amplifier.

The design of the amplifier for use in such a projection system must take into account the required single-pass gain and numerical aperture. It must also aim to maximise the spatial uniformity of the gain over that aperture, since the phase conjugate mirror is of course, incapable of compensating for unwanted amplitude fluctuations in the signal arriving from the amplifier. Initial calculations called for an amplifier with a single-pass gain of ~11 and a numerical aperture of ~0.05. Typical values of the small-signal gain in KrF[5] suggest that the gain region would need to be ~20 cm long and the amplifier cross-section ~2cm square. The aim of the present project is to construct such an amplifier and to investigate the magnitude and uniformity of the gain as functions of the electrical and preionisation subsystems and of the gas composition.

The laser head consists of a 20cm diameter metal tube containing the electrode structure and internal capacitor assembly. The circuit and laser cross-section are given in Fig 3.

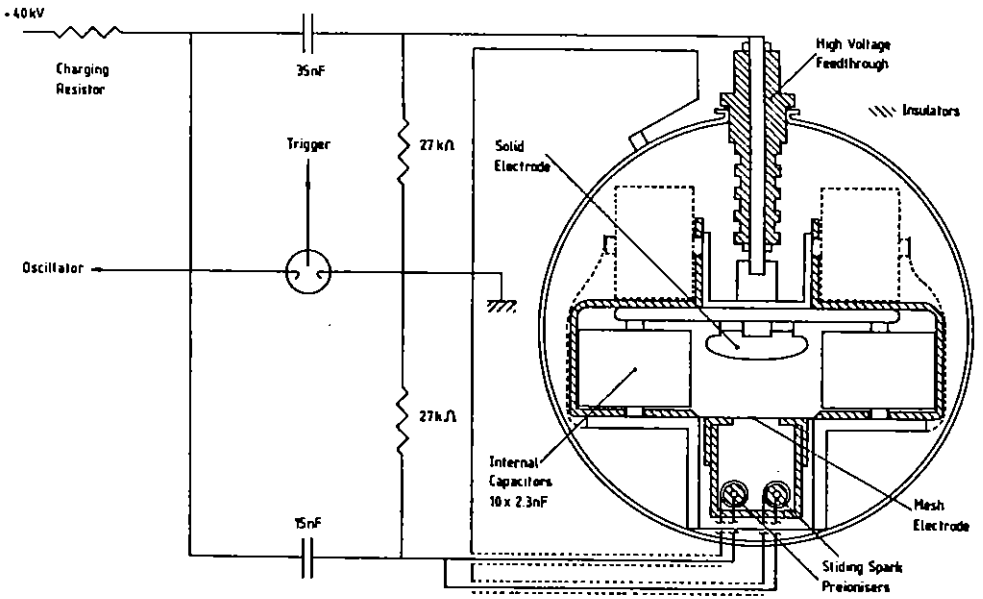

Fig 3 Discharge circuit and cross-section of KrF laser amplifier.

The values of the capacitors are those currently in use but it seems likely that these will need to be increased to achieve optimum performance. The electrodes consist of a solid cathode which is shaped to produce the required gain profile (efforts to optimise this profile are still in progress at the time of writing) and a flat, partially transparent mesh anode through which ultraviolet preionisation radiation can enter the laser discharge volume. The preionisation is provided by two parallel sliding-spark arrays made from lengths of cupro-nickel tube mounted on polytetrafluoroethylene (PTFE) supports. Each array carries 25 intense sparks for ~ 170ns before the main discharge breaks down. The entire preionisation assembly is mounted within an insulating liner made from polvinylidene fluoride (PVDF), this plastic being both mechanically strong and completely fluorine compatible. The advantage of preionising through one of the electrodes is that the unavoidable preionisation density gradient is then parallel to the main electric field and its effect on the spatial distribution

of current in the discharge is thus minimised. PVDF is also used to make the end flanges for the amplifier, allowing the tube length to be kept down to 30 cm without electrical flashover from the 25cm long high-voltage cathode. The windows are recessed into the end flanges and are mounted at 10° to the laser axis to suppress potential lasing between them.

Rare-gas halide lasers in general and wide aperture amplifiers in particular are reported to be sensitive to impurities in the gas mixture. Therefore in addition to using only fluorine-compatible materials within the laser head, we also circulate the gas through an Oxford Lasers GP2000 cryogenic gas purifier.[6] This traps out molecular contaminants formed within the discharge and increases the stability and longevity of the gas-mix considerably.

The high voltage design of the laser head and of the external circuit are now more or less complete and we are moving on to examine the dependence of the amplifier properties on gas mixture, voltage and driver circuit configuration.

The optical set-up used to study the performance of the amplifier is shown in Fig 4. The output beam from a small KrF oscillator module is passed through two 1 mm diameter pinholes placed 1.2m apart to produce a low-divergence probe beam whose intensity is ~160 kW cm^{-2}. A beam splitter and filter divert 2% of this beam into the amplifier while 92% is transmitted directly into a photodiode to provide a reference measurement of the energy from shot to shot. The beam which has passed through the amplifier is then spatially filtered to remove unwanted amplifier fluorescence before being passed to another photodiode which is used to record its energy. Each photodiode has a cell containing an organic dye (Coumarin 6 dissolved in methanol) in front of it. The dye fluorescence is monitored by the photodiodes since this is more diffuse and less intense then the laser light and does not suffer the same problems of photocathode response nonuniformity. The photodiodes are connected to a ratiometer constructed in the Clarendon Laboratory to produce the ratio Z/X of the energies in the two beams. The system was checked using independently calibrated UV neutral density filters and found to be linear over the range of use to better than 2%. Some

effort was also devoted to ensuring that the oscillator and amplifier were triggering simultaneously. The short pulse lengths involved required that the jitter between firing of the two lasers was not sufficient to lead to fluctuations in the energy extracted from the amplifier. By running the two lasers from the same pulsed power supply and by careful adjustment of the inductance of the oscillator circuit it was possible to synchronise the two lasers reproducible to within one nanosecond of one another.

To measure the spatial variation of the gain, the amplifier was mounted on a translation stage which allowed it to be scanned in both the horizontal and vertical directions. A map of the gain as a function of position can thus be built up. Moving the laser avoided the complex problems of trying to maintain precise optical alignment while scanning the probe beam. The only complication involved was the need for provision of a flexible high voltage feed to the laser tube.

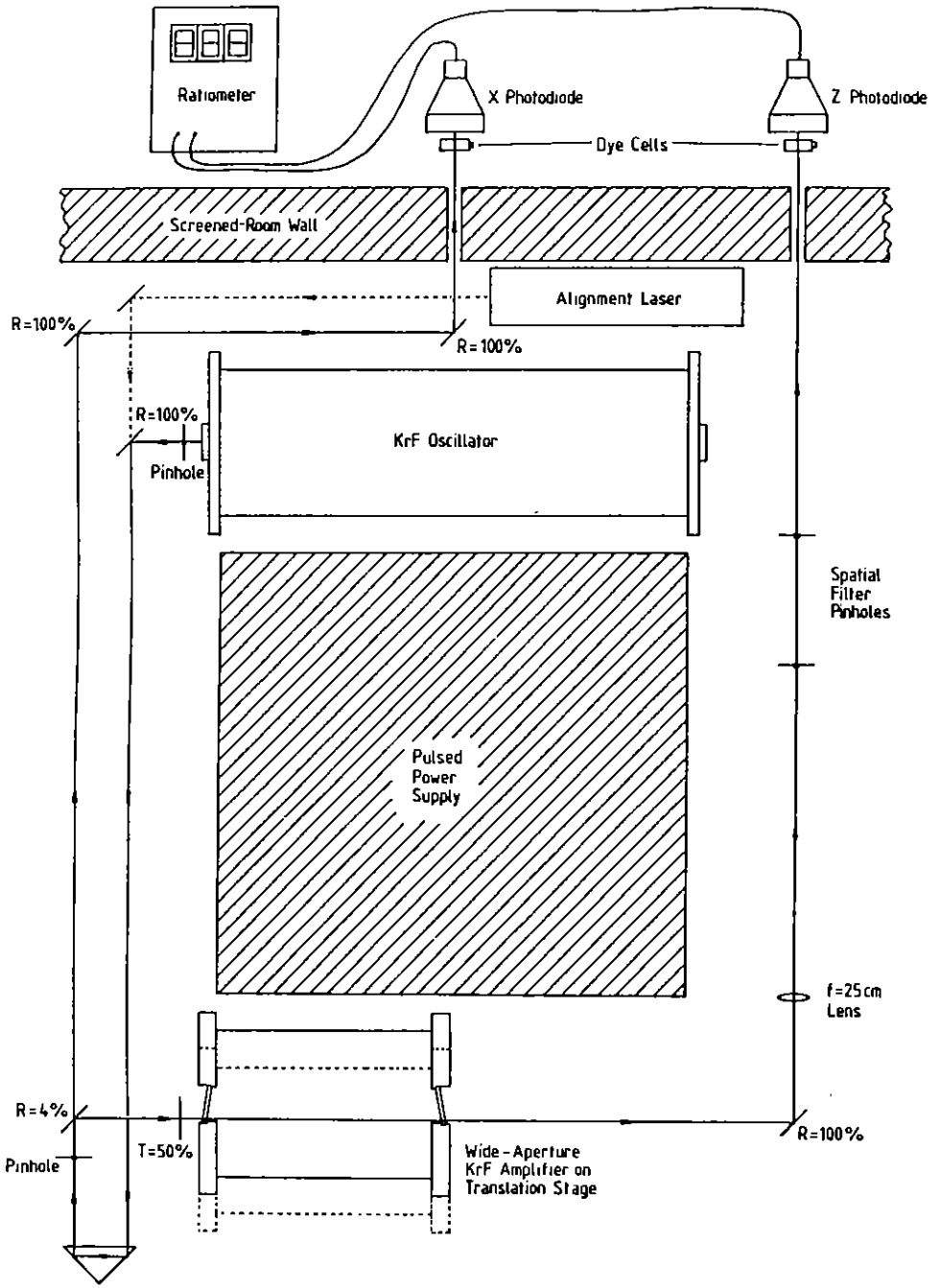

Fig 4 Optical arrangement used to measure gain of KrF laser amplifier.

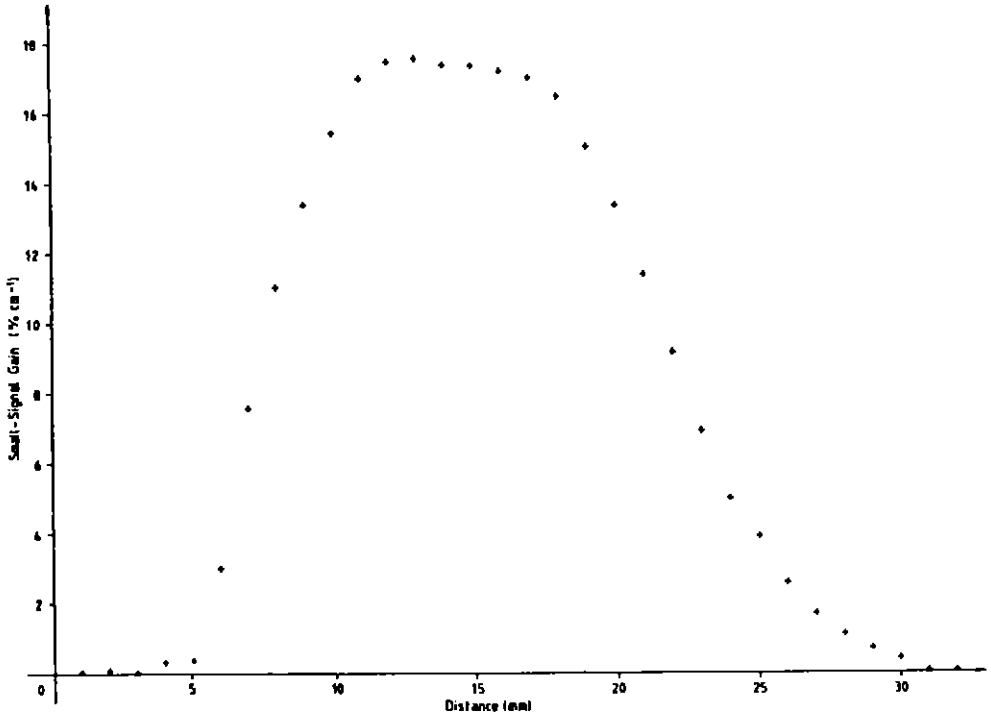

Fig 5 Typical gain profile (horizontal scan) for KrF laser amplifier with unoptimised electrodes.

A typical gain profile, scanning the laser horizontally through the probe beam, is shown in Fig 5. The gas mix used in the amplifier was 5 mbar F_2, 120 mbar Kr and 2500 mbar He and the external storage capacitor was charged to 40kV. The peak single-pass gain is ~80 implying a small-signal gain of ~17.5% cm^{-1}. The intensity at the output window should then be ~260 kW cm^{-2} which is well below the saturation intensity of KrF, so we are operating safely in the linear regime of the amplifier. The uncertainty in the position of the centre of the probe beam is $\pm$25μm and the uncertainty in the measured value of the gain results mainly from shot to shot fluctuations and is ~0.25%cm^{-1}. With the present unoptimised electrode profile the discharge FWHM is only 15mm. However, indications that a much broader beam is possible were obtained in earlier experiments using a similar but longer (60cm) device which achieved outputs that were 19mm wide. The long laser was set up as an oscillator and the beam width was

measured from burn-patterns on exposed Polaroid film so there was little information available about the shape of the gain profile. Difficulties associated with measuring the large gains produced by this laser caused us to transfer our attention to the present, much shorter unit once we had solved most of the electrical problems on the earlier device.

The first results available from the short amplifier suggest that its gain is more than sufficient to meet the design criteria. This allows some freedom in the choice of gas mix to improve the discharge width. (Reducing the F_2 concentration should widen the discharge at the expense of reducing the peak gain). We could also reduce the operating voltage of the laser which would simplify the design of a thyratron-based pulsed power circuit. The use of a thyratron would, in turn, allow easier interfacing of the amplifier to the rest of the projection system. Surprisingly we have been unable to detect any dependence of the amplifier performance on the discharge polarity. The obvious preionisation asymmetry might be expected to lead to a polarity asymmetry based on the tendence of the pre-breakdown electric field across the main discharge gap to cause bulk movement of the preionisation electrons. It may be, however, that the rapid electron attachment rate in gas mixtures containing F_2 ensures that the preionisation density depends predominantly on the instantaneous value of the current flowing through the preionisers, i.e. electrons are more likely to be attached than to be moved very far by the electric field.

Further work will involve a more detailed study of the amplifier properties and, based on the results of that study, we will produce a finished device which will then be fitted into the prototype projection system.

Dr V Rivano would like to acknowledge the "Fondazione Angelo Della Riccia" for financial support during his stay at the Clarendon Laboratory.

3. HOLOGRAPHY IN PHOTOLITHOGRAPHY

I N Ross (RAL) and G M Davis (Oxford)

Phase conjugation techniques can be regarded as 'real time' holography. Normal 'lapsed time' holography offers many of the same advantages such as high-resolution and inexpensive optics while offering one or two additional possibilities as a result of being a two-stage process. These well known advantages of holography have suggested that we should investigate its possibilities in photolithography alongside and in comparison with our work in phase conjugation. In consequence we have initiated some early trials into the feasibility of high-resolution holography using ultraviolet light from excimer lasers. Holograms made with such a pulsed source in the ultraviolet (probably the first group to do this) have shown considerable promise and this programme will continue.

4. DYNAMIC HOLOGRAPHY AND PHASE CONJUGATION

M C Gower (RAL)

The photorefractive effect refers to the light-induced refractive index changes which occur in certain crystals due to the migration and retrapping of charges in the presence of spatially nonuniform light fields. It was first noticed nearly twenty years ago as the mechanism responsible for causing the self-focussing of laser light in crystals of $LiNbO_3$ and $LiTaO_3$. Photorefraction has since been observed in many more crystals including $BaTiO_3$ $Bi_{12}SiO_{20}$(BSO), $Bi_{12}GeO_{20}$(BGO), $KTa_{1-x}Nb_xO_3$(KTN), $Sr_{1-x}Ba_xNb_2O_6$(SBN), $KNbO_3$, Rb_2ZnBr_4, $Bi_4Ti_3O_{12}$,CdS,InP and GaAs. It was soon recognised that when used as volume holographic recording media, photorefractive crystals could produce extremely large storage densities (up to 10^{12} bits/cm^3) while possessing exposure sensitivities comparable to the best photographic emulsions ($\lesssim$ 100 μJ/cm^2). Furthermore, just as with emulsions or photoresists, the hologram may be permanently 'fixed' by applying a suitable biasing voltage across the crystal during recording. However, unlike conventional media, photorefractive crystals can also be used

for dynamic or 'real-time' holography in which the writing and reading processes occur virtually continuously and simultaneously. Some recent remarkable discoveries in the field of dynamic holography using photorefractive materials may lead to a host of applications in the general area of real-time optical data processing - from optical image amplifiers, enhancers and pattern recognisers to optical switches and memories.[7] Unlike the relatively slow serial processing of current electronic devices, dynamic holograms offer the possibility of rapid parallel bit processing of information. Because the image wave is a complex or phase conjugate of the subject wave, real-time holography is closely analagous to the nonlinear optical method of degenerate four-wave mixing as used in producing phase conjugate (wavefront reversing) mirrors (see Fig. 6(a)). Thus these crystals can also be used as phase conjugate mirrors to correct for distortions on optical wavefronts and to project complex image patterns.

The migrating charges in photorefractive crystals - in $BaTiO_3$ for example they are positive while in BSO and BGO they are negative - are generated by photoexcitation of electrons or holes from impurity or donor levels in the band gap. The interference pattern set up between the subject and reference waves during recording causes the mobile charges to diffuse or drift (photoconduct) and become retrapped in the darker regions of the interference pattern, while leaving behind trapped ionised centres (for the case of negative mobile carriers see Fig. 6 (b)). In some polar ferroelectric crystals the photovoltaic effect can also produce charge motion. This spatial separation of charge creates local piezo-electrically induced stresses and strains caused by electric fields whose gradients (by Poisson's equation) are a maximum in regions of maximum space charge density, ρ_{sc}. Thus as shown in Fig. 6 (b), the space charge field, E_{sc}, is often shifted in phase from the original interference pattern. This space charge field then produces local variations of the refractive index, Δn, throughout the medium due to the linear electro-optic (Pockels) effect. In a similar manner the hologram is erased by uniform illumination of the crystal.

The maximum modulation of both the interference pattern and the induced space charge field occur when the recording beams have the same intensity - irrespective of their absolute values. Thus, in contrast

(a)

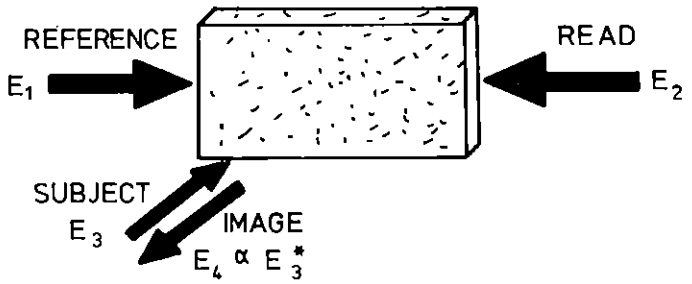

PHOTOREFRACTION

(b)

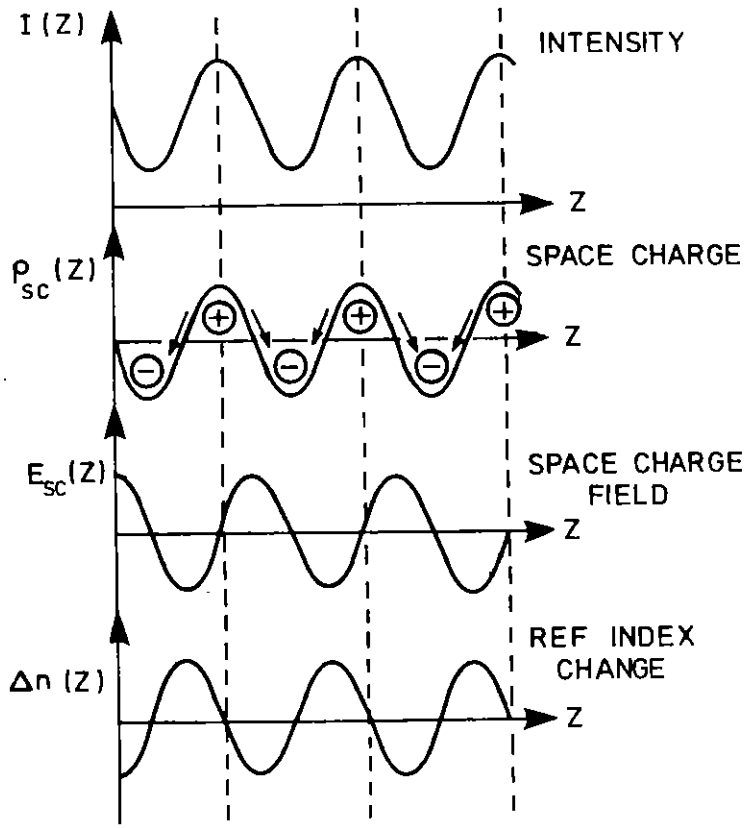

Fig 6 (a) Arrangement for producing real-time holograms and degenerate four-wave mixing phase conjugate mirrors

(b) The mechansisms responsible for photorefraction

to most other mechanisms used to produce phase conjugate mirrors, the normalised image wave light intensity (phase conjugate reflectivity) produced by the reading process is insensitive to the absolute values of the recording beam intensities. In $BaTiO_3$, for example, which has an extremely large electro-optic effect, an image intensity gain of 100 has been observed using low-powered continuous lasers.[8] Since this phase conjugate mirror had gain, oscillation could be produced between it and a relatively poor (non-aligned) reflector, such as a pair of scissors placed near the crystal! (see Fig. 7). If the scissors are moved then oscillation reappears at their new position demonstrating that the mirror can automatically track the location of the scissors.

If the intensity of the recording reference beam is chosen to be intermediate to that of the subject beam which contains a patterned object, then maximum reflectivity upon reading occurs for transmitted light near the edges of the pattern where the intensities of the two recording beams are equal. Thus the edges of the image can be preferentially enhanced which is often beneficial when trying to recognise complicated patterns. The holographic recording and erasure rates depend on the photoconductivity of the crystal, which in turn is proportional to the intensity of illumination so that the main effect of using high light intensities in recording and erasure is to make these rates faster. In $BaTiO_3$ for example, if the writing intensity I is in units of W/cm^2, a recording time of $\sim \frac{0.1}{I}$ sec is observed. Thus when using a low powered He-Ne laser, holograms are recorded in a few seconds, whereas when an intense (20 MW/cm^2) pulsed laser is used recording occurs in less than 10 nsec. On the other hand, provided it is kept in the dark the recorded hologram can be stored in the crystal for long periods - from a few hours in $BaTiO_3$, BSO and KTN to up to 10 years in $LiTaO_3$ - limited only by the dark conductivity of the crystal which eventually redistributes the charge carriers.

Because the volume hologram written in the crystal is often phase shifted from the original optical interference pattern (see Fig. 6(b)), the two writing beams can exchange energy by their self-diffraction from the hologram. This 'two-beam coupling' effect, while complicating the understanding of many of the observations made in the field of

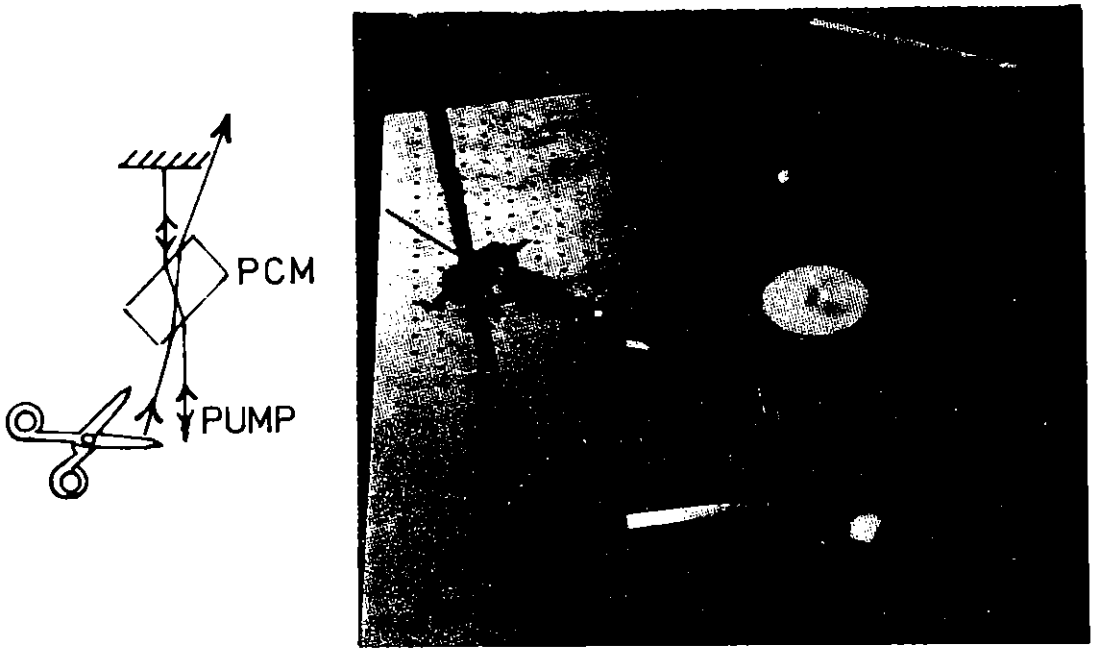

Fig 7 Phase conjugate mirror with gain causes oscillation to a reflecting surface (a pair of scissors, for example). The two spots on the upper right of the photograph are caused by oscillation to different parts of the scissors. Movement of the scissors causes these spots to automatically track their position.

photorefractive dynamic holography, leads to some remarkable effects. If a weak and a strong beam intersect in a crystal (Fig. 8) then the majority of the energy in the strong beam can be transfered to the transmitted weak beam (since the first-order Bragg reflection of one wave is phase shifted by $\pm\pi/2$ from the zero order transmitted wave of the other, then if the hologram is additionally shifted by $\pi/2$ then each of these two waves will interfere constructively or destructively). For example in $BaTiO_3$, for which diffusion processes alone cause migration, the hologram phase shift is $\pi/2$ and intensity gains of up to 600 can be observed for the transmitted weak beam.

In $BaTiO_3$ two-beam coupling between a single laser beam and scattered light propagating in the appropriate direction in the crystal can lead to self-defocussing or 'fanning' of the beam. If this fanned beam is then totally internally reflected from the far corner of the crystal (see Fig.9) then phase conjugate reflections can be produced with a reflectivity of up to 30% by using just one input beam to the crystal.[9] In this self-pumped arrangement there are at least two coupled interaction regions for which degenerate four-wave mixing can take place. In region 1 in Fig.9, waves E_1 and E_2 act as pump beams for the E_3 probe wave. E_3 and E_4 (α E_3^*) can also act as pumps for an E_1 probe beam to produce E_2 (α E_1^*) in this region. Thus maximum feedback will be obtained when E_1 and E_2 are phase conjugates of each other[10]. A similar arguement also applies to the coupled region 2 in Fig. 9. As far as requiring only one beam for its operation this type of self-pumped mirror retains the remarkable simplicity of a stimulated Brillouin scattering (SBS) phase conjugate mirror. However unlike the SBS mirror it can operate at extremely low ($<100mW/cm^2$) intensities. We have used such a self-pumped $BaTiO_3$ crystal to project high - resolution images. This image projector which consists of a self-pumped crystal and beam splitter cube combination as shown in Fig 10 has a numerical aperature close to unity. Using a 488nm CW Ar^+ laser source with this arrangement (Coherent Innova 90-5), as shown in Fig 11 we recorded on film the image of a test pattern. The laser speckle inherent in this image is due to scattering from the grains of photographic emulsion. As shown in Fig 12 laser speckle effects were completely absent when a photoresist was used as the recording medium. As first observed by Levenson et al[3] the phase conjugate mirror

TWO - BEAM COUPLING

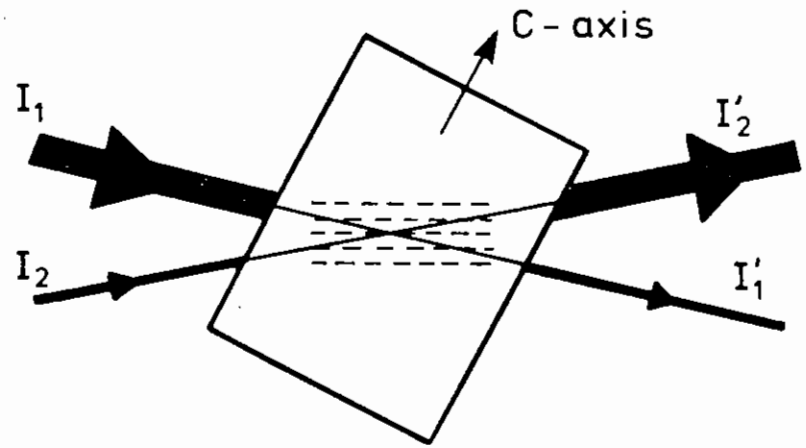

Fig 8 As a result of phase shifted holograms, energy is transferred between two intersecting beams.

SELF - PUMPED DFWM IN $BaTiO_3$

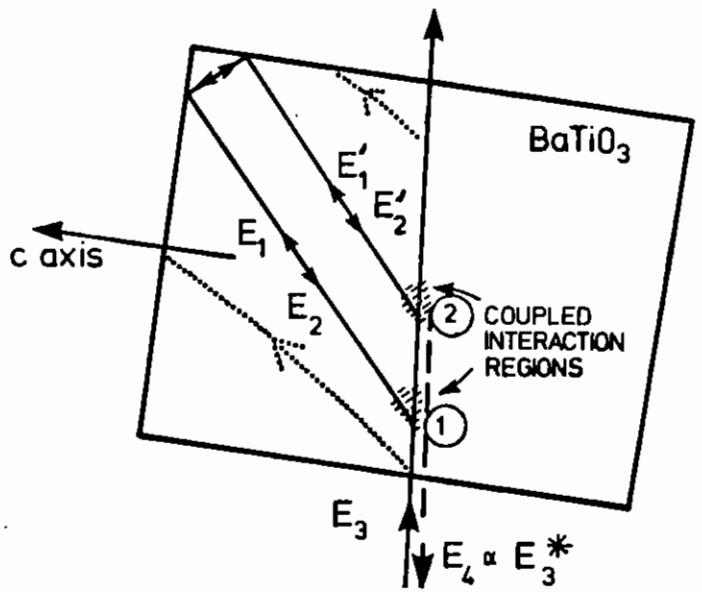

Fig 9 Beam focussing and total internal reflection in crystal gives rise to 2 coupled interaction regions for DFWM which then produce a self-pumped phase conjugate mirror.

IMAGE PROJECTION USING SELF-PUMPED $BaTiO_3$ CRYSTAL

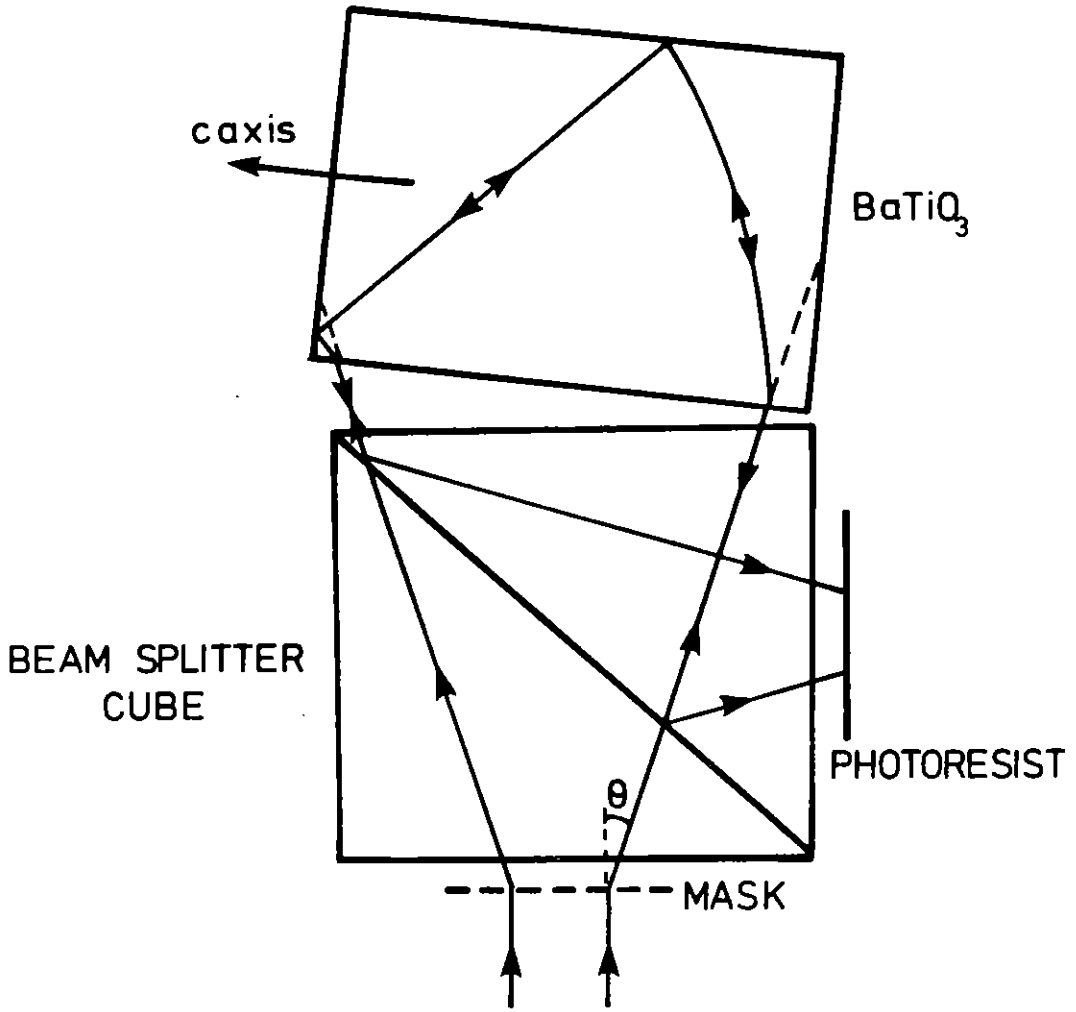

Fig 10 High-resolution image projection using self-pumped $BaTiO_3$ crystal and beam splitter cube.

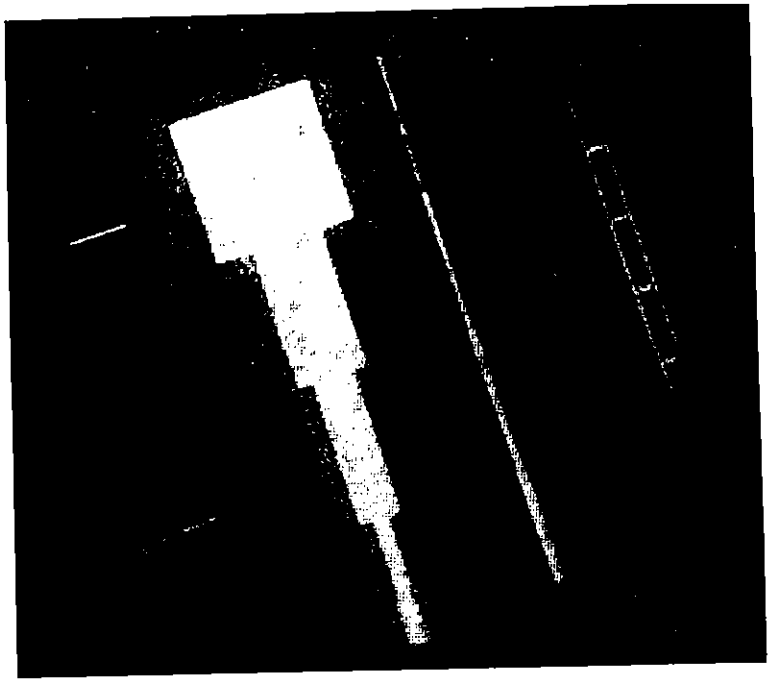

Fig 11 Image projected using a self-pumped $BaTiO_3$ crystal and CW 488nm Ar^+ laser. Photographed using a X9b microscope objective. The narrowest lines are 1μm.

CW Ar^+ LASER SOURCE

$\lambda = 488nm$

$P_{ave} = 6.4 W/cm^2$

$t_{exp} = 2min$

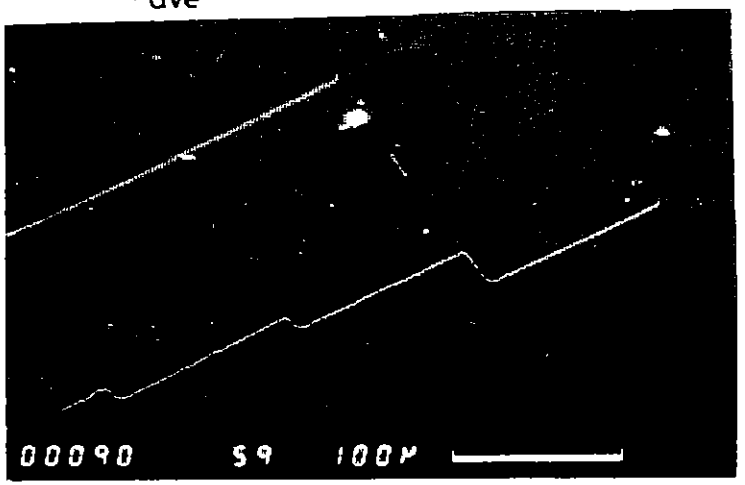

Fig 12 Scanning electron micrograph (SEM) of image projected into 0.5μm thick AZ 1350 photoresist spun on glass substrate by self-pumped $BaTiO_3$ crystal and CW 488nm Ar^+ laser.

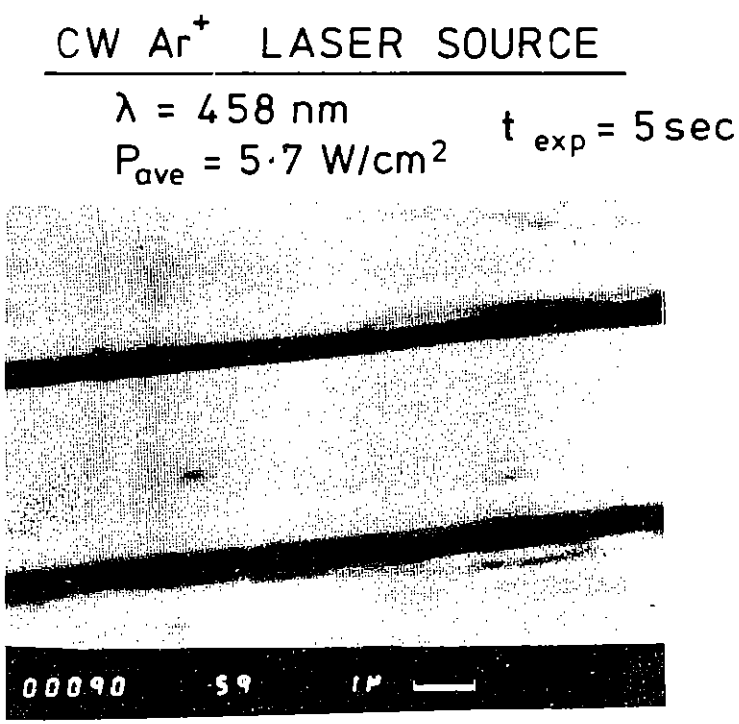

Fig 13 As Fig 12 but using the 458nm line from the Ar^+ laser. Note the reduction in photoresist exposure time.

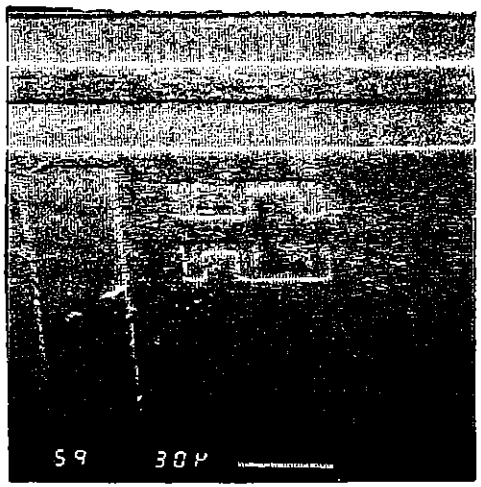

Fig 14 As Fig 12 but using a 460nm, 80pps pulsed dye laser. P_{ave} = 5W/cm^2, t_{exp} = 5 sec

corrects for all speckle efforts which may arise by scattering from surfaces between itself and the beamsplitter. Several beamsplitter cubes were tested from a variety of manufacturers and those with the least imperfections were selected for use in the projector. The exposure time needed to record the image shown in Fig. 12 was ~ 2 min which is much too long for any practical photolithographic system. This time was considerably reduced when the crystal was self-pumped with the 458nm Ar^+ laser line. 1μm mask features (unexposed lines) projected at this wavelength were recorded in 5sec in the Shipley 1350 resist (see Fig 13). Although at this shorter wavelength the AZ 1350 photoresist is ~15 times more sensitive than at 488nm, [11] measurements by Jahode et al[12] suggest that the reflectivity of the self-pumped $BaTiO_3$ crystal may be reduced by nearly this amount which would negate any improvement in exposure time. Clearly for our crystal the results in Fig. 13 show this not to be the case and that a significant reduction in the exposure time can be achieved in running the self-pumped image projector at short wavelengths. Indeed the 5sec exposure time used for taking the image shown in Fig.13 represents the shortest time yet achieved in any high resolution phase conjugate imaging system.

We are currently working to increase the field of view of this device from the present 0.2cm to 1cm while retaining exposure times of a few seconds. One approach has been to use a high repetition rate pulsed dye laser source operating at 460nm which had the same average intensity as the Ar^+ laser. High peak powers tended to damage the chrome on glass masks as well as the optical cement used in the beamsplitter cube. As shown in Fig. 14, a 5sec exposure time could also be achieved using this source. Since the size of single domain $BaTiO_3$ crystals which currently can be produced is limited to dimensions of ~5-7mm cubes, the size of this type of PCM is most conveniently increased by using a matrix of crystals, as shown in Fig 15. An average intensity of ~5W/cm^2 could be maintained over a much larger area when using the pulsed dye laser.

The high-resolution exposures shown in Fig 16(a) was obtained over an 8mm object field (for a low resolution picture see Fig 16(b) using this two- crystal projector (the crystals were actually positioned on top of

one other). The large (3cm) cube beamsplitter in conjunction with the 1cm PCM used for this experiment produced a numerical aperature NA ~ 0.12. The measured ~ 1.8 μm resolution obtained from this device was consistent with the value calculated from the Rayleigh limit ~ $\lambda/_{2NA}$. Work is continuing on this projector to further increase the object field area while continuing to reduce the resist exposure time.

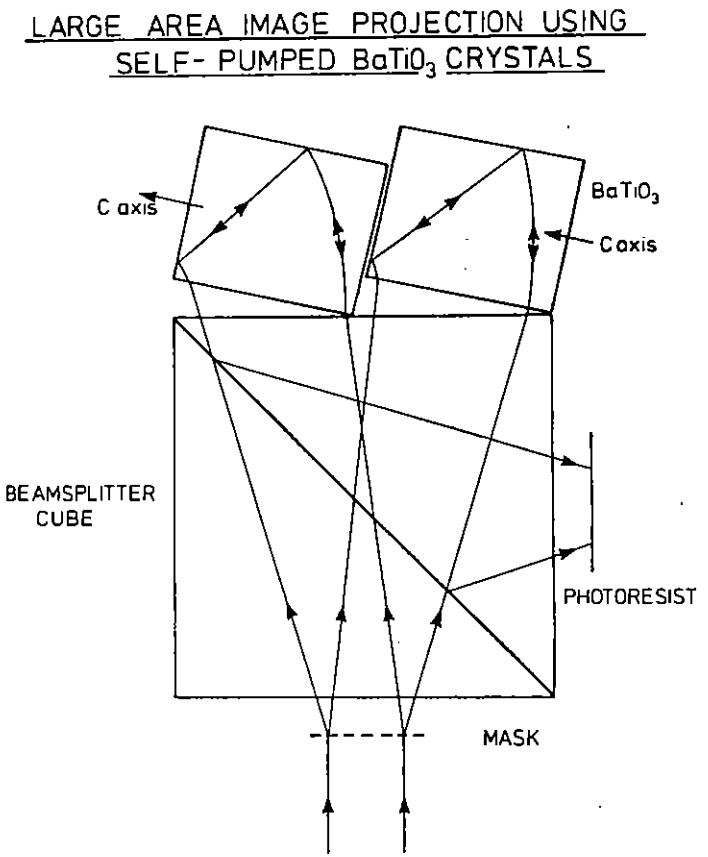

Fig 15 A larger area self-pumped PCM using two $BaTiO_3$ crystals.

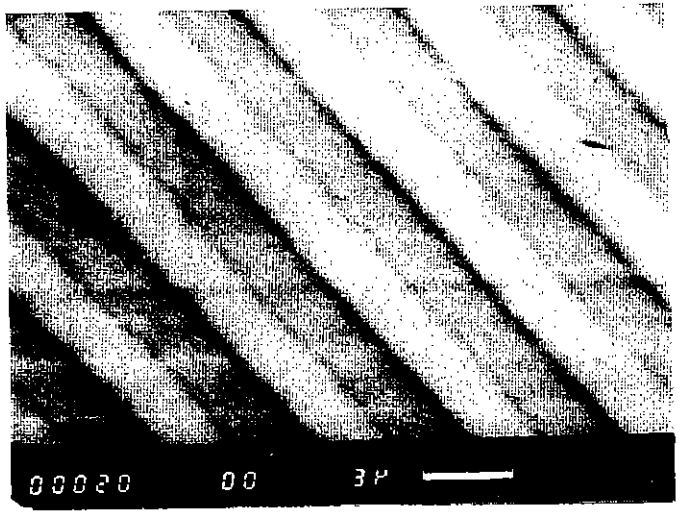

(a)

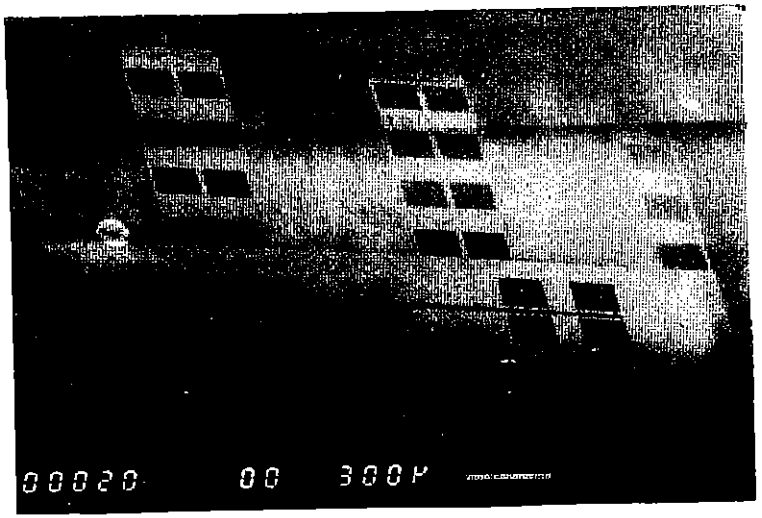

(b)

Fig 16 (a) high resolution SEM of 2.25μm lines and spaces obtained in AZ1350 photoresist using two crystal projector

(b) Low resolution SEM showing part of 8mm field

References

(1) M D Levenson, J. Appl. Phys. 54, 4305 (1983)

(2) M J Beesly, H Foster and K G Hambleton, Electron Lett, 4, 49 (1968)

(3) M D Levenson, K M Johnson, V C Hanchett and K Chiang JOSA 71, 737 (1981)

(4) R G Caro and M C Gower, Optics Letts 6, 557 (1981) Appl. Phys. Letts. 39, 855 (1981)

(5) J Banic, T Efthimiopoulos and B P Stoicheff, Appl. Phys. Letts. 37, 686 (1980)

(6) A J Kearsley, A J Andrews, C E Webb, K Errey and J Coutts, OSA Topical Meeting on Excimer Lasers, Lake Tahoe, Nevada A.I.P. Conference Proceedings no. 100 (1983)

(7) P Gunter, Physics Reports 93, 199 (1982)

(8) J Feinberg and R W Hellwarth, Opt. Letts. 5, 519 (1980)

(9) J Feinberg, Opt. Letts 7, 486 (1982)

(10) K R MacDonald and J Feinberg, JOSA 73, 548 (1983)

(11) S L Norman and M P Singh, Appl. Optics 14, 818 (1975)

(12) F C Jahoda, P G Weber, and J Feinberg, Opt. Letts. 9, 362 (1984)

CENTRAL LASER FACILITY PUBLICATIONS

CENTRAL LASER FACILITY PUBLICATIONS April 1984 - March 1985

(1) Journals and Books

V Aboites, E McGoldrick, S M L Sim, D Bassett, A R Bell and I N Ross
Harmonic imaging studies of illumination uniformity for 0.53 μm ablative compressions
Opt Comms, 52, 108, (1984)

K G H Baldwin, J P Marrangos, D D Burgess
Application of Coherent VUV radiation to measurement of Lyman and absorption lineshapes in dense hydrogen Z-pinch plasmas
J Phys B, 17 L169-L173 1984

K H G Baldwin, J P Marangos, D D Burgess and M C Gower
Generation of tunable coherent VUV radiation by anti-Stokes Raman scattering of excimer pumped dye laser radiation
Opt Comms, 52, 351 (1985)

H C Barr, T J M Boyd, G A Gardner and R Rankin
Raman Backscatter from an Inhomogeneous Magnetized Plasma
Phys Rev Letts, 53, 462 (1984)

H C Barr, R Rankin and T J M Boyd
Stimulated Raman Sidescatter from a Magnetized Plasma
J Plasma Physics, 32, 331 (1984)

H C Barr, R Rankin and T J M Boyd
Stimulated Raman Sidescattering in Magnetized Plasmas
Phys Letts, 105A, 218 (1984)

A R Bell
Non-Spitzer heat flow in a steadily ablating laser produced plasma
Phys Fluids (in press)

M A Bellhouse, I N Ross, C C Entwhistle and B J Bellhouse
Optical measurement of the viability of stored human platelets
Optics and Laser Technology, 17, 27 (1985)

J E Bennett, P M Killough, W E L Grossman and R E Hester
Resonance Raman spectra of alkyl nitroxyl radicals
J Raman Spectr, (in press)

T D Beynon and E H Smith
Properties of hot dense matter
J Quant Spect Rad Trans (in press)

T J M Boyd, G A Gardner and R Rankin
Finite Larmor radius effects in stimulated Raman scattering
Physics of Fluids, (in press)

T J M Boyd and R Rankin
Kinetic Theory of Stimulated Raman Scattering from a magnetised plasma
Plasma Physics, (in press)

D G Cunningham, D Denvir, I Duncan and T Morrow
Up-conversion using stimulated anti-Stokes Raman scattering and stimulated collisional induced fluorescence in Tl.
Optica Acta, 31, 249, (1984)

D G Cunningham, D Denvir, I Duncan and T Morrow
Raman and atomic resonance lasers in optically excited Thallium ($6P_{3/2}$,$_{1/2}$) - Xenon mixtures.
Optica Acta, 31, 1321 (1984)

C N Danson, C B Edwards and I N Ross
A pulse stacker for time resolved laser plasma diagnostics
Optics and Laser Technology, 17, 99 (1985)

G M Davis, M C Gower, C Fotakis, T Efthimiopoulos and P Argyrokis
Spectroscopic Studies of ArF Laser Photoablation of PMMA
Appl Phys, A36, 27 (1985)

R W Eason, D K Bradley, J D Kilkenny and G N Greaves
Improved laser-EXAFS studies of aluminium foil
J Phys C, 17, 5067 (1984)

C B Edwards, F O'Neill and M J Shaw
KrF-laser triggered swtich of a multiline pulsed power system
J Phys E, 18, 136 (1985)

E M Epperlein
The accuracy of Braginskii's transport coefficients for a Lorentz plasma
J Phys D, 17, 1823 (1984)

R G Evans
Non-uniform Illumination of Laser Targets
Lasers and Particle Beams, (in press)

R G Evans
Radiation driven instabilities in laser produced plasmas
J Quant Spect Rad Trans (in press)

R G Evans
Implosion Hydrodynamics
Heavy Ion Fusion (ed T D Beynon, Plenum Press) (in press)

R G Evans
Radiation Cooling Instabilities in Laser Driven Ablation
Plasma Phys (in press)

N Finn, T A Hall and E McGoldrick
A subnanosecond X-ray framing camera
Appl Phys Letts (in press)

M C Gower
Physics of phase conjugate mirrors
Prog Quant Electronics, 9, 101 (1984)

M C Gower
Mirrors that reflect time
Nature, 308, 110 (March 1984)

M C Gower
Dynamic Holography using Photorefraction
Nature (in press)

M C Gower
Application of excimer laser phase conjugate mirrors
SPIE, 476, 72 (1984)

M C Gower
Diagrammatical Analysis of phase conjugation using degenerate four-wave mixing in Kerr-like non saturated media
IEEE J Quant Elec, QE-21, 182 (1985)

M C Gower, G Davis and A F Gibson
Degenerate four-wave mixing using phase conjugate pump waves
Conference and Quant Optics V, 1187
Eds E Mandel, E Wolf, Plenum (1984)

R C Greenhow, D M Goodall and R W Eason
Ground-state repopulation time of BDN I and BDN II in a variety of solvent and plastic hosts
Chemical Phys, 83, 445 (1984)

T A Hall
A focusing x-ray crystal spectrograph
J Phys E, 17, 110 (1984)

A Hauer, W C Mead, O Willi, J D Kilkenny, D K Bradley, S D Tabatabaei and C J Hooker
Measurement and Analysis of near-classical thermal transport in one-micron laser-irradiated spherical plasmas
Phys Rev Letts, 53, 2563 (1984)

T H Kho
Relaxation of a system of charged particles
Phys Rev A (in press)

C Lewis and C R Mahoney
A simple technique to measure the response of Kodak Eastman 10101 film for approximately 70eV photon energies
J Phys E, 17, 744 (1984)

C L S Lewis and J McGlinchey
Quasi-monochromatic projection radiography of dense laser driven spherical targets
Optics Comms, 53, 179 (1985)

E McGoldrick, S M L Sim, R E Turner and O Willi
Simultaneous observations at $\omega_0/2$ and $3\omega_0/2$ harmonic emission from 526nm laser produced plasmas
Opt Comm, 50, 107 (1984)

Y Matsumoto, M J Shaw, F O'Neill, J P Partanen, M H Key, R Eason, I N Ross, E M Hodgson and Y Sakagami
X-ray emission from KrF laser-produced Al plasmas
Appl Phys Letts, 46, 28 (1985)

J N Moore, G H Atkinson, D Phillips, P N Killough and R E Hester
Time resolved resonance Raman spectra of the radical anion of anthaquinone-2,6-Disulphate
Chem Phys Letts, 107, 381 (1984)

A Nishiguchi, T Yake, M G Haines, M Psimopaulos and H Takewaki
Corrective amplification of magnetic fields in laser-produced plasmas by the Nernst effect
Phys Rev Letts, 53, 262 (1984)

G J Pert, L D Shorrock, G J Tallents, R Corbett, M J Lamb, C L S Lewis, E Mahoney, R Eason, C J Hooker and M H Key
Population inversion and gain in expanding carbon fibre plasmas
'Laser techniqeus in the extreme Ultra Violet',
Eds S E Harris and T B Lucatooto
Publ AIP, 480 (1984)

M H Key
Energy transport in laser produced plasmas
'Radiation in Plasmas'
Ed B McNamara, World Scientific, 458 (1984)

M H Key
Progress and prospects in the applications of laser produced plasmas
Plasma Phys, 26, 1383 (1984)

M H Key and R G Evans
A report on inertial confinement fusion
Nature, 313, 94 (1985)

J G Lunney et al
Ion implanted targets for soft X-ray laser investigations
Opt Commun, 50, 367 (1984)

D J Nicholas
The use of perturbed aspherics in multi-wavelength focusing optics
Optica Acta, 31, 1069 (1984)

R Rankin, G A Gardner, T J M Boyd and H C Barr
Inverse Resonance Absorption in an inhomogeneous magnetised plasma
Phys of Fluids, 28, 16 (1985)

S J Rose
The calculation of the radiative opacity in hot dense plasmas
J Quant Spect Rad Trans (in press)

S J Rose
The calculation of line coincidence in helium-like ions using the multiconfiguration Hartee-Fock method
J Quant Spect Rad Trans (in press)

I N Ross and E M Hodgson
Some opticalo designs for the generation of high quality linear foci
J Phys E, 18, 169 (1984)

I N Ross and A Mbanu
Optical monitoring of glucose concentration
Optics and Laser Tech, 17, 31 (1985)

R J Rosser et al
Soft X-ray contact microscopy with nanosecond exposure times
J Microscopy (in press)

P T Rumsby
Laser produced plasmas as intense X-ray sources for microscopy at the CLF
J Microscopy (in press)

Md Salimullah, Y G Liu and M G Haines
Modulation instabilities of upper-hybrid laser radiation in a strongly magnetised plasma
Phys Fluids, 28, 248 (1985)

P J Tonge, C W Wharton, R J Szawelski, R J Killough and R E Hester
Ultraviolet resonance Raman spectroscpy of a highly specific acyl-papain
Biochem Soc Trans (in press)

R Wilbrandt, W E L Grossman, P M Killough, J E Bennett and R E Hester
Triplet state resonance Raman spectra of trans, trans-diphenylbutadiene
J Phys Chem, 88, 5964 (1984)

O Willi, P H Y Lee and Z Q Lin
Non-uniform shock break-through of laser irradiated targets
Optics Comms (in press)

O Willi and P H Y Lee
Filamentation of an annular laser beam in a short wavelength laser produced plasma
Optics Comms (in press)

(2) Published Conference Proceedings

A R Bell
Solution of the Vlasov-Fokker-Planck equation for a laser-produced spherically-symmetric steadily ablating plasma
14th Conf on Anomalous Absoprtion, Charlottesville (1984)

A E Dangor, A Bradshaw, R Bingham, R G Evans, C B Edwards and W T Toner
The Rutherford Laboratory Beat Wave Experiment
Proc 2nd Workshop on 'Laser for Particle Acceleration' Malibu Jan 1985, APS (1985) (in press)

R G Evans et al
Constraints and achievements in directly driven laser compression
Proc 10th Int Conf on Plasma Phys and Controlled Thermonuclear Fusion Research, London (1984)

R G Evans
Efficiency Factors in the Beat Wave Accelerator
Proc 2nd Workshop on 'Lasers for Particle Acceleration' Malibu Jan 1985 APS (1985) (in press)

R G Evans
Radial Electric Fields in the Beat Wave Acclerator
Proc Workshop on 'Large Electric Fields for Particle Acceleration' Frascati Sept 1984, CERN (1985) (in press)

M C Gower
High resolution photolithographic image projection using a self-pumped $BaTiO_3$ phase conjugate mirror
CLEO, Baltimore, USA (1985)

M C Gower
Excimer Lasers in Photolithography
Invited paper in Proc 2nd Int Conf on Lasers in Manufacturing Birmingham, UK
Ed M KF Kimnett
IFS Publications (1985) (in press)

M C Gower
Physics of Phase Conjugate Mirrors and their applications
Proc Workshop on Optical Phase Conjugation
Int School of Quantum Electronics, Ettore
Majorana (1985) (in press)

M C Gower
Phase Conjugation
Invited paper in Proc 5th Int Conf on Gas Flow and Chemical Lasers
IOP Conf Series 72,
Eds AS Kaye and A C Walker, Adam Hilger (1984)

M C Gower
Phase Conjugate Mirrors- tutorial
International Society for Optical Engineering Technical Symposium East
1984, Washington DC
Tutorial T8, SPIE (1984)

M H Key
New Applications of Laser Produced Plasmas
PROC ICTP Commemorative Meeting (1964-1984)
Trieste September (1984) (in press)

M MacDonald et al
Oscillatory Continuum Emission from I_2 and Br_2
8th Int Symp on Gas Kinetics

S J Rose
Dense Plasma Physics
Invited Paper at 7th Int Conf on Spectral Line Shapes,
Aussois, France (1984)

S J Rose
Two centre electronic wave function in plasmas
2nd Int Workshop on Radiative Properties of Hot Dense Matter

P T Rumsby
Microtarget Fabrication activities in the UK
Proc IX Int Vacuum Congress Madrid, 635 (1983)

O Willi et al
Laser Interaction and Compression Studies at the Rutherford Appleton
Laboratory
Laser interaction and related plasma phenomena, 6, 209
Edited by Heinrich Hora and George H Miley (Plenum Publishing Corp)
(1983)

Proc 2nd Int Workshop on Atomic Physics for Ion Fusion (in press)
A P Fews et al
Thermonuclear track spectroscopy using CR-39 detectors
S J Rose
Absorption spectra of strongly coupled plasmas
W T Toner et al
Alphas particle measurements of stopping power in hot dense materials

(3) Reports

R Bingham, R A Cairns and R G Evans
Saturation of Plasma Beat Waves
RAL-84-122

R G Evans
Relativistic Saturation of Beat Waves
RAL-84-086

ACKNOWLEDGMENTS

Much effort has gone into the production of the report. Thanks are due to all the University contributors who (almost) met the manuscript deadline and to the section editors for their liaison work with University users and proof reading.

The brunt of the labour in drawing diagrams and producing wordprocessor text was carried out by Jan Smith, Carol Gavin, Chris Ayling and Clare Schroder to whom many thanks are due. Reproduction of the report was by the RAL Reprographics Section.

M H Key